SCHOLARLY PUBLICATIONS

A CURRENT AWARENESS BULLETIN
OF RESEARCH OUTPUT

@DTU

(72nd Edition)

DECEMBER, 2018

BY: CENTRAL LIBRARY

DELHI TECHNOLOGICAL UNIVERSITY
(FORMERLY *DELHI COLLEGE OF ENGINEERING)*
GOVT. OF N.C.T. OF DELHI
SHAHBAD DAULATPUR, MAIN BAWANA ROAD
DELHI 110042

PREFACE

This is the **Seventy Second** Issue of Current Awareness Bulletin started by Delhi Technological University, Central Library. The aim of the bulletin is to compile, preserve and disseminate information published by the faculty, students and alumni for mutual benefits. The bulletin also aims to propagate the intellectual contribution of Delhi Technological University (DTU) as a whole to the academia.

The bulletin contains information resources available in the internet in the form of articles, reports, presentations published in international journals, websites, etc. by the faculty and students of DTU. The publications of faculty and student which are not covered in this bulletin may be because of the reason that the full text either was not accessible or could not be searched by the search engine used by the library for this purpose.

The learned faculty and students are requested to provide their uncovered publications to the library either through email or in CD, etc. to make the bulletin more comprehensive.

This issue contains the information published during **December, 2018**. The arrangement of the contents is alphabetical. The full text of the article which is either subscribed by the university or available in the web is provided in this bulletin.

Central Library

CONTENTS

1. 5th Generation Millimeter Wave Wireless Communication Propagation Losses Dataset for Indian Metro Cities Based on Corresponding Weather Conditions, ***6.S. K. Agrawal*** and ***3.Kapil Sharma***, IT, DTU

2. A simple method to estimate the loading effects of A1/Si on the characteristic impedance of multilayer microstrip line, ***6.1.Sandhya M Patel***, ***3.Yogita Kalra***, V N Ojha and ***3.R K Sinha***, Applied Physics, DTU

3. Attracting millennial talent: a signal theory perspective, Anishya Obhrai Madan and ***Srishti Madan***, Electrical, DTU

4. Bandwidth enhancement using modified L-probe fed slotted patch antenna for WLAN and UMTS applications, Rakesh N. Tiwari, ***3.1.Prabhakar Singh*** and Binod Kumar Kanaujia, Physics, DTU

5. BEAM FORMING METHOD FOR A TRANSMITTING ANTENNA AND A DEVICE THERE OF, ***6.Sachin Kumar AGRAWAL*** and ***3.Kapil SHARMA*** , IT, DTU

6. Biodegradability and Mechanical Properties of Pineapple Leaf/Coir Fiber Reinforced Hybrid Epoxy Composites, ***6.Mohit Mittal*** and ***3.Rajiv Chaudhary***, Mechanical, Production, and Industrial, DTU

7. CFD ANALYSIS OF OGEE SPILLWAY HYDRUALICS, ***7.Dolon Banerjee*** and ***3.Dr. Bharat Jhamnani***, Civil, DTU

8. Coherence and entanglement under three-qubit cloning operations, Suchetana Goswami, ***3.Satyabrata Adhikari*** and A. S. Majumdar, DTU

9. Comparison of thermal performances of single effect, double effect and triple effect LiBr-H2O absorption system cascaded with vapour compression refrigeration systems using ecofriendly refrigerants, ***3.R.S. Mishra***, Mechanical & Production, DTU

10. Concentrated Solar Heat Integrated with Geothermal Energy for Thermal Energy Requirements in India, ***8.Shivam Sharma***, ***8.Yash Kumar Baghel***, ***8.Ajit Kumar*** and ***3.J. P. Kesari***, Mechanical, DTU

11. Design of Probability Density Function Targeting Efficient Coverage in Wireless Sensor Networks, ***3.1.Richa Mishra***, Rajeev K. Tripathi and Ajay K. Sharma, DTU

12. Development of PALF/Glass and COIR/Glass Fiber Reinforced Hybrid Epoxy Composites, ***6.Mohit Mittal*** and ***3.Rajiv Chaudhary***, Mechanical, Production, and Industrial, DTU

13. Effect of Fibber Surface Treatment on Mechanical Properties of Bio composites: a Review, ***3.Mohit Mittal*** and ***3.Rajiv Chaudhary***, Mechanical, DTU

14. Enhanced thermoelectric performance in p-type ZrCoSb based half-Heusler alloys employing nanostructuring and compositional modulation, Nagendra S. Chauhan, ***6.Sivaiah Bathula***, Avinash Vishwakarma, Ruchi Bhardwaj, Kishor Kumar Johari, Bhasker Gahtori and Ajay Dhar, Applied Physics, DTU

15. Experimental Study of a Low-Temperature Compressor-Ejector Refrigeration System, ***3.Samsher Gautam***, ***8.Apoorva Roy*** and ***8.Bhuvan Aggarwal***, Mechanical, DTU

16. Formulation & analysis of papaya fortified biscuits, Rupanjali Pathak, Vandana Thakur and ***3.Rajinder Kumar Gupta***, Applied Chemistry, DTU

17. Genre Classification using Feature Extraction and Deep Learning Techniques, ***Akshi Kumar***, ***Arjun Rajpal*** and ***Dushyant Rathore***, Computer Science, DTU

18. Improving Landmark Recognition using Saliency detection and Feature classication, ***8.Akash Kumar***, ***8.Sagnik Bhowmick***, ***3.N. Jayanthi***, and ***3.S. Indu***, Electronics and Communications, DTU

19. Intelligent Software Defined Atmospheric Effect Processing for 5th Generation (5G) Millimeter Wave (MMWave) Communication System, ***6.S. K. Agrawal*** and ***3.Kapil Sharma***, Computer Engineering, DTU

20. INTERNATIONAL JOURNAL OF ENGINEERING SCIENCES &MANAGEMENT OPPORTUNITIES AND CHALLENGES OF USING HYBRID VEHICLES IN INDIA, ***8.Akshit Tripathi*** and ***3.Dr J.P. Kesari***, Mech, DTU

21. Machine Learning from Theory to Algorithms: An Overview, Jafar Alzubi, Anand Nayyar and ***3.Akshi Kumar***, CSE, DTU

22. Mixed Dimensional 2D/3D Hybrid Perovskite Absorbers: The Future of Perovskite Solar Cells?, ***8.1.Anurag Krishna***, Sébastien Gottis, Mohammad Khaja Nazeeruddin and Frédéric Sauvage, Polymer Science and Chemical Technology, DTU

23. Modelling and Optimization of Process Parameters affecting machining involved in Electric Discharge Machining by GA-ANN, ***6.Shadab Ahmad, 6.Praveen, Prateek, 6Prateek Kalyani, 3.Ranganath M S, 3.R S Mishra and 6.Md Jamil Akhtar***, Mechanical, Production & Industrial and Automobiles, DTU

24. Multilingual Author Profiling from SMS, Deepanshu Gaur, Meghna Ayyar, ***8.1.Ashutosh Kumar Singh*** and Rajiv Ratn Shah, Computer, DTU

25. New approach for maximizing generation and optimal utilization of available space for solar PV system, Anirudh Dube, ***3.M. Rizwan*** and Majid Jamil, Electrical, DTU

26. Optimization of two-stage cascade refrigeration systems using HFO refrigerants in the high-temperature circuit and HFC-134a in low-temperature circuit, ***3.Radhey Shyam Mishra***, Mechanical, Production & Industrial and Automobiles, DTU

27. Performance parameters optimization of cascade refrigeration system using ecofriendly refrigerants, ***3.R.S. Mishra***, Mechanical & Production Engineering, DTU

28. raiden11@IECSIL-FIRE-2018 : Named Entity Recognition For Indian Languages, ***8.1.Ayush Gupta***, Meghna Ayyar, Ashutosh Kumar Singh, and Rajiv Ratn Shah, IT, DTU

29. STRESS VARATION DUE TO CHANGE IN CENTRE DISTANCE OF SPUR GEARS USING FINITE ELEMENT ANALYSIS, ***6.AKASH SHARMA***, ***6.HARISH DAKSHANA MOORTHY*** AND ***3.PARAS KUMAR***, MECHANICAL, DTU

30. Thermal performances (first law efficiency, exergy destruction ratio & exergetic efficiency) of cascade single effect ammonia-water (NH3-H20) vapour absorption refrigeration system coupled with vapour compression refrigeration using ecofriendly refrigerants in the low temperature cycle of VCRS system, ***3.R.S. Mishra***, Mechanical & Production, DTU

31. Thermodynamic analysis of vapour compression refrigeration system with mixing of TiO2 nano material in HFO refrigerants for replacing HFC-134a, ***3.R.S. Mishra***, Mechanical & Production, DTU

32. Variable Transconductance Voltage Differencing Current Conveyor and its Application in Filter Design, ***8.Suyash Kumar***, ***6.Gunit Dhingra*** and ***3.Pragati Kumar***, Electrical, DTU

33. ZnO nanoparticles modified with an amphipathic peptide show improved photoprotection in skin, Anusha Aditya, Sabyasachi Chattopadhyay, ***6.Nidhi Gupta***, Shamshad Alam, Archan Palillam Veedu, Mrinmoy Pal, Archana Singh, ***3.Deenan Santhiya***, Kausar M. Ansari and Munia Ganguli, Applied Chemistry and Polymer Technology, DTU

1. *Chancellor*

2. *Pro Vice Chancellor*	***2.1.*** *Ex Pro Vice Chancellor*
3. *Faculty*	***3.1.*** *Ex Faculty*
4. *Teaching-cum-Research Fellow*	***4.1.****Asst. Librarian*
5. *Alumni*	
6. *Research Scholar*	***6.1.*** *Ex Research Scholar*
7. *PG Scholar*	***7.1.*** *Ex PG Scholar*
8. *Undergraduate Student*	***8.1.*** *Ex Undergraduate Student*

Author's Accepted Manuscript

5th Generation Millimeter Wave Wireless Communication Propagation Losses Dataset for Indian Metro Cities Based on Corresponding Weather *Conditions*

S.K. Agrawal, Kapil Sharma



www.elsevier.com/locate/dib

PII: S2352-3409(18)31542-7
DOI: https://doi.org/10.1016/j.dib.2018.12.003
Reference: DIB3564

To appear in: *Data in Brief*

Cite this article as: S.K. Agrawal and Kapil Sharma, 5th Generation Millimeter Wave Wireless Communication Propagation Losses Dataset for Indian Metro Cities Based on Corresponding Weather *Conditions*, *Data in Brief,* https://doi.org/10.1016/j.dib.2018.12.003

This is a PDF file of an unedited manuscript that has been accepted for publication. As a service to our customers we are providing this early version of the manuscript. The manuscript will undergo copyediting, typesetting, and review of the resulting galley proof before it is published in its final citable form. Please note that during the production process errors may be discovered which could affect the content, and all legal disclaimers that apply to the journal pertain.

ACCEPTED MANUSCRIPT

Data Article

Title: *5th Generation Millimeter Wave Wireless Communication Propagation Losses Dataset for Indian Metro Cities Based on Corresponding Weather Conditions*

Authors: S. K. Agrawal* and Kapil Sharma**, Member, IEEE

Affiliations: *Department of Computer Engineering, Delhi Technological University (DTU) , Delhi, India

**Department of Information Technology, DTU, Delhi, India, e-mail : kapil@ieee.org

Abstract

In this paper, we present 5th generation (5G) millimeter wave (mmWave) wireless communication propagation losses dataset for four Indian major urban cities like Delhi, Mumbai, Kolkata and Chennai based on corresponding weather conditions. Weather effect on mmWave is calculated in terms of mmWave path losses by considering various atmospheric weather conditions. Propagation of mmWave is affected by weather impairments (WIs) and due to that mmWave attenuation takes place and Indian metro cities have variety in weather variations. 5G mmWave propagation attenuation is calculated due to WIs like water vapour, oxygen, rain and fog for frequencies 28GHz, 37GHz and 39GHz. Individual WI effects during the season are calculated and shown suing graphs and tables.

Keywords: 5th generation (5G), millimeter wave (mmWave), weather impairments (WIs)

Specifications Table

Subject area	*Engineering*
More specific subject area	*Telecommunication Engineering*
Type of data	*Tables, graphs and figures*
How data was acquired	*Dataset generation calculations are performed*
Data format	*Raw, analyzed*
Experimental factors	*Season or Weather Effects*
Experimental features	*Attenuation datasets*
Data source location	*Delhi, Mumbai, Kolkata and Chennai (Indian metro cities)*
Data accessibility	*Datasets are with this article*
Related research article	*S. K. Agrawal and P. Garg, "Calculation of Channel Capacity Considering the Effect of Different Seasons for Higher Altitude Platform System", Wireless Personal Communications, Springer,*

Accepted manuscript

ACCEPTED MANUSCRIPT

	Wireless Personal Communications: Volume 52, Issue 4 (2010), Page 719 [6].

Value of the Data

- In India, 5G research and deployment are under year 2020 plan and such dataset is not specifically available for Indian Metro cities (like Delhi, Mumbai, Kolkata and Chennai).
- This proposed data set of the mmWave attenuation values for various Indian metro cities in various seasons will be highly useful for future 5G research and 5G system deployment.
- This Indian scenario 5G dataset can be used during network planning, determine the additional transmission power margin and operations.
- It is quite important for mmWave power link budget and reliable system operations which is feasible using this data.
- Based on presented dataset adaptive mmWave power transmission techniques can be used for large fixed link power budget margins for 5G mmWave communication system.
- Based on the presented dataset the 5G can be used to utilize resources in an efficient manner and controls the power transmission in an optimum manner.

Data

Four major Indian cities are considered here to generate the mmWave frequencies propagation path losses data set for 5G mmWave communication system under various weather conditions. The various weather conditions are like; summer, rain and winter. The four major Indian cities are Delhi, Mumbai, Kolkata and Chennai. The summer season attenuation calculation considers propagation path losses due to atmospheric gases impairments (water vapour and oxygen) only for all four cities. The rainy season attenuation calculation considers propagation path losses due to atmospheric gases (water vapour and oxygen) and rain for all four cities. The winter season attenuation calculation considers propagation path losses due to atmospheric gases (water vapour and oxygen) and fog for Delhi. Further, the winter season attenuation calculation considers propagation path losses due to atmospheric gases (water vapour and oxygen) for rest three cities [1-5].

In this article, we have considered that both transceiver units are having direct or line of sight communication link and there is no non line of sight path. This data article calculates mmWave frequencies propagation path losses due to WIs for the certain mmWave frequencies. This article shows data for mmWave propagation under different WIs [5-10].

Figures 1-13 and Tables 1-5 are presented.

Accepted manuscript

ACCEPTED MANUSCRIPT

Experimental Design, Materials, and Methods

The calculations/experiments were carried out with MatLab for four Indian Metro cites during summer, rain and winter season. The seasons were considered along with their corresponding type of attenuation causes. As per recent analysis done by The United States Federal Communications Commission (FCC) for mmWave frequency bands: 28, 37 and 39 GHz, FCC authorizes and proposes broadband device operations in these mmWv bands [3-9]. Atmospheric parameters for the four Indian metro cities were collected as per literature and simulation was performed for the same using software experiment / calculations. The details about equations and related functions are explained the cited reference [5-10]. As per propagation loss equations; the attenuation due to atmospheric gases (combined water vapour and oxygen) has been plotted with mmWave frequencies for the four Indian metro cities i.e. Delhi, Mumbai, Kolkata and Chennai.

As per the Figures 1, 2, 3 and 4 atmospheric water vapor shows high value resonances at 22GHz for all four metro cities. The variation of attenuation due to the atmospheric gases along with mmWave frequencies is shown in the graphs. Tables 1-3 show the attenuation values for the four metro cities for various seasons like summer, rain and winter. Table 4 shows the attenuation values due to rain for 0.01% of a year for four Indian metro cities. Table 5 shows the attenuation values due to fog for Delhi. Further, the graphs also plots rain attenuation for the rain season for these four cities. Figures 5-8 represents the attenuation for four cities respectively. Figure 9 shows the fog attenuation for Delhi in winter season. Figures 10-13 show the plot of the total atmospheric attenuation due to water vapour, oxygen, rain and fog for Delhi, Mumbai, Kolkata and Chennai. The attenuation applicability due to water vapour, oxygen, rain and fog have been considered as per cities respectively Delhi, Mumbai, Kolkata and Chennai.

Accepted manuscript

Acknowledgments

The researchers are kindly thankful to Samsung India and Delhi Technological University (DTU) India. We don't have funding for this research.

References

[1] Sun, Shu, et al. "Investigation of prediction accuracy, sensitivity, and parameter stability of large-scale propagation path loss models for 5G wireless communications." IEEE Transactions on Vehicular Technology 65.5 (2016): 2843-2860.

[2] Agrawal, S. K., and Kapil Sharma. "5G Millimeter Wave (mmWave) Communication System with Software Defined Radio (SDR)." International Conference on Recent Trends in Engineering & Science (ICRTES-16), 29th-30th September. 2016.

ACCEPTED MANUSCRIPT

[3] Zhouye Pi et al., “An Introduction to Millimeter- Wave Mobile Broadband Systems, ” IEEE Communications Magazine, vol.49, no.6, pp.101- 107, Jun. 2011.
[4] Andrews J.G. et al., “What Will 5G Be?, ” IEEE JSAC Special Issue On 5G Wireless Communication Systems, May 2014.
[5] Theodore S. Rappaport et al., “Millimeter Wave Mobile Communications for 5G Cellular: It Will Work!, ” IEEE Access, vol.1, pp.335-349, May 2013.
[6] S. K. Agrawal and P. Garg, “Calculation of Channel Capacity Considering the Effect of Different Seasons for Higher Altitude Platform System", Wireless Personal Communications, Springer, Wireless Personal Communications: vol. pp-719-729, Issue 4 2010.
[7] S. K. Agrawal and P. Garg, “Calculation of the Channel Capacity in the Presence of Vegetation and Urban-site Environment for Higher Altitude Platform Communication System", to Wireless Personal Communications”, IET Microwaves, Antenna & Propagation, IET Microw. Antennas Propag., Vol. 3, Iss. 4, pp. 703–713, 2009.
[8] Agrawal, S. K., and Kapil Sharma. " Software Defined Radio Based Channel Capacity In 5G Millimeter Wave Communication System" International Virtual Conference on Computer Science, Engineering and Technology (25th - 28th December, 2016), Indore - India.
[9] S. K. Agrawal and K. Sharma, “5G Millimeter Wave (mmWave) Communication System with Software Defined Radio (SDR)”, International Journal for Innovative Research in Science & Technology, Volume 2, Issue 9, September 2016
[10] Agrawal, S. K., and Kapil Sharma. "5G Millimeter Wave (mmWave) Communication System with Software Defined Radio (SDR)." International Conference on Recent Trends in Engineering & Science (ICRTES-16), 29th-30th September. 2016.

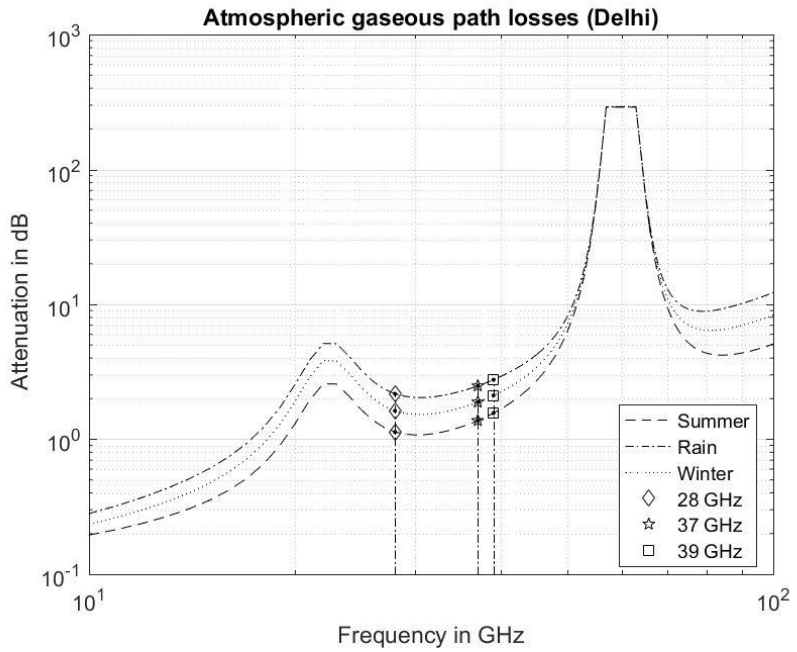


Fig. 1. Attenuation due to atmospheric gases for 5G mmWave Communication System (Delhi).

ACCEPTED MANUSCRIPT

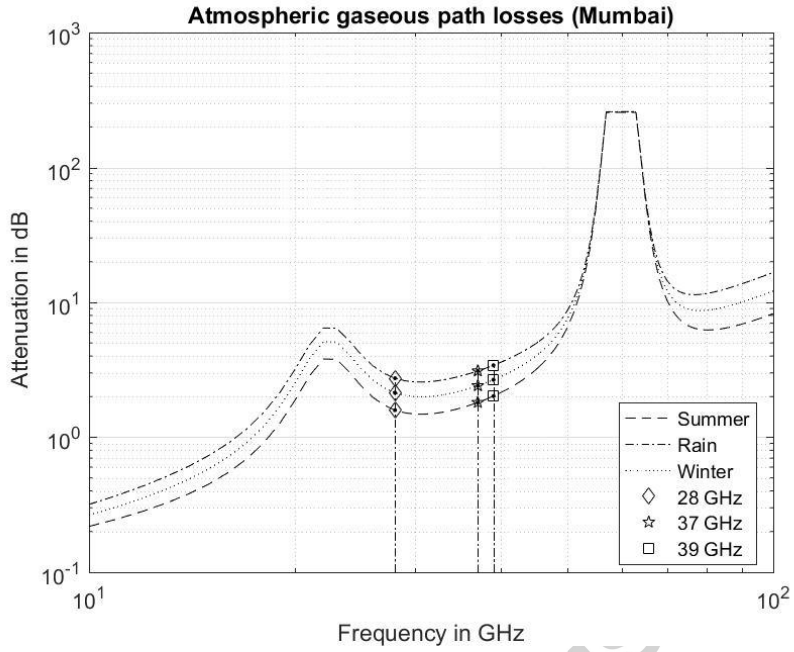


Fig. 2. Attenuation due to atmospheric gases for 5G mmWave Communication System (Mumbai).

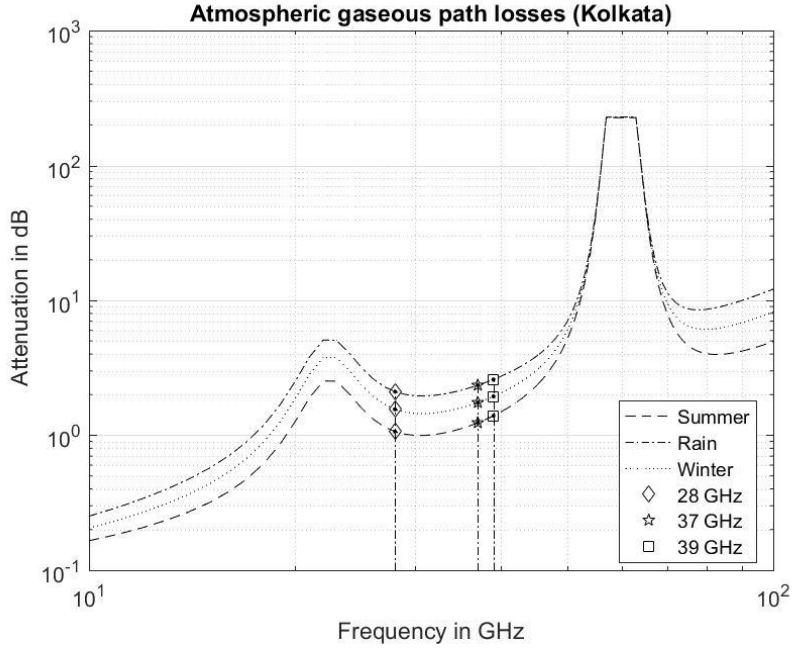


Fig. 3. Attenuation due to atmospheric gases for 5G mmWave Communication System (Kolkata).

ACCEPTED MANUSCRIPT

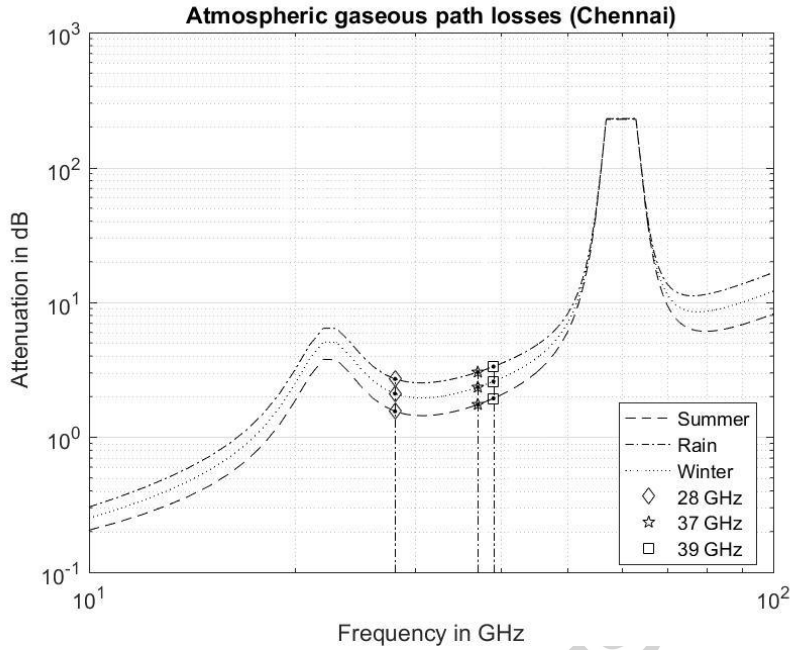


Fig. 4. Attenuation due to atmospheric gases for 5G mmWave Communication System (Chennai).

Total Atmospheric Attenuation (dB)	Frequency (28 GHz)	Frequency (37 GHz)	Frequency (39 GHz)
Delhi	0.81	0.73	0.77
Mumbai	1.31	1.21	1.30
Kolkata	0.82	0.75	0.7
Chennai	1.30	1.20	1.31

Table 1: Attenuation Due To Atmospheric Gases For Four Indian Metro Cities (Summer)

Total Atmospheric Attenuation (dB)	Frequency (28 GHz)	Frequency (37 GHz)	Frequency (39 GHz)
Delhi	1.80	1.81	1.93
Mumbai	2.41	2.52	2.71
Kolkata	1.85	1.86	1.99
Chennai	2.41	2.50	2.71

Table 2 : Attenuation Due To Atmospheric Gases For Four Indian Metro Cities (Rain)

Total Atmospheric Attenuation (dB)	Frequency (28 GHz)	Frequency (37 GHz)	Frequency (39 GHz)
Delhi	1.31	1.21	1.32

ACCEPTED MANUSCRIPT

Mumbai	1.81	1.82	1.91
Kolkata	1.31	1.21	1.33
Chennai	1.81	1.82	1.91

Table 3 : Attenuation Due To Atmospheric Gases For Four Indian Metro Cities (Winter)

Percentage (of Year)	Frequency (GHz)	Delhi Attenuation (dB)	Mumbai Attenuation (dB)	Kolkata Attenuation (dB)	Chennai Attenuation (dB)
0.01	28	26.71	37.29	36.65	30.09
0.01	37	33.43	45.58	44.09	37.29
0.01	39	34.12	47.03	45.48	38.79

Table 4 : Attenuation Due To Rain For 0.01% Of A Year For Four Indian Metro Cities

Temperature (˚C)	Frequency (GHz)	Attenuation (dB)
7	28.0	6.6
7	37.0	10.2
7	39.0	11.3

Table 5 : Attenuation values due to fog for Delhi.

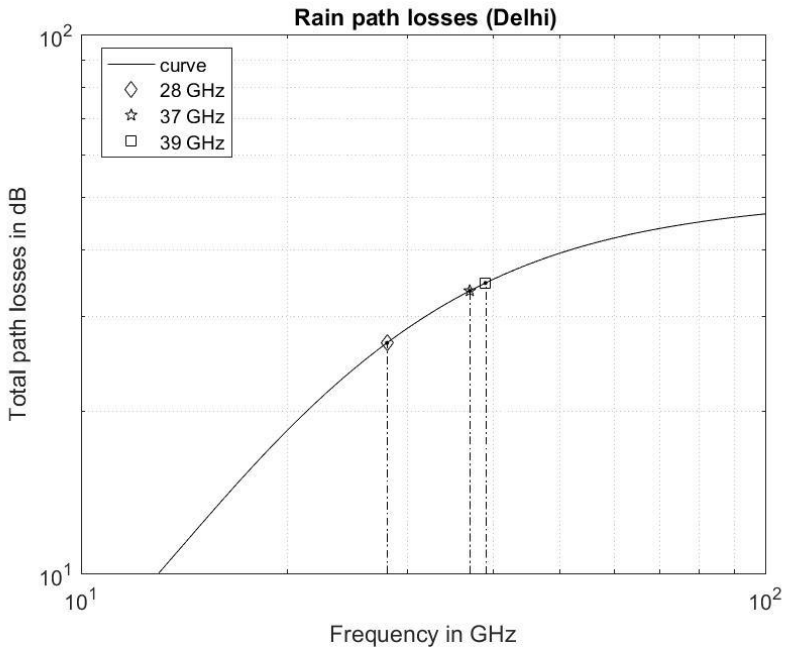


Fig. 5. Attenuation due to rain for 5G mmWave Communication System (Delhi) .

ACCEPTED MANUSCRIPT

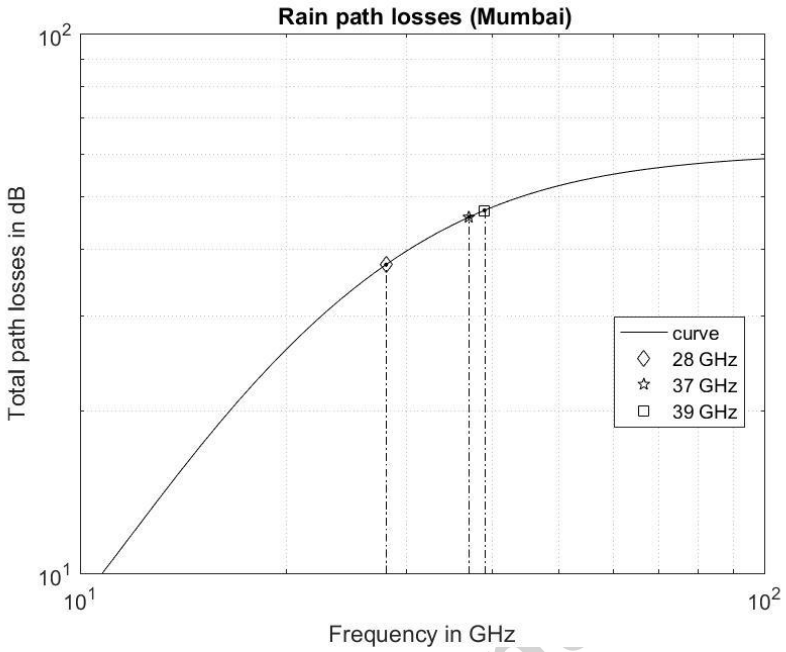


Fig. 6. Attenuation due to rain for 5G mmWave Communication System (Mumbai) .

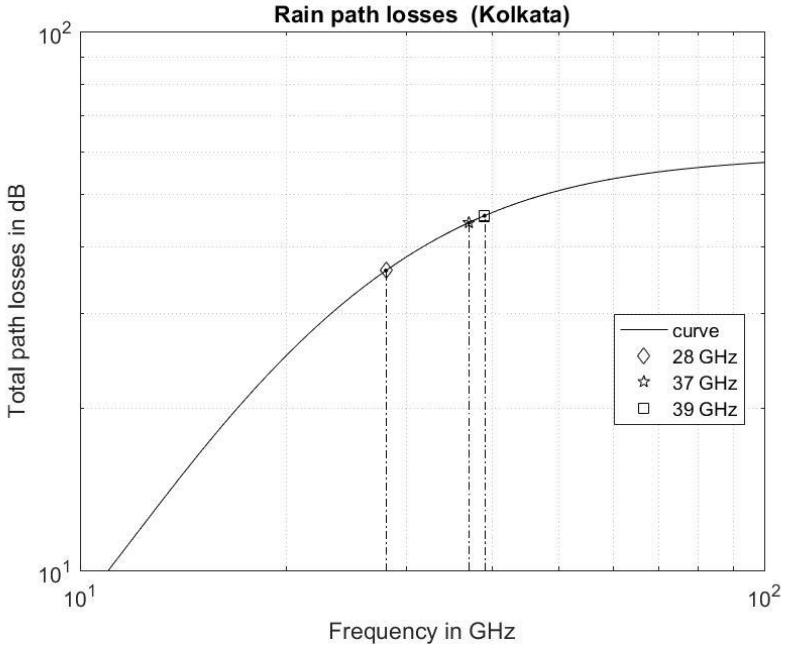


Fig. 7. Attenuation due to rain for 5G mmWave Communication System (Kolkata) .

ACCEPTED MANUSCRIPT

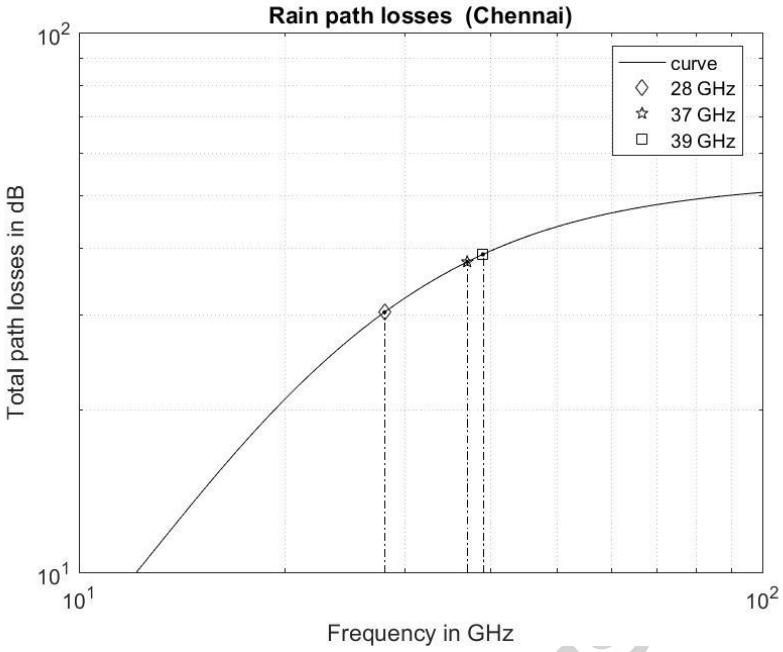


Fig. 8. Attenuation due to rain for 5G mmWave Communication System (Chennai) .

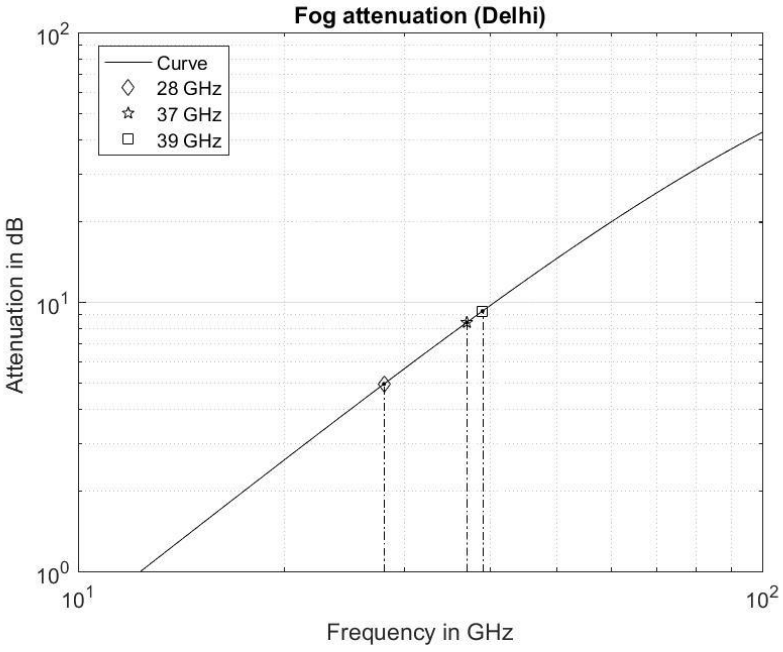


Fig. 9. Attenuation due to fog for 5G mmWave Communication System (Delhi).

ACCEPTED MANUSCRIPT

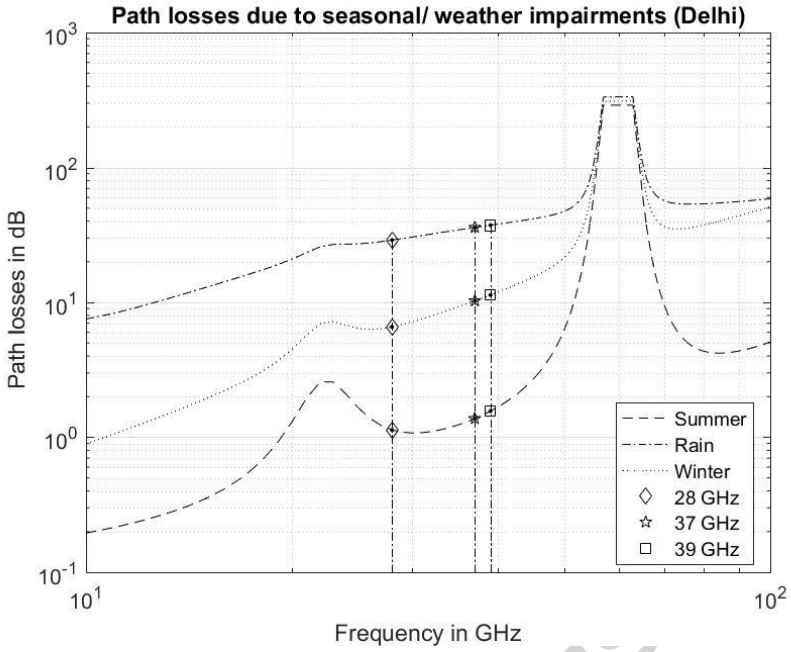


Fig. 10. Attenuation due to Seasons (Summer, Rain and Winter) for 5G mmWave Communication System (Delhi).

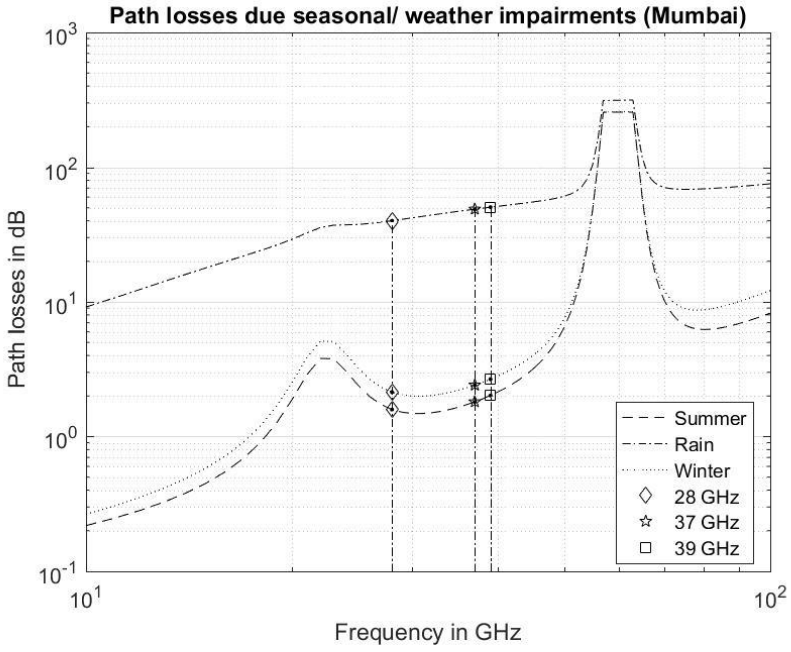


Fig. 11. Attenuation due to Seasons (Summer, Rain and Winter) for 5G mmWave Communication System (Mumbai).

ACCEPTED MANUSCRIPT

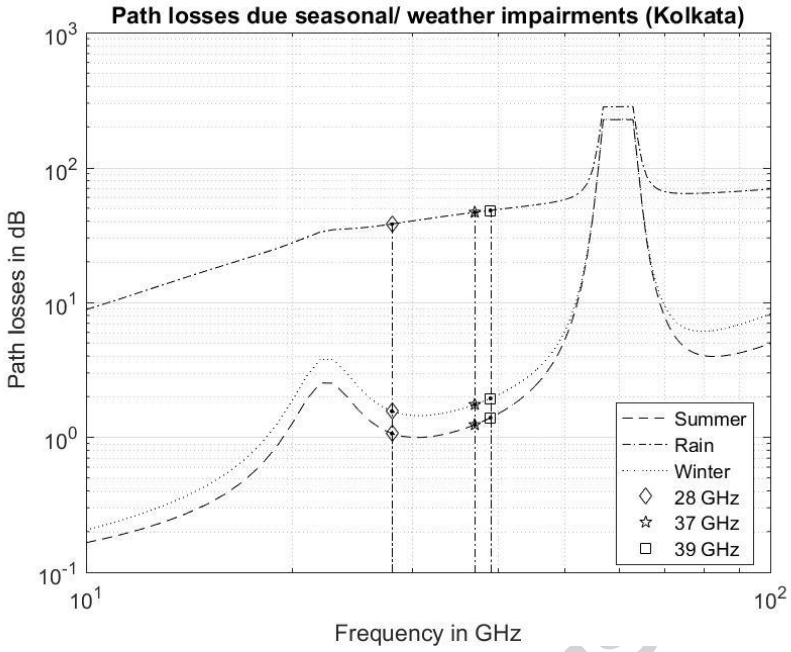


Fig. 12. Attenuation due to Seasons (Summer, Rain and Winter) for 5G mmWave Communication System (Kolkata).

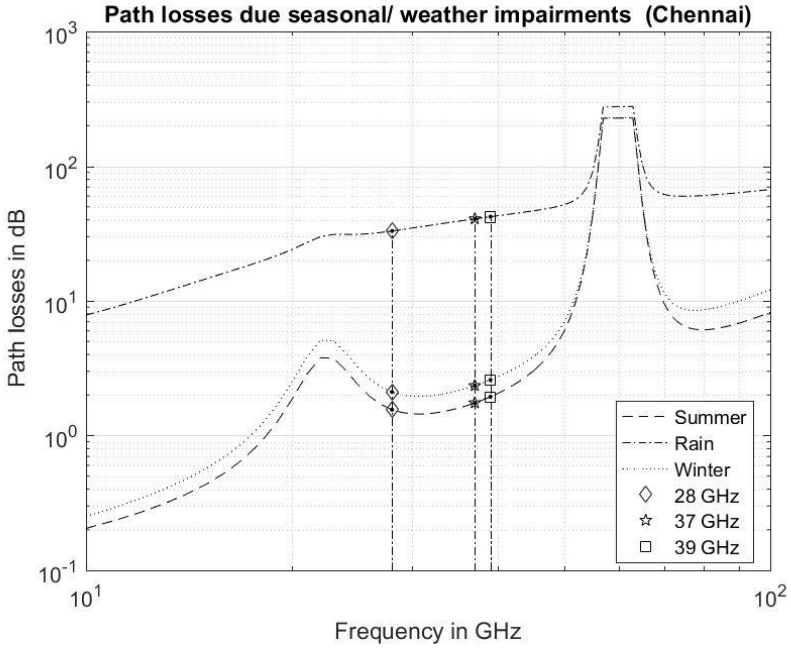


Fig. 13. Attenuation due to Seasons (Summer, Rain and Winter) for 5G mmWave Communication System (Chennai).

emeraldinsight

Evidence-based HRM: a Global Forum for Empirical Scholarship

Attracting millennial talent: a signal theory perspective
Anishya Obhrai Madan, Srishti Madan,

Article information:

To cite this document:
Anishya Obhrai Madan, Srishti Madan, (2018) "Attracting millennial talent: a signal theory perspective", Evidence-based HRM: a Global Forum for Empirical Scholarship, https://doi.org/10.1108/EBHRM-01-2018-0009
Permanent link to this document:
https://doi.org/10.1108/EBHRM-01-2018-0009

Downloaded on: 26 December 2018, At: 01:12 (PT)
References: this document contains references to 97 other documents.
To copy this document: permissions@emeraldinsight.com
The fulltext of this document has been downloaded 10 times since 2018*
Access to this document was granted through an Emerald subscription provided by emerald-srm:544911 []

For Authors

If you would like to write for this, or any other Emerald publication, then please use our Emerald for Authors service information about how to choose which publication to write for and submission guidelines are available for all. Please visit www.emeraldinsight.com/authors for more information.

About Emerald www.emeraldinsight.com

Emerald is a global publisher linking research and practice to the benefit of society. The company manages a portfolio of more than 290 journals and over 2,350 books and book series volumes, as well as providing an extensive range of online products and additional customer resources and services.

Emerald is both COUNTER 4 and TRANSFER compliant. The organization is a partner of the Committee on Publication Ethics (COPE) and also works with Portico and the LOCKSS initiative for digital archive preservation.

*Related content and download information correct at time of download.

Downloaded by Delhi Technological University At 01:12 26 December 2018 (PT)

The current issue and full text archive of this journal is available on Emerald Insight at:
www.emeraldinsight.com/2049-3983.htm

Attracting millennial talent: a signal theory perspective

Anishya Obhrai Madan
Training and Placement Unit,
Indian Institute of Technology Delhi, New Delhi, India and
HRM/OB Area, Management Development Institute, Gurugram, India, and
Srishti Madan
Department of Electrical Engineering,
Delhi Technological University, Delhi, India

Received 30 January 2018
Revised 30 June 2018
24 October 2018
29 October 2018
Accepted 30 October 2018

Downloaded by Delhi Technological University At 01:12 26 December 2018 (PT)

Abstract

Purpose – On the basis of an exploratory research, the purpose of this paper is to identify the criteria used by new entrants to the workforce (specifically premium millennial talent) while making job choices.
Design/methodology/approach – Using signal theory, the study attempts to explore what drives prospective millennial candidates to apply to a particular job role by identifying the components that form the initial anticipatory psychological contract (iAPC) of millennial talent from a tier-1 technological school in India and the factors that drive their job application intent. It is an exploratory study which uses survey data from 335 respondents.
Findings – The study identifies the critical components of the iAPC of this set of talent. It highlights the transactional approach of this cohort to evaluate prospective job roles.
Research limitations/implications – This research is based on an exploratory study which was carried out in a single school in India and may be used as a concept for designing and implementing more generalized studies using standardized tools of measurement in the future. The study highlights the fact that this cohort attends to the transactional components of the signals sent out by recruiters to a larger extent than to other kinds of signals which may be communicated by employers. HR communication strategies for connecting with this set may emphasize the unique employment proposition to potential recruits using the findings from this study to better engage with this cohort.
Practical implications – The current research gives indications on the components of the iAPC for this cohort and would help HR form appropriate strategies to attract this set of talent.
Originality/value – This research takes a fresh line of reasoning to explain what parameters would drive fresher millennial talent to apply for a job at an organization. It views the group through a generational theory paradigm and signaling theory forms the backdrop for this study. Further, since the study is based on an Indian sample, it contributes to literature from a non-western context.

Keywords Gen Y, Signal theory, Job choice, Initial anticipatory psychological contract (iAPC), Job preferences, Millennial talent

Paper type Research paper

1. Introduction

With over 1.21bn people and more than a sixth of the world's population, India is the second most populous country in the world after China. With 17.5 percent of the world's population, India is projected to be the world's most populous country by 2025 surpassing China, its population reaching 1.6bn by 2050 at present projected growth rates. India has more than 50 percent of its population below the age of 25 and more than 65 percent below the age of 35 (Registrar General, India, 2011; PTI, 2017; United Nations, 2017). It is expected that in 2020 the average age of an Indian will be 29 years, compared to 37 for China and 48 for Japan (Basu, 2007). India is thus a country with a predominantly young population compared to many developed nations which have aging populations.

Thus, managing this young workforce to unleash their productive potential gains importance. To this end, it becomes imperative to understand their motivations, ambitions and driving forces in the workplace and to design policies and processes to attract this talent pool and keep them engaged in the workplace.



Evidence-based HRM: a Global Forum for Empirical Scholarship
© Emerald Publishing Limited
2049-3983
DOI 10.1108/EBHRM-01-2018-0009

A gap exists in literature on how HR engages with this generation from the pre-recruitment phase to keeping them engaged during their life cycle within the company. This led the researchers to explore this phenomenon in an Indian context. The sample frame consisted of high-potential graduates (from a premier technological school in India). The following general research question was explored in this study:

RQ1. What are the criteria used by this cohort while applying for jobs? What criteria affect their job application intent?

Specific research questions included:

RQ2. What factors make up the initial psychological contract of high-potential graduates?

RQ3. What factors are prioritized over others and influence the initial anticipatory psychological contract (iAPC) of this set while applying for jobs?

This study views the group through a generational theory paradigm and signaling theory forms the backdrop for this study. It corroborates many previous studies while also pointing to some surprising trends.

2. Theoretical framework

2.1 Generational theory and millennials

The generational hypothesis states that a generation's (including millennials') expectations from work and life are determined by the characteristics of their generational cohort. A generational cohort can be defined as an "identifiable group that shares birth years, age, location and significant life events at critical developmental stages" (Kupperschmidt, 2000, p. 66). Each generation is purported to develop characteristics that differentiate it from those that precede and follow it; characteristics that are reflected in personality traits, work values, attitudes and motivations to work in ways presumed to be important to managers (Macky *et al.*, 2008). Young adulthood is a particularly impressionable developmental stage (Mannheim, 1952; Ryder, 1965). From adulthood onward, these personalities, values and expectations remain stable (Smola and Sutton, 2002).

The millennial generation/Generation Y (born between 1980 and 2000, the newest to enter the workforce) has been entering the workforce in large numbers, which has given them the power to reshape the rules of play at work (Smola and Sutton, 2002; Thompson and Gregory, 2012; Twenge and Campbell, 2008). As a result, practitioners have become increasingly interested in this new generation. They are interested in how organizations can successfully manage their (future) employment relationship with millennials by focusing on their work values, motivational drivers and career expectations (Cennamo and Gardner, 2008; Dries *et al.*, 2008; Smola and Sutton, 2002; Thompson and Gregory, 2012; Wong *et al.*, 2008). This led the researchers to investigate the driving factors affecting the job application intent of millennial talent at the stage of pre-entry to the workforce.

2.2 Signal-based context and job application intent

Signaling theory is fundamentally concerned with reducing information asymmetry between two parties (Spence, 2002). For example, Spence's (1973) seminal work on labor markets demonstrated how a job applicant might engage in behaviors to reduce information asymmetry that hampers the selection ability of prospective employers. Spence illustrated how high-quality prospective employees distinguish themselves from low-quality prospects via the costly signal of rigorous higher education. Potential employers lack information about the quality of job candidates. The candidates, therefore, obtain education to signal their quality and reduce information asymmetries, i.e., he deemphasizes the role of education for increasing worker productivity and focuses instead on education as a means to

Downloaded by Delhi Technological University At 01:12 26 December 2018 (PT)

Downloaded by Delhi Technological University At 01:12 26 December 2018 (PT)

communicate otherwise unobservable characteristics of the job candidate (Drover *et al.*, 2018; Weiss, 1995).

Rynes (1991) describes how job applicants use signals from recruiters to draw conclusions about facets of organizational quality. Recruitment researchers have argued that job seekers often have little information about recruiting organizations, so they rely on signals that they receive from whatever information they do have to make inferences about working conditions and other organizational characteristics (Drover *et al.*, 2018; Rynes, 1991; Rynes and Miller, 1983). Research shows that recruitment experiences do indeed provide signals that affect job seekers' attitudes and choices (e.g. Cable and Turban, 2003; Jaidi *et al.*, 2011; Rynes *et al.*, 1991).

Different applicants may not have the same concerns about their potential employers as they attend to different signals or interpret the same signal differently (Highhouse *et al.*, 2007). Receivers may apply weights to signals in accordance with preconceived notions about importance or cognitively distort signals so that their meanings diverge from the original intent of the signaler (Branzei *et al.*, 2004; Drover *et al.*, 2018; Ehrhart and Ziegert, 2005). Stiglitz (2002, p. 473) observed that some individuals wish to convey information and others wish not to have information conveyed, but "in either case, the fact that actions convey information leads people to alter their behavior, and […] this is why information imperfections have such profound effects." Signaling theory provides a unique, practical and empirically testable perspective on problems of social selection under conditions of imperfect information (Connelly *et al.*, 2011; Drover *et al.*, 2018).

Each signal-based context reflects something that job seekers and employees value and desire from their employment experience. Given that people are motivated to pursue favorable outcomes (Vroom, 1964), these signal-based mechanisms help to explain what signals job seekers look for while applying to organizations.

All the above are explored by the researcher in the current study under the variables of employer attractiveness (the signal) and the initial anticipated psychological contract (the receiver's interpretation of the signal) which leads to the action of exercising choice by applying for a particular job profile (Figure 1). Since the study is carried out in a premier technological school in India, the quality of applicants based on education achieved has been taken as a control variable.

3. The model detailed

3.1 Employer attractiveness as the signal

Job search is a dynamic decision-making process where job and organizational attributes affect final choice (Boswell *et al.*, 2003; Madan and Bhatnagar, 2014; Madan, 2017; Montgomery and Ramus, 2011; Rynes and Barber, 1990). These attributes are dominant because they have a direct positive effect on applicants' attraction to the firm and influence the decision to accept or reject a job offer (Turban *et al.*, 1998).

Among the various signals sent by an organization are signals about the organization's prestige, specific values and prosocial orientation. Further, a tight labor market gives highly competent employees many choices (Clarke, 2001; Jaidi *et al.*, 2011) especially in professional, information/knowledge based, technical and service-driven organizations (Ewing *et al.*, 2002; Inkson and King, 2011; Ployhart, 2006). Further, highly educated graduates are often

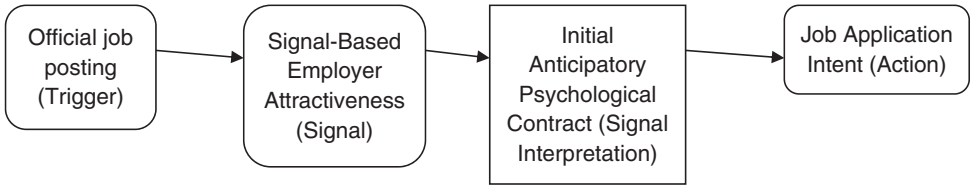


Figure 1.
Proposed conceptual model

exposed to recruitment practices of many different organizations and have multiple job pursuit options (Barber, 1998) and can choose their preferred employer (da Motta Veiga and Turban, 2018; Jaidi *et al.*, 2011). This underlines the requirement that an organization has to proceed by finding out what differentiates it from the competitors and then market the unique employment proposition it can offer (Breaugh, 2017; Drover *et al.*, 2018; Ewing *et al.*, 2002; Keefe, 2007).

There is an asymmetry of information regarding the actual work experience at an organization as well as the skills and competencies of the prospective candidate. Any information that job seekers examine builds their impressions of the hiring organization and can become important cues for what it would be like to work for that organization, including individuals' attraction to join the organization (Drover *et al.*, 2018; Rynes *et al.*, 1991; Turban, 2001). Hence, HR strategists are employing various strategies to ensure their job profiles appear in the preference lists of potential employees by highlighting the sum of benefits and culture of working with the organization while conveying the unique value proposition of the organization as an employer in an attempt to increase employer attractiveness to potential recruits.

3.2 Anticipatory psychological contract (APC) as a frame for signal interpretation

Individual career expectations can be understood from the prism of APC (Rousseau, 1995). The APC is defined as individuals' pre-employment beliefs about their future employment, including promises they want to make to their future employers and inducements they expect to receive in return (Anderson and Thomas, 1996; De Vos *et al.*, 2009). This contract is thus an overall set of expectations that an applicant holds with respect to his/her potential contributions to the organization and the organization's potential response to these contributions (Rousseau, 1990).

Nelson and Quick (1994) suggest that individuals expect to receive salary, status, advancement opportunities and challenging work to meet their needs while organizations expect to receive time, energy, skills, competences, talents and loyalty from the graduate. Inkson and King (2011) contend that individuals look at their careers through the lens of personal advantage, and consider how their careers may provide opportunities to optimize earnings, status, personal development and family life, both immediately and in the long term, while organizations consider those careers through the lens of organizational advantage, and as a means of maintaining or enhancing expertise, corporate culture and institutional memory as sources of long-term competitive advantage. The point at which these converge would form the backdrop for successful individuals' careers in specific organizations.

The APC is thus formed during the anticipatory socialization stage, i.e., the period which precedes organizational entry during which future employees develop expectations about what their new role will be (Feldman, 1976; Louis, 1980; Tomprou and Nikolaou, 2011). The APC is an imperfect schema about the future employment deal that enumerates the promises employees want to make to their future employer and the inducements they expect in return (Anderson and Thomas, 1996). It develops independently from the specific context of an employment relationship (Eilam-Shamir and Yaakobi, 2014). The APC is the lens through which employees view their future employment relationship and evolves with each new piece of information about the organization (Tomprou and Nikolaou, 2011). Individuals approach their future organization with career motives that will affect the saliency of the obligations that form part of their psychological contract (Rousseau, 1995; Shore and Tetrick, 1994; Sparrow, 1996).

This would impact the way an individual evaluates, prioritizes and applies to job profiles. Millennials' expectations regarding employer inducements are extremely high (Smola and Sutton, 2002; Twenge and Campbell, 2008). A discernment of this understanding of the iAPC can thus serve as a foundation to manage the employee–employer relationship over time (Sherman and Morley, 2015).

Downloaded by Delhi Technological University At 01:12 26 December 2018 (PT)

This study is an attempt to research, enumerate and identify the critical components of the iAPC for millennials at the cusp of deciding which job profiles advertised by employers during campus placement season they wish to consider while applying for jobs (job application intent) at the pre-entry stage to an employment relationship when expectations from career and work are still in the formation stage. This is still a greenfield area of research within APC literature.

Let us examine the various factors influencing job choice and hence the components of the iAPC in millennials as enumerated in literature.

3.2.1 Components of APC in millennials. The empirical research of Jurgensen (1978) has been conducted on job seekers' preferred job attributes. Millennials have been brought up in the era of globalization, employment outsourcing, foreign investments and a proliferation of information and communication technologies (Krywulak and Roberts, 2009). They are more globally educated, view themselves with confidence, assertiveness and entitlement, are highly optimistic, goal-oriented and idealistic (Chen and Choi, 2008). They like to voice their opinions and are work-oriented. They are connected 24×7 on social networking sites and are technologically adept. They are perceived to be healthier and more economically secure than any earlier generation (Raines, 2003; Deloitte, 2017). They have high expectations of self and employers (Armor, 2005) and believe in work-life balance. They have thus been brought up in an environment of changing family structures and rapidly evolving socio-economic and technological times. They are used to a fast pace of change.

Studies reveal that Generation Y/the millennial generation prefers a positive work environment and stimulating work that offers opportunities for advancement and long-term career progression, invested in training and development and allowed variety in their daily work (Eisner, 2005; Broadbridge *et al*., 2007; Terjesen *et al*., 2007). Millennials highly value mentoring and training within organizations because it will allow them to continuously develop new skills and remain attractive on the labor market (Loughlin and Barling, 2001; Sturges *et al*., 2002).

Millennials have low expectations regarding job security, although they still highly value it (Dries *et al*., 2008). Millennials realize that lifelong employment and organizational security are rare in today's workplace. Therefore, millennials take a more proactive approach toward their own security by enhancing their employability in the labor market (Tomlinson, 2007). Gen Y has an unorthodox approach to career management that does not parallel traditional paths. Job jumping every two years in search of greater compensation or purposeful work is the norm due to a boundaryless view of career and an awareness of their sought-after technological expertise (Zemke *et al*., 2000). Security is valued by younger workers, but is defined as career security whereby they build portfolios of transferable skills permitting them to change jobs (Lancaster and Stillman, 2002). Millennials increasingly expect meaningful and challenging jobs that yield learning opportunities and help them advance their careers (Dries *et al*., 2008; Deloitte, 2017; Inkson and King, 2011; Rawlins *et al*., 2008).

Millennials show a preference for intellectual challenge before geographic area and financial package (Montgomery and Ramus, 2011). They also have a strong need for independence and autonomy (Bush *et al*., 2004; Cennamo and Gardner, 2008). Used to taking part in family decisions, they are ready to provide inputs in the workplace, thus encouraging a collective management style and a supportive culture (Eisner, 2005; Broadbridge *et al*., 2007).

Millennials have high expectations regarding work-life balance, particularly young graduates preparing to enter the job market (Eisner, 2005; Cennamo and Gardner, 2008; Smola and Sutton, 2002), and look for personal enjoyment (Broadbridge *et al*., 2007). The millennial generation attaches more importance to freedom-related work values – i.e., work-life balance and autonomy – than did previous generational cohorts. Millennials have high expectations regarding their social connections at work and prefer a psychological contract that stresses social involvement (Cennamo and Gardner, 2008). Millennials score

Downloaded by Delhi Technological University At 01:12 26 December 2018 (PT)

higher on the affiliative trait than does any other generational cohort and that they are strongly motivated by a cooperative workplace (Wong *et al.*, 2008).

The literature gives mixed results when we examine Generation Y's salary expectations. Some researchers suggest that they consider salary less important than other attributes, such as a fulfilling private life (Eisner, 2005; Matuson, 2013), while others suggest that it is a major concern (Lowe *et al.*, 2008; Qenani-Petrela *et al.*, 2007). Although meaningful work and career satisfaction are rated more important than financial rewards, studies show that salary is still an important work value that helps to determine career success for all generations (Dries *et al.*, 2008).

With Gen Y declared "the most entrepreneurial generation in history"; characterized as entrepreneurial and independent; digitally savvy; rejecting micromanagement; and valuing empowerment, challenge and excitement (Izzo, 2002), organizations are confronted with the added weight of convincing young workers that working for a corporation has greater appeal than self-employment. Gen Y brings an impressive, portfolio of academic credentials and requisite skills in technology to the workplace along with lofty expectations for fast-track promotion, raises, perks, independence, flexible work arrangements, a need for fun (Zemke, 2001) and meaningful work that adds value to the organization's strategic direction (Rekar-Munro, 2009). They expect continuous recognition and daily feedback. They also call for managerial support as well as clear and comprehensive instructions, yet seek autonomy to chart the path and pace for achieving goals (Yeaton, 2008). Given their pressing sense of immediacy and impatience, Gen Y is unlikely to be enticed by promises of distant pay raises and promotions (Lancaster and Stillman, 2002).

Longitudinal studies reveal that millennials' expectations related to job content, career development, training, financial rewards and job security are affected by generational influences, while their expectations related to work-life balance and social atmosphere are affected by contextual influences (Deal, 2007; Macky *et al.*, 2008; Smola and Sutton, 2002). Furthermore, results indicate a positive relationship between millennials' level of optimism about their opportunities on the labor market and their expectations regarding job content, career development, training, financial rewards and social atmosphere especially in emerging markets (Deloitte, 2017) like India.

3.2.1.1 The case of Indian millennials. Various authors have described Indian millennials as ambitious, emphasizing financial reward, entrepreneurial, having business savvy, technologically capable and adept. Ghosh and Chaudhuri (2009) call them the Y2K generation. They find that chief among Gen Y's intrinsic motivators are equitable pay, responsibility and independence and achievement. Leading extrinsic motivators are considerate and sympathetic supervisor, restricted hours of work and sound company policies and practices. Gen Y looks for a company that invests in them by providing them with challenging learning opportunities on the job, training programs and the latest technology, an informal organizational culture with a "fun" working environment, supportive and approachable leaders, quick promotions and recognition of efforts and early exposure to all that the job has to offer. In return, the career-oriented Gen Yer is ready to work hard, longer hours, but is committed to the work rather than the organization.

Saxena and Jain (2012) found "Millennial don't live to work, they work to live." The Generation Y professionals generally aspire for brand identity, competence and a sense of service. They are motivated when they have an empathetic supervisor, good work-life balance, sound company policies and equitable pay. The Indian Generation Y places a high value on achievement in both the work and the social environment. They love to ask questions and despise unnecessary procedure and processes. A generation with a strong sense of social concise and purpose, it never loses an opportunity to create their own identity and space. The strong work ethic and an ability to learn rapidly and adapt are some of the attributes that make Generation Y employees highly valuable assets for an organization.

Downloaded by Delhi Technological University At 01:12 26 December 2018 (PT)

Singh *et al.* (2012) found that Indian millennials value personal growth, self-fulfillment, progressive orientation and community development in that order. On the other hand, HR professionals perceive millennials as energetic and enthusiastic, techno-savvy, curious, open to learning, creative but also as ambitious, over-confident, with a low respect for authority, materialistic, "Me" generation and entitlement centric.

Another study attempted to identify the critical factors being considered by millennials while making job choices and identified the interplay of critical organizational factors, job characteristics and the psychographic profile of the applicant (Madan and Bhatnagar, 2014). Thus, many of the drivers for Indian millennials appear to be similar to those found in other contexts. This also underlines the need for HR to understand and manage the career aspirations of Generation Y at the workplace.

The current study led the researchers to explore this phenomenon in an Indian context.

4. Methodology

4.1 Research design

An exploratory study was carried out in a leading technological school in India to investigate job preferences of millennials in a pre-placement situation. A questionnaire on work preferences was administered to a population of 1,000 under-graduate and post-graduate students at a premier technological school at the time they were applying for campus placement jobs. Voluntary sampling method was used for data collection.

The study used a mix of survey and open-ended questions for gathering data to identify the critical components going into the decision of whether or not to apply to a job available.

The current study was exploratory in nature with a non-experimental research design. It followed a descriptive mode of data gathering. Content analysis was used for analysis of the open-ended part of the questionnaire, while a weighted frequency analysis was used for the inventory scale. The individual respondent was the unit of analysis.

Validation of the inferences made on the basis of data from one analytic approach demands the use of multiple sources of information. If at all possible, the researcher should try to have some sort of validation study built into the design. In research, validation takes the form of triangulation. Triangulation lends credibility to the findings by incorporating multiple sources of data, methods, investigators or theories (Erlandson *et al.*, 1993). The use of different kinds of data (from open-ended survey responses as well as the inventory) was done to triangulate the findings of the research.

4.2 Sample

To fulfill validity requirements, the same group answered both kinds of questions. This is supported by the study of Diamantopoulos and Inglis (1998) which highlights that this helps in controlling specification and in balancing the familiarity of the respondents with specific issues. For reliability and consistency, similar study protocol as desired by Ashill *et al.* (2003) was used.

An online survey questionnaire was sent out (via e-mail) to 1,000 final year students (both under-graduate and graduate) of a leading technological school in India who would be appearing for campus placement interviews. These students had no prior full-time work experience. For the purposes of the current study, the entire set of respondents is treated as homogeneous. The questionnaire was administered about a month prior to the start of campus interview processes around the same time as the start of application processes to companies visiting the campus. Participation was completely voluntary. In total, 335 completed, valid responses were received. Thus, the response rate was 33.5 percent.

Downloaded by Delhi Technological University At 01:12 26 December 2018 (PT)

4.3 Analytic construct and measurement

This study attempts to capture impressions of the millennial generation in a pre-placement scenario to capture the job application intent of millennials while evaluating and applying for jobs advertised by employers during campus placement season.

To this end, a questionnaire containing a mix of open-ended questions to capture the critical components going into the decision of applying for a particular job profile at a particular organization as well as an inventory of 25 items culled out from the literature review above; of which the respondents were asked to pick the top 5 in their order of priority was administered

There are two approaches to coding data that operate with slightly different rules. With emergent coding, categories are established following some preliminary examination of the data. When dealing with *a priori* coding, the categories are established prior to the analysis based upon some theory. Professional colleagues agree on the categories, and the coding is applied to the data. Revisions are made as necessary, and the categories are tightened up to the point that maximizes mutual exclusivity and exhaustiveness (Weber, 1990). For purposes of the present study, we used both thematic *a priori* and emergent coding using conceptual analysis as the basis for content analysis.

The inventory was based on respondents picking out the top 5 criteria from the 25 listed (thematic *a priori* coding). This corresponds with an ordinal system of measurement. The content analysis of the open-ended questions yielded nominal data corresponding to the themes already identified in the inventory (thematic *a priori* coding) as well as a few new ones (emergent coding) (see Table I).

Content analysis was carried out on the open-ended part of the questionnaire and dominant themes were identified. These were then collated for all the respondents to arrive at loadings for each factor as culled out from the content analysis. Content analysis has been defined as a systematic, replicable technique for compressing many words of text into fewer content categories based on explicit rules of coding (Berelson, 1952; GAO, US, 1996; Krippendorff, 1980; Weber, 1990). It also allows inferences to be made which can then be corroborated using other methods of data collection. Content analysis extends far beyond simple word counts. Table I lists the 25 inventory items as well as the constructs which emerged from content analysis of the open-ended questions. In total, 15 new codes emerged making a total of 40 codes after the content analysis.

To triangulate the data, the responses from the open-ended part of the questionnaire and the inventory were analyzed. The responses received to the 25-item inventory were collated using a weighted frequency analysis paradigm. Preference 1 (highest preference) was given a value of 5, 2 a value of 4, 3 a value of 3, 4 a value of 2 and 5 (lowest preference) a value of 1. All values for each preference were aggregated to arrive at the loading of each factor for the group. The responses of the open-ended part of the questionnaire were collated with each factor identified through content analysis being given a weight of 1, i.e., simple frequency analysis was done. The loadings from each set of responses were collated and are presented in Table I.

5. Statistical analysis and results

To test the concordance of the rankings within sample, the statistic of Kendall's test of concordance was used. This is a measure of agreement among raters. The value for Kendall's W on the inventory scale was 0.0089 while that for the open-ended questions was 0.0002. This shows that the respondents form a random sample with virtually no inter-respondent concordance.

A simple correlation analysis between the simple frequency count of responses between the inventory and the open-ended questions as well as the weighted frequency of the inventory and responses to open-ended questions both yielded a value of 0.88. This suggests the existence of a significant relationship between the responses from the inventory and open-ended questions suggesting that respondents are giving similar responses to both sets of questions.

Downloaded by Delhi Technological University At 01:12 26 December 2018 (PT)

Parameter	Inventory weight	Inventory respondent count	Open-ended respondent count
Bond			11
Career progression	907	243	130
Cares about the health of employees	66	25	13
Challenging work			22
Company stage/size	204	69	38
Compensation/salary and benefits	864	258	272
Empowers people to take initiative and decisions	247	86	28
Enable innovation			9
Encourages people to voice their concerns and suggest improvements	45	19	8
Entrepreneurial			2
Ethical organization	144	55	9
Exit options			9
Flexibility			43
Fun at work	299	117	25
Has a strong brand value	246	88	68
Has the latest technology	39	15	7
Helps earn respect from society	47	21	2
Kid-friendly workplace			5
Location	423	154	132
Mentoring environment			4
People – boss	20	8	7
People – colleagues	94	37	9
Previous record/Alumni Feedback			18
Project based			2
Provide food			2
Provides a sense of community	18	7	5
Provides higher education opportunities			3
Provides job security	127	44	13
Recognizes performance	93	36	28
Role	335	97	138
Selection criteria/process			26
Socially responsible organization	37	13	7
Stock options	4	2	2
Technical domain	210	60	49
Time (hours at work)	139	57	17
Time to perform			2
Training opportunities/encourages learning	127	48	45
Travel	75	35	7
Values work-life balance	234	88	45
Work culture/employee-friendly work environment			138

Table I.
Frequency table of iAPC criteria

Table I shows that top 5 ratings were given to compensation, career progression, location, role and fun at work based on the inventory responses (both weighted and simple frequency). In the open-ended part of the questionnaire, the top 5 rated criterion included compensation, career progression, location, role and work culture.

Optimal scaling of the respondent data from both the inventory data as well as the open-ended questions was done for dimensional reduction using SPSS. In optimal scaling/ multi-dimensional scaling, a set of proximities between objects is approximated by a set of distances in a low dimensional space. These methods help reduce the observed variables to a smaller set of principal components/dimensions which explain most of the variance in the data. Another advantage of these methods is that they can handle nominal and ordinal data and discover non-linear relationships between variables and are apt for exploratory research.

Downloaded by Delhi Technological University At 01:12 26 December 2018 (PT)

Principal components analysis (PCA) for categorical data, an optimal scaling method, was carried out on the inventory data (ordinal data set) using the CATPCA function of SPSS. PCA focuses on the joint representation of respondents and variables in a low dimensional space (Linting *et al.*, 2007; Meulman *et al.*, 2004). From the output matrix of 25 variables, we found that compensation, career progression and location seem to be the critical components of the iAPC (with a component score greater than 0.5). Based on the output from the PCA and the Cronbach's α scores (Table II), the total variance accounted for by these three variables is 28.816.

The response matrix from the open-ended questions was analyzed using multiple correspondence analysis (MCA), another optimal scaling method. This is analogous to PCA above and is suitable to analyze nominal data with more than two categorical variables (Hair *et al.*, 2010; Husson and Josse, 2014). This was also done using SPSS. From the output matrix of 40 variables, we can infer that compensation, career progression, location, role and work culture seem to be the critical components of the iAPC (with a component score greater than 0.5). Based on the output from the MCA and the Cronbach's α scores (Table III), these five dimensions account for 28.04 percent variance in the data.

A frequentist analysis of the responses on each of the critical dimensions identified above from the inventory data is presented in Table IV. This highlights the progression orientation

Table II.
Principal components analysis for weighted inventory data

		Model summary		
			Variance accounted for	
Dimension	Variable	Cronbach's α	Total (eigenvalue)	% of variance
1	Compensation	0.790	4.145	16.579
2	Career progression	0.393	1.605	6.419
3	Location	0.325	1.454	5.817
Total		0.897[a]	7.204	28.816

Note: [a]Mean Cronbach's α is based on the mean eigenvalue

Table III.
Multiple correspondence analysis for open-ended survey data

		Model summary			
			Variance accounted for		
Dimension	Variable	Cronbach's α	Total (eigenvalue)	Inertia	% of variance
1	Compensation	0.792	4.396	0.110	10.989
2	Career progression	0.499	1.948	0.049	4.870
3	Location	0.418	1.688	0.042	4.221
4	Role	0.398	1.633	0.041	4.083
5	Work culture	0.365	1.551	0.039	3.878
Total			11.217	0.280	28.041
Mean		0.568[a]	2.243	0.056	5.608

Note: [a]Mean Cronbach's α is based on the mean eigenvalue

Table IV.
Frequentist analysis of preferences (on inventory data) (number of respondents)

Variable	Response as 5	Response as 4	Response as 3	Response as 2	Response as 1
Compensation	61	*72*	54	38	33
Career progression	*97*	60	33	30	23
Location	16	34	38	27	39

Downloaded by Delhi Technological University At 01:12 26 December 2018 (PT)

of this set of respondents since 97 of them chose progression as their highest preference. This is followed by compensation and then location.

6. Discussion

6.1 Research findings

Based on the above analysis of the top criteria being considered by premium millennial talent in India while deciding on which jobs to apply to leads us to see that they possess a strong progression orientation (Petrucelli, 2017). This is closely followed by compensation as a top criteria in the application decision followed by location. This points to the transactional component of the iAPC being more critical for this set (Eddy, 2016; Zupan *et al.*, 2017).

A systematic literature review reveals sparse and inconsistent literature on the millennial generations' expectations *vis-à-vis* a future employer especially in the Indian context. This study attempts to fill this gap. Thus, this study supports findings of many previous authors that compensation and financial reward is a major criterion in job preferences (Ghosh and Chaudhuri, 2009; Lowe *et al.*, 2008; Qenani-Petrela *et al.*, 2007; Saxena and Jain, 2012). It also endorses the view that this generation has a strong progression orientation and growth in the career is important to them (Broadbridge *et al.*, 2007; Eisner, 2005; Petrucelli, 2017; Singh *et al.*, 2012; Terjesen *et al.*, 2007).

This study also brings out the criticality of transactional components of the APC to this cohort at this stage of their career. This has also been found to be the case in another study on what millennials look for in recruitment advertisements (Eddy, 2016), as well as one on millennials from transition vs developed economies (Zupan *et al.*, 2017) and can be extrapolated to economies like India.

A new component, i.e., location, has been highlighted in this study. Thus, this cohort looks for progression with a good compensation and benefits structure at a convenient location while deciding on which job profiles to apply to.

6.2 Theoretical contributions

This study adds to theory by identifying the critical components of the iAPC of premium millennial talent from an emerging market like India at the stage of entry into the workplace. No similar study known to the authors has been carried out and thus, this is a contribution to literature on attracting millennial talent and the literature on APC. Literature on APC and how it evolves based on feedback of people already in a work environment is available but the APC of individuals at a pre-entry stage to the world of work is a greenfield area of research. This is a stage when the schema of what the work environment would be and what to expect is still being formed and thus, it is increasingly important to study this both from a theoretical and practitioner perspectives. The current study attempts to enumerate the critical components of the APC of this cohort. Since the individual applicant is the unit of analysis in this study, it is unique in that it attempts to bring out the critical components of this equation from the perspective of applicants. This would help extend understanding of how premium talent within this generation views signals from organizations and which are prioritized over others by them while attempting to make career choices.

The interdisciplinary approach of the study attempts to draw on economic theory as well as psychological theory to extend our comprehension of individual career decisions. It is a modest contribution to the interdisciplinary field of "career studies."

6.3 Practical implications

HR strategies which address the key criteria identified in this study would be more effective in attracting this talent pool. As HR practitioners look at innovative ways to engage with and attract this cohort into the workforce of their organizations, this study attempts to serve

Downloaded by Delhi Technological University At 01:12 26 December 2018 (PT)

as a modest contribution to fill the need to understand the psychographics of this generation. Understanding the psychographics of this generation would help HR frame policies to engage with this cohort more effectively.

In this age of hyper-competition, as organizations compete for talent – especially premium talent, the signals they send out to potential recruits needs to be customized to the cohort it is addressed to. Since "One Size" may not "Fit All," this study attempts to extend the understanding on millennial talent by documenting the bases of job application intent of premium talent within this generational cohort. The study highlights the fact that this cohort attends to the transactional components of the signals sent out by recruiters to a larger extent than to other kinds of signals which may be communicated by employers. HR communication strategies for connecting with this set may emphasize the unique employment proposition to potential recruits using the findings from this study to better engage with this cohort. By targeting HR strategies and communication geared to this cohort, HR may be better positioned to attract, engage with, deploy and utilize this critical talent pool for enhancing the long-term competitive advantage of their organizations.

6.4 Limitations and scope for future research

This study indicates the need for further research on the Millennial Talent pool especially one seen as "Premium Talent" at the cusp of entry to the world of work from academia. This research is based on an exploratory study which was carried out in a single school in India and may be used as a concept for designing and implementing more generalized studies using standardized tools of measurement in the future. It is a modest contribution to the existing literature in career theory from a non-western, emerging economy context.

References

Anderson, N. and Thomas, H.D.C. (1996), "Work group socialization", in West, M.A. (Ed.), *Handbook of Work Groups*, Wiley, Chichester, pp. 423-450.

Armour, S. (2005), "Generation Y: they've arrived at work with a new attitude", *USA Today*, June 11, available at: http://usatoday30.usatoday.com/money/workplace/2005-11-06-gen-y_x.htm (accessed January 29, 2018).

Ashill, N.J., Frederikson, M. and Davies, J. (2003), "Strategic marketing planning: a grounded investigation", *European Journal of Marketing*, Vol. 37 Nos 3/4, pp. 430-460.

Barber, A.E. (1998), *Recruiting Employees: Individual and Organizational Perspectives*, Vol. 8, Sage Publications.

Basu, K. (2007), "India's demographic dividend", BBC News, July 25, available at: http://news.bbc.co.uk/2/hi/south_asia/6911544.stm (accessed January 29, 2018).

Berelson, B. (1952), *Content Analysis in Communication Research*, Free Press, Glencoe, IL.

Boswell, W.R., Roehling, M.V., LePine, M.A. and Moynihan, L.M. (2003), "Individual job-choice decisions and the impact of job attributes and recruitment practices: a longitudinal field study", *Human Resource Management*, Vol. 42 No. 1, pp. 23-37.

Branzei, O., Ursacki-Bryant, T.J., Vertinsky, I. and Zhang, W. (2004), "The formation of green strategies in Chinese firms: matching corporate environmental responses and individual principles", *Strategic Management Journal*, Vol. 25 No. 11, pp. 1075-1095.

Breaugh, J.A. (2017), "The contribution of job analysis to recruitment", in Goldstein, H.W., Pulakos, E.D., Passmore, J. and Semedo, C. (Eds), *The Wiley Blackwell Handbook of the Psychology of Recruitment, Selection and Employee Retention*, John Wiley and Sons, pp. 12-28.

Broadbridge, A.M., Maxwell, G.A. and Ogden, S.M. (2007), "13_2_30: experiences, perceptions and expectations of retail employment for Generation Y", *Career Development International*, Vol. 12 No. 6, pp. 523-544.

Downloaded by Delhi Technological University At 01:12 26 December 2018 (PT)

Downloaded by Delhi Technological University At 01:12 26 December 2018 (PT)

Bush, A.J., Martin, C.A. and Bush, V.D. (2004), "Sports celebrity influence on the behavioral intentions of Generation Y", *Journal of Advertising Research*, Vol. 44 No. 1, pp. 108-118.

Cable, D.M. and Turban, D.B. (2003), "The value of organizational reputation in the recruitment context: a brand-equity perspective", *Journal of Applied Social Psychology*, Vol. 33 No. 11, pp. 2244-2266.

Cennamo, L. and Gardner, D. (2008), "Generational differences in work values, outcomes and person-organisation values fit", *Journal of Managerial Psychology*, Vol. 23 No. 8, pp. 891-906.

Chen, P.-J. and Choi, Y. (2008), "Generational differences in work values: a study of hospitality management", *International Journal of Contemporary Hospitality Management*, Vol. 20 No. 6, pp. 595-615.

Clarke, K. (2001), "What businesses are doing to attract and retain employees-becoming an employer of choice", *Employee Benefits Journal*, Vol. 26 No. 1, pp. 21-24.

Connelly, B.L., Certo, S.T., Ireland, R.D. and Reutzel, C.R. (2011), "Signaling theory: a review and assessment", *Journal of Management*, Vol. 37 No. 1, pp. 39-67.

da Motta Veiga, S.P. and Turban, D.B. (2018), "Who is searching for whom? Integrating recruitment and job search research", in Klehe, U.-C. and van Hooft, E. (Eds), *The Oxford Handbook of Job Loss and Job Search*, Oxford University Press, pp. 311-328.

Deal, J.J. (2007), *Retiring the Generation Gap: How Employees Young and Old Can Find Common Ground*, Vol. 35, John Wiley and Sons.

Deloitte (2017), "The Deloitte Millennial Survey, 2017", available at: www2.deloitte.com/global/en/pages/about-deloitte/articles/millennialsurvey.html (accessed January 29, 2018).

De Vos, A., De Stobbeleir, K. and Meganck, A. (2009), "The relationship between career-related antecedents and graduates' anticipatory psychological contracts", *Journal of Business and Psychology*, Vol. 24 No. 3, pp. 289-298.

Diamantopoulos, A. and Inglis, K. (1998), "Identifying differences between high and low involvement exporters", *International Marketing Review*, Vol. 5 No. 2, pp. 52-60.

Dries, N., Pepermans, R. and De Kerpel, E. (2008), "Exploring four generations' beliefs about career. Is satisfied the new successful?", *Journal of Managerial Psychology*, Vol. 23 No. 8, pp. 907-928.

Drover, W., Wood, M.S. and Corbett, A.C. (2018), "Toward a cognitive view of signalling theory: individual attention and signal set interpretation", *Journal of Management Studies*, Vol. 55 No. 2, pp. 209-231.

Eddy, C.P. (2016), "Millennial work expectations: can recruitment advertisements attract this generation to organizations?", doctoral dissertation, San Francisco State University, San Francisco.

Ehrhart, K.H. and Ziegert, J.C. (2005), "Why are individuals attracted to organizations?", *Journal of Management*, Vol. 31 No. 6, pp. 901-919.

Eilam-Shamir, G. and Yaakobi, E. (2014), "Effects of early employment experiences on anticipated psychological contracts", *Personnel Review*, Vol. 43 No. 4, pp. 553-572.

Eisner, S.P. (2005), "Managing Generation Y", *SAM Advanced Management Journal*, Vol. 70 No. 4, pp. 4-15.

Erlandson, D.A., Harris, E.L., Skipper, B.L. and Allen, S.D. (1993), *Doing Naturalistic Inquiry: A Guide to Methods*, Sage Publications, Newbury Park, CA.

Ewing, M.J., Pitt, L.F., de Bussy, N.M. and Berthon, P. (2002), "Employment branding in the knowledge economy", *International Journal of Advertising*, Vol. 21 No. 1, pp. 3-22.

Feldman, D.C. (1976), "A contingency theory of socialization", *Administrative Science Quarterly*, September, pp. 433-452.

GAO, US (1996), *Content Analysis: A Methodology for Structuring and Analyzing Written Material*, GAO/PEMD-10.3.1, General Accounting Office, Washington, DC (this book can be ordered free from the GAO).

Ghosh, R. and Chaudhuri, S. (2009), "Intergenerational differences in individualism/collectivism orientations: implications for outlook towards HRD/HRM practices in India and the United States", *New Horizons in Adult Education and Human Resource Development*, Vol. 23 No. 4, pp. 5-21.

Hair, J.F., Black, W.C., Babin, B.J. and Anderson, R.E. (2010), *Multivariate Data Analysis*, 7th ed., Pearson Education, Upper Saddle River, NJ.

Highhouse, S., Thornbury, E.E. and Little, I.S. (2007), "Social-identity functions of attraction to organizations", *Organizational Behavior and Human Decision Processes*, Vol. 103 No. 1, pp. 134-146.

Husson, F. and Josse, J. (2014), "Multiple correspondence analysis", in Blasius, J. and Greenacre, M. (Eds), *Visualization and Verbalization of Data*, Taylor & Francis Group, CRC Press, pp. 165-184.

Inkson, K. and King, Z. (2011), "Contested terrain in careers: a psychological contract model", *Human Relations*, Vol. 64 No. 1, pp. 37-57.

Izzo, J. (2002), *Values Shift: The New Work Ethic and What it Means for Business*, Prentice Hall, Toronto.

Jaidi, Y., Van Hooft, E.A. and Arends, L.R. (2011), "Recruiting highly educated graduates: a study on the relationship between recruitment information sources, the theory of planned behavior, and actual job pursuit", *Human Performance*, Vol. 24 No. 2, pp. 135-157.

Jurgensen, C.E. (1978), "Job preferences (What makes a job good or bad?)", *Journal of Applied Psychology*, Vol. 63 No. 3, pp. 267-276.

Keefe, T.J. (2007), "Know thyself: developing a strong employer brand", *American Water Works Association Journal*, Vol. 99 No. 8, pp. 20-21.

Krippendorff, K. (1980), *Content Analysis: An Introduction to Its Methodology*, Sage, Newbury Park, CA.

Krywulak, T. and Roberts, M. (2009), "Winning the 'generation wars' making the most of generational differences and similarities in the workplace", available at: www.aqesss.qc.ca/docs/pdf/i-media/20091126/ConferenceBoard_Compete_Generation_Wars.pdf (accessed January 29, 2018).

Kupperschmidt, B.R. (2000), "Multigeneration employees: strategies for effective management", *Health Care Manager*, Vol. 19 No. 1, pp. 65-76.

Lancaster, L.C. and Stillman, D. (2002), *When Generations Collide: Who They Are, Why They Clash, and How to Solve the Generational Puzzle at Work*, Harper, New York, NY.

Linting, M., Meulman, J.J., Groenen, P.J. and van der Koojj, A.J. (2007), "Nonlinear principal components analysis: introduction and application", *Psychological Methods*, Vol. 12 No. 3, pp. 336-358.

Loughlin, C. and Barling, J. (2001), "Young workers' work values, attitudes, and behaviours", *Journal of Occupational and Organizational Psychology*, Vol. 74 No. 4, pp. 543-558.

Louis, M.R. (1980), "Surprise and sense-making: what newcomers experience in entering unfamiliar organizational settings", *Administrative Science Quarterly*, pp. 226-251.

Lowe, D., Levitt, K.J. and Wilson, T. (2008), "Solutions for retaining Generation Y employees in the workplace", *Business Renaissance Quarterly*, Vol. 3 No. 3, pp. 43-58.

Macky, K., Gardner, D. and Forsyth, S. (2008), "Generational differences at work: introduction and overview", *Journal of Managerial Psychology*, Vol. 23 No. 8, pp. 857-861.

Madan, A.O. (2017), "Millennial talent's job application intent: a case from India", European Academy of Management (EURAM 2017), Glasgow, June 21–24.

Madan, A.O. and Bhatnagar, J. (2014), "Millennial Talent: person job fit criterion and job application heuristics – a literature review", *Global Conference on Managing in Recovering Markets (GCMRM), MDI, Gurgaon, March 5–7.*

Mannheim, K. (1952), "The problem of generations", in Kecskemeti, P. (Ed.), *Essays on the Sociology of Knowledge*, Routledge and Kegan Paul, London, pp. 276-322.

Matuson, R.C. (2013), *Talent Magnetism: How to Build a Workplace that Attracts and Keeps the Best*, Hachette.

Meulman, J.J., Van der Kooij, A.J. and Heiser, W.J. (2004), "Principal components analysis with nonlinear optimal scaling transformations for ordinal and nominal data", in Kaplan, D. (Ed.), *The Sage Handbook of Quantitative Methodology for the Social Sciences*, Sage Publications, pp. 49-72.

Montgomery, D.B. and Ramus, C.A. (2011), "Calibrating MBA job preferences for the 21st century", *Academy of Management Learning and Education*, Vol. 10 No. 1, pp. 9-26.

Nelson, D.C. and Quick, J.C. (1994), "Social support and newcomer adjustment in organizations: attachment to work?", *Journal of Organization Behaviour*, Vol. 12 No. 6, pp. 543-554.

Downloaded by Delhi Technological University At 01:12 26 December 2018 (PT)

Petrucelli, T. (2017), "Winning the 'cat-and-mouse game' of retaining millennial talent", *Strategic HR Review*, Vol. 16 No. 1, pp. 42-44.

Ployhart, R.E. (2006), "Staffing in the 21st century: new challenges and strategic opportunities", *Journal of Management*, Vol. 32 No. 6, pp. 868-897.

PTI (2017), "India's population to surpass that of China's around 2024", *The Economic Times*, June 21, available at: https://economictimes.indiatimes.com/news/politics-and-nation/indias-population-to-surpass-that-of-chinas-around-2024-un/articleshow/59257232.cms (accessed January 29, 2018).

Qenani-Petrela, E., Schlosser, J. and Pompa, R. (2007), "Satisfied employees are worth their weight in gold: what motivates Generation Y?", *Journal of Food Distribution Research*, Vol. 38 No. 1, pp. 113-118.

Raines, C. (2003), *Connecting generations: The Sourcebook for a New Workplace*, Thomson Crisp Learning, pp. 95-111.

Rawlins, C., Indvik, J. and Johnson, P.R. (2008), "Understanding the new generation: what the millennial cohort absolutely, positively must have at work", *Journal of Organizational Culture, Communications and Conflict*, Vol. 12 No. 2, pp. 1-8.

Registrar General, India (2011), "Census of India 2011: provisional population totals-India data sheet, office of the registrar general census commissioner, India", Indian Census Bureau, available at: www.censusindia.gov.in/2011census/C-series/C-14.html (accessed December 9, 2018).

Rekar-Munro, C. (2009), "Mentoring needs and expectations of generation-y human resources practitioners: preparing the next wave of strategic business partners", *Journal of Management Research*, Vol. 1 No. 2, pp. 1-25.

Rousseau, D. (1995), *Psychological Contracts in Organizations: Understanding Written and Unwritten Agreements*, Sage.

Rousseau, D.M. (1990), "Assessing organizational culture: the case for multiple methods", in Stirred, B. (Ed.), *Organizational Climate and Culture*, Sage, San Francisco, CA, pp. 153-192.

Ryder, N.B. (1965), "The cohort as a concept in the study of social change", *American Sociological Review*, Vol. 30, pp. 843-861.

Rynes, S.L. (1991), "Recruitment, job choice, and post-hire consequences: a call for new research directions", in Dunnette, M.D. and Howe, L.M. (Eds), *Handbook of Industrial and Organizational Psychology*, Consulting Psychologists Press, Palo Alto, CA, pp. 399-444.

Rynes, S.L. and Barber, A.E. (1990), "Applicant attraction strategies: an organizational perspective", *Academy of Management Review*, Vol. 15 No. 2, pp. 286-310.

Rynes, S.L. and Miller, H.E. (1983), "Recruiter and job influences on candidates for employment", *Journal of Applied Psychology*, Vol. 68 No. 1, pp. 147-154.

Rynes, S.L., Bretz, R.D. Jr and Gerhart, B. (1991), "The importance of recruitment in job choice: a different way of looking", *Personnel Psychology*, Vol. 44 No. 3, pp. 487-521.

Saxena, P. and Jain, R. (2012), "Managing career aspirations of Generation Y at work place", *International Journal of Advanced Research in Computer Science and Software Engineering*, Vol. 2 No. 7, pp. 114-118.

Sherman, U.P. and Morley, M.J. (2015), "On the formation of the psychological contract: a schema theory perspective", *Group & Organization Management*, Vol. 40 No. 2, pp. 160-192.

Shore, L.M. and Tetrick, L.E. (1994), "The psychological contract as an explanatory framework in the employment relationship", in Cooper, C.L. and Rousseau, D.M. (Eds), *Trends in Organizational Behavior*, Vol. 1, Wiley, New York, NY, pp. 91-109.

Singh, P., Bhandarker, A. and Rai, S. (2012), *Millennials and the Workplace*, Sage Publications, New Delhi.

Smola, K.W. and Sutton, C.D. (2002), "Generational differences: revisiting generational work values for the new millennium", *Journal of Organizational Behavior*, Vol. 23 No. 4, pp. 363-382.

Sparrow, P.R. (1996), "Transitions in the psychological contract: some evidence from the banking sector", *Human Resource Management Journal*, Vol. 6 No. 4, pp. 75-92.

Spence, M. (1973), "Job market signaling", *Quarterly Journal of Economics*, Vol. 87, August, pp. 355-374.

Downloaded by Delhi Technological University At 01:12 26 December 2018 (PT)

Spence, M. (2002), "Signaling in retrospect and the informational structure of markets", *American Economic Review*, Vol. 92 No. 3, pp. 434-459.

Stiglitz, J.E. (2002), "Information and the change in the paradigm in economics", *American Economic Review*, Vol. 92 No. 3, pp. 460-501.

Sturges, J., Guest, D., Conway, N. and Davey, K.M. (2002), "A longitudinal study of the relationship between career management and organizational commitment among graduates in the first ten years at work", *Journal of Organizational Behavior*, Vol. 23 No. 6, pp. 731-748.

Terjesen, S., Vinnicombe, S. and Freeman, C. (2007), "Attracting Generation Y graduates: organizational attributes, likelihood to apply and sex differences", *Career Development International*, Vol. 12 No. 6, pp. 504-522.

Thompson, C. and Gregory, J.B. (2012), "Managing millennials: a framework for improving attraction, motivation, and retention", *The Psychologist-Manager Journal*, Vol. 15 No. 4, pp. 237-246.

Tomlinson, M. (2007), "Graduate employability and student attitudes and orientations to the labour market", *Journal of Education and Work*, Vol. 20 No. 4, pp. 285-304.

Tomprou, M. and Nikolaou, I. (2011), "A model of psychological contract creation upon organizational entry", *Career Development International*, Vol. 16 No. 4, pp. 342-363.

Turban, D.B. (2001), "Organizational attractiveness as an employer on college campuses: an examination of the applicant population", *Journal of Vocational Behavior*, Vol. 58 No. 2, pp. 293-312.

Turban, D.B., Forret, M.L. and Hendrickson, C.L. (1998), "Applicant attraction to firms: influences of organization reputation, job and organizational attributes, and recruiter behaviours", *Journal of Vocational Behavior*, Vol. 52 No. 1, pp. 24-44.

Twenge, J.M. and Campbell, S.M. (2008), "Generational differences in psychological traits and their impact on the workplace", *Journal of Managerial Psychology*, Vol. 23 No. 8, pp. 862-877.

United Nations (2017), "World population prospects: the 2017 revision", available at: www.un.org/development/desa/publications/world-population-prospects-the-2017-revision.html (accessed January 30, 2018).

Vroom, V.H. (1964), *Work and Motivation*, Wiley, New York, NY.

Weber, R.P. (1990), *Basic Content Analysis*, 2nd ed., Sage Publications, Newbury Park, CA.

Weiss, A. (1995), "Human capital vs signaling explanations of wages", *Journal of Economic Perspectives*, Vol. 9 No. 4, pp. 133-154.

Wong, M., Gardiner, E., Lang, W. and Coulon, L. (2008), "Generational differences in personality and motivation. Do they exist and what are the implications for the workplace?", *Journal of Managerial Psychology*, Vol. 23 No. 8, pp. 878-890.

Yeaton, K. (2008), "Recruiting and managing the 'why' generation: Gen Y", *The CPA Journal*, Vol. 78 No. 4, pp. 68-72.

Zemke, R. (2001), "Here come the millennials", *Training*, Vol. 38 No. 7, pp. 44-49.

Zemke, R., Raines, C. and Filipczak, B. (2000), *Generations at Work: Managing the Clash of Veterans, Boomers, Xers, and Nexters in Your Workplace*, American Management Association, Washington, DC.

Zupan, N., Dziewanowska, K. and Pearce, A. (2017), "Wanting it all: the challenges of managing young talent in transition economies", *Baltic Journal of Management*, Vol. 12 No. 1, pp. 63-85.

Corresponding author
Anishya Obhrai Madan can be contacted at: anishya.madan@gmail.com

For instructions on how to order reprints of this article, please visit our website:
www.emeraldgrouppublishing.com/licensing/reprints.htm
Or contact us for further details: **permissions@emeraldinsight.com**

Downloaded by Delhi Technological University At 01:12 26 December 2018 (PT)

ResearchGate

See discussions, stats, and author profiles for this publication at: https://www.researchgate.net/publication/329374377

Bandwidth enhancement using modified L-probe fed slotted patch antenna for WLAN and UMTS applications

Article *in* International Journal of Microwave and Wireless Technologies · December 2018

DOI: 10.1017/S175907871800154X

CITATIONS
0

READS
18

3 authors:



Rakesh Nath Tiwari
Uttarakhand Technical University
15 PUBLICATIONS **17** CITATIONS
SEE PROFILE



Prabhakar Singh
Galgotias University
42 PUBLICATIONS **370** CITATIONS
SEE PROFILE



Binod K. Kanaujia
Jawaharlal Nehru University
222 PUBLICATIONS **1,031** CITATIONS
SEE PROFILE

Some of the authors of this publication are also working on these related projects:

micro strip antenna View project

RCS reduction of Antennas View project

All content following this page was uploaded by Rakesh Nath Tiwari on 05 December 2018.

The user has requested enhancement of the downloaded file.

International Journal of Microwave and Wireless Technologies

cambridge.org/mrf

Bandwidth enhancement using modified L-probe fed slotted patch antenna for WLAN and UMTS applications

Rakesh N. Tiwari[1], Prabhakar Singh[2,3] and Binod Kumar Kanaujia[4]

[1]Department of Electronics and Communication Engineering, Uttarakhand Technical University, Dehradun, Uttarakhand 248007, India; [2]Department of Physics, Galgotias University, Greater Noida, Uttar Pradesh 201310, India; [3]Department of Applied Sciences, Galgotias College of Engineering and Technology, Greater Noida, Uttar Pradesh 201306, India and [4]School of Computational and Integrative Sciences, Jawaharlal Nehru University, New Delhi 110067, India

Research Paper

Cite this article: Tiwari RN, Singh P, Kumar Kanaujia B (2018). Bandwidth enhancement using modified L-probe fed slotted patch antenna for WLAN and UMTS applications. *International Journal of Microwave and Wireless Technologies* 1–11. https://doi.org/10.1017/S175907871800154X

Received: 6 July 2017
Revised: 24 October 2018
Accepted: 31 October 2018

Key words:
Conducting strip; modified L-probe; slotted patch; wideband microstrip patch antenna

Author for correspondence:
Rakesh N. Tiwari,
E-mail: srakeshnath@gmail.com

Abstract

In this paper, two different radiating structures fed with modified L-probe, are reported using a circuit theory concept. The proposed antennas are operating in wireless local area network (WLAN) and universal mobile telecommunications system (UMTS) frequency bands. In the first design, an E-shaped patch is studied to increase the bandwidth. It is observed that the bandwidth is directly proportional to notch dimensions. In the second design, E-shaped patch is modified to reduce the antenna size up to 30% with high bandwidth. In the first design, measured bandwidth and gain achieved are 32.68% (1.92–2.67 GHz) and 8.43 dBi while in second design it is 34.19% (1.94–2.74 GHz) and 8.39 dBi, respectively. Radiation patterns for both the antennas are symmetrical and broadside in nature. The proposed antennas are fabricated and measured results compare well with the theoretical and simulated results.

Introduction

Many attempts have been made to overcome the low gain and narrow bandwidth of the microstrip antenna [1]. In this process, several measures were taken such as modifying the shape of radiating elements [2] and modifying the ground plane structure [3], use of low dielectric constant material, stacked patch antenna, use of impedance matching networks etc. [4–6] and creating defect in the ground plane [7]. Different feeding techniques such as L-strip proximity feeding, T-shape probe feeding etc. are also used to increase the bandwidth [8, 9]. In the literature some theoretical analysis of strip line fed, L-strip/L-probe fed patch antennas have also been reported for the wideband operation [10, 11]. When the strip line feeding is modified as L-strip/L-probe it provides better gain and directivity suitable for wideband operation and antenna array design. In such feeding an additional capacitance is created between the radiating patch and the feed which cancels the inductance of the vertical portion of the L-probe. Consequently, this effect broadens the impedance bandwidth of the antenna [12].

In this paper, symmetrical slots are etched in the radiating patch and modified L-probe feeding is used to increase the antenna bandwidth. The present design gives better impedance bandwidth and gain as compared with the previously reported results [13–16]. The antenna parameters are calculated using high frequency structure simulator (HFSS) and verified with IE3D simulators. The proposed designs are also analyzed using circuit theory concept. The theoretical and simulated results are validated with measured results.

Antenna geometry and theoretical analysis

In conventional design of L-probe feeding, probe is required to bend which makes the design process complicated. But, in the present paper a narrow horizontal conducting strip is printed on the upper side of the substrate of thickness t and the radiating patch on the lower side. In order to avoid the bending procedure, a vertical thick probe is soldered to the horizontal strip. A small portion of patch is removed so that unnecessary drilling of the patch can be avoided. The present structure looks like a capacitively loaded L-probe fed patch antenna. Figure 1 shows the top view and side view of the proposed antennas. In antenna-I, two symmetrical notches of dimensions $l_1 \times w_1$ are incorporated along one of the radiating side of the patch resulting an E-shaped structure. In antenna-II, two additional notches of dimensions $l_2 \times w_2$ and a center notch of dimensions $l_3 \times w_3$ are introduced in the opposite radiating edge. For the wideband operation air substrate of thickness H is used between ground plane and the patch. The design specification of the proposed antenna is presented in Table 1.

© Cambridge University Press and the European Microwave Association 2018

CAMBRIDGE UNIVERSITY PRESS

Downloaded from https://www.cambridge.org/core. University of Winnipeg, on 03 Dec 2018 at 14:52:43, subject to the Cambridge Core terms of use, available at https://www.cambridge.org/core/terms. https://doi.org/10.1017/S175907871800154X

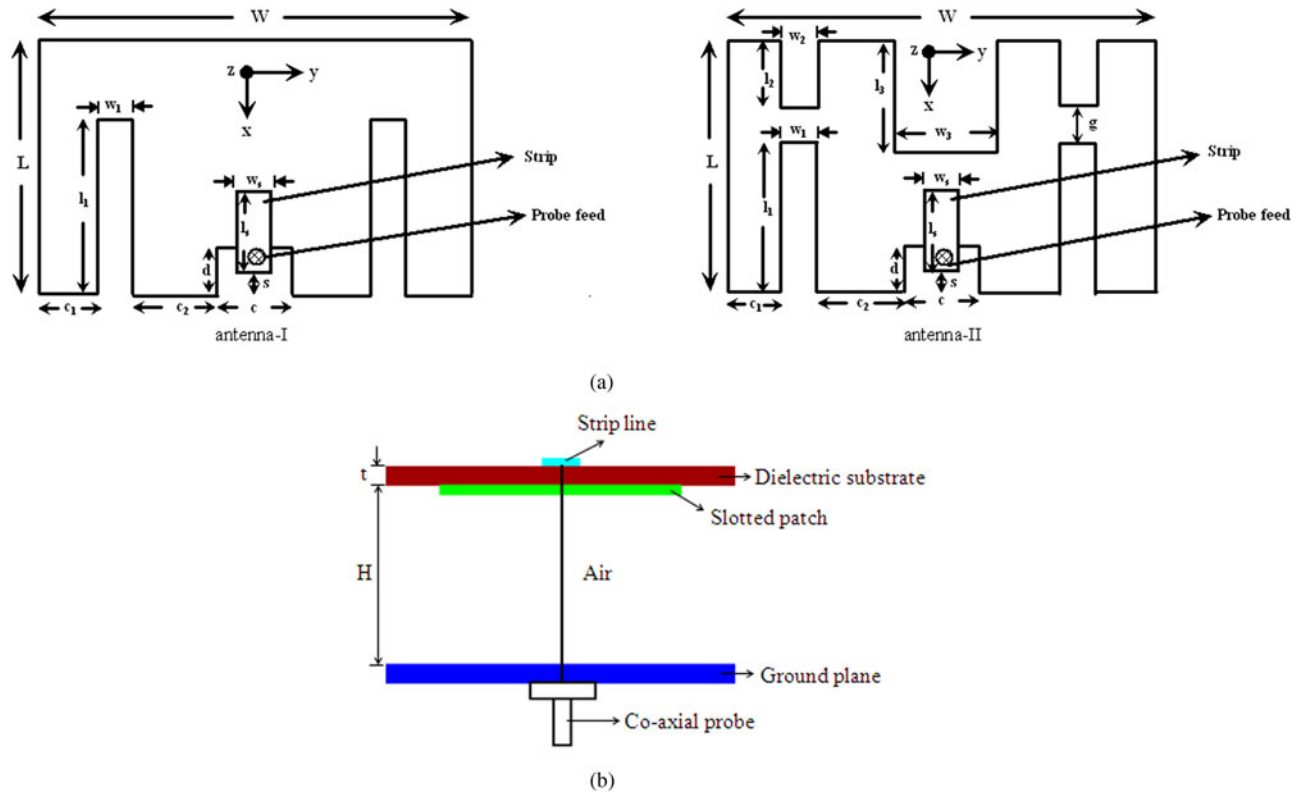


Fig. 1. Geometry of antenna (a) Top view (b) Side view for antenna-I and antenna-II.

Table 1. The design specification of the proposed antennas.

Parameter	Values
$W \times L$	72.0 × 50.0 mm^2
Air gap (H)	10.0 mm
Thickness of dielectric substrate (t)	1.59 mm
Substrate used	Rogers RT/duriod 5880 ($\varepsilon_r = 2.2$)
$l_1 \times w_1$	26.0 × 3.0 mm^2
$l_2 \times w_2$	20.0 × 3.0 mm^2
$l_3 \times w_3$	30.0 × 20.0 mm^2
Conducting strip ($w_s \times l_s$)	4.0 × 12.5 mm^2
$c \times d$	12.0 × 7.0 mm^2
c_1	11.0 mm
c_2	16.0 mm
g	4.0 mm
s	3.0 mm

Equivalent circuit for the modified L-probe

The modified L-probe can be considered as two sections, one is vertical probe and another is horizontal strip. Lumped elements of each section contribute in the total impedance of the antennas.

Vertical probe: From Fig. 2(a), the vertical probe can be analyzed as a series combination of resistance R_v and inductance L_v and can be given as [17]

$$R_v = \frac{\sqrt{\pi f \mu/\sigma}}{d_p}(H+t), \tag{1}$$

where μ = permeability of the probe conductor, f = frequency in GHz, d_p = diameter of probe and

$$L_v = 2.032(h+t)\left[\ln\frac{(H+t)}{d_p} + 0.2235\frac{d_p}{(H+t)} + 1.193\right] nH. \tag{2}$$

Horizontal strip: A series combination of distributive resistance R_s and inductance L_s is developed due to horizontal conducting strip and can be given as [18].

$$L_s = 0.2(H+t)\left[\ln\left\{\frac{2(H+t)}{w_s+t_s}\right\} + 0.2235\left\{\frac{w_s+t_s}{(H+t)}\right\} + 0.5\right](nH), \tag{3}$$

$$R_s = 4.13\times10^{-3}(H+t)\frac{\sqrt{f\rho_0}}{(w_s+t_s)} \text{ with } f \text{ in GHz}. \tag{4}$$

Here, w_s = width of the strip, t_s = thickness of the strip, ρ_0 = ratio of the specific resistance of strip and copper.

The distributive capacitance C_{sp} between the horizontal strip and the radiating patch can be given as:

$$C_{sp} = \frac{\varepsilon_r \varepsilon_0 l_s w_s}{t}. \tag{5}$$

Downloaded from https://www.cambridge.org/core. University of Winnipeg, on 03 Dec 2018 at 14:52:43, subject to the Cambridge Core terms of use, available at https://www.cambridge.org/core/terms.
https://doi.org/10.1017/S175907871800154X

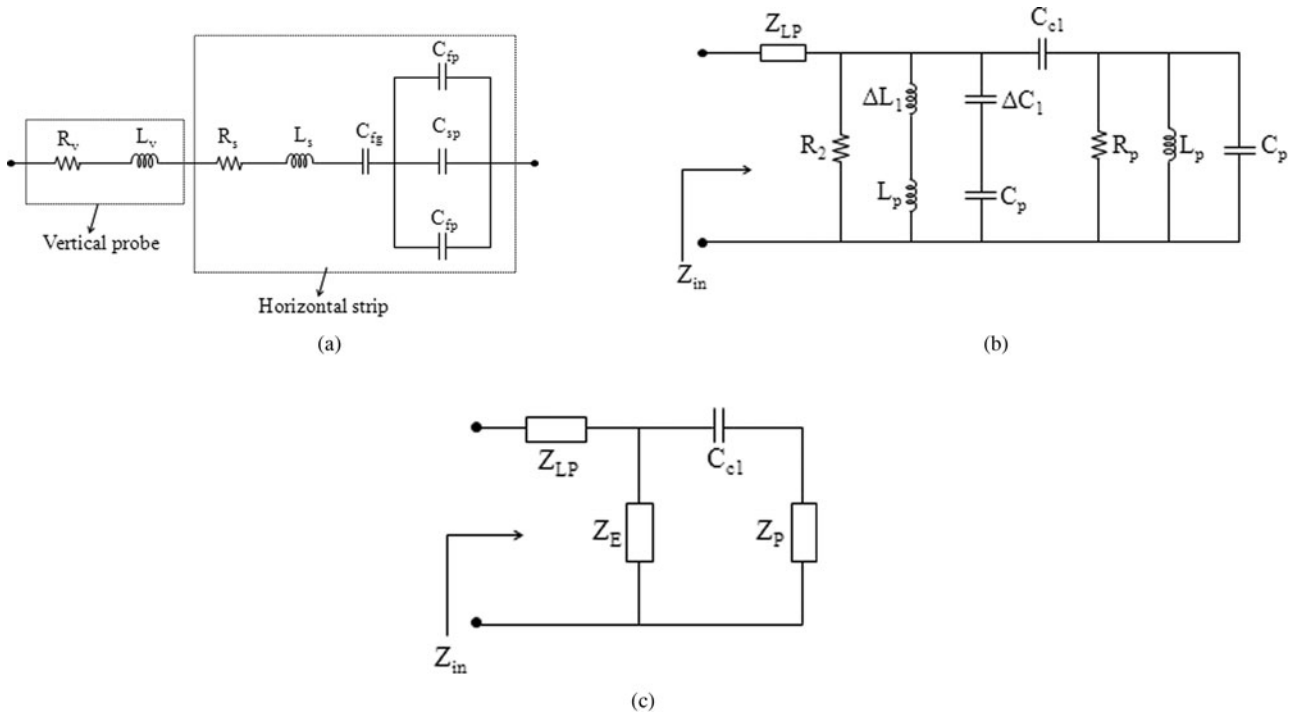


Fig. 2. (a) Equivalent circuit of modified L-probe (b) equivalent circuit of antenna-I and (c) modified circuit of (b).

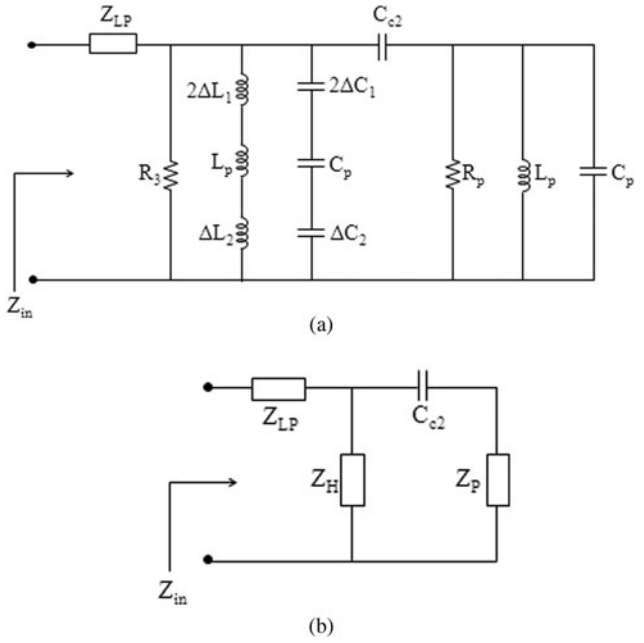


Fig. 3. (a) Equivalent circuit of antenna-II and (b) modified circuit of antenna-II.

Since the open ends of the horizontal strip above the radiating patch will have a fringing field, the effective length of the strip is increased. The increment of length will cause some extra capacitance which is fringing capacitance and it can be calculated as:

$$C_f = \frac{l_e \varepsilon_e^{-1/2}}{cZ_0} \tag{6}$$

here,

$$l_e = \frac{0.412\mathrm{h}(\varepsilon_e + 0.3)(w_s/h + 0.264)}{(\varepsilon_e - 0.258)(w_s/h + 0.8)},$$

in which, ε_e is the effective dielectric constant for the material under conducting strip [17]. The fringing capacitance C_{fp} between the open end of the strip and the patch is calculated by putting the substrate height $h = t$ and the fringing capacitance C_{fg} can be given by putting $h = (H + t)$. The entire feeding acts as a series L–C resonant element and connected in series with the radiating patch.

Equivalent circuit for antenna-I and antenna-II

The antenna-I is realized by introducing two parallel slits in the radiating edge and symmetrical with respect to the horizontal strip. This radiating structure is considered equivalent to two resonators, one as an original patch and another as a modified patch with additional series inductor ΔL_1 and capacitance ΔC_1 with the initial inductance L_p and capacitance C_p of the origin patch. The value of ΔL_1 and ΔC_1 can be given by [19, 20]. Now, these two resonators are coupled through the coupling capacitance C_{c1} (Fig. 2b) and its value can be given as:

$$C_{c1} = \frac{-(C_p + C') + \sqrt{((C_p + C')^2 - 4C_pC'(1 - (1/C_m^2)))}}{2}, \tag{7}$$

here,

$$C' = \frac{\Delta C_1 C_p}{\Delta C_1 + C_p},$$

$$C_m = \frac{1}{\sqrt{Q_1 Q_2}},$$

where Q_1 and Q_2 are the quality factors of the two resonators.

Downloaded from https://www.cambridge.org/core. University of Winnipeg, on 03 Dec 2018 at 14:52:43, subject to the Cambridge Core terms of use, available at https://www.cambridge.org/core/terms.
https://doi.org/10.1017/S175907871800154X

The microstrip patch is considered as a parallel combination of resistance (R_p), inductance (L_p) and capacitance (C_p) and the corresponding values are given as [18].

$$C_p = \frac{\varepsilon_0 \varepsilon_e \mathrm{LW}}{2\mathrm{H}} \cos^{-2}\left(\frac{L_s \pi}{L}\right), \tag{8}$$

$$L_p = \frac{1}{\omega^2 C_p}, \tag{9}$$

$$R_p = \frac{Q_r}{\omega C_p}. \tag{10}$$

In the proposed geometry, the effective dielectric constant for the fed patch is calculated by [21]:

$$\varepsilon_e = \frac{\varepsilon_{rs}+1}{2} + \frac{\varepsilon_{rs}-1}{2}\left(1+\frac{12H}{W}\right)^{-1/2}, \tag{11}$$

where, "H" is the thickness between ground and slotted patch, and

$$\varepsilon_{rs} = \frac{\sum_{i=1}^{n} h_i}{\sum_{i=1}^{n} \frac{h_i}{\varepsilon_{ri}}},$$

where n is the number of stacked layers.

The equivalent circuit of the modified L-probe fed antenna-I is shown in Fig. 2(b). The input impedance for this antenna can be calculated using Fig. 2(c).

$$Z_{in} = Z_{LP} + Z'', \tag{12}$$

where,

$$Z_{LP} = R_v + j\omega L_v + R_s + j\omega L_s + \frac{1}{j\omega C_{eq}}, \tag{13}$$

in which,

$$C_{eq} = \frac{(C_{fg})(2C_{fp}+C_{sp})}{(C_{fg}+2C_{fp}+C_{sp})},$$

and

$$Z'' = \frac{Z_E Z'}{Z_E + Z'},$$

where,

$$Z' = \frac{1}{j\omega C_{c1}} + Z_p,$$

$$Z_E = \frac{1}{(1/R_2) + (1/j\omega(L_p+\Delta L_1)) + j\omega C_{eq1}},$$

$$C_{eq1} = \frac{C_p \Delta C_1}{C_p + \Delta C_1},$$

$$Z_p = \frac{1}{(1/R_p) + (1/j\omega L_p) + j\omega C_p}.$$

The circuit diagram of antenna-II is shown in Fig. 3. For antenna-II, the input impedance Z_{in} is calculated as:

$$Z_{in} = Z_{LP} + Z_1'', \tag{14}$$

where,

$$Z_1'' = \frac{Z_H Z_1'}{Z_H + Z_1'},$$

$$Z_1' = \frac{1}{j\omega C_{c2}} + Z_p,$$

and

$$Z_H = \frac{1}{(1/R_3) + (1/j\omega(L_p + 2\Delta L_1 + \Delta L_2)) + j\omega C_{eq2}},$$

in which,

$$C_{eq2} = \frac{\Delta C_1 C_2 C_p}{C_2 C_p + \Delta 2 C_1 C_2 + 2 C_1 C_p},$$

here, C_{c2} can be calculated using equation 7 and Fig. 3(a).

Now, the return loss and voltage standing wave ratio (VSWR) can be obtained for both the antennas as:

$$\text{Reflection coefficient } (\Gamma) = \left|\frac{Z_{in}-Z_0}{Z_{in}+Z_0}\right|, \tag{15}$$

$$\text{VSWR} = \frac{1+|\Gamma|}{1-|\Gamma|}, \tag{16}$$

$$\text{Return loss (dB)} = 20\log\left|\frac{Z_{in}-Z_0}{Z_{in}+Z_0}\right|. \tag{17}$$

Antenna fabrications

The radiating patch is printed on substrate RT Duroid 5880 with the thickness 1.59 mm. The patch is separated by air gap spacing of 10 mm from the ground plane. The fabricated antenna is shown in Fig. 4. The patch is electromagnetically coupled by a conducting strip connected with the probe. This conducting strip of dimensions $l_s \times w_s$ is printed above the radiating patch and both are separated by a dielectric substrate of thickness $t =$ 1.59 mm. Such feeding method is more convenient than the conventional L-strip fed patch. The perturbed structure introduces some additional current to flow in the patch which causes the

Downloaded from https://www.cambridge.org/core. University of Winnipeg, on 03 Dec 2018 at 14:52:43, subject to the Cambridge Core terms of use, available at https://www.cambridge.org/core/terms.
https://doi.org/10.1017/S175907871800154X

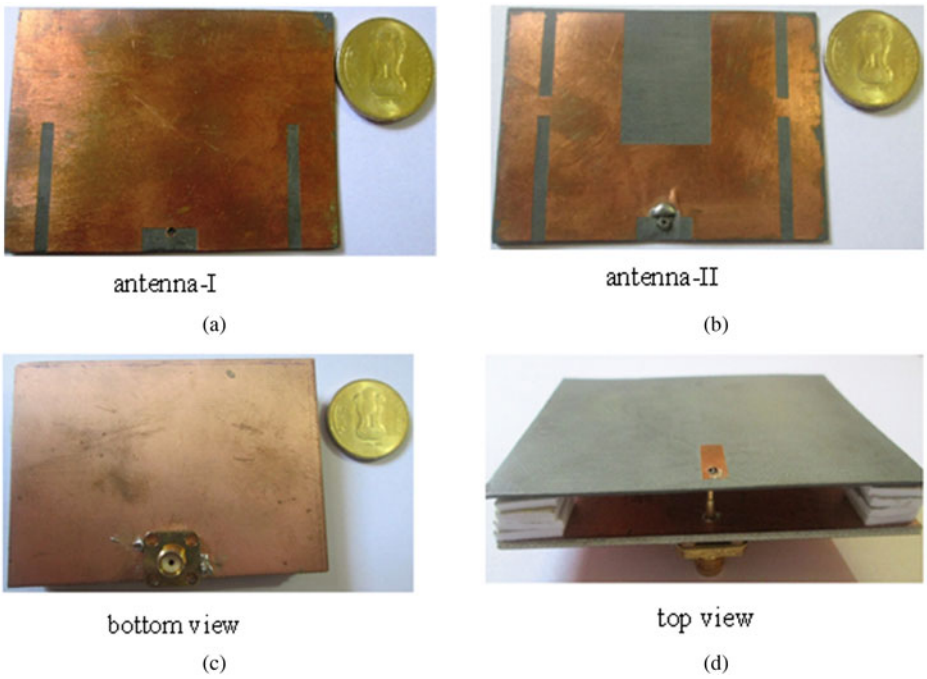


Fig. 4. Prototype of the fabricated antenna (a) antenna-I (b) antenna-II (c) bottom view (d) top view.

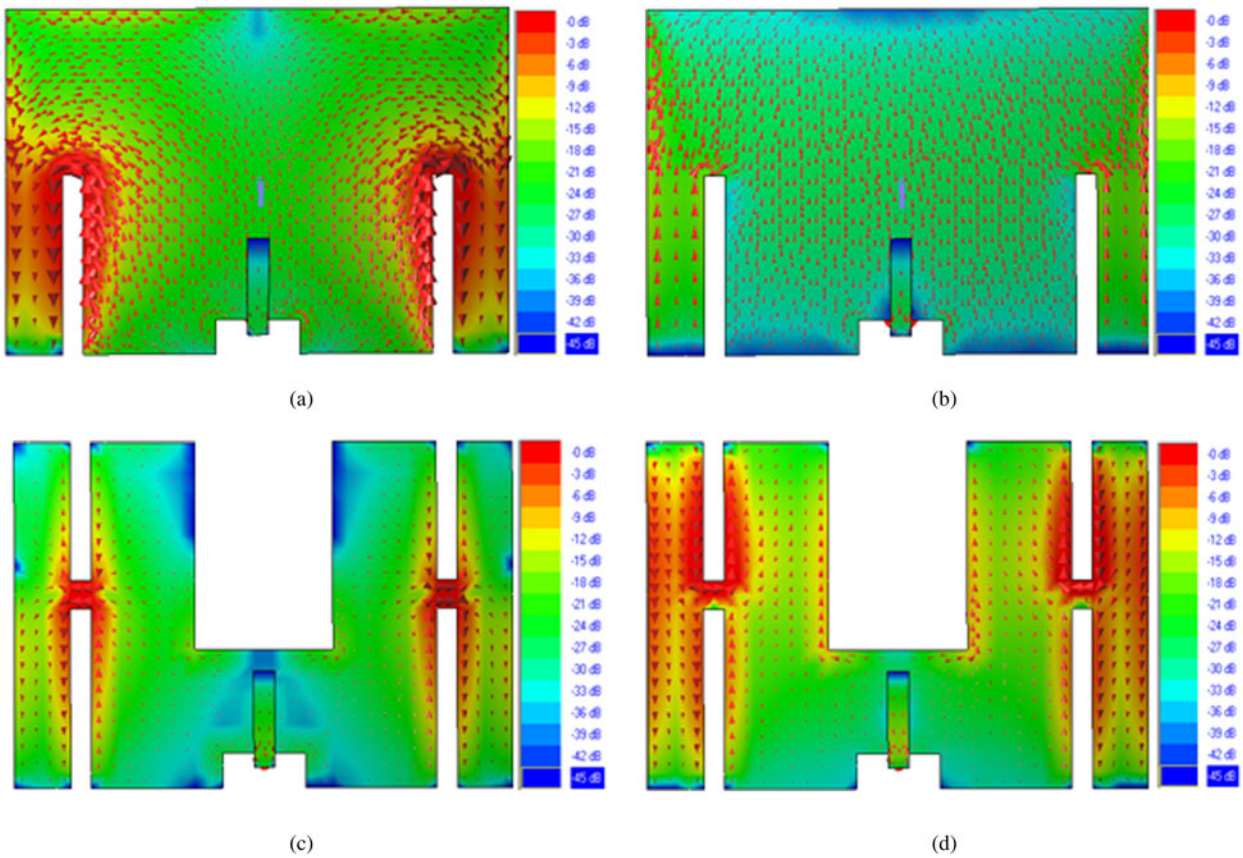


Fig. 5. Current distribution using IE3D at two resonant frequencies 2.1 and 2.5 GHz for antenna-I (a) and (b), and for antenna-II (c) and (d).

higher modes to shift closer and hence a wideband characteristics of the antenna is observed. Therefore, the current distributions on the two antennas are shown in Fig. 5 at two resonant frequencies 2.1 and 2.5 GHz, respectively. From this figure, it is clear that the current length can be optimized by introducing some notches along the radiating edges. The dimensions of the notches are taken in such a way so that the wideband nature of the antenna can be realized. The current distribution curves indicate that the

Downloaded from https://www.cambridge.org/core. University of Winnipeg, on 03 Dec 2018 at 14:52:43, subject to the Cambridge Core terms of use, available at https://www.cambridge.org/core/terms.
https://doi.org/10.1017/S175907871800154X

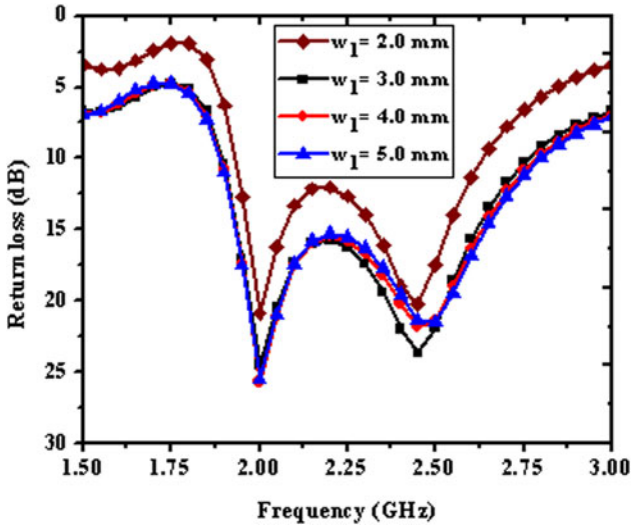


Fig. 6. Variation of return loss with frequency for different value of w_1 (l_1 = 26.0 mm is fixed) for antenna-I.

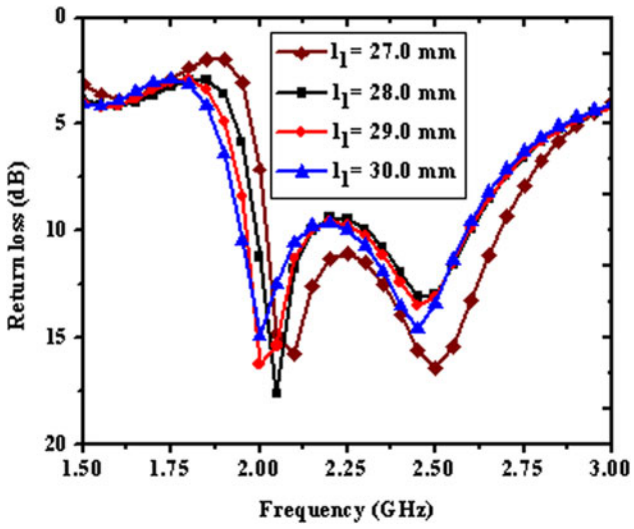


Fig. 7. Variation of return loss with frequency for different values of l_1 (w_1 = 3.0 mm is fixed) for antenna-I.

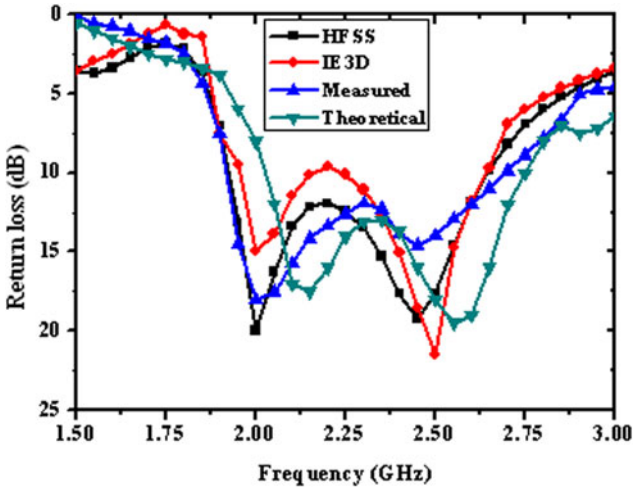


Fig. 8. Comparative graph of return loss with frequency for antenna-I, (w_1 = 3.0 mm and l_1 = 26.0 mm).

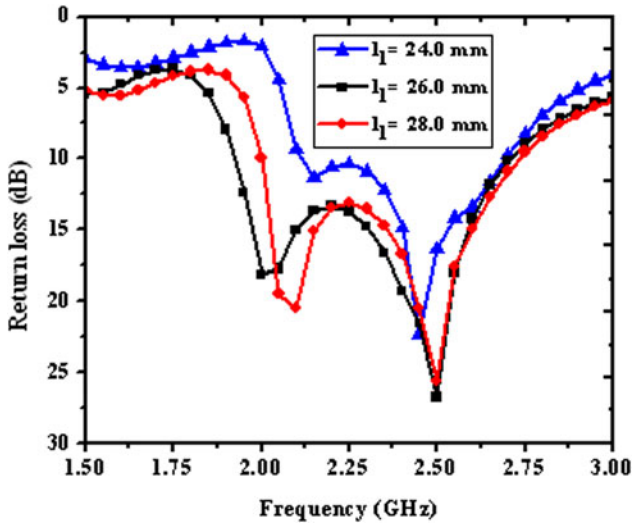


Fig. 9. Variation of return loss with frequency for different values of l_1 (l_2 = 20.0 mm, $w_1 = w_2$ = 3.0 mm) for antenna-II.

lower resonance is produced by two parallel notches in the patch while the higher one is created due to the combined effect of the initial patch and the notches.

Results and discussion

It is noted that all the antenna parameters are calculated using HFSS simulator for antenna-I and antenna-II. For antenna-I, the variation of return loss with frequency for different values of notch width (w_1) is shown in Fig. 6. From the figure, it is observed that the bandwidth increases as w_1 increases. It is found that as notch length l_1 increases (for a given value of w_1 = 3.0 mm) the operational frequency band shifts towards the lower side with a slight increase in bandwidth as shown in Fig. 7. The operational frequency band for antenna-I, calculated using HFSS, extends from 1.91–2.66 GHz and bandwidth obtained is 32.82%. The fabricated antenna is measured using Vector Network Analyzer with model type-Agilent N5230A. The measured bandwidth for antenna-I is found to vary from 1.92–2.67 GHz (32.68%). Theoretical and simulated return loss results are compared with the measured results which are in good agreement (Fig. 8). Return loss is also plotted for antenna-II in Fig. 9 and it is observed that the bandwidth significantly increases with the increasing value of l_1. Similar results are also found in case of increasing value of l_2 (Fig. 10).

From Fig. 11, it is found that the bandwidth marginally increases as the length of center notch l_3 increases, however; the patch size is reduced upto 30% as compared with the conventional rectangular patch. Thus, for a particular dimension, one can achieve a miniaturized antenna with appreciable bandwidth. The results for antenna-II obtained from HFSS, IE3D, and proposed theory are in agreement with the measured results (Fig. 12). The operational frequency band for this antenna, calculated using HFSS, is varying from 1.93 to 2.83 GHz and the bandwidth obtained is 37.82%. The measured frequency band for antenna-II is found to vary from 1.94 to 2.74 GHz (34.19%).

Downloaded from https://www.cambridge.org/core. University of Winnipeg, on 03 Dec 2018 at 14:52:43, subject to the Cambridge Core terms of use, available at https://www.cambridge.org/core/terms.
https://doi.org/10.1017/S175907871800154X

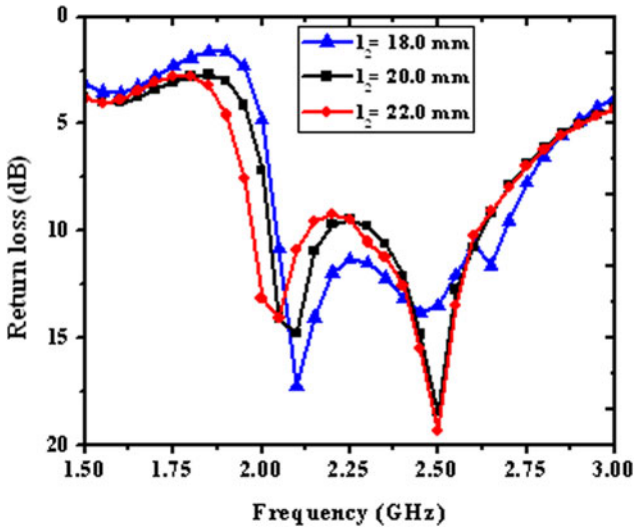


Fig. 10. Variation of return loss with frequency for different values of l_2 (l_1 = 26.0 mm, $w_1 = w_2$ = 3.0 mm) for antenna-II.

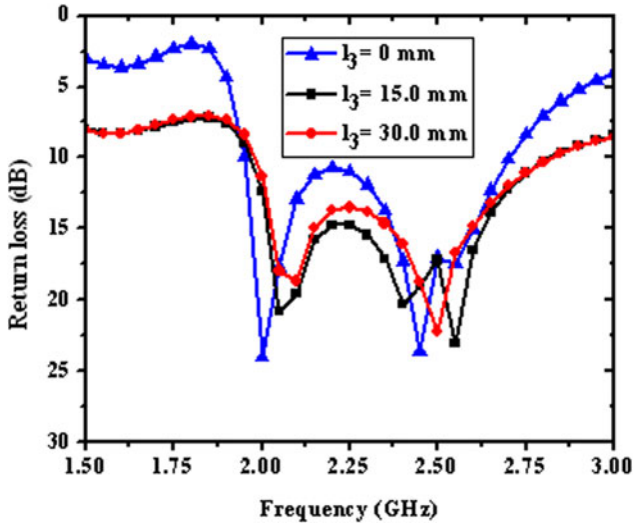


Fig. 11. Variation of return loss with frequency for different values of l_3 (w_3 = 20.0 mm is fixed) for antenna-II.

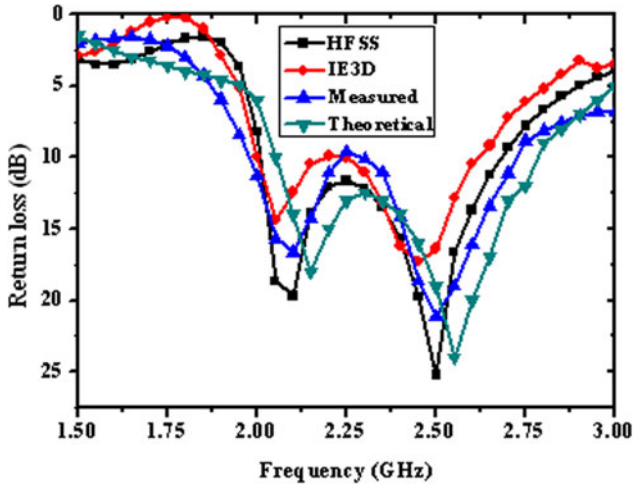


Fig. 12. Comparative plot of return loss with frequency for antenna-II (l_3 = 30 mm, w_3 = 20.0 mm, l_1 = 26 mm, $w_1 = w_2$ = 3 mm).

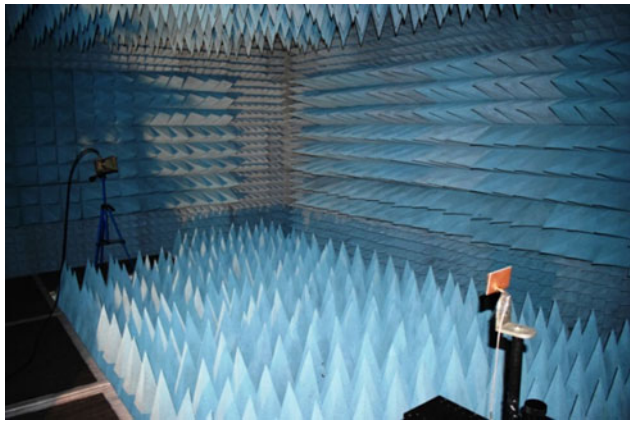


Fig. 13. Gain measurement setup.

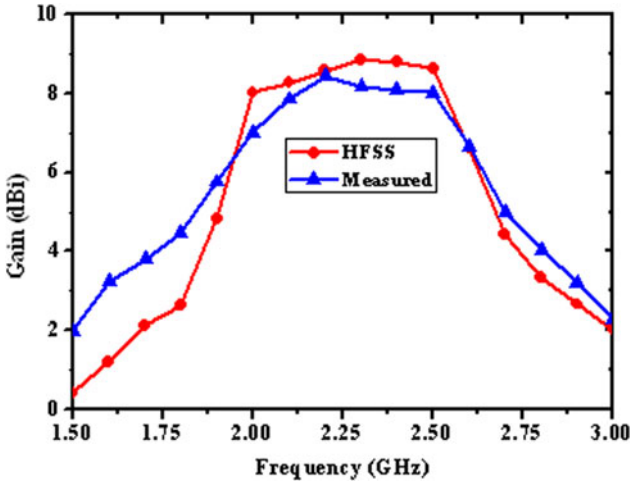


Fig. 14. Measured gain for antenna-I.

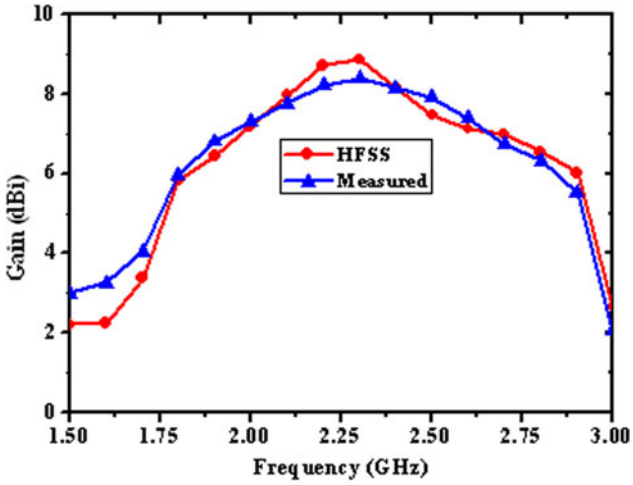


Fig. 15. Measured gain for antenna-II.

Downloaded from https://www.cambridge.org/core. University of Winnipeg, on 03 Dec 2018 at 14:52:43, subject to the Cambridge Core terms of use, available at https://www.cambridge.org/core/terms.
https://doi.org/10.1017/S175907871800154X

Table 2. Comparison of the proposed antennas with earlier reported antennas.

Ref. No.	Patch dimensions (mm^2)	Bandwidth (GHz)	Bandwidth (%)	Antenna Gain (dBi)
[13]	72 × 50	1.92–2.51	26.50	7.8
[14]	120 × 60	1.17~0.89	26.70	7.0
[15]	76.4 × 76.4	2.02–2.88	36.00	2.0
[16]	56.7 × 56.7 (Parasitic), 48.6 × 48.6 (Radiating)	1.66–2.27	30.00	7.5
Proposed (Antenna-I)	72 × 50	1.92–2.67	32.68	8.43
Proposed (Antenna-II)	72 × 50	1.94–2.74	34.19	8.39

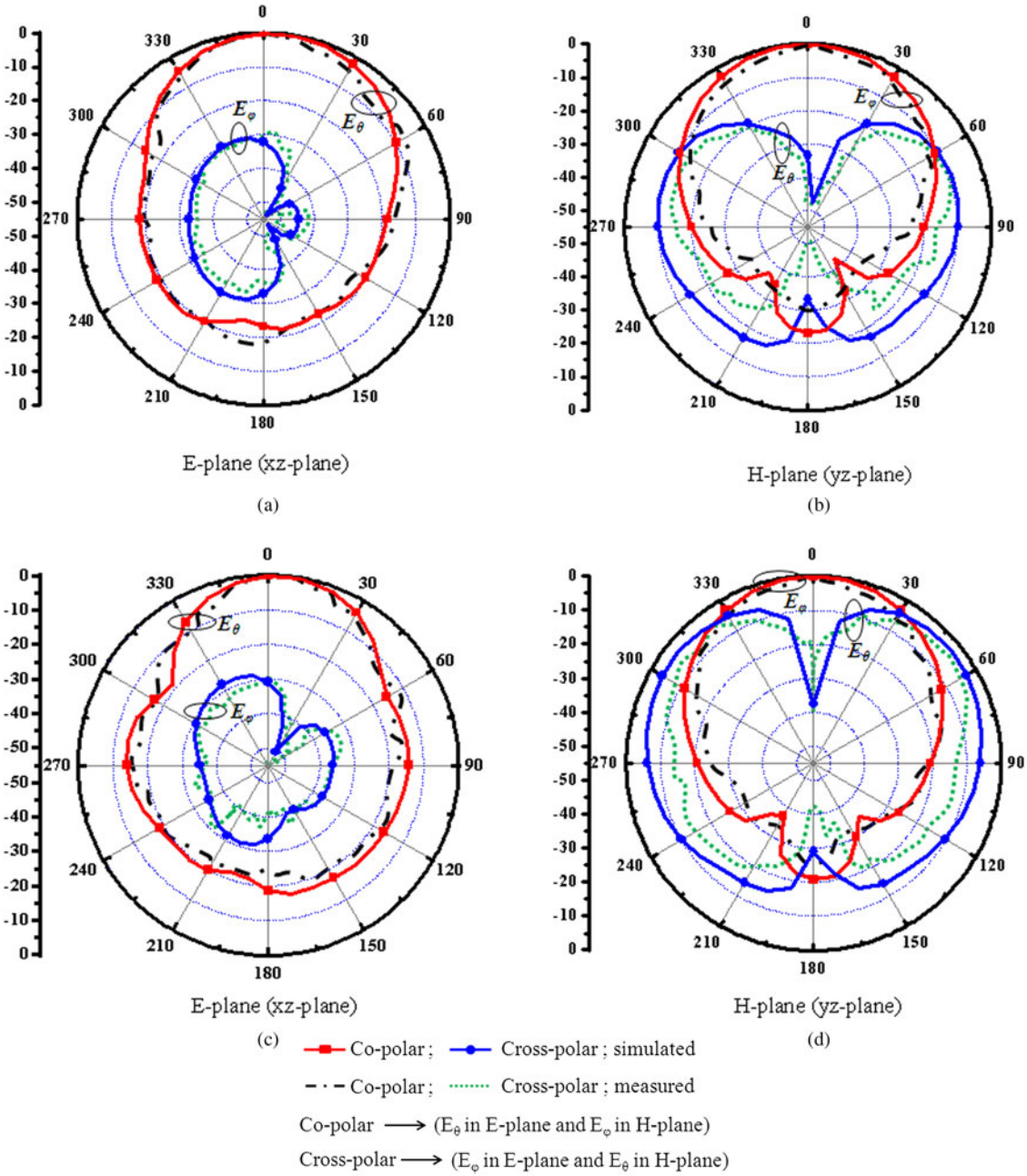


Fig. 16. Simulated (HFSS) and measured radiation pattern of antenna–I at $f = 2.1$ GHz (a and b) and at $f = 2.5$ GHz (c and d).

Downloaded from https://www.cambridge.org/core. University of Winnipeg, on 03 Dec 2018 at 14:52:43, subject to the Cambridge Core terms of use, available at https://www.cambridge.org/core/terms.
https://doi.org/10.1017/S175907871800154X

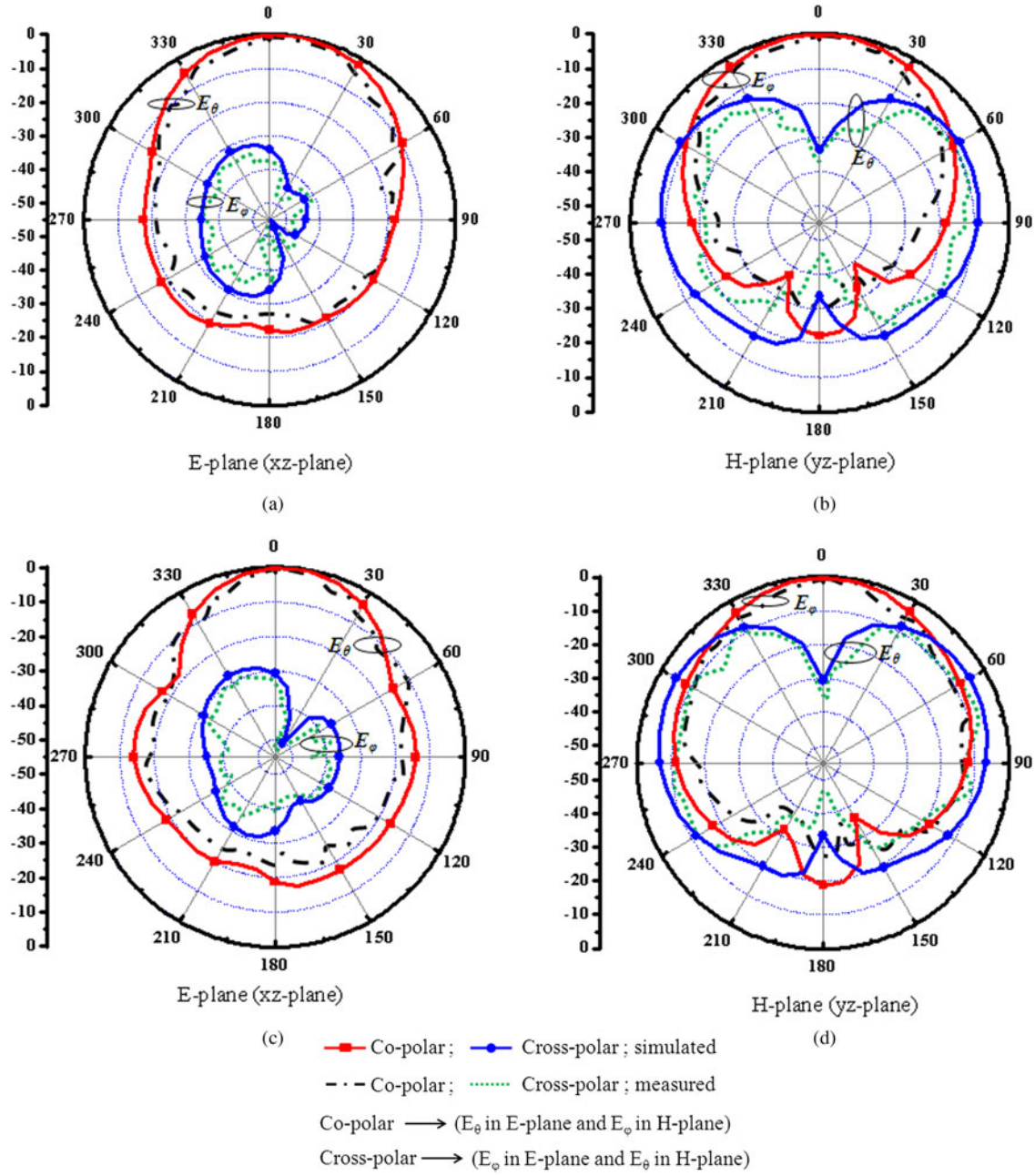


Fig. 17. Simulated (HFSS) and measured radiation pattern of antenna–II at $f = 2.1$ GHz (a and b) and at $f = 2.5$ GHz (c and d).

Some deviation in the simulated and measured results is due to fabrication imperfection and the misalignment of SMA connector. The gain measurement is performed inside an in-house anechoic chamber of physical dimensions $7.0 \times 5.0 \times 3.0$ m^3 and shown in Fig. 13. A Dual Ridge Horn Antenna (DRH20) of size $56 \times 41 \times 18$ cm^3 is used for the gain measurement. The gains of antenna-I and antenna-II are measured from 1.5 to 3.0 GHz with an equal frequency interval of 0.1 GHz. Measured gains for both the antennas are shown in Figs 14 and 15, respectively. The discrepancy between simulated and measured gain of antennas may be due to the fact that no near-field to far-field correction is applied for the direct measurement. Another reason is due to the use of DRH horn antenna which is somewhat not suitable for such type of correction. It is observed that the gain is always above 6.5 dBi for the entire band of operation. The maximum measured gain for antenna-I and antenna-II are 8.43 and 8.39 dBi, respectively. The measured average gain for antenna-I and antenna-II are calculated and found to be 7.23 and 7.63 dBi, respectively. The comparisons of the proposed antennas performance are illustrated in Table 2. The proposed antennas exhibit sufficient bandwidth and high gain as compared with the earlier reported antennas.

The radiation patterns measured for antenna-I and II are plotted in Figs 16 and 17 at $\varphi = 0^0$ (E plane) and $\varphi = 90^0$ (H plane) for two resonant frequencies (2.1 and 2.5 GHz), respectively. The cross-polarization level is quite low as compared with co-polarization level for both the antennas at $\varphi = 0°$ and $\varphi = 90°$. The radiation patterns of the proposed antennas are symmetrical, broadside in nature and linearly polarized. E and H plane half power beamwidths (HPBW) is measured for both the antennas

Downloaded from https://www.cambridge.org/core. University of Winnipeg, on 03 Dec 2018 at 14:52:43, subject to the Cambridge Core terms of use, available at https://www.cambridge.org/core/terms.
https://doi.org/10.1017/S175907871800154X

at 2.1 and 2.5 GHz, respectively. For antenna-I, the *E* and *H* plane HPBW are 57.8° and 61° at 2.1 GHz and 45.48° and 58.68° at 2.5 GHz, respectively. For antenna-II, the *E* and *H* plane beamwidths are 58.14° and 63.05° at 2.1 GHz and 45.41° and 54.24° at 2.5 GHz, respectively. Also, it is noted that the simulated and measured values of beamwidths are in good agreement.

Conclusion

A modified L-strip feeding technique is used to study the slotted patch antennas. The circuit theory is successfully implemented to calculate the antenna parameters. From this study it is inferred that the antenna bandwidth is function of dimensions of the notches incorporated in the patch. Antenna size is also reduced along with the enhancement of bandwidth. Radiation pattern is stable and gain is acceptable across the entire operational band. The dimension of conducting strip may also be the key parameters for further improvement in the antenna performance, which is not studied in the present paper. The proposed antennas can be used for WiFi/Bluetooth, UMTS, radio frequency identification device (RFID) and other communication systems.

Author ORCIDs. Prabhakar Singh, Binod Kumar Kanaujia 0000-0001-8272-3293, 0000-0003-1272-1561.

References

1. **Garg R, Bhartia P, Bahl IJ and Ittipiboon A** (2001) *Microstrip Antenna Design Handbook*. Norwood: Artech House.
2. **Tarange V, Gite T, Musale P and Khobragade SV** (2011) A U-slotted H-shaped micro strip antenna with capacitive feed for broadband application. *International Conference on Emerging Trends in Networks and Computer Communications*, pp. 182–184.
3. **Mondal K and Sarkar PP** (2017) Enhancement of the gain and bandwidth of the microstrip patch antenna with modified ground plane. *International Journal of Microwave and Wireless Technologies* **9**, 1179–1184.
4. **Khidre A, Lee KF, Yang F and Elsherbeni AZ** (2013) Circular polarization reconfigurable wideband E-shaped patch antenna for wireless applications. *IEEE Transactions on Antennas and Propagation* **61**, 960–964.
5. **Liu WC, Chen YL and Wu CM** (2013) A compact wideband strip antenna for wireless USB dongle application. *Microwave and Optical Technology Letters* **55**, 302–304.
6. **Sung Y** (2012) Bandwidth enhancement of a microstrip line-fed printed wide-slot antenna with a parasitic center patch. *IEEE Transactions on Antennas and Propagation* **60**, 1712–1716.
7. **Gautam AK, Bisht A and Kanaujia BK** (2016) A wideband antenna with defected ground plane for WLAN/WiMAX applications. *International Journal of Electronics and Communications* **70**, 354–358.
8. **Singh P and Kumar D** (2011) L-strip proximity fed broadband circular disk patch antenna. *International Journal of Microwave and Optical Technology* **6**, 64–99.
9. **Mak CL, Lee KF and Luk KM** (2000) Broadband patch antenna with a T-shaped probe. *IEE Proceedings – Microwaves, Antennas and Propagation* **147**, 73–76.
10. **. Meshram MK** (2007) Analysis of L-strip proximity fed rectangular microstrip antenna for mobile base station. *Microwave and Optical Technology Letters* **49**, 1817–1824.
11. **Yadav NP, Wu W, Fang DG and Singh P** (2014) L-strip proximity fed C-band half circular disk patch antenna for WLAN network. *International Journal of Microwave and Optical Technology* **9**, 317–324.
12. **Singh AK, Gangwar RK and Kanaujia BK** (2016) Wideband and compact slot loaded annular ring microstrip antenna using L-probe proximity-feed for wireless communications. *International Journal of Microwave and Wireless Technologies* **8**, 1085–1093.
13. **Park J, Na H-G and Baik S-H** (2004) Design of a modified L-probe fed microstrip patch antenna. *IEEE Antennas and Wireless Propagation Letters* **3**, 117–119.
14. **Deshmukh AA and Ray KP** (2009) Compact broadband slotted rectangular microstrip antenna. *IEEE Antennas and Wireless Propagation Letters* **8**, 1410–1413.
15. **Sun X-B, Cao M-Y, Hao J-J and Guo Y-J** (2012) A rectangular slot antenna with improved bandwidth. *International Journal of Electronics and Communications* **66**, 465–466.
16. **Bilgic MM and Yeğin K** (2015) Design of L-plate proximity fed base station antenna element. *International Journal of Microwave and Wireless Technologies* **7**, 205–208.
17. **Bahl IJ and Bhartia P** (1980) *Microstrip Antenna*. Dedham, MA: Artech House.
18. **Hoffman RK** (1987) *Handbook of Microstrip Integrated Circuits*. Norwood, MA: Artech House.
19. **Zhang XX and Yang F** (1998) Study of a slit cut on a microstrip antenna and its applications. *Microwave and Optical Technology Letters* **18**, 297–300.
20. **Bahl I** (2003) *Lumped Elements for RF and Microwave Circuits*. Boston: Artech House, pp. 728–746.
21. **Liu Z-F, Kooi P-S, Li L-W, Leong M-S and Yeo T-S** (1999) A method for designing broad-band microstrip antennas in multilayered planar structures. *IEEE Transactions on Antennas and Propagation* **47**, 1416–1420.



Rakesh Nath Tiwari received his B.Sc. and M.Sc. (Electronics) degree from University of Allahabad and Deen Dayal Upadhyaya Gorakhpur University, Gorakhpur, India in 2002 and 2004, respectively. He received M.Tech. degree in Optical & Wireless Communication Technology from Jaypee University of Information Technology, Waknaghat, Solan, India in 2008. He has published more than 21 papers in peer-reviewed International/National journals and conferences. Currently, he is a Ph.D. scholar in Electronics and Communication Engineering from Uttarakhand Technical University, Dehradun, India. His research interests include design and modeling of slot patch antennas, UWB antennas, microwave/millimeter wave integrated circuits & devices.



Prabhakar Singh was born in village Semara, Chandauli (U.P), India in 1984. He received his B.Sc. and M.Sc. degree from V. B. S. Purvanchal University in 2004 and 2006, respectively. He received his Ph.D. degree from J. K. Institute of Applied Physics, Department of Electronics and Communication, University of Allahabad, India in 2010. He taught B. Tech. and M. Tech. students at Delhi Technological University, Delhi, India for 1 year from 2009 to 2010. He worked as an assistant professor at Bahra University, Shimla Hills, Himanchal Pradesh, India from 2010 to 2011. Presently, he is working at Galgotias University, Greater Noida, India. He has published more than 50 research papers in peer reviewed International/National journals and conference proceedings with more than 400 citations. He is reviewer of many International and National journals. He is presently working on broadband microstrip antennas, size miniaturization techniques in patch antennas, UWB and photonic band gap antennas.



Binod Kumar Kanaujia is working as Professor in School of Computational and Integrative Sciences, Jawaharlal Nehru University, New Delhi since August, 2016. Before joining Jawaharlal Nehru University, he had been in the Department of Electronics & Communication Engineering in Ambedkar Institute of Advanced Communication Technologies & Research (formerly, Ambedkar Institute of Technology), Delhi as a Professor since February 2011& Associate Professor (2008–2011). Earlier, Dr. Kanaujia held the positions of Lecturer (1996–2005), Reader

Downloaded from https://www.cambridge.org/core. University of Winnipeg, on 03 Dec 2018 at 14:52:43, subject to the Cambridge Core terms of use, available at https://www.cambridge.org/core/terms.
https://doi.org/10.1017/S175907871800154X

(2005–2008) and Head of Department in Department of Electronics & Communication Engineering, M.J.P. Rohilkhand University, Bareilly, India. Prior to his career in academics, Dr. Kanaujia had worked as Executive Engineer in the R&D division of M/s UPTRON India Ltd.

Dr. Kanaujia had completed his B.Tech. in Electronics Engineering from KNIT Sultanpur, India in 1994. He did his M.Tech. and Ph.D. in 1998 and 2004; respectively from Department of Electronics Engineering, Indian Institute of Technology Banaras Hindu University, Varanasi, India. He has been awarded Junior Research Fellowship by UGC Delhi in the year 2001–2002 for his outstanding work in the electronics field. He has a keen research interest in design and modeling of microstrip antenna, dielectric resonator antenna, left-handed metamaterial microstrip antenna, shorted microstrip antenna, ultra-wideband antennas, reconfigurable and circular polarized antennas for wireless communication.

He has been credited to publish more than 220 research papers with more than 1000 citations with h-index of 17 in several peer-reviewed journals and conferences. He had supervised 50 M.Tech. and 15 Ph.D. research scholars in the field of microwave engineering. He is a reviewer for several journals of international repute i.e. IET Microwaves, Antennas & Propagation, IEEE Antennas and Wireless Propagation Letters, Wireless Personal Communications, Journal of Electromagnetic Wave and Application, Indian Journal of Radio and Space Physics, IETE Technical Review, International Journal of Electronics, International Journal of Engineering Science, IEEE Transactions on Antennas and Propagation, AEU-International Journal of Electronics and Communication, International Journal of Microwave and Wireless Technologies, etc. Dr. Kanaujia had successfully executed 05 research projects sponsored by several agencies of Government of India i.e. DRDO, DST, AICTE, and ISRO. He is also a member of several academic and professional bodies i.e. IEEE, Institution of Engineers (India), Indian Society for Technical Education and The Institute of Electronics and Telecommunication Engineers of India.

Downloaded from https://www.cambridge.org/core. University of Winnipeg, on 03 Dec 2018 at 14:52:43, subject to the Cambridge Core terms of use, available at https://www.cambridge.org/core/terms.
https://doi.org/10.1017/S175907871800154X
View publication stats

US 20180331738A1

(19) **United States**

(12) **Patent Application Publication** (10) **Pub. No.: US 2018/0331738 A1**

AGRAWAL et al. (43) **Pub. Date: Nov. 15, 2018**

(54) **BEAM FORMING METHOD FOR A TRANSMITTING ANTENNA AND A DEVICE THEREOF**

(71) Applicants: **Samsung Electronics Co., Ltd.**, Suwon-si (KR); **DELHI TECHNOLOGICAL UNIVERSITY**, New Delhi (IN)

(72) Inventors: **Sachin Kumar AGRAWAL**, Ghaziabad (IN); **Kapil SHARMA**, Delhi (IN)

(21) Appl. No.: **15/975,162**

(22) Filed: **May 9, 2018**

(30) **Foreign Application Priority Data**

May 11, 2017 (IN) 201711016629

Publication Classification

(51) **Int. Cl.**

H04B 7/06 (2006.01)

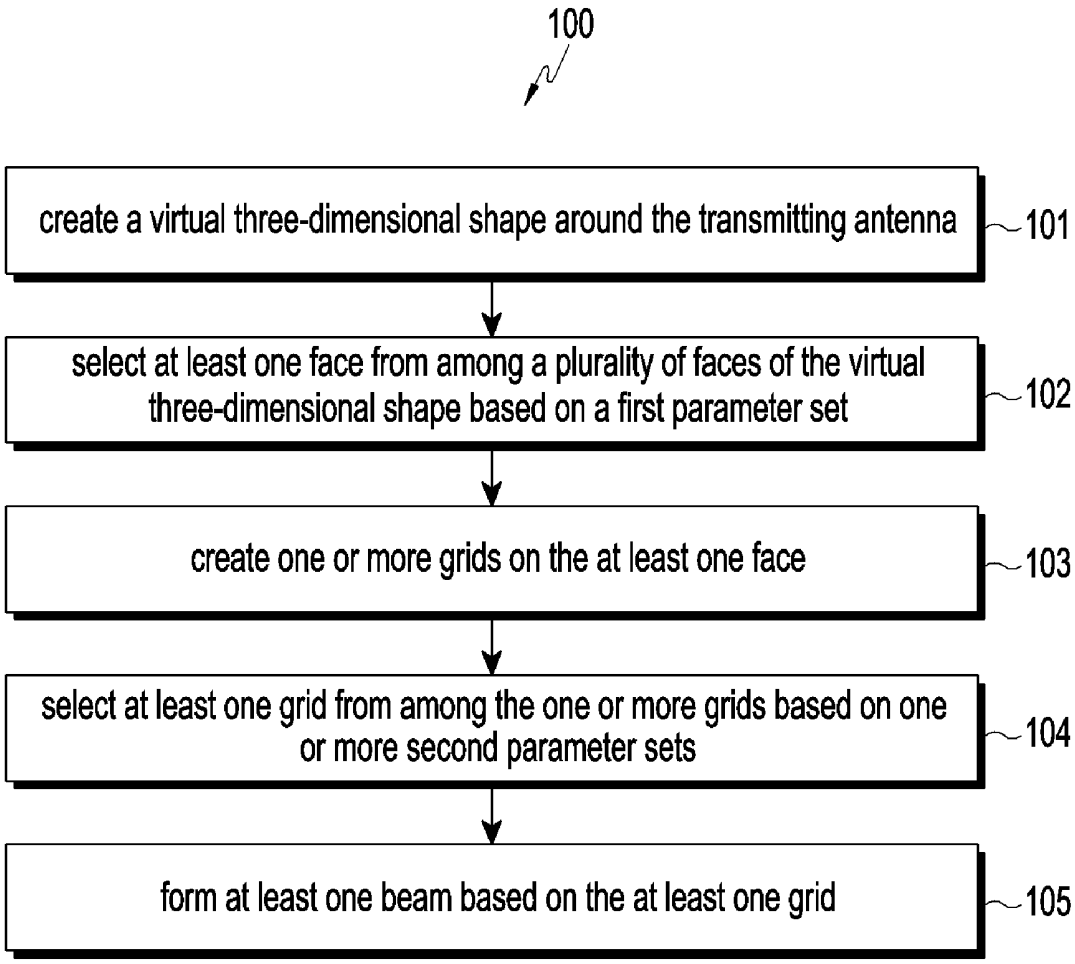
H04B 7/08 (2006.01)

(52) **U.S. Cl.**

CPC ***H04B 7/0608*** (2013.01); ***H04B 7/0617*** (2013.01); *H04B 7/0456* (2013.01); ***H04B 7/0695*** (2013.01); ***H04B 7/0802*** (2013.01)

(57) **ABSTRACT**

A method and a device for beam forming in cellular communication systems are provided. The method includes creating a virtual three-dimensional shape around the transmitting antenna, selecting at least one face from among a plurality of faces of the virtual three-dimensional shape based on a first set of parameters, creating one or more grids on the at least one selected face, selecting at least one grid from among the one or more grids as an optimum grid set based on a second set of parameters, and forming at least one beam based on the at least one grid.



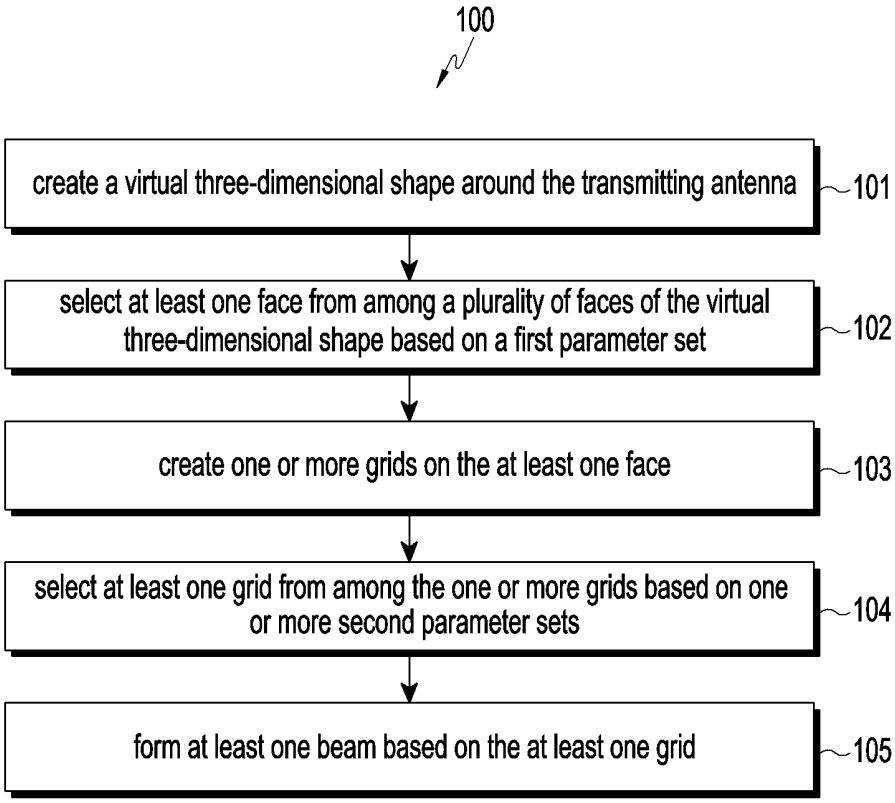

100
create a virtual three-dimensional shape around the transmitting antenna
101
select at least one face from among a plurality of faces of the virtual three-dimensional shape based on a first parameter set
102
create one or more grids on the at least one face
103
select at least one grid from among the one or more grids based on one or more second parameter sets
104
form at least one beam based on the at least one grid
105

FIG.1

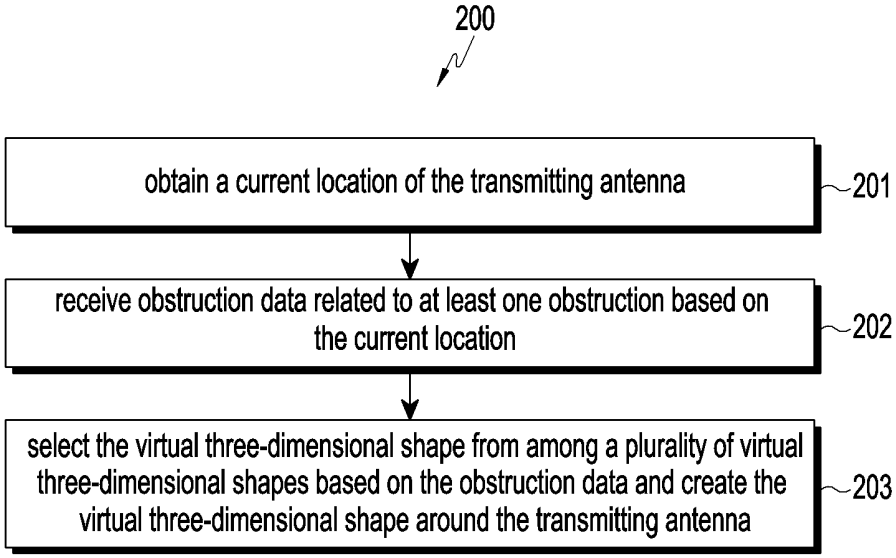

200
obtain a current location of the transmitting antenna
201
receive obstruction data related to at least one obstruction based on the current location
202
select the virtual three-dimensional shape from among a plurality of virtual three-dimensional shapes based on the obstruction data and create the virtual three-dimensional shape around the transmitting antenna
203

FIG.2

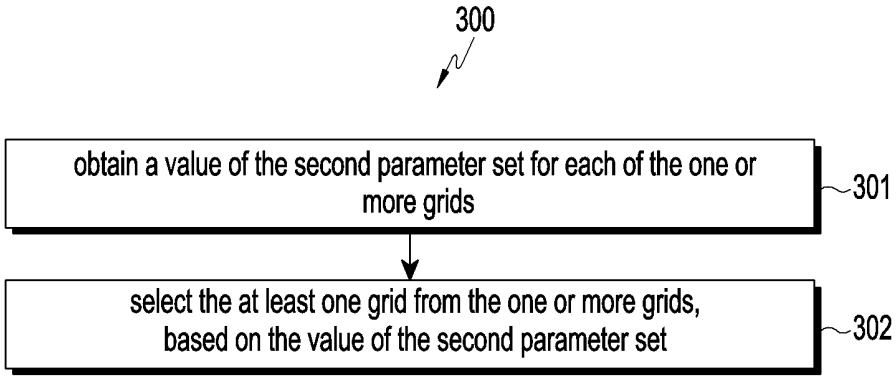

300
obtain a value of the second parameter set for each of the one or more grids
301
select the at least one grid from the one or more grids, based on the value of the second parameter set
302

FIG.3

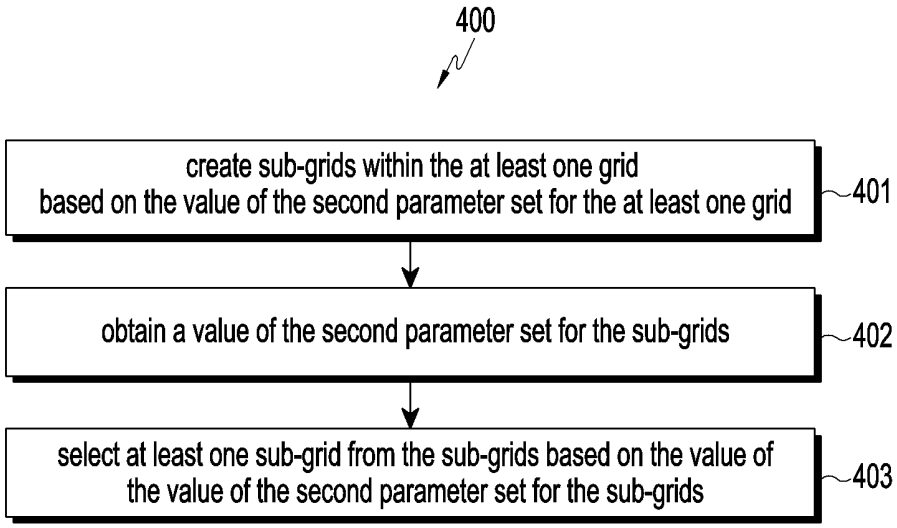

400
create sub-grids within the at least one grid based on the value of the second parameter set for the at least one grid
401
obtain a value of the second parameter set for the sub-grids
402
select at least one sub-grid from the sub-grids based on the value of the value of the second parameter set for the sub-grids
403

FIG.4

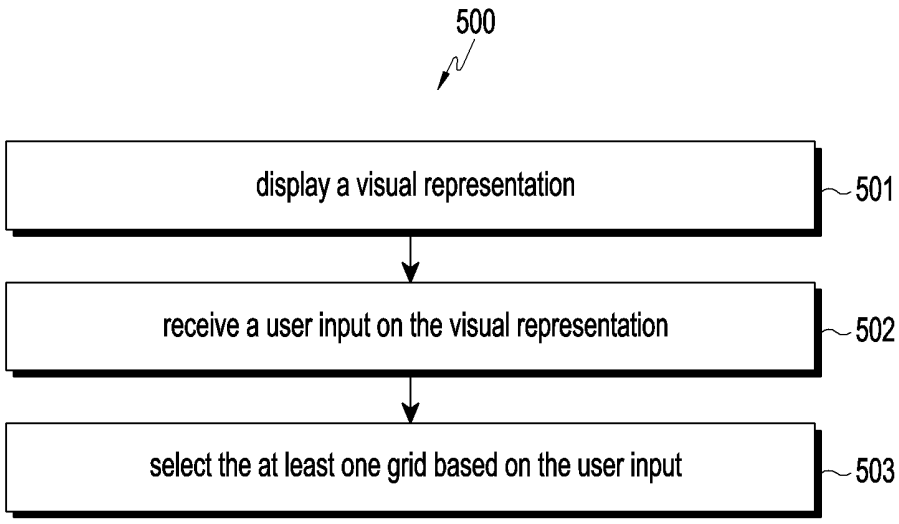

500
display a visual representation
501
receive a user input on the visual representation
502
select the at least one grid based on the user input
503

FIG.5

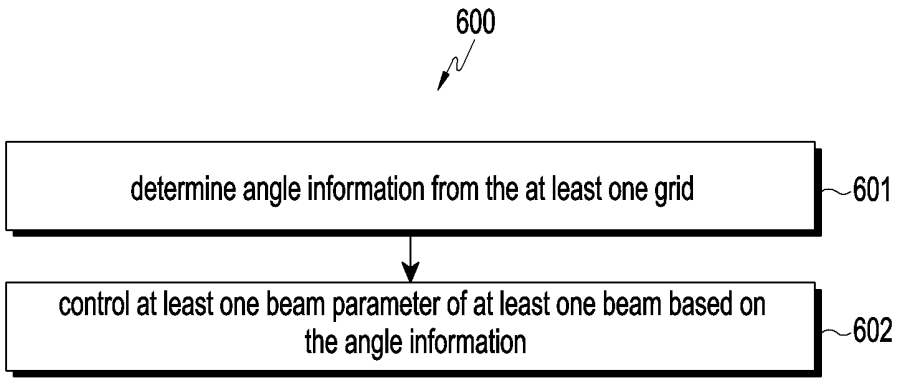

600
determine angle information from the at least one grid
601
control at least one beam parameter of at least one beam based on the angle information
602

FIG.6

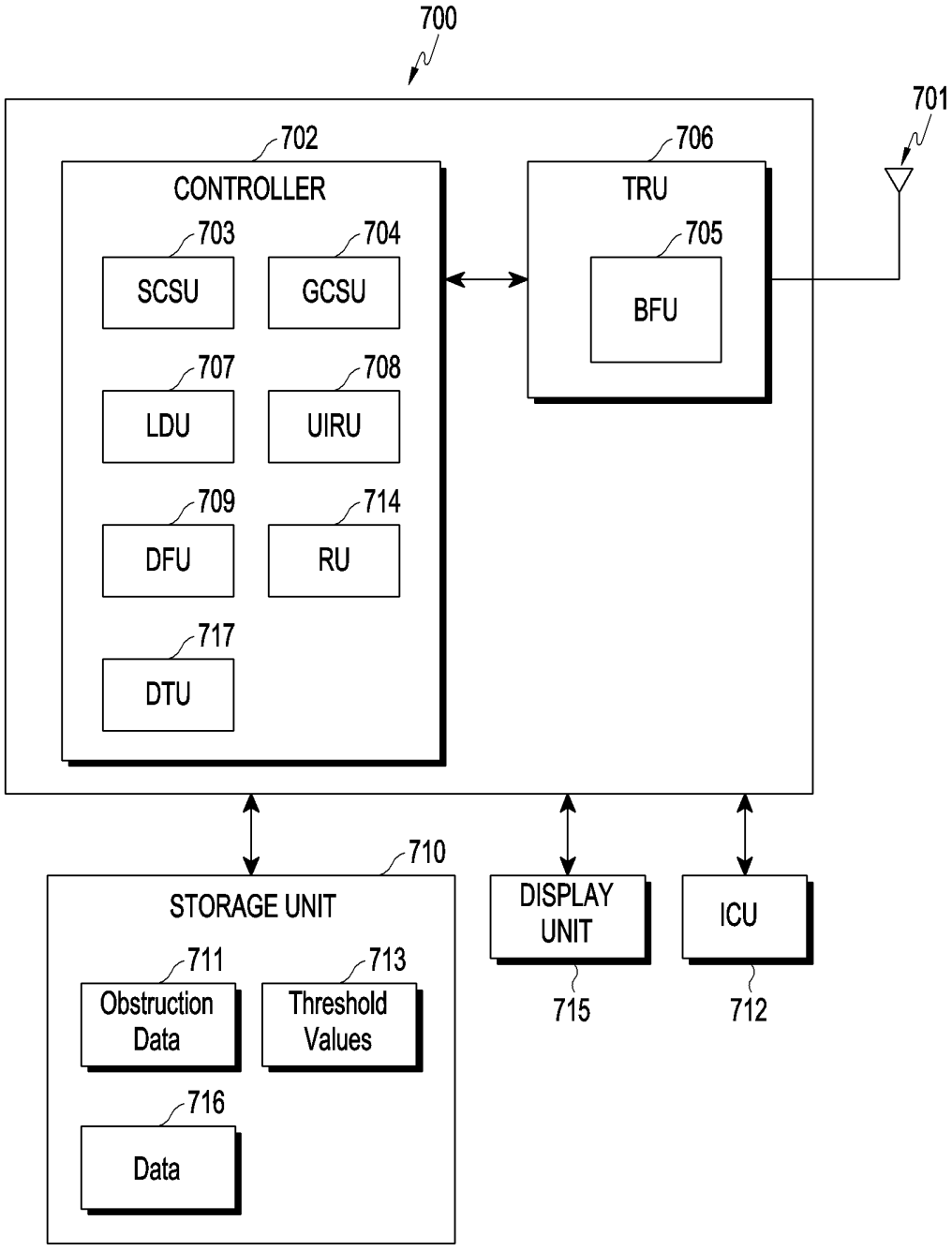

700
701
702
CONTROLLER
703
SCSU
704
GCSU
706
TRU
705
BFU
707
LDU
708
UIRU
709
DFU
714
RU
717
DTU
710
STORAGE UNIT
711
Obstruction Data
713
Threshold Values
716
Data
DISPLAY UNIT
715
ICU
712

FIG.7

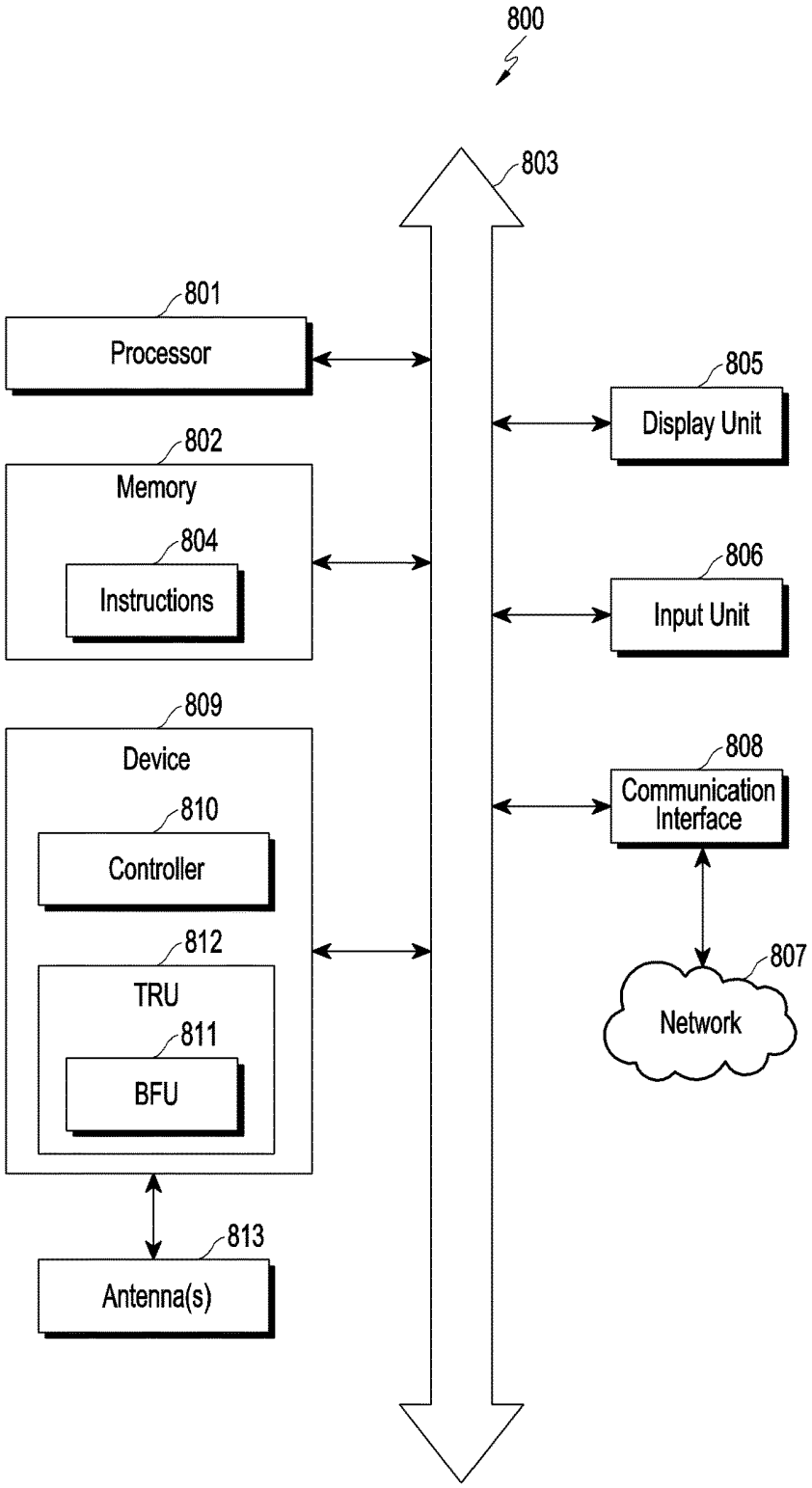

800
803
801
Processor
805
Display Unit
802
Memory
804
Instructions
806
Input Unit
809
Device
808
Communication Interface
810
Controller
812
TRU
807
Network
811
BFU
813
Antenna(s)

FIG.8

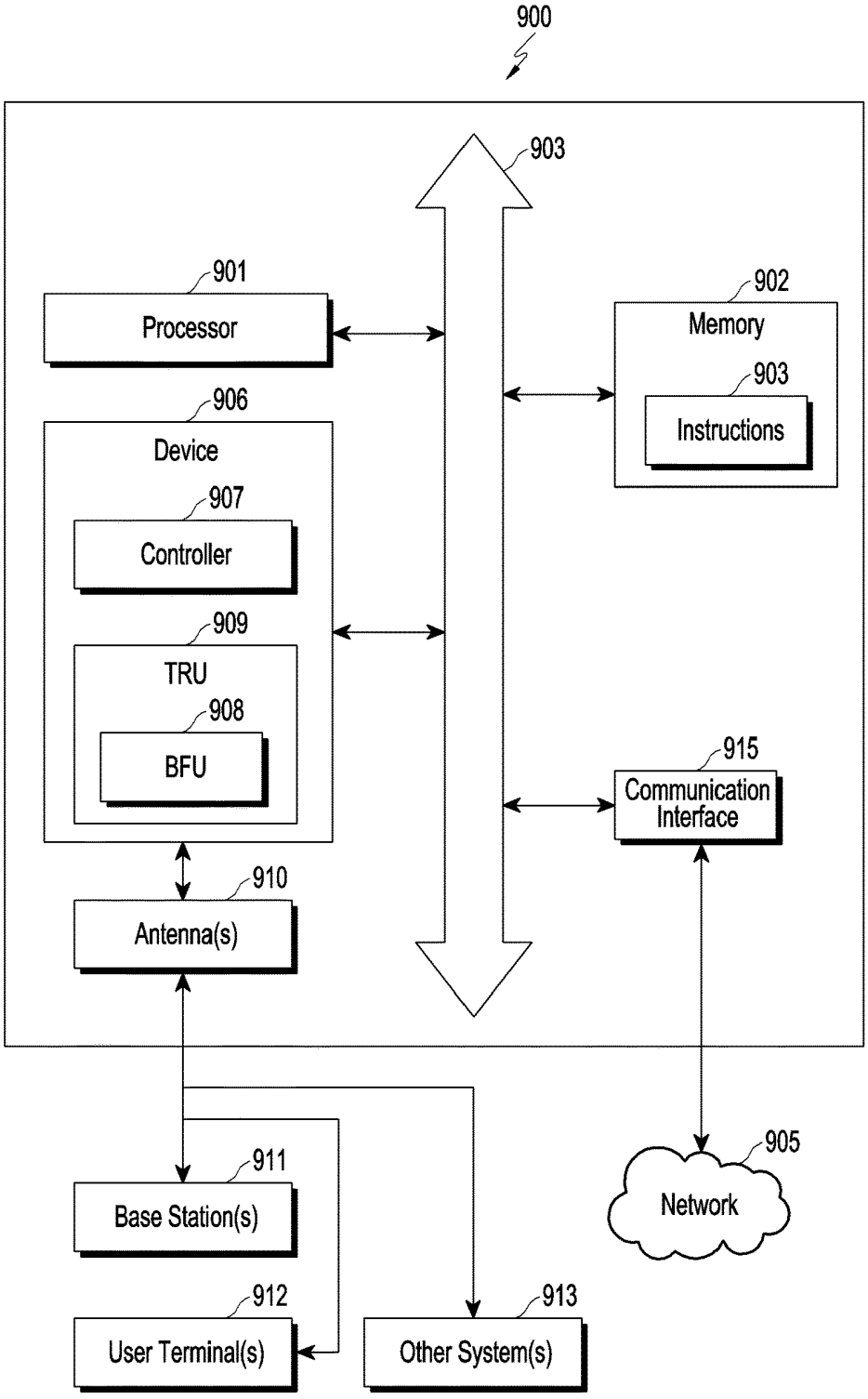

900
903
901
Processor
902
Memory
903
Instructions
906
Device
907
Controller
909
TRU
908
BFU
915
Communication Interface
910
Antenna(s)
905
Network
911
Base Station(s)
912
User Terminal(s)
913
Other System(s)

FIG.9

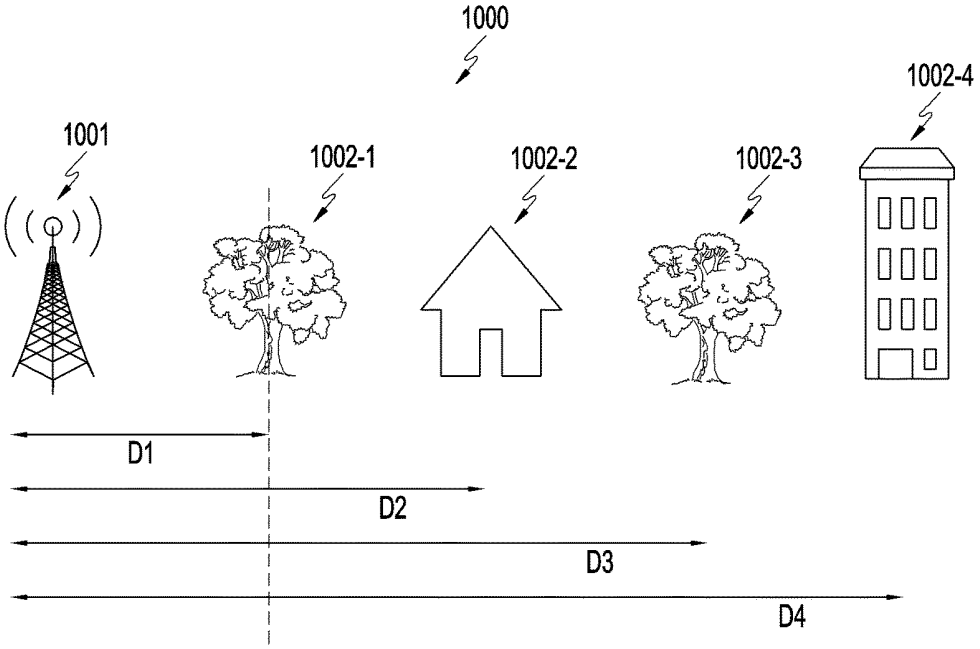


FIG.10A

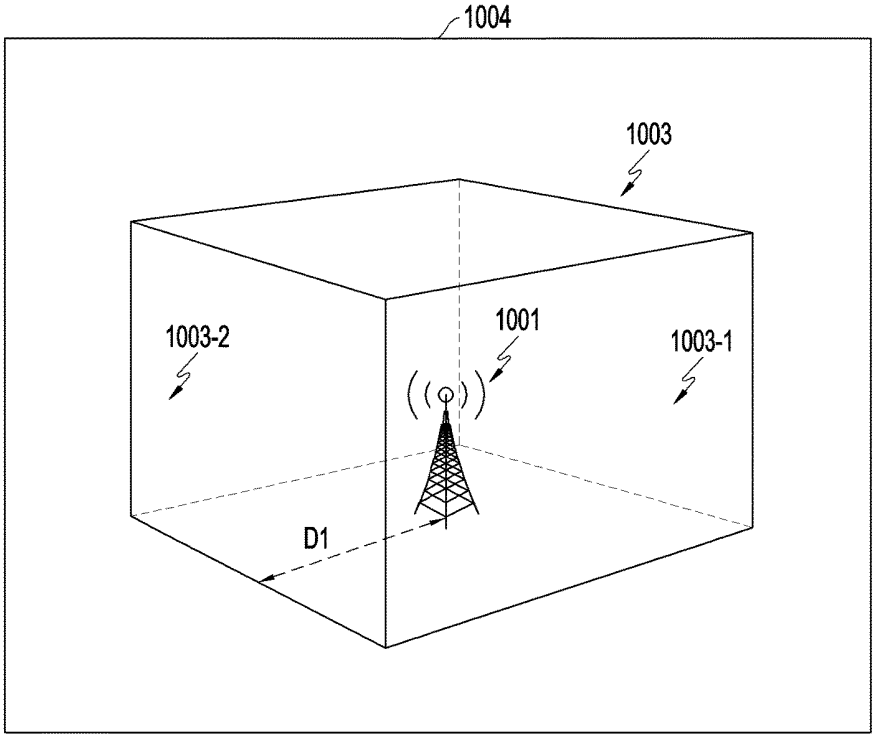


FIG.10B

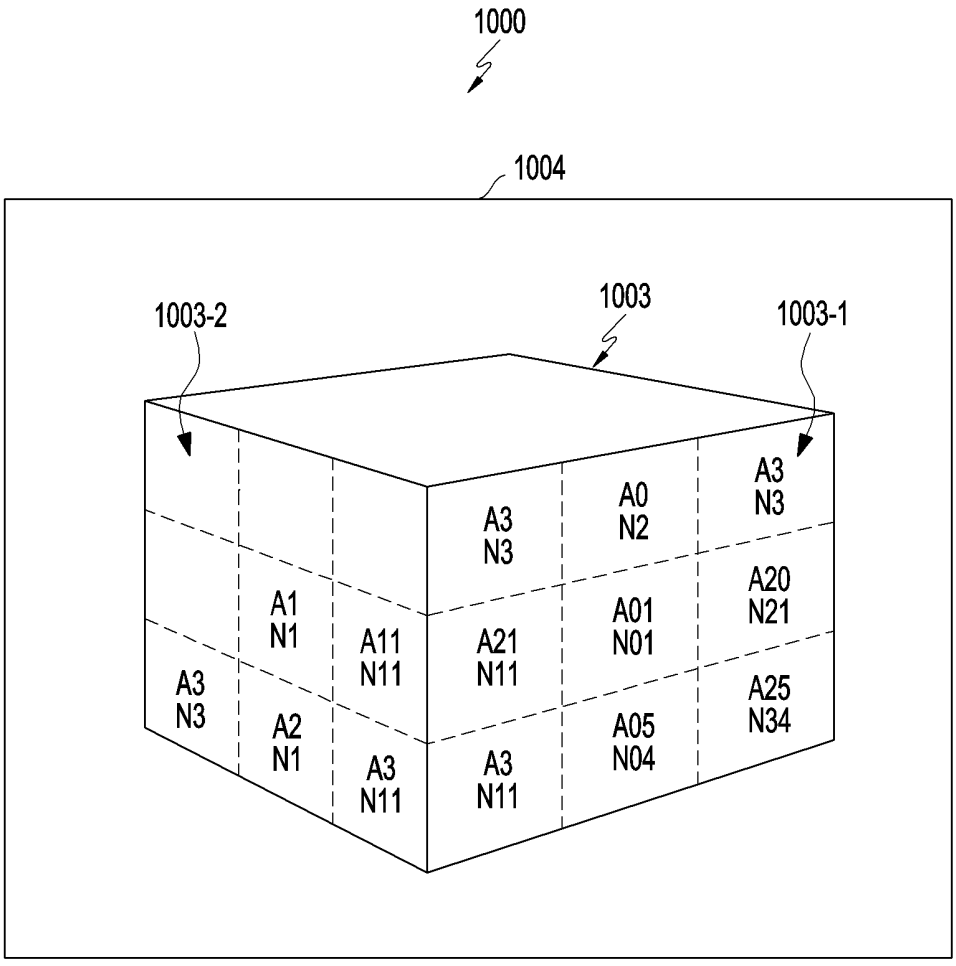

1000
1004
1003-2
1003
1003-1
A3
N3
A0
N2
A3
N3
A1
N1
A11
N11
A21
N11
A01
N01
A20
N21
A3
N3
A2
N1
A3
N11
A3
N11
A05
N04
A25
N34

FIG.10C

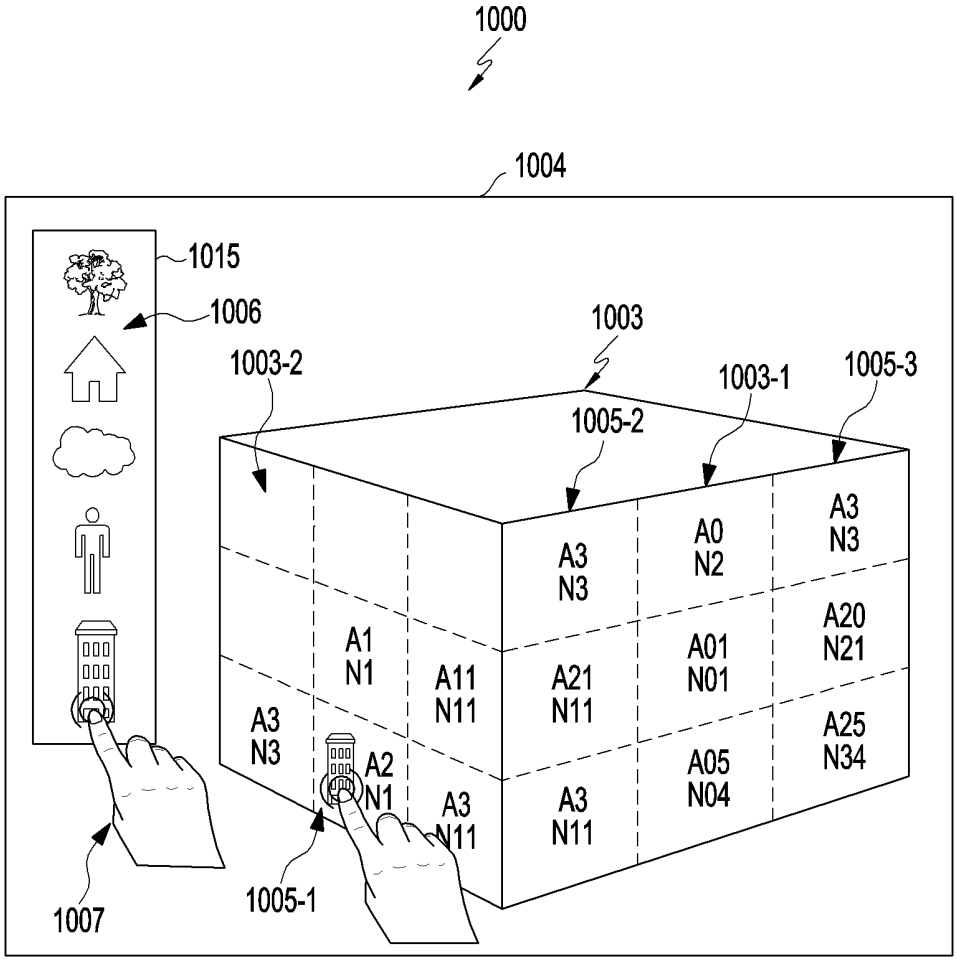

1000
1004
1015
1006
1003
1003-2
1003-1
1005-3
1005-2
A3
N3
A0
N2
A3
N3
A1
N1
A11
N11
A21
N11
A01
N01
A20
N21
A3
N3
A2
N1
A3
N11
A3
N11
A05
N04
A25
N34
1007
1005-1

FIG.10D

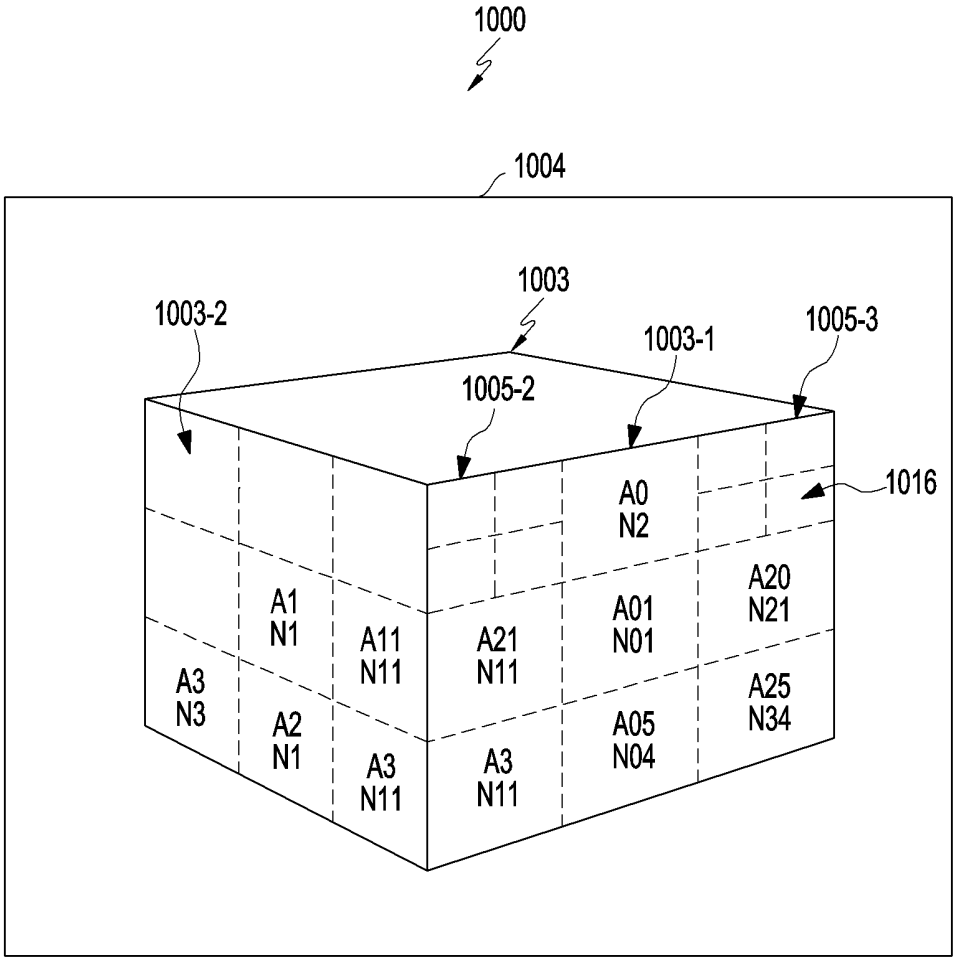

1000
1004
1003
1003-2
1003-1
1005-3
1005-2
1016
A0
N2
A1
N1
A11
N11
A21
N11
A01
N01
A20
N21
A3
N3
A2
N1
A3
N11
A3
N11
A05
N04
A25
N34

FIG.10E

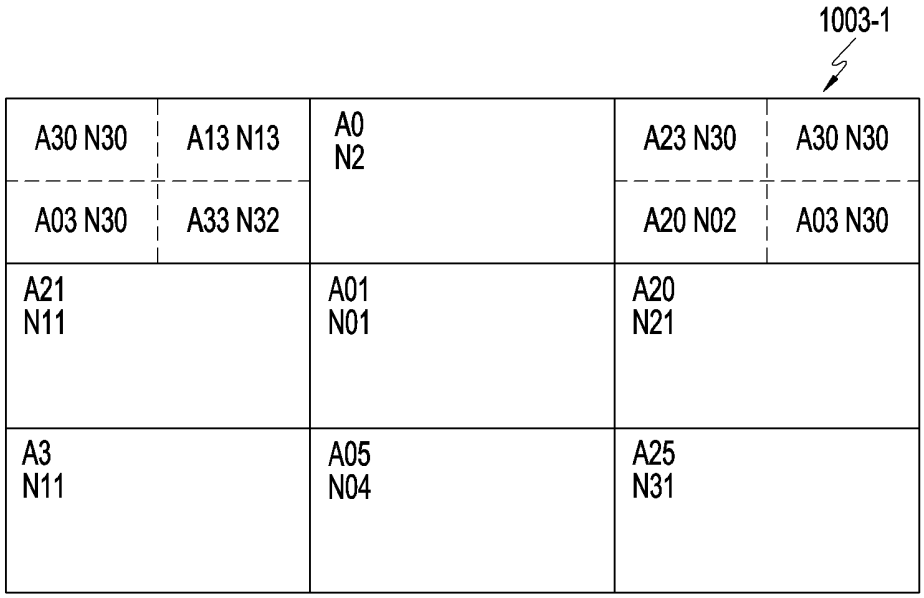

1003-1
A30 N30
A13 N13
A0
N2
A23 N30
A30 N30
A03 N30
A33 N32
A20 N02
A03 N30
A21
N11
A01
N01
A20
N21
A3
N11
A05
N04
A25
N31

FIG.10F

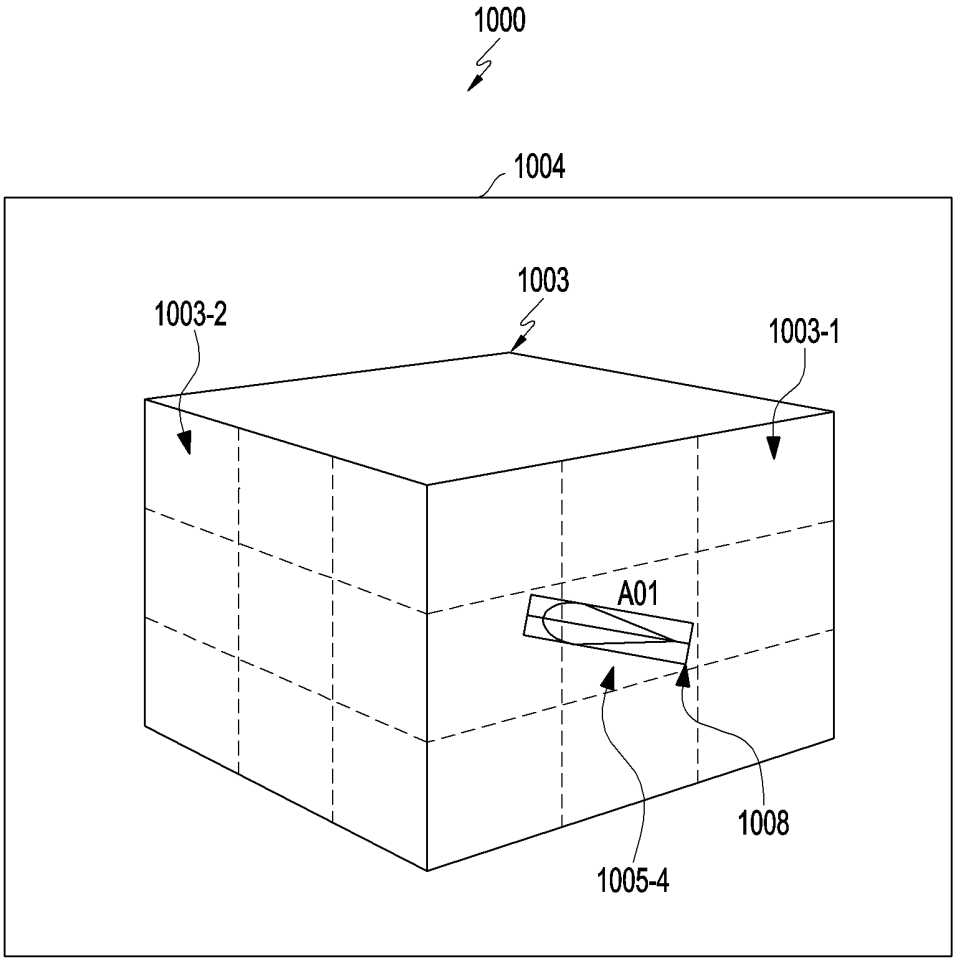


FIG.10G

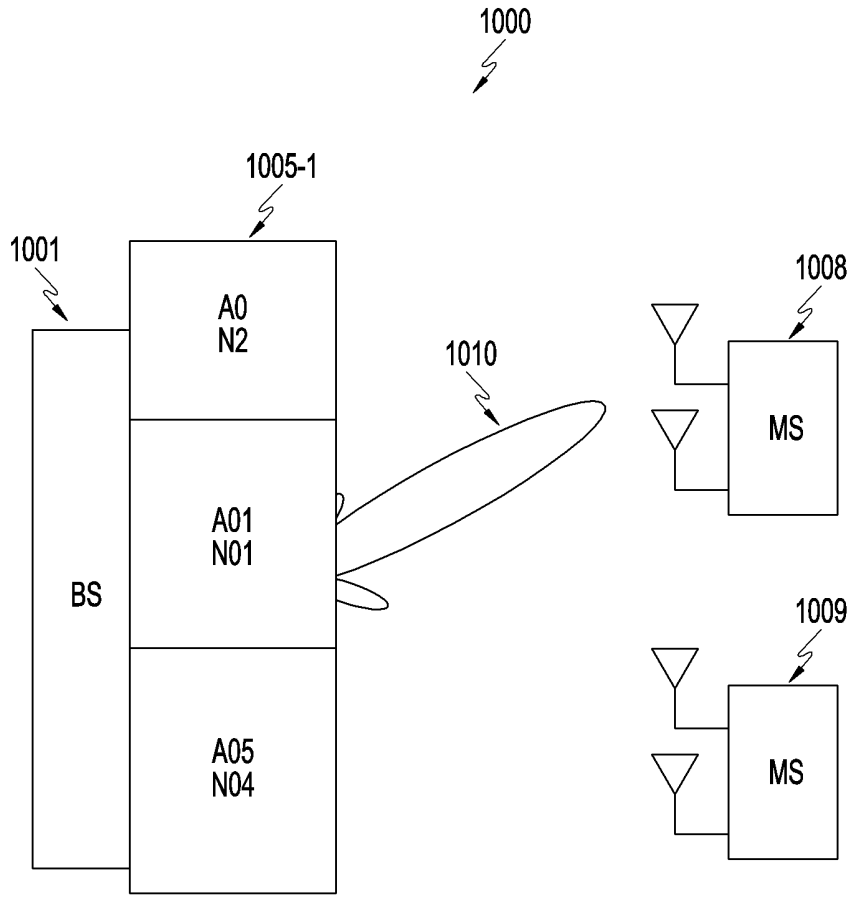


FIG.10H

BEAM FORMING METHOD FOR A TRANSMITTING ANTENNA AND A DEVICE THEREOF

CROSS-REFERENCE TO RELATED APPLICATION

[0001] This application is based on and claims priority under 35 U.S.C. § 119(a) of an Indian patent application number 201711016629, filed on May 11, 2017, in the Indian Intellectual Property Office, the disclosure of which is incorporated by reference herein in its entirety.

BACKGROUND

1. Field

[0002] The disclosure relates to a method and device for beam forming in cellular communication systems. More particularly, the disclosure relates to selecting an antenna for beam forming based on obstructions.

2. Description of Related Art

[0003] To meet the demand for wireless data traffic having increased since deployment of 4G (4^{th}-Generation) communication systems, efforts have been made to develop an improved 5G (5^{th}-Generation) or pre-5G communication system. Therefore, the 5G or pre-5G communication system is also called a 'Beyond 4G Network' or a 'Post LTE System'.

[0004] The 5G communication system is considered to be implemented in higher frequency (mmWave) bands, e.g., 60 GHz bands, so as to accomplish higher data rates. To decrease propagation loss of the radio waves and increase the transmission distance, the beamforming, massive multiple-input multiple-output (MIMO), Full Dimensional MIMO (FD-MIMO), array antenna, an analog beam forming, large scale antenna techniques are discussed in 5G communication systems.

[0005] In addition, in 5G communication systems, development for system network improvement is under way based on advanced small cells, cloud Radio Access Networks (RANs), ultra-dense networks, device-to-device (D2D) communication, wireless backhaul, moving network, cooperative communication, Coordinated Multi-Points (CoMP), reception-end interference cancellation and the like.

[0006] In the 5G system, Hybrid FSK and QAM Modulation (FQAM) and sliding window superposition coding (SWSC) as an advanced coding modulation (ACM), and filter bank multi carrier (FBMC), non-orthogonal multiple access (NOMA), and sparse code multiple access (SCMA) as an advanced access technology have been developed.

[0007] In a cellular communication system that supports beam forming, a base station and a terminal may form a plurality of beams for signal transmission and reception. Particularly, each of the base station and the terminal may select an optimal beam of a plurality of beams according to a beam forming protocol, and transmit and receive a signal using the selected beam. In general, the beam forming protocol includes a beam tracking procedure that is performed continuously in a background. The beam tracking procedure involves scanning a wide spectrum of reflected signals to obtain relevant parameters for optimal beam forming, thereby increasing time, load, and power consumption.

[0008] Thus, there exists a need for a solution to overcome above-mentioned deficiencies.

[0009] The above information is presented as background information only to assist with an understanding of the disclosure. No determination has been made, and no assertion is made, as to whether any of the above might be applicable as prior art with regard to the disclosure.

SUMMARY

[0010] Aspects of the disclosure are to address at least the above-mentioned problems and/or disadvantages and to provide at least the advantages described below. Accordingly, an aspect of the disclosure is to provide a selection of concepts in a simplified format that are further described in the detailed description of the disclosure. This summary is not intended to identify key or essential inventive concepts of the claimed subject matter, nor is it intended for determining the scope of the claimed subject matter.

[0011] In accordance with an aspect of the disclosure, the method and the device for beam forming in cellular communication systems are provided. The method and the device includes selecting an antenna for beam forming based on obstructions.

[0012] In an embodiment of the disclosure, a beam is formed for a transmitting antenna. Accordingly, a virtual three-dimensional shape is created around the transmitting antenna. Thereafter, at least one face from among a plurality of faces of the virtual three-dimensional shape is selected based on a first set of parameters. One or more grids are then created on the at least one selected face. The one or more grids divide a face of the virtual three-dimensional shape into an n by m matrix, wherein a value of n is equal to or more than one (1); and a value of m is equal to or more than one (1). At least one grid is then selected from among the one or more grids as an optimum grid set based on a second set of parameters. Based on the at least one grid, at least one beam is formed.

[0013] The advantages of the disclosure include, but not limited to, forming an efficient and high direction beam based on at the optimum grid set with minimal losses. Further, by creating a virtual three-dimensional shape and creating the at least one grid on at least one face of the virtual three-dimensional shape, a three-dimensional beam forming is facilitated. Thereby, the beam formation is highly directional. This further reduces complexity of the cellular communication systems and optimizes performance parameters. Further, time, load, and power consumption for beam forming may be considerably reduced, as the beam is formed based on the at least one selected grid rather than linear scanning.

[0014] These aspects and advantages will be more clearly understood from the following detailed description taken in conjunction with the accompanying drawings and claims.

[0015] Other aspects, advantages, and salient features of the disclosure will become apparent to those skilled in the art from the following detailed description, which, taken in conjunction with the annexed drawings, discloses various embodiments of the disclosure.

BRIEF DESCRIPTION OF THE DRAWINGS

[0016] The above and other aspects, features, and advantages of certain embodiments of the disclosure will be more apparent from the following description taken in conjunction with the accompanying drawings, in which:

[0017] To further clarify advantages and aspects of the disclosure, a more particular description of the disclosure will be rendered by reference to specific embodiments thereof, which is illustrated in the appended drawings. It is appreciated that these drawings depict only typical embodiments of the disclosure and are therefore not to be considered limiting its scope. The disclosure will be described and explained with additional specificity and detail with the accompanying drawings, which are listed below for quick reference.

[0018] FIGS. **1**, **2**, **3**, **4**, **5**, and **6** illustrates method for beam forming for a transmitting antenna, according to various embodiments of the disclosure.

[0019] FIG. **7** illustrates device implementing the method for beam forming illustrated in FIGS. **1**, **2**, **3**, **4**, **5**, and **6**, according to the embodiment of the disclosure.

[0020] FIG. **8** is a block diagram illustrating an example of architecture of a system configured for use in wireless communication, according to the embodiment of the disclosure.

[0021] FIG. **9** is a block diagram illustrating an example of architecture of a base station configured for use in wireless communication, according to the embodiment of the disclosure.

[0022] FIGS. **10**A, **10**B, **10**C, **10**D, **10**E, **10**F, **10**G, and **10**H illustrate an example of implementing the method for beam forming in a base station, in accordance with the disclosure.

[0023] It may be noted that to the extent possible, like reference numerals have been used to represent like elements in the drawings. Further, those of ordinary skill in the art will appreciate that elements in the drawings are illustrated for simplicity and may not have been necessarily drawn to scale. For example, the dimensions of some of the elements in the drawings may be exaggerated relative to other elements to help to improve understanding of aspects of the disclosure. Furthermore, the one or more elements may have been represented in the drawings by conventional symbols, and the drawings may show only those specific details that are pertinent to understanding the embodiments of the disclosure so as not to obscure the drawings with details that will be readily apparent to those of ordinary skill in the art having benefit of the description herein.

[0024] Throughout the drawings, it should be noted that like reference numbers are used to depict the same or similar elements, features, and structures.

DETAILED DESCRIPTION

[0025] The following description with reference to the accompanying drawings is provided to assist in a comprehensive understanding of various embodiments of the disclosure as defined by the claims and their equivalents. It includes various specific details to assist in that understanding but these are to be regarded as merely exemplary. Accordingly, those of ordinary skill in the art will recognize that various changes and modifications of the various embodiments described herein can be made without departing from the scope and spirit of the disclosure. In addition, descriptions of well-known functions and constructions may be omitted for clarity and conciseness.

[0026] The terms and words used in the following description and claims are not limited to the bibliographical meanings, but, are merely used by the inventor to enable a clear and consistent understanding of the disclosure. Accordingly, it should be apparent to those skilled in the art that the following description of various embodiments of the disclosure is provided for illustration purpose only and not for the purpose of limiting the disclosure as defined by the appended claims and their equivalents.

[0027] It is to be understood that the singular forms "a," "an," and "the" include plural referents unless the context clearly dictates otherwise. Thus, for example, reference to "a component surface" includes reference to one or more of such surfaces.

[0028] Certain terms or phrases used herein may be defined merely for ease of description. For example, the terms "include" and "comprise" and their derivatives may indicate doing so without any limitations. As used herein, the term "or" may be used interchangeably with the term "and/or." As used herein, the phrases "associated with," "associated therewith" and their derivatives may be used interchangeably with the terms "include," "be included within," "interconnect with," "contain," "be contained within," "connect to or with," "couple to or with," "be communicable with," "cooperate with," "interleave," "juxtapose," "be proximate to, "be bound to or with, "have, and "have a property of." As used herein, the term "controller" may indicate any device, system, or part thereof controlling at least one operation. As used herein, the term "device" may indicate a device that may be implemented in hardware, firmware, software, and some combination of at least two thereof. It should be noted that functions, whatever certain controller is associated therewith, may be concentrated, distributed, and implemented locally or remotely. It should be appreciated by one of ordinary skill in the art that the definitions of certain terms or phrases as used herein may be adopted for the present or the future in many cases.

[0029] The terms coming with ordinal numbers such as "first" and "second" may be used to denote various components, but the components are not intended to be limited by the terms. The terms are used only to distinguish one component from another. For example, a first component may be referred to as a second component, and vice versa without departing from the scope of the present disclosure. The term "and/or" may refer to a combination(s) of a plurality of related items as listed or any of the items.

[0030] The terms as used herein are provided merely to describe embodiments of the present disclosure, but are not intended to limit the present disclosure. It will be further understood that the terms "comprise" and/or "have," when used in the present disclosure, indicate the presence of stated features, integers, steps, operations, elements, and/or components, but do not preclude the presence or addition of one or more other features, integers, steps, operations, elements, components, and/or groups thereof.

[0031] It should be understood at the outset that although illustrative implementations of the embodiments of the disclosure are illustrated below, the disclosure may be implemented using any number of techniques, whether currently known or in existence. The disclosure should in no way be limited to the illustrative implementations, drawings, and techniques illustrated below, including the design and

implementation illustrated and described herein, but may be modified within the scope of the appended claims along with their full scope of equivalents.

[0032] The term "some" as used herein is defined as "none, or one, or more than one, or all." Accordingly, the terms "none," "one," "more than one," "more than one, but not all" or "all" would all fall under the definition of "some." The term "some embodiments" may refer to no embodiments or to one embodiment or to several embodiments or to all embodiments. Accordingly, the term "some embodiments" is defined as meaning "no embodiment, or one embodiment, or more than one embodiment, or all embodiments."

[0033] The terminology and structure employed herein is for describing, teaching and illuminating some embodiments and their specific features and elements and does not limit, restrict or reduce the spirit and scope of the claims or their equivalents.

[0034] More specifically, any terms used herein such as but not limited to "includes," "comprises," "has," "consists," and grammatical variants thereof do NOT specify an exact limitation or restriction and certainly do NOT exclude the possible addition of one or more features or elements, unless otherwise stated, and furthermore must NOT be taken to exclude the possible removal of one or more of the listed features and elements, unless otherwise stated with the limiting language "MUST comprise" or "NEEDS TO include."

[0035] Whether or not a certain feature or element was limited to being used only once, either way it may still be referred to as "one or more features" or "one or more elements" or "at least one feature" or "at least one element." Furthermore, the use of the terms "one or more" or "at least one" feature or element do NOT preclude there being none of that feature or element, unless otherwise specified by limiting language such as "there NEEDS to be one or more . . . " or "one or more element is REQUIRED."

[0036] Unless otherwise defined, all terms, and especially any technical and/or scientific terms, used herein may be taken to have the same meaning as commonly understood by one having an ordinary skill in the art.

[0037] Reference is made herein to some "embodiments." It should be understood that an embodiment is an example of a possible implementation of any features and/or elements presented in the attached claims. Some embodiments have been described for the purpose of illuminating one or more of the potential ways in which the specific features and/or elements of the attached claims fulfil the requirements of uniqueness, utility and non-obviousness.

[0038] Use of the phrases and/or terms such as but not limited to "a first embodiment," "a further embodiment," "an alternate embodiment," "one embodiment," "an embodiment," "multiple embodiments," "some embodiments," "other embodiments," "further embodiment", "furthermore embodiment", "additional embodiment" or variants thereof do NOT necessarily refer to the same embodiments. Unless otherwise specified, one or more particular features and/or elements described in connection with one or more embodiments may be found in one embodiment, or may be found in more than one embodiment, or may be found in all embodiments, or may be found in no embodiments. Although one or more features and/or elements may be described herein in the context of only a single embodiment, or alternatively in the context of more than one embodiment, or further alternatively in the context of all embodiments, the features and/or elements may instead be provided separately or in any appropriate combination or not at all. Conversely, any features and/or elements described in the context of separate embodiments may alternatively be realized as existing together in the context of a single embodiment.

[0039] Any particular and all details set forth herein are used in the context of some embodiments and therefore should NOT be necessarily taken as limiting factors to the attached claims. The attached claims and their legal equivalents can be realized in the context of embodiments other than the ones used as illustrative examples in the description below.

[0040] FIGS. **1**, **2**, **3**, **4**, **5**, and **6** illustrates method for beam forming for a transmitting antenna, according to various embodiments of the disclosure. FIG. **7** illustrates device implementing the method for beam forming according to the embodiment of the disclosure.

[0041] Referring to FIG. **1** and FIG. **7**, a beam forming method **100** and a device **700** implementing the beam forming method for a transmitting antenna **701** are described. To implement the method **100**, the device **700** includes a controller **702**. The controller **702** may be at least one processor. Examples of the transmitting antenna **701** can include, but not limited to, a beam antenna and an array antenna that can form one or more beams in a specific direction. The transmitting antenna **701** can be integral part of a user terminal such as a smart phone, wearable devices, a virtual reality (VR) device, a base station, a vehicle, unmanned aerial vehicles (UAVs), low earth orbit (LEO) satellites, autonomous small size robot such as drones, radar, internet of things (IoT) devices such as wireless modems and smart TV, etc. As such, the device **700** can also be integral to the user terminal, the base station, the vehicle, the UAVs, the LEO satellites, the autonomous small size robot, radar and the IoT devices. The transmitting antenna **701** transmits a signal in a direction of a receiving antenna (not shown in the figure). The receiving antenna can be integral part of a user terminal such as smart phone, wearable devices, a VR device, a base station, a vehicle, UAVs, (LEO satellites, an autonomous small size robot such as drones, radar, IoT devices such as wireless modems, and smart TV, etc.

[0042] At operation **101** of FIG. **1**, a virtual three-dimensional shape is created around the transmitting antenna. The transmitting antenna may be included in a base station. The virtual three-dimensional (3D) shape can be any three-dimensional polygon having a plurality of faces. Examples of such three-dimensional polygon include, but not limited to, cube, pyramid, L-cube, etc.

[0043] At operation **102**, at least one face may be selected from among a plurality of faces of the virtual three-dimensional shape based on a first set of parameters. The first set of parameters include, but not limited to, channel sense information, data related to the transmitting antenna, data related to a receiving antenna, a direction of the receiving antenna, cellular information, and user-input.

[0044] To create the virtual three-dimensional shape and select the at least one face, the controller **702** includes a shape creating and selecting unit (SCSU) **703**. The SCSU **703** creates the virtual three-dimensional shape around the

transmitting antenna. Thereafter, the SCSU **703** obtains the first set of parameters and selects at least one face based on the first set of parameters.

[0045] At operation **103**, one or more grids are created on the at least one selected face. The one or more grids divide a face of the virtual three-dimensional shape into an n by m matrix, wherein a value of n is equal to or more than one (1); and a value of m is equal to or more than one (1).

[0046] At operation **104**, at least one grid may be selected from among the one or more grids as an optimum grid set based on a second set of parameters. The second set of parameters includes attenuation, propagation delay, network efficiency, quality of service (QoS), latency, signal-to-noise ratio (SNR), channel capacity, and signal-to-interference ratio.

[0047] To this end, the controller **702** includes a grid creator and selector unit (GCSU) **704**. The GCSU **704** creates the one or more grids on the at least one selected face and selects the at least one grid based on the second set of the parameters.

[0048] At operation **105**, at least one beam is formed based on the optimum grid set. As would be understood, beam forming is used to direct and steer an antenna's directivity beam in a particular direction. The optimum grid set allows formation of beam in a direction of a particular location with minimal attenuation/losses, thereby allowing control over shape and steering of antenna's directivity pattern. Thus, formation of the at least one beam based on the optimum grid set generates a high directional and efficient beam with minimal losses and overheads.

[0049] To form the at least one beam at operation **105**, the device **700** includes a beam-forming unit (BFU) **705**. The BFU **705** forms at least one beam in accordance with the input, i.e., the at least one optimum grid, provided by the controller **702**. The BFU **705** can be included within a transmitting and receiving unit (TRU) **706**. The TRU **706** controls and performs a function of transmitting a signal to the receiving antenna through the at least one beam formed by the BFU **705**. The transmitting antenna **701** then transmits the signal in the direction of the receiving antenna.

[0050] Further, during the formation of the at least one beam at operation **102**, the BFU **705** can employ various techniques as known in the art to form the beam. Examples of such techniques include analogue beam forming technique using a phase shifter, digital beam forming technique, hybrid beam forming technique, and physically moving the transmitting antenna to a previously defined direction. Examples of the digital beam forming technique include fixed beam forming technique, adaptive beam forming technique, azimuth beam forming technique, and elevation beam forming technique. Fixed beam forming technique is typically used when signal source location and noise source location is fixed with respect to the transmitting antenna **701**. Examples of fixed beam forming technique include, but not limited to, Delay-and-Sum, Filter-and-Sum, and Weighted-Sum based technique. Adaptive beam forming technique is typically used when signal source location and noise source location are moving with respect to the transmitting antenna **701**. Examples adaptive beam forming technique includes, but not limited to, generalised sidelobe canceller (GSC), linearly constrained minimum variance (LCMV, Frost), in situ calibrated microphone array (ICMA), and minimum mean squared error (MMSE).

[0051] Referring to FIG. **1**, in accordance with the disclosure, the creation of the virtual three-dimensional shape, as defined at operation **101**, is performed by implementing operations of method **200** as described in FIG. **2**. Thus, referring to FIG. **2** and FIG. **7**, the device **700** implementing the beam forming method are described below.

[0052] Accordingly, to create the virtual three-dimensional shape, a current location of the transmitting antenna is determined at operation **201** of FIG. **2**.

[0053] In one implementation, the current location is determined based on dynamic determination of geolocation of the transmitting antenna. In such implementation, referring to FIG. **7**, the controller **702** includes a location detection unit (LDU) **707** to determine the current location. The LDU **707** dynamically detects the current location of the transmitting antenna **701** using various techniques as known in the art. As described earlier, the device **700** and the transmitting antenna **701** can be an integral part of the user terminal, the base station, the vehicle, the autonomous small size robot, and the IoT devices. As such, the LDU **707** can detect the current location using techniques such as, but not limited to, inbuilt-global positioning system (GPS) sensor, GPS techniques, deriving geo-location from an IP address, an indoor position system (IPS), local positioning system (LPS), base station assisted (BS assisted) position determination technique, mobile station assisted (MS assisted) reverse position determination technique, etc. As would be understood, the IPS can be based on various technologies.

[0054] In another implementation, the current location is determined based on user-input. In such implementation, referring to FIG. **4**, the controller **702** includes a user-input receiving unit (UIRU) **708** to receive the user-input. In one example of such implementation, the user-input can be a text data indicating the current location. In one example of such implementation, the user-input can be touch-based input indicating the current location. Accordingly, in such implementation, the SCSU **703** can provide a user-interface on a display unit (not shown in the figure) communicatively coupled with the device **700**. The display unit can be integral part of or external to the user terminal, the base station, the vehicle, the UAVs, the LEO satellites, the autonomous small size robot, and the IoT devices. In one example, the user-interface can provide text field(s) to input text data indicating the current location. In another example, the user-interface can provide a list to select the current location. The UIRU **708** can receive the user-input a provided through the user-interface via input unit (not shown in the figure and communicatively coupled to the device **700**).

[0055] Upon determining the current location, at operation **202**, data related to at least one obstruction is received based on the current location thus determined. The obstruction(s) can be manmade obstruction(s) or natural obstruction(s). Examples of the obstruction include, but not limited to, buildings/high-rise structures, trees, vegetation, vehicles, rain, clouds, fog, smog, other weather condition, and a human body. As such, the received data related to the at least one obstruction includes type of obstruction present at or available in proximate to the determined current location and characteristics of the at least one obstruction. The characteristics include depth of the at least one obstruction, a width of the at least one obstruction, and a property of the at least one obstruction such as material and movable/static.

[0056] In one implementation, the data is received or fetched from a storage unit. Accordingly, the controller **702**

includes a data-fetching unit (DFU) **709** to fetch above-mentioned data from a storage unit **710** upon determining the current location of the transmitting antenna **701**. The storage unit **710** stores the data related to at least one obstruction as obstruction data **711**. Such obstruction data **711** can be determined, evaluated or processed prior to the current instance of time. In addition, such obstruction data **711** can be determined, evaluated or processed for various terminals/devices/systems used by various users and having the device **700** prior to the current instance of time and stored in the storage unit **710**. In addition, such obstruction data **711** can be obtained from system(s) capable of predicting/forecasting obstruction details such as future building projects and weather condition at later instance of time. In one implementation, the storage unit **710** can be internal to the device **700**. In one example of such implementation, the device **700** and the storage unit **710** can be integral to a base station. In another implementation, the storage unit **710** can be external to the device **700**, as illustrated in the figure. In one example of such implementation, the device **700** can be integral to a user terminal and the storage unit **710** can be associated with a network operator.

[0057] Further, in one implementation, the data is obtained from at least one reflected signal received from the current location. Accordingly, the SCSU **703** obtains the reflected signal using various techniques as known in the art. In one example, the SCSU **703** obtains the reflected signals using 3D scanning technique. In one example, the SCSU **703** obtains the reflected signals using 2D scanning technique. Upon obtaining the reflected signal, the SCSU **703** obtains the at least one parameter of the received signal using techniques as known in the art. The at least one parameter of the reflected signal includes an intensity, angle of arrival (AOA), elevation angle, azimuth angle, frequency/Doppler shift, time of arrival (TOA), time difference of arrival (TDOA), power of the signal, signal to noise ratio, signal to interference plus noise ratio, interference, offset, coherent energy, incoherent energy, variance, and correlation. Upon obtaining the at least one parameter, the SCSU **703** derives the characteristics of the at least one obstruction, if any, present in the current location from where reflected signals are being received using techniques as known in the art. The characteristics include depth of the at least one obstruction, a width of the at least one obstruction, and a property of the at least one obstruction.

[0058] In one implementation, the data is obtained based on user-input. In such implementation, the SCSU **703** can provide a user-interface on the display unit (not shown in the figure) to receive the user-input. The user-input is received by the UIRU **708** via a user-interface and consequently the SCSU **703** derives the characteristics of the at least one obstruction.

[0059] Upon receiving the data related to at least one obstruction, the SCSU **703** selects and creates the virtual three-dimensional shape based on the received data in operation **203**. The virtual three-dimensional shape is selected and created such that the the transmitting antenna **701** is at center of the virtual three-dimensional shape. Further, the virtual three-dimensional shape is selected and created such that the distance from the center of virtual three-dimensional shape to a face of the three-dimensional shape is a minimum distance between the transmitting antenna **701** and the at least one obstruction.

[0060] To this end, the SCSU **703** determines a nearest obstruction in the current location based on the received data and determines a minimum distance between the transmitting antenna **701** and the nearest obstruction. The determined minimum distance is calculated on all sides/directions of the transmitting antenna **701**. Based on the determined minimum distance, the SCSU **703** selects the virtual three-dimensional shape from among a plurality of three-dimensional shapes and creates the virtual three-dimensional shape around the transmitting antenna **701**. The virtual three-dimensional shape is having a plurality of faces and is created such that the transmitting antenna **701** is at the center from each of the faces at a distance equal to the minimum distance. The virtual three-dimensional shape can be created using techniques as known in the art. In an example, the virtual three-dimensional shape can be a cube based on the received data. In an example, the virtual three-dimensional shape can be a pyramid based on the received data. Thus, the virtual three-dimensional shape indicates an obstruction free area around the transmitting antenna **701** at the current location for beam forming such that obstruction free area reduces interference and distortion of the beam due to the obstructions during signal transmission and avoids communication dead zones. In accordance with the disclosure, referring to FIG. **1**, upon creating the virtual three-dimensional shape, at least one face is selected from among the plurality of faces at operation **102** based on the first set of parameters. Accordingly, the SCSU **703** obtains values of the first set of parameters using various techniques. As described earlier, the first set of parameters include, but not limited to, channel sense information, data related to the transmitting antenna, data related to a receiving antenna, a direction of the receiving antenna, cellular information, and user-input. In one example, the SCSU **703** obtains channel sense information by sensing whether there is signal energy at the frequency bands designated for transmission. In on example, the SCSU **703** obtains direction of the receiving antenna as a user-input via the UIRU **708**. In one another example, the SCSU **703** obtains selection of the face(s) itself as a user-input via the UIRU **708**. Based on the values of the first set of parameters, the SCSU **703** selects at least one face of the virtual three-dimensional shape in the direction of the receiving antenna with minimal attenuation/losses due to the obstructions. In one example, the three-dimensional shape is a cube with six faces and the selected faces can be two adjacent side faces based on the values of the first set of parameters. Thus, the selected faces(s) can be a specific zone or geographical area (within the total obstruction free area represented by the virtual three-dimensional shape) that has minimal obstruction(s) and consequently provides minimal propagation/path losses during transmission of signals. In one example, the zone can be geographical area covered by a single cell within the obstruction free area. In one example, the zone can be a small geographical area within a larger area covered by the obstruction free area.

[0061] Further, referring to FIG. **1**, one or more grids are created on the selected at least one face at operation **103**. Accordingly, based on the values of the first set of parameters and the received data, the GCSU **704** divides the at least one selected face of the virtual three-dimensional shape into an n by m matrix that form the one or more grids. A value of n is equal to or more than 1; and a value of m is equal to or more than 1. In one implementation, the GCSU **704** obtains the values of the first set of parameters and the

received data from the SCSU **703**. In one implementation, the GCSU **704** obtains the values of the first set of parameters and the received data in a similar manner as the SCSU **703** obtains the values of the first set of parameters and the received data, as described above. In one implementation, the GCSU **704** divides the at least one selected face into the n-by-m matrix based on a size of the at least one selected face. In one implementation, the GCSU **704** divides the at least one selected face into the n-by-m matrix based on a user-input. The user-input can be indicative of the number of grids to be formed and/or the size of the matrix, i.e., values of n and m. In one example of such implementation, the user-input can be a text data indicating the number of grids to be formed and/or the size of the matrix. In one example of such implementation, the user-input can be touch-based input indicating the number of grids to be formed and/or the size of the matrix. Accordingly, in such implementation, the GCSU **704** can provide a user-interface on the display unit (not shown in the figure). In one example, the user-interface can provide text field(s) to input text data indicating the number of grids to be formed and/or the size of the matrix. In another example, the user-interface can provide a list to select the number of grids to be formed and/or the size of the matrix. The UIRU **708** can receive the user-input provided through the user-interface via the input unit (not shown in the figure and communicatively coupled to the device **700**). In this manner, the GCSU **704** further divides the specific zone or area into smaller zones or areas that have negligible obstruction(s) and consequently provides negligible propagation/path losses during transmission of signals. In one example, the smaller zones can small geographic area within the single cell. It would be understood that a 3D beam forming improves cell average and edge grid throughput, and eliminates interference to adjacent cells by combining elevation beam forming and azimuth beam forming. Thus, the creation of one or more grids enhances the performance of the 3D beam forming. Although, only one (1) grid from 1-×-1 matrix or four (4) grids from a 2×2 matrix can be formed, it would be understood that greater the number of grids created on the face, the higher is the improvement in the performance of 3D beam forming.

[0062] Referring to FIG. **1**, the selection of at least one grid from among the one or more grids as the optimum grid set based on the second set of parameters, as defined at operation **104**, is performed by implementing operations of method **300**, **400**, and **500** as described in FIGS. **3**, **4**, and **5**, respectively. Thus, referring to FIGS. **3**, **4**, and **5**, and FIG. **7**, the device **700** implementing the beam forming method are described below.

[0063] Accordingly, at operation **301** of FIG. **3**, a value of the second set of parameters for each of the one or more grids is determined. As described earlier, the second set of parameters include, but not limited to, attenuation, propagation delay, network efficiency, quality of service (QoS), latency, signal-to-noise ratio (SNR), channel capacity, and signal-to-interference ratio. The attenuation can be channel impairment attenuation or channel impairment dynamic attenuation.

[0064] In one implementation, the value of the second set of parameters can be determined/obtained from at least one reflected signal received from the current location. Accordingly, the GCSU **704** receives at least one reflected signal from the one or more grids using various techniques as known in the art. In one example, the GCSU **704** obtains/receives the reflected signals using 3D scanning technique. In one example, the GCSU **704** obtains/receives the reflected signals using 2D scanning technique. Upon obtaining the reflected signal, the GCSU **704** obtains the at least one parameter of the received signal using techniques as known in the art. The at least one parameter of the reflected signal includes an intensity, AOA, elevation angle, azimuth angle, frequency/Doppler shift, TOA, TDOA, power of the signal, signal to noise ratio, signal to interference plus noise ratio, interference, offset, coherent energy, incoherent energy, variance, and correlation. Upon obtaining the at least one parameter of the reflected signal, the GCSU **704** derives the characteristics of the at least one obstruction, if any, present in the current location from where reflected signals are being received using techniques as known in the art. The characteristics include depth of the at least one obstruction, a width of the at least one obstruction, and a property of the at least one obstruction. From the characteristics of the at least one obstruction, the GCSU **704** derives/determines the values of the second set of parameters using techniques as known in the art.

[0065] In one implementation, the value of the second set of parameters can be determined from pre-stored data corresponding to at least one obstruction available in one or more grids. The pre-stored data corresponding to the at least one obstruction includes: information related to geographic location of the one or more grids; information related to characteristics of at least one obstruction located in proximate to the geographic location; metadata associated with one or more optimum grids prior to current instance of time; and ranking associated with one or more optimum grids prior to current instance of time.

[0066] Accordingly, the LDU **707** determines location coordinates of the one or more grids and the DFU **709** fetches the obstruction data **711** from the storage unit **710** based on the location coordinates. Upon receiving the data, the GCSU **704** derives/determines the values of the second set of parameters using techniques as known in the art.

[0067] In one implementation, the value of the second set of parameters can be determined from current data corresponding to at least one obstruction available in one or more grids by capturing an image of the at least one obstruction. Accordingly, in one implementation, the device **700** is communicatively coupled with an image-capturing unit (ICU) **712** to capture an image or a video of the at least one obstruction. In another implementation, the ICU **712** is internal to the device **700**. Upon capturing the image or video, the GCSU **704** analyses the captured image or video and derives/determines the values of the second set of parameters based on the analysis, using techniques as known in the art.

[0068] In one implementation, the value of the second set of parameters can be determined based on a user-input corresponding to at least one obstruction available in the one or more grids. In one example, the user-input can be a text data indicating the at least one obstruction at the one or more grids. In one example, the user-input can be an image of the at least one obstruction at the one or more grids. In one example, the user-input can be a touch-based user-input corresponding to at least one obstruction available in one or more grids. Examples of such touch-based input include, but not limited to, gesture input such as drag and drop. Upon receiving the user-input, the GCSU **704** obtains data corresponding to the obstructions in the one or more grids as

described earlier. The GCSU **704** then determines/derives the value of the second set of parameters from the data as described earlier.

[0069] Upon determining the value of the second set of parameter, referring to FIG. **3**, at least one grid having an optimum value of the second set of parameters is selected as the optimum grid at operation **302**. The at least one grid is selected in the direction of the receiving antenna. To this end, the GCSU **704** fetches predefined threshold values **713** stored in the storage unit **710**. Upon fetching, the GCSU **704** compares the determined value of the parameters with the predefined threshold value **713** and determines if the value is optimal with respect to the threshold value. In an implementation, the value is optimal if the value is lower than the predefined threshold value. In an implementation, the value is optimal if the value is higher than the predefined threshold value. Upon determining the value is optimal, the GCSU **704** selects the at least one grid with parameters having optimal value as the optimum grid. In an example, the GCSU **704** selects the optimum grid set with optimal value of one or more parameters as mentioned below, but not limited to: attenuation of signal passing through a grid is lower than a predefined threshold value; propagation delay of signal passing through a grid is lower than a predefined threshold value; latency of signal passing through a grid is lower than a predefined threshold value; single-to-noise-ratio at a grid is higher than a predefined threshold value; and quality of service for signal propagation through a grid is higher than a predefined threshold value; channel capacity is higher than a predefined threshold value; and signal-to-interference ratio is lower than a predefined threshold value.

[0070] In one implementation, the selection of the optimum grid(s) at operation **302** may include further operations as illustrated in FIG. **4**. Referring to FIG. **4**, at operation **401**, a plurality of further sub-grids are created within at least one grid from among the one or more grids based on the value of the second set of parameters for the at least one grid. The further sub-grids divide a face of the grid into a by b matrix, wherein a value of "a" is equal to or more than one (1); and a value of "b" is equal to or more than one (1); and wherein "a"="b" **1**. In one implementation, the further sub-grids within at least one grid can be created when the value of the second set of parameters of the at least one grid can be further optimized. In one implementation, the further sub-grids can be created based on a user-input. The user-input can be indicative of the number of grids to be formed or the size of the matrix. As discussed earlier, such user-input is received by the UIRU **708** via a user-interface provided by the GCSU **704**. As such, the GCSU **704** creates further sub-grids in the grid in a manner as discussed earlier while creation of the one or more grids on the at least one selected face.

[0071] At operation **402**, a value of the second set of parameters is determined for the further sub-grids. At operation **403**, at least one further sub-grid having an optimum value of the second set of parameters is selected as the optimum grid set in the direction of a receiving antenna. As such, the GCSU **704** selects the optimum grid set from the further sub-grids in a manner as described earlier while selecting the optimum grid set from among the one or more grids.

[0072] In another implementation, the selection of the optimum grid(s) at operation **302** may include further operations as illustrated in FIG. **5**.

[0073] Referring to FIG. **5**, at operation **501** a visual representation is presented on a display unit. The visual representation includes (a) the transmitting antenna, (b) the virtual three-dimensional shape around the transmitting antenna, (c) the at least one selected face, (d) the one or more grids on the at least one selected face, and (e) the value of the second set of parameters for each of the one or more grids. To this end, the controller **702** includes a representation unit (RU) **714** to present the virtual representation on a display unit **715** communicatively coupled with the device **700**. The RU **714** may obtain necessary details from the SCSU **703** and the GCSU **704** present the visual representation.

[0074] In addition, the RU **714** provides a preview user-interface including a plurality of obstructions available at the location of the transmitting antenna **701** to enable determination of second set of parameters for the grids, as described earlier. In an example, the RU **714** provides the preview user-interface as a preview edge on the display unit **715**. Upon receiving the user-input, the GCSU **704** obtains data corresponding to the obstructions in the one or more grids as described earlier. The GCSU **704** then again determines/derives the value of the second set of parameters from the data as described earlier.

[0075] At operation **502**, a user-input is received on the visual representation. The user-input is indicative of the selection of at least one grid on the visual representation as the optimum grid(s). At operation **503**, the at least one grid as the optimum grid set based on the user-input. Accordingly, the UIRU **708** receives the user-input on the visual representation Thereafter, the GCSU **704** selects the at least one grids as the optimum grid(s).

[0076] Further, in one implementation, the SCSU **703** may continually track at least one obstruction based on the received data. In such case, the at least one obstruction is dynamic or movable such as, but not limited to, autonomous small size robots, unmanned aerial vehicle (UAV), vehicle, bird, human, and holding a mobile device. Further, in such case, the tracking of the at least one obstruction is performed to determine/predict a trajectory or path of the at least one movable obstruction. Based on such tracking, the GCSU **704** may continually determine the value of the second set of parameters at current instance time and/or forecast/predict the value of the second set of parameters for a later instance time. This enables both dynamic creation of the grids and selection of optimum grid set at current instance of time. In addition, such data including the at least one movable obstruction, the trajectory, determined values at the current instance of time, and the predicted values for the later instance of time are stored in the storage unit **710**. As such, the GCSU **704** may obtain this stored data at the later instance time to update the trajectory, dynamically create the grids, and select optimum grid set at the later instance time. This results in elimination of creation of further grids and consequently beams jumping.

[0077] Further, referring to FIG. **1**, the beam forming based on the selected optimum grid, as defined at operation **105**, is performed by implementing operations of method **600** as described in FIG. **6**, respectively. Thus, referring to FIG. **6** and FIG. **7**, the device **700** implementing the beam forming method are described below.

[0078] At operation **601**, angle information is determined from the at least one grid thus selected. As described earlier, the 3D beam forming combines elevation beam forming and

azimuth beam forming. As such, the BFU **705** determines optimal electric down tilt for the selected optimum grid set and consequently determines optimal elevation angle and optimal azimuth angle based on the second set of parameters determined for the selected optimum grid.

[0079] At operation **602**, at least one beam is formed by controlling at least one beam parameter of at least one beam based on the angle information thus determined. The at least one beam parameter includes weight gain, frequency, phase, amplitude, direction, width, intensity, power, signal to noise ratio, signal to interference plus noise ratio, interference, output energy, variance, correlation, elevation angle, and azimuth angle. In one implementation, at operation **602**, one beam is formed corresponding to each of the selected optimum grids. In one implementation, at operation **602**, multiple beams are formed corresponding to each of the selected optimum grids. In one implementation, at operation **602**, the at least one beam is formed corresponding to a combination of plurality of selected optimum grids. As such, the BFU **705** forms the at least one beam by continually controlling elevation angle and azimuth angle in accordance with the angle information.

[0080] In an implementation, the BFU **705** may further continually control the other beam parameter(s) based on a set of predefined threshold values defined for the beam parameters and satisfy predetermined conditions. The predetermined conditions include at least one of: weight gain of the at least one beam is lower than a third predefined threshold value; weight gain of the at least one beam is higher than a predefined threshold value; weight gain of the at least one beam is equal to a predefined threshold value; variance of the at least one beam is lower than a predefined threshold value; output energy of the at least one beam is lower than a predefined threshold value; power of the at least one beam is lower than a first predefined threshold value; signal to noise ratio of the at least one beam is higher than a predefined threshold value; signal to interference plus noise ratio of the at least one beam is higher than a predefined threshold value; and interference of the at least one beam is lower than a predefined threshold value.

[0081] In one implementation, the predefined threshold values, as indicated above, can be stored in the storage unit **710** as the threshold values **713**. It would be understood that the threshold value(s) might not be defined/set for all parameters. The threshold values may be added/updated/modified/after the beam formation for subsequent evaluation/scanning.

[0082] In one implementation, the BFU **705** may further control at least one beam parameter of at least one beam based on the data corresponding to at least one obstruction available in one or more grids. Such data can be obtained from the storage unit **710** or can be obtained from the GCSU **704** as described earlier. This results in elimination of beams jumping and creating too many beams.

[0083] In one implementation, the BFU **705** can also employ artificial intelligence to control the beam parameters. In another one implementation, the BFU **705** can also employ machine learning to control the beam parameters.

[0084] Upon forming the at least beam, the transmitting antenna **701** then transmits a signal through the at least one formed beam in the direction of the receiving antenna. Accordingly, the TRU **706** controls and performs a function of transmitting a signal to the receiving antenna through the at least one beam formed by the BFU **705**. The transmitting antenna **701** then transmits the signal in the direction of the receiving antenna.

[0085] Further, upon forming the at least one beam and transmitting the signal, at least one function is performed with respect to data related to one or more of (a) the virtual three-dimensional shape, (b) the at least one selected face, (c) the at least one optimum grid, and (d) the at least one beam. The at least one function can include, but not limited to, such as storing, transmitting, metadata associating, tagging, ranking, and recommending.

[0086] Thus, in one implementation, data related to one or more of (a) the virtual three-dimensional shape, (b) the at least one selected face, (c) the at least one optimum grid, and (d) the at least one beam is stored in a storage unit. In such implementation, the controller **702** can store the data related to one or more of data related to one or more of (a) the virtual three-dimensional shape, (b) the at least one selected face, and (c) the at least one grid in the storage unit **710**. Similarly, the BFU **705** can store data related to the at least one beam in the storage unit **710**. Such data can be stored as data **716** in the storage unit **710**.

[0087] In one implementation, metadata is associated with one or more of (a) the virtual three-dimensional shape, (b) the at least one selected face, (c) the at least one optimum grid, and (d) the at least one beam and the metadata is stored in the storage unit **710** as data **716**. In such implementation, any one or all of the controller **702**, the BFU **705**, and the TRU **706** may generate metadata indicating beam experience as good, bad, better, worst, etc., and/or signal transmission result as successful, unsuccessful, etc. upon transmission of the signal by the transmitting antenna **701**. The generated metadata may then be associated with the one or more of (a) the virtual three-dimensional shape, (b) the at least one selected face, (c) the at least one optimum grid, and (d) the at least one beam. The associated metadata is then stored in the storage unit **710**. Such metadata can be used for performing the face selection and the grid selection later, as described above. In addition, to the beam experience and transmission result, the controller **702**, the BFU **705**, and the TRU **706** can determine corresponding geographical location, time-period, and other details, and store as metadata in the storage unit **710**.

[0088] In one implementation, data related to one or more of (a) the virtual three-dimensional shape, (b) the at least one selected face, (c) the at least one optimum grid, and (d) the at least one beam is transmitted to a receiver. In such implementation, the controller **702** includes a data-transmitting unit (DTU) **717** to transmit the stored data **716** to a receiver (not shown in the figure) automatically upon or prior to or along with transmission of the signal by the transmitting antenna **701**. Examples of such receiver include, but not limited to, user terminal such as smart phone, wearable devices, and a VR device, a base station, vehicle, UAVs, LEO satellites, autonomous small size robot such as drones, and IoT devices such as wireless modems, smart TV, etc. The DTU **717** may transmit the stored data **716** using techniques as known in the art.

[0089] In one implementation, a further user-input indicative of access control information is received. The access control information is then stored in the storage unit in a mapped relationship with data related to one or more of (a) the virtual three-dimensional shape, (b) the at least one selected face, (c) the at least one optimum grid, and (d) the

at least one beam. In such implementation, the user-input is received via an input unit communicative coupled with the user terminal, the base station, the vehicle, and the autonomous small size robot of which the device **700** is the integral part, as described earlier. The UIRU **708** receives the user-input indicative of access control information. As would be understood, the access control information provides information of users and/or devices/apparatuses/systems that can access the stored data **716**, thereby providing selective access to the storage unit **710**. Upon receiving the access control information, the controller **702** stores the access control information in a mapped relationship with data related to virtual three-dimensional shape, selected face, optimum grid, beam, and metadata as the stored data in the storage unit **710**. In a similar manner, the controller **702** may receive data from the receiver and store the received data in the storage unit **710** as the stored data **716**.

[0090] In one implementation, a further user-input indicative of tagging one or more of (a) the virtual three-dimensional shape, (b) the at least one selected face, (c) the at least one optimum grid, and (d) the at least one beam is received. In such implementation, the controller **702** may present the aforesaid data on a display unit (not shown in the figure) in a manner as known in the art. Upon presenting the data, the UIRU **708** receives the user-input indicative of tagging the data. The tagging of data can be indicative of beam experience as good, bad, better, worst, etc., and/or signal transmission result as successful, unsuccessful, etc. Upon receiving the user-input, the controller **702** stores the data in a mapped relationship with above the data as the stored data in the storage unit **710**.

[0091] In one implementation, a further user-input indicative of ranking one or more of (a) the virtual three-dimensional shape, (b) the at least one selected face, (c) the at least one optimum grid, and (d) the at least one beam is received. The ranking is then stored in the storage unit. In such implementation, the controller **702** may present the aforesaid data on the display unit, in a manner as known in the art. Upon presenting the data, the UIRU **708** receives the user-input indicative of ranking the data. The ranking can be based on at least one of beam experience, signal transmission result, geographical location, time-period, and other details. Upon receiving the user-input, the controller **702** stores the data in in a mapped relationship with the above mentioned data in the storage unit **710**. In a similar manner, the controller **702** may receive ranking via the data sharing application and store the recommendation in the storage unit **710** as the stored data **716**. In addition, the received data can be stored with respect to each user. In addition, the received data can be stored with respect to each user. This enables selection of required data based on users. For example, user A receives recommendation from user B and user C. Thus, when user A again tries to send data using the disclosure to user B, the data corresponding to user B will be preferred. Similarly, when user A again tries to send data using the disclosure to user C, the data corresponding to user C will be preferred. In addition, the reception of data related to other users enables performing a combined evaluation of data for selecting most suitable optimum grid.

[0092] In one implementation, a further user-input indicative of sharing data related to one or more of (a) the virtual three-dimensional shape, (b) the at least one selected face, (c) the at least one optimum grid, and (d) the at least one beam at least one data sharing application is received. In such implementation, the controller **702** may be linked/connected with a data sharing application via mechanism knows in the art.

[0093] Examples of such data sharing application include, but not limited to, a chat application, an instant messaging application, a messaging application, and social media application. Examples of such mechanisms include, but not limited to, extensions, plug-ins, and in-built mechanisms. Accordingly, the UIRU **708** receives the user-input indicative of sharing the data sharing application. Upon receiving the user-input, the controller **702** enables the user to select and share data in a manner as known in the art. In a similar manner, the controller **702** may receive data via the data application and store the received data in the storage unit **710** as the stored data **716**. In addition, the reception of data related to other users enables performing a combined evaluation of data for selecting most suitable optimum grid.

[0094] In one implementation, a further user-input indicative of recommending data related to one or more of (a) the virtual three-dimensional shape, (b) the at least one selected face, (c) the at least one optimum grid, and (d) the at least one beam via the at least one data sharing application is received. In such implementation, the UIRU **708** receives the user-input indicative of sharing the data sharing application, as described above. Upon receiving the user-input, the controller **702** enables the user to select and recommend data in a manner as known in the art. The recommendation can be based on at least one of beam experience, signal transmission result, geographical location, time-period, and other details. In a similar manner, the controller **702** may receive recommendation via the data sharing application and store the recommendation in the storage unit **710** as the stored data **716**. In addition, the received data can be stored with respect to each user. This enables selection of required data based on users. For example, user A receives recommendation from user B and user C. Thus, when user A again tries to send data using the disclosure to user B, the data corresponding to user B will be preferred. Similarly, when user A again tries to send data using the disclosure to user C, the data corresponding to user C will be preferred. In addition, the reception of data related to other users enables performing a combined evaluation of data for selecting most suitable optimum grid.

[0095] Although, the above description explains the method of beam forming in accordance with the disclosure for the transmitting antenna, it is to be understood that same method can be implemented for the receiving antenna. As such, the receiving antenna may also be coupled with a device (not shown in the figure) having units as explained above.

[0096] Thus, the disclosure enables forming an efficient and high direction beam based on at the least one grid with minimal losses. This reduces time required to search for a beam path with minimal propagation loss.

[0097] As such, the disclosure can be implemented for various communication systems for transmitting and receiving signals with minimal losses and minimal delay. Examples of communication systems include, but not limited to, multiple input multiple output (MIMO) communication systems, multiple input single output (MISO) communication systems, single input multiple output (SIMO) communication systems, etc.

[0098] Similarly, the disclosure can be implemented within devices/systems/apparatus operating in various wire-

less/cellular networks for transmitting and receiving data with minimal losses and minimal delay. Examples of network include, but not limited to, indoor wireless networks, outdoor wireless networks, core network interfaces, back end networks, cloud based networks such as device-to-device (D2D) network and machine-to-machine (M2M) network, etc.

[0099] FIG. **8** is a block diagram illustrating an example of architecture of a system **800** configured for use in wireless communication, according to an embodiment of the disclosure.

[0100] Referring to FIG. **8**, the system **800** can be part of MIMO communication systems, MISO communication systems, SIMO communication systems, etc., that can send or receive signals in either of indoor environments and outdoor environments. Thus, in one implementation, the system **800** can be user terminal such as smart phone, wearable devices, and a VR device, UAVs, LEO satellites, autonomous small size robot such as drones, and IoT devices such as wireless modems, smart TV, etc. In another implementation, the system **800** can also be part of a vehicle.

[0101] The system **800** may include a processor **801**, e.g., a central processing unit (CPU), a graphics processing unit (GPU), or both. The processor **801** may be a component in a variety of systems. For example, the processor **801** may be part of a standard personal computer or a workstation. The processor **801** may be one or more general processors, digital signal processors, application specific integrated circuits, field programmable gate arrays, servers, networks, digital circuits, analog circuits, combinations thereof, or other now known or later developed devices for analyzing and processing data The processor **801** may implement a software program, such as code generated manually (i.e., programmed). The processor **801** may include at least one central processing unit (CPU). The processor **801** may be operated as a controller.

[0102] The system **800** may include a memory **802**, such as a memory **802** that can communicate via a bus **803**. The memory **802** may be a main memory, a static memory, or a dynamic memory. The memory **802** may include, but is not limited to computer readable storage media such as various types of volatile and non-volatile storage media, including but not limited to random access memory, read-only memory, programmable read-only memory, electrically programmable read-only memory, electrically erasable read-only memory, flash memory, magnetic tape or disk, optical media and the like. In one example, the memory **802** includes a cache or random access memory for the processor **801**. In alternative examples, the memory **802** is separate from the processor **801**, such as a cache memory of a processor, the system memory, or other memory. The memory **802** may be an external storage device or database for storing data. Examples include a hard drive, compact disc ("CD"), digital video disc ("DVD"), memory card, memory stick, floppy disc, universal serial bus ("USB") memory device, or any other device operative to store data. The memory **802** is operable to store instructions **804** executable by the processor **801**. The functions, acts or tasks illustrated in the figures or described may be performed by the programmed processor **801** executing the instructions stored in the memory **802**. The functions, acts or tasks are independent of the particular type of instructions set, storage media, processor or processing strategy and may be performed by software, hardware, integrated circuits, firmware, micro-code and the like, operating alone or in combination. Likewise, processing strategies may include multiprocessing, multitasking, parallel processing and the like.

[0103] The system **800** may further include a display unit **805**, such as a liquid crystal display (LCD), an organic light emitting diode (OLED), a flat panel display, a solid state display, a cathode ray tube (CRT), a projector, a printer or other now known or later developed display device for outputting determined information. The display unit **805** may act as an interface for the user to see the functioning of the processor **801**, or other units. The system **800** may further include other output devices (not shown in the figure).

[0104] The system **800** may further include an input unit **806** configured to allow a user to interact with any of the components of system **800**. The input device may be a number pad, a keyboard, or a cursor control device, such as a mouse, or a joystick, touch screen display, remote control or any other device operative to interact with the system **800**.

[0105] The system **800** may be connected to a network **807** to communicate voice, video, audio, images or any other data over the network **807**. Further, the instructions **804** may be transmitted or received over the network **807** via a communication interface **808** or network **807** or using the bus **803**. The communication interface **808** or network **807** may be a part of the processor **801** or may be a separate component. The communication interface **808** may be created in software or may be a physical connection in hardware. The communication interface **808** may be configured to connect with the network **807**, external media, the display unit **805**, or any other components in system **800**, or combinations thereof. The connection with the network **807** may be a physical connection, such as a wired Ethernet connection or may be established wirelessly as discussed later. Likewise, the additional connections with other components of the system **800** may be physical connections or may be established wirelessly. The network **807** may alternatively be directly connected to the bus **803**. The communication interface **808** may be a transceiver.

[0106] The network **807** may include wired networks, wireless networks, Ethernet AVB networks, or combinations thereof. The wireless network may be a cellular telephone network, an 802.11, 802.16, 802.70, 802.1Q or Wi Max network. Further, the network **807** may be a public network, such as the Internet, a private network, such as an intranet, or combinations thereof, and may utilize a variety of networking protocols now available or later developed including, but not limited to TCP/IP based networking protocols.

[0107] The system **800** may further include a device **809** for forming a beam in accordance with the disclosure. The device **809** can include a controller **810** to select at least one obstruction free zone and at one obstruction free beam window, as described in various embodiments above. The device **809** further includes forming unit (BFU) **811** within a TRU **812**. The BFU **811** forms at least one beam based on the optimum grids selected by the controller **810**, as described in various embodiments above. The TRU **812** transmits or receives a signal to/from a receiver through the at least one beam formed by the BFU **811** via one or more antennas **813**. In one implementation, the antenna(s) **813** transmit or receive the signal over millimeter waves (mmWV). Examples of the antenna(s) **813** can include, but

not limited to, a beam antenna and an array antenna that can form one or more beams in a specific direction.

[0108] Further, in one implementation, the device **809** can be a separate component. In one implementation, the device **809** can be part of a dedicated radio frequency (RF) unit (not shown in the figure) connected to the antenna(s) **813**. In one implementation, the device **809** can be a software component implemented in a physical layer of a digital RF interface, as per current communications standards.

[0109] Further, the receiver can be part of MIMO communication systems, MISO communication systems, SIMO communication systems, etc., that can send or receive signals in either of indoor environments and outdoor environments. For example, the receiver can be a base station, a user-terminal, a vehicle, an IOT device, and an autonomous small size robot.

[0110] Although, specific components have been illustrated in the figure, the system **800** may include further components (hardware/software/combination thereof) necessary for proper functioning/operation of the system **800** as required.

[0111] FIG. **9** is a block diagram illustrating an example of architecture of a system **900** configured for use in wireless communication, according to an embodiment of the disclosure. The system **900** can be base station.

[0112] Referring to FIG. **9**, the system **900** may include a processor **901**, e.g., a CPU, a GPU, or both. The processor **901** may be a component in a variety of systems. For example, the processor **901** may be part of a standard personal computer or a workstation. The processor **901** may be one or more general processors, digital signal processors, application specific integrated circuits, field programmable gate arrays, servers, networks, digital circuits, analog circuits, combinations thereof, or other now known or later developed devices for analyzing and processing data The processor **901** may implement a software program, such as code generated manually (i.e., programmed). The processor **901** may include at least one central processing unit (CPU). The processor **901** may be operated as a controller.

[0113] The system **900** may include a memory **902**, such as a memory **902** that can communicate via a bus **903**. The memory **902** may be a main memory, a static memory, or a dynamic memory. The memory **902** may include, but is not limited to computer readable storage media such as various types of volatile and non-volatile storage media, including but not limited to random access memory, read-only memory, programmable read-only memory, electrically programmable read-only memory, electrically erasable read-only memory, flash memory, magnetic tape or disk, optical media and the like. In one example, the memory **902** includes a cache or random access memory for the processor **901**. In alternative examples, the memory **902** is separate from the processor **901**, such as a cache memory of a processor, the system memory, or other memory. The memory **902** may be an external storage device or database for storing data. Examples include a hard drive, "CD", "DVD", memory card, memory stick, floppy disc, "USB" memory device, or any other device operative to store data. The memory **902** is operable to store instructions **904** executable by the processor **901**. The functions, acts or tasks illustrated in the figures or described may be performed by the programmed processor **901** executing the instructions stored in the memory **902**. The functions, acts or tasks are independent of the particular type of instructions set, storage media, processor or processing strategy and may be performed by software, hardware, integrated circuits, firmware, micro-code and the like, operating alone or in combination. Likewise, processing strategies may include multiprocessing, multitasking, parallel processing and the like.

[0114] The system **900** may be connected to a network **905** to communicate voice, video, audio, images or any other data over the network **905**. Further, the instructions **904** may be transmitted or received over the network **905** via a communication interface **915** or network **905** or using the bus **903**. The communication interface **915** or network **905** may be a part of the processor **901** or may be a separate component. The communication interface **915** may be created in software or may be a physical connection in hardware. The communication interface **915** may be configured to connect with the network **905**, external media, a display unit (not shown in the figure), or any other components in system **900**, or combinations thereof. The connection with the network **905** may be a physical connection, such as a wired Ethernet connection or may be established wirelessly as discussed later. Likewise, the additional connections with other components of the system **900** may be physical connections or may be established wirelessly. The network **905** may alternatively be directly connected to the bus **903**. The communication interface **915** may be a transceiver.

[0115] The network **905** may include wired networks, wireless networks, Ethernet AVB networks, or combinations thereof. The wireless network may be a cellular telephone network, an 802.11, 802.16, 802.70, 802.1Q or Wi Max network. Further, the network **905** may be a public network, such as the Internet, a private network, such as an intranet, or combinations thereof, and may utilize a variety of networking protocols now available or later developed including, but not limited to TCP/IP based networking protocols.

[0116] The system **900** may further include a device **906** for forming a beam in accordance with the disclosure. The device **906** can include a controller **907** to select at least one obstruction free zone and at one obstruction free beam window, as described in various embodiments above. The device **906** further includes BFU **908** within a TRU **909**. The BFU **908** forms at least one beam based on the optimum grids selected by the controller **907**, as described in various embodiments above. The TRU **909** transmits or receives a signal to/from a receiver through the at least one beam formed by the BFU **908** via one or more antennas **910**. In one implementation, the antenna(s) **910** transmit or receive the signal over mmWV. Examples of the antenna(s) **910** can include, but not limited to, a beam antenna and an array antenna that can form a beam in a specific direction. The receiver can be base station(s) **911**, user terminal(s) **912** such as smart phone whose architecture was illustrated in FIG. **8**, and other system(s) **913** such as an IOT device, vehicle, and an autonomous small size robot.

[0117] FIGS. **10**A to **10**H illustrates an example **1000** of implementing the method of beam forming as described above by a base station **1001** according to an embodiment of the disclosure.

[0118] Referring to FIG. **10**A, to create the virtual three-dimensional shape, data related to a plurality of obstructions **1002** at current location of base station **1001** is obtained. For the sake of brevity, only a side view is illustrated for illustrating distance between the base station **1001** and a plurality of obstructions. The base station **1001** may include

one or more transmitting antennas. As illustrated, a first obstruction **1002-1** such as tree is determined to be at distance D**1** from the base station **1001** based on the received data. Similarly, a second obstruction **1002-2** such as house is determined to be at distance D**2** from the base station **1001** and a third obstruction **1002-3** such as tree is determined to be at distance D**3** from the base station **1001** based on the received data. Likewise, a fourth obstruction **1002-4** such as building is determined to be at distance D**4** from the base station **1001**. As can be gathered, the first obstruction **1002-1** is nearest to the base station **1001** and the distance D**1** is the minimum distance from among the distances between the obstructions. In a similar manner, the minimum distance is calculated from all sides/directions of the base station **1001**. As such, the virtual three-dimensional shape is created such that the base station **1001** is at the center of the virtual three-dimensional shape and a radius/distance from the center of virtual three-dimensional shape to a face of the three-dimensional shape is D**1**, the minimum distance (represented by dashed line).

[0119] Referring to FIG. **10**B, illustrates an example virtual three-dimensional shape **1003** in form of cube created around the transmitting antenna with minimum distance D**1**. The virtual three-dimensional shape **1003** is also depicted on a display unit **1004**. In the example, a receiving antenna may be located in the direction of the side faces **1003-1** and **1003-2**. Therefore, side faces **1003-1** and **1003-2** are selected based on the first set of parameters as described above.

[0120] Referring to FIG. **10**C, a plurality of grids **1005** (represented by squares formed by dashed line) are formed on the side faces **1003-1** and **1003-2**, in a manner as described above. The plurality of grids **1005** are formed by dividing the faces into 3-×-3 matrix, in a manner as described earlier. For each of the grid, a value of the second set of parameters is determined. For the sake of brevity, only two parameters attenuation as A and network efficiency as N are depicted, and the base stations has not been depicted. Further, reference numerals 0, 1, 2, and 3 indicate a value of the parameter which three (3) being higher value and zero (0) being lower value.

[0121] Referring to FIG. **10**D, a preview user-interface **1015** is provided on the display unit **1004**. The user-interface **1015** displays a plurality of icons **1006** indicative of obstructions as available near the base station **1001**. A user-input **1007** can be received to indicate presence of an obstruction in a grid **1005-1**.

[0122] Referring to FIG. **10**E, based on the user-input, the data corresponding to the obstruction is fetched and the value of attenuation and network efficiency is re-determined for the grid **1005-1** from A2N1 to A22N12. Based on the values of attenuation and network efficiency, A3N3, the further sub-grids of 2×2 matrix are created in grids of face **1003-1**.

[0123] Referring to FIG. **10**F illustrates a front view of the face **1003-1** depicting the grids **1005-2** and **1005-3**, and sub-grids **1016** (represented by squares formed by dashed lines) within the grids **1005-2** and **1005-3** along with values of attenuation A and network efficiency N.

[0124] Referring to FIG. **10**G, grid **1003-1** with attenuation A01 and network efficiency N01 as optimal values, is selected as the optimum grid, and a beam **1010** is formed by determining angle information.

[0125] Referring to FIG. **10**H, the base station **1001** transmits signal via the beam **1010** formed in accordance with grid **1005-4** towards the receiving antenna of a target mobile device **1008**. This enables creating highly-directional beam towards the target mobile device **1008** such that a coverage area of the beam only includes target mobile device **1008** and not any interfering mobile device **1009**.

[0126] According to various embodiments, a beam forming method for a transmitting antenna may comprise: creating a virtual three-dimensional shape around the transmitting antenna; selecting at least one face from among a plurality of faces of the virtual three-dimensional shape based on a first parameter set; creating one or more grids on the at least one face; selecting at least one grid from among the one or more grids based on a second parameter set; and forming at least one beam based on the at least one grid.

[0127] According to various embodiments, the beam forming method may further comprise: obtaining a current location of the transmitting antenna; receiving obstruction data related to at least one obstruction based on the current location; selecting the virtual three-dimensional shape from among a plurality of virtual three-dimensional shapes based on the obstruction data, wherein the transmitting antenna is at a center of the virtual three-dimensional shape; and creating the virtual three-dimensional shape around the transmitting antenna. Additionally, a distance from the center of the virtual three-dimensional shape to a face of the three-dimensional shape may be a minimum distance between the transmitting antenna and the at least one obstruction.

[0128] Additionally, the obstruction data may be received from at least one of a storage unit, at least one reflected signal that is received from the current location, or a user input. The first parameter set may include at least one of channel sense information, first data related to the transmitting antenna, second data related to a receiving antenna, a direction of the receiving antenna, cellular information, or a user input. The second parameter set includes at least one of an attenuation, a propagation delay, a network efficiency, a quality of service (QoS), a latency, a signal-to-noise ratio (SNR) channel capacity, or a signal-to-interference ratio. The one or more grids may divide a face of the virtual three-dimensional shape into an N×M matrix.

[0129] According to various embodiments, the beam forming method may further comprise: obtaining a value of the second parameter set for each of the one or more grids; and selecting the at least one grid from the one or more grids, based on the value of the second parameter set, the at least one grid being in a direction of a receiving antenna.

[0130] According to various embodiments, the beam forming method may further comprise: receiving at least one reflected signal, the at least one reflected signal being received from the one or more grids; receiving data corresponding to at least one obstruction available in the one or more grids from a storage unit; receiving image data corresponding to the at least one obstruction available in the one or more grids from an image capturing unit; or receiving a user input corresponding to the at least one obstruction available in the one or more grids.

[0131] Additionally, the image data includes at least one of: information related to a geographic location of the one or more grids; information related to characteristics of the at least one obstruction located in proximity to the geographic location; metadata associated with the at least one grid prior

to current instance of time; or a rank associated with the at least one grid prior to the current instance of time.

[0132] According to various embodiments, the beam forming method may further comprise: creating sub-grids within the at least one grid based on the value of the second parameter set for the at least one grid; obtaining a value of the second parameter set for the sub-grids; selecting at least one sub-grid from the sub-grids based on the value of the second parameter set for the sub-grids, the at least one sub-grid being in a direction of a receiving antenna.

[0133] While the disclosure has been shown and described with reference to various embodiments thereof, it will be understood by those skilled in the art that various changes in form and details may be made therein without departing from the spirit and scope of the disclosure as defined by the appended claims and their equivalents.

What is claimed is:

1. A beam forming method for a transmitting antenna, the method comprising:
- creating a virtual three-dimensional shape around the transmitting antenna;
- selecting at least one face from among a plurality of faces of the virtual three-dimensional shape based on a first parameter set;
- creating one or more grids on the at least one face;
- selecting at least one grid from among the one or more grids based on a second parameter set; and
- forming at least one beam based on the at least one grid.

2. The beam forming method of claim **1**, wherein the creating of the virtual three-dimensional shape comprises:
- obtaining a current location of the transmitting antenna;
- receiving obstruction data related to at least one obstruction based on the current location;
- selecting the virtual three-dimensional shape from among a plurality of virtual three-dimensional shapes based on the obstruction data, wherein the transmitting antenna is at a center of the virtual three-dimensional shape; and
- creating the virtual three-dimensional shape around the transmitting antenna;
- wherein a distance from the center of the virtual three-dimensional shape to a face of the virtual three-dimensional shape is a minimum distance between the transmitting antenna and the at least one obstruction.

3. The beam forming method of claim **2**, wherein the obstruction data is received from at least one of a storage unit, at least one reflected signal that is received from the current location, or a user input.

4. The beam forming method of claim **1**,
- wherein the first parameter set includes at least one of channel sense information, first data related to the transmitting antenna, second data related to a receiving antenna, a direction of the receiving antenna, cellular information, or a user input, and
- wherein the second parameter set includes at least one of an attenuation, a propagation delay, a network efficiency, a quality of service (QoS), a latency, a signal-to-noise ratio (SNR) channel capacity, or a signal-to-interference ratio.

5. The beam forming method of claim **1**, wherein the one or more grids divide a face of the virtual three-dimensional shape into an N×M matrix.

6. The beam forming method of claim **1**, wherein the selecting of the at least one grid comprises:
- obtaining a value of the second parameter set for each of the one or more grids; and
- selecting the at least one grid from the one or more grids, based on the value of the second parameter set, the at least one grid being in a direction of a receiving antenna.

7. The beam forming method of claim **6**,
- wherein the obtaining of the value of the second parameter set comprises at least one of:
- receiving at least one reflected signal, the at least one reflected signal being received from the one or more grids;
- receiving data corresponding to at least one obstruction available in the one or more grids from a storage unit;
- receiving image data corresponding to the at least one obstruction available in the one or more grids from an image capturing unit; or
- receiving a user input corresponding to the at least one obstruction available in the one or more grids.

8. The beam forming method of claim **7**, wherein the image data includes at least one of:
- information related to a geographic location of the one or more grids;
- information related to characteristics of the at least one obstruction located in proximity to the geographic location;
- metadata associated with the at least one grid prior to current instance of time; or
- a rank associated with the at least one grid prior to the current instance of time.

9. The beam forming method of claim **6**, further comprising:
- creating sub-grids within the at least one grid based on the value of the second parameter set for the at least one grid;
- obtaining a value of the second parameter set for the sub-grids;
- selecting at least one sub-grid from the sub-grids based on the value of the second parameter set for the sub-grids, the at least one sub-grid being in a direction of the receiving antenna.

10. The beam forming method of claim **6**, wherein selecting the at least one grid comprises:
- displaying a visual representation including the transmitting antenna, the virtual three-dimensional shape around the transmitting antenna, the at least one face, the one or more grids on the at least one face, and the value of the second parameter set for each of the one or more grids;
- receiving a user input on the visual representation; and
- selecting the at least one grid based on the user input.

11. The beam forming method of claim **1**, wherein the forming of the at least one beam comprises:
- determining angle information from the at least one grid; and
- controlling at least one beam parameter of the at least one beam based on the angle information.

12. The beam forming method of claim **11**, wherein the at least one beam parameter includes at least one of a gain, a frequency, a phase, an amplitude, a direction, a width, an intensity, a power, a signal to noise ratio, a signal to interference plus noise ratio, an interference, an output energy, a variance, a correlation, an elevation angle, or azimuth angle.

13. The beam forming method of claim 1, wherein the controlling of the at least one beam parameter is further based on obstruction data related to at least one obstruction based on a current location.

14. A device implementing a beam forming method for a transmitting antenna, the device comprising:

a transceiver;

a memory; and

at least one processor coupled to the transceiver and the memory,

wherein the at least one processor is configured to:

create a virtual three-dimensional shape around the transmitting antenna,

select at least one face from among a plurality of faces of the virtual three-dimensional shape based on a first parameter set,

create one or more grids on the at least one face,

select at least one grid from among the one or more grids based on a second parameter set, and

form at least one beam based on the at least one grid.

15. The device of claim 14,

wherein the at least one processor is further configured to obtain a current location of the transmitting antenna.

16. The device of claim 15,

wherein when the at least one processor creates the virtual three-dimensional shape, the at least one processor is further configured to:

receive obstruction data related to at least one obstruction based on the current location,

select the virtual three-dimensional shape from among a plurality of virtual three-dimensional shapes based on the obstruction data, wherein the transmitting antenna is at a center of the virtual three-dimensional shape; and

create the virtual three-dimensional shape around the transmitting antenna,

wherein a distance from the center of the virtual three-dimensional shape to a face of the virtual three-dimensional shape is a minimum distance between the transmitting antenna and the at least one obstruction.

17. The device of claim 14,

wherein the first parameter set includes at least one of channel sense information, first data related to the transmitting antenna, second data related to a receiving antenna, a direction of the receiving antenna, cellular information, or a user input, and

wherein the second parameter set includes at least one of an attenuation, a propagation delay, a network efficiency, a quality of service (QoS), a latency, a signal-to-noise ratio (SNR) channel capacity, or a signal-to-interference ratio.

18. The device of claim 14, wherein the one or more grids divide a face of the virtual three-dimensional shape into an N×M matrix.

19. The device of claim 14, wherein, when the at least one processor selects the at least one grid, the at least one processor is further configured to:

obtain a value of the second parameter set for each of the one or more grids, and

select the at least one grid from the one or more grids, based on the value of the second parameter set, the at least one grid being in a direction of a receiving antenna.

20. The device of claim 19, wherein, when the at least one processor selects the at least one grid, the at least one processor is further configured to:

create sub-grids within the at least one grid based on the value of the second parameter set,

obtain a value of the second parameter set for the sub-grids,

select at least one sub-grid from the sub-grids, based on the value of the second set for the sub-grids, the at least one sub-grid being in a direction of the receiving antenna.

21. The device of claim 19, wherein, when the at least one processor selects the at least one grid, the at least one processor is further configured to:

display a visual representation including the transmitting antenna, the virtual three-dimensional shape around the transmitting antenna, the at least one face, the one or more grids on the at least one selected face, and the value of the second parameter set for each of the one or more grids,

receive a user input on the visual representation, and

select the at least one grid based on the user input.

22. The device of claim 14, wherein, when the at least one processor forms the at least one beam, the at least one processor is further configured to:

determine angle information from the at least one grid; and

control at least one beam parameter of the at least one beam based on the angle information.

23. The device of claim 22, wherein the at least one beam parameter includes at least one of a gain, a frequency, a phase, an amplitude, a direction, a width, an intensity, a power, a signal to noise ratio, a signal to interference plus noise ratio, an interference, an output energy, a variance, a correlation, an elevation angle, or azimuth angle.

24. The device of claim 14, wherein the at least one processor is further configured to control the at least one beam based on obstruction data related to at least one obstruction based on a current location.

* * * * *

Materials Research Express

ACCEPTED MANUSCRIPT

Biodegradability and mechanical properties of Pineapple Leaf/Coir Fiber reinforced hybrid epoxy composites

To cite this article before publication: Mohit Mittal *et al* 2018 *Mater. Res. Express* in press https://doi.org/10.1088/2053-1591/aaf8d6

Manuscript version: Accepted Manuscript

Accepted Manuscript is "the version of the article accepted for publication including all changes made as a result of the peer review process, and which may also include the addition to the article by IOP Publishing of a header, an article ID, a cover sheet and/or an 'Accepted Manuscript' watermark, but excluding any other editing, typesetting or other changes made by IOP Publishing and/or its licensors"

This Accepted Manuscript is **© 2018 IOP Publishing Ltd**.

During the embargo period (the 12 month period from the publication of the Version of Record of this article), the Accepted Manuscript is fully protected by copyright and cannot be reused or reposted elsewhere.
As the Version of Record of this article is going to be / has been published on a subscription basis, this Accepted Manuscript is available for reuse under a CC BY-NC-ND 3.0 licence after the 12 month embargo period.

After the embargo period, everyone is permitted to use copy and redistribute this article for non-commercial purposes only, provided that they adhere to all the terms of the licence https://creativecommons.org/licences/by-nc-nd/3.0

Although reasonable endeavours have been taken to obtain all necessary permissions from third parties to include their copyrighted content within this article, their full citation and copyright line may not be present in this Accepted Manuscript version. Before using any content from this article, please refer to the Version of Record on IOPscience once published for full citation and copyright details, as permissions will likely be required. All third party content is fully copyright protected, unless specifically stated otherwise in the figure caption in the Version of Record.

View the article online for updates and enhancements.

This content was downloaded from IP address 14.139.251.107 on 26/12/2018 at 09:12

Biodegradability and Mechanical Properties of Pineapple Leaf/Coir Fiber Reinforced Hybrid Epoxy Composites

Mohit Mittal [a,*], Rajiv Chaudhary [a]

[a] *Department of Mechanical, Production, and Industrial Engineering, Delhi Technological University, Delhi, 110042, India*

[*] Corresponding author. *E-mail address*: **mohit.30mittal@gmail.com**; Tel. +91-9971698741.

Abstract

Environmental policies set the boundary conditions for industries and commercial market regarding the maximum utilization of biodegradable material. In this context, the current research work deals with the development of cellulosic fiber filled epoxy composites and test for biodegradability in the natural soil environment. Moreover, an experimental investigation has been carried out to study the effect of relative fiber volume content and alkaline treatment of cellulosic fibers on the biodegradability and mechanical properties of Pineapple leaf/Coir fiber reinforced hybrid epoxy composites. To accomplish the desired objectives, the total of 23 biocomposite specimens (untreated and alkali-treated) has been developed by hand lay-up molding technique and test for tensile, flexural, impact, and weight loss properties as per ASTM standard. In all composite specimens, the total fiber to polymer resin ratio was kept fixed at 40:60 (v/v). The total of four samples for each composite specimen was tested and their average values were reported. The experimental results showed that the hybrid composites exhibit rapid loss of mechanical strength in natural soil environment than the pure Pineapple leaf-Epoxy composite. The single pineapple leaf fiber reinforced material revealed a higher rate of biodegradation and greater loss of tensile and flexural strength as compared to the pure Coir-Epoxy composite. The alkali-treated coir fiber enriched composites have a higher weight loss and greater reduction in mechanical strength than the untreated one. The mechanical strength and biodegradability of an epoxy thermoset were increased with the incorporation of PALF and COIR fibers which leads to easy and smooth adoption in engineering applications.

***Keywords*:** natural fiber, hybrid biocomposites, biodegradable, mechanical properties, alkali treatment

Accepted Manuscript

1. Introduction

Recently, the cellulosic materials are earning a lot of concern in industrial applications, academia, and fundamental research. Furthermore, people are also looking for those materials which can biodegrade at the end of product life-cycle. Therefore, the researchers and technologists are putting their efforts to develop a high-performance material based on lignocellulosic fibers. The natural fiber reinforced composites (NFRC's) have an adequate potential to supplant synthetic materials in wide varieties of engineering applications. This was because of their exceptional features such as lightweight, low cost, renewability, non-hazardousness, biodegradability, easy availability, high specific strength and stiffness, corrosion resistant, safe manufacturing, and good acoustic, thermal, and electrical insulation etc. [1]. A lot of research work has already done on the deployment of local cheap and efficient natural fibers such as jute, banana, rice straw, bamboo, and sisal, etc. as reinforcement in polymer composites. H.S Kim et al. [2] studied the mechanical properties of agro flour filled polybutylene succinate biocomposites. S.H Lee et al. [3] studied the mechanical and thermal properties of Bamboo/PLA and Bamboo/PBS composites. G. Romhany et al. [4] investigated the tensile fracture and failure behavior of flax fiber reinforced starch composites. T.T. L Doan et al. [5] studied the effect of coupling agents on the properties of Jute fiber/PP composites. J. Wehsener et al. [6] investigated the influence of jute fiber addition on the formability of partially densified wood structure. Amongst all the commonly used natural fibers, the pineapple leaf (PALF) and coconut husk (COIR) fibers have significant potential to be used as reinforcement in fiber or powder form to develop a high strength, lightweight, and biodegradable biocomposite material. The PALF and COIR are multi-cellular fibers, extracted from the leaves of pineapple and the husk (mesocarp) of coconut fruit respectively. The primary reasons to select PALF and COIR fibers over the other natural fibers are:

- PALF contains high cellulose content (70-85%) which results in higher tensile and flexural properties than the flax, sisal, jute, OPEFB, and cotton fibers.
- The flexural and torsional rigidity of PALF is also comparable with jute fiber.
- Easy availability, low density, favorable aspect ratio, and low microfibrillar angle of PALF.
- COIR fiber has high lignin content (40-45%) which makes it more durable and stable under a wide range of temperature and humid conditions as well as provides excellent resistant properties against microbial and fungus attack.

Accepted Manuscript

S. Mishra et al. [7] reported that the PALF has a great potential to be used in rubber industries and this was due to its high modulus (34.5-82.5 GPa). U. Wisittanawat et al. [8] stated that the tensile and tear strength of NBR composite was increased to 10 MPa and 100kN/mm respectively by the loading of 30phr PALF. N. Kengkhekit et al. [9] reported that the PALF can be effectively used in a polypropylene matrix. Inspite of a large number of advantageous properties, the PALF exhibits poor impact toughness than that of COIR. Our previous research work reported that the PALF absorbs more water than that of COIR fiber and it was due to the presence of high cellulose content in PALF [10]. D. Verma et al. [11] reported that the COIR fiber is largely available in India and about 52 billion coconuts are yearly produced in the world. So, it is beneficial to develop and explore the materials based on PALF and COIR fibers. To combine their properties synergistically, it becomes necessary to reinforce PALF and COIR fibers in the same polymer matrix. The hybridization of a stiff and low elongation fiber with the high strain to failure fiber leads to an increment in the impact strength of resulting composite material. Moreover, the hybridization of one type of natural fiber with another provides a prominent and feasible solution which results in a multifunctional composite material having high creep and fatigue resistance with improved fracture toughness. Table 1 illustrates the literature on fiber hybridization and provides adequate assurance to the reviewers regarding its benefits. The properties of a hybrid composite depend not only on the individual properties of constituents but also on the fiber-matrix volume ratio, relative fiber volume content, an aspect ratio of individual fibers, arrangement and orientation of each kind of reinforcing fibers, fiber-matrix interfacial interaction, and the extent of an intermingling of the fibers. The failure of one kind of fiber can be overcome by the hybridization with a suitable kind of another fiber. In most of the cases, the hybrid composites exhibit better and comparable performance than the natural and synthetic fiber reinforced materials respectively. Inspite of It is difficult for engineers to select fully biodegradable material used in outdoor applications. Therefore, most of the practicing and experienced researchers have suggested to compound lignocellulosic fibers with a synthetic polymer resin which leads to a partially biodegradable high-performance composite material. We believe that the epoxy thermoset is a best suitable synthetic polymer for semi-structural and structural applications and this was because of its low viscosity; high mechanical strength; good adhesive and electrical properties; excellent resistance to chemicals, moisture, and environmental degradation; easy processing; and ability to easily cured at a temperature from 5^0C to 150^0C. However, the hydrophobic characteristics of an epoxy thermoset may increase the probability of poor compatibility with hydrophilic

Accepted Manuscript

cellulosic fibers. Therefore, it becomes necessary to alter the surface chemistry of natural fibers by the employment of the chemical treatment process. The previous research work reported in Table 2 also assured the researchers about the positive attributes of a chemical treatment process. The primary goal of this research work is to develop a biodegradable high strength biocomposite material. Therefore, an experimental investigation has been carried out to study the biodegradability and mechanical properties of untreated and alkali treated Pineapple leaf/Coir fiber reinforced composites in the natural soil environment. The primary reason behind this is to compare the relative performance of hybrid composites in terms of their ability to sustain mechanical strength in unfavorable conditions like water, sand etc.

Table 1 Previous research work reported on the hybrid fiber reinforced composites

Authors	Factors explored by researchers	Results	References
R. Shrivastava et al. (2016)	Development of a Coir/Glass fiber reinforced hybrid epoxy composite	The mechanical properties of a Coir-Epoxy composite were increased substantially after the hybridization with glass fiber.	[12]
R. Siakeng et al. (2018)	Physical properties of PALF/COIR fiber reinforced-PLA composites.	The density, water absorption, and thickness swelling of COIR-PLA composites were decreased after the hybridization with PALF.	[13]
T. Rihayat et al. (2018)	Investigated the mechanical properties of Bamboo, PALF, and COIR fibers reinforced hybrid composites.	The hybrid composite made up of bamboo, PALF, and COIR fibers exhibits higher mechanical strength than that of single fiber reinforced composites.	[14]
A. Shahzad et al. (2011)	Impact and fatigue properties of hemp/Glass fiber reinforced composites.	The impact and fatigue strength of pure hemp fiber composite were increased after the hybridization with glass fiber.	[15]
A. Atiqah et al. (2014)	Mechanical characterization of Kenaf/Glass fiber reinforced polyester composites.	The hybrid composite reinforced with alkali-treated kenaf fiber and glass fiber in volume ratio of 15/15 has higher tensile, flexural, and impact strength as compared to the other hybrid formulations.	[16]
M. Mittal et al. (2018)	Experimental investigation on the mechanical properties of PALF/COIR fiber reinforced hybrid epoxy composites	The tensile and flexural properties (strength and modulus) of Coir/Epoxy composite were increased after the hybridization with pineapple leaf fiber.	[17]
M. Jawaid et al. (2012)	Physical and chemical resistant properties of Jute/EFB-Epoxy hybrid composites.	The void content of hybrid composite was reduced and the stability towards chemical reagents (benzene, toluene, CCl_4, HNO_3, CH_3COOH, NaOH, and Na_2CO_3) was increased with the increase of jute fiber content.	[18]
S. Panthapulakkal et al. (2006)	Mechanical, water absorption and thermal characterization of hybrid hemp/glass fiber polypropylene composites.	The mechanical strength and thermal stability of Hemp/PP composite were increased after the incorporation of a glass fiber.	[19]
M. Haq et al. (2008)	Development of a high performance hybrid composite made up of UPE and soybean oil.	A Synergistic hybrid composite having balanced stiffness and toughness properties was developed after the partial substitution (10%) of UPE with EMS and reinforced with 1.5% nanoclay.	[20]
V.S. Chevali et al. (2015)	Effect of the loading of sunflower hull and distiller dried grains fiber on the physical properties of ABS polymer.	The tensile, flexural, and impact strength of ABS polymer were decreased after the addition of SFH and DDGS filler in ABS polymer. It was due to the poor compatibility between reinforcing fillers and polymer.	[21]

Accepted Manuscript

M.M Davoodi et al. (2011)	Compared the overall performance of a kenaf/glass-epoxy composite with GMT material for car bumper beam.	The Kenaf/Glass fiber reinforced hybrid epoxy composite in double hat profile (DHP) has significant potential to be used in a small-sized car bumper beam.	[22]
V.S. Uppin et al. (2016)	Interlaminar fracture toughness of Glass/Cellulose fiber reinforced epoxy composites	The interlaminar fracture toughness of a Glass-Epoxy composite was increased by 32% after the hybridization with cellulose fiber.	[23]
F. Cheng et al. (2014)	Characterization of Glass/Coir fiber reinforced polyester composites.	The flexural strength, impact strength, and modulus of elasticity of COIR-Polyester composite were increased by 419%, 562%, and 708% respectively after the addition of glass fabric.	[24]
V.K. Bhagat et al. (2014)	Studied the physical and mechanical properties of Coir/Glass hybrid epoxy composites.	The hybrid composite reinforced with 10 wt% coir fiber (15 mm length) and 20 wt% glass fiber exhibits the maximum mechanical strength.	[25]
V. Arumugaprabhu et al. (2016)	Mechanical characterization of the Palmyra/Coir fiber reinforced polyester composites.	The tensile, flexural, and impact strength of pure Palmyra/Polyester composite were increased significantly after the hybridization with Coir fiber in the ratio of 40:60 (Palmyra/Coir).	[26]
N.M. Nurazzi et al. (2018)	Effect of fiber hybridization on the mechanical properties of Sugar palm/Glass fiber reinforced polyester composites.	The hybrid composite consists of 40 wt% total fiber content with equal volume of each fiber (50:50 Sugar palm yarn: Glass fiber) exhibits a higher tensile, flexural, and compressive strength than the other hybrid formulations.	[27]
H.P.S Abdul Khalil et al. (2017)	Effect of the loading of coconut shell nano-fillers on the mechanical properties of kenaf/coconut fiber reinforced composites.	The incorporation of coconut shell nano-fillers up to 3 wt% leads to the increment in tensile, flexural, and impact strength of kenaf/coconut fiber reinforced composites.	[28]
IS. Aji et al. (2012)	Effect of the hybridization on the mechanical properties and water absorption behavior of Kenaf/PALF fiber reinforced HDPE composites.	The tensile and flexural properties of Kenaf/HDPE composite were increased after the hybridization with PALF. The equal volume content of PALF and Kenaf in HDPE matrix possess the optimum mechanical properties.	[29]
B. Bakri et al. (2017)	Effect of relative fiber volume content on the mechanical properties of Coir/Angustifolia Haw Agave fiber reinforced epoxy composites.	The hybrid composite reinforced with 15:15 v/v (Coir: Agave) yields higher tensile strength, tensile modulus, and flexural modulus than that of the other hybrid formulations (Coir: Agave = 10:20 and 20:10).	[30]
M.S Teja et al. (2016)	Effect of SiC filler loading on the mechanical properties of sisal fiber reinforced composite.	The SiC filled sisal-polyester composite possess 2.53 and 1.73 times higher tensile and impact strength than that of the unfilled composite.	[31]
R. Yahaya et al. (2016)	Effect of kenaf fiber content on the physical properties of kenaf-kevlar hybrid epoxy composites.	The void content was increased from 3.15% to 25.67% with the increase of kenaf fiber content from 22% to 68%.	[32]

Table 2 Previous research work reported on the chemically treated fiber reinforced composites

Authors	Factors explored by researchers	Results	References
L.Y. Mwaikambo et al. (2001)	Alkalization of hemp, sisal, jute, and kapok fibers	The mechanical properties and thermal stability were improved by the alkali treatment of cellulosic fibers.	[33]

Accepted Manuscript

M.J. John et al. (2008)	Effect of chemical modification on the properties of Sisal/OPEFB hybrid composite.	The 4% NaOH treated hybrid composite exhibits maximum tensile strength and torque value.	[34]
Xue Li et al. (2007)	Chemical treatment of natural fiber for high strength biocomposite material.	An alkali treatment significantly improved the static and dynamic mechanical properties of NFRC's with the increased resistance to moisture sorption.	[35]
M.J. John et al. (2007)	Characterization of chemically modified NFRC's.	Alkali treatment is one of the most efficient and reliable chemical treatments which favors the formation of a strong covalent bond between fibers and matrix.	[36]
P.J Jandas et al. (2011)	Effect of chemical treatment on the mechanical properties of PLA/Banana fiber reinforced composites.	The tensile strength, impact strength, glass transition temperature, and storage modulus of biocomposite were increased after the chemical treatments i.e. NaOH, APS, and Si69.	[37]
R. Ranjan et al. (2013)	Effect of alkali treatment on the mechanical properties of Banana/Sisal fiber reinforced PLA composites.	The 2 wt% NaOH treated hybrid composite yields better mechanical properties (tensile, flexural, and impact strength) than that of the untreated composites.	[38]
L. Uma Devi et al. (2011)	Effect of chemical treatment (NaOH and vinyl silane) and glass fiber content on the water absorption behavior of PALF/GF reinforced polyester composites.	The alkaline treated hybrid composite having glass fiber content of 0.46 V_f exhibits lowest water sorption affinity.	[39]
M. Rahman et al. (2018)	Effect of an alkali treatment, fiber content, and fiber volume ratio on the mechanical properties of Banana/PALF fiber reinforced polypropylene composites.	The hybrid composite reinforced with NaOH treated PALF and Banana fiber at a ratio of 3:1exhibits the best set of mechanical properties.	[40]
A. Atiqah et al. (2018)	Effect of chemical treatment on the mechanical properties of Sugar Palm/Glass fiber reinforced polyurethane composites.	The tensile, flexural, and impact strength of a hybrid composite were improved by 16%, 39%, and 18% respectively after the chemical treatment with 6 wt% alkaline + 2 wt% silane solution.	[41]
A. Oushabi et al. (2017)	Effect of alkali treatment on the mechanical and thermal properties of date palm fiber-polyurethane composites.	The tensile strength, interfacial bond strength, and thermal stability of DPF composites were increased after an alkali treatment. The optimal concentration for alkali treatment of DPF is 5 wt%.	[42]
K. Panyasart et al. (2014)	Effect of alkaline treatment on the mechanical properties of PALF/Polyamide 6 composites.	The alkali treated pineapple leaf fiber reinforced composite yields higher tensile strength and modulus of elasticity as compared to the untreated composites.	[43]
N.P.G Suardana et al. (2011)	Effect of chemical treatment on the mechanical properties of Coir/PLA biocomposites	The biocomposite treated with NaOH and 0.5 wt% acrylic acid solution yields higher tensile and flexural strength than the untreated composite and the composite treated only with NaOH solution.	[44]
E. Lopez et al. (2016)	Effect of surface treatment on the mechanical properties of Agave, Coir, and Pine fiber reinforced composites.	Treated fiber composites have better mechanical properties than the untreated and neat polymer composites.	[45]
G. Goud et al. (2010)	Effect of alkali treatment on the mechanical properties of *Roystonea regia* fiber reinforced epoxy composites	Alkali-treated fiber reinforced composite has better tensile and flexural properties than that of the untreated composite.	[46]
P. Anand et al. (2014)	Effect of alkali treatment on the mechanical properties of hemp fiber reinforced cellulose filled epoxy composite	The alkali-treated hemp fiber composite yields better mechanical properties than the untreated composite. It was due to the better interfacial interaction between fiber and matrix.	[47]

Accepted Manuscript

C.U Maheshwari et al. (2013)	Compared the mechanical properties of untreated, alkali-treated, and alkali-silane treated tamarind fiber reinforced polyester composites.	The composite reinforced with alkali-silane treated tamarind fiber (25 wt%) has higher tensile and flexural strength than the others.	[48]
S.C Venkateshappa et al. (2011)	Influence of an alkali treatment on the mechanical properties of areca fiber reinforced epoxy composites	The tensile, flexural, and compressive strength of composites were increased after the alkali treatment of areca fiber.	[49]

2. Experimental details

2.1 Materials

The medium viscosity epoxy resin [DGEBA (diglycidyl bisphenol A); LY 556; density: 1.16 g/cm^3; average molecular weight (M_n): 2300 g/mol] and hardener [TETA (triethylene tetraamine); HY 951; density: 0.95 g/cm^3; average molecular weight (M_n): 146.23 g/mol] were procured from M/s Sakshi Dies and Chemicals, Delhi (India). The chemical reaction involved during the curing process of an epoxy thermoset is illustrated in Figure 1. The lignocellulosic pineapple leaf (PALF, *Ananas-comosus*) and coconut husk (COIR, *Cocos-nucifera*) fibers were obtained from M/s Go Green Products, Chennai (India). The surface morphology of untreated and alkali-treated PALF and COIR fibers is illustrated in Figure 2 and 3 respectively. Table 3 and 4 revealed the typical properties of an epoxy thermoset and cellulosic fibers (PALF and COIR) respectively. For mercerization (*Alkali-treatment*) of natural fibers, the sodium hydroxide (NaOH) was used and obtained from the *Applied Chemistry Department*, DTU (Delhi), India.

Table 3 Typical properties of an epoxy matrix

The appearance of liquid resin	**A clear pale yellow**
Density (Kg/m^3)	1200-1250
Viscosity at 25^{0}C (cps)	550
Tensile strength (MPa)	11.14
Tensile modulus (GPa)	0.48
Flexural strength (MPa)	25.29
Flexural modulus (GPa)	1.53
Max. Elongation (%)	4.2-5.6
Impact strength (kJ/m^2)	1.2
Flashpoint	> 200^{0}C

(Authors observations)

Accepted Manuscript

Table 4 Physical properties of pineapple leaf and coir fiber [50]

Physical properties	Pineapple leaf fiber	Coir fiber
Density (g/cm^3)	0.98	1.2
Cellulose (%)	70-82	32-43
Hemicellulose (%)	18.8	0.15-0.25
Lignin (%)	5-12.7	40-45
Pectin (%)	1.1	3-4
Moisture content (%)	11.8	8
Microfibrillar angle (deg)	14	30-49
Diameter (µm)	20-80	100-460
Tensile strength (MPa)	413-1627	131-220
Young's modulus (GPa)	34.5-82.5	4-6
Elongation at break (%)	1.6	15-40

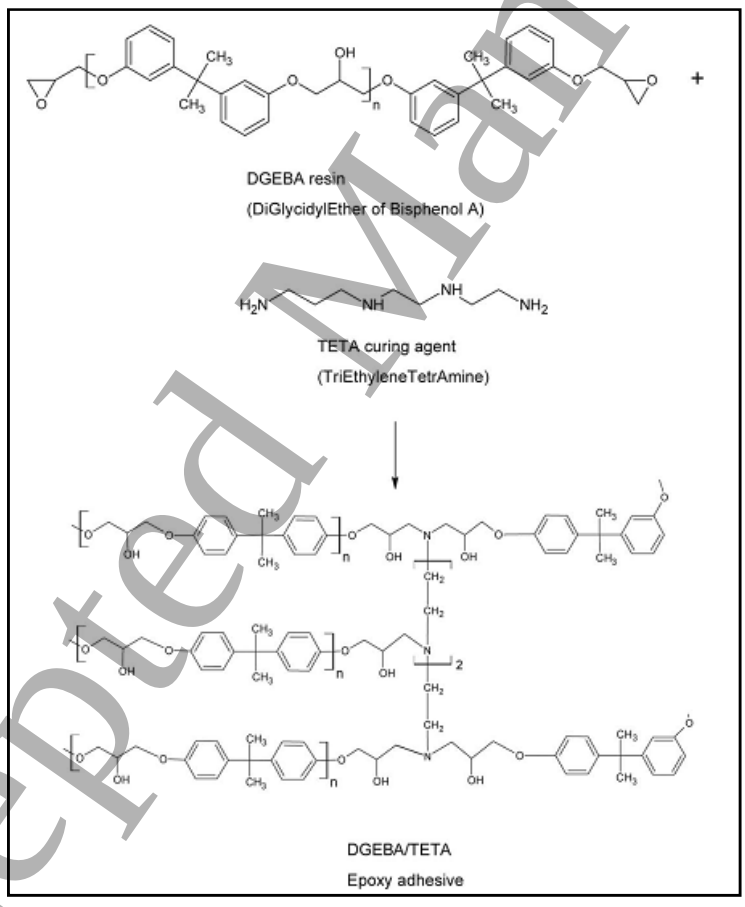
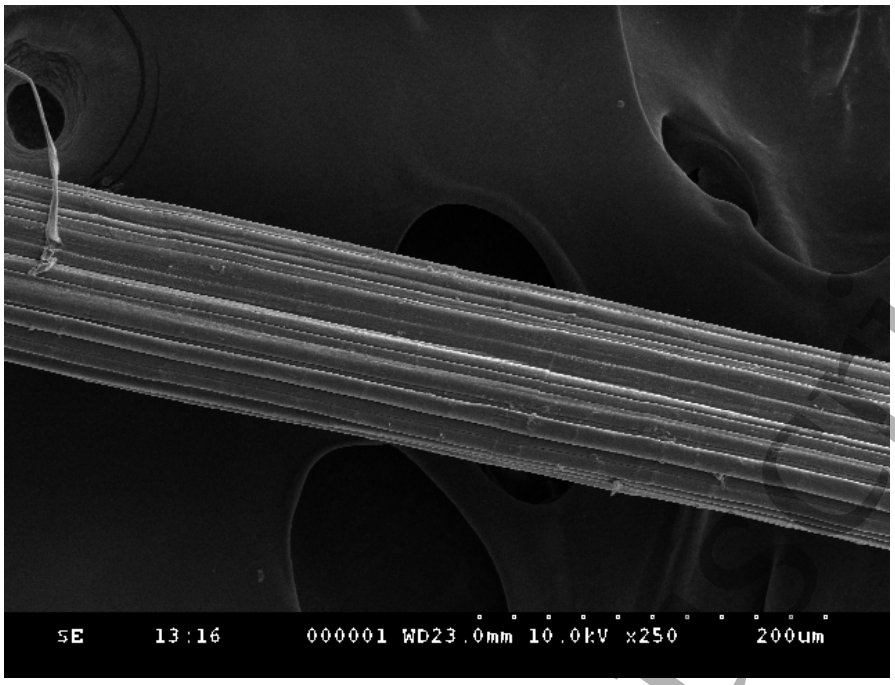
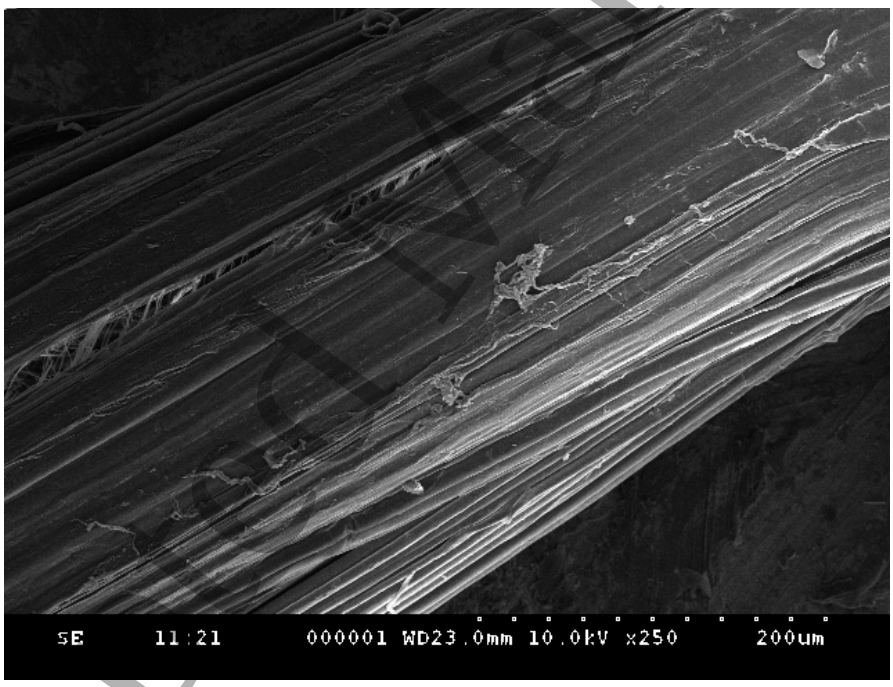


Figure 1 Curing reaction between epoxy resin (DGEBA) and hardener (TETA)

Accepted Manuscript



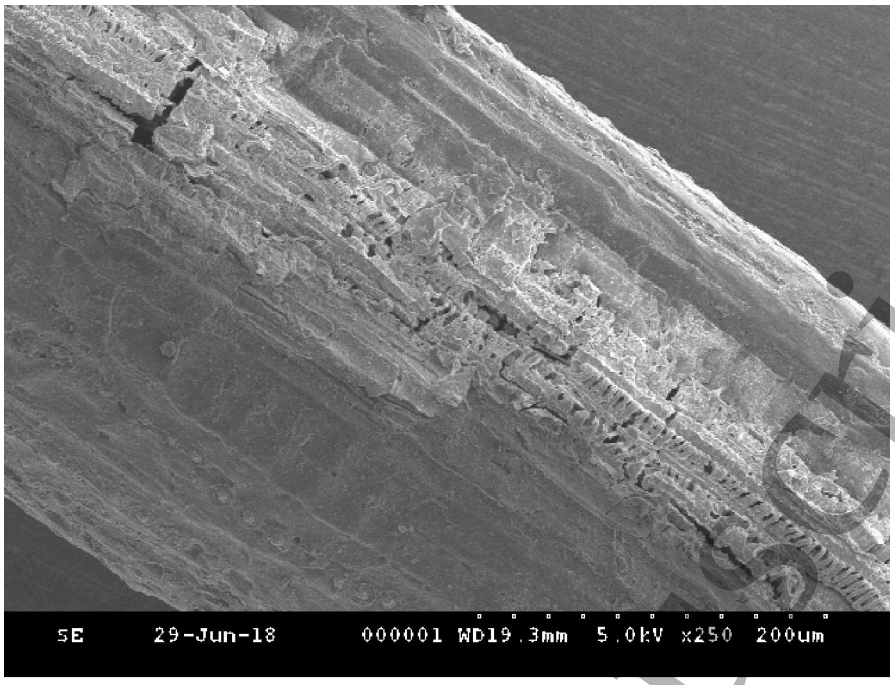
(a)



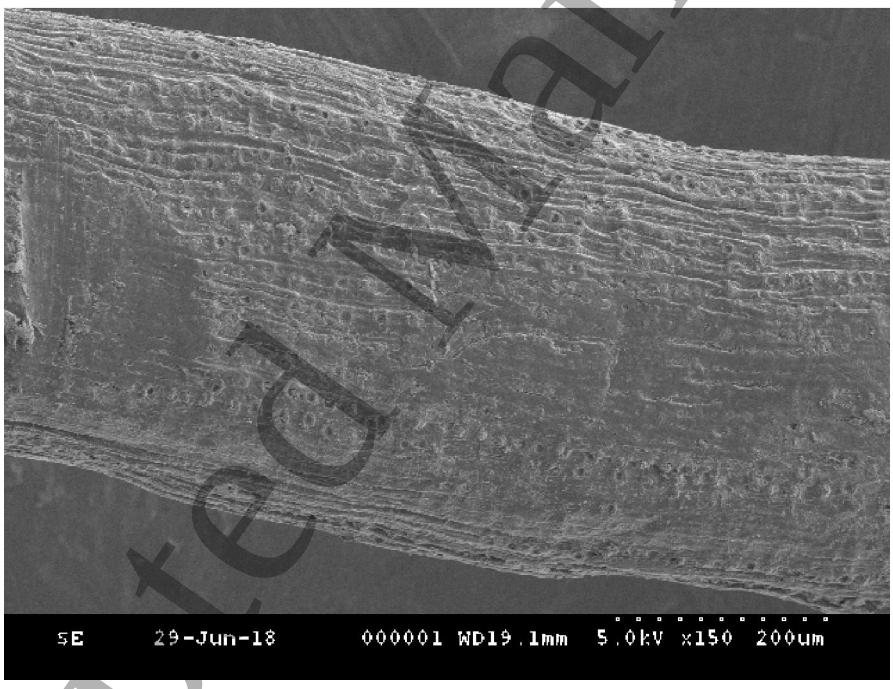
(b)

Figure 2 Surface morphology of (a) untreated PALF (b) 4% NaOH treated PALF

Accepted Manuscript



(a)



(b)

Figure 3 Surface morphology of (a) untreated COIR (b) 4% NaOH treated COIR

2.2 Alkali treatment of cellulosic fibers

In order to analyze the effect of an alkaline treatment on biodegradability and mechanical properties of developed composites, the PALF and COIR fibers were treated with a 4 wt% NaOH solution. Initially, the fibers were washed in tap water and then dried in sunlight for

Accepted Manuscript

three days to eliminate the surface impurities and absorbed water molecules. The cleaned cellulosic fibers were immersed in an alkaline solution for 24 hr at room temperature, followed by the treatment with 2 wt% acetic acid (CH_3COOH) solution and then rinsed in distilled water to control the pH level at 7. The neutralized wet fibers were dried again at room temperature and followed by oven drying at 70^0C for 24 hr.

2.3 Development of composites and sample preparation

The hand lay-up molding technique was employed to impregnate and compound the cellulosic fibers with an epoxy polymer resin an open mold cavity of size 200 mm X 100 mm X 4 mm. Before molding process, ensure that the epoxy resin (DGEBA) was mixed completely and thoroughly with a curing agent (TETA) and no air bubbles were present. To accomplish this objective, the epoxy resin was mixed slowly with hardener in a necked round glass flask through mechanical stirrer. Initially, the surface of a mold was covered with a Teflon sheet and sprayed with a releasing gel (*Mirror Glaze*) to prevent the sticking of an adhesive polymer resin. The intimately mixed short and randomly oriented fibers were placed in a glass mold cavity and impregnated with the premixed epoxy matrix. Ensure that the distribution of fibers and polymeric resin are uniforms throughout the mold space. During the fabrication of a composite sheet, the air bubbles are abstracted cautiously by using a steel roller. In the end, closed the mold and then pressed with 35 kg dead weight for 24 hr curing at room temperature. The total of 23 specimens (untreated and alkali-treated) was formulated by varying the relative fiber volume content (Table 5). In all composite samples, the volume ratio between resin-hardener and fibers-matrix were taken as 2:1 and 40:60 respectively. Further increase of total fiber content in a composite leads to the inadequate wetting of fiber with polymeric resin. Moreover, the effect of hybridization and alkaline treatment can be analyzed effectively at this optimum fiber-matrix ratio. The specimens for biodegradability and mechanical tests (Tensile, Flexural, and Impact) were cut from the molded sheet as per ASTM standard.

Table 5 Designation and composition of developed composites

Sr. No	Designation	Composition
1	EP	Epoxy matrix (100 vol.%)
2	P100	Epoxy (60 vol.%) + untreated pineapple leaf fiber (40 vol.%) + untreated coir fiber (0 vol.%)
3	P90-C10	Epoxy (60 vol.%) + untreated pineapple leaf fiber (36 vol.%) + untreated coir fiber (4 vol.%)
4	P80-C20	Epoxy (60 vol.%) + untreated pineapple leaf fiber (32 vol.%) + untreated coir fiber (8 vol.%)
5	P70-C30	Epoxy (60 vol.%) + untreated pineapple leaf fiber (28 vol.%) + untreated coir fiber (12 vol.%)

Accepted Manuscript

6	P60-C40	Epoxy (60 vol.%) + untreated pineapple leaf fiber (24 vol.%) + untreated coir fiber (16 vol.%)
7	P50-C50	Epoxy (60 vol.%) + untreated pineapple leaf fiber (20 vol.%) + untreated coir fiber (20 vol.%)
8	P40-C60	Epoxy (60 vol.%) + untreated pineapple leaf fiber (16 vol.%) + untreated coir fiber (24 vol.%)
9	P30-C70	Epoxy (60 vol.%) + untreated pineapple leaf fiber (12 vol.%) + untreated coir fiber (28 vol.%)
10	P20-C80	Epoxy (60 vol.%) + untreated pineapple leaf fiber (8 vol.%) + untreated coir fiber (32 vol.%)
11	P10-C90	Epoxy (60 vol.%) + untreated pineapple leaf fiber (4 vol.%) + untreated coir fiber (36 vol.%)
12	C100	Epoxy (60 vol.%) + untreated pineapple leaf fiber (0 vol.%) + untreated coir fiber (40 vol.%)
13	P100 (T)	Epoxy (60 vol.%) + NaOH treated pineapple leaf fiber (40 vol.%) + NaOH treated coir fiber (0 vol.%)
14	P90-C10 (T)	Epoxy (60 vol.%) + NaOH treated pineapple leaf fiber (36 vol.%) + NaOH treated coir fiber (4 vol.%)
15	P80-C20 (T)	Epoxy (60 vol.%) + NaOH treated pineapple leaf fiber (32 vol.%) + NaOH treated coir fiber (8 vol.%)
16	P70-C30 (T)	Epoxy (60 vol.%) + NaOH treated pineapple leaf fiber (28 vol.%) + NaOH treated coir fiber (12 vol.%)
17	P60-C40 (T)	Epoxy (60 vol.%) + NaOH treated pineapple leaf fiber (24 vol.%) + NaOH treated coir fiber (16 vol.%)
18	P50-C50 (T)	Epoxy (60 vol.%) + NaOH treated pineapple leaf fiber (20 vol.%) + NaOH treated coir fiber (20 vol.%)
19	P40-C60 (T)	Epoxy (60 vol.%) + NaOH treated pineapple leaf fiber (16 vol.%) + NaOH treated coir fiber (24 vol.%)
20	P30-C70 (T)	Epoxy (60 vol.%) + NaOH treated pineapple leaf fiber (12 vol.%) + NaOH treated coir fiber (28 vol.%)
21	P20-C80 (T)	Epoxy (60 vol.%) + NaOH treated pineapple leaf fiber (8 vol.%) + NaOH treated coir fiber (32 vol.%)
22	P10-C90 (T)	Epoxy (60 vol.%) + NaOH treated pineapple leaf fiber (4 vol.%) + NaOH treated coir fiber (36 vol.%)
23	C100 (T)	Epoxy (60 vol.%) + NaOH treated pineapple leaf fiber (0 vol.%) + NaOH treated coir fiber (40 vol.%)

2.4 Mechanical tests

For mechanical characterization of developed hybrid composites, the tensile, flexural (3 point bending), and impact tests were performed as per ASTM D 638, 790, and 256 standards respectively. The tensile and flexural bending tests were carried out on a calibrated Table Top Tinius Olsen Horizon H50KS, Universal Testing Machine. While the impact strength of biocomposites was determined by using an Izod impact tester (installed in the SOM Laboratory, DTU (Delhi), India). All the tests were performed at room temperature (27 ± 3 ^{0}C) and their important details with standardized dimensions of test specimens are reported in Table 6. The total of four samples for each composite specimen was tested and their average values were reported.

Table 6 Important test details and standardized dimensions of test specimens

Test details	Formulas used	Specimen dimensions
Tensile test (Cross head speed = 1mm/min)	$\sigma_t = \frac{F}{bt}$ Young's modulus = Tensile stress/Tensile strain	Flat dog-bone shape (50 mm gauge length, 13 mm width, and 4 mm thickness)
Flexural test (Cross head speed = 3mm/min)	$\sigma_f = \frac{3FL}{2bt^2}$ Flexural strain = $\frac{6st}{L^2}$ Flexural modulus = $\frac{L^3F}{4sbt^2}$	80 mm (l) X 15 mm (b) X 4 mm (t); Span length to depth ratio = 20:1

Accepted Manuscript

Izod impact test	Impact strength = Total absorbed energy (kJ)/Area (m^2)	65 mm (l) X 13 mm (b) X 4 mm; Notch angle = 45^0;

2.5 Biodegradability

The biodegradability of untreated and an alkali treated composites was studied in natural soil burial condition for 110 days. The specimens were dug out after every 10 days of soil burial, followed by washed in distilled water and then dried in an oven at 70^0C for 24 hr. The weight loss (%) was measured by using a digital highly calibrated weighing machine (0.001 g accuracy, DTU (Delhi), India). The total four measurements were taken for each composite specimen and their average values were reported.

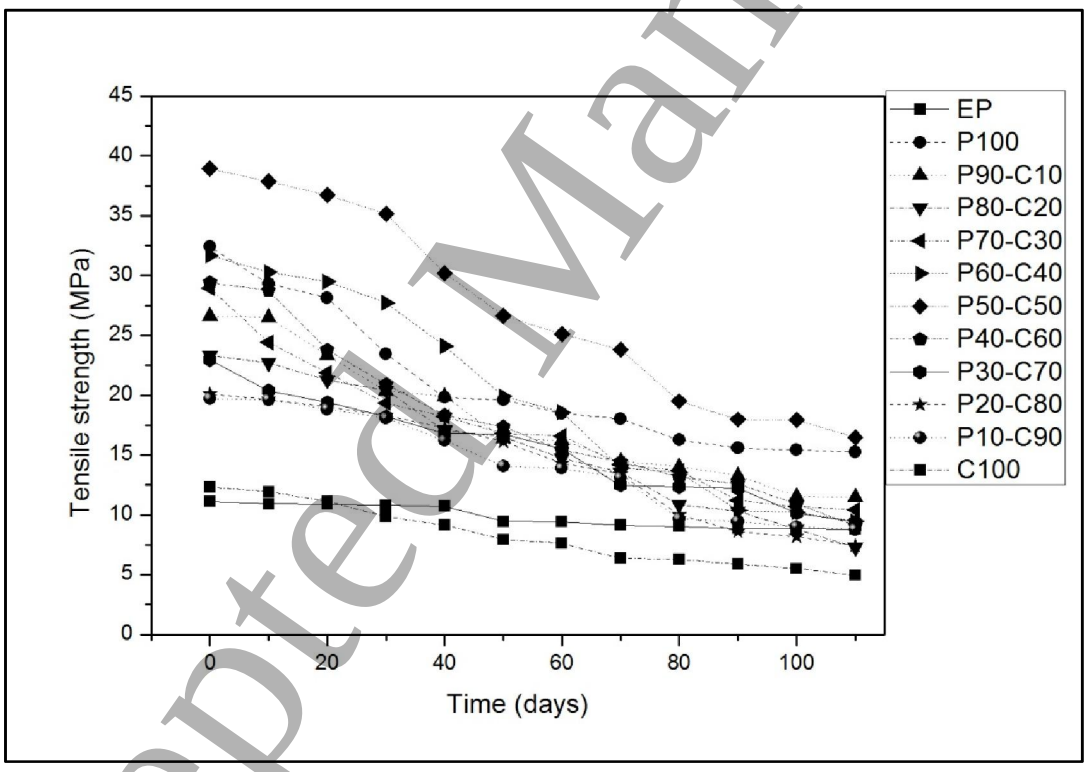
3. Results and Discussion

3.1 Tensile strength

The variation in tensile strength of untreated and alkali treated composites as a special function of burial time is shown in Figure 4(a) and 4(b) respectively. It was observed that the epoxy thermoset exhibits a very small decrement in tensile strength (about 2.35 MPa) after the 110 days of burial in the natural soil. This was attributed to the highly cross-linked network structure of an epoxy matrix. The rate of reduction and total loss of tensile strength in virgin epoxy matrix were increased with the incorporation of cellulosic fibers (PALF and COIR). It was due to the inherent characteristic of cellulosic fibers that they can biodegrade by the action of microorganisms. H. Kim et al. [51] also reported that the agro-flour filled PBS composite exhibits a higher rate of reduction in tensile strength than the unfilled PBS matrix. Figure 4 clearly revealed that the tensile strength of pure PALF-Epoxy composite was reduced rapidly in natural soil environment as compared to the COIR-Epoxy composite. It can be explain by the fact that the COIR fiber contains high lignin content (40-45%) which provides higher stability against the attack of microorganisms. In all the formulated biocomposites, the natural fibers were hydrolyzed significantly which leads to the weakening of interfacial bond strength between the fibers and a matrix resin. From Figure 5, we can conclude that the hybrid composites possess greater reduction in tensile strength as compared to the pure PALF-Epoxy composite. This negative effect of hybridization in natural soil environment is due to the penetration of water molecules at the interface between fiber-matrix and fiber-fiber which results in an easy fiber pull-out under mechanical loading conditions. The hybrid composite (P60-C40) drops 70% of tensile strength in the natural soil.

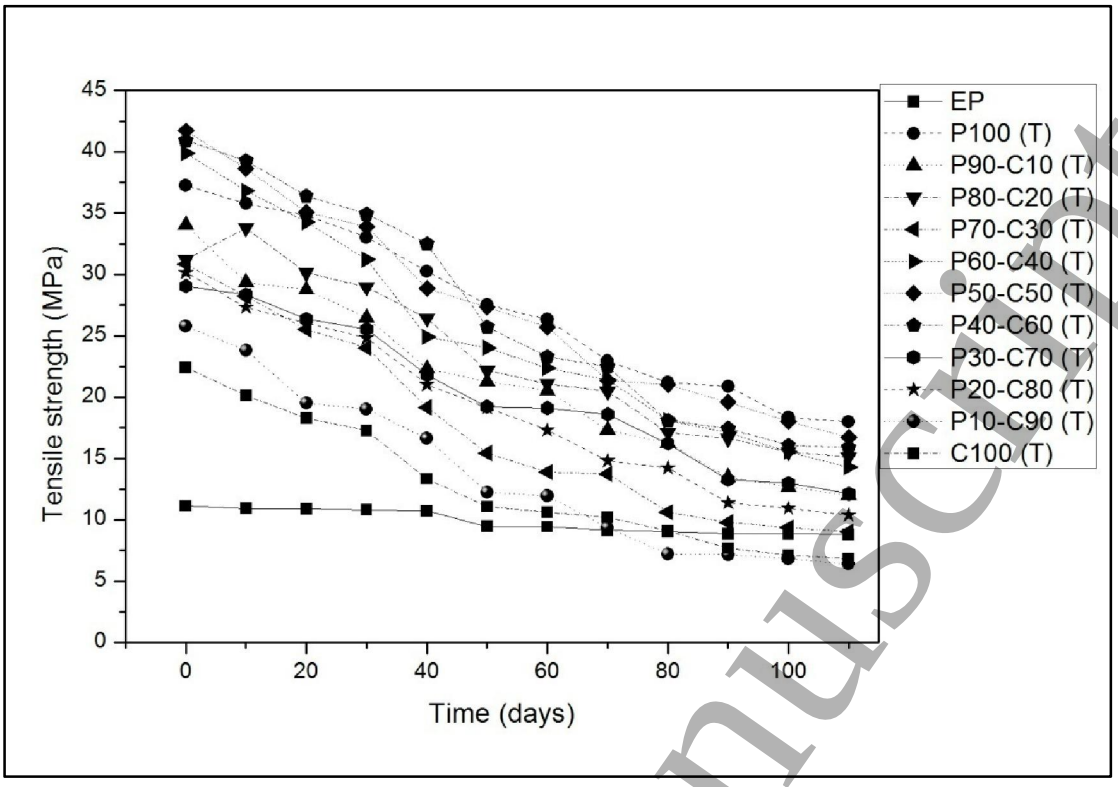
Accepted Manuscript

This was due to the attack of microorganisms and the hydrolysis of lignocellulosic fibers. It can be observed that the NaOH treated Coir-Epoxy composite possess a higher rate of reduction in tensile strength as compared to the untreated one. This was attributed to the removal of lignin compound from the fiber cell wall which results in rough and porous morphology of coir fiber surface (shown in Figure 3). Amongst all the developed composites, the NaOH treated P10-C90 possess maximum reduction of tensile strength (75.12%) in the natural soil environment. However, the alkaline treated P80-C20 hybrid composite exhibits 13% lower reduction in tensile strength as compared to the untreated one because of the removal of hemicellulose by mercerization process. In most of the untreated and alkali treated composites, the tensile strength of biocomposites was reduced significantly after 30 days of soil burial due to the substantial hydrolysis of cellulosic fibers. It is worth to note that the P60-C40 and P50-C50 composites exhibit a high rate of tensile strength reduction after 30 days.



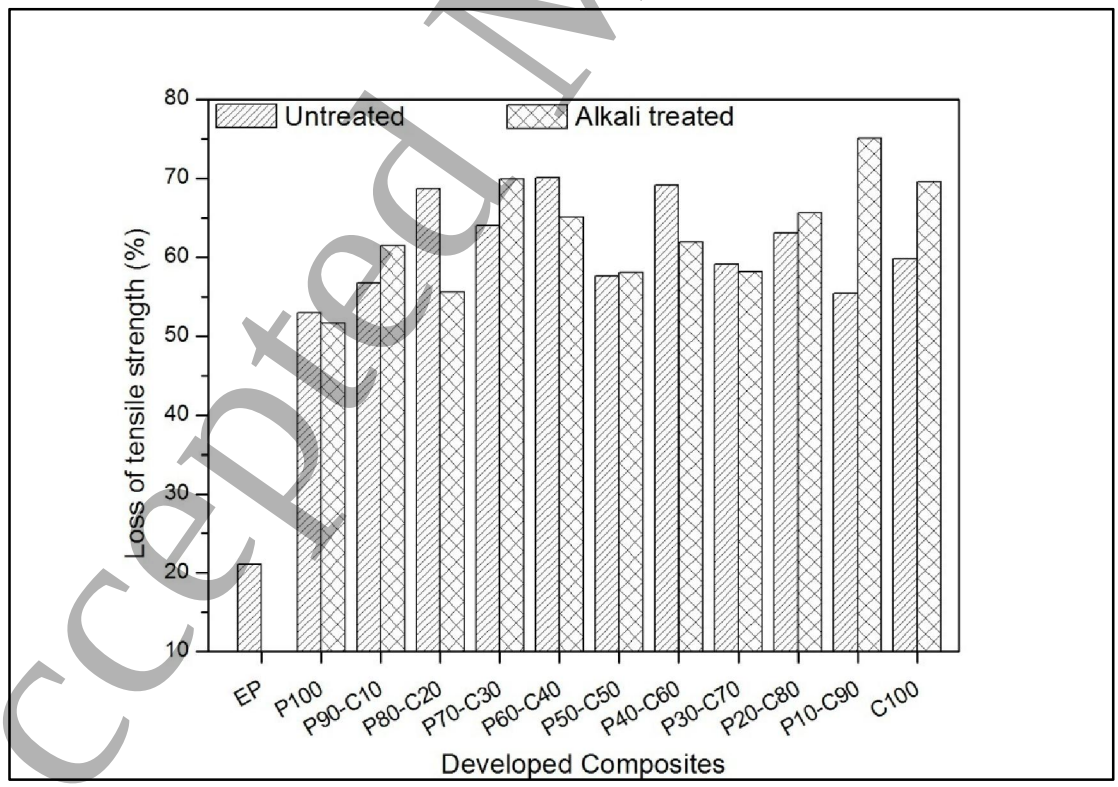
(a) Untreated biocomposites

Accepted Manuscript



(b) 4% NaOH treated biocomposites

Figure 4 Effect of the natural soil burial time on the tensile strength of (a) untreated biocomposites (b) alkali treated biocomposites



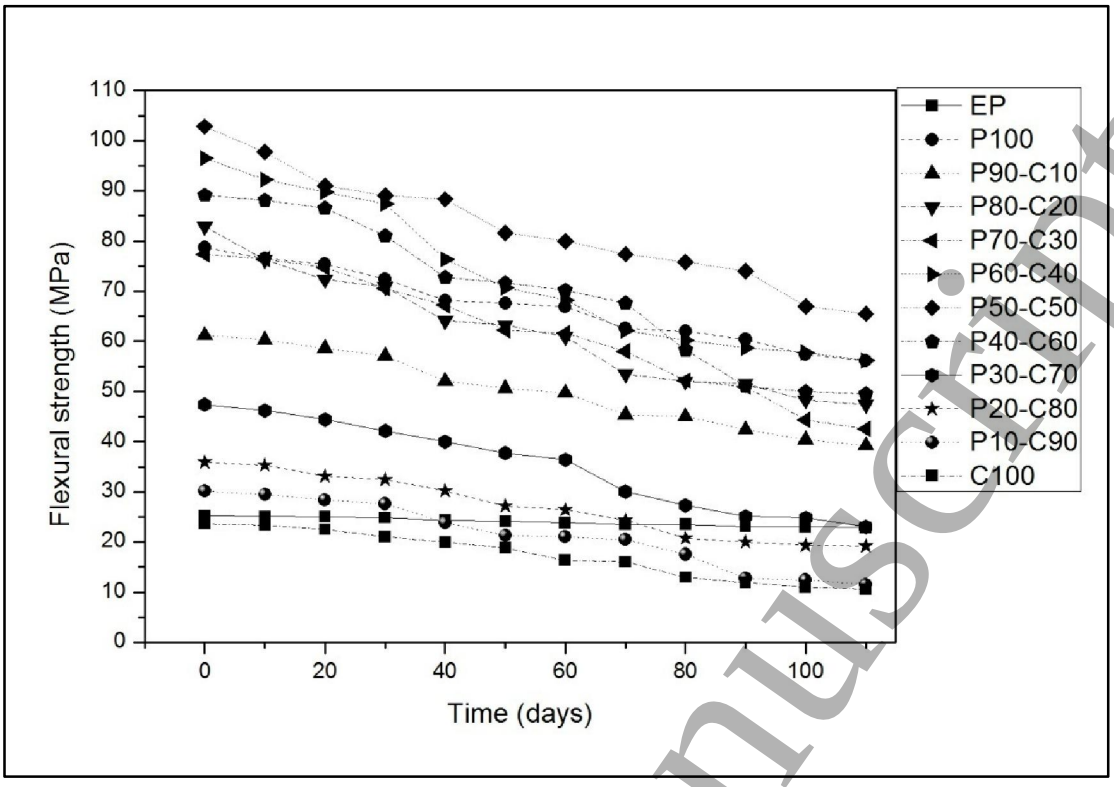
Accepted Manuscript

Figure 5 Comparison of the maximum loss in tensile strength after 110 days of burial in the natural soil environment

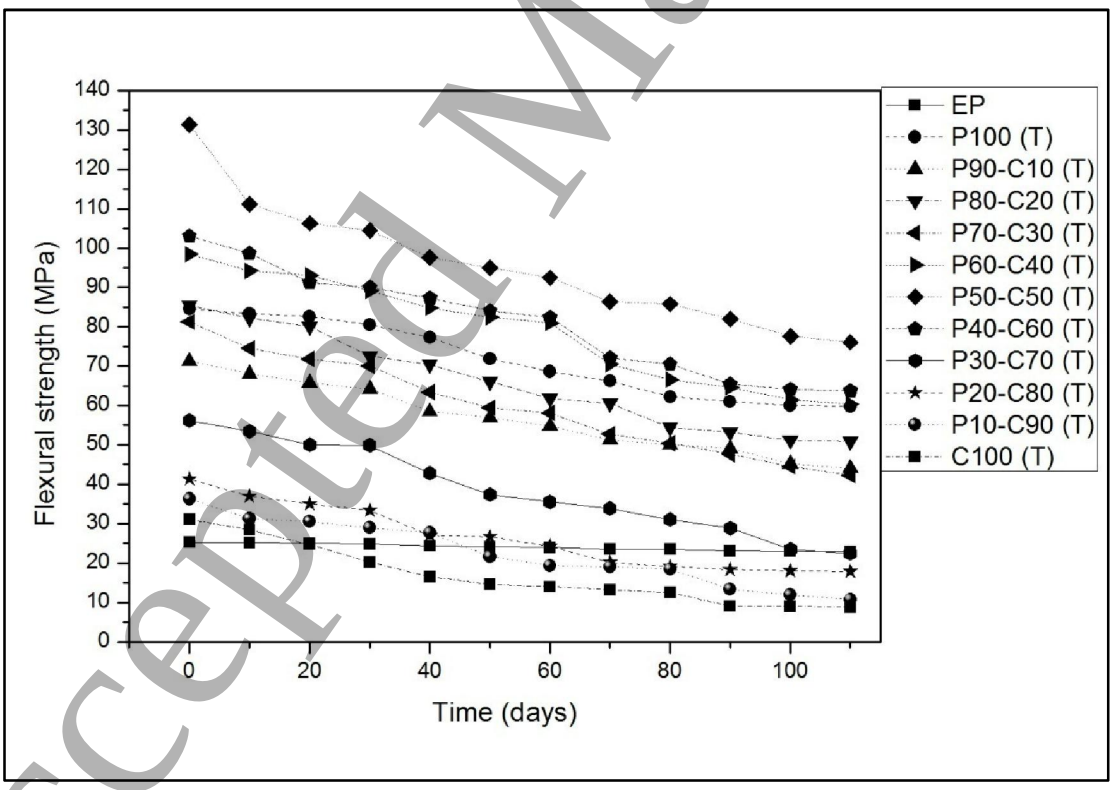
3.2 Flexural strength

Figure 6 (a)-(b) illustrates the flexural strength of untreated and alkali-treated biocomposites in response to natural soil burial time. It was observed that the bending strength of an epoxy thermoset was increased considerably after the addition of reinforcing PALF and COIR fibers. However, the fiber reinforced composites exhibit a higher rate of reduction in flexural strength than the unfilled epoxy thermoset. This was attributed to the easy and selective hydrolysis of cellulosic fibers; entrapment of water molecules inside the pores, cavity, and an interfacial region between fiber and matrix; anisotropic nature of composites; scission and depolymerization of cellulosic chains; and localized stress concentration in micropores. The pure COIR fiber reinforced composite possess a slow rate of reduction in flexural strength as compared to the PALF-Epoxy composite. It was observed that the flexural strength of a hybrid composite in natural soil environment was reduced rapidly with the increase of coir fiber content. Amongst all the untreated hybrid composites, the P10-C90 one exhibits maximum reduction (%) in flexural strength. It was attributed to the poor stress transfer from PALF to COIR fiber and the presence of a large number of micropores and cavities at this particular composition which results in the absorption and adsorption of water molecules by capillary action. From Figure 6, we can conclude that most of the composites revealed an accelerated rate of reduction after 30 days of burial in the natural soil environment. It is worth to note that the flexural strength of developed composites was reduced substantially in burial state after an alkaline treatment of cellulosic fibers. This finding was due to the removal of lignin and waxy substances from the surface of natural fibers. The flexural strength of NaOH treated P50-C50 composite was reduced significantly after 10 days of burial in natural soil. Amongst all the developed composites, the alkaline treated Coir-Epoxy composite exhibits a maximum reduction in flexural strength after 110 days of burial. This was because of the significant removal of highly stable lignin compound after the mercerization process.

Accepted Manuscript



(a) Untreated biocomposites



(b) 4% NaOH treated biocomposites

Accepted Manuscript

Figure 6 Effect of the natural soil burial time on the flexural strength of (a) untreated biocomposites (b) alkali treated biocomposites

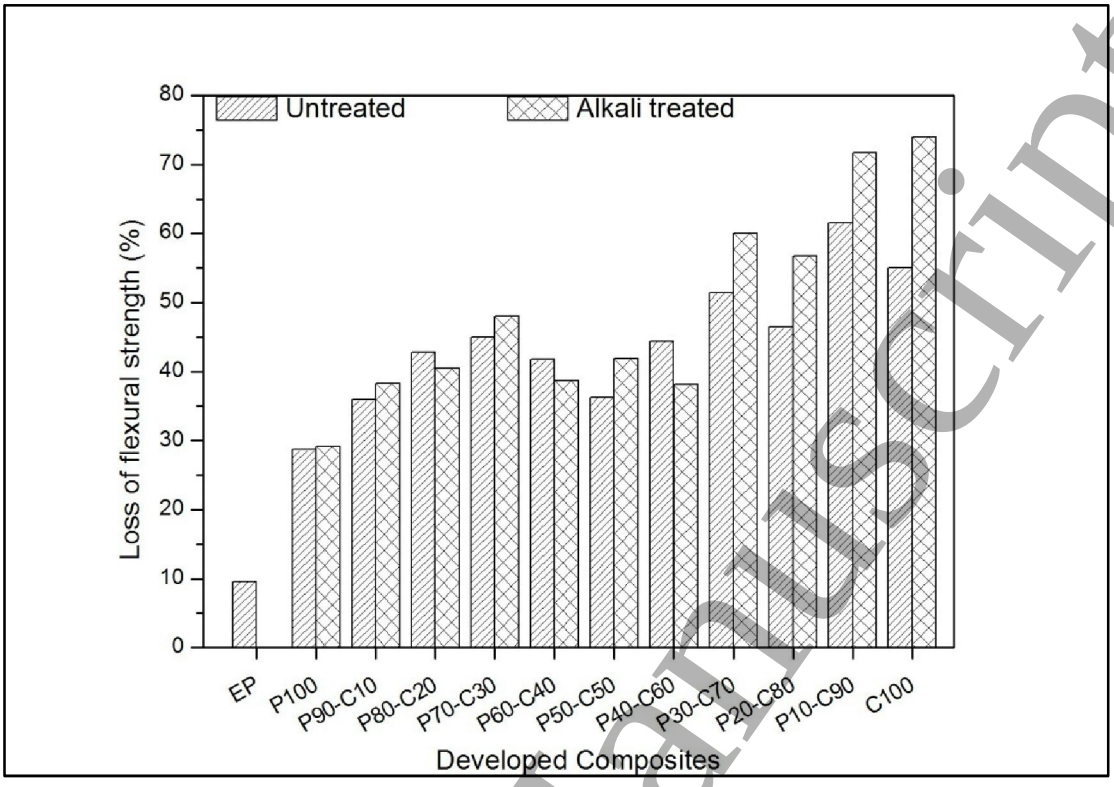


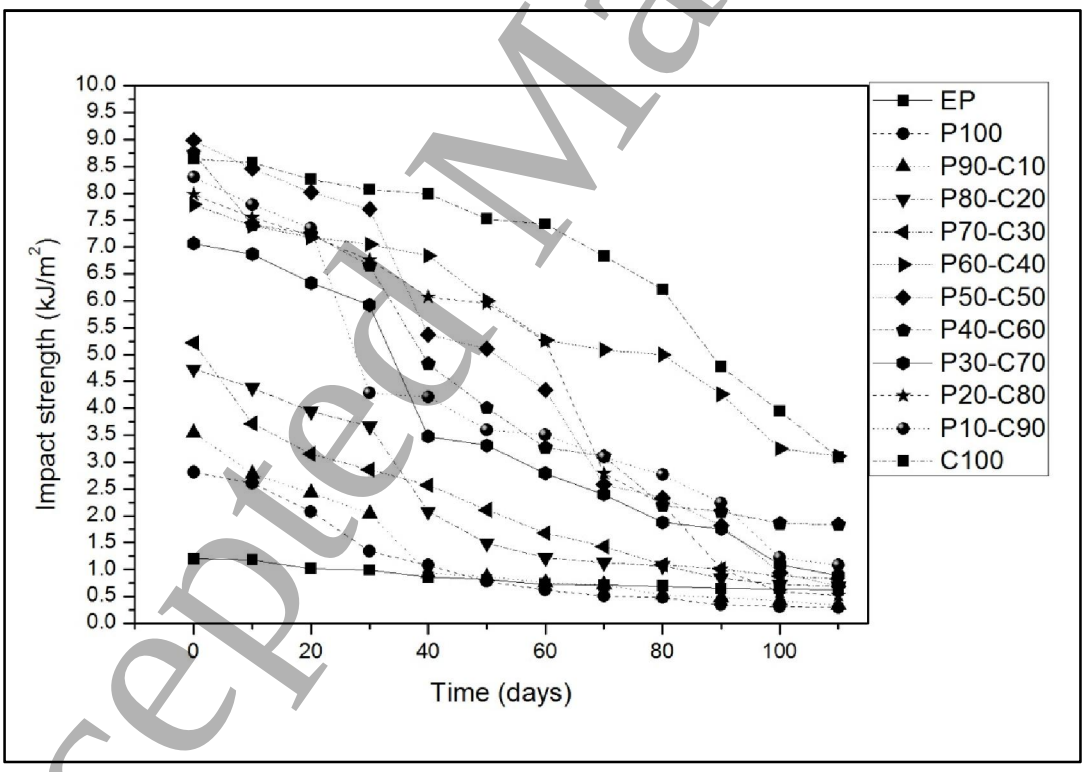
Figure 7 Comparison of the maximum loss in flexural strength after 110 days of burial in the natural soil environment

3.3 Impact strength

Figure 8(a)-(b) depicts the impact strength of formulated composites (untreated and alkali treated) as a special function of natural soil burial time. The brittleness of an epoxy thermoset was reduced significantly with the incorporation of PALF and COIR fibers. Similar to the tensile and flexural strength, the impact strength of developed composites was also decreased in the natural soil environment. This kind of behavior is due to the entrapment of water molecules at the fiber-matrix interfacial region which leads to easy and smooth fibers pull-out from the viscoelastic medium. Irrespective of the chemical composition of PALF and COIR fibers (mentioned in Table 4), the pure Coir-Epoxy composite exhibits a higher rate of reduction in impact strength after the 60 days of burial than that of the PALF-Epoxy composite. However, the total loss (%) in an impact strength of Coir-Epoxy composite was 15.9% less as compared to the PALF-Epoxy composite (Figure 9). This outcome can be defined by the excellent characteristics of coir fiber to resist microbial and fungus attack. Figure 8 clearly demonstrates that the impact strength of hybrid composites was reduced rapidly with the increase of coir fiber content. This was attributed to the large penetration of

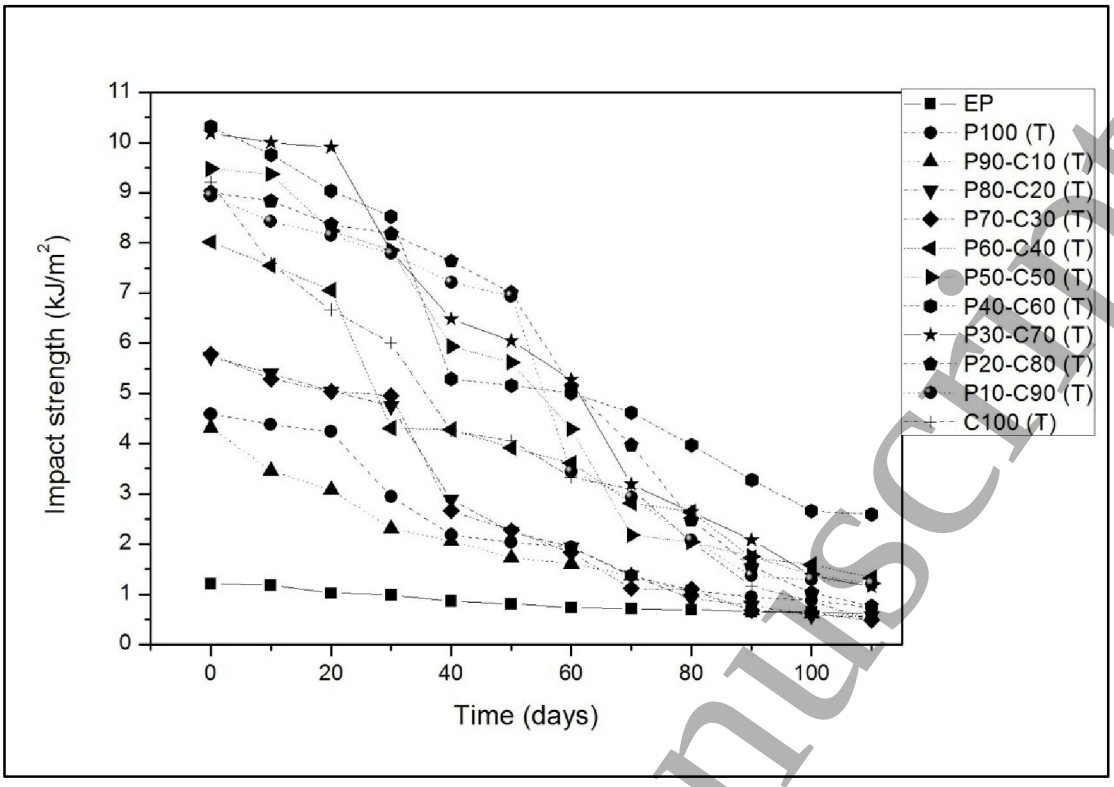
Accepted Manuscript

water molecules in the interfacial region between coir fiber and the matrix resin. Amongst all the untreated hybrid composites, the P20-C80 revealed the maximum loss (%) of impact strength in the natural soil environment. This was because of the localized stress concentration, substantial scission of polymeric chains, selective hydrolysis of reinforcing fibers, and avulsion of fiber bundles into individual fibers. From Figure 9, we can conclude that the alkali treatment imparts a positive effect on the impact strength of a pure PALF-Epoxy composite. This was due to the removal of hydroxyl (-OH) and other polar functional groups after the mercerization process which leads to a substantial reduction in the hydrolysis of pineapple leaf fiber. However, the NaOH treated COIR-Epoxy composite exhibits a higher rate of reduction in impact strength as compared to the untreated one. This was attributed to the change in chemical composition of coir fiber (removal of highly durable and stable lignin component) after an alkaline treatment. From Figure 8(a)-(b), we can also conclude that the rate of reduction in impact strength was more accelerated after the 30 days of burial in the natural soil environment. The overall discussion clearly revealed that the mechanical strength was reduced significantly due to the action of microorganisms.



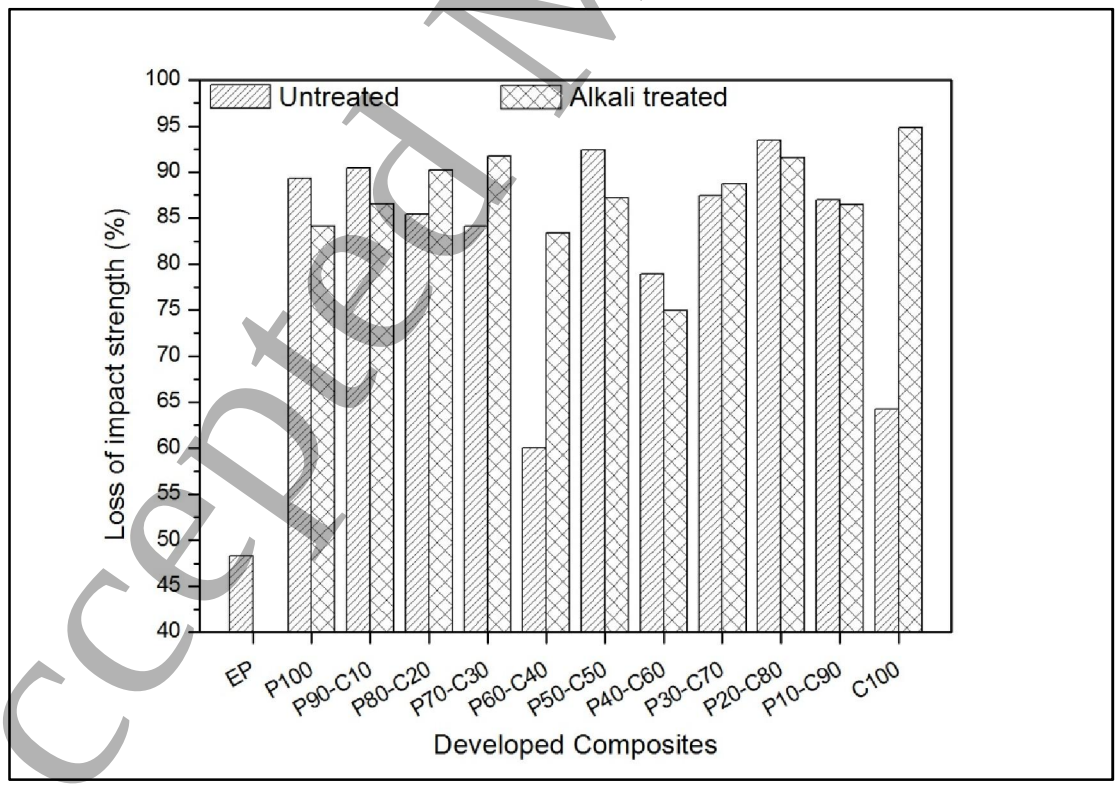
(a) Untreated biocomposites

Accepted Manuscript



(b) 4% NaOH treated biocomposites

Figure 8 Effect of the natural soil burial time on the impact strength of (a) untreated biocomposites (b) alkali treated biocomposites



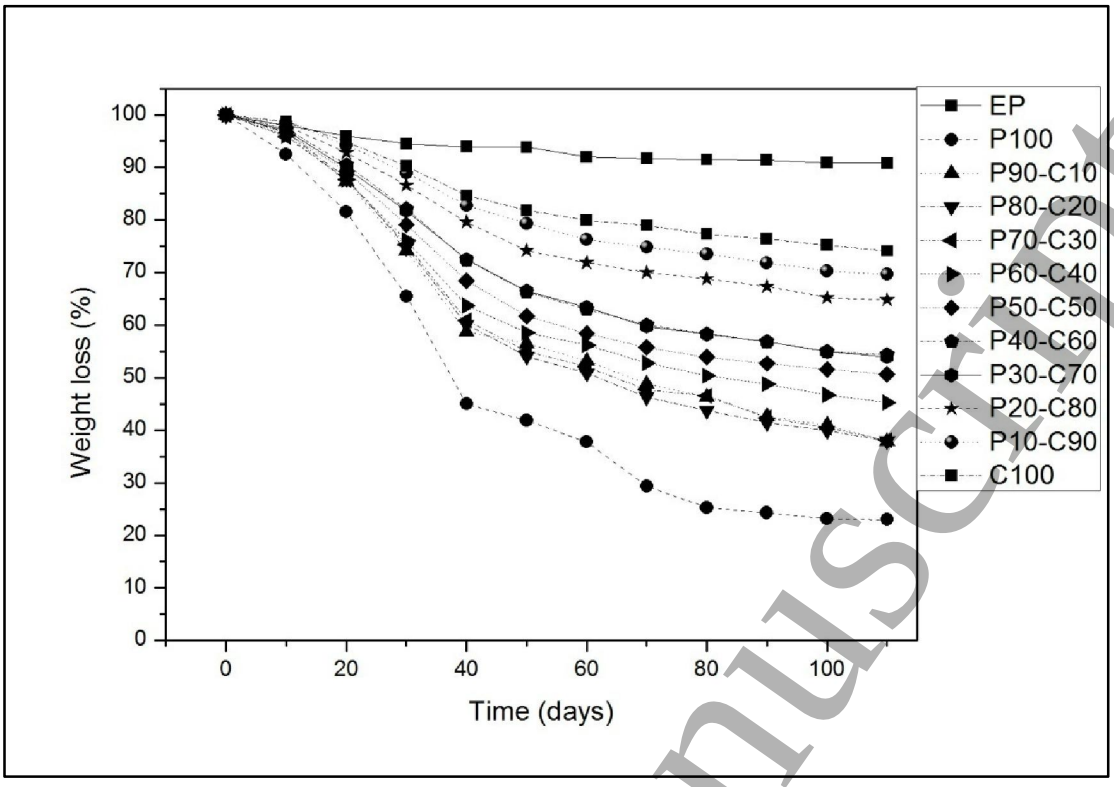
Accepted Manuscript

Figure 9 Comparison of the maximum loss in impact strength after 110 days of burial in the natural soil environment

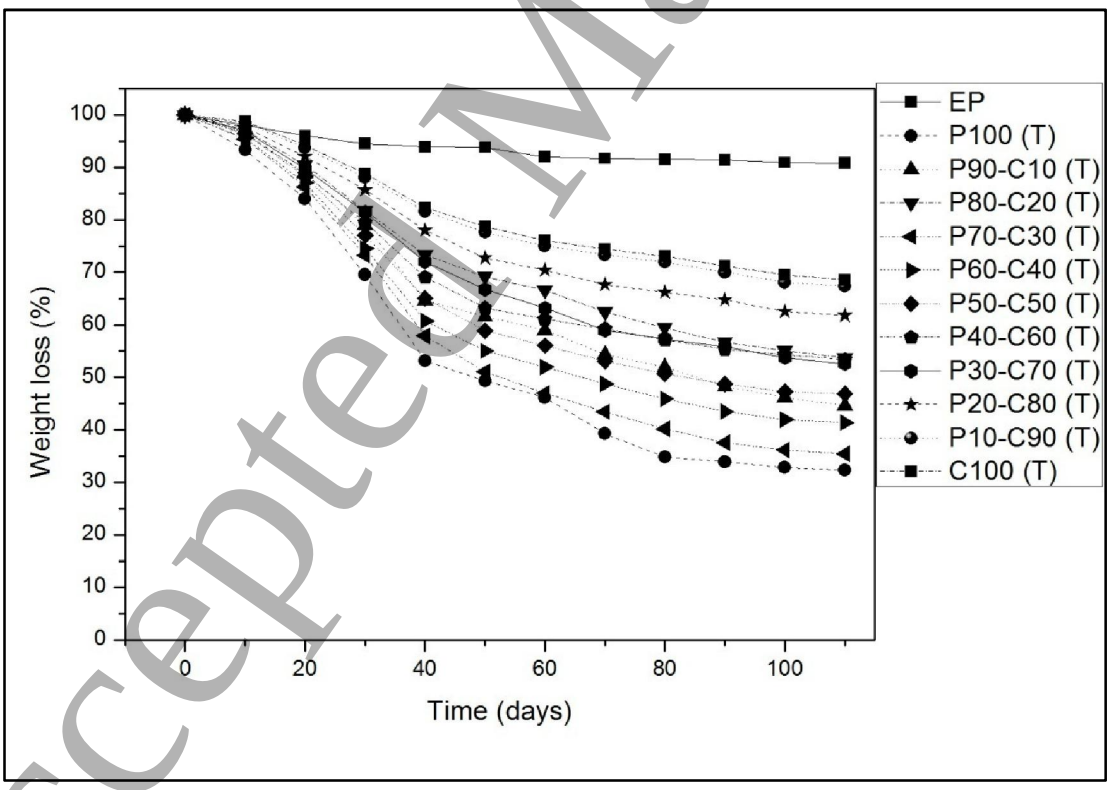
3.4 Weight loss

The weight loss of untreated and alkali treated biocomposites in the response of natural soil burial time is shown in Figure 10(a) and 10(b) respectively. The weight loss (%) of an epoxy thermoset was increased considerably in natural soil environment after the incorporation of PALF and COIR fibers (As expectedly). Amongst all the developed materials, the pure PALF-Epoxy composite shows a maximum percentage of weight loss in the natural soil environment (Figure 11). This result is attributed to the substantial hydrolysis of PALF which leads to the depolymerization and chain scission of cellulosic material into small monomer units. It was observed that the weight loss percentage of hybrid composites was reduced with the increase of coir fiber content. This was because of the high resisting power of COIR fiber to be biodegrade. The coir fiber consists of high lignin content (40-45%) which makes it and their composites to resist the attack of bacteria, fungi, and microorganisms. Figure 10 clearly depicts that the single coir fiber reinforced composite exhibits least biodegradability in the natural soil environment. Moreover, the total weight loss (%) in the Coir-Epoxy composite was 51.1% less than that of the pure PALF-Epoxy composite. This result was attributed to the presence of high cellulose content in PALF which results in easy and fast absorption of water molecules. The mechanism of bio-degradation involves penetration of water molecules, breakage of strong covalent bonds, and deterioration of hemicellulose & cellulose by the action of microorganisms. Bharat K.N et al. [52] also reported that the biodegradation involves bond scission reactions in the backbone of polymers. We can expect that the alkali treated fiber reinforced composites have a higher rate of biodegradation as compared to the untreated composites. However, the NaOH treated composites (P100, P90-C10, and P80-C20) possess lower weight loss (%) as compared to the untreated ones (Figure 11). This was because of the removal of hydroxyl (-OH) and other polar functional groups from the surface of cellulosic fibers after the mercerization process.

Accepted Manuscript



(a) Untreated biocomposites



(b) 4% NaOH treated biocomposites

Accepted Manuscript

Figure 10 Percentage weight loss of (a) untreated biocomposites (b) alkali treated biocomposites in natural soil environment

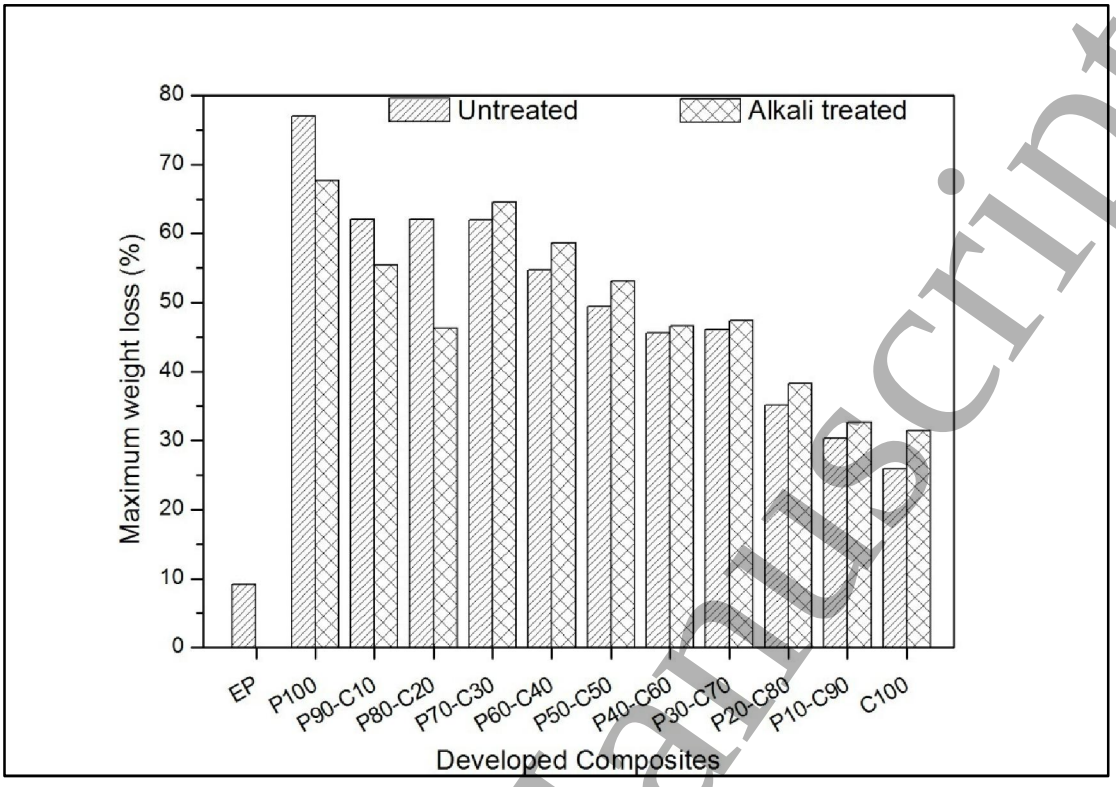


Figure 11 Comparison of the maximum weight loss after 110 days of burial in the natural soil environment

4. Conclusions

The current research work deals with the biodegradability and mechanical properties of untreated and alkali treated PALF/COIR fiber reinforced composites in the natural soil environment. On the basis of the above-mentioned research work, the following conclusions can be made:

- In the natural soil environment, the PALF-Epoxy composite exhibits a higher rate of reduction in tensile and flexural strength than that of the COIR-Epoxy composite. It was due to the substantial hydrolysis of PALF.
- Amongst all the developed composites, the pure PALF-Epoxy revealed a maximum percentage of weight loss in the natural soil burial condition.
- Most of the hybrid composites drop their mechanical strength rapidly in burial condition than that of the pure PALF-Epoxy composite.

Accepted Manuscript

- The biodegradability of a hybrid composite was reduced with the increase of coir fiber content. This was attributed to the high resistance power of a coir fiber against the microbial and fungus attack.
- Most of the developed composites revealed an accelerated rate of reduction in mechanical strength after 30 days of soil burial. This was attributed to the selective hydrolysis of reinforcing fibers and substantial scission of polymeric chains.
- The biodegradability of a pure Coir-Epoxy composite was increased significantly after an alkaline treatment. The NaOH treated PALF-Epoxy composite possess higher stability against the attack of microorganisms than the untreated one. This was because of the removal of hydroxyl (-OH) and other polar functional groups due to the mercerization process.
- Amongst all the developed composites, the NaOH treated P10-C90 possess maximum reduction (%) in mechanical strength after 110 days of burial in the natural soil environment.
- The mechanical strength and biodegradability of a Coir-Epoxy composite were increased with the incorporation of pineapple leaf fiber.

Overall, we can conclude that the fiber hybridization and alkaline treatment of cellulosic fibers play a major role to affect the biodegradation. The experimental work proved that the developed hybrid composites are more environment-friendly and have good mechanical strength as compared to the conventional plastics which results in they can be employed to fabricate helmets; roofing; floor furnishing materials; different parts of automobile such as door panels, headliner panel, package and floor trays, noise insulation panels; low cost cellular beam; raw material for particleboard; printed circuit boards etc.

Acknowledgment: The authors extend their gratitude to the Delhi Technological University, Delhi (India) for supporting this research work.

Conflicts of Interest: The authors declare no conflict of interest.

Funding: This research work received no specific grant from any funding agency in the public, commercial, and non profit sectors.

Accepted Manuscript

References

1. Saba N, Paridah M T, and Jawaid M 2015 Mechanical properties of kenaf fiber reinforced polymer composite: A Review *Constr. Build. Mater.* **76**: 87-96.

2. Kim H S, Yang H S, and Kim H J 2005 Biodegradability and mechanical properties of agro-flour-filled polybutylene succinate biocomposites *J. Appl. Polym. Sci.* **97**: 1513-1521.

3. Lee S H and Wang S 2005 Biodegradable polymers/bamboo fiber biocomposite with bio-based coupling agent *Compos. Part A* **37**: 80-91.

4. Romhany G, Kocsis J K, and Czigany T 2003 Tensile fracture and failure behavior of thermoplastic starch with unidirectional and cross-ply flax fiber reinforcements *Macromol. Mater.Eng.* **288**: 699-707.

5. Doan T T L, Gao S L, and Mader E 2006 Jute/Polypropylene composites I. Effect of matrix modification *Compos. Sci. Technol.* **66**: 952-963.

6. Wehsener J, Weser T, Haller P, Diestel O, and Cherif C 2014 Textile reinforcement of multidimensional formable wood *Eur. J. Wood. Prod.* **72**: 463-475.

7. Mittal M and Chaudhary R 2018 Experimental study on the water absorption and surface characteristics of alkali treated pineapple leaf fiber and coconut husk fiber *Int. J. Appl. Eng. Res.* **13**(15): 12237-12243.

8. Mishra S, Mohanty A K, Drzal L T, Mishra M, and Hinrichsen G 2004 A review on pineapple leaf fibers, sisal fibers and their biocomposites *Macromol. Mater.Eng.* **289**: 955-974.

9. Wisittanawat U, Thanawan S, and Amornsakchai T 2014 Mechanical properties of highly aligned short pineapple leaf fiber reinforced–Nitrile rubber composite: Effect of fiber content and bonding agent *Polym. Test.* **35:** 20-27.

10. Kengkhekit N and Amornsakchi T 2012 Utilisation of pineapple leaf waste for plastic reinforcement: 1. A novel extraction method for short pineapple leaf fiber *Ind. Crops Prod.* **40**: 55-61.

Accepted Manuscript

11. Verma D, Gope P C, Shandilya A, Gupta A, and Maheshwari M K 2012 Coir fiber reinforcement and applications in polymer composites: A Review, *J. Mater. Environ. Sci.* **4**(2): 263-276.

12. Shrivastava R, Telang A, Rana R S, and Purohit R 2017 Mechanical properties of Coir/Glass fiber epoxy resin hybrid composite, *Mater. Today: Proc.* **4**: 3477-3483.

13. Siakeng R, Jawaid M, Ariffin H, and Sapuan S M 2018 Physical properties of coir and pineapple leaf fiber-reinforced polylactic acid hybrid composites *IOP Conf. Ser. Mater. Sci. Eng.* **290**, doi: 10.1088/1757-899X/290/1/012031.

14. Rihayat T, Suryanil S, Fauzi T, Agusnar H, Wirjosentono B, Syafruddin Helmi Zulkifil, and Alam P N 2018 Mechanical properties evaluation of single and hybrid composites polyester reinforced bamboo, PALF, and Coir fiber *IOP Conf. Ser. Mater. Sci. Eng.* **334**, doi: 10.1088/1757-899X/334/1/012081.

15. Shahzad A 2011 Impact and fatigue properties of hemp-glass fiber hybrid biocomposites *J. Reinf. Plast. Compo.* **30**(16): 1389-1398.

16. Atiqah A, Maleque M A, Jawaid M, and Iqbal M 2013 Development of kenaf-glass reinforced unsaturated polyester hybrid composite for structural applications *Compos. Part B* **56**: 68-73.

17. Mittal M and Chaudhary R 2018 Experimental investigation on the mechanical properties and water absorption behavior of randomly oriented short pineapple/coir fiber-reinforced hybrid epoxy composites, *Mater. Res. Express* https://doi.org/10.1088/2053-1591/aae944.

18. Jawaid M, Abdul Khalil H P S, Hassan A, and Abdallah E 2012 Bi-Layer hybrid biocomposites: Chemical resistant and physical properties *BioResources* **7**(2): 2344-2355.

19. Panthapulakkal S and Sain M 2006 Injection-molded short hemp fiber/glass fiber-reinforced polypropylene hybrid composites-Mechanical, water absorption and thermal properties *J. Appl. Polym. Sci.* **103**: 2432-2441.

Accepted Manuscript

20. Haq M, Burgueno R, Mohanty A K, and Misra M 2008 Hybrid bio-based composites from blends of unsaturated polyester and soybean oil reinforced with nanoclay and natural fibers *Compos. Sci. Technol.* **68**: 3344-3351.

21. Chevali V S, Nerenz B A, Ulven C A, and Kandare E 2015 Mechanical properties of hybrid lignocellulosic fiber-filled acrylonitrile butadiene styrene (ABS) biocomposites *Polym. Plast. Technol. Eng.* **54**: 375-382.

22. Davoodi, M.M., Sapuan, S.M., Ahmad, D., Aidy, A., Khalina, A., and Jonoobi, M. (2011). Concept selection of car bumper beam with developed hybrid bio-composite material, *Mater. Design,* **32**: 4857-4865.

23. Uppin V S, Ashok Joshi A, Sridhar I, and Gouda P S S 2016 Interlaminar fracture toughness in Glass-Cellulose reinforced epoxy hybrid composites *IOP Conf. Ser. Mater. Sci. Eng.* **149**, doi: 10.1088/1757-899X/149/1/012113.

24. Cheng F, Hu Y, and Yuan J 2014 Preparation and characterization of Glass fiber-Coir hybrid composites by a novel and facile prepreg/press process *Fiber. Polym.* **15**(8): 1715-1721.

25. Bhagat V K, Biswas S, and Dehury J 2014 Physical, Mechanical, and Water absorption behavior of Coir/Glass fiber reinforced epoxy based hybrid composites *Polym. Compos.* doi: 10.1002/pc.22736.

26. Arumugaprabhu V, Uthayakumar M, Cardona F, and Sultan M T H 2016 Mechanical characterization of Coir/Palmyra waste fiber hybrid composites *IOP Conf. Ser. Mater. Sci. Eng.* **152**, doi: 10.1088/1757-899X/152/1/012054.

27. Nurazzi N M, Khalina A, Sapuan S, Rahmah M 2018 Development of sugar palm yarn/glass fiber reinforced unsaturated polyester hybrid composites *Mater. Res. Express* http://doi.org/10.1088/2053-1591/aabc27.

28. Abdul Khalil H P S, Masri M, Saurabh C K, Fazita M R N, Azniwati A A, Aprilla N A, Rosamah E, and Dungani R 2017 Incorporation of coconut shell based nanoparticles in kenaf/coconut fibers reinforced vinyl ester composites *Mater. Res. Express* http://doi.org/10.1088/2053-1591/aa62ec.

Accepted Manuscript

29. Aji IS, Zainudin ES, Abdan K, Sapuan SM, and Khairul MD 2012 Mechanical properties and water absorption behavior of hybridized kenaf/pineapple leaf fiber reinforced high-density polyethylene composite *J. Compos.Mater.* **47**(8): 979-990.

30. Bakri B, Chandrabakty S, and Putra K 2017 Evaluation of mechanical properties of Coir-Angustifolia Haw Agave fiber reinforced hybrid epoxy composite *Jurnal. Mekanikal.* **8**(1): 679-685.

31. Teja M S, Ramana M V, Sriramulu D, and Rao C J 2016 Experimental investigation of mechanical and thermal properties of sisal fiber reinforced composite and effect of SiC filler material *IOP Conf. Ser. Mater. Sci. Eng.* **149**: 1-10.

32. Yahaya R, Sapuan S M, Jawaid M, Leman Z, and Zainudin E S 2016 Water absorption behavior and impact strength of Kenaf-Kevlar reinforced epoxy hybrid composites *Adv. Compo. Lett.* **25**(4): 98-102.

33. Mwaikambo L Y and Ansell M P 2001 Chemical modification of hemp, sisal, jute, and kapok fibers by alkalization *J. Appl. Polym. Sci.* **84**: 2222-2234.

34. John M J, Francis B, Varughese K T, and Thomas S 2008 Effect of chemical modification on properties of hybrid fiber biocomposites *Compos. Part A* **39**: 352-363.

35. Li Xue, Tabil L G, and Panigrahi S 2007 Chemical treatments of natural fiber for use in natural fiber-reinforced composites *J. Polym. Environ.* **15**: 25-33.

36. John M J and Anandjiwala R D 2008 Recent developments in chemical modification and characterization of natural fiber-reinforced composites *Polym. Compos.* DOI: 10.1002/pc.20461.

37. Jandas P J, Mohanty S, Nayak S K, and Shrivastava H 2011 Effects of surface treatments of banana fiber on mechanical, thermal, and biodegradability properties of PLA/Banana fiber biocomposites *Polym. Compos.* DOI: 10.1002/pc.21165.

38. Ranjan R, Bajpai P K, and Tyagi R K 2013 Mechanical characterization of Banana/Sisal fiber reinforced PLA hybrid composites for structural applications *Eng. Int.* **1**(1): 39-49.

Accepted Manuscript

39. Devi L, Bhagawan S S, Nair K C, and Thomas S 2011 Water absorption behavior of PALF/GF hybrid polyester composites *Polym. Compos* DOI: 10.1002/pc.21034.

40. Rahman M, Das S, and Hasan M 2018 Mechanical properties of chemically treated banana and pineapple leaf fiber reinforced hybrid polypropylene composites *Adv. Mater. Process. Technol.* http://doi.org/10.1080/2374068X.2018.1468972.

41. Atiqah A, Jawaid M, Sapuan S M, and Ishak M R 2018 Dynamic mechanical properties of sugar palm/glass fiber reinforced thermoplastic polyurethane hybrid composites *Polym. Compos* DOI: 10.1002/pc.24860.

42. Oushabi A, Sair S, Hassani F, Abboud Y, Tanane, O, and Bouari A 2017 The effect of alkali treatment on mechanical, morphological, and thermal properties of date palm fibers (DPFs): Study of the interface of DPF-Polyurethane composite, *S. Afr. J. Chem. Eng.* http://dx.doi.org/10.1016/j.sajce.2017.04.005.

43. Panyasart K, Chaiyut N, Amornsakchai T, and Santawitee O 2014 Effect of surface treatment on the properties of pineapple leaf fibers reinforced polyamide 6 composites *Energy. Procedia.* **56**: 406-413.

44. Suardana N P G, Lokantara I P, and Lim J K 2011 Influence of water absorption on mechanical properties of coconut coir fiber/Polylactic acid biocomposites *Mater. Phy. Mech.* **12**, 113-125.

45. Lopez E, Lopez M, Fonseca A, Nunez R, Rodrigue D, and Ortiz J 2016 Effect of fiber content and surface treatment on the mechanical properties of natural fiber composites produced by rotomolding, *Compos. Interface* http://dx.doi.org/10.1080/09276440.2016.1184556.

46. Goud G and Rao R N 2010 Effect of fiber content and alkali treatment on mechanical properties of *Roystonea regia*-reinforced epoxy partially biodegradable composites *B. Mater. Sci.* **34**(7): 1575-1581.

47. Anand P and Anbumalar V 2014 Mechanical properties of cellulose-filled epoxy hybrid composites reinforced with alkali-treated hemp fiber *Polym.* **39**(1): 46-55.

48. Maheshwari C, Reddy K, Muzenda E, Shukla M, and Rajulu A V 2013 Mechanical properties and chemical resistance of short tamarind fiber/unsaturated polyester

Accepted Manuscript

composites: Influence of fiber modification and fiber content *Int. J. Polym. Anal. Charact.* **18**(7): 520-533.

49. Venkateshappa S C, Jayadevappa S Y, and Puttiah P K W 2011 Mechanical behavior of areca fiber reinforced epoxy composites, *Adv. Polym. Technol.* **31**(4): 319-330.

50. Mohanty A K, Misra M, Drzal L T 2005 Natural fibers, biopolymers, and biocomposites, *CRC Press*, ISBN-10: 0-8493-1741-X.

51. Kim H, Yang H, and Kim H 2005 Biodegradability and mechanical properties of agro-flour-filled polybutylene succinate biocomposites *J. Appl. Polym. Sci.* **97**: 1513-1521.

52. Bharat K N, Swamy R P, and Mohan Kumar G C 2010 Experimental studies on biodegradable and swelling characteristics of natural fibers composites *Int. J. Agr. Sci.* **2**(1):01-04.

Accepted Manuscript

Scientific Journal Impact Factor (SJIF) : 5.278
International Journal of Modern Trends in Engineering and Research
ISSN (ONLINE) : 2349 - 9745
ISSN (PRINT) : 2393 - 8161

CFD ANALYSIS OF OGEE SPILLWAY HYDRUALICS

Dolon Banerjee[1] and Dr. Bharat Jhamnani[2]
[1]*M.Tech Student, Department of Civil Engineering, Delhi Technological University*
[2]*Professor, Department of Civil Engineering, Delhi Technological University*

Abstract— This piece of work aims to use CFD modelling to validate the phenomenon of the flow over a ogee spillway model in laboratory. Since this simulation consists of the pure interaction of the water flowing through the spillway and the air present in the surrounding, hence we use Volume of Fluid (VOF) to simulate the free surface of the flow which is having the two phases: Air and Water. Then we have used the most versatile turbulence model "k- ε" for the simulation of the flow turbulence. For CFD modelling, a commercially available Computational Fluid Dynamics (CFD) package, Ansys-Fluent, was used. In order to get the exact geometry of the physical model, the use of Reynolds-Averaged Navier-Stokes(RANS) equations in combination with the realizable "k-ε" eddy-viscosity closure model was adopted. The procedure of CFD model development and the theory related to those model parameter selection are also discussed in this work briefly. We have simulated the pressure readings in steady state and fully hydrodynamic stages. Besides this the level of water along the spillway profile and the water surcharge at the crest produced by numerical models are also presented here. Finally, we have carried out a validation process of the results of CFD model in 2D and 3D by comparing them with the results obtained from physical models. From this comparison it was proved that CFD modelling of the hence experimented ogee spillway was in very good accordance with the test data and only slight differences were revealed between them. Hence CFD modelling was accurately able to model the two phase system along with all the real life conditions originated during the test.

Keywords— Ogee Spillway, CFD-Ansys Fluent, VOF(Volume of Fluid), "k-ε" turbulence model, Water Surcharge

I. INTRODUCTION

In recent times numerical modeling techniques have been rapidly evolved and they are now developed to such an extent that they now can be used for many different studies and hence these are now preferred as a standard design tool in many engineering disciplines. Even though they can be used for a wide range of problems but their basic remains the same. First of all there is a problem whose solution is required. Now this problem is denoted as a set of Partial Differential Equations (PDE). After getting the PDEs, we use Finite Volume Analysis or Finite Element Analysis to change the PDEs into a set of Algebraic Equations. Now the solution to these algebraic equations is calculated using either an Iterative Method or by using Matrix Method but in both these cases the solution is often very computationally intensive and hence we use the Numerical Models to solve these without the tedious solving procedure. Apart from saving time and energy these numerical models are less pricey than physical models because they do not require any space or material or construction and they can be easily customized to any design changes made later on in the process. All we require for performing simulations is a computer, any simulation software and the engineering knowledge to interpret the results obtained. Also Flow 3D has the benefit that it can ignore the air contiguous to the flowing water by using Volume of Fluid(VOF) method invented by Hirt and Nichols[4]. In this work we have derived the physical model experiment data from a previously performed Laboratory tests and used it to validate our CFD modelling as we being the Hydraulics Engineers are interested in CFD and its ability of simulating different flow conditions as

found by Gessler[3]. Even though CFD is mostly utilized for modelling flow in many different areas but in this study we will be focusing on the use of CFD to model the flow of water through an ogee spillway.

Spillway is a hydraulic structure catered at the dam to discharge floodwater that cannot be held safely in the reservoir. To get a hydraulically efficient spillway we need to check on its Discharge, Water Surcharge, Pressures generated and quantify them into safe limit. These parameters further are dependent on type of spillway. As we know there are several types of spillways but the ogee-crested spillways are the most common because they have the ability to release excess water from upstream to downstream proficiently when properly designed and implemented[5]. These ogee type spillways have larger water holding capacity, higher hydraulic agreements, and are easily adaptable to all type of dams.

Kjellesvig[7] carried out the numerical modelling of flow over a spillway in 2D and 3D for several geometries and found that the discharge and pressure were in good consensus with physical test results. Johnson and Savage[6] estimated the discharge and crest pressures over an uncontrolled ogee spillway using a FLOW-3D. Then those results were compared to physical model results data and was found to be within limit of physical model study and the USBR data up to $0.1H_d$ to $0.7H_d$. But for heads higher than this, up to 1.2 times H_d, the Flow-3D results showed slight over-prediction in discharge, however, the deviation remained within 1% of the physical model results. Azmoudeh and Kamanbedast[1] simulated the best location of aeration system to cease cavitation and found it to be in accordance with physical model. Further Bhajantri[2] also conducted the formation and development of a 2-D free surface flow mathematical model for flow over a spillway and found good agreement with physical test results. Zhenwei[9] studied about the flow over a spillway using CFD and chose hexahedral grid with "k-ε" model and again got fine similarity in both model results .

II. NUMERICAL METHOD

In the field of hydraulic engineering, computational modelling of spillway flows has been very rapidly gaining popularity but a validation with a physical model test results is required to ensure competency. Several approaches have been established, including modelling in 1, 2 or 3 dimensions which use various equations and discretization methods. Here we will be dealing with 2-D and 3-D simulations only.

2.1 Setup physics

The physical modeling referred here consisted of one ogee spillway installed, in a glass flume of 1.25 m high, 0.50 m wide and 22 m in length. The maximum flow rate obtained in the laboratory from a constant head tank was 130 l/s. The laboratory Setup is shown in Figure 1 below. The spillway was a 1:30 size model of a large dam.

The Model Dimensions along with other hydraulic parameters are tabulated in Table 1 and Table 2

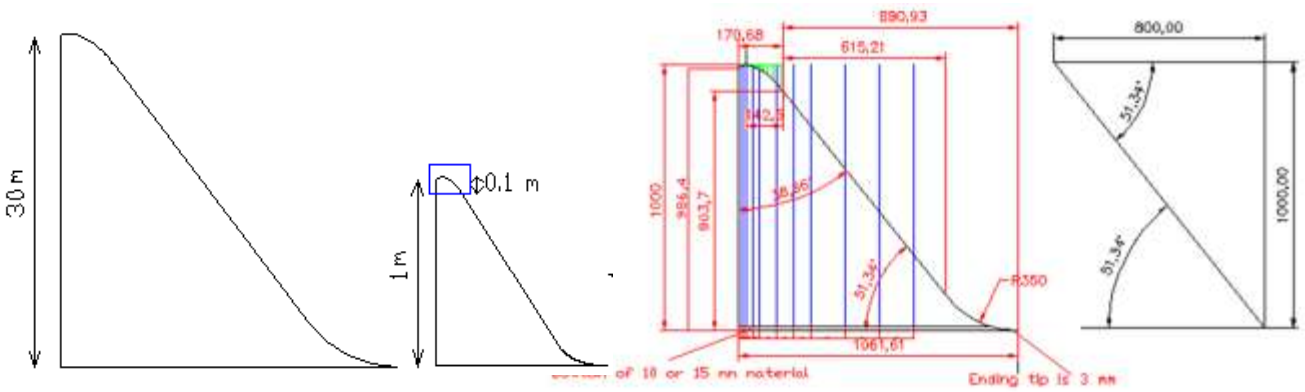


Figure 1: Physical model geometry of 1:30 scale model

Table 1: Model dimensions

Model Type	Spillway Approach Depth	Crest Depth	Radii	
1:30 scaled	1.00	0.50	0.06(R_1)	0.03(R_2)

Table 2: Design Surcharge, coefficient of discharge and design discharge for model

Model Type	Design Surcharge(H_o) in m	Coefficient of Discharge(C_o)	Design Discharge(m^3/s)
1:30 model	0.20	2.10	0.045

2.2 Numerical setup & meshing

The laboratory setup shown above was designed in the CFD simulation package and the 2-D and 3-D geometry were made as shown below:

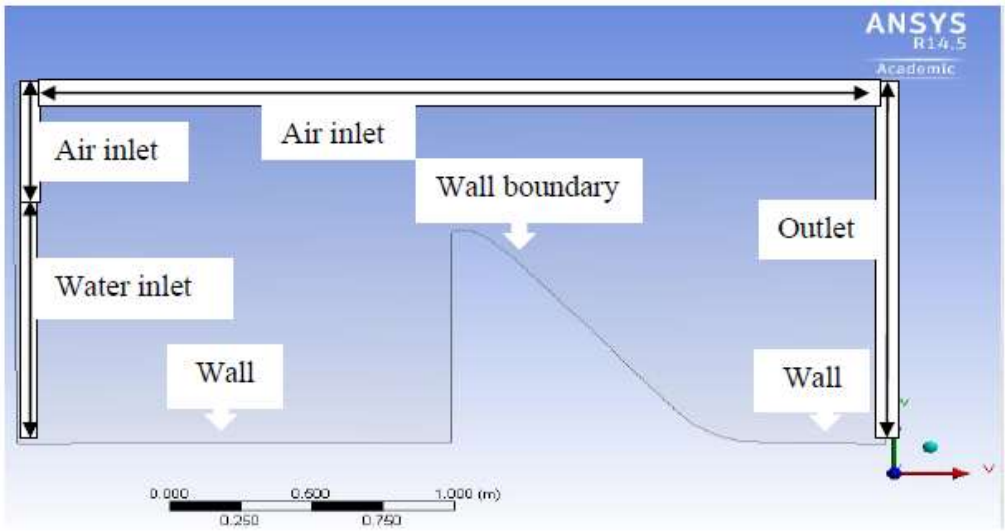


Figure 2: Model geometry constructed in 2-D with boundary labels

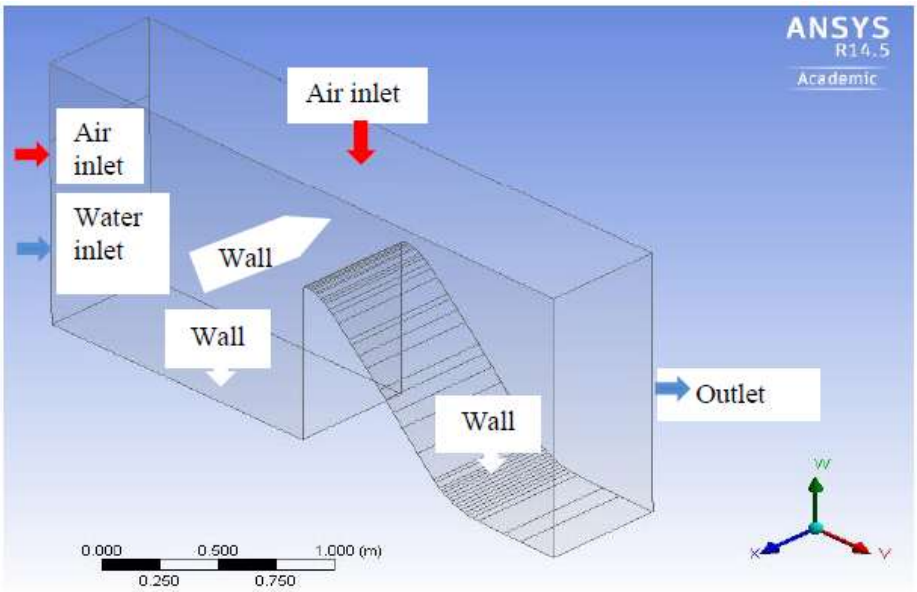


Figure 3: Model geometry constructed in 3-D with boundary labels

Now for the meshing part due care is required as this part decides the accuracy of the simulation. The correctness of a CFD solution is influenced by the number of cells contained by the mesh i.e. the finer is the meshing, the better is the solution accuracy. A number of trials with smaller and non-overlapping computational cells were performed to obtain the most suitable mesh so that a better solution accuracy could be achieved. The areas with highest concerns were meshed with the

finest cells while others were relatively coarsely meshed. Triangular meshing was used in this case because of its superiority in accuracy of results. Also at the spillway downstream refinement was done. Figure 4 and Figure 5 show the meshing in 2-D and 3-D respectively.

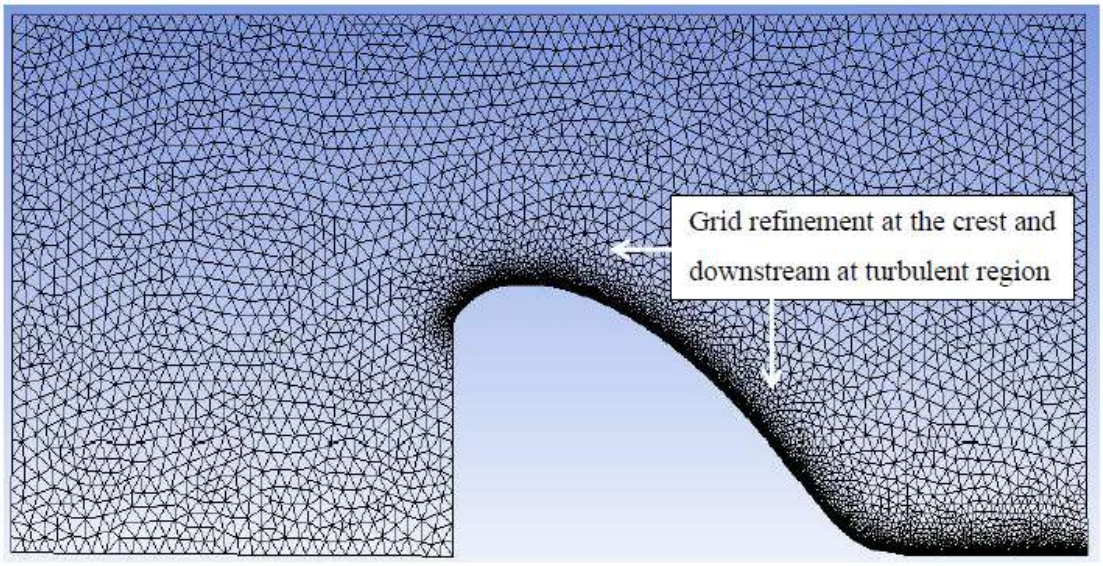


Figure 4: Meshing geometry of 2D model

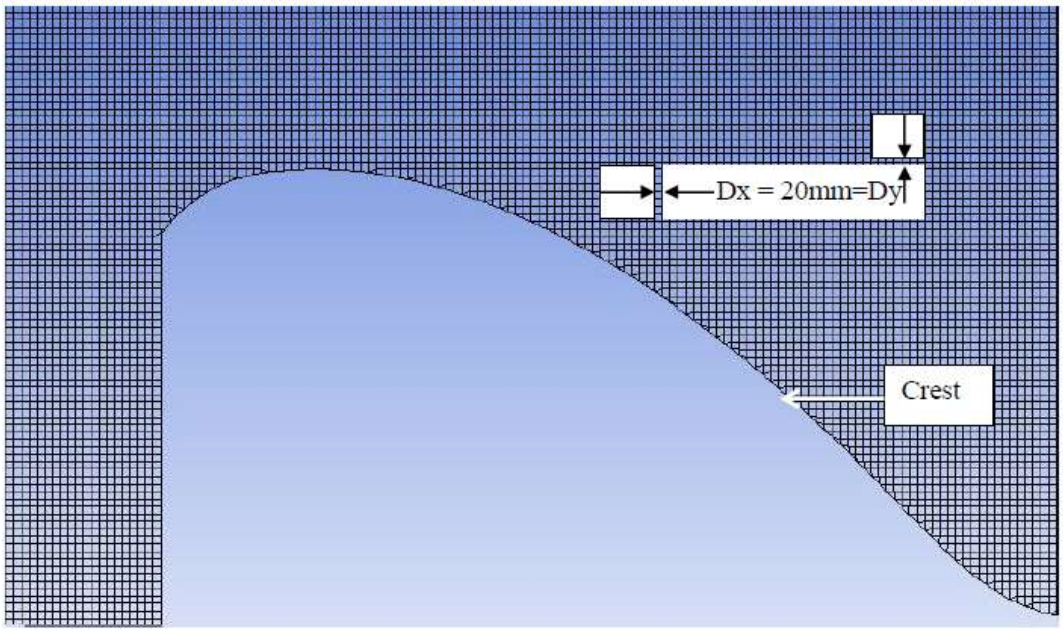


Figure 3-5: Meshing geometry of 3D model

2.3 Solver

For this work the realisable "$k-\varepsilon$" model was used. This model was used because of its latest turbulent viscosity formulation and latest transport equation for the Kinetic Energy (K.E) dissipation rate as studied by Singh[8]. For carrying out the multiphase modelling we have used the VOF (Volume of Fluid) in which the two Eulerian Phases were Air as Primary Phase and Water as Secondary Phase.

2.4 Boundary conditions

This is another important aspect of simulation as it controls the whole phenomenon going on in the geometry and directly affects the outcomes of the process. Since walls and internal faces have direct interaction with the water so they are also given appropriate boundary conditions.

@IJMTER-2018, All rights Reserved

A. Inlet

The inlet is defined at the upstream side of the spillway with pressure boundary as Atmospheric Pressure and since there is water entering at bottom and air at the top so to simulate this situation Velocity-Inlet was given at inlet.

B. Oulet

At the outlet to get the atmospheric condition, outlet boundary was defined and the flow was allowed to flow back into system.

C. Walls

For walls a no-slip condition with stationary throughout the test was used.

After defining these conditions initialization of the simulation was done under steady condition till the solution showed convergence. Further 2D and 3D tests with discharge of 130 l/s was conducted for both steady and fully hydrodynamic stages. In steady state stage, the convergence is monitored while for the fully hydrodynamic condition the test was performed for a longer time i.e. 5 minutes to get the fully developed flow with less fluctuations but reading showed that after a short time interval there was no fluctuations in pressure so finally the time for this was fixed at 20 seconds.

2.5 Simulation outcomes

A. Density contours and pathlines

In this work we have used Density contours and Pathlines to show the flow pattern of water through the spillway. As shown below, water (dark blue color) and air (red color) has a density of 998.2 kg/m^3 and a density of 1.225 kg/m^3 respectively while the yellowish color in between represents the interface of water and air and also signifies the aeration effect.

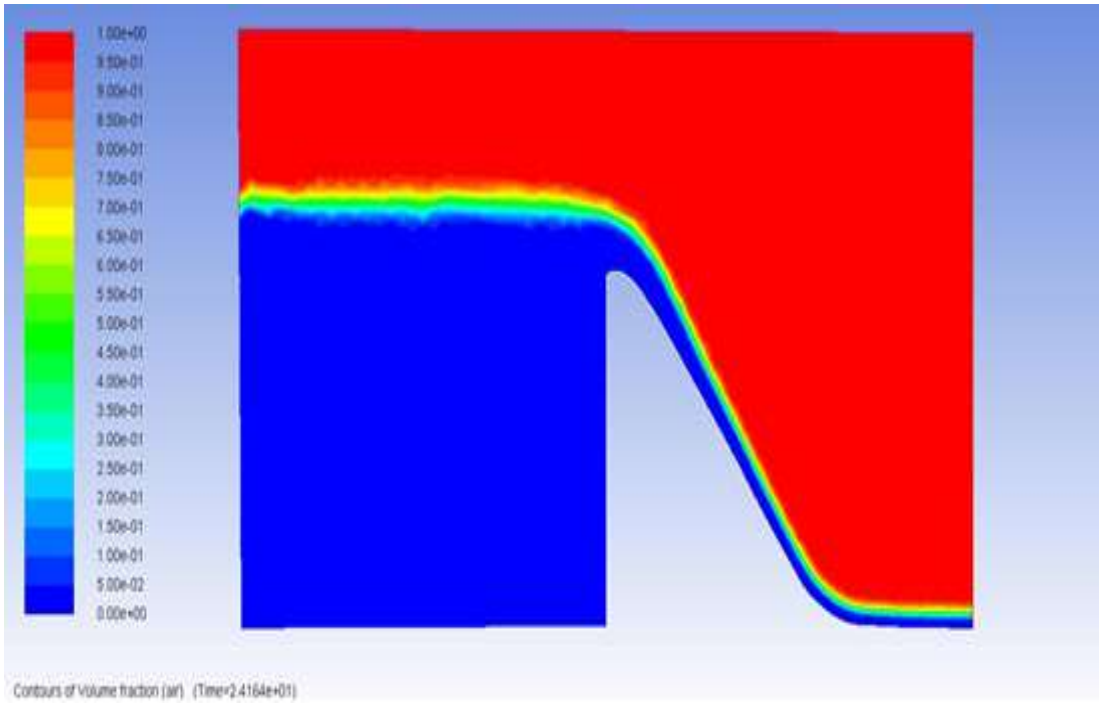


Figure 6: Density contours simulated by CFD model for 130 l/s

For better understanding of flow aeration Path line diagram can be used. Here the red band on the water surface shows the aeration which signifies that the aeration of the flowing water continuously increases as it flows through the spillway profile.

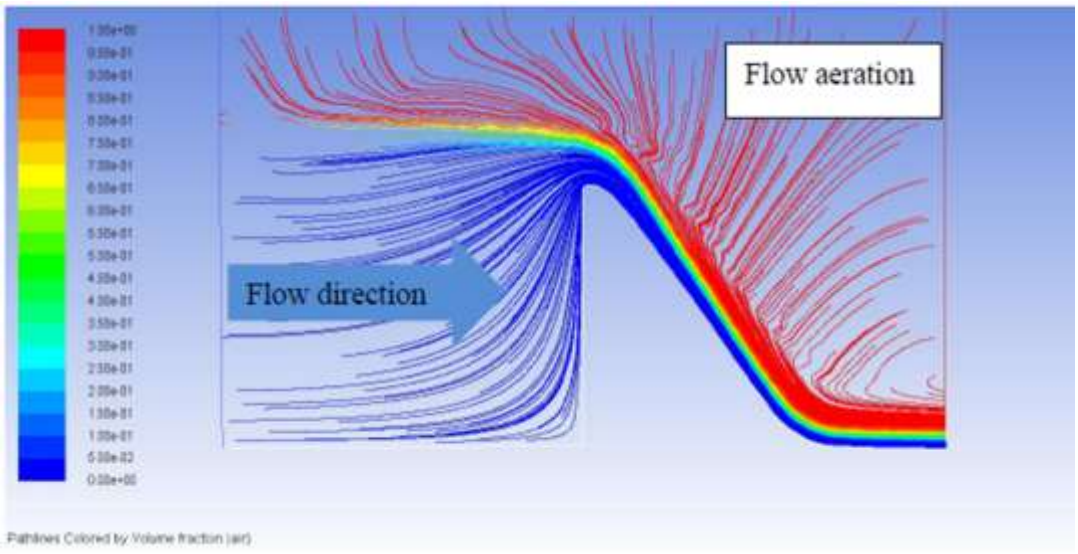


Figure 7: Simulated path lines of particles by volume fraction of air

B. Water surcharge

The water surface profile and the surcharge over the crest were also measured by the help of multiphase modelling. Both these parameters were measured at the centerline of spillway to avoid effect of spillway boundaries. The steady and fully hydrodynamic flows showed nearly the same water surface profile. Also it was noticed that the at crest the upstream side had higher water level than downstream side hence formation and thickening of boundary layer took place there along with increase in velocity.

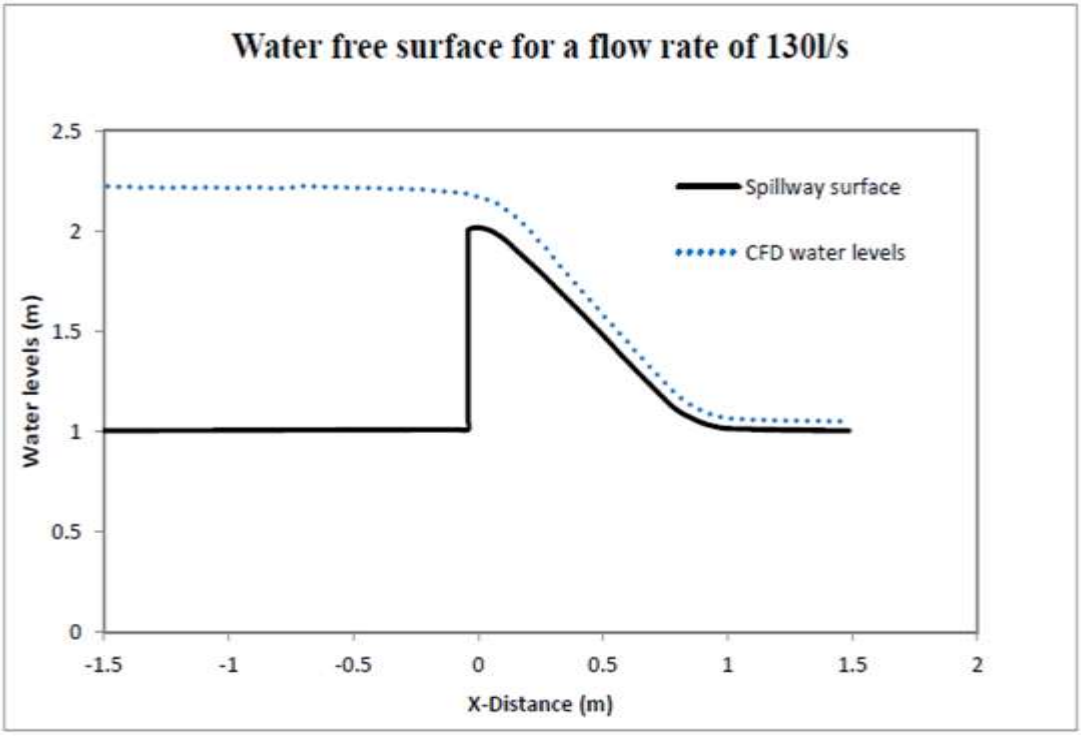


Figure 9: Water free surface over spillway model

C. Pressure results

Pressure results of both steady and fully hydrodynamic case were measured for both 2D and 3D cases. To get these in case of steady state 2500 iterations were used while for fully hydrodynamic case 20 second time was used.

@IJMTER-2018, All rights Reserved

Table 3: CFD simulated steady state pressure results for 2D model

Flow Rate(l/s)	Sensor 1	Sensor 2	Sensor 3	Sensor 4	Sensor 5	Sensor 6	Sensor 7
	CFD modelling: Average Sensor pressure (m)						
130	-0.118	-0.034	0.009	0.041	0.017	-0.031	0.036

The sensors were installed at the physical model along the profile of the spillway starting from the crest and then downward.

Table 4: CFD simulated fully hydrodynamic pressure results for 2D model

Flow Rate(l/s)	Sensor 1	Sensor 2	Sensor 3	Sensor 4	Sensor 5	Sensor 6	Sensor 7
	CFD modelling: Average Sensor pressure (m)						
130	-0.120	-0.034	0.009	0.040	0.017	-0.029	0.036

Table 5: CFD simulated steady state pressure results for 3D model

Flow Rate(l/s)	Sensor 1	Sensor 2	Sensor 3	Sensor 4	Sensor 5	Sensor 6	Sensor 7
	CFD modelling: Average Sensor pressure (m)						
130	-0.072	-0.038	0.012	0.046	0.030	-0.004	0.044

Table 6: CFD simulated fully hydrodynamic pressure results for 3D model

Flow Rate(l/s)	Sensor 1	Sensor 2	Sensor 3	Sensor 4	Sensor 5	Sensor 6	Sensor 7
	CFD modelling: Average Sensor pressure (m)						
130	-0.073	-0.035	0.012	0.047	0.031	-0.003	0.044

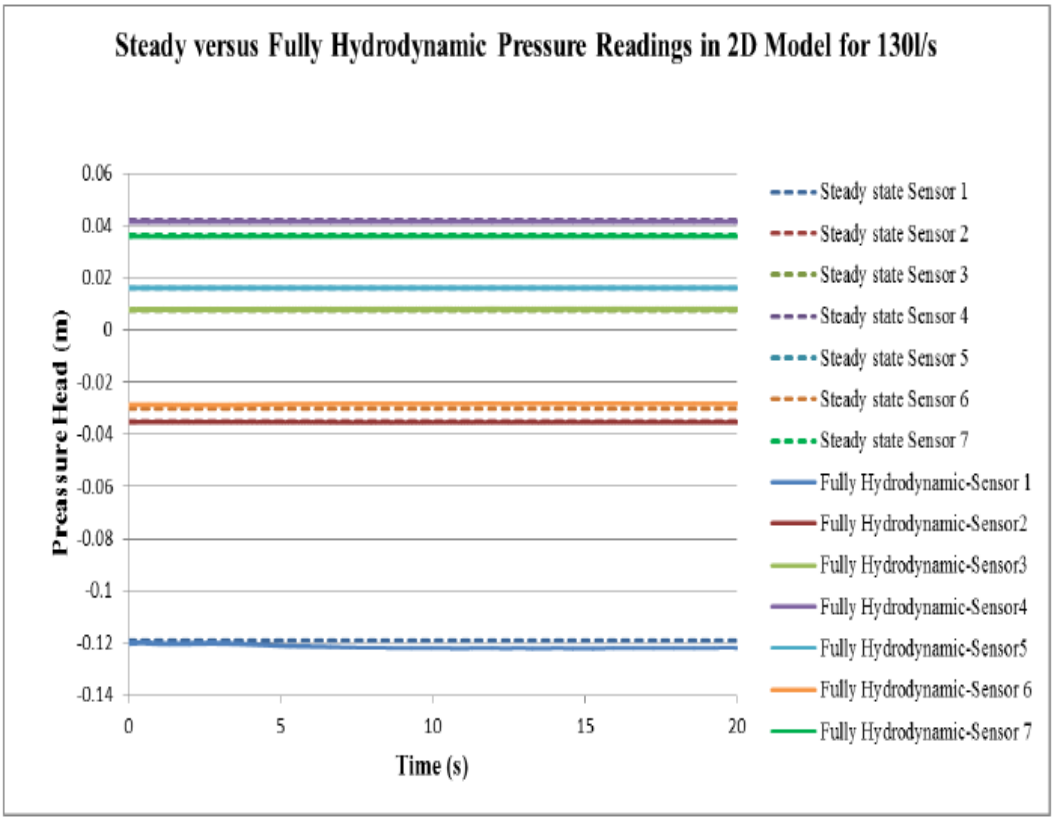


Figure 11: Comparison between 2D steady and fully hydrodynamic state models

@IJMTER-2018, All rights Reserved

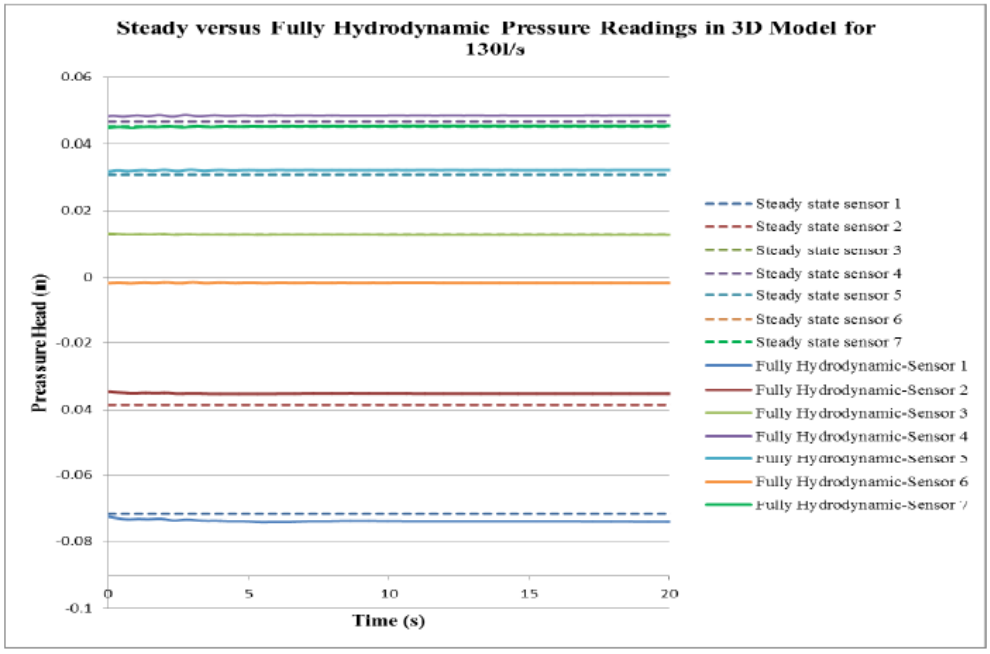


Figure 12: Comparison between 3D steady and fully hydrodynamic state models

III. VALIDATION OF CFD SIMULATION OUTCOMES

3.1 Water surcharge

For this section we will be comparing the Water Surface profile along the spillway profile and the Water surcharge upstream of the crest. To get the graphical representation of the water surcharge we have considered a number of diccharges and from the Figure 13 we can quantify that maximum deviation of surcharge is seen at highest discharge i.e. 130 l/s and is of 14 mm only hence validating the great similarity between both the model readings.

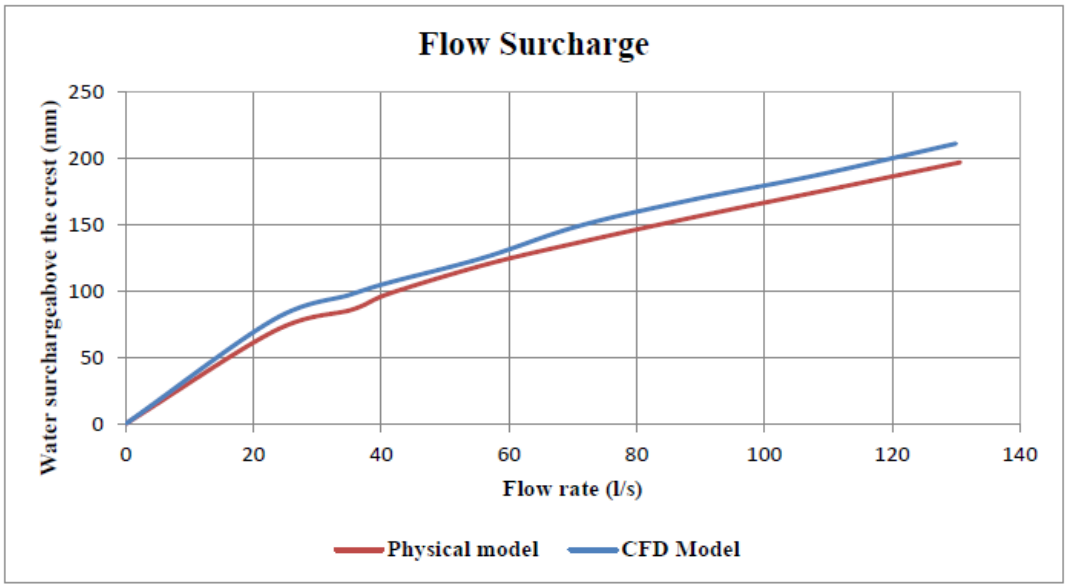


Figure 13: Water Surcharge of CFD Model and Physical Model

Secondly we look into the water surface profile and as shown in Figure 14, we can clearly see that the water free surface simulated by CFD models are in good agreement with those measured in physical modelling hence it can be noted that the CFD models can simulate the surcharge of flow for ogee spillways consistently.

@IJMTER-2018, All rights Reserved

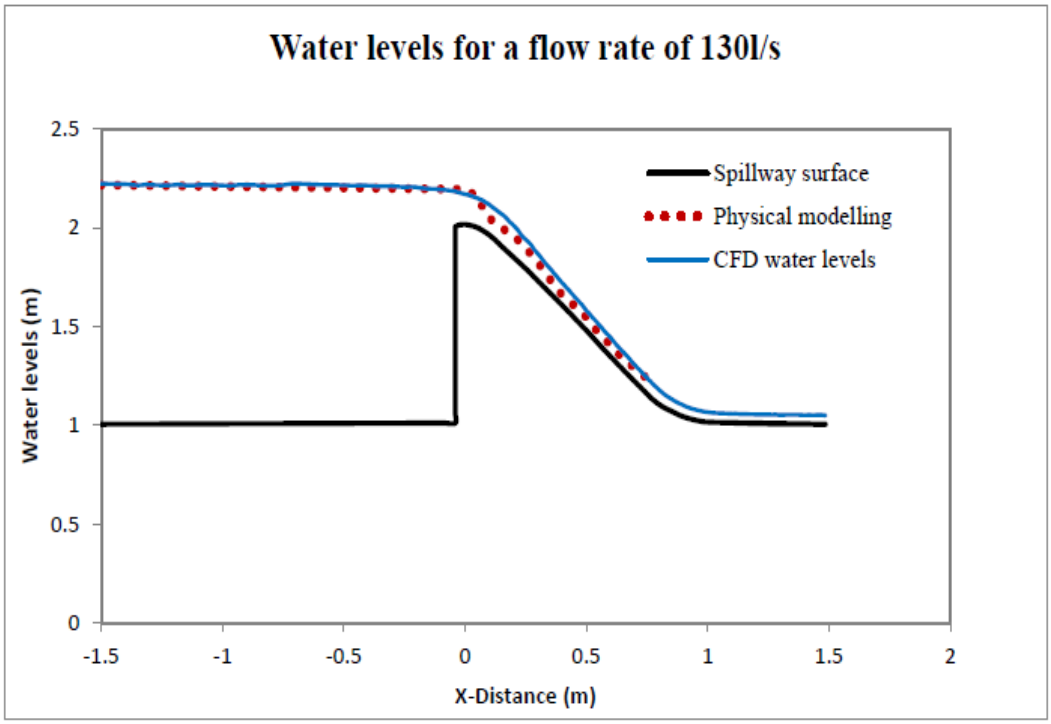


Figure 14: Free water surface of CFD Model and Physical Model

3.2 Pressure results

As already stated the steady state and fully hydrodynamic state have very similar pressure results. So here we will compare the 2D and 3D results of pressure with the Physical Model results.

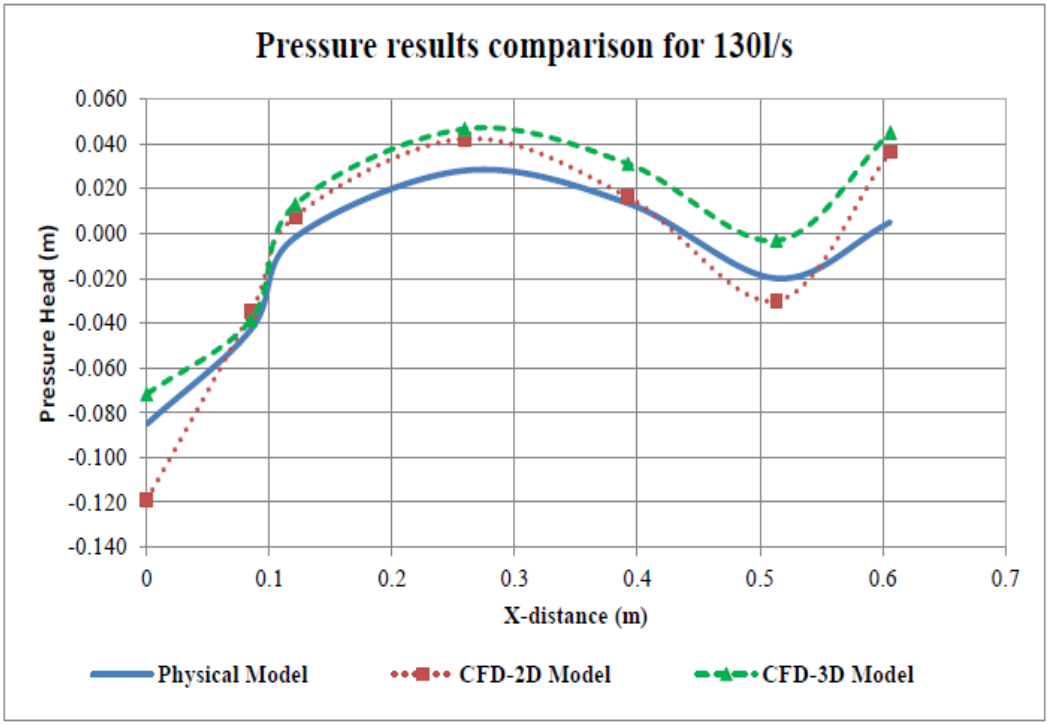


Figure 15: Comparison of 2D, 3D and Physical pressure results

As seen from Figure 15, there is very minute difference between the 2D Model and Physical Model and the 3D Model has larger deviation but the magnitude of this difference is very low and so it can be said that the CFD pressure results confirm to Physical Model results.

@IJMTER-2018, All rights Reserved

IV. CONCLUSION

The flow over an ogee spillway was simulated in this work and compared with the pre obtained physical test results. We here compared mainly the Pressure results and the Water Surcharge results. After the comparison we saw that the in case of pressure, a Negative pressure was obtained when the discharge was greater than Design discharge with a flow separation over the crest and a Positive pressure was obtained for discharge less than Design discharge. Also in case of Water Surcharge and Water Surface Profile we saw a minimal difference of 14 mm in their profile obtained from CFD and Physical tests.

Hence the meshing done in 2D case i.e. Triangular meshing with refinement at lower part proved to be a very successful tool for simulating the phenomenon. Finally we can say that the Multiphase modelling chosen here which was Volume of Fluid (VOF) was able to show the Water surcharge and Water surface profile accurately and also was able to simulate the Pressure with high conformity to the Physical test data.

REFERENCES

[1] Azmoudeh, M.H.E., Kamanbedast, A.A., (2013), Determine The Appropriate Location Of Aerator System On Gotvandolidam's Spillway Using Flow 3D,American-Eurasian J. Agric. & Environ. Sci., 13 (3): Page 378-383. J. Breckling, Ed., The Analysis of Directional Time Series: Applications to Wind Speed and Direction, ser. Lecture Notes in Statistics. Berlin, Germany: Springer, 1989, vol. 61.

[2] Bhajantri, M. E., Deolalikar, P. (2006). Hydrodynamic modelling of flow over a spillway using a two-dimensional finite volume-based numerical model. Sadhana, Page 743-754.

[3] Gessler, D. (2005). CFD Modelling of Spillway performance, EWRI 2005: Impacts of global climate change in Proceedings of the World Water and Environmental Resources Congress. Anchorage, Alaska: American Society of Civil Engineers.

[4] Hirt, C. W., & Nicholas, B. (1981). Volume of Fluid Method (VOF) for the Dynamics of Free Boundaries. J.Comp. Physics, Vol. 39, Page 201-205.

[5] ICOLD. (2001). Tailings Dams- Risk of dangerous occurrences, lessons learnt from practical experiences. ICOLD Comittee on Tailings Dam and Waste Lagoons (p. Bulletin 121). Paris: United Nations Environmental Programme (UNEP), Division of Technology, Industry and Economics (DTIE) and International Commission on Large Dams (ICOLD).

[6] Johnson, M., & Savage, M. B. (2006). Physical And Numerical Comparison of Flow Over Ogee Spillway in the Presence of Tailwater. Journal of Hydraulic Engineering, Vol. 132, No.12.

[7] Kjellesvig, H. (1996). Numerical Modelling of Flow over a Spillway. Hydroinformatics- 96.

[8] Singh, C., & Zhou, F. (1999). Simulation of Free Surface Flow over Spillway. Journal of hydraulic Engineering 125(9),Page 959-967.

[9] Zhenwei, M., Zhiyan, Z., Tao, Z., (2012), Numerical Simulation Of 3-D Flow Field Of Spillway Based On VOF Method, 2012 International Conference On Modern Hydraulic Engineering, SciVerse ScienceDirect, Procedia Engineering 28 (2012) Page 808-812.

@IJMTER-2018, All rights Reserved

Quantum Information Processing (2019) 18:36
https://doi.org/10.1007/s11128-018-2150-0



Coherence and entanglement under three-qubit cloning operations

Suchetana Goswami[1] · Satyabrata Adhikari[2] · A. S. Majumdar[1]

Received: 25 May 2018 / Accepted: 7 December 2018
© Springer Science+Business Media, LLC, part of Springer Nature 2018

Abstract
Coherence and entanglement are the two most crucial resources for various quantum information processing tasks. Here, we study the interplay of coherence and entanglement under the action of different three-qubit quantum cloning operations. Considering certain well-known quantum cloning machines (input state independent and dependent), we provide examples of coherent and incoherent operations performed by them. We show that both the output entanglement and coherence could vanish under incoherent cloning operations. Coherent cloning operations, on the other hand, could be used to construct a universal and optimal coherence machine. It is also shown that under coherent cloning operations, the output two-qubit entanglement could be maximal even if the input coherence is negligible. Also it is possible to generate a fixed amount of entanglement independent of the nature of the input state.

Keywords Quantum correlations · Coherence · Entanglement · Cloning operations

1 Introduction

Out of three nonlocal quantum correlations (such as entanglement [1], steering [2–5] and Bell-nonlocality [6]), entanglement is the most widely applied resource in the field of quantum information [7]. Various manifestations of entanglement among discrete,

✉ Suchetana Goswami
suchetana.goswami@gmail.com

Satyabrata Adhikari
tapisatya@gmail.com

A. S. Majumdar
archan@bose.res.in

1 S. N. Bose National Centre for Basic Sciences, Block JD, Sector-III, Salt Lake, Kolkata 700106, India

2 Delhi Technological University, Shahbad Daulatpur, Main Bawana Road, New Delhi, Delhi 110042, India

Published online: 13 December 2018

continuous and hybrid physical variables have been studied in the context of applications in information theoretic protocols such as dense coding [8], teleportation [9] and cryptography [10]. Investigations of the resource theory of entanglement have uncovered rich tenets [11], and some surprising features such as intra-particle entanglement [12–14]. The connection of entanglement with other defining features of quantum theory such as the uncertainty principle has been rigorously examined [15,16].

Recently, quantum coherence [17] has come to be appreciated as one of the fundamental features of quantum theory. It has been realized that coherence embodies basic quantumness responsible for superposition of quantum states, from which all quantum correlations arise in composite systems. As with entanglement, several measures have been suggested to quantify coherence [18–20]. Interesting connections of coherence with thermodynamic properties of multipartite systems have been pointed out [21–23]. Efforts are on to develop resource theories of coherence enabling it to be used for detection of genuine non-classicality in physical states, and advantage in physical tasks over those performed using classical resources [24–26].

The relation of coherence with other resources in quantum theory forms an interesting arena of study. In a recent work, Streltsov et al. [27] have provided an important insight into the linkage of coherence with entanglement. Based upon the observation that two-qubit incoherent operations can generate entanglement only when the input state is coherent, they have shown that the input state coherence provides an upper bound on the generated two-qubit entanglement. In another recent work, the complementarity of local coherence measures has been used to derive a nonlocal advantage of coherence in the form of enabling quantum steering [28]. In entanglement theory, it is known that the robustness (robustness of the state means here that the state does lose less quantum information in the quantum teleportation through noisy channels.) of GHZ and W states depends on the types of noisy channel [29], while W state is more robust against qubit loss [30]. In the resource theory of coherence, Luo et. al. [31] have shown that if one qubit is lost from GHZ state then the state will become incoherent but in case of W state, if one qubit is lost then the remaining two-qubit state remain coherent. Moreover, they have defined inequivalent classes of multipartite coherence states in the same spirit as in entanglement theory. The connection between coherence and nonlocal resources such as entanglement is important to understand from both the perspective of quantum foundations and information theoretic applications, and thus deserves further study in various contexts.

In the present work, we pose the question as to how the linkage between coherence and entanglement fares in the presence of additional parties or qubits. Specifically, we study the relationship between two-qubit entanglement and coherence under three-qubit operations. Quantum cloning provides a prototypical example of three-qubit operations, and here, we employ coherent and incoherent cloning operations to investigate the connection between coherence and entanglement of the input and output states. For this purpose we consider different categories of cloning machines, such as the Wootters–Zurek [32] mechanism which acts as an incoherent operation, the Buzek–Hillary state independent cloning machine [33] which performs coherent operations. Also we consider phase covariant [34] and state dependent universal [35] cloning machines in order to undertake our study. Cloning could play an efficient role

in resource replication, and in the present context, we propose an optimal quantum coherence machine using our analysis.

The plan of the paper is as follows. In Sect. 2, we discuss three-qubit incoherent operations which could lead to vanishing coherence and entanglement at the output. In Sect. 3, we study three-qubit coherent operations and show how they could be used to construct a universal and optimal coherence machine that generates a fixed value of output coherence irrespective of the input state parameters. In Sect. 4, we investigate further the relation between coherence and entanglement in the context of coherent cloning operations. We find that maximally entangled two-qubit output states could be generated even if the input state coherence is negligible. Lastly, in Sect. 5, we study the behavior of coherence and entanglement of the output single party and two party states for state dependent cloning operations. A summary of our main results is provided in Sect. 6.

2 Entanglement and coherence in reduced two-qubit system under incoherent quantum operations

In this section, we consider a three-qubit incoherent quantum operation and investigate the coherence and entanglement generated in two-qubit reduced state when third ancilla qubit is traced out. Coherence is an elementary property of quantum theory, which is basically a measure of quantumness arising from the superposition principle of quantum mechanics. Also this is a basis dependent quantity and also it might exist in a single partite systems. Based on the superposition principle, an arbitrary state can be classified into two types: incoherent and coherent state. A state ρ is said to be incoherent if it can be expressed in the form

$$\rho = \sum_i \rho_i \, |i\rangle \, \langle i| \tag{1}$$

where $|i\rangle$ represents a fixed reference basis of the state. Otherwise, it is said to be a coherent state. This definition holds not only for single-qubit systems but also for higher dimensional quantum systems. Now, an incoherent quantum operation is defined as a completely positive trace preserving map which takes an incoherent state into another. There are different classes of incoherent operation as well [36]. Mathematically, an incoherent quantum operation Λ can be written as:

$$\Lambda(\rho) = \sum_l K_l \rho K_l^\dagger \tag{2}$$

where the operators K_l are incoherent Kraus operators. There are different types of measures to quantify the amount of coherence in a given quantum state. In our present analysis, we will employ the l_1 norm measure [17] defined as

$$C_{l_1}(\rho) = \sum_{i \neq j} |\rho_{ij}| \tag{3}$$

On the other hand, for the purpose of measuring entanglement, here we consider concurrence [37] of the quantum state (as it is sufficient for two-qubit scenario) and for any two-qubit state ρ it is given by,

$$C(\rho) = \max\left\{\left(\sqrt{\lambda_1} - \sqrt{\lambda_2} - \sqrt{\lambda_3} - \sqrt{\lambda_4}\right), 0\right\} \tag{4}$$

where λ_1, λ_2, λ_3, λ_4 are the eigenvalues of the matrix ρ_f, with $\rho_f = \rho \cdot \tilde{\rho}$ ($\tilde{\rho} = (\sigma_y \otimes \sigma_y)\rho \cdot (\sigma_y \otimes \sigma_y)$). In order to motivate our study, let us here briefly return to the case of two-qubit incoherent operations discussed earlier by Streltsov et al. [27]. Consider the tensor product of an input coherent state

$$|\psi\rangle_a = c_1 |0\rangle_a + c_2 |1\rangle_a , \quad |c_1|^2 + |c_2|^2 = 1 \tag{5}$$

with the ancilla state $|0\rangle_b$, and the state of the composite system is given by

$$\begin{aligned} |\Phi\rangle_{ab} &= |\psi\rangle_a \otimes |0\rangle_b \\ &= c_1 |00\rangle_{ab} + c_2 |10\rangle_{ab} \end{aligned} \tag{6}$$

Now, a two-qubit unitary CNOT operation which is given as,

$$U_{\text{CNOT}} = |00\rangle\langle 00| + |01\rangle\langle 01| + |10\rangle\langle 11| + |11\rangle\langle 10| \tag{7}$$

applied on $|\Phi\rangle_{ab}$, results in the two-qubit state given by

$$|\phi\rangle_{\text{out}} = c_1 |00\rangle_{ab} + c_2 |11\rangle_{ab} \tag{8}$$

One may now consider the following cases. If either $c_1 = 0$ or $c_2 = 0$, the input state (5) is incoherent and it remains an incoherent state even after the application of CNOT operation. Since the CNOT operation takes an incoherent state to another incoherent state and takes the set of incoherent basis $\{|00\rangle, |01\rangle, |10\rangle, |11\rangle\}$ into another $\{|00\rangle, |01\rangle, |11\rangle, |10\rangle\}$, it can be regarded as an incoherent operation. If both $c_1 \neq 0$ and $c_2 \neq 0$, the input state is a coherent state and the application of the CNOT operation on the tensor product (6) will generate an entangled state which basically reproduces the fact that to generate entanglement through an incoherent operation one has to start with a coherent state. In this case, we find that the amount of entanglement generated is equal to the amount of coherence present in the input state. In general, it has been shown [27] that the maximum entanglement generated by an incoherent operation is given by the amount of coherence present in the input qubit. In other words, a two-qubit incoherent operation generates entanglement, only if the input state has non-vanishing coherence. It is hence natural to ask the question if such a result can be extended to systems involving additional qubits. Note also that the coherence of the two-qubit input state $|\Phi\rangle_{ab}$ is equal to the coherence of the two-qubit output state (8) and it is given by $2|c_1||c_2|$. Thus, the coherence of the output state depends on the input state parameters. If, on the other hand, we trace out the second system, i.e., the mode b from the two-qubit system (8), the qubit in mode a is left in an incoherent state. By

generating entanglement through this incoherent operation, one has to pay the price in terms of reducing the amount of coherence in the outputs ρ_A and ρ_B compared to that present in the input state [27]. In fact, in this case, the single-qubit state at the output end is incoherent, while we have started with a coherent state. In our subsequent analysis with three-qubit operations, we investigate further this issue of the amount of coherence retained in the output states and its relation to the entanglement generated using three-qubit operations.

Let us first consider the Wootters–Zurek cloning operation, which is a three-qubit quantum operation expressed as [32]

$$|0\rangle\,|0\rangle\,|0\rangle \rightarrow |0\rangle\,|0\rangle\,|0\rangle \tag{9}$$

$$|1\rangle\,|0\rangle\,|0\rangle \rightarrow |1\rangle\,|1\rangle\,|1\rangle \tag{10}$$

where the first ket vector represents the input state, the second ket vector represents the blank state in which the input state is to be copied and the third ket vector represents the machine state. It is clear from Eqs. (9) and (10) that the cloning operation transforms incoherent input state into incoherent output state and also it takes the set of incoherent basis $\{|0\rangle, |1\rangle\}$ into another $\{|0\rangle, |1\rangle\}$; thus, the above-defined cloning operation is an example of a three-qubit incoherent operation. Note that in [38] the WZ cloning machine has been studied for higher dimensional systems. From the transformation rule of this type of higher dimensional cloning machines, it is clear that it keeps an incoherent input state incoherent.

Now, if we take the input qubit to be coherent in nature, we see that this incoherent operation (9), (10) does not generate entanglement between the input qubit and the blank qubit, when the ancillary machine state is traced out. Let us take the input qubit to be of the form

$$|\psi^{\text{in}}\rangle = \alpha\,|0\rangle + \beta\,|1\rangle\,, \quad |\alpha|^2 + |\beta|^2 = 1 \tag{11}$$

When the state (11) passes through the cloning transformation given in (9), (10), the resulting two-qubit state at the output end after tracing out the machine qubit is given by

$$\rho_{12}^{\text{out}} = |\alpha|^2\,|00\rangle\,\langle 00| + |\beta|^2\,|11\rangle\,\langle 11| \tag{12}$$

Also, the density operators of the copy qubits is given by

$$\rho_1^{\text{out}} = \rho_2^{\text{out}} = |\alpha|^2\,|0\rangle\,\langle 0| + |\beta|^2\,|1\rangle\,\langle 1| \tag{13}$$

The following observations can be made from the Eqs. (12), (13). It can easily be seen that the state described by the density operator ρ_{12}^{out} is not entangled. Therefore, the transformation (9), (10) is an example of a three-qubit incoherent operation that does not generate entanglement between the input qubit and the blank qubit when machine qubit is traced out, even if we start with a coherent input state. We further find that the state described by the density operator ρ_{12}^{out} is an incoherent two-qubit state. The copy qubits generated at the output described by the density operators $\rho_1^{\text{out}} = \rho_2^{\text{out}}$

are incoherent states too. Now, the quality of copying of the cloning machine can be expressed in terms of the distance between the initial and the reduced copied state at the output end, measured by the Hilbert–Schmidt norm given as,

$$D_a = Tr[(\rho^{\text{in}} - \rho_1^{\text{out}})^2] \tag{14}$$

In case of Wootters–Zurek cloning machine, one obtains the distance as,

$$D_a = 2|\alpha|^2(1 - |\alpha|^2) \tag{15}$$

where D_a is known as the copy quality index. Averaging over all input states, one can obtain the copy quality as,

$$D_a = \frac{1}{3} \tag{16}$$

Note that there is another cloning operation which does not generate entanglement at the output end, named phase covariant cloning [34] which can be regarded as an incoherent operation in single-qubit level (but generates coherence in two-qubit output) and it is given as:

$$\begin{aligned} |0\rangle|\Sigma\rangle|Q\rangle \rightarrow & \left[\left(\frac{1}{2}+\sqrt{\frac{1}{8}}\right)|00\rangle + \left(\frac{1}{2}-\sqrt{\frac{1}{8}}\right)|11\rangle\right]|\uparrow\rangle \\ & + \frac{1}{\sqrt{8}}(|01\rangle + |10\rangle)|\downarrow\rangle \end{aligned} \tag{17}$$

$$\begin{aligned} |1\rangle|\Sigma\rangle|Q\rangle \rightarrow & \left[\left(\frac{1}{2}+\sqrt{\frac{1}{8}}\right)|11\rangle + \left(\frac{1}{2}-\sqrt{\frac{1}{8}}\right)|00\rangle\right]|\downarrow\rangle \\ & + \frac{1}{\sqrt{8}}(|01\rangle + |10\rangle)|\uparrow\rangle \end{aligned} \tag{18}$$

Here, without any loss of generality we consider, $|\Sigma\rangle = |0\rangle$, $|Q\rangle = |0\rangle$, $|\uparrow\rangle = |0\rangle$ and $|\downarrow\rangle = |1\rangle$. Likewise in this scenario, it is never possible to generate any entanglement starting even from a coherent state, as one can check starting from a most general form of single-qubit coherent state in computational basis, given in Eq. (11) with $\alpha \neq 0$ and $\beta \neq 0$. So this type of cloning machine is also not effective for the purpose of generating entanglement. The above results motivate us to consider next three-qubit quantum operations which may not be incoherent and can not only generate entanglement between the input qubit and the blank qubit when ancillary machine qubit is traced out, but also generate coherence in the copy qubits at the output.

3 Optimal universal two-qubit quantum coherence machine

In this section, we will consider the Buzek–Hillary (B–H) cloning operations [33] to see that there exist two classes of three-qubit coherent quantum operations that

generate coherence in the reduced two-qubit system. In the first class, the generated coherence depends on input state parameters, while in the second class, the coherence in reduced two-qubit system does not depend on the input state parameters.

To begin with, let us consider the three-qubit quantum operation given by [33]

$$|0\rangle_a |0\rangle_b |0\rangle_c \rightarrow \sqrt{\frac{2}{3}} |0\rangle_a |0\rangle_b |0\rangle_c + \sqrt{\frac{1}{6}}(|0\rangle_a |1\rangle_b + |1\rangle_a |0\rangle_b) |1\rangle_c \tag{19}$$

$$|1\rangle_a |0\rangle_b |0\rangle_c \rightarrow \sqrt{\frac{2}{3}} |1\rangle_a |1\rangle_b |1\rangle_c + \sqrt{\frac{1}{6}}(|0\rangle_a |1\rangle_b + |1\rangle_a |0\rangle_b) |0\rangle_c \tag{20}$$

The above transformation is a two-qubit coherent quantum operation as it takes an incoherent state to two-qubit coherent state. The above transformation is also known as the optimal state independent B–H cloning transformation in the $\{|0\rangle, |1\rangle\}$ basis. If we take the partial trace over the ancillary machine qubit c at the output end of (19) and (20), the corresponding reduced two-qubit density operators are given by

$$\rho_{ab}^{\text{out1}} = \frac{2}{3} |00\rangle \langle 00| + \frac{1}{6}(|01\rangle \langle 01| + |10\rangle \langle 01| + |01\rangle \langle 10| + |10\rangle \langle 10|) \tag{21}$$

$$\rho_{ab}^{\text{out2}} = \frac{2}{3} |11\rangle \langle 11| + \frac{1}{6}(|01\rangle \langle 01| + |10\rangle \langle 01| + |01\rangle \langle 10| + |10\rangle \langle 10|) \tag{22}$$

The entanglement [39,40] and coherence of the states ρ_{ab}^{out1} and ρ_{ab}^{out2} are equal and given by $\frac{1}{3}$. Thus, the B–H cloning machine generates a two-qubit coherent state starting from an incoherent input qubit.

Let us next consider the input state $|\psi^{\text{in}}\rangle$ (11) with non-zero state parameters α and β. If we apply the optimal universal B–H cloning transformations given in (19) and (20) on $|\psi^{\text{in}}\rangle$, the two-qubit cloned state at the output end comes out to be of the form,

$$\rho_{ab}^{\text{out}} = \frac{2}{3}|\alpha|^2 |00\rangle \langle 00| + \frac{\sqrt{2}\alpha\beta^*}{3} |00\rangle \langle +| + \frac{\sqrt{2}\alpha^*\beta}{3} |+\rangle \langle 00| + \frac{1}{3} |+\rangle \langle +| + \frac{\sqrt{2}\alpha\beta^*}{3} |+\rangle \langle 11| + \frac{\sqrt{2}\alpha^*\beta}{3} |11\rangle \langle +| + \frac{2}{3}|\beta|^2 |11\rangle \langle 11| \tag{23}$$

where $|+\rangle = \frac{1}{\sqrt{2}}(|01\rangle + |10\rangle)$. The amount of coherence contained in the state described by the density operator ρ_{ab}^{out} is given by $\frac{4(\alpha^*\beta+\alpha\beta^*)+1}{3}$. ($*$ denotes the corresponding complex conjugate) Thus, in case of the B–H quantum cloning machine,

the generated cloned two-qubit output is always coherent. It can be observed that the coherence of the state ρ_{ab}^{out} depends on the state parameters α and β of the input. But it should be noted that the concurrence of this two party output state turns out to be $\frac{1}{3}$, which is independent of the input state parameters. Also, it is quite interesting to note that this cloning machine generates a constant amount of entanglement starting from any single-qubit input state. Hence, it can be used as a source of constant entanglement.

We have seen that if we use this coherent quantum operation (19), (20), the coherence of the reduced two-qubit output state depends on the input state. It would be interesting to design a universal coherence transformation that transforms an arbitrary state $|\Psi\rangle_{ab}$ which may or may not be coherent, to a two-qubit coherent state. We demand the transformation to be universal in the sense that the coherence of the two-qubit output state should not be depending on the input state parameters. To construct such a coherence transformation, let us start with the most general form B–H quantum cloning transformation given by

$$\begin{aligned} |0\rangle_a |0\rangle_b |Q\rangle_c \rightarrow\ & |0\rangle_a |0\rangle_b |Q_0\rangle_c + (|0\rangle_a |1\rangle_b \\ & + |1\rangle_a |0\rangle_b) |Y_0\rangle_c \end{aligned} \tag{24}$$

$$\begin{aligned} |1\rangle_a |0\rangle_b |Q\rangle_c \rightarrow\ & |1\rangle_a |1\rangle_b |Q_1\rangle_c + (|0\rangle_a |1\rangle_b \\ & + |1\rangle_a |0\rangle_b) |Y_1\rangle_c \end{aligned} \tag{25}$$

Unitarity of the transformation gives the relations

$$ {}_c\langle Q_i|Q_i\rangle_c + 2\,{}_c\langle Y_i|Y_i\rangle_c = 1, \quad i = 0, 1 \tag{26}$$

$$ {}_c\langle Y_0|Y_1\rangle_c = 0, \tag{27}$$

Let us further assume the following orthogonality relations between the machine state vectors:

$$ {}_c\langle Q_i|Y_i\rangle_c = 0, \quad i = 0, 1 \tag{28}$$

$$ {}_c\langle Q_0|Q_1\rangle_c = 0, \tag{29}$$

First let us apply the cloning transformation given in (24) and (25) on an incoherent input state, say, $|0\rangle$ ($|1\rangle$). At the output end, the coherence and concurrence of the final two party state (while the state of the ancillary system is traced out) turn out to be the same and it is given by, 2μ, where, μ is given by,

$$ {}_c\langle Y_0|Y_0\rangle_c =_c \langle Y_1|Y_1\rangle_c = \mu \tag{30}$$

Secondly, applying the cloning transformation (24) and (25) on $|\psi^{\text{in}}\rangle$ given by Eq. (11), and taking the partial trace over the ancillary machine qubit c, we obtain the cloned two-qubit state described by the density operator

$$\begin{aligned}\varrho_{ab}^{\text{out}} &= |\alpha|^2(1-2\mu)|00\rangle\langle 00| + \alpha\beta^*\frac{\nu}{\sqrt{2}}|00\rangle\langle +| + \alpha^*\beta\frac{\nu}{\sqrt{2}}|+\rangle\langle 00| \\ &+ 2\mu|+\rangle\langle +| + \alpha\beta^*\frac{\nu}{\sqrt{2}}|+\rangle\langle 11| + \alpha^*\beta\frac{\nu}{\sqrt{2}}|11\rangle\langle +| \\ &+ |\beta|^2(1-2\mu)|11\rangle\langle 11|) \end{aligned} \tag{31}$$

where μ is given as Eq. (30) and ν is given by

$$_c\langle Y_0|Q_1\rangle_c =_c \langle Q_0|Y_1\rangle_c = \frac{\nu}{2} \tag{32}$$

Using the Schwarz inequality, the range of the parameters μ, ν are given by

$$0 \le \mu \le \frac{1}{2} \quad \text{and} \quad 0 \le \nu \le 2\sqrt{\mu}\sqrt{1-2\mu} \le \frac{1}{\sqrt{2}} \tag{33}$$

Now, the coherence of the state described by the density operator $\varrho_{ab}^{\text{out}}$ is given by

$$C_{l_1}(\varrho_{ab}^{\text{out}}) = 2\mu + 2(\alpha^*\beta + \alpha\beta^*)\nu \tag{34}$$

The quantity $C_{l_1}(\varrho_{ab}^{\text{out}})$ is input state independent if $\nu = 0$. In this case Eq. (34) reduces to $C_{l_1}(\varrho_{ab}^{\text{out}}) = 2\mu$. The maximum value of $C_{l_1}(\varrho_{ab}^{\text{out}})$ can be obtained by putting $\mu = \frac{1}{2}$, which leads to

$$C_{l_1}(\varrho_{ab}^{\text{out}}) = 1 \tag{35}$$

For these particular values of μ and ν, it can be seen that the concurrence of the two party state is maximum. Also note that the copy quality index in this case turns out to be $\frac{1}{18}$ which is much less than that of WZ cloning machine (hence better quality of cloning) and also independent of the input state parameter [33].

Equation (35) is the evidence of the fact that the coherence present in the two-qubit output state is optimal and independent of the input state parameters. Thus, we are successful in constructing a universal quantum coherence machine starting from the B–H quantum cloning machine. Particularly, the optimal universal quantum coherence transformation is given by

$$|0\rangle_a|0\rangle_b|0\rangle_c \to \sqrt{\frac{1}{2}}(|0\rangle_a|1\rangle_b + |1\rangle_a|0\rangle_b)|0\rangle_c \tag{36}$$

$$|1\rangle_a|0\rangle_b|0\rangle_c \to \sqrt{\frac{1}{2}}(|0\rangle_a|1\rangle_b + |1\rangle_a|0\rangle_b)|1\rangle_c \tag{37}$$

It is now clear that optimal universal quantum coherence transformation can be obtained from B–H quantum cloning transformation by choosing the machine vector in such a way that $\mu = \frac{1}{2}$ and $\nu = 0$. Let us now ascertain how well the B–H copying

machine with machine parameters $\mu = \frac{1}{2}$ and $\nu = 0$ copies the input qubit described by the density operator

$$\begin{aligned}\rho^{\text{in}} &= |\psi_{\text{in}}\rangle \langle\psi_{\text{in}}| \\ &= |\alpha|^2 |0\rangle \langle 0| + \alpha\beta^* |0\rangle \langle 1| + \alpha^*\beta |1\rangle \langle 0| + |\beta|^2 |1\rangle \langle 1| \end{aligned} \tag{38}$$

Since the B–H quantum cloning machine is considered to be symmetric in nature, the copies of the input state at the output end of the copying machine are identical and are given by

$$\begin{aligned}\rho_a^{\text{out}} = \rho_b^{\text{out}} = (|\alpha|^2(1-2\mu) + 2\mu)|0\rangle\langle 0| + \sqrt{2}\nu\alpha\beta^*|0\rangle\langle 1| \\ + \sqrt{2}\nu\alpha^*\beta|1\rangle\langle 0| + (|\beta|^2(1-2\mu) + 2\mu)|1\rangle\langle 1| \end{aligned} \tag{39}$$

The distance between ρ^{in} and $\rho_a^{\text{out}}/\rho_b^{\text{out}}$ can be measured by the Hilbert Schmidt norm, given as

$$\begin{aligned} D_a &= Tr[(\rho^{\text{in}} - \rho_a^{\text{out}})^2] = Tr[(\rho^{\text{in}} - \rho_b^{\text{out}})^2] \\ &= 2\mu^2(1 - 4|\alpha|^2|\beta|^2) + 2|\alpha|^2|\beta|^2(\nu - 1)^2 \end{aligned} \tag{40}$$

Note that, for $\nu = 1 - 2\mu$, the quality of copy for the B–H cloning machine becomes input state independent and particularly for $\mu = \frac{1}{2}$ and $\nu = 0$, the distance D_a reduces to

$$D_a = \frac{1}{2} \tag{41}$$

Equation (41) indicates that the quality of the copy also does not depend on the input state parameter. Therefore, for the cloning machine parameter $\mu = \frac{1}{2}$ and $\nu = 0$, the B–H quantum cloning machine becomes an input state independent quantum cloning machine, but it should be noted that this cloning machine is not optimal in terms of quality of cloning.

4 Generation of entanglement from coherent operations

A quantum operation is said to be a coherent operation if it generates coherence even from an incoherent state. It has been already seen that under the application of any coherent operation it is possible to generate entanglement starting even from an incoherent state. Unlike incoherent quantum operations (free operation in coherence resource theory), we have seen that when a coherent operation (19) acts on the tensor product of an incoherent input state and an incoherent ancilla state, it generates entanglement in the two-qubit reduced state when the ancilla state is traced out. We found that the amount of entanglement generated in the two-qubit reduced state is equal to the amount of coherence in it. This leads us to the following result.

Result If we construct a coherent operation Λ^c in such a way that it generates a two-qubit mixed state of the form

$$\begin{aligned}\rho_{AB} = a|00\rangle\langle 00| + b|01\rangle\langle 01| + c|01\rangle\langle 10| + c^*|10\rangle\langle 01| \\ + d|10\rangle\langle 10| + e|11\rangle\langle 11|\end{aligned} \tag{42}$$

when applied on the tensor product of an incoherent input state and an incoherent ancilla state, the output entanglement and coherence are related by

$$C(\rho_{AB}) \leq C_{l_1}(\rho_{AB}) \tag{43}$$

where $C(\rho_{AB})$ is the concurrence of the output two-qubit state and C_{l_1} is the l_1 norm measure of coherence of the corresponding state.

Proof It is known that the concurrence of the two-qubit mixed entangled state (42) is given by [40,41],

$$C(\rho_{AB}) = \max\{0, 2(|c| - \sqrt{ae})\} \tag{44}$$

From (44), we find that

$$C(\rho_{AB}) \leq 2|c| \tag{45}$$

Again, the l_1 norm of coherence of the two-qubit mixed state (42) is given by

$$C_{l_1}(\rho_{AB}) = |c| + |c| = 2|c| \tag{46}$$

Using (45) and (46), we have

$$C(\rho_{AB}) \leq C_{l_1}(\rho_{AB}) \tag{47}$$

Hence proved. □

In this section, we consider a coherent operation in the form of B–H quantum cloning machine to study the entanglement structure of the two-qubit output state. Depending on the (coherent/incoherent) nature of the input state, we analyze the entanglement structure of two-qubit state at the output end of the cloning machine. First, let us consider the case when the input state to be cloned is an incoherent state which is either of the form $|0\rangle$ or $|1\rangle$. When $|0\rangle$ goes through the cloning transformation given by Eqs. (24) and (25), the two-qubit output state is given by

$$\rho_{ab}^{\text{out3}} = (1 - 2\mu)|00\rangle\langle 00| + 2\mu|+\rangle\langle +| \tag{48}$$

It is clear that the concurrence of the two-qubit state ρ_{ab}^{out3} given by Eq. (48) is non-zero and given by 2μ. A similar result can be obtained when the input state to be cloned is of the form $|1\rangle$. Therefore, the general B–H quantum cloning transformation

generates an entangled two-qubit cloned state when the input state is an incoherent. A maximally entangled state is generated when $\mu = \frac{1}{2}$. The structure of the cloning transformation that generates the maximally entangled state of two cloned copies out of the incoherent input state is the same as the state independent quantum coherence transformation given by (36), (37).

In the second scenario, let us consider that the input state to be cloned is a coherent state $|\psi_{\text{in}}\rangle$ given by (11). When the general B–H quantum cloning transformation is applied on $|\psi_{\text{in}}\rangle$ and tracing out the cloning machine state vector, the resulting two-qubit state of two cloned copies is entangled. We study the entanglement of the output two-qubit state for two cases.

Case-I If we perform a state independent B–H quantum cloning transformation given by (24) and (25) with $\nu = 1 - 2\mu$, on any arbitrary coherent input state $|\psi_{\text{in}}\rangle$, the output state is given by

$$\begin{aligned}\varrho_{ab}^{\text{out}} = {} & |\alpha|^2(1-2\mu)|00\rangle\langle 00| + \alpha\beta^*\frac{1-2\mu}{\sqrt{2}}|00\rangle\langle +| + \alpha^*\beta\frac{1-2\mu}{\sqrt{2}}|+\rangle\langle 00| \\ & + 2\mu|+\rangle\langle +| + \alpha\beta^*\frac{1-2\mu}{\sqrt{2}}|+\rangle\langle 11| + \alpha^*\beta\frac{1-2\mu}{\sqrt{2}}|11\rangle\langle +| \\ & + |\beta|^2(1-2\mu)|11\rangle\langle 11|) \end{aligned} \tag{49}$$

We find that the generated two-qubit cloned state is entangled and it is clearly evident from the plot given below (Fig. 1).

From the plot, it can be seen that there exist state independent B–H quantum cloning transformations that cannot be used to generate two-qubit entangled states. Additionally, one may note that the optimal state independent B–H quantum cloning machine can be used to generate a two-qubit cloned state from a coherent input state. Also, one may observe that there exists a cloning transformation which generates maximum entanglement at the output end even when the coherence of the input is negligible.

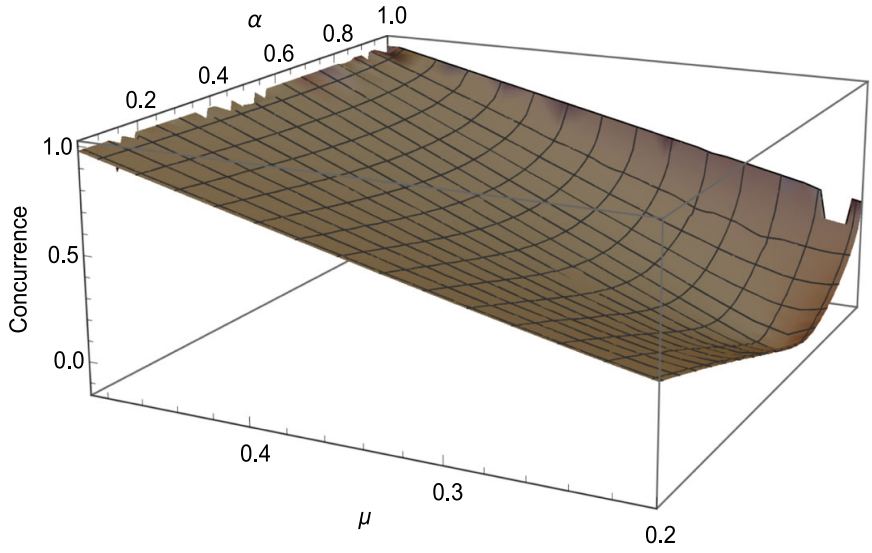


Fig. 1 Concurrence of the two-qubit output state is plotted against the machine parameter μ and the input state parameter α

Case-II If we apply the optimal state independent quantum coherence transformation given by (36), (37) on the coherent input state $|\psi_{\text{in}}\rangle$ (or may be on any incoherent input state, i.e. $|\psi_{\text{in}}\rangle$ either with $\beta = 0$ or $\alpha = 0$), then the two party output state is given by,

$$\varrho_{ab}^{\text{out}} = \frac{1}{2}(|01\rangle\langle 01| + |01\rangle\langle 10| + |10\rangle\langle 01| + |10\rangle\langle 10|) \tag{50}$$

The concurrence of this state is unity for any type of input state. So even for negligible amount of coherence it generates maximal entanglement.

5 Study of coherence and entanglement in case of general state dependent cloning machine

In this type of cloning [35], the cloner operates a unitary operation on the composite Hilbert space of the three party state in the following way,

$$\begin{aligned} |0\rangle\,|0\rangle\,|X\rangle \rightarrow\ & a\,|00\rangle\,|A\rangle + b_1\,|01\rangle\,|B_1\rangle + b_2\,|10\rangle\,|B_2\rangle + \\ & c\,|11\rangle\,|C\rangle \end{aligned} \tag{51}$$

$$\begin{aligned} |1\rangle\,|0\rangle\,|X\rangle \rightarrow\ & \tilde{a}\,|11\rangle\,\left|\tilde{A}\right\rangle + \tilde{b_1}\,|01\rangle\,\left|\tilde{B_1}\right\rangle + \tilde{b_2}\,|10\rangle\,\left|\tilde{B_2}\right\rangle + \\ & \tilde{c}\,|00\rangle\,\left|\tilde{C}\right\rangle \end{aligned} \tag{52}$$

The above cloning operations are corresponding to the incoherent input states $|0\rangle$ and $|1\rangle$, respectively. Here, the state $|X\rangle$ represents the initial ancillary machine state and $|A\rangle$, $|B_1\rangle$, $|B_2\rangle$, $|C\rangle$, $\left|\tilde{A}\right\rangle$, $\left|\tilde{B_1}\right\rangle$, $\left|\tilde{B_2}\right\rangle$, $\left|\tilde{C}\right\rangle$ signify the ancillary machine state at the output end. As the operation of cloning is unitary, the coefficients in each case should satisfy the normalization conditions,

$$a^2 + {b_1}^2 + {b_2}^2 + c^2 = 1 \tag{53}$$

$$\tilde{a}^2 + \tilde{b_1}^2 + \tilde{b_2}^2 + \tilde{c}^2 = 1 \tag{54}$$

Here, we chose that $c = 0$ and $\tilde{c} = 0$ as the terms corresponding to these coefficients do not produce any productive output (neither it copies the state properly nor gives back the original state).

Now for our convenience let us choose (without any loss of generality), $|A\rangle = |0\rangle$, $|B_1\rangle = |1\rangle$, $|B_2\rangle = |1\rangle$ and hence $\left|\tilde{A}\right\rangle = |1\rangle$, $\left|\tilde{B_1}\right\rangle = |0\rangle$, $\left|\tilde{B_2}\right\rangle = |0\rangle$. Let us first start with an incoherent state $|0\rangle$ ($|1\rangle$), and under the transformation 51 (52) it can be observed that the single party cloned state at the output end is incoherent in nature. So, we can call it as a single-qubit incoherent cloning operation. It is interesting to notice that under such type of cloning operation on these incoherent states, it is possible to generate an entangled state at the output end, whose concurrence is given by, $2b_1$ (or, $2\tilde{b_1}$) with $b_1 = b_2$ (and, $\tilde{b_1} = \tilde{b_2}$)(assuming the cloning machine

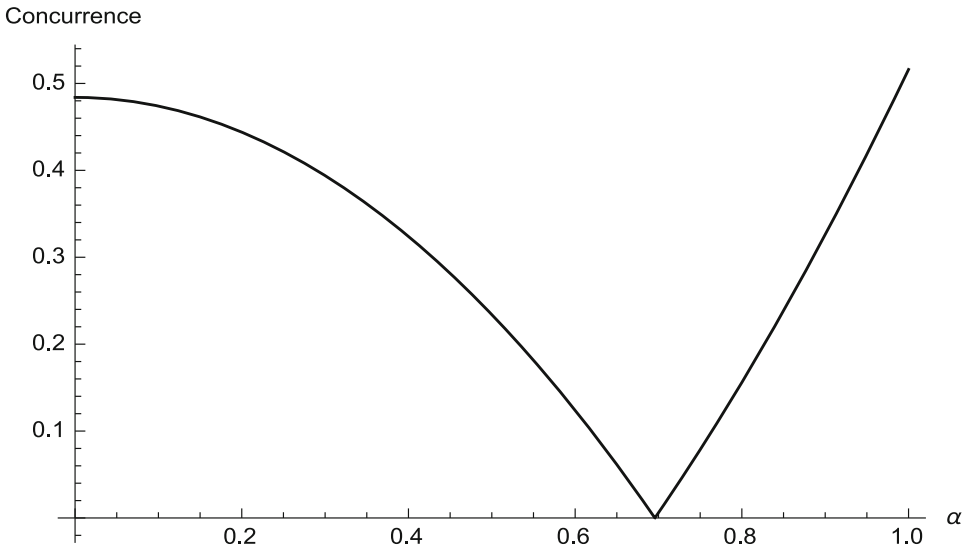


Fig. 2 Concurrence of the two-qubit output state for general state dependent cloning machine is plotted against the input state parameter α

to be symmetric). Now let us consider the initial state to be coherent as given in 11. Now after passing through the cloning machine, the output three party state becomes, $|\psi_{out}\rangle = \alpha[a\,|000\rangle + b_1\,|011\rangle + b_2\,|101\rangle] + \beta[\tilde{a}\,|111\rangle + \tilde{b_1}\,|100\rangle + \tilde{b_2}\,|010\rangle]$. Now to find the coherence of the copied state or the original state after the operation, one needs to trace out the two party state with respect to either the first party or with respect to the second party. For this cloning machine to be symmetric in nature, one should have the coherence of both the states to be equal. By assuming the symmetry of the operation, one can get the coherence as $2(\tilde{a}b_2 + a\tilde{b_2})\alpha\beta = 2(\tilde{a}b_2 + a\tilde{b_2})\alpha\sqrt{1-\alpha^2}$. Now optimization with respect to $a, \tilde{a}, b_1, \tilde{b_1}$ gives that the maximum value of coherence of the final one party state for this type of cloning is $\sqrt{2}\alpha\beta$. The corresponding values of the parameters are $a = \frac{3}{4\sqrt{2}} = 0.695654$, $b_1 = b_2 = \frac{\sqrt{23}}{8} = 0.507969$, $\tilde{a} = \frac{\sqrt{\frac{23}{2}}}{4} = 0.718377$ and $\tilde{b_1} = \tilde{b_2} = \frac{3}{8} = 0.491902$. One can easily see that compared to the state independent cloning, the coherence of the final state is better in this case. Also, the entanglement also shows an improvement with respect to optimal BH cloning machine. The variation of concurrence with respect to the state parameter, for the optimized set of parameters of the machine is shown in Fig. 2, and it can be seen for most of the values of state parameter α the output two party state remains entangled.

6 Conclusions

In this work, we have considered three-qubit cloning operations and studied the two-qubit output coherence and entanglement. The cloning operations have different copy quality indices, and here, we have considered cloning machines with different copying efficiency. In some cases, it is independent of the input state parameters and for others, efficiency is dependent on the same. Recently, a bound has been obtained on the two-qubit entanglement in terms of the coherence of a single-qubit input state when an

incoherent operation is performed on it [27]. Our motivation for the present study is to investigate further the connection between entanglement and coherence in the context of cloning operations involving additional qubits. For this purpose, we have considered here two types of well-known cloning operations, *viz.*, the Wootters–Zurek copier [32], and the Buzek–Hillery copier [33]. As we have discussed, our cloning operations could be categorized into three-qubit coherent and incoherent operations. We have shown that the WZ cloning machine does not generate either coherence or entanglement at the output. Cloning operations may be regarded as resource replicators in quantum information processing. In the present work, we next show that the BZ copier could act as a universal coherence machine that generates a fixed amount of coherence in the two-qubit output state irrespective of the input state parameters. Under the action of coherent cloning operations, a relation is obtained among the two-qubit output coherence and entanglement. We have further shown that under such operations, the output entanglement could be maximal even if the input state coherence is negligible.

References

1. Einstein, A., Podolsky, D., Rosen, N.: Can quantum-mechanical description of physical reality be considered complete? Phys. Rev. **47**, 777 (1935)
2. Schrödinger, E.: Discussion of probability relations between separated systems. Proc. Camb. Philos. Soc. **31**, 555 (1935)
3. Schrödinger, E.: Discussion of probability relations between separated systems. Proc. Camb. Philos. Soc. **32**, 446 (1936)
4. Wiseman, H.M., Jones, S.J., Doherty, A.C.: Steering, entanglement, nonlocality, and the Einstein–Podolsky–Rosen paradox. Phys. Rev. Lett. **98**, 140402 (2007)
5. Jones, S.J., Wiseman, H.M., Doherty, A.C.: Entanglement, Einstein–Podolsky–Rosen correlations, bell nonlocality, and steering. Phys. Rev. A **76**, 052116 (2007)
6. Bell, J.S.: On the Einstein Podolsky Rosen paradox. Physics **1**, 195 (1964)
7. Nielsen, M., Chuang, I.: Quantum Computation and Quantum Information. Cambridge University Press, Cambridge (2000)
8. Bennett, C.H., Wiesner, S.J.: Communication via one- and two-particle operators on Einstein–Podolsky–Rosen states. Phys. Rev. Lett. **69**, 2881 (1992)
9. Bennett, C.H., Brassard, G., Crpeau, C., Jozsa, R., Peres, A., Wootters, W.K.: Teleporting an unknown quantum state via dual classical and Einstein–Podolsky–Rosen channels. Phys. Rev. Lett. **70**, 1895 (1993)
10. Ekert, A.K.: Quantum cryptography based on Bells theorem. Phys. Rev. Lett. **67**, 661 (1991)
11. Horodecki, R., Horodecki, P., Horodecki, M., Horodecki, K.: Quantum entanglement. Rev. Mod. Phys. **81**, 865 (2009)
12. Boschi, D., Branca, S., De Martini, F., Hardy, L., Popescu, S.: Experimental realization of teleporting an unknown pure quantum state via dual classical and Einstein–Podolsky–Rosen channels. Phys. Rev. Lett. **80**, 1121 (1998)
13. Michler, M., Weinfurter, H., Zukowski, M.: Experiments towards Falsification of noncontextual hidden variable theories. Phys. Rev. Lett. **84**, 5457 (2000)
14. Barreiro, J.T., Wei, T.-C., Kwiat, P.G.: Beating the channel capacity limit for linear photonic superdense coding. Nat. Phys. **4**, 282 (2008)
15. Berta, M., Christandl, M., Colbeck, R., Renes, J.M., Renner, R.: The uncertainty principle in the presence of quantum memory. Nat. Phys. **6**, 659 (2010)
16. Pramanik, T., Chowdhury, P., Majumdar, A.S.: Fine-grained lower limit of entropic uncertainty in the presence of quantum memory. Phys. Rev. Lett. **110**, 020402 (2013)
17. Baumgratz, T., Cramer, M., Plenio, M.B.: Quantifying coherence. Phys. Rev. Lett. **113**, 140401 (2014)
18. Girolami, D.: Observable measure of quantum coherence in finite dimensional systems. Phys. Rev. Lett. **113**, 170401 (2014)

19. Napoli, C., Bromley, T.R., Cianciaruso, M., Piani, M., Johnston, N., Adesso, G.: Robustness of coherence: an operational and observable measure of quantum coherence. Phys. Rev. Lett. **116**, 150502 (2016)
20. Yao, Y., Dong, G.H., Xiao, X., Sun, C.P.: Frobenius-norm-based measures of quantum coherence and asymmetry. Sci. Rep. **6**, 32010 (2016)
21. berg, J.: Catalytic coherence. Phys. Rev. Lett. **113**, 150402 (2014)
22. Narasimhachar, V., Gour, G.: Low-temperature thermodynamics with quantum coherence. Nat. Commun. **6**, 7689 (2015)
23. wikliski, P., Studziski, M., Horodecki, M., Oppenheim, J.: Limitations on the evolution of quantum coherences: towards fully quantum second laws of thermodynamics. Phys. Rev. Lett. **115**, 210403 (2015)
24. Gour, G., Marvian, I., Spekkens, R.W.: Measuring the quality of a quantum reference frame: the relative entropy of frameness. Phys. Rev. A **80**, 012307 (2009)
25. Marvian, I., Spekkens, R.W.: The theory of manipulations of pure state asymmetry: I. Basic tools, equivalence classes and single copy transformations. New J. Phys. **15**, 033001 (2013)
26. Marvian, I., Spekkens, R.W., Zanardi, P.: Quantum speed limits, coherence, and asymmetry. Phys. Rev. A **93**, 052331 (2016)
27. Streltsov, A., Singh, U., Dhar, H.S., Bera, M.N., Adesso, G.: Measuring quantum coherence with entanglement. Phys. Rev. Lett. **115**, 020403 (2015)
28. Mondal, D., Pramanik, T., Pati, A.K.: Nonlocal advantage of quantum coherence. Phys. Rev. A **95**, 010301 (2017)
29. Jung, E., Hwang, M.-R., Ju, Y.H., Kim, M.-S., Yoo, S.-K., Kim, H., Park, D., Son, J.-W., Tamaryan, S., Cha, S.-K.: Greenberger–Horne–Zeilinger versus W states: quantum teleportation through noisy channels. Phys. Rev. A **78**, 012312 (2008)
30. Kang, Y.-H., Chen, Y.-H., Wu, Q.-C., Huang, B.-H., Song, J., Xia, Y.: Fast generation of W states of superconducting qubits with multiple Schrodinger dynamics. Sci. Rep. **6**, 36737 (2016)
31. Luo, Y., Li, Y., Hsieh, M-H: Inequivalent multipartite coherence classes and new coherence monotones. arxiv:1807.06308
32. Wootters, W.K., Zurek, W.H.: A single quantum cannot be cloned. Nat. (Lond.) **299**, 802 (1982)
33. Buzek, V., Hillery, M.: Quantum copying: beyond the no-cloning theorem. Phys. Rev. A **54**, 1844 (1996)
34. Bruss, D., Cinchetti, M., DAriano, G.M., Macchiavello, C.: Phase-covariant quantum cloning. Phys. Rev. A **62**, 12302 (2000)
35. Bruss, D., DiVincenzo, D.P., Ekert, A., Fuchs, C.A., Macchiavello, C., Smolin, J.A.: Optimal universal and state-dependent quantum cloning. Phys. Rev. A **57**, 2368 (1998)
36. Streltsov, A., Adesso, G., Plenio, M.B.: Colloquium: quantum coherence as a resource. Rev. Mod. Phys. **89**, 041003 (2017)
37. Coffman, V., Kundu, J., Wootters, W.K.: Distributed entanglement. Phys. Rev. A **61**, 052306 (2000)
38. Ying, M.: WoottersZurek Quantum-copying machine: the higher-dimensional case. Phys. Lett. A **299**, 107 (2002)
39. Wootters, W.K.: Entanglement of formation of an arbitrary state of two qubits. Phys. Rev. Lett. **80**, 2245 (1998)
40. O'Connor, K.M., Wootters, W.K.: Entangled rings. Phys. Rev. A **63**, 052302 (2000)
41. Bruss, D., Macchiavello, C.: On the entanglement structure in quantum cloning. Found. Phys. **33**, 1617 (2003)

International Journal of Research in Engineering and Innovation (IJREI)
journal home page: http://www.ijrei.com
ISSN (Online): 2456-6934



Comparison of thermal performances of single effect, double effect and triple effect LiBr-H_2O absorption system cascaded with vapour compression refrigeration systems using ecofriendly refrigerants

R.S. Mishra

Department of Mechanical & Production Engineering, Delhi Technological University Delhi, India

Abstract

This paper mainly deals with comparisons of three cascade vapour compression systems cascaded with evaporator of LiBr-H_2O vapour absorption refrigeration system cascaded by condenser of vapour compression refrigeration system using ecofriendly refrigerants (i.e. R1234yf, R134a, R-32, R507a, R227ea, R236fa, R245fa , R717) and energy and exergy analysis of all three systems were carried out because exergy (Second law) analysis used to facilitates the identification of the system components with high exergy loss. The performance parameters have been compared with three cascade vapour absorption-compression refrigeration system and it was observed that 122% first law efficiency enhancement using triple effect VARS cascaded with VCRS and 79.45% enhancement in second law efficiency using triple effect VARS cascaded with VCRS. Similarly exergy reduction is 56.60% using triple effect VARS cascaded with VCRS and 25.9% reduction using double effect VARS cascaded with VCRS An Similarly performance parameters have been compared with three cascade vapour absorption-compression refrigeration system and it was observed that 22.87% first law efficiency enhancement using triple effect VARS cascaded with VCRS and 46.3% enhancement in second law efficiency using triple effect VARS cascaded with VCRS as compared with double effect vapour absorption refrigeration cascaded with vapour compression refrigeration system. Similarly exergy reduction is 41.4% using triple effect VARS cascaded with VCRS as compared to double effect VARS cascaded with VCRS.
© 2018 ijrei.com. All rights reserved

Keywords: Thermodynamic Analysis, Energy-Exergy Analysis, Entropy Generation principle, Irreversibility Analysis

1. Introduction

Refrigeration and air conditioning (RAC) plays very importance role in our day to day working for cooling and heating requirements. Refrigeration systems are widely used for controlling temperature in working/living environment to provide thermal comfort to mankind. The use of refrigeration technology for cooling is not new; however, air-conditioning technology is required to evolve due to many environmental regulations. Its applications are many in different fields and sectors. Refrigeration systems also used for storages of perishable food, and pharmaceutical formulations. Conventional systems of refrigeration and air conditioning consume a huge amount of (high-grade) electrical energy produced by burning of fossil fuels. The prices of fossil fuels are increasing day by day and source availability is also declining due to huge consumption. The concerns of increasing fuel price for electricity generation, environmental pollution & environmental damage in terms of global warming is a world –wide concern. Key reasons attributing to this increasing power consumption include: 75% Growth in population 75% Greater demand for building services 75% Need for better comfort levels 75%. Longer duration of occupants spent time inside buildings. It is not only in the developed but also in the developing countries.

The vapour absorption refrigeration system is one of the oldest methods of producing refrigeration effect. The principle of vapour absorption was discovered by the Micheal Faraday in 1824 while performing a set of experiments to liquify certain gases. The first vapour absorption refrigeration machine using NH3-H_2O was developed by a French scientist, Ferd Carre in 1860 and this system was used in both domestic and large

Corresponding author: R. S. Mishra
Email Address: hod.mechanical.rsm@dtu.ac.in

industrial plants. The vapour absorption system uses heat energy instead of mechanical energy as in vapour compression refrigeration system. In the vapour absorption refrigeration system, the compressor is replaced by an absorber, pump, generator and pressure reducing valves. These components in vapour absorption system perform the same function as that of a compressor in vapour compression refrigeration system. In the vapour absorption refrigeration system, the vapour refrigerant from evaporator is drawn into an absorber where it is absorbed by the weak solution of refrigerant forming strong solution. This strong solution is pumped to the generator where it is heated by some solar energy source. During the heating process, the vapour refrigerant is driven off by the solution and enters into the condenser where it is liquified. The liquid refrigerant then flows into the evaporator and thus the cycle is completed. The LiBr-H_2O vapour absorption system can achieve temperature not below (5^0C) as required while NH_3-H_2O can be used up to 5^0 C are required [1].

This paper mainly deals with comparisons of three cascade vapour compression systems cascaded with evaporator of LiBr-H_2O vapour absorption refrigeration system cascaded by condenser of vapour compression refrigeration system using ecofriendly refrigerants (i.e. R1234yf, R134a, R-32, R507a, R227ea, R236fa, R245fa , R717) and energy and exergy analysis of all three systems were carried out because exergy (Second law) analysis used to facilitates the identification of the system components with high exergy loss.

2. Literature Review

S.C. Kaushik and Akhilesh Arora [2] carried out , the energy and exergy analysis of single effect and series flow double effect water–lithium bromide absorption systems and developed computational model by using property equations of water lithium bromide solution and found that the effects of generator, and effectiveness of heat exchangers absorber and evaporator temperatures, the effects of pressure drop between evaporator and absorber, on the energetic and exergetic performances in terms of coefficient of performance, exergy destruction, efficiency defects and exergetic efficiency found Irreversibility highest occurred in the absorber in both systems when compared to other system components. Their results indicate that coefficient of performance of the single effect system lies in range of 0.6–0.75 and double effect system lies in the range 1–1.28 respectively.

Rabah Gomri [3-4] carried out exergy analysis and thermo-economic optimization of the triple-effect LiBr-water absorption refrigerating system and found maximum exergetic efficiency of triple effect refrigeration system is about 35.1 % for condenser 30°C , absorber cooling water temperature (25°C/) and chilled water temperature (12°C/7°C) respectively Thermax's [5] developed the world's greenest and highest efficiency absorption machine using Triple effect vapour absorption chiller known as absorption chiller as a viable energy efficient alternative with a COP of 1.8 as against double effect vapour absorption chiller (1.4) is driven by various heat sources such as hot water, steam, exhaust and direct fuel fired, by using high pressure steam (15-25 bar) for optimum utilization of heat source. The system utilizes smaller size cooling tower due to lower heat load and also ensures water saving by reducing evaporation loss (10-12%)enabled 25-30% more output from engine exhaust, 25-30% lower fuel consumption for direct fired and reduction in $C0_2$ emission by 30%. In the U.S Patent [6] , the inventor to provide an absorption chiller method by utilizing two separate singe-effect absorption refrigeration circuits operating at relatively higher and lower temperatures, respectively, in which the external heat input is effectively utilized three times to thereby improve the coefficient of performance. This is achieved by an absorption apparatus comprising: a first absorption system circuit for operation within a first temperature range, a second absorption system circuit for operation within a second lower temperature range relative to the first circuit, the first circuit having generator means, condenser means, evaporator means, and absorber means operatively connected together, the second circuit having generator means, condenser means, evaporator means, and absorber means operatively connected together, the first circuit condenser means and the first circuit absorber means being in heat exchange communication with the second circuit generator means, and the first and second evaporator means being in heat exchange communication with an external heat load. Performance can be improved by using the double-effect evaporation principle. With a water lithium bromide pair, two generators can be used. One, at high temperature and pressure, is heated by an external source of thermal energy. A second, at lower pressure and temperature, is heated by condensation of the vapor from the first generator. Condensate from both generators moves to the evaporator. This enables the external thermal energy to be effectively utilized twice in the high and low temperature generators, thereby increasing the overall thermal efficiency as compared to single effect absorption systems. The cooling thermal efficiency (COP) of a single effect cycle is typically about 0.5 to 0.7. The thermal efficiency of double-effect cycles is typically about 1.0 to 1.2, while the 1.3 COP reported for double-effect absorption machine. Ravi Kumar T.S., Suganthi S, Anand A.S [7] carried out Exergy analysis of solar assisted double effect water lithium bromide absorption refrigeration system and found 60% higher COP than Single effect LiBR-H_2O system with optimized generation temperature of 150^oC in double effect VARS and 91^0C generator temperature using found using energy analysis in single effect LIBr-H_2O system along with highest exergy destruction in high pressure generator and also found using exergy analysis, the optimum generator temperature of 130^oC in double effect LiBr-H_20 System and 80^oC in single effect LiBr -H_20 System .

A.K. Prithar, S.C. Kaushika , R.S. Agrawal [8] carried out the Simulation of an Ammonia water compression absorption refrigeration system and found that 16% enhancement of COP by increasing 30% of solution heat exchanger area using R22 in the vapour compression refrigeration system.

Vaibahv Jain , S.S. Kachhawaha, Gulson Sachdeva [9]

Developed thermodynamic model for cascade vapour compression single effect absorption refrigeration and found around 61% of reduction in power consumption by using R410a, R407c and R134a refrigerants in VCRS and observed reduction in total irreversibility by reducing condenser temperature and also reduction in irreversibilities by increasing evaporator temperature**.** M Dixit, SC Kaushik, A Arora [10] studied, the absorption-Compression Cascade Refrigeration, comprising of a VCR system in low temperature stage and a vapour absorption refrigeration system at the high temperature stage, is analyzed. CO_2, NH_3 and R134a have been considered as refrigerants in the compression stage and the H_2O-LiBr refrigerant absorbent pair in the absorption stage. The analysis has been realized by means of a mathematical model of the refrigeration system. The study presents the results obtained regarding the performance of the refrigeration system based on energy and exergy analysis. The comparative study helps to find out the best refrigerant and appropriate operation parameters. It is found in the study that cascade condenser, compressor and refrigerant throttle valve are the major source of exergy destruction.

3. Result and Discussion

Following numerical values have been taken for validatation of thermal models for cascade vapour compression-absorption refrigeration systems .

3.1 Tripple Effect Cascade vapour compression-absorption refrigeration system using ecofriendly refrigerants.

$T_{_Generator}$=180^{o}C.T_Cond=30^{o}C,$T_{_Eva}$=5^{o}C,T_absorber=30^{o}C , Compressor Efficiency=0.80, T_Eva_LTC=-50^{o}C, Approach (Temperature Overlapping)=10^{o}C) Table-1 shows the variation of thermal performance parameters of triple effect cascade vapour absorption refrigeration system using lithium bromide water solution coupled with vapour compression refrigeration system using 10 tons of load. The evaporator of VARS is cascaded with condenser of vapour compression refrigeration systems using following nine ecofriendly refrigerants. It is found that overall first law efficiency in terms of coefficient of performance (COP) of cascade refrigeration system using R245fa refrigerant is highest and lowest by using R227ea as shown in fig-1 .while exergy destruction of cascade system is lowest by using R141b and highest while using R227ea as shown in Fig-2. The cascade system exergetic efficiency is highest by using R141b and lowest by using R227ea as shown in Fig-3. The thermal performances using ecofriendly refrigerants in the low temperature circuit of vapour compression refrigeration system is shown in Table-1 and it is found that maximum coefficient of performance (COP)of vapour compression refrigeration system by using R141b and lower COP by using R227ea respectively as shown in Fig-4. Similarly exergy destruction of vapour compression refrigeration system is lowest by using R141b and highest while using R227ea as shown in Fig-5. The exergetic efficiency of vapour compression of refrigeration system is highest by using R141b and lowest by using R227ea as shown in Fig-6.

3.2 Double Effect Cascade vapour compression-absorption refrigeration system using ecofriendly refrigerants

$T_{_Generator}$=150^{o}C,T_Cond=30^{o}C,$T_{_Eva}$=10^{o}C,T_absorber=30^{o} C, Compressor Efficiency=0.80, T_Eva_LTC=-50^{o}C, Approach (Temperature Overlapping) =10^{o}C)
Table-2 shows the variation of thermal performance parameters of double effect cascade vapour absorption refrigeration system using lithium bromide -water solution coupled with vapour compression refrigeration system using 10 tons of load. The evaporator of VARS is cascaded with condenser of vapour compression refrigeration systems using nine ecofriendly refrigerants. It is found that overall first law efficiency in terms of coefficient of performance (COP) of cascade refrigeration system using R245fa refrigerant is highest and lowest by using R227ea as shown in fig-7 .while exergy destruction of cascade system is lowest by using R141b and highest while using R227ea as shown in Fig-8. The cascade system exergetic efficiency is highest by using R141b and lowest by using R227ea as shown in Fig-9. The thermal performances using ecofriendly refrigerants in the low temperature circuit of vapour compression refrigeration system is shown in Table-2 and it is found that maximum coefficient of performance (COP)of vapour compression refrigeration system by using R141b and lower COP by using R227ea respectively as shown in Fig-10. Similarly exergy destruction of vapour compression refrigeration system is lowest by using R141b and highest while using R227ea as shown in Fig-11. The exergetic efficiency of vapour compression of refrigeration system is highest by using R141b and lowest by using R227ea as shown in Fig-12.

3.3 Single Effect Cascade vapour compression-absorption refrigeration system using ecofriendly refrigerants

$T_{_Generator}$=110^{o}C.T_Cond=35^{o}C, $T_{_Eva}$=10^{o}C, T_absorber =30^{o}C, Compressor Efficiency=0.80, T_Eva _LTC =-50^{o}C, Approach (Temperature Overlapping) =10^{o}C)
Table-3 shows the variation of thermal performance parameters of single effect cascade vapour absorption refrigeration system using lithium bromide-water solution coupled with vapour compression refrigeration system using 10 tons of load. The evaporator of VARS is cascaded with condenser of vapour compression refrigeration systems using nine ecofriendly refrigerants. It is found that overall first law efficiency in terms of coefficient of performance (COP) of cascade refrigeration system using R245fa refrigerant is highest and lowest by using R227ea as shown in fig-13 .while exergy destruction of cascade system is lowest by using R141b and highest while using R227ea as shown in Fig-14. The

cascade system exergetic efficiency is highest by using R141b and lowest by using R227ea as shown in Fig-15. The thermal performances using ecofriendly refrigerants in the low temperature circuit of vapour compression refrigeration system is shown in Table-3 and it is found that maximum coefficient of performance (COP)of vapour compression refrigeration system by using R141b and lower COP by using R227ea respectively as shown in Fig-16. Similarly exergy destruction of vapour compression refrigeration system is lowest by using R141b and highest while using R227ea as shown in Fig-17. The exergetic efficiency of vapour compression of refrigeration system is highest by using R141b and lowest by using R227ea as shown in Fig-18.

Table 1: thermal performances of triple effect vapour absorption refrigeration system using vapour compression refrigeration system

Refrigerant	COP_Overall	Overall Exergy Destruction Ratio (EDR)	Overall Exergetic Efficiency	COP_VCRS	VCRS Exergy Destruction Ratio (EDR)	VCRS Exergetic Efficiency
R134a	1.782	1.371	0.4218	2.05	0.4501	0.6896
R1234yf	1.754	1.46	0.4065	1.951	0.5243	0.6560
R141b	1.850	1.210	0.4526	2.258	0.3170	0.7593
R717	1.782	1.382	0.4199	2.037	0.4594	0.6852
R32	1.776	1.398	0.4170	2.019	0.4729	0.6789
R-507a	1.738	1.507	0.3988	1.902	0.5634	0.6396
R227ea	1.701	1.616	0.3823	1.796	0.6534	0.6048
R236fa	1.756	1.455	0.4074	1.956	0.5199	0.6579
R245fa	1.805	1.323	0.4305	2.107	0.4109	0.7068

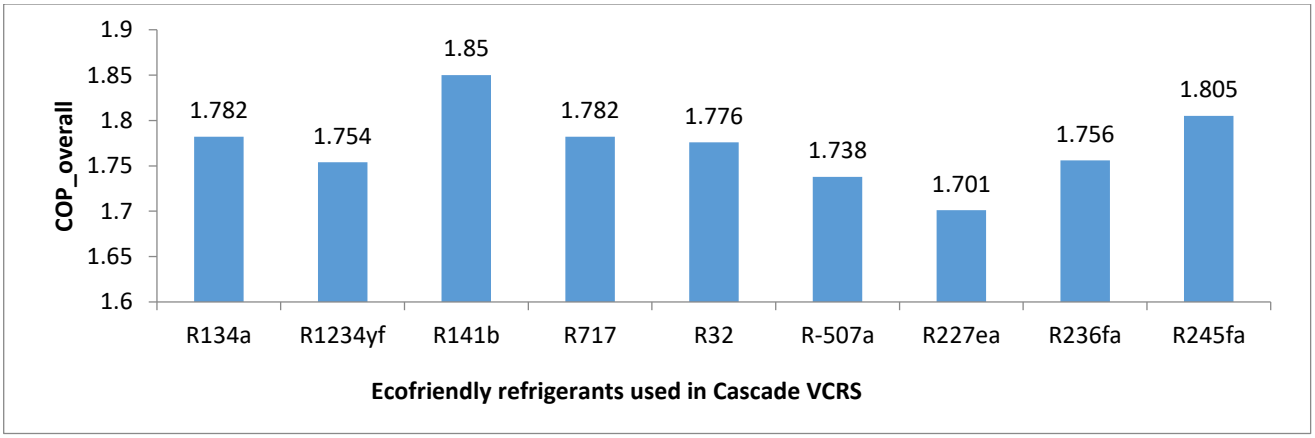


Figure 1: Thermal first law performances (COP_Over all) of cascade triple effect LiBr vapour absorption refrigeration system coupled with vapour compression refrigeration using ecofriendly refrigerants in the low temperature cycle of VCRS system

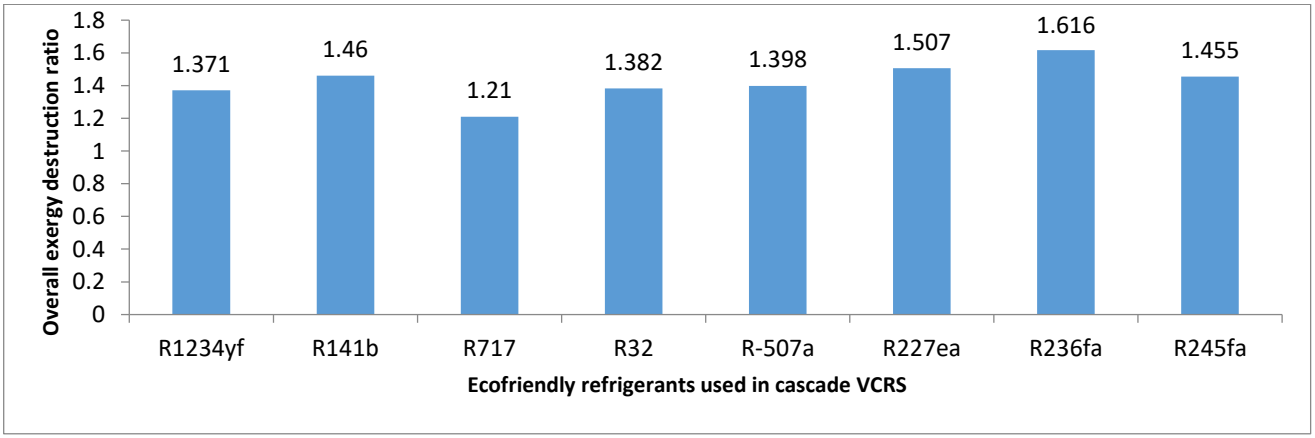


Figure 2: Thermal performances in terms of exergy destruction ratio (EDR_VCRS) of cascade triple effect LiBr vapour absorption refrigeration system coupled with vapour compression refrigeration using ecofriendly refrigerants in the low temperature cycle of VCRS system

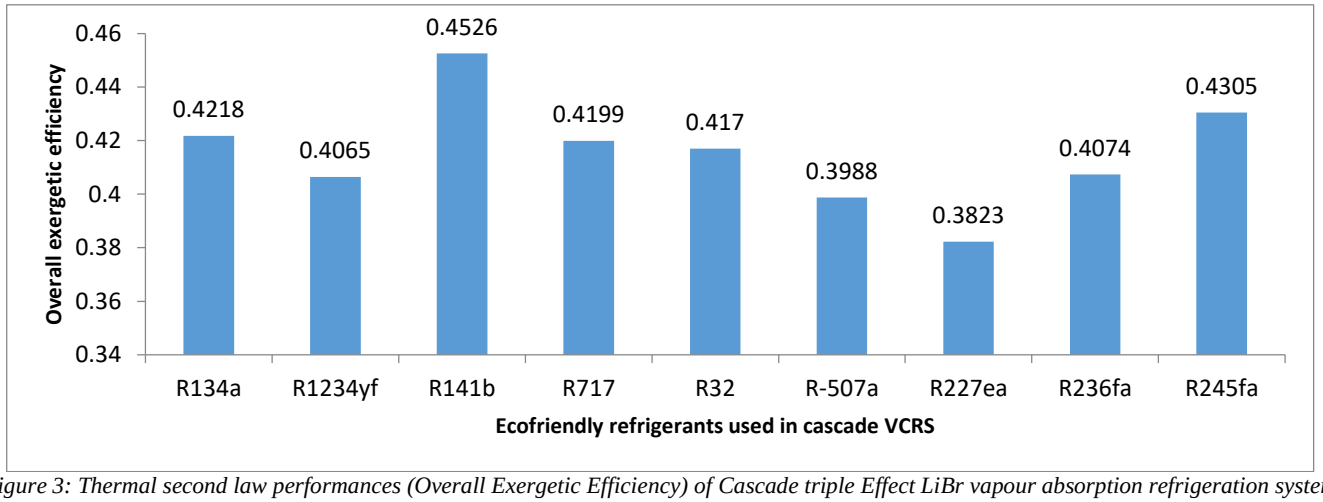


Figure 3: Thermal second law performances (Overall Exergetic Efficiency) of Cascade triple Effect LiBr vapour absorption refrigeration system coupled with vapour compression refrigeration using ecofriendly refrigerants in the low temperature cycle of VCRS system

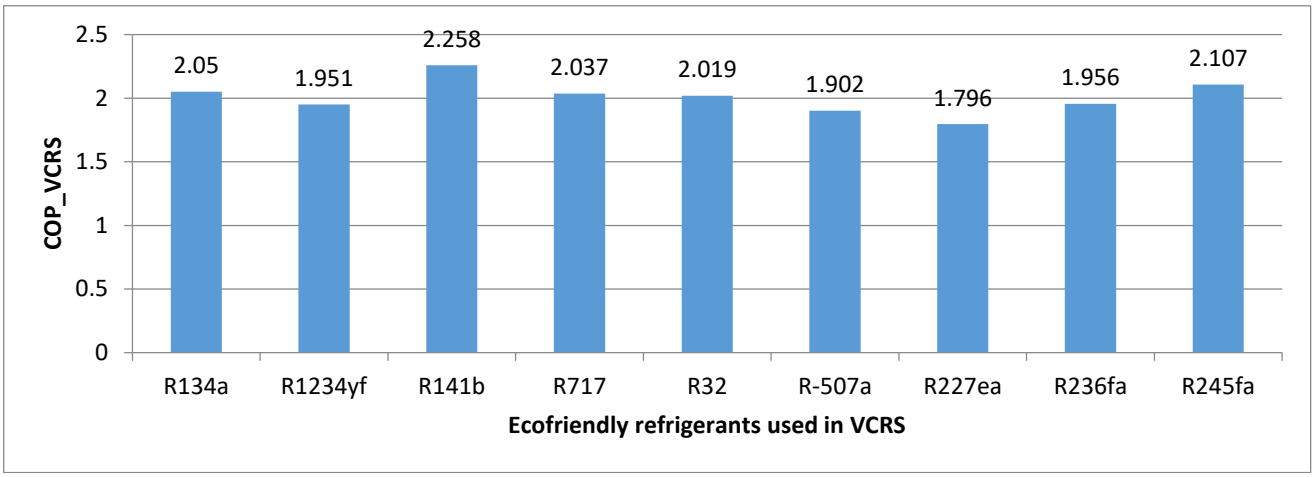


Figure 4: Thermal first law performances (COP_VCRS) of cascade triple effect LiBr vapour absorption refrigeration system coupled with vapour compression refrigeration using ecofriendly refrigerants in the low temperature cycle of VCRS system

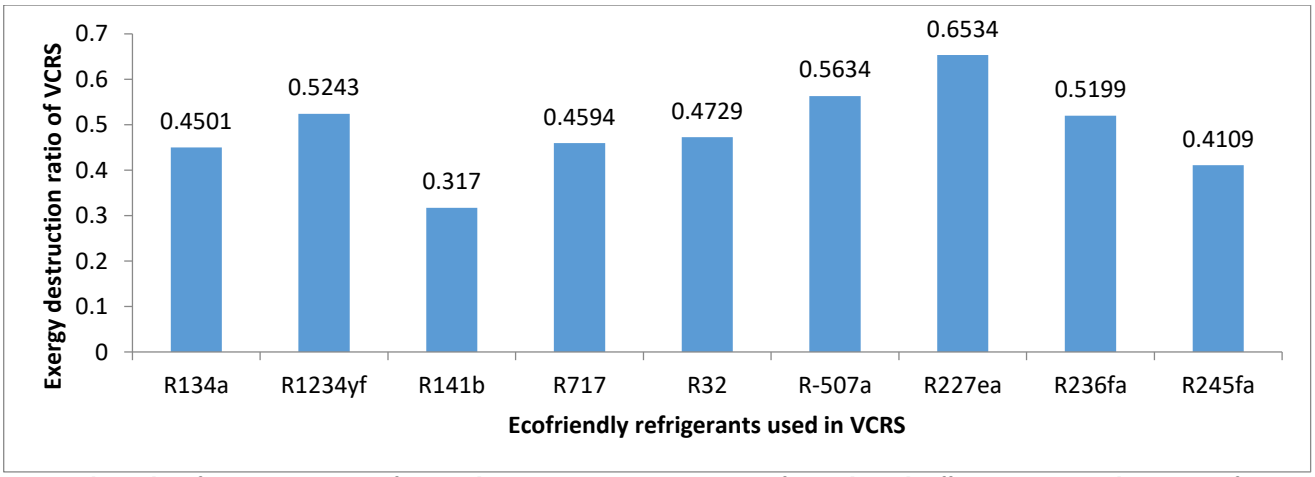


Figure 5: Thermal performances in terms of exergy destruction ratio(EDR_VCRS) of cascade triple effect LiBr vapour absorption refrigeration system coupled with vapour compression refrigeration using ecofriendly refrigerants in the low temperature cycle of VCRS system

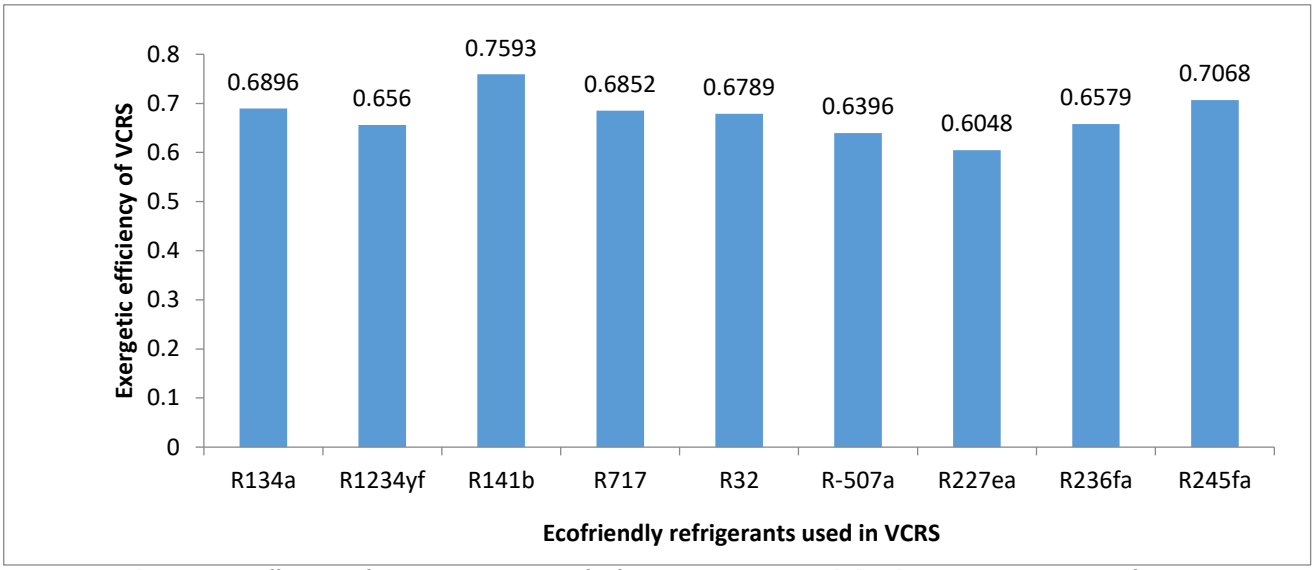


Figure 6: The exergetic efficiency of vapour compression of refrigeration system coupled with vapour compression refrigeration using ecofriendly refrigerants in the low temperature cycle of VCRS system

Table 2: Thermal performances of double effect vapour absorption refrigeration system using vapour compression refrigeration system

Refrigerant	COP_Overall	Overall Exergy Destruction Ratio (EDR)	Overall Exergetic Efficiency	COP_VCRS	VCRS Exergy Destruction Ratio (EDR)	VCRS Exergetic Efficiency
R134a	1.536	1.595	0.3854	1.838	0.6174	0.6183
R1234yf	1.503	1.719	0.3676	1.729	0.7196	0.5815
R141b	1.596	1.389	0.4186	2.054	0.4476	0.6908
R717	1.539	1.582	0.3873	1.850	0.6068	0.6224
R32	1.530	1.615	0.3823	1.819	0.6343	0.6119
R-507a	1.488	1.778	0.3599	1.681	0.7686	0.5654
R227ea	1.452	1.928	0.3416	1.838	0.8916	0.5286
R236fa	1.505	1.709	0.3691	1.572	0.7115	0.5843
R245fa	1.553	1.534	0.3947	1.898	0.5668	0.6383

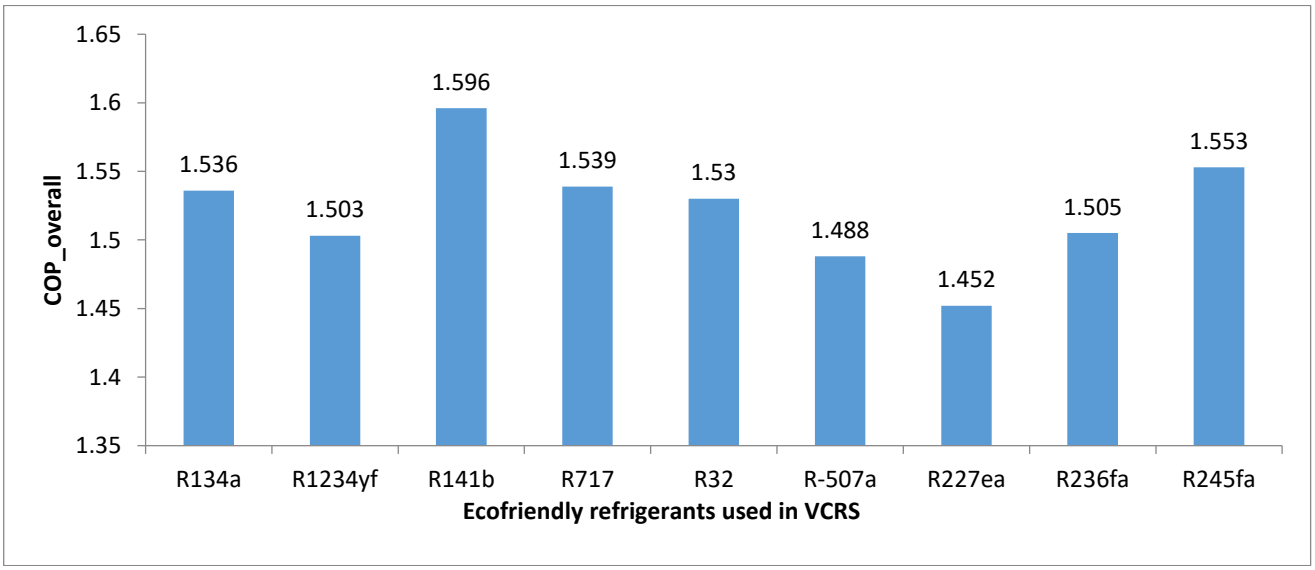


Figure 7: Thermal first law performances (COP_Over all) of cascade double effect LiBr vapour absorption refrigeration system coupled with vapour compression refrigeration using ecofriendly refrigerants in the low temperature cycle of VCRS system

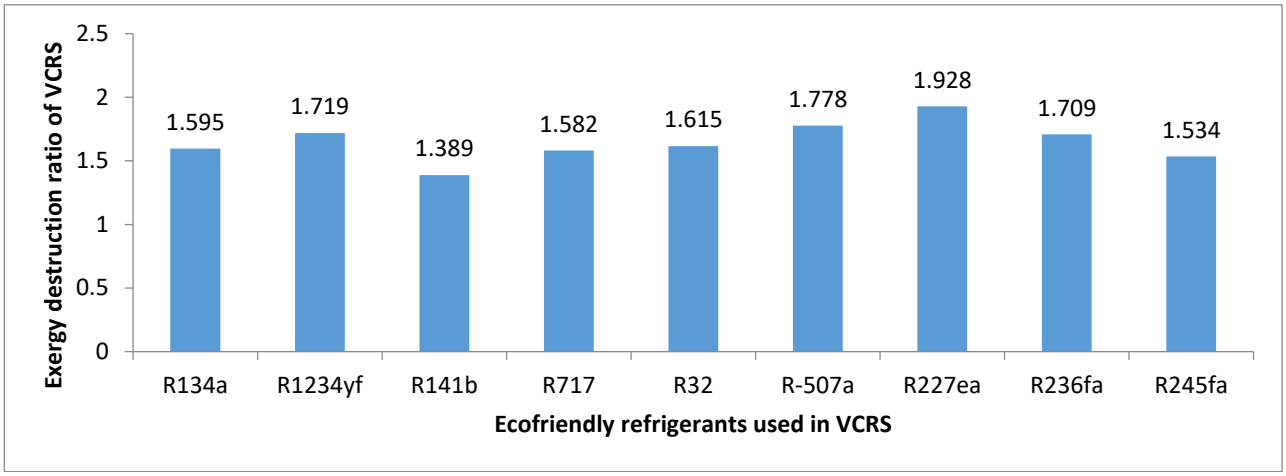


Figure 8: Thermal performances in terms of exergy destruction ratio (EDR_VCRS) of cascade double effect LiBr Vapour absorption refrigeration system coupled with vapour compression refrigeration using ecofriendly refrigerants in the low temperature cycle of VCRS system

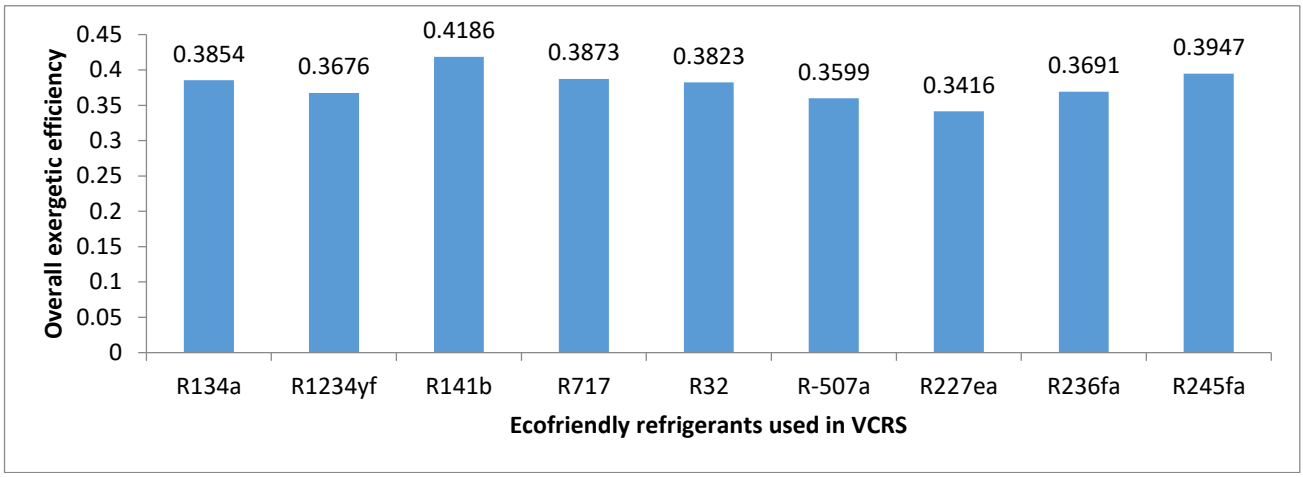


Figure 9: Thermal second law performances (Overall Exergetic Efficiency) of Cascade double effect LiBr Vapour absorption refrigeration system coupled with vapour compression refrigeration using ecofriendly refrigerants in the low temperature cycle of VCRS system

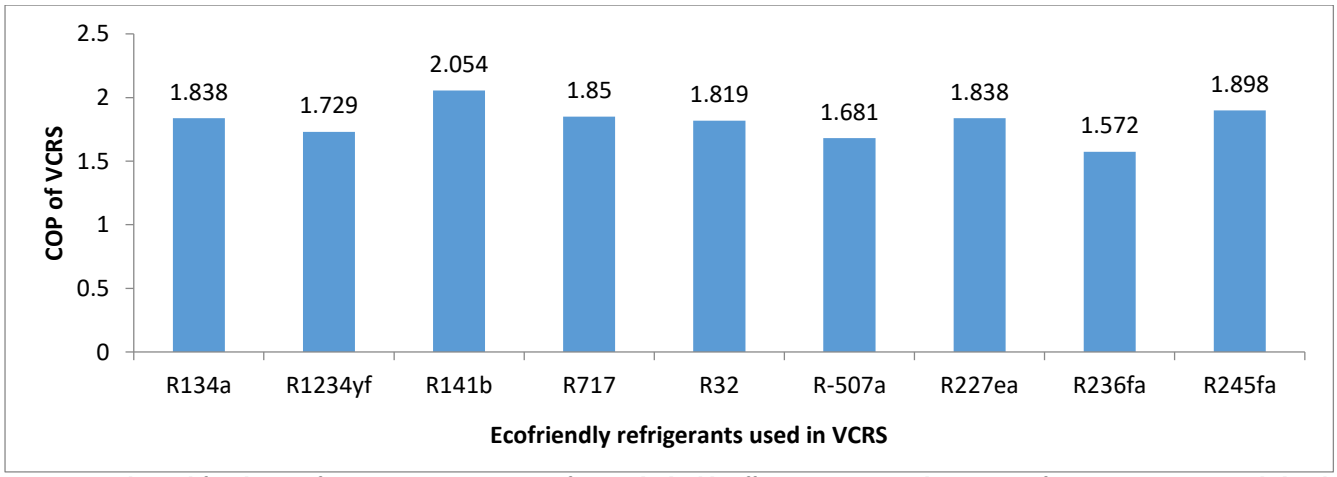


Figure 10: Thermal first law performances (COP_VCRS) of Cascade double effect LiBr Vapour absorption refrigeration system coupled with vapour compression refrigeration using ecofriendly refrigerants in the low temperature cycle of VCRS system

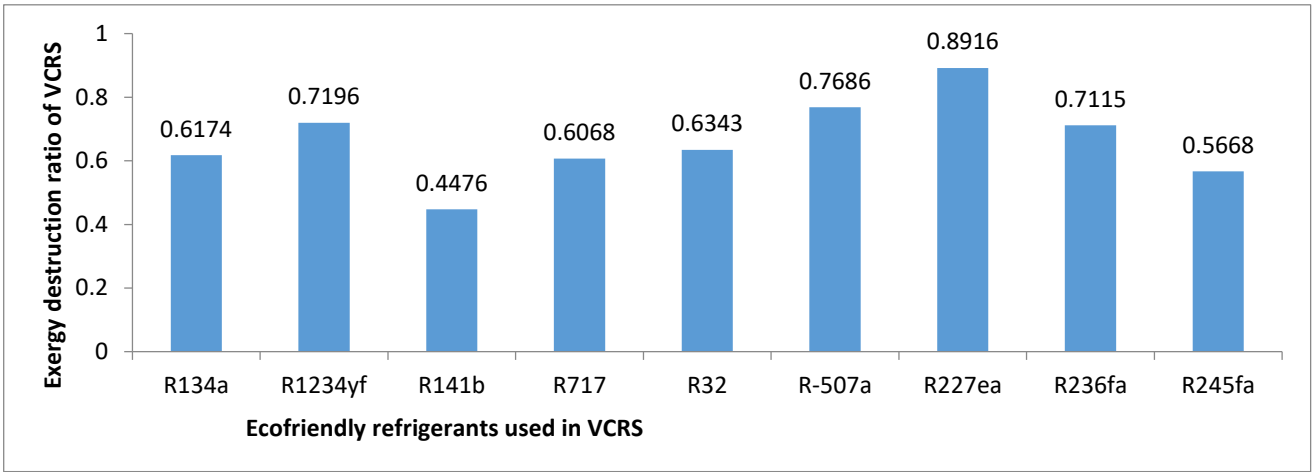


Figure 11: Thermal performances in terms of exergy destruction ratio (EDR_VCRS) of cascade double effect LIBr vapour absorption refrigeration system coupled with vapour compression refrigeration using ecofriendly refrigerants in the low temperature cycle of VCRS system

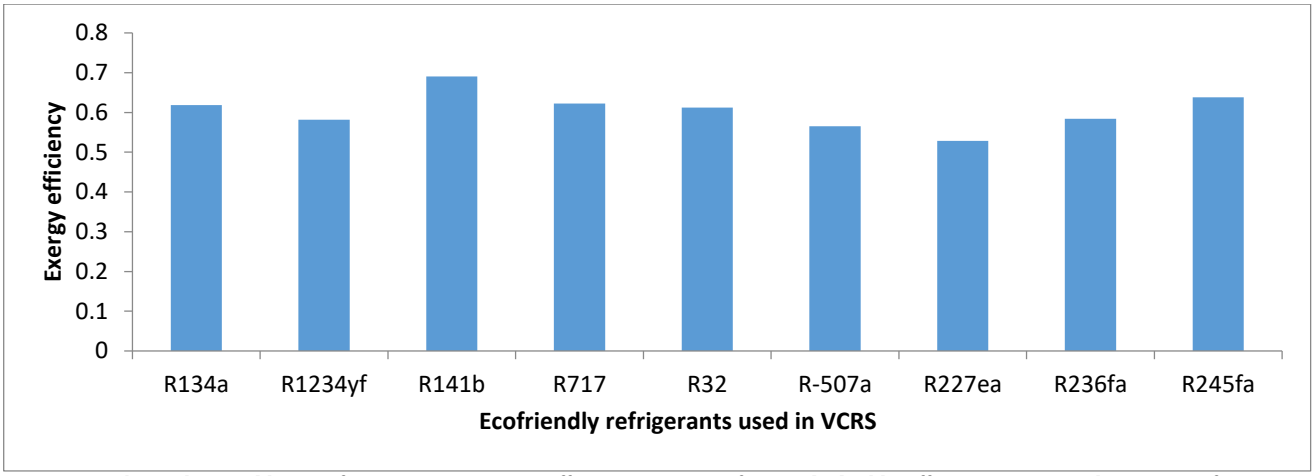


Figure 12: Thermal second law performances (Exergetic Efficiency _VCRS) of Cascade double Effect LiBr vapour absorption refrigeration system coupled with vapour compression refrigeration using ecofriendly refrigerants in the low temperature cycle of VCRS system

Table 3: Thermal performances of single effectvapourabsorption refrigeration system using vapour compression refrigeration system

Refrigerant	COP_Overall	Overall Exergy Destruction Ratio (EDR)	Overall Exergetic Efficiency	COP_VCRS	VCRS Exergy Destruction Ratio (EDR)	VCRS Exergetic Efficiency
R134a	0.9887	1.888	0.3463	1.920	0.60	0.6457
R1234yf	0.9736	2.004	0.3329	1.814	0.6250	0.6157
R141b	1.017	1.688	0.3463	2.132	0.3946	0.7171
R227ea	0.9496	2.023	0.3122	1.859	0.7921	0.5580
R236fa	0.9747	1.996	0.3338	1.821	0.6324	0.6126
R245fa	0.9967	1.828	0.3536	1.978	0.5030	06653
R32	0.9853	1.913	0.3433	1.896	0.5683	0.6376
R717	0.9890	1.885	0.3466	1.922	0.5471	0.6464
R507a	0.9664	2.062	0.3266	1.766	0.6835	0.5940

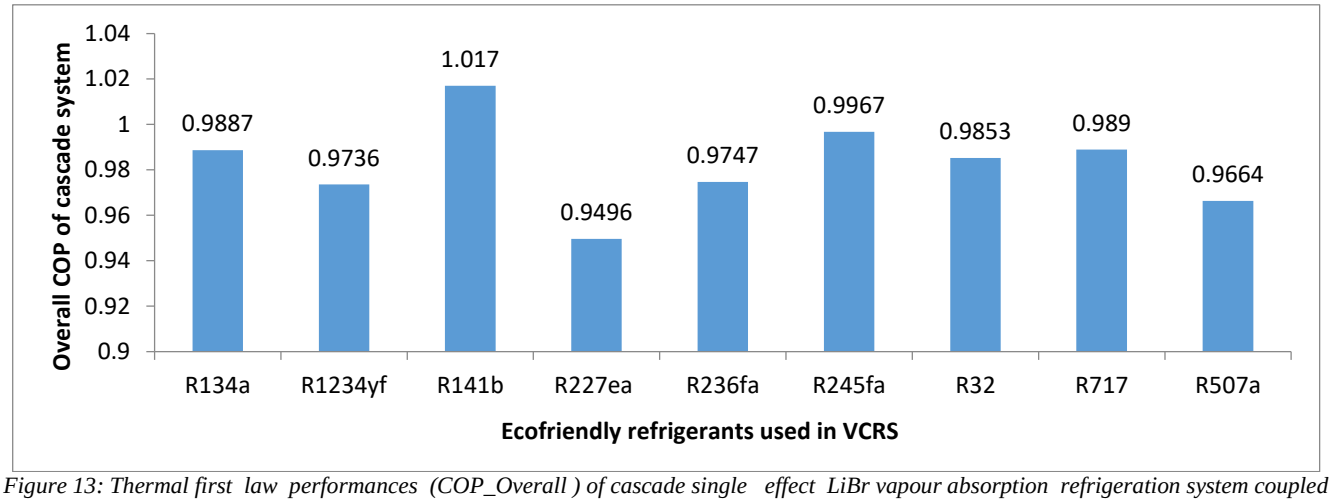


Figure 13: Thermal first law performances (COP_Overall) of cascade single effect LiBr vapour absorption refrigeration system coupled with vapour compression refrigeration using ecofriendly refrigerants in the low temperature cycle of VCRS system

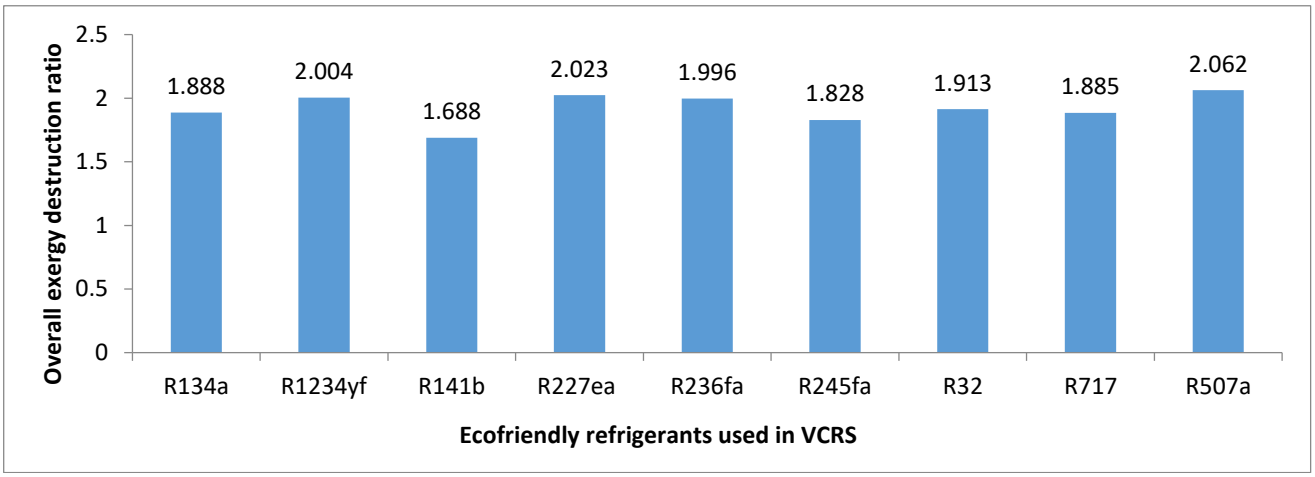


Figure 14: Thermal performances in terms of exergy destruction Ratio (EDR_VCRS) of cascade single effect LiBr vapour absorption refrigeration system coupled with vapour compression cycle

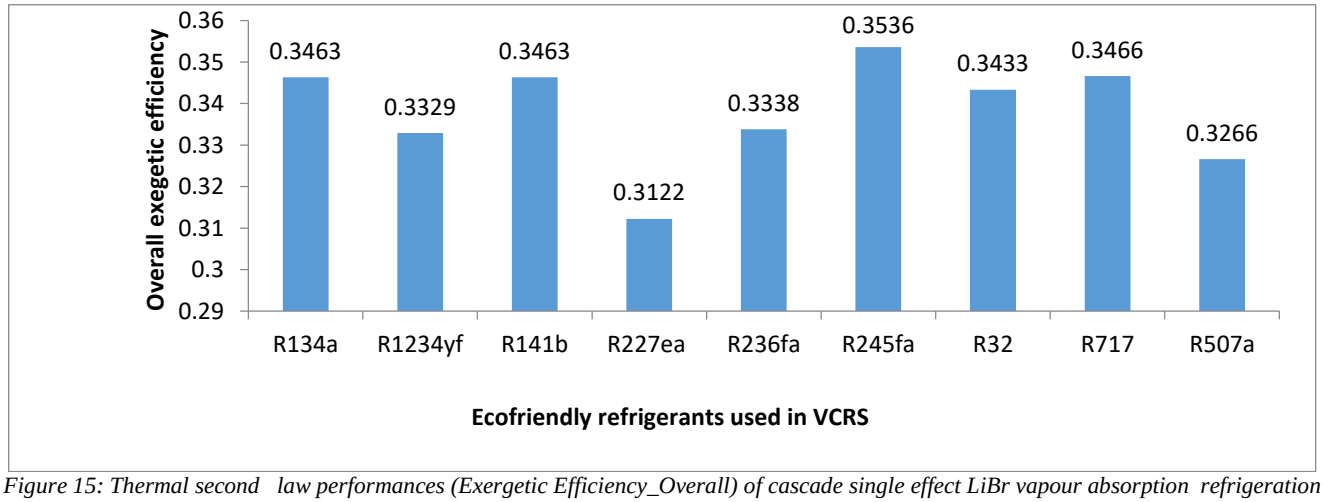


Figure 15: Thermal second law performances (Exergetic Efficiency_Overall) of cascade single effect LiBr vapour absorption refrigeration system coupled with vapour compression refrigeration using ecofriendly refrigerants in the low temperature cycle of VCRS system

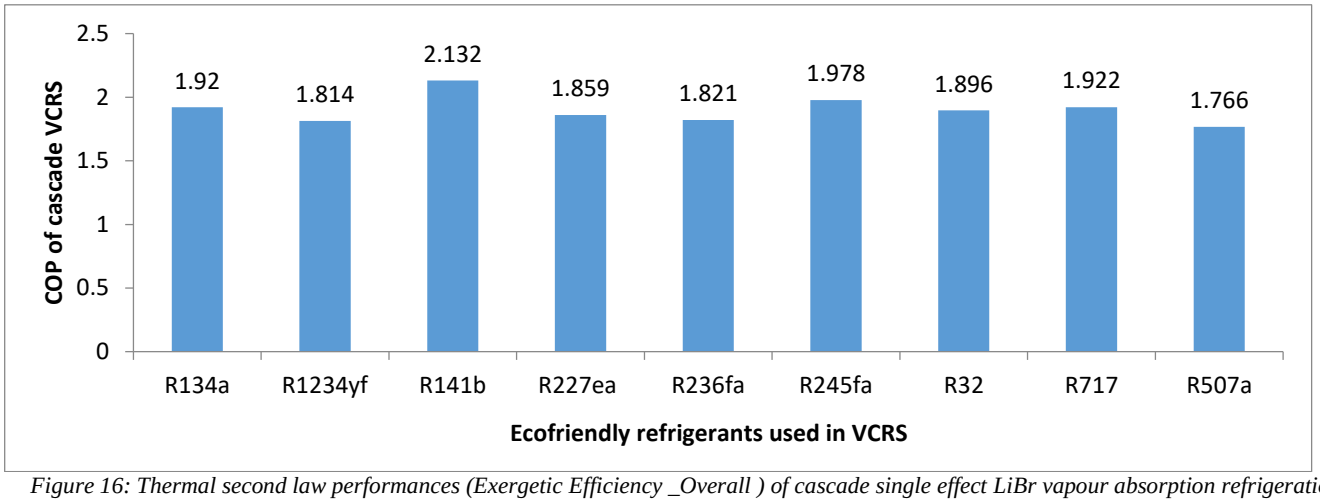


Figure 16: Thermal second law performances (Exergetic Efficiency _Overall) of cascade single effect LiBr vapour absorption refrigeration system coupled with vapour compression refrigeration using ecofriendly refrigerants in the low temperature cycle of VCRS system

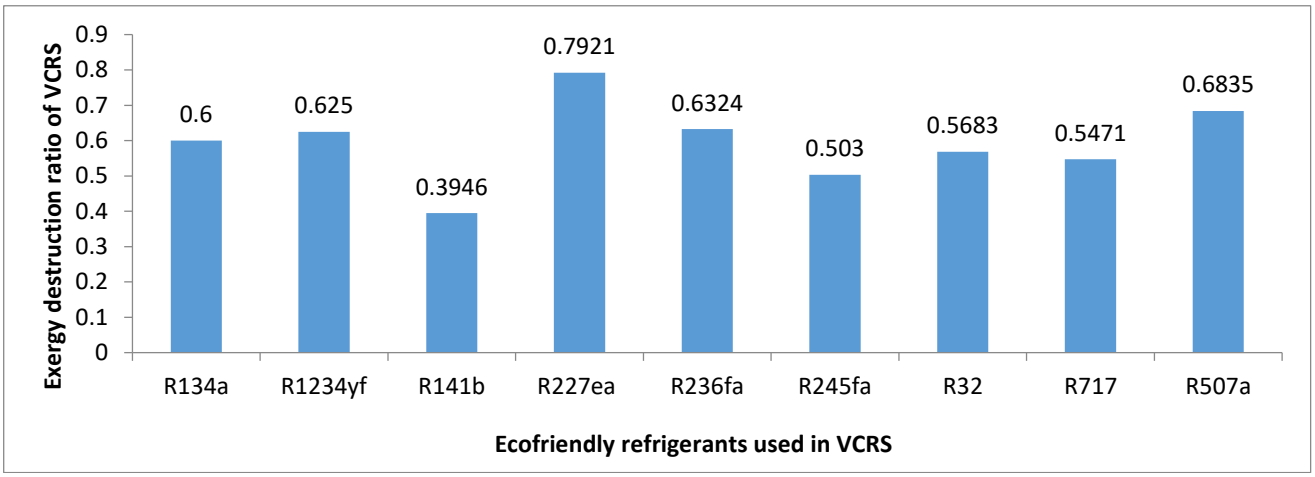


Figure 17: Thermal performances in terms of exergy destruction ratio (EDR_VCRS) of cascade single effect LiBr vapour absorption refrigeration system coupled with vapour compression refrigeration using ecofriendly refrigerants in the low temperature cycle of VCRS system

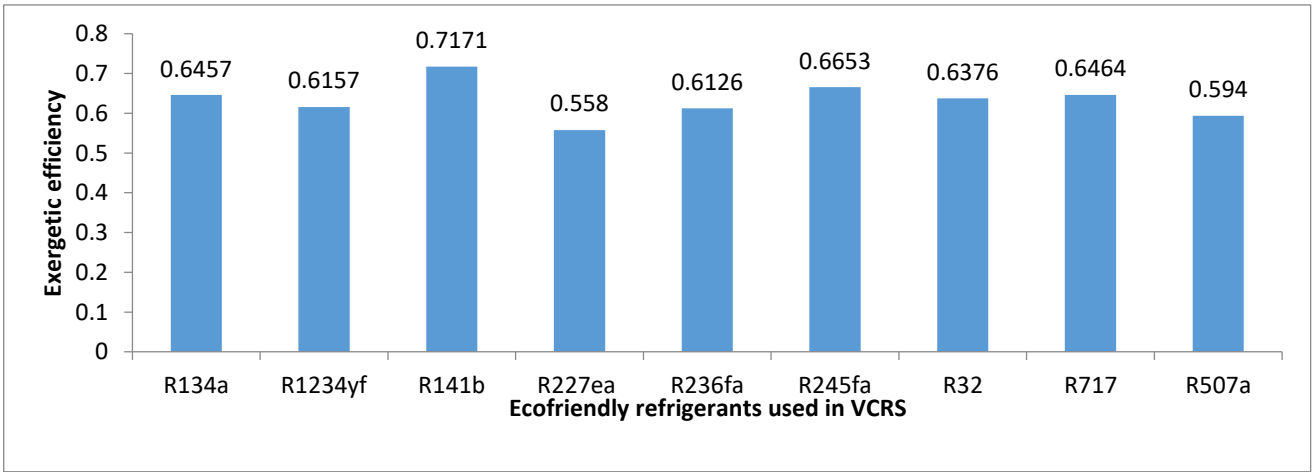


Figure 18: Thermal second law performances(Exergetic Efficiency _VCRS) of cascade single effect LiBr vapour absorption refrigeration system coupled with vapour compression refrigeration using ecofriendly refrigerants in the low temperature cycle of VCRS system

The performance parameters have been compared with three cascade vapour absorption-compression refrigeration system and it was observed that 122% first law efficiency enhancement using triple effect VARS cascaded with VCRS and 79.45% enhancement in second law efficiency using triple effect VARS cascaded with VCRS. Similarly exergy reduction is 56.61% using triple effect VARS cascaded with VCRS and 25.92% reduction using double effect VARS cascaded with VCRS as shown in Table-4(a)-Table 4(c) respectively.

Table 4(a): Performance parameters obtained from computed Results obtained from developed model for vapour absorption LiBr-H_2O refrigeration systems (only)

Performance Parameters	Single Effect VARS	Double Effect VARS	% Incre-ment	Tripple Effect VARS	% Increment
First Law Efficiency of VARS (COP_{VARS})	0.7496	1.338	78.495	1.644	121.99
Exergetic_ Efficiency of _ VARS	0.1927	0.2364	22.68	0.3458	79.45
Irreversibility Ratio/EDR (EDR_{VARS})	4.36	3.230	25.92 Reduction	1.892,	56.61 Reduction

Table 4(b): Overall cascade system performance parameters obtained from computed results from developed model using vapour compression refrigeration system (only) using R134a for10^oC of temperature overlapping (approach).

Performance Parameters	Single Effect VARS	Double Effect VARS	% Incre-ment	Tripple Effect VARS	% Incre-ment
First Law Efficiency of VARS (COP_{VARS})	0.9887	1.536	55.36	1.782	80.30
Exergetic_ Efficiency of _ VARS	0.3463	0.3854	11.29	0.4218	21.80
Irreversibility Ratio/EDR (EDR_{VARS})	1.888	1.595	15.52 Reduction	1.371	37.10

Table 4(c): Overall cascade system performance parameters obtained from computed results obtained from developed model using cascaded condenser of vapour compression system using R134a coupled with LiBr absorption Refrigeration Systems

Performance Parameters	Single Effect VARS	Double Effect VARS	% Increment	Tripple Effect VARS	% Increment
First Law Efficiency of VARS (COP_{VARS})	1.921	1.838	4.32 Reduction	2.05	6.72
Exergetic_ Efficiency of _ VARS	0.6457	0.6183	4.24 Reduction	0.6896	6.80
Irreversibility Ratio/EDR based on exergy output (EDR_{VARS})	0.60	0.6174	2.90	0.4501	24.98 Reduction

Similarly performance parameters have been compared with three cascade vapour absorption-compression refrigeration system and it was observed that 22.87% first law efficiency enhancement using triple effect VARS cascaded with VCRS and 46.28% enhancement in second law efficiency using triple effect VARS cascaded with VCRS as compared with double effect vapour absorption refrigeration cascaded with vapour compression refrigeration system. Similarly exergy reduction is 41.42% using triple effect VARS cascaded with VCRS as compared to double effect VARS cascaded with VCRS as shown in Table-5(a)-Table 5(c) respectively.

Table 5(a): Performance parameters obtained from computed Results obtained from developed model for Vapour Absorption LiBr-H_2O refrigeration systems (only)

Performance Parameters	Double Effect VARS	Tripple Effect VARS	% Incre-ment
First Law Efficiency of VARS (COP_{VARS})	1.338	1.644	22.87
Exergetic_ Efficiency of _ VARS	0.2364	0.3458	46.28
Irreversibility Ratio/EDR (EDR_{VARS})	3.230	1.892,	41.42%Reduction

Table 5(b): Performance parameters obtained from computed results obtained from developed model using vapour compression refrigeration system (only) using R134a for 10^oC of temperature overlapping (approach).

Performance Parameters	Double Effect VARS	Tripple Effect VARS	% Incre-ment
First Law Efficiency of VARS (COP_{VARS})	1.536	1.782	16.01
Exergetic_ Efficiency of _ VARS	0.3854	0.4218	9.44
Irreversibility Ratio/EDR (EDR_{VARS})	1.595	1.371	-14.04

Table 5(c): Overall Cascade system performance parameters obtained from computed results obtained from developed model using cascaded condenser of vapour compression system using R134a coupled with LiBr absorption refrigeration systems

Performance Parameters	Double Effect VARS	Tripple Effect VARS	% Increment
First Law Efficiency of VARS (COP_{VARS})	1.838	2.05	11.534
Exergetic_ Efficiency of _ VARS	0.6183	0.6896	11.532
Irreversibility Ratio/EDR based on exergy output (EDR_{VARS})	0.6174	0.4501	-27.10

4. Conclusion

The following conclusions were drawn.

(i) The 122% increment of first law efficiency (i.e. over all COP) of the triple effect vapour absorption refrigeration cascade system and 78.495% increment of first law efficiency (i.e. over all COP) of the double effect vapour absorption refrigeration system cascade system as compared to single effect vapour absorption compression refrigeration system.

(ii) The 80.30% increment of first law efficiency (i.e. over all COP) of the triple effect vapour absorption refrigeration system and 55.36% increment of first law efficiency (i.e. over all COP) of the double effect vapour absorption refrigeration system cascade system as compared to single effect vapour absorption -compression refrigeration system.

(iii) The 6.72% increment of first law efficiency (i.e. over all COP) of the triple effect vapour absorption refrigeration system and 4.32% reduction in first law efficiency (i.e. over all COP) of the double effect vapour absorption refrigeration system cascade system as compared to single effect vapour absorption -compression refrigeration system.

(iv) The 22.87% increment of first law efficiency (i.e. over all COP) of the triple effect vapour absorption refrigeration system and 46% increment of exergetic efficiency and 41.42% reduction in EDR as compared to double effect vapour absorption -compression refrigeration system.

(v) The 16.01% increment of first law efficiency (i.e. over all COP) of the triple effect vapour absorption refrigeration system as compared to double effect vapour absorption -compression refrigeration system with reduction in system exergy destruction ratio as compared to vapour compression system.

References

[1] Khurmi R,S (2011) A text book of refrigeration and air conditioning, ISBN : 978-81-219-2781-9, Eurasia publishing house, Private limited, Ram Nagar, New Delhi Page-273-274.

[2] S.C. Kaushika and A Rrrora [2009] Energy and exergy analysis of single effect and series flow double effect water–lithium bromide absorption refrigeration systems, International Journal of Refrigeration, Volume 32, Issue 6, September 2009, Pages 1247-1258.

[3] Rabah Gomri R and Hakimi R [2009] second law analysis of double effect vapour absorption cooler system , International journal of energy conversion and management, Elsevier , Vol-49, page-3343-48.

[4] Rabah Gomri R [2008] second law comparison of single and double effect vapour absorption refrigeration system, International journal of energy conversion and management, Elsevier , Vol-50, page-1279-1287.

[5] Published in: 2008 Second International Conference on Thermal Issues in Emerging Technologies DOI: 10.1109/THETA.2008.5188778 , ,Cairo, Egypt, 17-20 Dec. 2008, IEEE Xplore: 04 August 2009The second.

[6] (U.S. Pat. No. 4,542,628).and U.S. Pat. Nos. 3,483,710)on Triple effect absorption chiller utilizing two refrigeration circuits.

[7] Ravi Kumar T.S.,Suganthi S, Anand A.S. Exergy analysis of solar assisted double effect absorption refrigeration system, Renewable energy, Vol-14, (1-4) page-55-59.

[8] A.K. Prithar, S.C. Kaushika , R.S. Agrawal [2010] , Simulation of an Ammonia water compression absorption refrigeration system , International journal of refrigeration, Vol-33, page-1386-1394.

[9] Vaibahv Jain , S.S. Kachhawaha, Gulson Sachdeva (2013) , Energy Conversion and Management , Vol-75, (2013) page-685-700.

[10] M Dixit, SC Kaushik, A Arora[2016] energy and exergy analysis of absorption-compression cascade refrigeration system, journal of thermal engineering,Vol-2, No-6, page-995-1006

Cite this article as: R.S. Mishra, Comparison of thermal performances of single effect, double effect and triple effect LiBr-H_2O absorption system cascaded with vapour compression refrigeration systems using ecofriendly refrigerants, *International journal of research in engineering and innovation (IJREI),* vol 2, issue 6 (2018), 610-621.

International Journal of Research in Engineering, Science and Management
Volume-1, Issue-12, December-2018
www.ijresm.com | ISSN (Online): 2581-5792

Concentrated Solar Heat Integrated with Geothermal Energy for Thermal Energy Requirements in India

Shivam Sharma[1], Yash Kumar Baghel[2], Ajit Kumar[3], J. P. Kesari[4]
[1,2,3]*B. Tech. Student, Department of Mechanical Engineering, Delhi Technological University, Delhi, India*
[4]*Associate Professor, Department of Mechanical Engineering, Delhi Technological University, Delhi, India*

***Abstract*: Geothermal and Solar Energy Sources are the only two natural sources of heat energy which provide heat as it is, without any burning or conversion requirement. These technologies are being used for power generation and heating applications. Power generation will be the center focus of this paper while simultaneously focusing on other industrial heating applications as well. During their operational life, Geothermal Power Plants often lose their pressure, temperature, and mass flow rate and they are unable to run on their full capacities as desired or expected. This loss in energy over time can be recovered by integrating the power plant with some other energy resource. Concentrated Solar Power (CSP) can be one such green energy resource which can directly supply heat energy derived from sun. Such operational hybrid plants and their working were studied. Apart from power generation, CSP is a great resource to be tapped for other mechanical and industrial heating processes. While both of them are being used separately or collectively (on a small scale), using them collectively can help us achieve greater efficiency and energy volume. Data of surveys and research in Indian scenario were compared with already functional plants to draw conclusion on the potential that lies ahead in the field of geothermal energy in India.**

***Keywords*: Concentrated Solar Power, Geothermal Energy, Green energy, Hybrid, Process heating**

1. Introduction

This paper discusses the scope and advantages of using the two direct heat energy resources of nature for heating applications in industry. Energy requirements are ever increasing and these need to be met in ways which are sustainable and leave behind least carbon footprint possible. Since a major amount of energy is lost in conversion from one form to another, it becomes all the more necessary to maximize the usage of energy in its original form. Converting solar heat into electrical energy and again reconverting it into heat energy through some electrical heater for industrial heating leads to huge amount of energy being lost to efficiency losses of conversions. Power generation, being one major and central process involving heating process, is discussed majorly in this paper.

Coming to power generation sector, geothermal energy apart from being green and renewable source of energy has quite a few added advantages. Geothermal Power Plants are capable of running all round the clock 365 days a year without being dependent on weather conditions. These plants also have less water consumption and greenhouse gases emissions through their lifespan when compared to other conventional energy resources. These plants can reuse the waste water of cities by injecting them into the geothermal wells to maintain the steam output pressure. The solid waste generated by these plants often contains minerals which can be sold to recover some part of the cost.

CSP in comparison with other energy resources is a better suited resource to integrate with a geothermal power plant as there is no energy conversion needed. The energy is absorbed as heat energy and transferred to geothermal plant as heat energy itself. Thermal Energy Storage has higher energy dispatchability and also cheaper to store energy in comparison to the batteries which need regular replacement too. The efficiency losses are way lesser when using CSP due to the above cited reasons. This way the life of the plant can be extended and also the cost of drilling extra wells can be saved. India has abundant solar energy resource, even if 10% of available usable land is used for installation that may result into solar energy potential of 8 million MW [1].

Talking about India, Geothermal Energy is untapped but has some great potential when integrated with CSP to bridge the thermal energy gap present. Investigations and surveys have been conducted and in-process at various sites across India. Their findings when compared with the operational plants and processes abroad can be concluded in the opportunities and challenges that lie ahead of us.

2. Review of literature

CSP is a proven technology. Around the world total power produced through CSP has reached beyond 4GW. Solar to electric efficiency for CSP plants range from 15% to 25%. However, the thermal energy when used directly without any conversion involves no cyclic losses and just the heat transfer losses. Thermal Storage losses are almost negligible. That is why CSP should be used in its raw form as much as possible

without involving any conversion. Conversion efficiency however, increases with higher operating temperature; therefore, working fluids capable of running at higher temperatures have to be employed.

A Reliance Power subsidiary, Rajasthan Sun Technique Energy has commissioned a 100MW CSP plant facility in Rajasthan, India. As of 2017, Spain leads in overall installed CSP generating capacity with 2300 MW.

Review of [2] shows that: The main ground of superiority of CSP technology over other renewable resources is the ability to provide dispatchable power by storing the energy through thermal energy storage (TES). Land requirement for parabolic trough without storage and for Linear Fresnel without storage is 2 hectare and 4 hectare per MW. It also has the capability to compete with steam powered plants due to technologies which can handle 540°C and above also. CSP is expected to meet 11.5% of global energy needs by 2050. National Solar Mission which commenced in Jan'10 with the aim of establishing India as global leader in Solar Power Generation. CSP and PV projects had equal share in the first phase mission but it was subsequently slashed due to expensive bids compared to average electricity price then. Rajasthan is the richest state in terms of its solar resource and if tapped even partially, the state can play a pivotal role in meeting the electricity demand of India by 2052. The Thar Desert region with a border by Jodhpur district has the highest Direct Normal Irradiance (DNI) of 5.89KWh/m^2/day. Rajasthan has the potential to generate 456 TWh/year electricity by 2052 by CSP plants with accelerated advancement and modernization of higher temperature technologies.

Review [3] shows that: Performance or biddings in the first phase of Jawaharlal Nehru Mission lead to reduction of share of CSP projects in its second phase to 30% from 50% initially. Theoretically, India has a good potential for generating 700-2100GW of energy. A report by National Renewable Energy Laboratory (NREL) suggested that Capacity Utilization Factor (CUF) which gives the measure of sensibility of a particular technology in a specific geographical location, of CSP plant can go up to 40%-50% with 6-7.5 hours of storage. Higher efficiencies of hybrid plants were supported if we use the CSP heat to preheat the boiler hence reducing the dependency on the primary resource. However, there are a few challenges too, like: No reliable data as the previously available data didn't turn out to be accurate, Projects are yet underway and no big successful project. Financially, high cost of operation and maintenance and unavailability of local manufacturers also added to the high costs.

Review of [4] shows that: currently there is no geothermal power plant in operation anywhere in the country. Seven regions on the basis of surveys and magneto telluric surveys have been recognized. Main R&D priorities are life cycle analysis, sustainable production from geothermal resources and conversion efficiency cycles. Main cost, almost 33% to 50% of the total cost can be attributed to drilling the wells which are around 2 kms deep. Hard hot rocks are used to heat the production fluids in a cyclic manner. Steam or hot water is not transportable beyond 2 miles. Barriers in setup of geothermal plants are: location surveying and drilling, competition with established wind, solar and hydro sources. Exploration stage is expensive and risky due to terrain difficulties. While there is also an added risk of harmful gases but there is also added profit earnings through selling the solid waste that comes along and contains minerals.

Review of [5] shows that: Annual temperature decrement for geothermal plants range from 0.5%-0.8% and these underperforming plants can be brought back to life by additional thermal heat by addition of solar heat. There can be five ways to do this out of which direct heat addition to the geothermal fluid is the most efficient one. Levelized Cost of Energy (LCOE) is also found to be lower for the hybrid system in comparison to standalone CSP plant.

Review of [6] shows that: Solar Industrial Process Heat (SIPH) consumption and potential was studied in California due to its high DNI resource. In most industrial purposes, the direct-heat temperatures needed mostly is less than 260°C. The focus was laid on the five industries that are the largest users of natural gas for these applications: food, paper, petroleum, chemicals, and primary metals manufacturing. The annual requirement of about 48 TWhth, when met with solar energy was found to be cost effective at the state of technology and costs then.

3. Materials and methods

For using Integrated Concentrated Solar Power and Geothermal Energy for power generation, there are basically two ways to integrate them depending on whether the geothermal or CSP is the primary energy source.

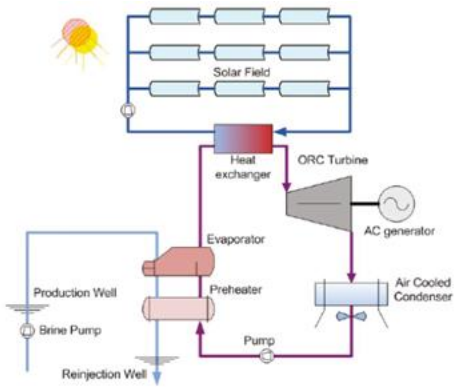


Fig. 1. Hybrid geothermal/ solar thermal system with solar heating of the ORC working fluid [8]

If the major energy source is CSP and Geothermal has to provide the supporting role, following methods can be used [7]:

- Preheating Binary cycle brine
- Preheating flash cycle brine to increase vapour fraction in the flash tank

- Superheating the Organic Rankine Cycle (ORC) working fluid
- Reheating brine and recycling the fluid to power cycle

It was concluded by the authors of the paper "Geothermal / Solar Hybrid Designs: Use of Geothermal Energy for CSP Feedwater Heating [8]" that by annual geothermal energy input of 11.4%, the power output of the integrated plant was 8.5% higher compared to a standalone CSP plant with same solar input.

If the major/primary energy source is Geothermal and CSP provides the minor share of energy to maintain or add to the potential of the Geothermal Power Plant, there are five methods to do this [5]:

- Addition of solar thermal energy to the brine that has to be re-injected into the geothermal reservoir.
- Adding solar thermal energy to re-injection brine until it is 50% vapor.
- Adding solar thermal energy to condenser water.
- Adding solar thermal energy directly to the geothermal production fluids.
- Adding solar thermal energy to the brine that leaves the first flash tank.

On the basis of studies conducted on geothermal plants in California and Nevada, the authors of the paper "Hybridizing a geothermal power plant with concentrating solar power and thermal storage to increase power generation and dispatchability [5]" observed that:

- The first law efficiency and net power generated over the whole range of varying thermal power added to the process is highest for the direct heat addition to geothermal production fluids. Solar Collectors when to directly raise the temperature of the geothermal fluids increase its enthalpy and steam generation.
- The hybrid power plants solar thermal energy to electricity efficiency is 24% and the power output of the earlier 22MW to 24MW (9% increment).
- It was also found to be the most cost-effective way to increase the output and efficiency of the geothermal power plant.

For using Concentrated Solar Power for industrial heating purposes, the type of solar collector or CSP system is chosen depending upon the operating temperature of the heating process (Table 1) and then narrowing down on the types of collectors which can meet the temperature demand. Following this the total energy requirement is estimated and through the data available on the factors such as solar irradiance, no. of sunny days in the year, the size of solar field is estimated [9].

The solar resource can be used in parallel with conventional heating resources by using Thermal Energy Storage, which uses molten salt technology to store thermal energy with minimal loss of efficiency. Assessments in 2006 foretold an annual productivity of 99%, a reference to the energy retained by collecting heat before turning it into electricity, versus transforming heat into electricity directly [10]. This way the solar thermal energy can be provided at the times when there is no sun i.e. during night or cloudy days.

Table 1
Key features of five CSP technology categories

Technology	Annual Solar to electricity efficiency	Practical operating temp. (°C)	Commercial maturity
Parabolic trough	12-15%	150 to 400	High
Central Receiver Tower	20-30%	300 to 1200	Medium
Linear Fresnel	8-10%	150 to 400	Medium
Fresnel lens	12-15%	150 to 400	Medium
Parabolic Dish	20-30%	300 to 1500	Low

For using Geothermal Energy for industrial heating purposes, any industrial heating requirement can be met if the heating temperatures required aren't too high (more than 130°C). Most of the sources in India are lying in this range and hence it makes them fit to be used directly. Some of the industries which use this heat are pulp and paper, cement, food, aquaculture, lumber, and more [11]. Hot water from the geothermal fields can be directly utilized to meet the heating and cooling needs of buildings, towns using heat pump. The heat pump can be reversed in summers to provide cooling effect. Also, if we study the temperature pattern in the region, we can directly use hot water to provide heat in the industrial heating processes. Current methods are used for direct usage where a well is drilled into a geothermal reserve to yield a steady stream of warm water. Steam or the hot water is drawn up from the well through pumps and pipes which transfers the warmth directly for its designed usage.

For using Integrated CSP and geothermal energy for Industrial Applications, Thermal Energy Storage needs to be utilized to combine the heat energy of the two sources and use it throughout the day. Also, the brine from geothermal source can be used as the working fluid which absorbs heat from the heated brine of CSP circuit and then is re-injected into the ground. For this even waste water of cities can be used after minimal processing.

4. Opportunities and challenges in India

As we can see in the map (Fig. 2), around 2.5 million sq. kms area of Indian mainland receives Annual Global Horizontal Irradiance (GHI) 5.0-6.0 kWh/m2/day. GHI gives the total amount of shortwave radiation received from above by a horizontal surface on the ground. It includes both the Direct Normal Irradiance (DNI) and Diffuse Horizontal Irradiance (DHI). India's renewable energy sector has been ranked third in the Renewable Energy Country Attractiveness Index (RECAI) which is majorly due to the solar resources that India possesses. India's current installed capacity is less than 1% of the potential that surveys claim. Indian states of Gujarat and Rajasthan receive the highest avg. solar energy per unit area per day.

Roughly the whole southern and western parts of India receive high average solar energy.

As we can see in the geothermal map of India (Fig. 3), Chhattisgarh-MP belt and J&K region are the hotspots of Geothermal Energy in India. It has been estimated from geological, geochemical, shallow geophysical and shallow drilling data that India has about 10,000 MW of geothermal energy potential that can be utilised for various purposes [4]. Indian geothermal resources are divided into 7 provinces according to their geographical locations out of which the Puga Valley of Ladakh is the most promising one. Geothermal Atlas of India, which is developed by the Geological Survey of India (GSI) provides knowledge/data of around 340 geothermal potential sites. Geothermally heated water can be used for various purposes which need heat. Its uses involve providing heat to buildings (separately or whole locality) during winters, cultivating plants in nurseries, heating water at fish farms, drying crops, and other industrial processes, such as pasteurizing milk. According to an article on livemint.com dated 9th June, 2016, India aims to harness 10 GW of geothermal energy by the next decade by an effective global collaboration with nations such as USA, Philippines, Mexico and New Zealand.

When we compare the maps of Solar and Geothermal Energy simultaneously, common sites with abundant resources of both the energies lie in the northern part of Rajasthan, Gujarat, western coast of Maharashtra and the MP- Chhattisgarh belt. These sites can be utilized for setting up integrated CSP and geothermal power generation plants. NTPC is already on its way to setup a geothermal plant in Chhattisgarh's Tatapani reservoir.

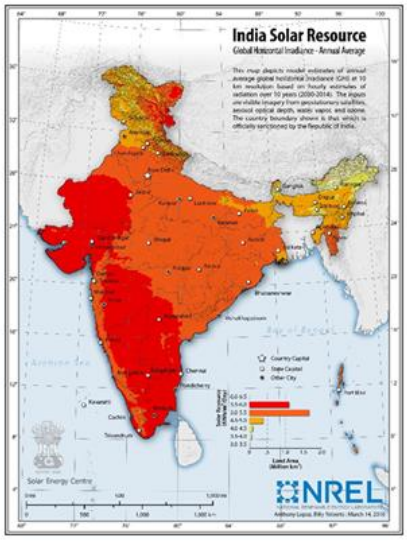


Fig. 2. Annual Global Horizontal Irradiance (GHI) of India (Source: NREL)

The industries in consideration are textile, paper & pulp, Dairy, Leather and Automobile. The results of "Solar Energy for Process Heating: A Case Study of Select Indian Industries by Suresh N S and Badri S Rao [9]" for these industries are combined with their geographical locations to suggest possible geographical sites where solar and geothermal resources can be directly utilized to derive thermal energy.

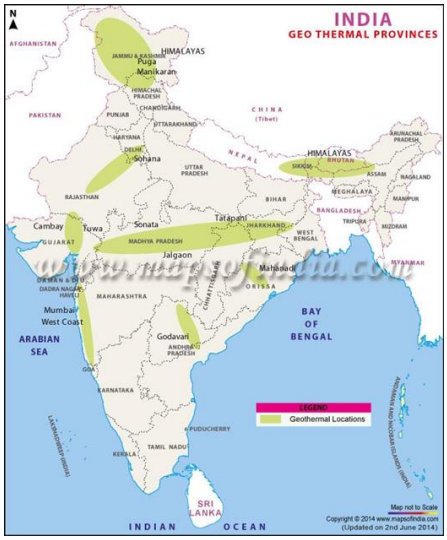


Fig. 3. Geothermal Locations (Source: mapsofindia.com)

Table 2
Status of geothermal fields in India [4]

Geothermal Field	Estimated (min.) Temp (Approx.)	Status
Puga, Ladakh	240°C at 2000m	From geochemical and deep geophysical studies
Tattapani Sarguja (Chhattisgarh)	120°C-150°C at 500m 200°C at 2000m	Magneto telluric survey done by NGRI
Tapoban Chamoli (Uttarakhand)	100°C at 430m	Magneto telluric survey done by NGRI
Cambay Garben (Gujarat)	160°C at 1900m	Steam discharge was estimated 3000 cu meter/ day with high temperature gradient.
Badrinath Chamoli (Uttarakhand)	150°C estimated	Magneto-telluric study was done by NGRI Deep drilling required to ascertain geothermal field
Surajkund Hazaribagh (Jharkhand)	110°C	Magneto-telluric study was done by NGRI. Heat rate 128.6 mW/m^2
Manikaran Kullu (H P)	100°C	Magneto-telluric study was done by NGRI Heat flow rate 130 mW/m^2
Kasol Kullu (H P)	110°C	Magneto-telluric study was done by NGRI

All of these industries mostly require temperatures below 150°C and the sites with availability of temperatures above this should be tapped for power generation. The suggestions with the map links being considered are presented in a tabulated form (Table 3).

Table 3
Key features of five CSP technology categories

Type of Industry	Temperature Requirement (°C)	Geographical Location (Major Cluster)	Map link	Suggested Thermal Energy Resources
Textile	60-110	Western and Southern Part	https://business.mapsofindia.com/india-industry/textile.html	Abundant Solar Radiation through Evacuated Tube Collector Woolen Industry in Kashmir can utilise Geothermal resources
Paper & Pulp	60-150	Maharashtra-Telangana Border and Orissa	https://business.mapsofindia.com/paper-and-pulp-industry/	Abundant Solar Radiation through Evacuated Tube Collector Godavari Geothermal Province can be utilised in Telangana
Dairy	< 120	Western half of country	http://i1.wp.com/mpstudy.com/wp-content/uploads/2016/06/9815369933_1c807c1289_o.png?w=560	Solar Radiation through Linear Fresnel or Evacuated Tube Collector
Leather	< 100	Tamil Nadu & around Delhi	https://www.mapsofindia.com/maps/india/leather-industry.htm	Solar Radiation through Evacuated Tube Collector
Automobile	200 approx. for drying	Spread throughout	https://business.mapsofindia.com/automobile/automobiles-industries-in-india.jpg	Solar Radiation through Parabolic Dish

5. Conclusion and future recommendations

Concluding the paper, it can be said that:

- Geothermal should be the focus of India for the next decade to achieve its target of 10GW geothermal energy by 2030. Also, it is an utilizable green resource going waste in 21st century.
- Due to its nature, Geothermal Power Plant needs a partner to assist in achieving its potential for a longer and healthy duration for which CSP is best suited. Common hotspots of both these resources like Rajasthan, Gujarat, Sonata and Tatapani should be targeted for integrated Power Plants.
- Failure and delay of CSP in Phase 1 of National Solar Mission due to technical, financial or policy problems should be worked upon rather than completely neglecting the potential of CSP.
- CSP and Geothermal Energy for Thermal Industrial Purposes should be promoted by the government in the areas where it is not feasible to set up power generation facilities.
- If standalone power plants of Geothermal or CSP are not feasible in some area of abundant resources, it should be tried to be integrated with gas, coal or biomass power plants.
- More R&D and support is needed to develop the parts for CSP within the nation. This would make the technology cheaper and affordable.
- Lethargic policies and behavior towards projects and investors have led to failure and delay of previous projects which has resulted in hesitation and air of doubt among the stakeholders/prospective investors.

References

[1] *Solar Energy*, www.indiaenergyportal.org/subthemes.php?text=solar
[2] P.R. Arora. "A Vital Role of Concentrating Solar Power Plants of Rajasthan in Future Electricity Demand of India", *International Journal of Scientific and Research Publications*, Volume 3, Issue 6, June 2013
[3] Chandra Bhushan, Aruna Kumarankandath and Nayanjyoti Goswami 2015, "The State of Concentrated Solar Power in India: A Roadmap to Developing Solar Thermal Technologies in India", *Centre for Science and Environment, New Delhi*
[4] *India Geothermal Energy*, www.eai.in/ref/ae/geo/geo.html
[5] J. K. Joshua D. McTigue, Jose Castro, et al. "Hybridizing a geothermal power plant with concentrating solar power and thermal storage to increase power generation and dispatchability" *Science Direct Applied Energy*, Vol. 228, 15 October 2018, Pages 1837-1852
[6] Parthiv Kurup and Craig Turchi "Potential for solar industrial process heat in the United States: A look at California", *AIP Conf. Proc*. 2015.
[7] Zhou, C.E. Doroodchi and B.Moghtaderi, 2013. "An in-depth assessment of hybrid solar—geothermal power generation", *Energy Conversion and Management*, vol. 74, pp. 88-101.
[8] Craig Turchi, Guangdong Zhu, Michael Wagner, Tom Williams, and Daniel Wendt "Geothermal / Solar Hybrid Designs: Use of Geothermal Energy for CSP Feedwater Heating", *Geothermal Resouces Council 2014 Annual Meeting, Portland, Oregon.*
[9] Suresh N S and Badri S Rao "Solar Energy for Process Heating: A Case Study of Select Indian Industries", *Journal of Cleaner Production* (2017).
[10] *Thermal Energy Storage*, https://en.wikipedia.org/wiki/Thermal_energy_storage
[11] *Geothermal Industrial Heat*, https://energyeducation.ca/encyclopedia/Geothermal_industrial_heat

Wireless Personal Communications
https://doi.org/10.1007/s11277-018-6103-9

Design of Probability Density Function Targeting Efficient Coverage in Wireless Sensor Networks

Richa Mishra[1] · **Rajeev K. Tripathi**[1] · **Ajay K. Sharma**[1]

© Springer Science+Business Media, LLC, part of Springer Nature 2018

Abstract
Wireless sensor networks (WSNs) incorporate small devices known as sensors. These sensors monitor the deployment field and are responsible for communicating the sensed data periodically to the base station. Therefore, conserving the battery power of these sensors and the efficient coverage are the two important issues that need to be addressed especially in the cases where the sensors are having limited sensing range. In this paper, we intent to address the above mentioned issues by judiciously deploying the sensor nodes in WSN such that the energy efficient network along with the desirable coverage is obtained. In this paper, the considered deployment field is divided into concentric circles such that the area of each annulus is equal. Probability density function (PDF) is designed based on node density in each annulus. A node distribution algorithm is then proposed using the above PDF. The execution of the proposed distribution scheme is assessed with regard to the network life, energy balancing and the coverage obtained in the network. The results of the proposed scheme is compared with the other present schemes through simulation. It is noticed that the suggested scheme shows better results than other node distribution schemes.

Keywords Wireless sensor network (WSN) · Probability density function (PDF) · Node distribution strategy (NDS) · Cumulative density function (CDF)

1 Introduction

A classic WSN is composed of large number of self governing sensors that monitor and communicate the data to an information collector known as base station (BS). WSNs are used in variety of applications such as temperature monitoring [1, 2], surveillance [3], health [4], earthquake [5], monitoring [6, 7] and battelfield monitoring [8]. These sensor

✉ Richa Mishra
richas.phoenix@gmail.com

Rajeev K. Tripathi
rajivtripathi@nitdelhi.ac.in

Ajay K. Sharma
sharmaajayk@nitj.ac.in

[1] National Institute of Technology Delhi, New Delhi, Delhi, India

Published online: 15 December 2018

nodes are battery operated and sometimes deployed in areas where human interference is difficult. As battery is the only source of energy for these sensors, it should be effectively used to increase the lifetime of the WSN. Lifetime of a WSN is a measure of the stretch from the initialization of the network till all the nodes fail to handover the information to the BS. Therefore, efficient utilization of energy is of utmost concern here.

Traditionally nodes act as both data creator as well as router. The data traffic in the WSN usually follows from many nodes to one node paradigm. Therefore, the nodes nearby BS die out early as they carry heavier traffic. This creates energy-hole in the areas closer to the BS. Once this hole is created further data cannot be transported to the BS thereby resulting in premature end of the WSN. It has been showed experimentally that approximately 90% of the battery power of live nodes is left unused once the lifetime of WSN is over. This is especially true in the cases where the sensor nodes are distributed deterministically in the deployment area. The rate of energy depletion in WSN usually relies on the nature of the distribution of the sensors which in turn is determined by the application area. To prevent the aforementioned scenario the nodes should be distributed in such a way that the energy dissipated by all the nodes in the WSN is even. Different node deployment schemes result in unlike network lifetime and network coverage depending upon their network design criteria. A network design criteria in WSN is governed by network topology, power consumption and transmission errors. Therefore, developing a WSN for any application introduces various implementation challenges among which node deployment problem is one. One solution to resolve the problem of uneven energy dissipation in WSN is to place more number of nodes closer to the BS. In this paper, we aim to propose a PDF based on non-uniform node distribution strategy (NDS) which provides better coverage as well as increase in the lifetime of the WSN. Here, the sensors are disseminated such that the energy-hole problem is eliminated and energy balanced network is obtained.

The paper has been organized as given below: Section 2 surveys the current literature on the design of energy efficient strategies in the WSNs. Section 3 formulates the problem. Section 4 presents energy model for the proposed work in WSN. Section 5 yields the answer to the formulated problem. Experimental set up and results are discussed in Sect. 6. Finally, we conclude the work in Sect. 7.

2 Literature Review

In this section, the literature review has been classified into the following categories namely: analysing the problem of energy-hole, strategies for node distribution and designing energy efficient protocols.

2.1 Analysing the Problem of Energy-Hole

Li and Mahapatra [9] in their mathematical model analyse the energy-hole problem and show that when the nodes are uniformly distributed in concentric circles the lifetime of WSN is limited as the problem of energy-hole do occur. The authors further investigate the work to mitigate the energy-hole problem. Finally, they conclude that simply increasing the number of nodes in the considered scenario does not increase the lifetime of the network. However, they have not discussed the schemes to avoid the problem of energy-hole in WSNs. Similar work has been reported in [10]. Olariu and Stojmenvoic [11] are the first one to address the problem of avoiding the energy-hole problem in corona based network

architecture wherein the nodes are uniformly distributed in each corona. It is further shown that by adjusting the transmission range of the nodes such problem can be avoided. However, such a solution creates imbalance in energy consumption in the WSNs. Further, the authors in the work discussed in [12] provide a non-uniform node distribution scheme that avoids energy-hole problem. Authors prove that the balanced energy consumption in each corona is obtained when the node densities of the two adjacent coronas is proportional with respect to each other.

2.2 Strategies for Node Distribution

Lian et al. [13] present a non-uniform node distribution scheme. The author also made use of additional nodes called the relay nodes in the network. They proposed a routing algorithm in which some of the nodes were put to sleep mode once in a while based on energy saving schemes. This led to increase in lifetime of the network. Lian et al. [14] also proposed a non-uniform node distribution scheme that dealt with another problem called sink-hole problem. Here, the nodes were distributed based on the power of the sensor nodes. Sink-hole problem is similar to energy-hole problem in WSNs. The author solve the sink-hole problem by proposing a long term connectivity in WSN to address the above problem. In both [13, 14], energy-hole problems are not addressed. Halder et al. [15] distributed nodes non-uniformly in their considered architecture. The authors have designed PDF in order to obtain the number of nodes to be distributed in each corona. The author have also derived intrinsic characteristics such as cumulative density function (CDF), expectations and covariance of the PDF. Reference [16] is an extension of the work discussed in [17]. In this the questions such as how many number of node should be distributed in each annulus to achieve uniform energy dissipation in WSNs has been answered. The authors validated the performance of their scheme through qualitative and quantitative analysis. The advantage of the PDF here is that it provides an energy balance among nodes.

2.3 Designing Energy Efficient protocols

LEACH [18] is the first distributed protocol that forms clusters. Cluster head of each cluster is selected probabilistically in the network. All the members of the cluster send the data to their cluster head. Cluster head send this data to the BS through multi-hop [19] or single-hop communication. In [20] clusters were formed based on the strength of local radio signal. Further, load balancing algorithm was proposed that provides some energy balancing in the sensor network. However, this scheme may not be suitable for certain application as data was gathered periodically [21]. In HEED [22] clusters are formed based on the the residual energies and the cost associated with communication of the sensor nodes. Similarly, in [20, 23, 24] clusters of different sizes are formed. The aim of all the work discussed above is to achieve the balanced energy consumption in network.

Perillo et al. [25] have discussed two scenarios that leads to uneven energy consumption when the nodes are distributed uniformly in the network. In first case, when the sensor nodes transmit the data directly to the BS i.e. in one hop count, the nodes farthest away from the BS die out first. In the second case, when the nodes transmit the data to the BS through multiple hop counts, the nodes near the BS die out first due to excessive load transmission. The authors in their work have assumed varying transmission range for all the sensors and model the network lifetime maximization as linear optimization problem. Girdhar and Kumar [26] also formulate the network lifetime maximization as linear

programming problem. They derive the lifetime bounds of the WSN using linear and $2D$ networks and arrive at a conclusion that the optimal lifetime can be acheived by sending the data to the nearby neighbour in WSN field. In order to solve the problem of imbalance energy depletion and extending the network lifetime, mobility was introduced. Wang et al. [27] made use of relay nodes in their work. These relay nodes were placed nearly two hop-counts away from the BS to enhance the lifetime of the network. The authors also proposed joined mobility and routing algorithms and validated the performance of the algorithm. Luo and Hubaux [28] used mobile sink to improve the lifetime of the network. The authors showed that using mobile sink, the imbalance of energy near the sink can be mitigated. The authors proved that the best position of the static sink is at the center of the deployment, provided that the deployment field is circular in architecture. Further, it has been proved that using mobile sink is beneficial and that the mobility trajectory should be the periphery of the WSN. Similarly, in the paper [29], the authors have proposed distributed clustering protocol. In this protocol, few nodes volunteer for the election of cluster head. The other nodes decide to join the nearest cluster head based on hop count (h).

In this paper, we propose a corona based NDS that provides better coverage and increased lifetime of WSN. The main objectives of the paper are:

- It has been analysed that the node density plays a vital part in governing the lifetime of the network. A PDF has been devised based on the above said analysis.
- The node distribution algorithm is constructed based on the PDF design.
- The nodes are disseminated in conformity with the node distribution algorithm.
- The performance of the proposed NDS has been analysed theoretically in terms of lifetime and balanced energy consumption.
- Finally, the proposed NDS has been compared with the other present NDSs through simulation.

3 Formulation of the Problem

An emerging application area in WSN is monitoring a deployment field with the objectives such as intrusion detection, covering an area of interest etc. In such applications, the sensor nodes are randomly distributed across the deployment field. As sensor nodes have limited energy, minimization of the energy consumption by each sensor node and the efficient coverage of the network are the two issues that need to be addressed while designing the WSN. The network lifetime can be remarkably enhanced by the energy utilization of each sensor node. Ideally, it is required that all the nodes in the network die out almost at the same time. This corroborates that very little residual energy is left when the network becomes non-operational i.e., when the connectivity or the coverage is lost. But obtaining such a uniform distribution of energy utilization amongst the sensor nodes with the objective to achieve enhanced lifetime still remains a challenge.

The performance in terms of coverage/connectivity and lifetime of WSN to a large extent depends upon the way the nodes are distributed across the WSN field. In this paper, we propose a NDS with the aim to achieve better coverage with increase in network lifetime along with the balanced energy consumption by the sensor nodes across the WSN.

4 Energy Model

The channel model [18] similar to LEACH has been used in this work. The energy consumed during transmission is given as

$$E_{Tx}(a,d) = \begin{cases} aE_{Tx_{elec}} + aE_{fs}d^2, & \text{if } d < d_0 \\ aE_{Tx_{elec}} + aE_{mp}d^4, & \text{if } d \geq d_0 \end{cases} \quad (1)$$

Here E_{Tx}, $E_{Tx_{elec}}$, $E_{fs}d^2$ and $E_{mp}d^4$ are the energy consumed in transmission, hardware circuitry, free-space loss and multi-path loss at a distance d respectively. The free-space loss and multi-path loss depicts the two kinds of amplifications that is used in the radio model. Here, d_0 is the threshold distance. Energy consumed in receiving E_{Rx} is given by

$$E_{Rx}(a) = E_{Rx_{elec}}(a) = aE_{elec} \quad (2)$$

Here E_{elec} is the energy used in receiving $a-$ bit data.

5 Solution Approach

We adduce a node distribution scheme for the considered model in order to maximize lifetime and the coverage in the WSN field. The area of the deployment field is divided based on the sensing range of the sensor node. The field is partitioned in a way that the region of each corona remains constant throughout the field. The mathematical expressions have been formulated based on which the PDF has been developed. Finally, nodes are distributed using the node distribution algorithm that is proposed using the designed PDF.

5.1 The Network Model

Network domain consists of a square field $ABCD$ having an area $H \times H$ square units. The network field is then divided into a number of concentric circles (NoCC) with the BS positioned at the center $O(X_c, Y_c)$ of the field as shown in Fig. 1. Here, the innermost

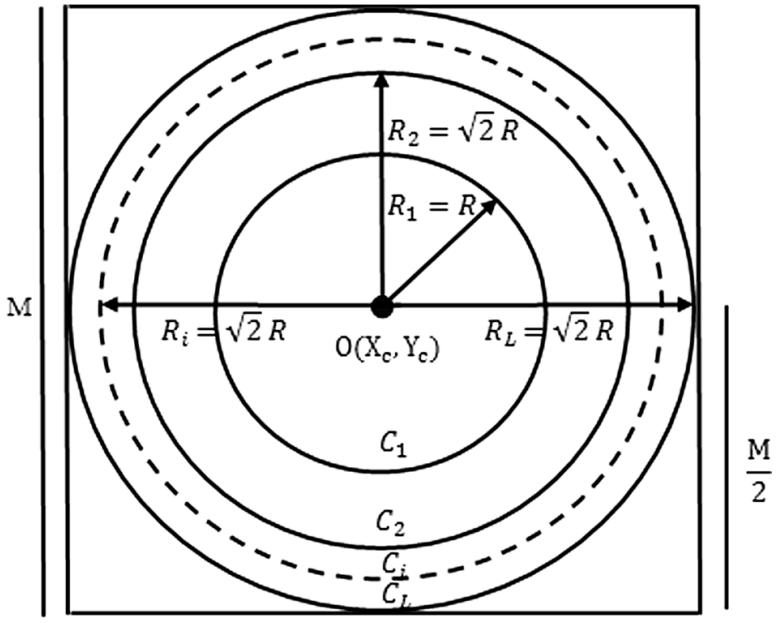


Fig. 1 Network architecture

corona and its radius is denoted by C_1 and R_1 respectively. Similarly, the next concentric corona C_2 has the radius that is denoted by R_2 and so on. The field is partitioned in such a manner that the area of each corona in the field is equal. The radius, width of each corona and the number of coronas in the network is determined using Lemmas 1, 2 and Theorem 1 respectively.

Lemma 1 *Radius of* ith *corona denoted by* C_i *in the considered network domain is given by*

$$R_i = \sqrt{i}\, R$$

where R_i *is the radius of* ith *corona.*

Proof Let us assume that the radius of corona C_i is equal to R_i. Using this relation, the radius of coronas C_1 and C_2 is R_1 and R_2 respectively. Then, the area A_1 of the corona C_1 can be calculated by πR_1^2. Now, the area A_2 of the corona C_2 can be obtained by

$$A_2 = \pi R_2^2 - \pi R_1^2 = \pi (R_2^2 - R_1^2) \tag{3}$$

As the area of each corona is equal i.e., $A_2 = A_1$, the new expression can be obtained and is given by,

$$\pi (R_2^2 - R_1^2) = \pi R_1^2 \tag{4}$$

Simplifying the above equation we get,

$$R_2^2 = 2 R_1^2 \tag{5}$$

$$R_2 = \sqrt{2} R_1 \tag{6}$$

Similarly, area of corona C_3 can be calculated by,

$$A_3 = \pi R_3^2 - \pi R_2^2 \tag{7}$$

$$= \pi (R_3^2 - R_2^2) \tag{8}$$

As area of corona C_3 is equal to area of corona C_1, we get,

$$\pi (R_3^2 - R_2^2) = \pi R_1^2 \tag{9}$$

Substituting the value of R_2 as obtained in Eq. (6) in the above equation, we get

$$\pi (R_3^2 - 2R_1^2) = \pi R_1^2 \tag{10}$$

$$R_3^2 = 3 R_1^2 \tag{11}$$

$$R_3 = \sqrt{3} R_1 \tag{12}$$

Substituting $R_1 = R$ and using the Eqs. (6) and (12) the radius of ith corona is given by

$$R_i = \sqrt{i}\, R \tag{13}$$

Hence proved. □

Lemma 2 *The width W_i of each corona C_i is given by*

$$W_i = (\sqrt{i+1} - \sqrt{i})\, R$$

Proof The width W_2 of corona C_2 is given by,

$$W_2 = R_2 - R_1 \tag{14}$$

Similarly, width W_3 of Corona C_3 can be given by

$$W_3 = R_3 - R_2 \tag{15}$$

Using Lemma 1 and the Eqs. (14) and (15), the width of ith corona is given by

$$W_i = (\sqrt{i+1} - \sqrt{i})\, R \tag{16}$$

□

Theorem 1 *The network area is divided into La layers and is given by*

$$La = \frac{H^2}{4 \times R^2} \tag{17}$$

Where H and R is the length of one side and the length of the radius of the innermost corona C_1 of the deployment field respectively .

Proof The radius of the outermost circle can be given by

$$R_{La} = \frac{H}{2} \tag{18}$$

Using the Eq. (13) obtained in Lemma 1, the above equation can be rewritten as

$$\sqrt{La} \times R = \frac{H}{2} \tag{19}$$

We assume that the communication range R_c of sensor node is equal to twice the sensing range of a sensor node i.e., $R_c \geq 2 \times R_s$. Simplifying the above equation using this relation we get,

$$La = \frac{H^2}{4 \times R^2}$$

Hence proved. □

Lemma 3 *The area A_i of any corona C_i in the deployment field is given as*

$$A_i = \left[(\sqrt{i+1})^2 - (\sqrt{i})^2\right] \times \pi R^2 \tag{20}$$

Proof Using Lemmas 1 and 2

$$A_i = \pi \times \left[(\sqrt{i+1}R)^2 - (\sqrt{i}R)^2\right] \tag{21}$$

Hence proved. □

5.2 Definitions

Definition 1 The lifetime of a network is defined as the duration from the initialization of the network till all the nodes in any one corona except the last one die out.

Definition 2 Node density (ND) is defined as the total number of nodes distributed per unit area in the considered network field.

Definition 3 Coverage is defined as the ratio of the product of the sensing range of a sensor node and total number of sensors deployed to the area of the deployment field.

5.3 Analysis of Network Lifetime

The lifetime of any node can be determined by the proportion of its initial energy to its energy dissipation rate (EDR) and is given by

$$LT_i = \frac{E_o}{EDR_i} \tag{22}$$

Here EDR_i and E_o are the energy dissipation rate and initial energy of the ith node in the network respectively. The lifetime of any layer can be expressed by

$$LT_j = \frac{E_o \times T_j}{EDR_j \times T_j} \tag{23}$$

Here T_j is total nodes distributed in jth layer. Hence, from the above equation it can be said that lifetime of one node is equal to lifetime of one layer. Data communication rate (DCR) of a node can be determined by the proportion of all the data produced to the ND in that layer and it is given by

$$DCR_j = \frac{\chi \times A_j}{\delta_j \times A_j} = \frac{\chi}{\delta_j} \tag{24}$$

Here A_j, χ, and δ_j are the area, data production rate (DPR) of a node, and the ND of the jth layer respectively. The nodes in the jth layer transmit their own data and the data received

from its successive outer layer i.e., $(j+1)$, to the next consecutive layer towards the BS and is given by

$$DCR_{avg} = \frac{\chi \delta_{j+1} A_{j+1}}{\delta_j A_j} \tag{25}$$

Using the above equation, the average DCR of $(j+1)$th layer towards a node in the jth layer is given by

$$DCR_{avg} = \frac{\chi \delta_{j+1} \left[(\sqrt{(j+2)})^2 - (\sqrt{(j+1)})^2 \right]}{\delta_j \left[(\sqrt{(j+1)})^2 - (\sqrt{j})^2 \right]} \tag{26}$$

Here δ_{j+1} and DCR_{avg} are the the ND and the average DCR respectively. We assume that the greedy mechanism is used to forward the data from a node in a layer to a node in the next consecutive layer towards the BS (NCLtBS). The average DCR of $(j+1)$th layer is given as $DCR_{j+1} = \frac{\chi \delta_{j+1} \left[(\sqrt{(j+2)})^2 - (\sqrt{(j+1)})^2 \right]}{\delta_j \left[(\sqrt{(j+1)})^2 - (\sqrt{j})^2 \right]}$. Therefore, the sum of all the data forwarded by a node in the jth layer is the sum of the average data communicated by all the successive layers farther away and is given by

$$DCR_{Total} = \frac{\chi \left[\sum_{h=j+1}^{La} \delta_h (\sqrt{(h+1)})^2 - (\sqrt{h})^2 \right]}{\delta_j \left[(\sqrt{(j+1)})^2 - (\sqrt{j})^2 \right]} \tag{27}$$

Here La is the total layer in the network. DCR_{Total} is the sum of data relayed by the outer layers to its inner successive layer respectively. Using Eqs. (24) and (27), the DCR of each node in the jth layer can calculated by,

$$DCR_j = \begin{cases} \frac{\chi}{\delta_j} + \frac{\chi \left[\sum_{h=j+1}^{La} \delta_h (\sqrt{(h+1)})^2 - (\sqrt{h})^2 \right]}{\delta_j \left[(\sqrt{(j+1)})^2 - (\sqrt{j})^2 \right]}, & \text{for } j = 1, 2, \ldots, (La-1) \\ \frac{\chi}{\delta_L a}, & \text{for } j = La \end{cases} \tag{28}$$

The first part $\frac{\chi}{\delta_j}$ is the self generated data by a layer that is to be communicated and the second part $\frac{\chi \sum_{h=j+1}^{La} \delta_h (\sqrt{(h+1)} - \sqrt{h})}{\delta_j (\sqrt{(j+1)} - \sqrt{j})^2}$ is the sum of all the data from the outer consecutive layers that needs to be communicated by the jth layer. The energy required to communicate nodes own data is given by

$$E_i = \frac{\chi}{\delta_j} \times E_{Tx} \tag{29}$$

Here E_i and E_{Tx} is the total energy dissipated by the ith node and the energy needed to communicate the data respectively. The energy needed by the inner layer to communicate the total relayed data from the outer consecutive layers is given by

$$E_{relayed} = \left[\frac{\chi \sum_{h=j+1}^{La} \delta_h \left\{ (\sqrt{(h+1)})^2 - (\sqrt{h})^2 \right\}}{\delta_j \{ (\sqrt{(j+1)})^2 - (\sqrt{j})^2 \}} \right] \times E_{Tx} \tag{30}$$

Here $E_{relayed}$ is the total energy dissipated in forwarding all the data from the outer layers. The energy dissipated by each node in jth layer is calculated from Eqs. (29) and (30) and is given by

$$EDR_j^{Tx} = \begin{cases} \left[\frac{\chi}{\delta_j} + \frac{\chi \sum_{h=j+1}^{La} \delta_h \{ (\sqrt{(h+1)})^2 - (\sqrt{h})^2 \}}{\delta_j \{ (\sqrt{(j+1)})^2 - (\sqrt{j})^2 \}} \right] \times E_{Tx}, & \text{for } j = 1, 2, \ldots, (La-1) \\ \frac{\chi}{\delta_{La}} \times E_{Tx}, & \text{for } j = La \end{cases} \tag{31}$$

where EDR_j^{Tx} is the energy consumed in transmission by the layer j. Similarly, energy consumed in receiving the data from the farther consecutive layers is given by

$$EDR_j^{Rx} = \left[\frac{\chi \sum_{h=j+1}^{La} \delta_h \{ (\sqrt{(h+1)})^2 - (\sqrt{h})^2 \}}{\delta_j \{ (\sqrt{(j+1)})^2 - (\sqrt{j})^2 \}} \right] \times E_{Rx} \tag{32}$$

Here E_{Rx} is energy consumed in reception of data. EDR_j^{Rx} is the energy dissipated in receiving the data by the jth layer . Sum of all the energy dissipated by the ith node is given by

$$EDR_i = EDR_i^{Tx} + EDR_i^{Rx} \tag{33}$$

Here EDR_i^{Tx}, EDR_i^{Rx} and EDR_i are the energy dissipated in communication, the energy dissipated in reception and the total energy dissipated by a node i in the layer j respectively. Therefore, the sum of all the energy dissipated by the nodes in jth layer is given by

$$EDR_j = \begin{cases} EDR_j^{Tx} + EDR_j^{Rx}, & \text{for } j = 1, 2, \ldots, (La-1) \\ EDR_{La}^{Tx}, & \text{for } j = La \end{cases} \tag{34}$$

Substituting Eqs. (31) and (32) in the above equation, we get,

$$EDR_j = \begin{cases} \left[\frac{\chi}{\delta_j} + \frac{\chi \sum_{h=j+1}^{La} \delta_h \{ (\sqrt{(h+1)})^2 - (\sqrt{h})^2 \}}{\delta_j \{ (\sqrt{(j+1)})^2 - (\sqrt{j})^2 \}} \right] \times E_{Tx} \\ \quad + \left[\frac{\chi \sum_{h=j+1}^{La} \delta_h \{ (\sqrt{(h+1)})^2 - (\sqrt{h})^2 \}}{\delta_j \{ (\sqrt{(j+1)})^2 - (\sqrt{j})^2 \}} \right] \times E_{Rx}, \\ \quad \text{for } j = 1, 2, \ldots, (La-1) \\ \frac{\chi}{\delta_{La}} \times E_{Tx}, \quad \text{for } j = La \end{cases} \tag{35}$$

The above equation can be rewritten as given by

$$EDR_j = \begin{cases} \frac{\chi}{\delta_j} E_{Tx} + \left[\frac{\chi \sum_{h=j+1}^{La} \delta_h \{ (\sqrt{(h+1)})^2 - (\sqrt{h})^2 \}}{\delta_j \{ (\sqrt{(j+1)})^2 - (\sqrt{j})^2 \}} \right] (E_{Tx} + E_{Rx}), \\ \quad \text{for } j = 1, 2, \ldots, (La-1) \\ \frac{\chi}{\delta_{La}} \times E_{Tx}, \quad \text{for } j = La \end{cases} \tag{36}$$

Energy balancing is a condition where the nodes in all the layers drain their energy around similar time. Therefore, it needs to satisfy the following condition.

$$EDR_j = ECR_{j+1} = EDR_{j+2} = \cdots = EDR_{j+La} \tag{37}$$

Now substituting Eq. (36) in the above equation, we get

$$\begin{aligned} &\frac{\chi}{\delta_j} E_{Tx} + \left[\frac{\chi \sum_{h=j+1}^{La} \delta_h \{(\sqrt{(h+1)})^2 - (\sqrt{h})^2\}}{\delta_j \{(\sqrt{(j+1)})^2 - (\sqrt{j})^2\}} \right] (E_{Tx} + E_{Rx}) \\ &= \frac{\chi}{\delta_{j+1}} E_{Tx} + \left[\frac{\chi \sum_{h=j+2}^{La} \delta_h \{(\sqrt{(h+1)})^2 - (\sqrt{h})^2\}}{\delta_j \{(\sqrt{(j+2)})^2 - (\sqrt{j+1})^2\}} \right] (E_{Tx} + E_{Rx}) \end{aligned} \tag{38}$$

On simplifying Eq. (38) we get Eq. (39) and is given by

$$\delta_j = \delta_{j+1} \frac{\left[\chi E_{tx} + (E_{tx} + E_{rx}) \left(\frac{\chi \sum_{h=j+1}^{La} \delta_h \{(\sqrt{(h+1)})^2 - (\sqrt{h})^2\}}{\delta_j \{(\sqrt{(j+1)})^2 - (\sqrt{j})^2\}} \right) \right]}{\left[\chi E_{tx} + (E_{tx} + E_{rx}) \left(\frac{\chi \sum_{h=j+2}^{La} \delta_h \{(\sqrt{(h+1)})^2 - (\sqrt{h})^2\}}{\delta_j \{(\sqrt{(j+2)})^2 - (\sqrt{j+1})^2\}} \right) \right]} \tag{39}$$

The above equation indicates that the ratio of ND depends upon the successive layers and the total number of layers. ND should be non-uniform in each layer *i.e.*, $\delta_j > \delta_{j+1} > \delta_{j+2} > \cdots > \delta_N$. It can be assumed that if the node is distributed according to the above equation, the nodes would deplete the energy approximately at similar time. The lifetime of a node of the *j*th layer can be calculated using Eq. (22). Substituting value of *EDR* in Eq. (22) we get,

$$LT_j = \frac{E_o}{EDR_j^{Tx} + EDR_j^{Rx}} \tag{40}$$

Using Eq. (36) in the above equation, the network lifetime can be calculated as given by,

$$LT_j = \begin{cases} \frac{E_o \{(\sqrt{j+1})^2 - (\sqrt{j})^2\} \delta_j}{\{(\sqrt{j+1})^2 - (\sqrt{j})^2\} E_{Tx} + \chi (E_{Tx} + E_{Rx}) \delta_h \{\sum_{h=j+1}^{La} (\sqrt{h+1})^2 - (\sqrt{h})^2\}}, \\ \qquad \text{for } j = 1, 2, \ldots, (La-1) \\ \frac{E_o \delta_{La}}{E_{Tx} \chi}, \qquad \text{for } j = La \end{cases} \tag{41}$$

Here LT_j is the lifetime of the *j*th layer.

5.4 The Probability Based Node Deployment Scheme (PBNDS)

In this subsection, the probability of a node lying in a corona *i* is designed using the aforementioned lemmas and theorems. The probability of the number of nodes (NoNs) disseminated in each corona is designed on the basis of decreasing width of each corona such that the area of each corona remains the equal. Maximal nodes are scattered in the innermost corona and

it decreases as one progresses far from it. Such kind of node distribution provides balanced energy in each corona thereby maximizing the life of WSN. The PDF of a point $Y(u, v)$ lying in ith corona is given by

$$\eta(u, v; R, i, H, La) = \frac{\varphi(\sqrt{i+1} - \sqrt{i})}{i\sqrt{(La)}} \quad \forall\ i R^2 < u^2 + v^2 \leq (i-1) R^2 \tag{42}$$

Here φ is constant and is given as

$$\varphi = \frac{\sqrt{La}}{\left\{\pi \times R^2 \sum_{i=1}^{La} \frac{1}{i}(\sqrt{i+1} - \sqrt{i}) \times [(\sqrt{i+1})^2 - (\sqrt{i})^2]\right\}} \tag{43}$$

Theorem 2 *Given a deployment field consisting of area $H \times H$ square units having divided into La number of coronas, the constant φ is given by*

$$\varphi = \frac{\sqrt{La}}{\left\{\pi \times R^2 \sum_{i=1}^{La} \frac{1}{i}(\sqrt{i+1} - \sqrt{i}) \times [(\sqrt{i+1})^2 - (\sqrt{i})^2]\right\}} \tag{44}$$

Proof The probability $P(i)$ at any point $Y(u, v)$ lying in the ith corona given by

$$P(i) = \frac{\varphi(\sqrt{i+1} - \sqrt{i})}{i\sqrt{(La)}} \iint f(u, v)\, du\, dv \tag{45}$$

Here $\iint f(u, v)\, du\, dv$ is the area of each corona in the deployment field and is given by

$$A_i = \pi \times [(\sqrt{i+1})^2 - (\sqrt{i})^2] R^2 \tag{46}$$

Substituting the above equation in Eq. (45) we get,

$$P(i) = \frac{\varphi(\sqrt{i+1} - \sqrt{i})[R^2 \pi((\sqrt{i+1})^2 - (\sqrt{i})^2)]}{i\sqrt{(La)}} \tag{47}$$

According to the definition of probability $\sum_{i=1}^{La} P_{(i)} = 1$, therfore, the equation now can be drafted as

$$\frac{\varphi(\sqrt{i+1} - \sqrt{i})[R^2 \pi((\sqrt{i+1})^2 - (\sqrt{i})^2)]}{i\sqrt{(La)}} = 1 \tag{48}$$

Simplifying the above equation, we get

$$\varphi = \frac{\sqrt{La}}{\left\{\pi \times R^2 \sum_{i=1}^{La} \frac{1}{i}(\sqrt{i+1} - \sqrt{i}) \times \left[(\sqrt{i+1})^2 - (\sqrt{i})^2\right]\right\}} \tag{49}$$

Hence proved. □

5.5 Node Distribution

The algorithm for the node dissemination in the deployment field is given in Algorithm 1. At first, the network domain is divided into NoCC as discussed in the earlier section. NoCC/Layers is obtained using Eq. (17). Now the nodes are disseminated based on the PDF design. The value of the constant φ is calculated using Eq. (44). Once the value of constant φ is obtained, the probability (P_i) can be obtained using Eq. (47). Now, using Eqs. (47), the total nodes in corona i is calculated by

$$T_i = P_i \times Total \tag{50}$$

Here T_i is the NoN in ith corona.

Illustrative example is as given below:

Example Consider a network architecture consisting of 100×100 square units with $Total = 500$ and sensing radius $R_s = 20$. The number of coronas the network is divided into is computed utilizing Eq. (17) and constant φ is calculated using Eq. (49) are 6 and 0.0024 respectively. Now, the probability and the total NoN in each corona is calculated using Eqs. (42) and (50) and is as laid out by Table 1.

Algorithm 1 Node Deployment ( )

Input : Side H, Sensing Radius (R_s), Total nodes ($Total$)
Output : Total nodes in every corona.
Obtain La from the Equation (17);
Obtain φ using Equation (44);
for $i = 1$ to La **do**
  Calculate P_i from the Equation (42);
  Obtain T_i Equation (50);
end for

6 Performance Analysis

The performance of the proposed NDS is analysed using qualitative and quantitative techniques as discussed below.

6.1 Qualitative Analysis

Performance of the proposed scheme is measured on the basis of three parameters namely; lifetime, energy balancing and coverage density of the network.

Table 1 Distribution of nodes

Layer (La_i)	La_1	La_2	La_3	La_4	La_5	La_6
Probability (P_i)	0.51	0.199	0.1121	0.0741	0.0536	0.0410
Node distribution (T_i)	260	100	56	37	27	21

6.1.1 Balancing Energy

The energy balancing is a condition where all the nodes end up their energy at the same time. Similarly, in layered architecture, the energy balancing is achieved when the nodes in all the layers end up their battery power at the similar time. Nodes deployed in the farthest layer transmit their data to the NCLtBS. The energy required to transmit the data is given by

$$E_{TX}(a,d) = E_{tx_{elec}}\, a + a\, E_{tx_{amp}}(R_c^2) \tag{51}$$

The above equation can be rewritten as

$$E_{TX}(a,d) = a\, E_{Tx} \tag{52}$$

Here $E_{Tx} = E_{tx_{elec}}\, a + a\, E_{tx_{amp}}(R_c^2)$. Similarly, energy required to receive $a-$bit data is given by

$$E_{RX}(k) = a\, E_{rx_{elec}} = aE_{RX} \tag{53}$$

Here $E_{RX} = E_{rx_{elec}}$.Energy consumed by the last layer in transmitting its data is given by

$$EDR_L = ETX \times \delta \times A_{La} \tag{54}$$

Here $(\alpha \times A_{La})$ is data to be transmitted by layer La. Rest of the layers transmit their own sensed data and received data from their outer layers. Therefore, energy consumed by the layers other than the outer layer is given by

$$EDR_j = E_{TX} \times \delta \times A_j + \left[(E_{TX} + E_{RX}) \sum_{j=i+1}^{La} (\delta \times A_j) \right] \tag{55}$$

To achieve the condition for balanced energy consumption, below given condition must be fulfilled.

$$\frac{T_1 \times E_o}{EDR_1} = \frac{T_2 \times E_o}{EDR_2} = \cdots = \frac{T_i \times E_o}{EDR_i} \tag{56}$$

Here T_1 and E_o are the NoNs in the innermost layer and the initial energy of the nodes in all the layers respectively. From the above equation, the condition for the balance energy is given as

$$\frac{ECR_i}{T_i} = \frac{ECR_{i+1}}{T_{i+1}} \tag{57}$$

Using Eqs. (55) and (57), we get

$$\frac{T_i}{T_{i+1}} = \frac{E_{TX} \times \alpha \times A_i + \left[(E_{TX} + E_{RX}) \sum_{j=i}^{L} (\alpha \times A_j) \right]}{E_{TX} \times \alpha \times A_{i+1} + \left[(E_{TX} + E_{RX}) \sum_{j=i+1}^{L} (\alpha \times A_j) \right]} \tag{58}$$

Substituting A_i by $\pi(\sqrt{i}\,R)^2$ and by dropping α, we get

$$\frac{T_i}{T_{i+1}} = \frac{E_{TX} \times \times \pi(\sqrt{i}\,R)^2 + \left[(E_{TX} + E_{RX}) \sum_{j=i}^{L} \pi(\sqrt{j}\,R)^2\right]}{E_{TX} \times \pi(\sqrt{i+1}\,R)^2 + \left[(E_{TX} + E_{RX}) \sum_{j=i+1}^{L} \pi(\sqrt{j}\,R)^2\right]} \tag{59}$$

Simplifying the above equation, we obtain,

$$\frac{T_i}{T_{i+1}} = \frac{E_{TX} \times (\sqrt{i})^2 + \left[(E_{TX} + E_{RX}) \sum_{j=i}^{L} (\sqrt{j})^2\right]}{E_{TX} \times (\sqrt{i+1})^2 + \left[(E_{TX} + E_{RX}) \sum_{j=i+1}^{L} (\sqrt{j})^2\right]} \tag{60}$$

By using the proposed PDF discussed in Sect. 5, the LHS of the above expression can be written as

$$\frac{T_i}{T_{i+1}} = \frac{(\sqrt{i+1} - \sqrt{i})\left[R^2\pi((\sqrt{i+1})^2 - (\sqrt{i})^2)\right]}{(\sqrt{i+2} - \sqrt{i+1})\left[R^2\pi((\sqrt{i+2})^2 - (\sqrt{i+1})^2)\right]} \tag{61}$$

Equating the above Eqs. (60) and (61), we get

$$\begin{aligned} &\frac{(\sqrt{i+1} - \sqrt{i})[R^2\pi((\sqrt{i+1})^2 - (\sqrt{i})^2)]}{(\sqrt{i+2} - \sqrt{i+1})[R^2\pi((\sqrt{i+2})^2 - (\sqrt{i+1})^2)]} \\ &= \frac{E_{TX} \times (\sqrt{i})^2 + \left[(E_{TX} + E_{RX}) \sum_{j=i}^{L} (\sqrt{j})^2\right]}{E_{TX} \times (\sqrt{i+1})^2 + \left[(E_{TX} + E_{RX}) \sum_{j=i+1}^{L} (\sqrt{j})^2\right]} \end{aligned} \tag{62}$$

In the above equation, the LHS and RHS are approximately equal. Hence, the objective of energy balancing is fulfilled if the nodes are deployed using the proposed scheme.

6.1.2 Network Lifetime

Energy dissipation rate by each node in *i*th layer per unit $u(t)$ time is given by

$$ED_i = \frac{EDR_i}{T_i \times u(t)} \tag{63}$$

For the energy balanced network the life of each node is equivalent to the life of one corona and is given by The lifetime of a node in *i*th layer is given as

$$LT_i = \frac{E_o}{EC_i} \tag{64}$$

Putting the values of ED_i in Eq. (64) we get

$$LT_i = \frac{E_o \times T_i}{EDR_i} \times u(t) \tag{65}$$

Substituting the value of EDR_i as given in Eq. (55) in the above equation, we get

$$LT_i = \frac{E_o \times T_i}{E_{TX} \times \alpha \times A_i + \left[(E_{TX} + E_{RX}) \sum_{j=i+1}^{L} (\alpha \times A_j)\right]} \tag{66}$$

The parameters such as $E_o, T_i, E_{TX}, e_r, \alpha, A_i$ and $u(t)$ affect the lifetime of the network. As the parameter $E_0, E_{TX}, E_{RX}, \delta$ and A_i are constant, we discuss the impact of other parameters affecting the lifetime of the network.

Absolute NoNs in Each Layer From the Eq. (66), it can be observed that increasing the NoNs in *i*th layer increases the lifetime of the network, keeping the other parameters as fixed. Therefore, it can be said that the lifetime of each layer in layered network is directly proportional to the total number of nodes in that layer.

Data Collection Period Increasing the period of data collection alludes the lesser number of data collected by the sensor nodes. This leads to less energy consumption by the nodes in each layer. Therefore, it can be said that by increasing the period of data collection, the lifetime of the network is increased, assuming the other parameters as constant.

Data Production Rate (DPR) Life of WSN is inversely proportional to DPR. This indicated that if the DPR is increased, the nodes sense more data which leads in an increase in energy dissipation by each node therefore the life of the WSN is decreased.

6.1.3 Coverage Analysis

Using the definition of coverage as defined in the previous section, the coverage obtained for the *i*th layer is given by

$$La^i_{Cov} = \frac{T_i \times \pi \times R_S^2}{A_i} = \frac{T_i \times \pi \times R_S^2}{\pi(\sqrt{i}\,R)^2} \tag{67}$$

The coverage of a WSN is given as

$$Network_{AvgCov} = \frac{\sum_{i=1}^{La} \left(\frac{T_i \times \pi \times R_S^2}{\pi(\sqrt{i}\,R)^2}\right)}{La} \tag{68}$$

6.2 Quantitative Analysis

Considered network consists of $H \times H$ square units. This area is separated into various regions denoted by corona. The NoNs in every corona/region is distributed using the Algorithm 1. The nodes considered in this work are static and homogeneous in nature. The simulation parameters are as given in Table 2. Here, the size of one message (packet) is 4000 bits. Therefore, data rate is 4000 bits/s.

Table 2 Simulation parameter

Symbol	Denotation	Value
Area (H)	Domain area	100 to 500 sq. units
Nodes (total)	Total nodes	100–500
E_o	Initial energy	0.01 J
E_{Tx}	Transmission energy	50 nJ/bit
E_{Rx}	Reception energy	50 nJ/bit
E_{elec}	Hardware electronics	50 nJ/bit
a	Message size	4000 bits

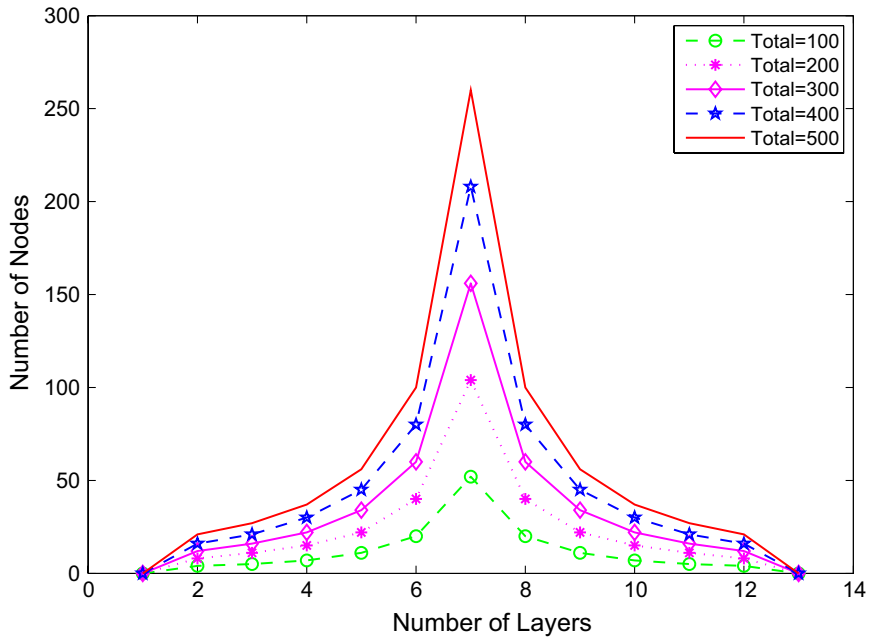


Fig. 2 Node distribution in 6-*layered* architecture

6.2.1 Analysis of PBNDS

The considered deployment field is divided into successive coronas with each corona having the equal area. The nodes are distributed as given in Algorithm 1.

NoNs disseminated in each layer in a 6-layered architecture is plotted in Fig. 2. It is observed from the figure that the maximum NoNs are distributed towards the innermost corona of the deployment field in all the considered cases i.e., when Total is 100, 200, 300, 400 and 500 keeping the sensing radius $R_s = 20$ and the area of the deployment field as 100×100. Total 52, 104, 156, 208 and 260 nodes are distributed in layer-1 of the deployment field when Total is 100, 200, 300, 400 and 500 respectively. Layer-1 is the innermost corona with the BS positioned at the origin of each corona. The NoNs distributed in the next consecutive outer coronas in layer-2 is 20, 40, 60, 80 and 100, layer-3 is 11, 22, 34, 45 and 56, layer-4 is 7, 15, 22, 30 and 37, layer-5 is 5, 11, 16, 21 and 27 and finally layer-6 is 4, 8, 12, 16 and 21 with total NoNs Total as 100, 200, 300, 400 and 500 respectively. It is observed from the figure that the total number of node distributions keep decreasing as one progresses towards the outer coronas.

Number of nodes in each layer with varying sensing range of a sensor node is plotted in Fig. 3. The case is analysed keeping the area as 100×100 and $Total = 100$ for all the considered cases. It is observed that with the parameter $R_s = 18$, the deployment field is divided into 8-*layers*. The maximum number of nodes distributed are in the innermost corona in *layer*-1. The number of nodes distributed in consecutive outer coronas decreases as one moves towards the outermost corona in *layer*-8. When $R_s = 20$, the deployment field is divided into 6-*layered* architecture. The distribution of number of nodes is similar to case where $R_s = 18$ in sense that the number of node distribution decreases towards the successive outer coronas. Similarly, with $R_s = 24$ and $R_s = 28$ the network is divided into 4 and 5-*layered* architecture respectively. The node distribution pattern is similar as discussed.

The network coverage obtained in various layered architecture is plotted in Fig. 4. It is observed that the maximum network coverage is obtained when a network is divided into a 3-*layered* architecture. This is because the sensing range R_s of the sensor node is large and is equal to 28, when compared to other cases in layered architecture. This is evident from the Fig. 3. As the sensing radius of a sensor node decreases, the number of coronas in the deployment field increases thereby, increasing the number of layers in the network. Hence it can be said that the number of layers in the network is dependent on the sensing range of a sensor node. Using the graph shown in Fig. 3, it is seen that when $R_s = 24$, the 4-*layered* architecture is obtained. The network coverage obtained in the 4-*layered* architecture is 25.25. Similarly, in case of 5, 6 and 7-*layered* architecture the network coverage obtained is 20, 16.5 and 12.62 respectively as shown in Fig. 4.

6.2.2 Comparison with Existing Schemes

The proposed NDS is compared with the existing schemes such as PDFND [16], NDGD [30], NDUD [31] and PDFBNDS [32]. The number of dead nodes for each round has been

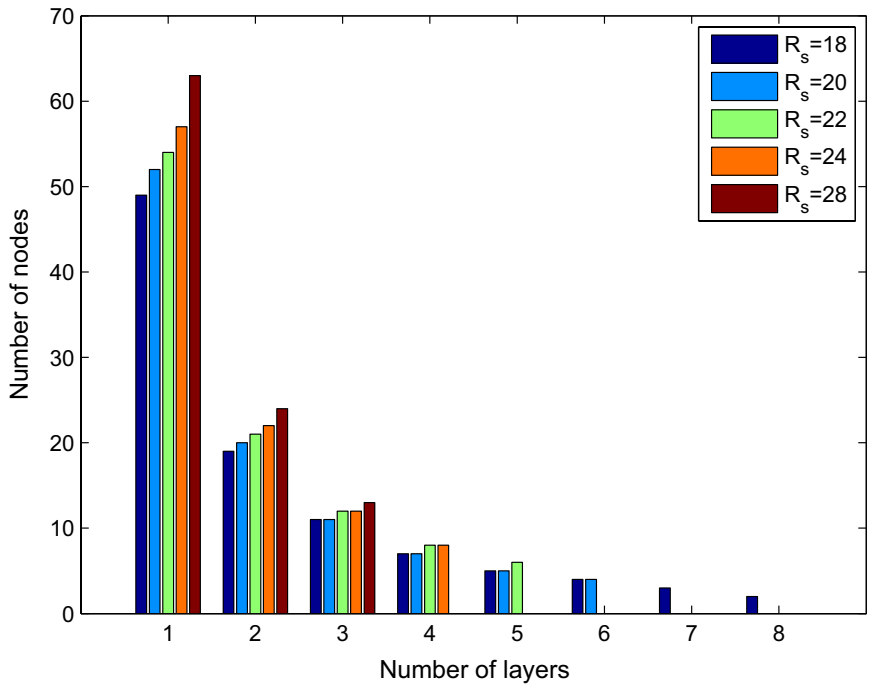


Fig. 3 Node distribution with varying sensing range

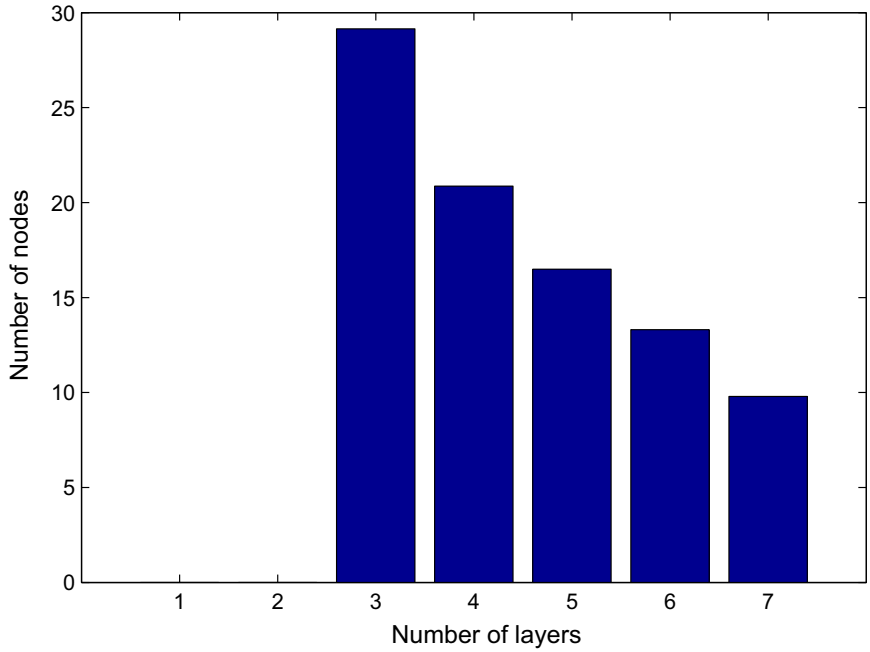


Fig. 4 Network coverage in various layerd architecture

plotted in the Fig. 5. The parameters namely network area and sensing radius are kept constant in order to analyse the lifetime of the network. It is seen that the lifetime of the network with both the deployment scheme is the same. It is observed from the figure that all the nodes die out approximately at the same time in both the schemes. Therefore, it can be said that the energy is balanced through out the network.

Coverage obtained in each layer using both the schemes i.e.,PBNDS and PDFND is plotted in Figs. 6 and 7. From the Fig. 6 it is noticed that the coverage obtained in $layer - 1$ is greater with respect to other successive layers namely layers 2, 3, 4, 5 and 6 respectively

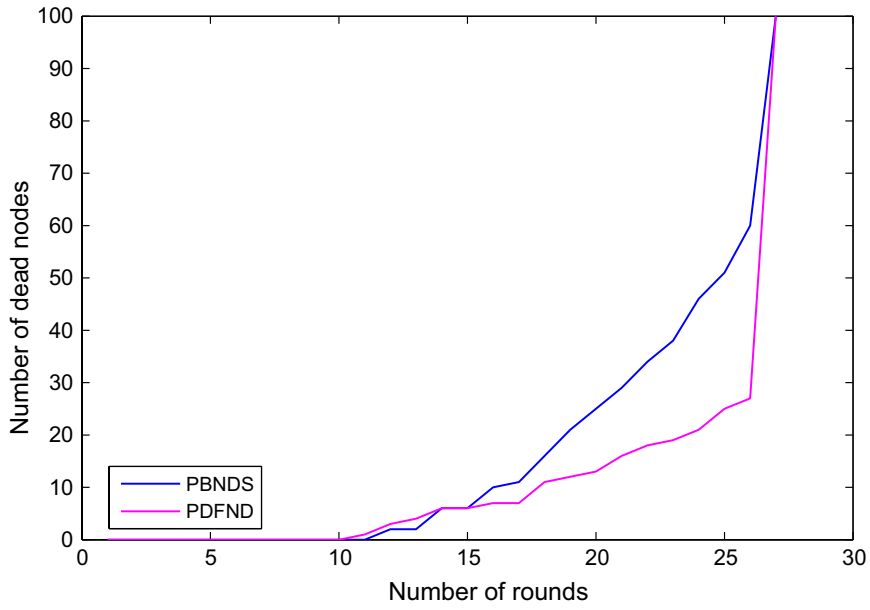


Fig. 5 Comparison of lifetime

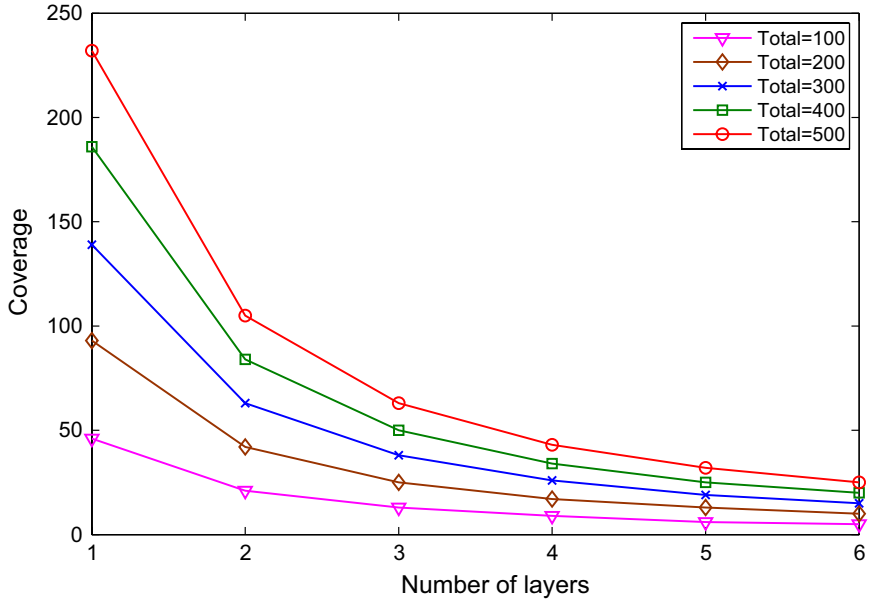


Fig. 6 Coverage obtained in each layer in PBNDS

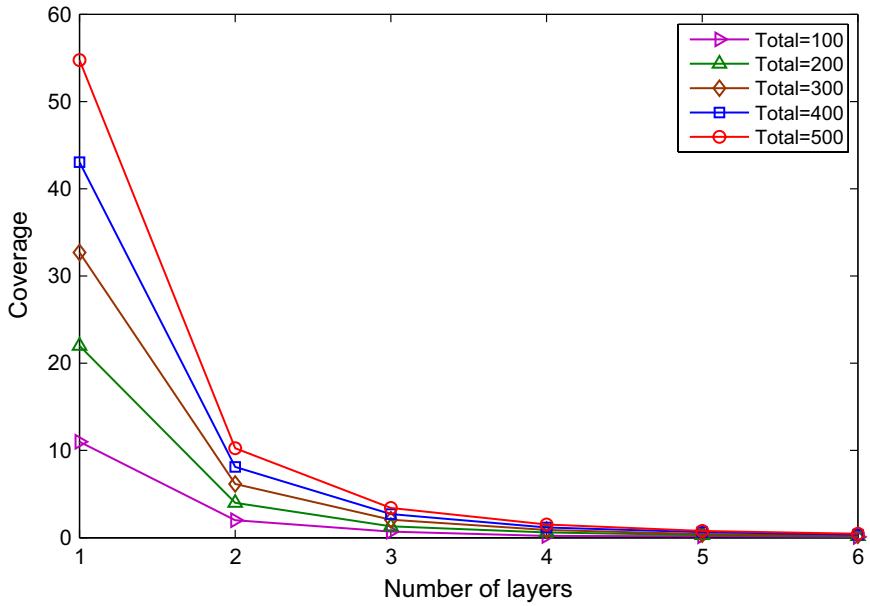


Fig. 7 Coverage obtained in each layer in PDFND

in all the cases where Total is 100, 200, 300, 400 and 500 in 6-*layered* architecture. Minimum and maximum coverage in each layer is obtained when nodes are distributed with $Total = 100$ and $Total = 500$ keeping the sensing radius R_s and the area of deployment field constant respectively. We also notice a gradual slope in all the considered cases. This is because the division of the deployment field is such that the area of each corona remains the same through the deployment field. Only the number of nodes distributed in each corona keep changing as one moves from the innermost to the outermost corona in the deployment field.

In case of PDFND, the network architecture is divided in such a way that the innermost corona has minimum area while the area increases exponentially as one moves from the center to the outer most corona. Also the number of nodes distributed with this scheme is inversely proportional to the area. In other words, the maximum number of nodes

distributed are in the innermost corona where the area is small while it is at its minimum where the area is large in this node distribution scheme. This type of deployment scheme affects the coverage parameter. This is evident from the result plotted Fig. 7. As observed from the figure, the maximum coverage obtained is in $layer - 1$ while it decreases in other successive layers in all the considered cases keeping all the other parameters such as area of the deployment field and sensing range of a node constant. A steep curve starting from $layer - 1$ to $layer - 6$ is observed in the graph. Maximum coverage is obtained in $layer - 1$ while it decreases exponentially in other consecutive layers in a 6-*layered* architecture.

The dead NoN for each iteration is plotted in Fig. 8. It is evident from the graph that if the nodes are disseminated according to the proposed strategy, the lifetime of WSN is increased. It is observed that when the node is distributed through the PBNDS, better coverage is obtained in all the layers when compared to the NDS through PDFND. Finally, the scheme was compared with all the NDSs in Fig. 9. The average energy consumed in each layer is calculated and is plotted as shown in figure. It is seen that in case of nodes distribution through using NDUD and NDGD, more energy is consumed in 1{st}-*layer* and decreases in other two layers. Therefore, it can be said that the energy consumption in each corona is not same or similar. Whereas, the energy consumption rate in other three schemes are nearly same. All the coronas in the considered architecture exhaust their energies nearly at the same times. This leads to the energy balanced network in WSN. Therefore, it can be concluded that the proposed scheme is superior as it avoids energy-hole problem and provides better coverage with the increase in the lifetime of the network.

7 Conclusion

In this paper, an energy efficient node distribution scheme for WSN is proposed. The considered network architecture is divided into a number of coronas with the BS positioned at the middle of the network. The division of the network is such that the area of each corona is kept the same. The node distribution scheme with the objective of better coverage and

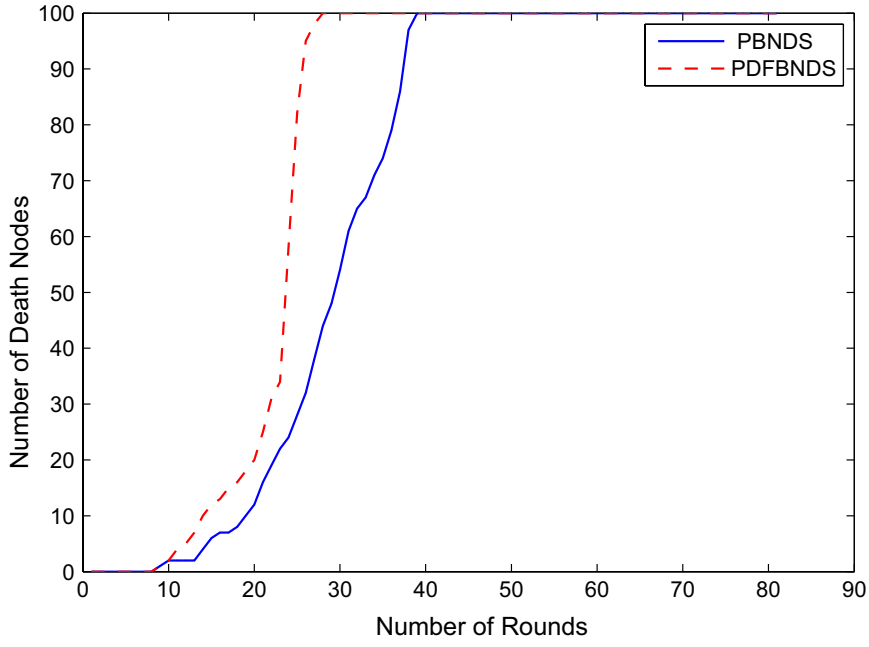


Fig. 8 Comparison of lifetime

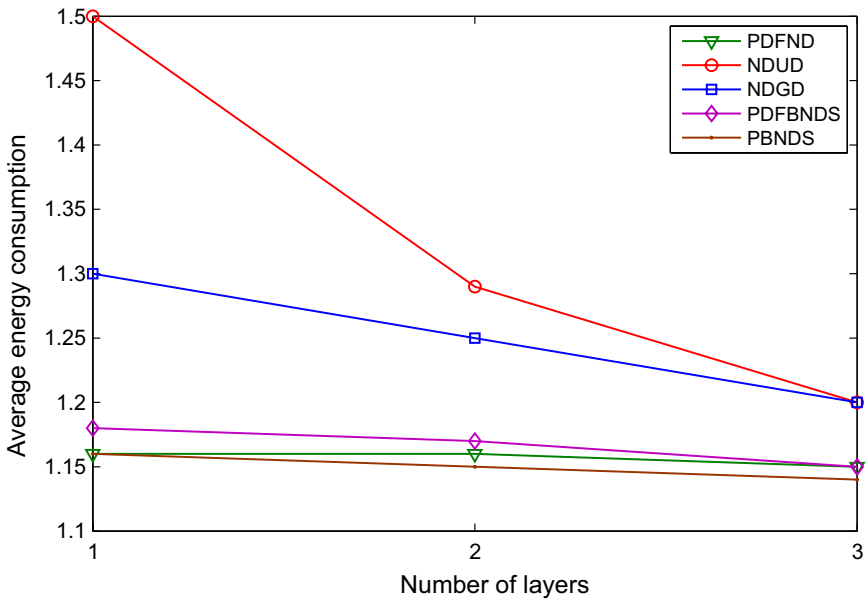


Fig. 9 Average energy consumption energy in each layer

energy efficient transmission based on PDF design is proposed. The proposed NDS is analysed with respect to the current NDSs such as NDUD, NDGD, PDFND and PDFBNDS. The performance of the proposed scheme is assessed based on the coverage and lifetime of the WSN. The outcome achieved through simulation confirm the superiority of the proposed node distribution scheme over other existing NDSs.

References

1. Mathew, J., Hauser, C., Stoll, P., Kenel, C., Polyzos, D., Havermann, D., et al. (2017). Integrating fiber fabry-perot cavity sensor into 3-d printed metal components for extreme high-temperature monitoring applications. *IEEE Sensors Journal*, *17*(13), 4107–4114.
2. Mishra, R., Jha, V., Tripathi, R. K., & Sharma, A. K. (2017). Energy efficient approach in wireless sensor networks using game theoretic approach and ant colony optimization. *Wireless Personal Communications*, *95*(3), 3333–3355.
3. Mishra, R., Kumar, P., Chaudhury, S. & Indu, S. (2013). Monitoring a large surveillance space through distributed face matching. In *2013 Fourth national conference on computer vision, pattern recognition, image processing and graphics (NCVPRIPG)* (pp. 1–5).
4. Rajwade, K. C., & Gawali, D. H. (2016). Wearable sensors based pilgrim tracking and health monitoring system. In *2016 International conference on computing communication control and automation (ICCUBEA)* (pp. 1–5).
5. Lin, S. C., Alshehri, A. A., Wang, P., & Akyildiz, I. F. (2017). Magnetic induction-based localization in randomly deployed wireless underground sensor networks. *IEEE Internet of Things Journal*, *4*(5), 1454–1465.
6. Tanenbaum, A. S., Gamage, C., & Crispo, B. (2006). Taking sensor networks from the lab to the jungle. *Computer*, *39*(8), 98–100.
7. Meng, S., Kashyap, S. R., Venkatramani, C., & Liu, L. (2012). Resource-aware application state monitoring. *IEEE Transactions on Parallel and Distributed Systems*, *23*(12), 2315–2329.
8. Dempsey, T., Sahin, G., Morton, Y. T., & Hopper, C. M. (2009). Intelligent sensing and classification in ad hoc networks: A case study. *IEEE Aerospace and Electronic Systems Magazine*, *24*(8), 23–30.
9. Li, J., & Mohapatra, P. (2007). Analytical modeling and mitigation techniques for the energy hole problem in sensor networks. *Pervasive and Mobile Computing*, *3*(3), 233–254.
10. Li, J., & Mohapatra, P. (2005). An analytical model for the energy hole problem in many-to-one sensor networks. In *2005 IEEE 62nd vehicular technology conference on VTC-2005-Fall* (Vol. 4, pp. 2721–2725).

11. Olariu, S. & Stojmenovic, I. (2006). Design guidelines for maximizing lifetime and avoiding energy holes in sensor networks with uniform distribution and uniform reporting. In *Proceedings IEEE INFOCOM 2006, 25th IEEE international conference on computer communications* (pp. 1–12).
12. Stojmenovi, I., & Olariu, S. (2005). *Data-centric protocols for wireless sensor networks* (pp. 417–456). New York: Wiley.
13. Lian, J., Naik, K., & Agnew, G. B. (2006). Data capacity improvement of wireless sensor networks using non-uniform sensor distribution. *International Journal of Distributed Sensor Networks*, *2*(2), 121–145.
14. Liu, Y., Ngan, H., & Ni, L. M. (2006). Power-aware node deployment in wireless sensor networks. In *IEEE international conference on sensor networks, ubiquitous, and trustworthy computing (SUTC'06)* (Vol. 1, p. 8).
15. Halder, S., Ghosal, A., Chaudhuri, A., & DasBit, S. (2011). *A probability density function for energy-balanced lifetime-enhancing node deployment in WSN* (pp. 472–487). Berlin: Springer.
16. Halder, S., & DasBit, S. (2014). Design of a probability density function targeting energy-efficient node deployment in wireless sensor networks. *IEEE Transactions on Network and Service Management*, *11*(2), 204–219.
17. Halder, S., Ghosal, A., Chaudhuri, A., & DasBit, S. (2011). A probability density function for energy-balanced lifetime-enhancing node deployment in wsn. In *Proceedings of the 2011 international conference on computational science and its applications-volume part IV (ICCSA'11)* (pp. 472–487). Berlin: Springer.
18. Heinzelman, W. B., Chandrakasan, A. P., & Balakrishnan, H. (2002). An application-specific protocol architecture for wireless microsensor networks. *IEEE Transactions on Wireless Communications*, *1*(4), 660–670. https://doi.org/10.1109/TWC.2002.804190.
19. Farooq, M. O., Dogar, A. B., & Shah, G. A. (2010). Mr-leach: Multi-hop routing with low energy adaptive clustering hierarchy. In *2010 Fourth international conference on sensor technologies and applications (SENSORCOMM)* (pp. 262–268).
20. Ye, M., Li, C., Chen, G., & Wu, J. (2005). Eecs: An energy efficient clustering scheme in wireless sensor networks. In *IPCCC*.
21. Lara, R., Bentez, D., Caamao, A., Zennaro, M., & Rojo-lvarez, J. L. (2015). On real-time performance evaluation of volcano-monitoring systems with wireless sensor networks. *IEEE Sensors Journal*, *15*(6), 3514–3523.
22. Younis, O., & Fahmy, S. (2004). Heed: A hybrid, energy-efficient, distributed clustering approach for ad hoc sensor networks. *IEEE Transactions on Mobile Computing*, *3*(4), 366–379.
23. Soro, S., & Heinzelman, W. B. (2005). Prolonging the lifetime of wireless sensor networks via unequal clustering. In *19th IEEE international parallel and distributed processing symposium* (p. 8).
24. Ye, M., Li, C., Chen, G., & Wu, J. (2005). An energy-efficient unequal clustering mechanism for wireless sensor networks. In *IEEE international conference on mobile adhoc and sensor systems conference* (pp. 8–604).
25. Perillo, M., Cheng, Z., & Heinzelman, W. (2004). On the problem of unbalanced load distribution in wireless sensor networks. In *IEEE global telecommunications conference workshops. GlobeCom Workshops 2004.* (pp. 74–79).
26. Giridhar, A., & Kumar, P. R. (2005). Maximizing the functional lifetime of sensor networks. In *IPSN 2005, Fourth international symposium on information processing in sensor networks* (pp. 5–12).
27. Wang, W., Srinivasan, V., & Chua, K. C. (2005). Using mobile relays to prolong the lifetime of wireless sensor networks. In *Proceedings of the 11th annual international conference on mobile computing and networking (MobiCom '05)* (pp. 270–283). New York, NY: ACM.
28. Luo, J., & Hubaux, J. P. (2005). Joint mobility and routing for lifetime elongation in wireless sensor networks. In *Proceedings IEEE 24th annual joint conference of the IEEE computer and communications societies* (Vol. 3, pp. 1735–1746).
29. Bandyopadhyay, S., & Coyle E. J. (2003). An energy efficient hierarchical clustering algorithm for wireless sensor networks. In *INFOCOM 2003, twenty-second annual joint conference of the IEEE computer and communications* (Vol. 3, pp. 1713–1723). IEEE Societies.
30. Wang, D., Xie, B., & Agrawal, D. P. (2008). Coverage and lifetime optimization of wireless sensor networks with Gaussian distribution. *IEEE Transactions on Mobile Computing*, *7*(12), 1444–1458.
31. Wu, X., Chen, G., & Das, S. K. (2008). Avoiding energy holes in wireless sensor networks with nonuniform node distribution. *IEEE Transactions on Parallel and Distributed Systems*, *19*(5), 710–720.

32. Mishra, R., Jha, V., Tripathi, R. K., & Sharma, A. K. (2017). Design of probability density function targeting energy efficient network for coalition based WSNS. *Wireless personal communications, 99*(2), 651–680. https://doi.org/10.1007/s11277-017-5134-y.

Publisher's Note Springer Nature remains neutral with regard to jurisdictional claims in published maps and institutional affiliations.



Richa Mishra received M.E. degree from University of Mumbai, India in the year 2008. She has received Ph.D. Degree from National Institute of Technology, Delhi, India in the year 2018. She has served 5 years as Assistant Professor in Guru Gobind Singh Indraprastha University and Delhi Technological University (Formerly known as Delhi College of Engineering), India. She is currently working as an Assistant Professor in National Institute of Technology Delhi, India. Her current area of interest includes energy efficient protocols in wireless sensor network.



Rajeev K. Tripathi received Ph.D. degree from Indian Institute of Technology, Kanpur, India. He is currently working as an Assistant Professor in Electronics and Communication Engineering at National Institute of Technology, Delhi, India. His current area of interest includes clustering algorithms for Wireless Sensor Networks.



Ajay K. Sharma is working as Director at National Institute of Technology (An Institute of National Importance), Ministry of Human Resource Development, Government of India, New Delhi since October 2013. He received his BE in Electronics and Electrical Communication Engineering from Punjab University Chandigarh, India in 1986, M.S. in Electronics and Control from Birla Institute of Technology (BITS), Pilani in the year 1994 and Ph.D. in Electronics Communication and Computer Engineering in the year 1999. His Ph.D. thesis was on "Studies on Broadband Optical Communication Systems and Networks". After serving various organizations from 1986 to 1995, he has joined National Institute of Technology (Erstwhile Regional Engineering College) Jalandhar as Assistant Professor in the Department of Electronics and Communication Engineering in the year 1996. From November 2001, he has worked as Professor in the ECE department and thereafter he has worked as Professor in Computer Science and

Engineering from 2007 to 2013 in the same institute. His major areas of interest are broadband optical wireless communication systems and networks, dispersion compensation, fiber nonlinearities, optical soliton transmission, WDM systems and networks, Radio-over-Fiber (RoF) and wireless sensor networks and computer communication. He has published 290 research papers in the International/National Journals/Conferences and 12 books. He has supervised 22 Ph.D. and 52 M.Tech. theses. He has completed two R&D projects funded by Government of India and one project is ongoing. He was associated to implement the World Bank project of 209 Million for TEQIP-I programme of the institute. He has been appointed as member of technical Committee on Telecom under International Association of Science and Technology Development (IASTD) Canada for the term 2004–2007 and he is Life Member of Optical Society of America, USA, (LM ID-361253), Computer Society of India, Mumbai, India, (LM-Associate: 01099298), Advanced Computing and Communications Society, Indian Institute of Science, Bangalore, India, (L284M1100306), SPIE, USA, (ID: 619838), Indian Society for Technical Education (I.S.T.E.), New Delhi, India, (LM-11724), Fellow The Institution of Electronics and Telecommunication Engineers (IETE), (F-224647).

Journal of Materials Science & Surface Engineering, 6(5): 851-861
ISSN (Online): 2348-8956; 10.jmsse/2348-8956/6-5.1

Development of PALF/Glass and COIR/Glass Fiber Reinforced Hybrid Epoxy Composites

Mohit Mittal · Rajiv Chaudhary

Department of Mechanical, Production, and Industrial Engineering, Delhi Technological University, Delhi, 110042, India.

ABSTRACT

To meet the industrial and environmental policy regarding the selection of a material for structural applications, it becomes necessary to compound recyclable cellulosic material with the high-performance synthetic material. In this regard, the untreated and alkali treated PALF/Glass and Coir/Glass hybrid epoxy-based composites were developed by hand lay-up technique, keeping the total fiber to resin ratio 30:70 v/v. The hybrid composites were characterized in terms of tensile, flexural, impact, and water absorption properties according to the ASTM D 638, 790, 256, and 570 standards respectively. The results showed that the 15/15 (v/v) PALF/Glass hybrid composite has higher tensile and flexural properties as compared to the other hybrid formulations. The alkali treated 15/15 (v/v) PALF/Glass composite possess 35.13% higher flexural strength than that of pure Glass-Epoxy composite. Amongst all the developed materials, the mercerized 15/15 (v/v) Coir/Glass fiber reinforced epoxy composite exhibits the maximum impact strength and resistance to water molecules.
© 2018 JMSSE and Science IN. All rights reserved

ARTICLE HISTORY
Received 13-10-2018
Revised 04-09-2018
Accepted 06-11-2018
Published 27-11-2018

KEYWORDS
Pineapple leaf fiber
Coir fiber
Glass fiber
Epoxy matrix
Polymer composite
Mechanical properties

List of abbreviations

NFRC's	*Natural Fiber Reinforced Composites*
PALF	*Pineapple Leaf Fiber*
ASTM	*American Society for Testing and Materials*
OPEFB	*Oil Palm Empty Fruit Bunch Fiber*
DGEBA	*Di-Glycidal Ether Bisphenol A*
TETA	*Tri-Ethylene Tetra-Amine*
PG-EP	*Pineapple Glass-Epoxy Composite*
CG-EP	*Coir Glass-Epoxy Composite*
KP-PE	*Kenaf Pineapple-Polyethylene Composite*

Introduction

Natural fibers and their composites are received a lot of attention for the employment in varieties of engineering applications. This was because of their large number of profitable properties such as low cost, lightweight, high specific strength and stiffness, problem-free disposal at the end of use, energy and ecological balance, non-abrasive to molding and mixing equipment, recyclability, and biodegradability [1]. The progressive consumption of natural fibers in industrial and consumer goods will help to generate the local economy, and widening availability of the products to ordinary people at low cost. Among all the lignocellulosic materials, the pineapple leaf and coconut husk fibers are the most promising and desirable candidates to be select as a reinforcing agent in polymer-based materials. Pineapple and coir are multi-cellular fiber, extracted from the leaves of pineapple and the husk (mesocarp) of coconut fruit respectively. The primary reasons to select PALF and COIR fibers over the other natural fibers are: 1) Pineapple leaf fiber contains high cellulose (70-85%) content which results it has higher tensile and flexural properties than that of flax, sisal, jute, OPEFB, and cotton fibers. 2) Easy availability, low density, favourable aspect ratio, and low microfibrillar angle of PALF. 3) Coir fiber consists of high lignin content (40-45%) which makes it more durable and stable under a wide range of temperature, humid environmental conditions, and also has excellent resistant properties to microbial and fungus attack. Inspite of their fruitful features, the cellulosic fibers are far away to smoothly adopt in structural applications. It was due to the poor match between natural and synthetic fibers in the context of mechanical properties [2-5]. The most commonly used synthetic fiber is E-glass having good tensile and compressive properties. However, the higher cost, non-biodegradability, abrasive nature, and associated health hazards problems favour the exploration and exploitation of natural fibers [6]. In order to increase the probability of natural fibers as a preferred choice for semi-structural and structural applications, it becomes necessary to modify and improve their properties by the exploitation of hybridization and chemical treatment tools. The previous research work mentioned in Table 1 confirmed this fact and provide sufficient assurance to the benefits of fiber hybridization and chemical modifications. Hybrid composites offer the tailor-made properties at low cost according to the requirements for a particular application. The properties of a hybrid composite are mainly depends on the nature of reinforcing fibers and matrix; relative volume content of each kind of reinforcing fiber; arrangement, orientation, and distribution of fibers; morphology of the system; and the compatibility between fibers and matrix. The failing of one kind of fiber can be overcome by the hybridization with a suitable type of fiber. The positive hybridization is a result of synergistic compatibility between reinforcing fibers which results in the balanced combination of strength, stiffness, ductility, and toughness. In most of the cases, the hybrid composites have better and comparable performance to that of natural and synthetic fiber reinforced composites respectively. Therefore, the hybridization with synthetic glass fiber can surmount the problems of natural fibers. A high-performance structural material can be developed at a low cost by employing the hybridization concept. The incorporation of thermoset polymer as a matrix resin leads to the improvement in performance of a structural

Corresponding Author: Mohit Mittal, Tel: +91-9971698741
Email: mohit.30mittal@gmail.com
Contents lists available at http://www.jmsse.org/ & http://www.jmsse.in/
© 2018 Science IN. All rights reserved

Table 1: Previous research work reported on the hybrid and chemically treated natural fiber reinforced composites

Authors	Factors explored by researchers	Results	Reference
A. Atiqah et al. (2014)	Development and mechanical characterization of Kenaf/Glass reinforced polyester hybrid composites.	The hybrid composite reinforced with alkali-treated kenaf fiber and glass fiber in 15/15 (v/v) showed higher tensile, flexural, and impact strength than that of other hybrid formulations.	[7]
M. Jawaid et al. (2012)	Effect of Jute fiber loading on physical and chemical resistant properties of Jute/EFB-Epoxy hybrid composites.	Void content reduced and stability towards chemical reagents (benzene, toluene, CCl_4, HNO_3, CH_3COOH, NaOH, Na_2CO_3) increased with the increase of jute fiber content.	[8]
R. Ranjan et al. (2013)	Effect of alkali treatment on mechanical properties of Banana/Sisal fiber reinforced PLA composites.	The 2 wt% NaOH treated hybrid composite shows better mechanical properties (tensile, flexural, and impact strength) than that of untreated composites.	[9]
S. Panthapulakkal et al. (2006)	Mechanical, water absorption and thermal characterization of hybrid hemp/glass fiber reinforced-polypropylene composites.	Low cost and high performance composite was obtained by the hybridization of hemp and glass fibers. The tensile, flexural, and impact strength of Hemp/PP composite was increased with the incorporation of a small amount (15 wt%) of glass fiber. Glass fiber loading improves the thermal stability of Hemp-PP composite	[10]
A. Shahzad et al. (2011)	Effect of hybridization on impact and fatigue strength of Hemp/Glass fiber reinforced unsaturated polyester composites.	Impact and fatigue strength of Hemp/UPE composite was increased by the replacement of 11% hemp fiber with glass fiber.	[11]
M. Haq et al. (2008)	Development of hybrid composites from blends of UPE and soybean oil reinforced with nanoclay and hemp fiber	A Synergistic hybrid composite having balanced stiffness and toughness properties was developed by the partial substitution (10%) of UPE with EMS and reinforced with 1.5% nanoclay.	[12]
V.S. Chevali et al. (2015)	Effect of the loading of sunflower hull and distiller's dried grains fiber on the physical properties of ABS polymer.	Tensile, Flexural, and impact strength was reduced with the addition of SFH and DDGS filler in ABS polymer. It showed the poor compatibility between reinforcing fillers and polymer.	[13]
M.M Davoodi et al. (2011)	Compared the overall performance of hybrid kenaf/glass-epoxy composite with traditionally used GMT material in car bumper beam	The Kenaf/Glass fiber reinforced hybrid epoxy composite in double hat profile (DHP) has significant potential to be used in small-sized car bumper beam.	[14]
P.J Jandas et al. (2011)	Effect of chemical treatment on mechanical properties of PLA/Banana fiber reinforced composites.	Tensile strength, impact strength, glass transition temperature, and storage modulus was increased by the effect of chemical treatments (NaOH, APS, and Si69) on PLA/Banana fiber biocomposites.	[15]
L.Y. Mwaikambo et al. (2001)	Alkalization of hemp, sisal, jute, and kapok fibers.	Mechanical properties and thermal stability were improved by the alkali treatment.	[16]
M.J. John et al. (2008)	Effect of chemical modification on the properties of Sisal/OPEFB hybrid composite.	The 4% NaOH treated Sisal/OPEFB fiber reinforced natural rubber hybrid composite exhibits maximum tensile strength and torque value with minimum swelling index.	[17]
Xue Li et al. (2007)	Chemical treatments of natural fiber for high strength biocomposite material.	Alkali treatment significantly improves the static and dynamic mechanical properties of NFRC's with the increased resistance to moisture sorption.	[18]
M.J. John et al. (2007)	Characterization of chemically modified NFRC's.	Alkali treatment is one of the most efficient and reliable chemical treatments which favors the formation of a strong covalent bond between fibers and matrix.	[19]
V.S. Uppin et al. (2016)	Interlaminar fracture toughness of Glass/Cellulose fiber reinforced epoxy composites	Interlaminar fracture toughness of Glass-Epoxy composite was increased by 32% with the incorporation of cellulose fiber.	[20]

©2018 Science IN. All rights reserved

Table 1: continues....

F. Cheng et al. (2014)	Characterization of Glass/Coir fiber reinforced polyester composites.	The improvement in flexural strength (419%), modulus of elasticity (708%), and impact strength (562%) was observed by the addition of glass fabrics in coir-polyester composites.	[21]
L. Uma Devi et al. (2011)	Effect of chemical treatment (NaOH and vinyl silane) and glass fiber content on the water absorption behavior of PALF/GF reinforced polyester composites.	Alkaline treated hybrid composites having 0.46 V_f content of glass fiber possess lowest water sorption affinity.	[22]
V.K. Bhagat et al. (2014)	Study of physical and mechanical properties of Coir/Glass hybrid epoxy composites.	The hybrid epoxy based composite consists of 10 wt% coir fiber (15 mm length) and 20 wt% glass fiber revealed the maximum mechanical strength.	[23]
M. Rahman et al. (2018)	Effect of alkali treatment, fiber content, and fiber volume ratio on the mechanical properties of Banana/PALF fiber reinforced hybrid polypropylene composites.	The hybrid composite reinforced with NaOH treated PALF and Banana fiber at a ratio of 3:1 with a 5 wt% total fiber content showed the best set of mechanical properties.	[24]
V. Arumugaprabhu et al. (2016)	Mechanical characterization of Palmyra/Coir fiber reinforced polyester hybrid composites.	Tensile, flexural, and impact strength of Palmyra/Polyester composite was increased by the hybridization with Coir fiber in ratio of 40:60 (Palmyra/Coir).	[25]
N.M. Nurazzi et al. (2018)	Effect of fiber hybridization on mechanical properties of Sugar palm/Glass fiber reinforced polyester composites.	The hybrid composite reinforced with 40 wt% fiber in the ratio of 50:50 (Sugar palm yarn: Glass fiber) revealed the higher tensile, flexural, and compressive strength than that of other hybrid formulations.	[26]
H.P.S Abdul Khalil et al. (2017)	Effect of the loading of coconut shell nano-fillers on the mechanical properties of kenaf/coconut fiber reinforced composites.	The incorporation of coconut shell nano-fillers up to 3 wt% leads to the increment in tensile, flexural, and impact strength of kenaf/coconut fiber reinforced composites.	[27]
A. Atiqah et al. (2018)	Effect of chemical treatment on the mechanical properties of Sugar Palm/Glass fiber reinforced polyurethane composites.	The tensile, flexural, and impact strength of a hybrid composite was improved by 16%, 39%, and 18% respectively by the chemical treatment with 6 wt% alkaline + 2 wt% silane.	[28]
IS. Aji et al. (2012)	Effect of hybridization on mechanical properties and water absorption behavior of Kenaf/PALF fiber reinforced HDPE composites.	Tensile and flexural properties of Kenaf/HDPE composite were increased by the hybridization with pineapple leaf fiber. The equal volume content of PALF and Kenaf in HDPE matrix possess the optimum mechanical properties.	[29]
B. Bakri et al. (2017)	Effect of relative fiber volume content on the mechanical properties of Coir/Angustifolia Haw Agave fiber reinforced epoxy composites.	The hybrid composite reinforced with 15:15 v/v (Coir: Agave) yields higher tensile strength, tensile modulus, and flexural modulus than that of other hybrid formulations (Coir: Agave = 10:20 and 20:10).	[30]
A. Oushabi et al. (2017)	Effect of alkali treatment on mechanical and thermal properties of date palm fiber-polyurethane composites.	The tensile strength, interfacial bond strength, and thermal stability of DPF composites were increased by the effect of alkali treatment. The optimal concentration for alkali treatment of DPF is 5 wt%.	[31]
K. Panyasart et al. (2014)	Effect of alkaline treatment on the mechanical properties of PALF/Polyamide 6 composites.	The tensile strength and modulus of composites was increased by the alkali treatment of pineapple leaf fiber which leads to the increased interfacial adhesion between treated PALF and polyamide matrix resin.	[32]

composite material for outdoor applications. The epoxy resin is a best suitable thermoset matrix for use in primary construction and marine industry. It was due to the high mechanical and electrical properties; good resistance to chemicals, moisture, and environmental degradation; good adhesive properties; low viscosity with easy processing; and easily cured at a temperature from 5^0C to 150^0C. In the present research work, the two different kinds of epoxy based hybrid composites (PALF/Glass and Coir/Glass) were developed and characterized their mechanical

©2018 Science IN. All rights reserved

properties. Moreover, the effect of relative fiber volume content and the alkaline treatment on mechanical properties and water absorption behavior of PALF/Glass and Coir/Glass fiber reinforced hybrid epoxy composites have been also investigated.

Experimental

Materials

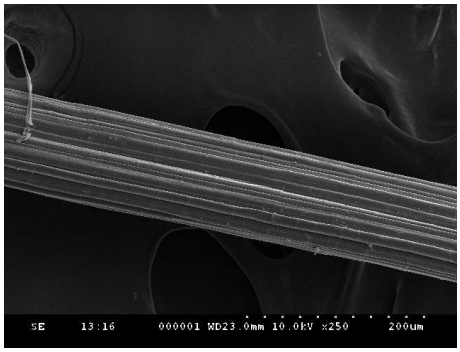
The chopped strand glass fiber mat (E-glass), coconut husk fiber (*Cocos-nucifera*), and pineapple leaf fiber (*Ananas-comosus*) were all obtained from M/s Go Green Products Chennai, India. Both type of cellulosic fibers (PALF and COIR) were of the long form and cut into the length of 20 mm by scissor. The glass fiber mat was also cut according to the size of the mold (200 X 100 X 4 mm^3). To impregnate the dried cellulosic and synthetic fibers in an open glass mold cavity, the medium viscosity epoxy thermoset resin was used. The epoxy resin (DGEBA) and curing agent (hardener, TETA) were procured from M/s Sakshi Dies and Chemicals, Delhi, India. The physical properties of reinforcing fibers (PALF, COIR, and E-GLASS) and the matrix resin are reported in Table 2 and 3 respectively. Sodium hydroxide (NaOH) used for mercerization (alkali treatment) was of laboratory reagent and received from the Chemistry Department, DTU (Delhi), India. The surface morphology of untreated and alkali treated pineapple leaf and coir fibers are depicted in Figure 1 and 2 respectively.

Table 2: Physical properties of Pineapple leaf, Coir, and E-Glass fiber

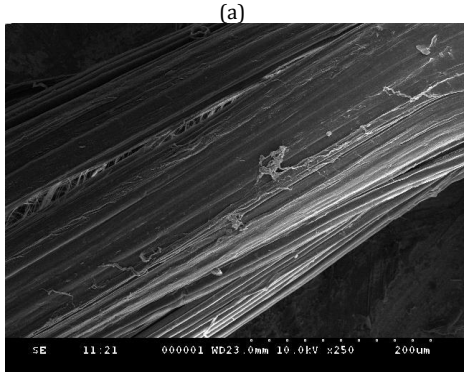
Physical properties	Pineapple leaf fiber	Coir fiber	E-Glass fiber
Density (g/cm^3)	0.98	1.2	2.55
Cellulose (%)	70-82	32-43	-
Hemicellulose (%)	18.8	0.15-0.25	-
Lignin (%)	5-12.7	40-45	-
Pectin (%)	1.1	3-4	-
Moisture content (%)	11.8	8	-
Microfibrillar angle (deg)	14	30-49	-
Diameter (µm)	20-80	100-460	<17
Tensile strength (MPa)	413-1627	131-220	3400
Young's modulus (GPa)	34.5-82.5	4-6	73
Elongation at break (%)	1.6	15-40	2.5

Table 3: Physical properties of epoxy thermoset matrix

The appearance of liquid resin	A clear pale yellow
Density (Kg/m^3)	1200-1250
Viscosity at 25^{0}C (cps)	550
Tensile strength (MPa)	11-15
Tensile modulus (GPa)	0.45-0.52
Flexural strength (MPa)	23-28
Flexural modulus (GPa)	1.3-1.7
Max. Elongation (%)	4.2-5.6
Impact strength (kJ/m^2)	1.2
Flashpoint	> 200^{0}C

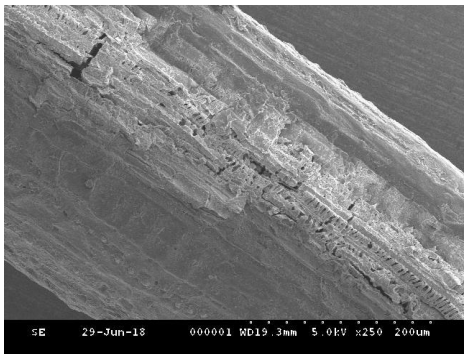


(a)

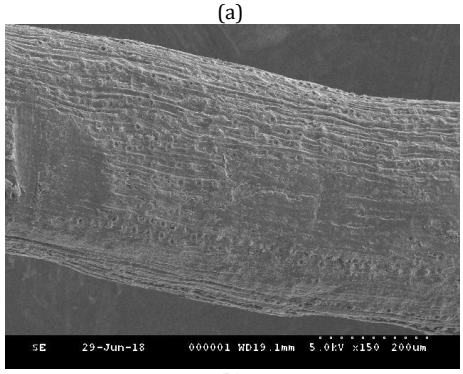


(b)

Figure 1: Surface morphology of Pineapple leaf fiber (a) Untreated, (b) 4% alkaline treated



(a)



(b)

Figure 2: Surface morphology of Coir fiber (a) Untreated, (b) 4% alkaline treated

Alkaline treatment of natural fibers

In order to ameliorate the interfacial interaction between natural fibers (PALF and COIR) and epoxy thermoset resin, the most commonly used chemical treatment known as 'mercerization' was employed. Initially, both type of fibers were washed in tap water and dried in sunlight for 3 days to remove the surface impurities and absorbed water

©2018 Science IN. All rights reserved

molecules. The cleaned and dried cellulosic fibers were immersed in 4 wt% alkali (NaOH) solution for 24 hr at room temperature, followed by the treatment with 2 wt% acetic acid (CH_3COOH) solution and then rinsed in distilled water to control the pH level at 7. The neutralized wet fibers were dried again at room temperature for 24 hr and then followed by oven drying at 70^0C for 24 hr (until the constant weight was obtained).

Development of hybrid composites

For the molding of a biocomposite sheet, two thick glass plates of same dimensions (250 mm X 150 mm X 3mm) are used. A hand lay-up method was employed to position the reinforcing fibers in the desired pattern and to impregnate them with the viscous thermoset resin. Before the sheet molding process, it is highly desirable to treat the mold surface with a releasing wax (*Mirror Glaze*) to avoid the sticking of adhesive polymer epoxy matrix to the mold surface and for easy removal of the developed composite parts. Figure 3 shows the arrangement of glass and cellulosic fibers with an epoxy matrix in a glass mold cavity. Before the molding process, ensure that the epoxy resin (DGEBA) and the hardener (TETA) were uniformly mixed and no air bubbles were present. The surface of the mold must be smoothen and flatten which confirms the good surface finish of a molded part. During the fabrication of a laminate sheet, the air bubbles are abstracted carefully by using a steel roller. To obtain good results, ensure that the fiber and matrix content per unit area of the mold is constant and the fibers were completely impregnated with the matrix resin. In the end, closed the mold and then pressed with external heavy weight for 24 hrs curing at room temperature. Table 4 depicts the designation and composition of developed hybrid composites. The four samples of each composite specimen were cut from the molded sheet as per ASTM standard for tensile, flexural, impact, and water absorption tests.

Characterization of developed composites

To characterize the physical properties of developed hybrid composites, the tensile, flexural (*3 point bending*), impact, and water absorption tests were performed as per ASTM D 638, 790, 256, and 570 standards respectively. The tensile and flexural bending tests were carried out on calibrated Table Top Tinius Olsen Horizon H50KS, Universal Testing Machine. While the impact strength was determined by using an Izod impact tester (installed in the SOM Laboratory, DTU (Delhi), India). All the tests were performed at room temperature and their important details with standardized dimensions of test specimens are reported in Table 5. The total of four samples for each composite specimen was tested and their mean values were reported.

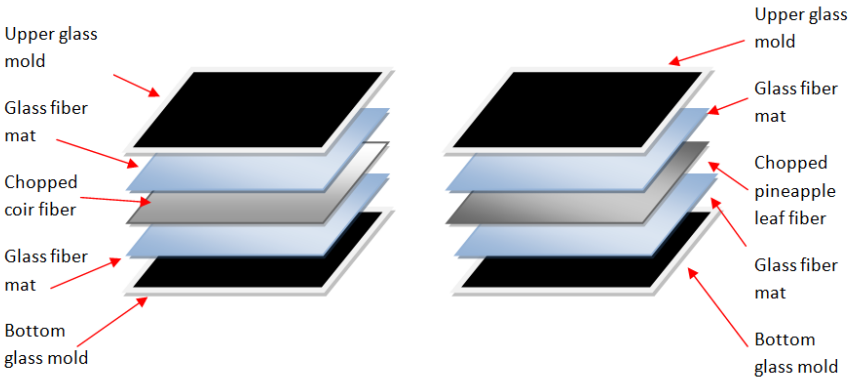


Figure 3: Schematic diagram of fibers sequence in an open glass mold

Table 4: Designation and composition of developed PALF/Glass and Coir/Glass hybrid composites

Designation		Composition
Un-treated	S1	Epoxy (70 vol.%) + untreated pineapple leaf fiber (30 vol.%)
	S2	Epoxy (70 vol.%) + untreated pineapple leaf fiber (20 vol.%) + chopped E-glass fiber mat (10 vol.%)
	S3	Epoxy (70 vol.%) + untreated pineapple leaf fiber (15 vol.%) + chopped E-glass fiber mat (15 vol.%)
	S4	Epoxy (70 vol.%) + untreated pineapple leaf fiber (10 vol.%) + chopped E-glass fiber mat (20 vol.%)
	S5	Epoxy (70 vol.%) + chopped E-glass fiber mat (30 vol.%)
	S6	Epoxy (70 vol.%) + untreated coir fiber (10 vol.%) + chopped E-glass fiber mat (20 vol.%)
	S7	Epoxy (70 vol.%) + untreated coir fiber (15 vol.%) + chopped E-glass fiber mat (15 vol.%)
	S8	Epoxy (70 vol.%) + untreated coir fiber (20 vol.%) + chopped E-glass fiber mat (10 vol.%)
	S9	Epoxy (70 vol.%) + untreated coir fiber (30 vol.%)
Treated	S1	Epoxy (70 vol.%) + treated pineapple leaf fiber (30 vol.%)
	S2	Epoxy (70 vol.%) + treated pineapple leaf fiber (20 vol.%) + chopped E-glass fiber mat (10 vol.%)
	S3	Epoxy (70 vol.%) + treated pineapple leaf fiber (15 vol.%) + chopped E-glass fiber mat (15 vol.%)
	S4	Epoxy (70 vol.%) + treated pineapple leaf fiber (10 vol.%) + chopped E-glass fiber mat (20 vol.%)
	S6	Epoxy (70 vol.%) + treated coir fiber (10 vol.%) + chopped E-glass fiber mat (20 vol.%)
	S7	Epoxy (70 vol.%) + treated coir fiber (15 vol.%) + chopped E-glass fiber mat (15 vol.%)
	S8	Epoxy (70 vol.%) + treated coir fiber (20 vol.%) + chopped E-glass fiber mat (10 vol.%)
	S9	Epoxy (70 vol.%) + treated coir fiber (30 vol.%)

©2018 Science IN. All rights reserved

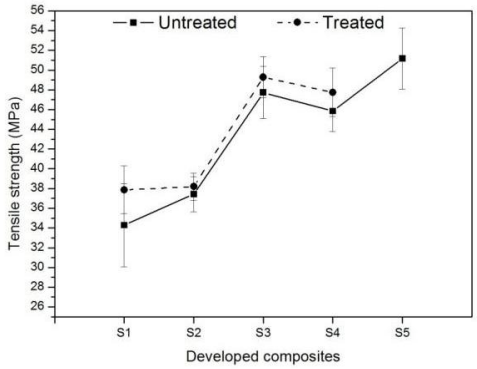
Table 5: Important test details and standardized dimensions of test specimens

Test details	Formulas used	Specimen dimensions
Tensile test (Cross head speed = 1mm/min)	$\sigma_t = \frac{F}{bt}$ Young's modulus = Tensile stress/Tensile strain	Flat dog-bone shape (50 mm gauge length, 13 mm width, and 4 mm thickness)
Flexural test (Cross head speed = 3mm/min)	$\sigma_f = \frac{3FL}{2bt^2}$ Flexural strain = $\frac{6st}{L^2}$ Flexural modulus = $\frac{L^3F}{4sbt^2}$	80 mm (l) X 15 mm (b) X 4 mm (t); Span length to depth ratio = 20:1
Izod impact test	Impact strength = Total absorbed energy (kJ)/Area (m^2)	65 mm (l) X 13 mm (b) X 4 mm; Notch angle = 45^0;
Water absorption test (Immersion time = 120 hr)	$Weight\ gain\ (\%) = \frac{(W_t - W_0)}{W_0} \times 100$ where W_t and W_0 are the weight of the specimen after immersion time "t" and the oven dried weight respectively	20 mm (l) X 20 mm (b) X 4 mm

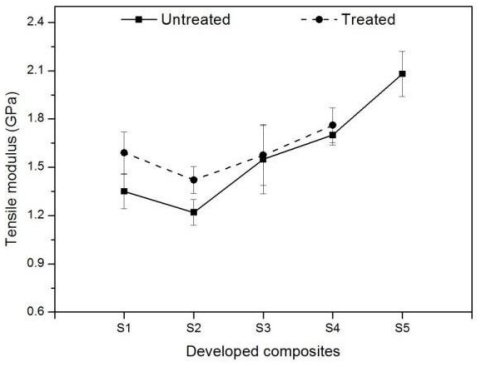
Results and Discussion

Tensile Properties

The tensile properties (strength and modulus) of developed PALF/Glass and Coir/Glass hybrid epoxy composites are shown in Figure 4 and 5 respectively. It was observed that the tensile properties of alkali treated hybrid composites were slenderly better than the untreated composite materials. The strength and modulus values of specimens S1 (pure PALF-Epoxy composite) and S9 (pure COIR-Epoxy composite) were increased by (9.45% and 3.7%) and (44.75% and 48.93%) respectively by alkali treatment. This was because of the better compaction, consolidation, and adhesion of treated reinforcements in the thermoset polymer matrix. Similar results of mercerization were reported by M.J John et al. [17] on sisal and OPEFB reinforced natural rubber composites. From Figure 4, it is clear that the NaOH treated 15/15 (v/v) PALF/Glass hybrid material possess higher and comparable tensile strength than that of other hybrid formulations and to the pure E-glass/epoxy composite respectively. This can be attributed to the synergistic compatibility between cellulosic and glass fiber at this relative volume fraction which results in the effective and uniform transfer of load from fiber to fiber and matrix to fibers without the cracking of matrix. The NaOH treated coir fiber reinforced composite having equal volume content of coir and glass fiber (15/15 v/v, sample S7) showed higher stiffness as compared to the other hybrid specimens (S6, S8, and S9). It was due to the rapid and effective stress transfer from viscoelastic medium to reinforcing fibers without the substantial deformation of thermoset matrix, an absence of localized stress concentration, and the presence of optimum total fiber to resin ratio and coir to glass fiber relative volume content. The surface of treated coir fiber being roughens with regularly placed pinholes due to the removal of fatty, waxy, and lignin compounds (Figure 2) which leads to the improvement in the interfacial interaction between fiber and matrix. The PALF reinforced epoxy material has higher tensile strength and modulus than that of Coir/Epoxy composite (As expectedly). This was because of the better inherent tensile properties of pineapple leaf fiber.

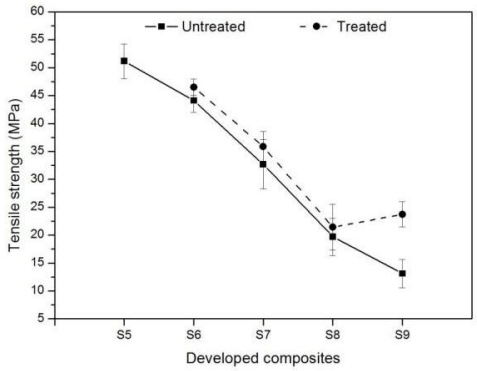


(a)



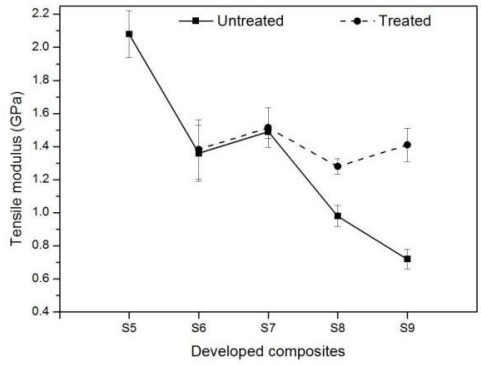
(b)

Figure 4: Tensile properties of untreated and alkali treated PALF/Glass fiber reinforced hybrid epoxy composites (a) Tensile strength, (b) Tensile modulus



(a)

©2018 Science IN. All rights reserved
Contents lists available at http://www.jmsse.org/ & http://www.jmsse.in/



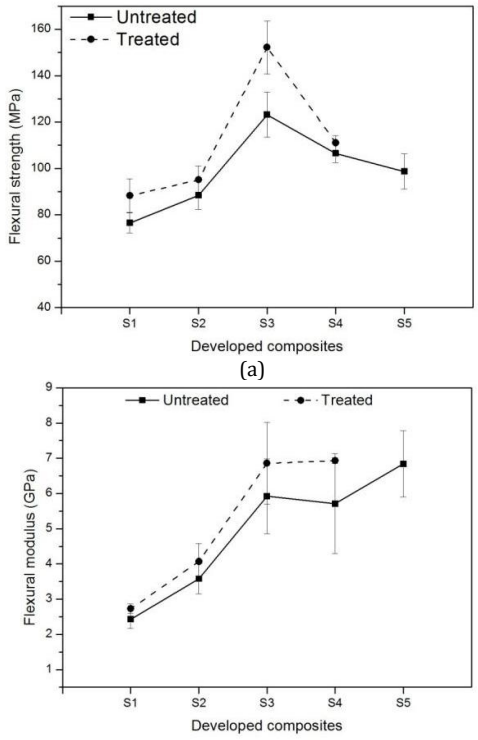
(b)

Figure 5: Tensile properties of untreated and alkali treated Coir/Glass fiber reinforced hybrid epoxy composites (a) Tensile strength, (b) Tensile modulus

From Fig. 4 and 5, it can be observed that the tensile properties of Glass/Epoxy composite were reduced with the increase of pineapple leaf or coir fiber volume content. This outcome was attributed to the better strength and stiffness of glass fiber than that of PALF and COIR fibers (Table 2). However, the hybrid composite consists of alkaline treated 15/15 (v/v) PALF/Glass fiber shows soundly mechanical behavior which results it can compete with pure synthetic fiber reinforced composites and can be employed as a structural material in automotive application.

Flexural Properties

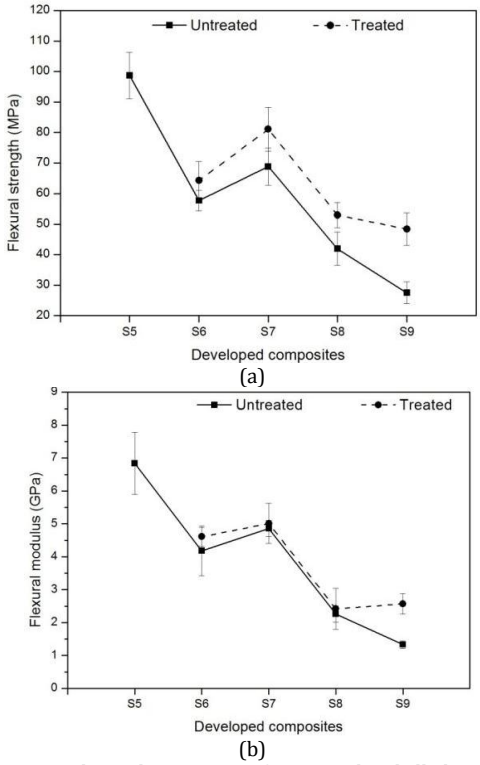
The flexural or 3 point bending test on fabricated composites (PALF/Epoxy, Coir/Epoxy, PALF/Glass/Epoxy, Coir/Glass/Epoxy, and Glass/Epoxy) was performed as per ASTM D 790 standard and the test results are reported in Figure 6 and 7. Similar to the tensile test results, the chemically treated (4% NaOH) fiber reinforced unhybridized and hybridized epoxy-based composites exhibit typically greater values of flexural strength and modulus as compared to the untreated composites. The treated PALF/Glass hybrid composites (Specimen S3 and S4) possess higher values of flexural properties than that of pure Glass/Epoxy material. It is worth to note that the flexural strength and modulus of treated 15/15 (v/v) PALF/Glass hybrid composite was highest amongst all the composite specimens. This was mainly because of the rapid and effective stress transfer from matrix to fiber, restrictions to crack propagation along the fiber-matrix interface, and increased shear and tear resistance of fibers with better dispersion and distribution. Moreover, fiber fibrillation (*avulsion of fiber bundles into individual fibers*) as a result of mercerization takes place which elevates the fiber effective surface area for bonding with the matrix resin. In a flexural bending test, the specimen was subjected to tensile, compressive, and shear load at the lower, upper, and axisymmetrical plane respectively. As we increase the coir fiber volume content in Coir/Glass-epoxy composite, the flexural strength decreases considerably. However, this trend was in opposite situation as compared with PALF/Glass hybrid composites in which the flexural strength increases with the incorporation of pineapple leaf fiber up to 15% V_f ($V_f = 0.3V_c$). This kind of different behavior was due to the poor interaction between coir and glass fiber as compared to the PALF-Glass fiber. The alkali treated pineapple leaf fiber reinforced 15/15 (v/v) PALF/Glass hybrid composite revealed 35.13%, 41.98%,



(a)

(b)

Figure 6: Flexural properties of untreated and alkali treated PALF/Glass fiber reinforced hybrid epoxy composites (a) Flexural strength, (b) Flexural modulus



(a)

(b)

Figure 7: Flexural properties of untreated and alkali treated Coir/Glass fiber reinforced hybrid epoxy composites (a) Flexural strength, (b) Flexural modulus

and 68.21% higher bending strength as compared to the Glass/Epoxy, treated PALF/Epoxy, and Coir/Epoxy composite respectively. Moreover, it can be observed that

©2018 Science IN. All rights reserved

the alkali treated pineapple leaf fiber exert a great impact on tensile and flexural properties of hybrid composites. Ultimately, we can conclude that the 15/15 PALF/Glass hybrid material with treated pineapple leaf fiber is the optimum one which displays better mechanical properties (tensile strength, flexural strength, and flexural modulus) amongst the other hybrid formulations.

Impact strength

The impact strength of developed PALF/Glass and Coir/Glass hybrid composites is shown in Figure 8 and 9 respectively. After the examination of test results, we can easily state that the alkaline treated (4% NaOH) fiber reinforced composites depicts higher values of strength during impact loading as compared to the untreated single and hybrid composite materials. In both cases (PALF/Glass and Coir/Glass), the mercerized 15/15 (v/v) hybrid composites [Sample S3 and S7] exhibit greater impact toughness amongst all the reinforced materials. The treated 15/15 (v/v) PALF/Glass and Coir/Glass hybrid specimens possess 18.24% and 38.84% higher impact strength than the single Glass/Epoxy composite respectively.

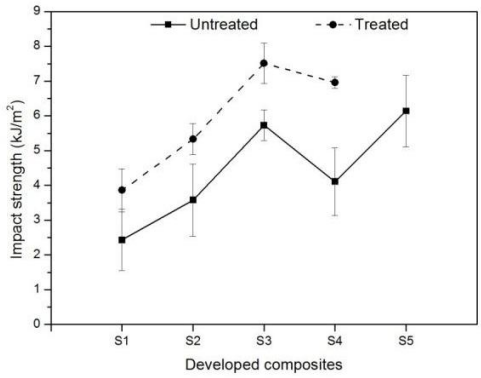


Figure 8: Impact strength of untreated and alkali treated PALF/Glass fiber reinforced hybrid epoxy composites

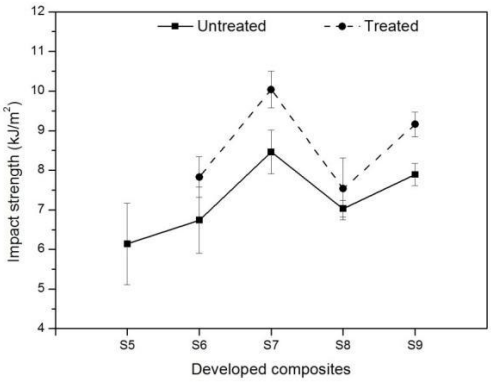


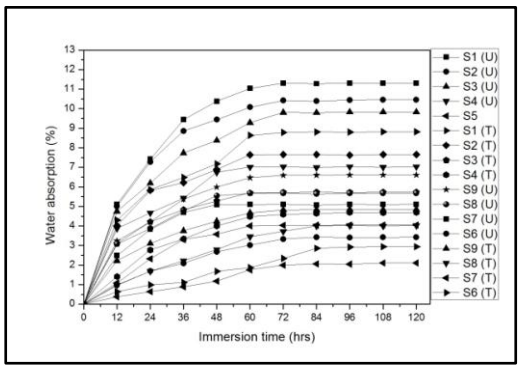
Figure 9: Impact strength of untreated and alkali treated Coir/Glass fiber reinforced hybrid epoxy composites

It was due to the synergistic hybridization between cellulosic and synthetic fiber; and positive attributes of alkaline treatment against the surface impurities, wax, pectin, and hemicellulose content which leads to the higher interfacial bond strength, less void content and higher restrictions to crack propagation along the interface between fiber and matrix. The overall impact strength of a polymer-based composite material mainly depends on the ability of the matrix to transfer load uniformly and efficiently to reinforcing fibers. It was observed that the coir fiber reinforced unhybridized and hybridized composites have a higher value of impact strength than that of pineapple leaf fiber reinforced composites. This was attributed to the greater value of the microfibrillar angle in COIR fiber (15-40^0). The impact strength of Glass/Epoxy composite was significantly improved by the addition of treated pineapple leaf or coir fiber up to 15% of total fiber volume content. The impact resistance of a hybrid fibrous material is greatly depends on the yarn geometry and structure, orientation and arrangement of each kind of fibers in a matrix material, inherent ability of fibers to dissipate or absorb energy, and their relative volume content in the same matrix system. The treated and untreated pure coir and pineapple leaf fiber reinforced composites absorbs less amount of energy or shows brittleness in comparison to 15/15 (v/v) hybrid specimen. From all the three crucial mechanical tests (Tensile, Flexural, and Impact), we can conclude that the alkaline treated hybrid composites (PALF/Glass, 15/15 v/v) and (Coir/Glass, 15/15 v/v) are the most appropriate material which shows substantial higher tensile, flexural and impact properties respectively.

Water absorption

The moisture sorption demeanour of untreated and alkali treated pineapple leaf fiber and coir fiber reinforced composites as a special reference of immersion time is depicted in Figure 10. It can be easily conclude that the composites consist of chemically treated fibers have better dimensional stability in a humid environment than that of untreated NFRC's. From the experimental test results reported in Figure 13, it was observed that the NaOH treated pineapple leaf fiber [S1 (T)] and coir fiber [S9 (T)] reinforced composites absorbs 22.01% and 26.62% less water than that of untreated pure PALF/Epoxy [S1 (U)] and Coir/Epoxy [S9 (U)] Composites. This was because of the removal of hydroxyl and polar functional groups as a result of mercerization which leads to the greater compatibility and adhesion between reinforcing fibers and matrix. Figure 11 clearly demonstrates that the dimensional stability of Glass/Epoxy composite [S5] in wet conditions was deteriorated with the incorporation of untreated and alkali treated pineapple leaf fiber. In all cases, the amount of water absorption increases linearly with the immersion time up to 72 hr and then becomes saturated (moisture equilibrium condition) at 120 hr. The composites reinforced with coconut husk fiber have better impedance to water molecules than that of pineapple leaf fiber reinforced composites. This was attributed to the presence of more hydrophobic lignin and waxy substances on the surface of COIR fiber. From Figure 10 and 12, we can finally conclude that the treated hybrid composite reinforced with equal volume content of coir and glass fibers [Coir: Glass = 15:15 v/v, S7 (T)] absorbs the least amount of water among all the developed composite specimens. The 15/15 (v/v) Coir/Glass hybrid composite was absorbed 47.91% less moisture as compared to the pure Glass/Epoxy composite. It was due to the presence of less void content, better interaction between fibers and matrix resin at the surface, high lignin content in coir fiber cell wall, the greater value of the microfibrillar angle, and synergistic hybrid effect of Coir and Glass fibers.

©2018 Science IN. All rights reserved



*U = Untreated, T = Alkaline treated

Figure 10: Water absorption behavior of developed composites as a function of immersion time

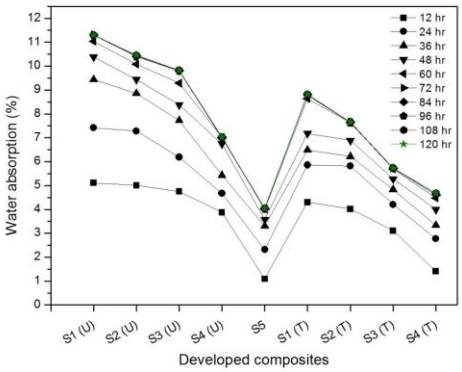


Figure 11: Water absorption of untreated and alkali treated PALF/Glass fiber reinforced hybrid epoxy composites

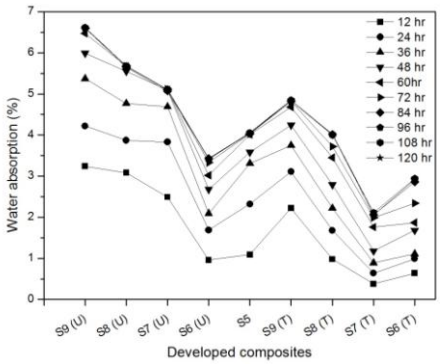


Figure 12: Water absorption of untreated and alkali treated Coir/Glass fiber reinforced hybrid epoxy composites

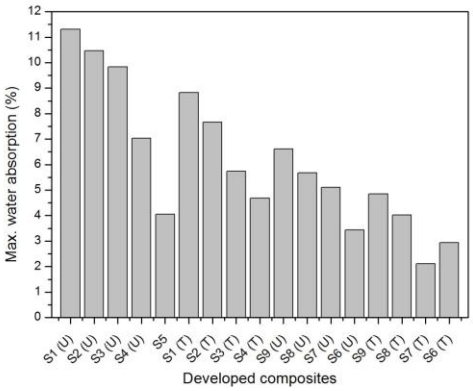


Figure 13: Maximum Water absorption of developed hybrid composites

The tensile, flexural, impact and water absorption properties of treated PG-EP and CG-EP composites (sample S3 and S7) were compared with the hybrid KP-PE (Kenaf/Pineapple-Polyethylene) composite [29] in Figure 14, 15, 16, and 17 respectively. It was observed that the alkaline treated 15/15 (v/v) PG-EP composite possess significantly higher tensile and flexural properties (strength and modulus) than that of KP-PE and CG-EP composites. However, the impact strength and moisture resistance properties of treated pineapple leaf fiber reinforced hybrid composite were slightly lower than the KP-PE composite. Therefore, it becomes necessary to improve the toughness and moisture sorption affinity of PALF/Glass hybrid material by the incorporation of high strain to failure COIR fiber which may results a high performance structural biocomposite material having an optimum combination of strength, stiffness, and ductility.

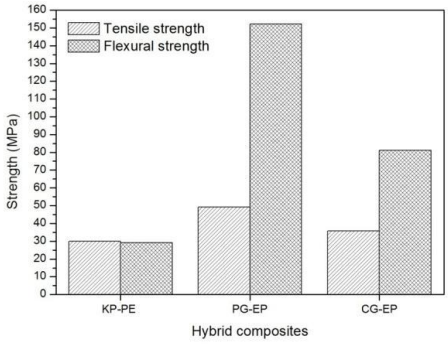


Figure 14: Comparison of tensile and flexural strength for KP-PE, PG-EP, and CG-EP hybrid composites

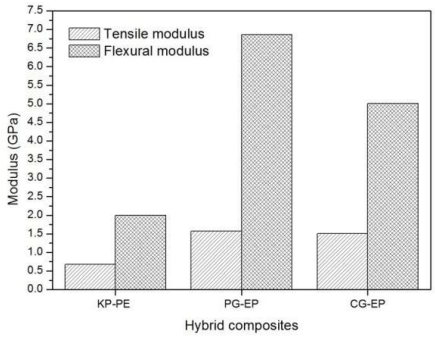


Figure 15: Comparison of tensile and flexural modulus for KP-PE, PG-EP, and CG-EP hybrid composites

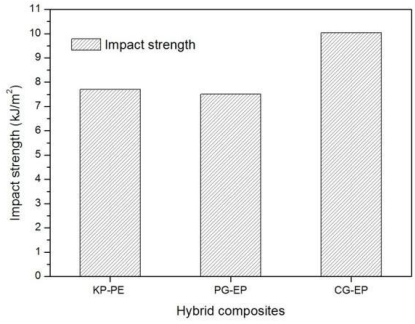


Figure 16: Comparison of impact strength for KP-PE, PG-EP, and CG-EP hybrid composites

©2018 Science IN. All rights reserved

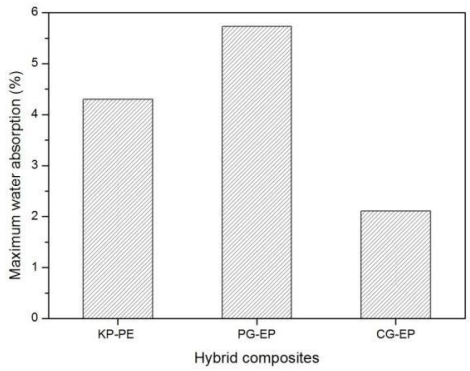


Figure 17: Comparison of maximum water absorption for KP-PE, PG-EP, and CG-EP hybrid composites

Conclusions

On the basis of the above experimental findings, the following conclusions can be made:

- The optimum fiber volume ratio of cellulosic and glass fiber is 15:15. The 15/15 (v/v) PALF/Glass hybrid composite exhibits higher tensile strength, flexural strength, and flexural modulus than that of other hybrid formulations.
- Alkali-treated composites have better mechanical and water resistance properties than that of untreated reinforced composites. This was because of the good interfacial adhesion between reinforcing fibers and polymer matrix. The 15/15 (v/v) hybrid composite reinforced with mercerized pineapple leaf fiber depicts 35.13% and 18.24% higher flexural and impact strength as compared to the pure Glass/Epoxy composite respectively. This was attributed to the synergistic hybridization between pineapple leaf fiber and glass fiber.
- Among all the developed composites, the alkali treated 15/15 (v/v) Coir/Glass fiber reinforced material possess the highest impact toughness and dimensional stability. The composite reinforced with equal volume content of NaOH treated coir and glass fiber [15/15 (v/v) Coir/Glass] exhibits 38.84% and 25.19% greater impact strength as compared to the Glass/Epoxy and treated 15/15 (v/v) PALF/Glass hybrid composite respectively.
- The alka1i treated 15/15 (v/v) Coir/Glass hybrid composite absorbs less amount of water than that of other hybrid formulations. It absorbs 47.90% less water than the pure synthetic Glass/Epoxy composite.

Overall, we can conclude that the hybrid composite developed by the combination of chemically treated cellulosic and glass fibers in an optimum volume ratio has better properties than that of single glass fiber reinforced material. From this significant and valuable research work, we have found that the alkaline treated 15/15 (v/v) PALF/Glass hybrid epoxy composite has better tensile and flexural properties. Whereas the 15/15 (v/v) Coir/Glass hybrid material possess highest impact toughness and impedance to moisture sorption. Therefore, to develop a high-performance structural cellular based material, it becomes necessary to optimally combine pineapple leaf fiber, coir fiber, and glass fiber in an epoxy thermoset matrix resin. It may produce a structural biocomposite material for load-bearing applications.

Acknowledgments: The authors extend their gratitude to the Delhi Technological University, Delhi (India) for supporting this research work.

References

1. Mohanty A.K., Misra M., Drzal L.T., Natural fibers, biopolymers, and biocomposites, *CRC Press*, 2005, ISBN-10: 0-8493-1741-X.
2. Sharba M.J., Leman Z., Sultan M.T.H., Ishak M.R., Hanim M.A., Effect of kenaf fiber orientation on mechanical properties and fatigue life of Glass/Kenaf hybrid composites, *BioResources*, 2016, 11(1),1448-1465.
3. Salman S.D., Leman Z., Sultan M.T.H., Ishka M.R., Cardona F., Kenaf/Synthetic and Kevlar/Cellulosic fiber reinforced hybrid composites: A Review, *BioResources*, 2015, 10(4), 8580-8603.
4. Mansor M.R., Sapuan S.M., Zainudin E.S., Nuraini A.A., Hambali A., Hybrid natural and glass fibers reinforced polymer composites material selection using analytical hierarchy process for automotive brake lever design, *Mater. Design.,* 2013, 51, 484-492.
5. Jawaid M., Abdul Khalil H.P.S., Cellulosic/Synthetic fiber reinforced polymer hybrid composites: A Review, *Carbohydr. Polym.*, 2011, 86, 1-18.
6. Shrivastava R., Telang A., Rana R.S., Purohit, R. Mechanical properties of Coir/Glass fiber epoxy resin hybrid composite, *Mater. Today. Proc.*, 2017, 4, 3477-3483.
7. Atiqah A., Maleque M.A., Jawaid M., Iqbal M., Development of kenaf-glass reinforced unsaturated polyester hybrid composite for structural applications, *Compos. Part B.*, 2013, 56, 68-73.
8. Jawaid M., Abdul Khalil H.P.S., Hassan A., Abdallah E., Bi-Layer hybrid biocomposites: Chemical resistant and physical properties, *BioResources*, 2012, 7(2), 2344-2355.
9. 9 Ranjan R., Bajpai P.K., Tyagi R.K., Mechanical characterization of Banana/Sisal fiber reinforced PLA hybrid composites for structural applications, *Eng. Int.*, 2013, 1(1), 39-49.
10. Panthapulakkal S., Sain M., Injection-molded short hemp fiber/glass fiber-reinforced polypropylene hybrid composites-Mechanical, water absorption and thermal properties, *J. Appl. Polym. Sci.*, 2006, 103, 2432-2441.
11. Shahzad A., Impact and fatigue properties of hemp-glass hybrid biocomposites, *J. Reinf. Plast. Compos.*, 2011, 30(16), 1389-1398.
12. Haq M., Burgueno R., Mohanty A.K., Misra M., Hybrid bio-based composites from blends of unsaturated polyester and soybean oil reinforced with nanoclay and natural fibers, *Compos. Sci. Technol.*, 2008, 68, 3344-3351.
13. Chevali V.S., Nerenz B.A., Ulven C.A., Kandare E., Mechanical properties of hybrid lignocellulosic fiber-filled acrylonitrile butadiene styrene (ABS) biocomposites, *Polym. Plast. Technol. Eng.,* 2015, 54, 375-382.
14. Davoodi M.M., Sapuan S.M., Ahmad D., Aidy A., Khalina A., Jonoobi M., Concept selection of car bumper beam with developed hybrid bio-composite material, *Mater. Design.,* 2011, 32, 4857-4865.
15. Jandas P.J., Mohanty S., Nayak S.K., Shrivastava H., Effects of surface treatments of banana fiber on mechanical, thermal, and biodegradability properties of PLA/Banana fiber biocomposites, *Polym. Compos.*, 2011, DOI: 10.1002/pc.21165.
16. Mwaikambo L.Y., Ansell M.P., Chemical modification of hemp, sisal, jute, and kapok fibers by alkalization, *J. Appl. Polym. Sci.*, 2001, 84, 2222-2234.
17. John M.J., Francis B., Varughese K.T., Thomas S. Effect of chemical modification on properties of hybrid fiber biocomposites, *Compos. Part A.*, 2008, 39, 352-363.
18. Li X., Tabil L.G., Panigrahi S., Chemical treatments of natural fiber for use in natural fiber-reinforced composites, *J. Polym. Environ.*, 2007, 15, 25-33.

©2018 Science IN. All rights reserved

19. John M. J., Anandjiwala R.D., Recent developments in chemical modification and characterization of natural fiber-reinforced composites, *Polym. Compos.*, 2008, DOI: 10.1002/pc.20461.
20. Uppin V.S., Ashok Joshi A., Sridhar I., Gouda P.S.S., Interlaminar fracture toughness in Glass-Cellulose reinforced epoxy hybrid composites, *IOP Conf. Ser. Mater. Sci. Eng.*, 2016, 149, DOI: 10.1088/1757-899X/149/1/012113.
21. Cheng F., Hu Y., Yuan J., Preparation and characterization of Glass fiber-Coir hybrid composites by a novel and facile prepreg/press process, *Fiber. Polym.*, 2014, 15(8), 1715-1721.
22. 22. Devi L., Bhagawan S.S., Nair K.C., Thomas S., Water absorption behavior of PALF/GF hybrid polyester composites, *Polym. Compos.*, 2011, DOI: 10.1002/pc.21034.
23. Bhagat V.K., Biswas S., Dehury J., Physical, Mechanical, and Water absorption behavior of Coir/Glass fiber reinforced epoxy based hybrid composites, *Polym. Compos.*, 2014, DOI: 10.1002/pc.22736.
24. Rahman M., Das S., Hasan M., Mechanical properties of chemically treated banana and pineapple leaf fiber reinforced hybrid polypropylene composites, *Adv. Mater. Process. Technol.,* 2018, http://doi.org/10.1080/2374068X.2018.1468972.
25. Arumugaprabhu V., Uthayakumar M., Cardona F., Sultan M.T.H., Mechanical characterization of Coir/Palmyra waste fiber hybrid composites, *IOP Conf. Ser. Mater. Sci. Eng.*, 2016, 152, DOI: 10.1088/1757-899X/152/1/012054.
26. Nurazzi N.M., Khalina A., Sapuan S., Rahmah M., Development of sugar palm yarn/glass fiber reinforced unsaturated polyester hybrid composites, *Mater. Res. Express.*, 2018, http://doi.org/10.1088/2053-1591/aabc27.
27. Abdul Khalil H.P.S., Masri M., Saurabh C.K., Fazita M.R.N., Azniwati A.A., Aprilla N.A., Rosamah E., Dungani R., Incorporation of coconut shell based nanoparticles in kenaf/coconut fibers reinforced vinyl ester composites, *Mater. Res. Express.*, 2017, http://doi.org/10.1088/2053-1591/aa62ec.
28. Atiqah A., Jawaid M., Sapuan S.M., Ishak M.R., Dynamic mechanical properties of sugar palm/glass fiber reinforced thermoplastic polyurethane hybrid composites, *Polym. Compos.*, 2018, DOI: 10.1002/pc.24860.
29. Aji IS., Zainudin ES., Abdan K., Sapuan SM., Khairul MD., Mechanical properties and water absorption behavior of hybridized kenaf/pineapple leaf fiber reinforced high-density polyethylene composite, *J. Compos.Mater.*, 2012, 47(8), 979-990.
30. Bakri B., Chandrabakty S., Putra K., Evaluation of mechanical properties of Coir-Angustifolia Haw Agave fiber reinforced hybrid epoxy composite, *Jurnal Mekanikal*, 2017, 8(1). 679-685.
31. Oushabi A., Sair S., Hassani F., Abboud Y., Tanane O., Bouari A., The effect of alkali treatment on mechanical, morphological, and thermal properties of date palm fibers (DPFs): Study of the interface of DPF-Polyurethane composite, *S. Afr. J. Chem. Eng.*, 2017, http://dx.doi.org/10.1016/j.sajce.2017.04.005.
32. Panyasart K., Chaiyut N., Amornsakchai T., Santawitee O., Effect of surface treatment on the properties of pineapple leaf fibers reinforced polyamide 6 composites, *Energy Procedia,* 2014, 56, 406-413.

©2018 Science IN. All rights reserved

ResearchGate

See discussions, stats, and author profiles for this publication at: https://www.researchgate.net/publication/320872285

Effect of Fibber Surface Treatment on Mechanical Properties of Bio composites: a Review

Article · October 2017

DOI: 10.22214/ijraset.2017.10292

CITATIONS
0

READS
21

1 author:



Mohit Mittal
Delhi Technological University
11 PUBLICATIONS **1** CITATION

SEE PROFILE

Some of the authors of this publication are also working on these related projects:

Corrugation process parameters optimization View project

Water absorption behaviour of natural Fibers View project

All content following this page was uploaded by Mohit Mittal on 24 June 2018.

The user has requested enhancement of the downloaded file.

International Journal for Research in Applied Science & Engineering Technology (IJRASET)
ISSN: 2321-9653; IC Value: 45.98; SJ Impact Factor:6.887
Volume 5 Issue X, October 2017- Available at www.ijraset.com

Effect of Fibber Surface Treatment on Mechanical Properties of Bio composites: a Review

Mohit Mittal[1], Rajiv Chaudhary[2]
[1]*Faculty of Mechanical Engineering Department, B.S Anangpuria Institute of Technology & Management, Faridabad.*
[2] *Faculty of Mechanical Engineering Department, Delhi Technological University, Delhi*

Abstract: Bio composites have become more popular in automotive, aerospace, packaging, and construction sectors because of their wide varieties of advantageous properties like good specific strength as well as modulus, environment friendly, low cost and low density etc. Inspite of their enormous favourable features they also have poor interfacial adhesion, poor wet ability of natural fibbers within the matrix. To overcome these barriers and for efficient utilization of bio composites in structural as well as non structural applications, it is highly required to change fiber surface morphology by removal of various surface impurities like wax, pectin, lignin, and hemicelluloses. Various chemical treatments i.e. alkalization, silane treatment, carination, permanganate, peroxide etc. are widely adopted for this purpose. The mechanical and thermal properties of treated bio composites are higher than the untreated one. It may be attributed to improvement in fiber-matrix interfacial adhesion as well as good wet ability of fibber within the matrix. The main focus of this work is to study the effect of fiber surface treatments on the mechanical properties of biocomposites. Outcomes from most of the cases show that the incorporation of chemical treated fiber compared to untreated fiber in biocomposites leads to increase the tensile and flexural properties but impact strength are reduced.

Key Words: Surface treatment, Biocomposite, Interfacial adhesion, Surface Morphology, Wettability, Mechanical properties

I. INTRODUCTION

Lignocelluloses fibbers attract the engineers to use as reinforcement filler in polymeric resin matrices. The attraction towards them is due to their low cost, low density, acceptable mechanical and thermal properties, recycling, and biodegradation ability. Inspite of their wide varieties of advantages, biofiber also have many drawbacks which create obstacle in effective reinforcement. The main drawback of natural fiber is their hydrophilic nature that causes poor interfacial adhesion with polymeric resin which results development of low strength biocomposite material [8]. To reduce moisture uptake behaviour of natural fiber and to increase the interfacial adhesion with polymeric resin, it is highly required to change the surface topology of natural fiber and make compatible with hydrophobic matrices. Surface modification of biofiber by physical or chemical treatment leads to alleviate their uses in structural applications such as exterior components of automobile, aerospace, building components etc [9]. Surface modification also results in enhancement of aspect ratio, improves the wet ability of fibers, and forms a strong adhesion between polar natural fiber and nonpolar matrix [10].The objective of this paper is to review the effect of fiber surface treatment on mechanical properties of natural fiber reinforced composites.

II. EFFECT OF FIBER SURFACE TREATMENT ON TENSILE PROPERTIES OF BIOCOMPOSITES

A. Effect of fiber surface treatments on tensile properties of Jute fiber/PLA composites

Bhanu K. Goriparthi et al. [1] analyzed the effect of jute fiber surface treatments on tensile properties of Jute/PLA composites. It was observed in fig 1 & 2 that tensile strength and moduli of composites had significantly increased with fiber surface treatment. It may be attributed to better fiber/matrix adhesion of treated composites as compared to untreated composite. The order of tensile properties improvement follows the order: Silane 2 (tri-methoxy methyl silane)> Silane 1(3-amino propyl tri-methoxy silane)>peroxide>permanganate>alkalization>untreated. The maximum improvement in tensile strength and modulus is by 35% and 38% respectively is due to silane 2 treatment.

©IJRASET (UGC Approved Journal): All Rights are Reserved

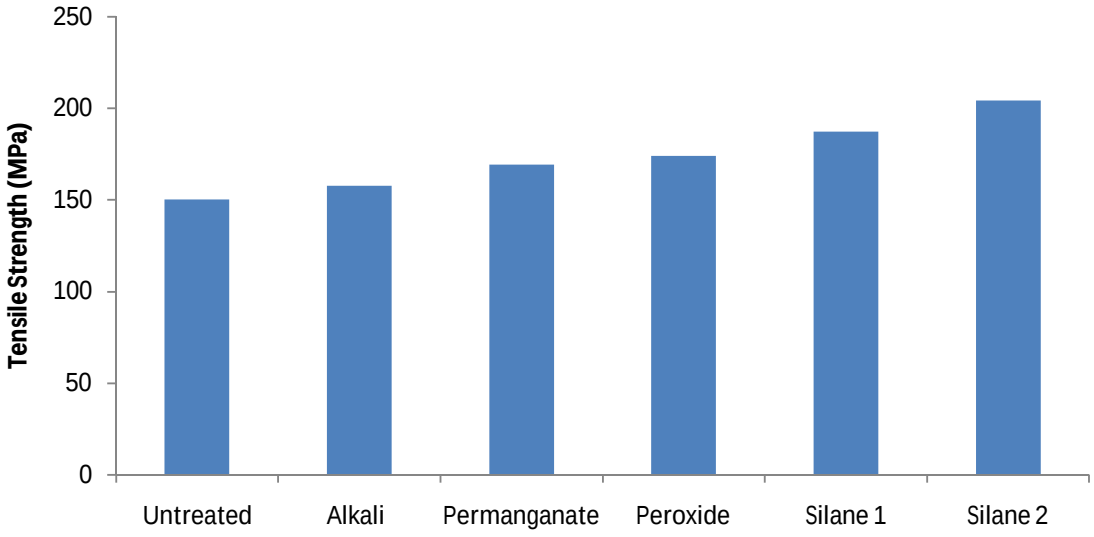


Fig.1. Variations of tensile strength with jute fiber treatments

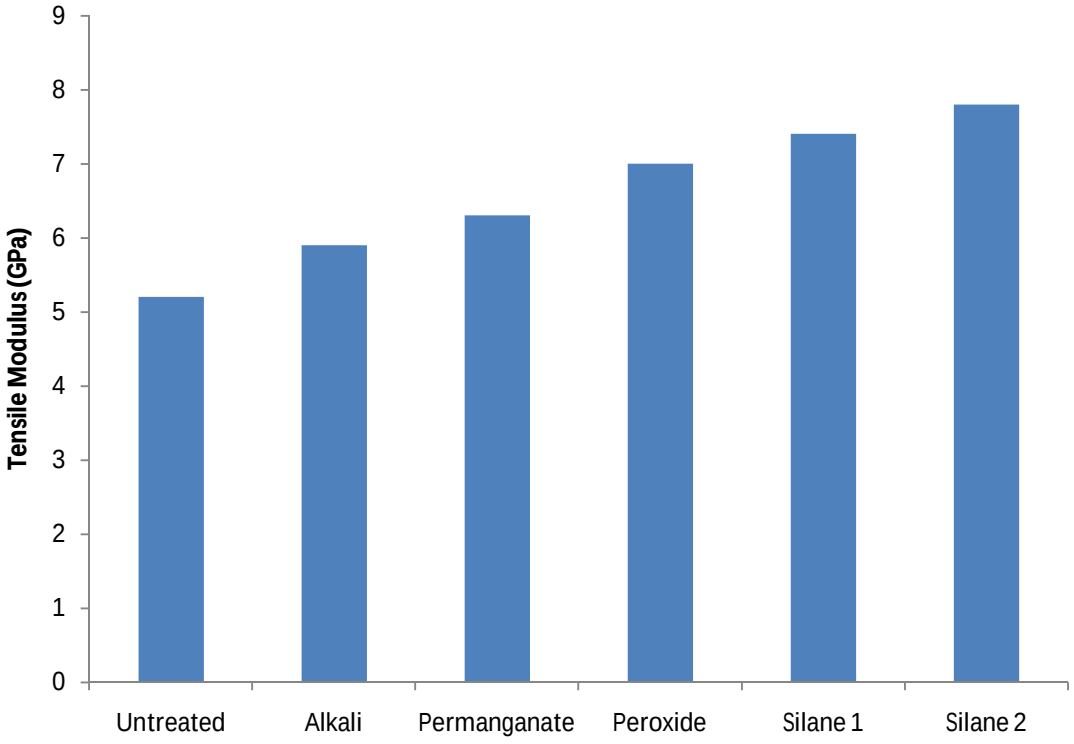


Fig.2. Variations of tensile modulus with jute fiber treatments

B. Effect of fiber surface treatments on tensile strength of Ramie/PLA composites

Hae Young Choi et al. [2] investigated the effect of various surface treatments of fiber on tensile strength of Ramie/PLA composites. Fig 3 clearly reveals that the tensile strength of PLA was decreased by 18.2, 49.82, and 41.08% when PLA was reinforced with FIBNA, FIBNASI, and FIBNAPO composites. It may be attributed to poor dispersion of ramie fiber in the PLA matrix.

©IJRASET (UGC Approved Journal): All Rights are Reserved

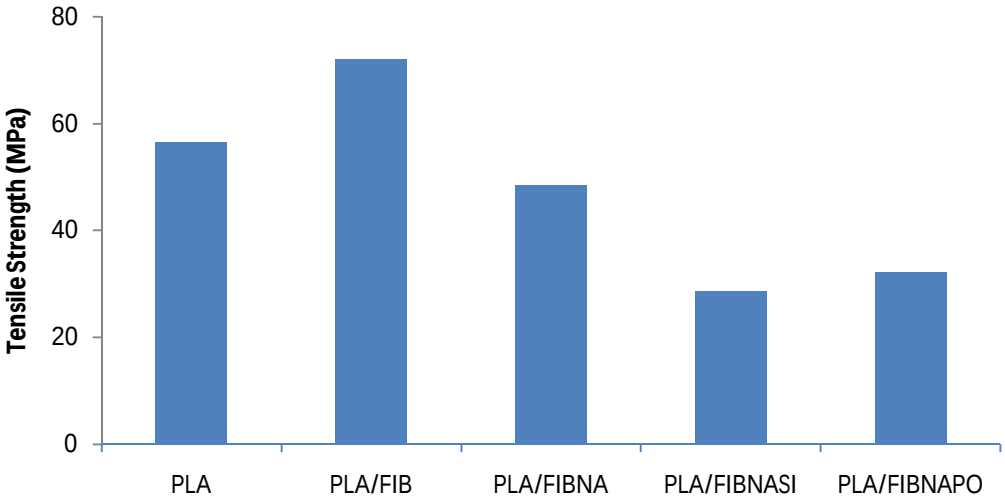


Fig 3. Tensile strength of PLA and chemically treated ramie fiber-reinforced composites

C. Effect of fiber surface treatments on tensile strength of non woven hemp fiber/PLA composites

Geeta Mehta et al. [3] examined the effect of various surface treatments on tensile strength of non woven hemp fiber/PLA composites. Fig 4 clearly shows that the tensile strength of alkaline treated fiber based biocomposite was 34% higher, silane treated biocomposite was 48% higher, UPE-MEKP treated composite was 57% higher, and acrylonitrile treated fiber composite was 80% higher than that of untreated non woven hemp fiber-PLA composites. This increase in tensile strength of the chemically-treated biocomposites is due to the improved adhesion between the fiber and the matrix which results effective stress transfer from matrix to fiber.

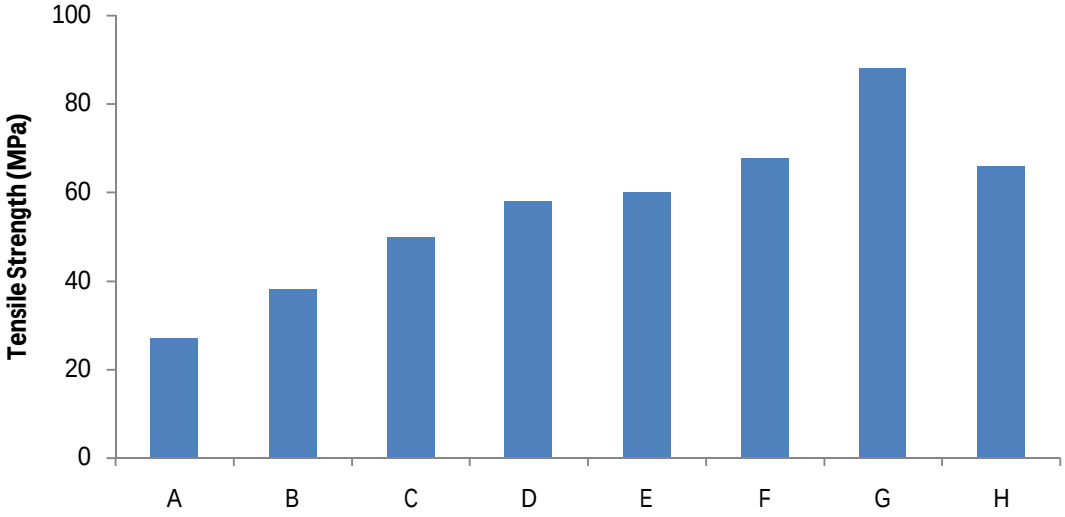


Fig 4. Comparison of tensile strength of surface-treated composites: A, UPE control; B, untreated hemp mat (30% vol.)-UPE; F, acrylonitrile treated hemp mat (30% vol.)-UPE; G, E-glass mat-UPE; H, E-glass mat-hemp mat-UPE.

D. Effect of alkalization on tensile properties of Coir/PBS composites

Tran Huu Nam et al. [4] conduct experiments to analyze the effect of alkalization on tensile properties of Coir/PBS composites. It can be concluded from fig 5 and 6 that the tensile strength and modulus of 5N72 treated Coir fiber/PBS composite at 10, 15, 20, 25, and 30% fiber mass content was 21, 22.1, 22.4, 24.1, and 24.1% and 29.4, 20.5, 40.8, 14.2, and 25.2% respectively higher than untreated Coir fiber/PBS composites. It may be attributed to the greater fiber/matrix interfacial and physical bonding.

©IJRASET (UGC Approved Journal): All Rights are Reserved

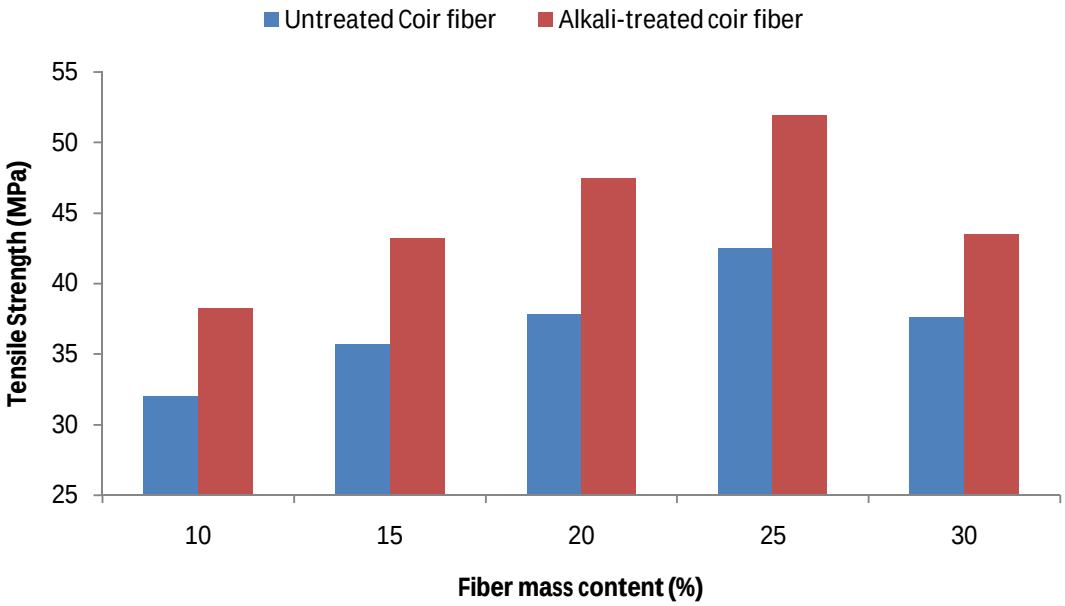


Fig 5. Tensile strength of untreated and 5N72 treated Coir fiber/PBS biocomposites

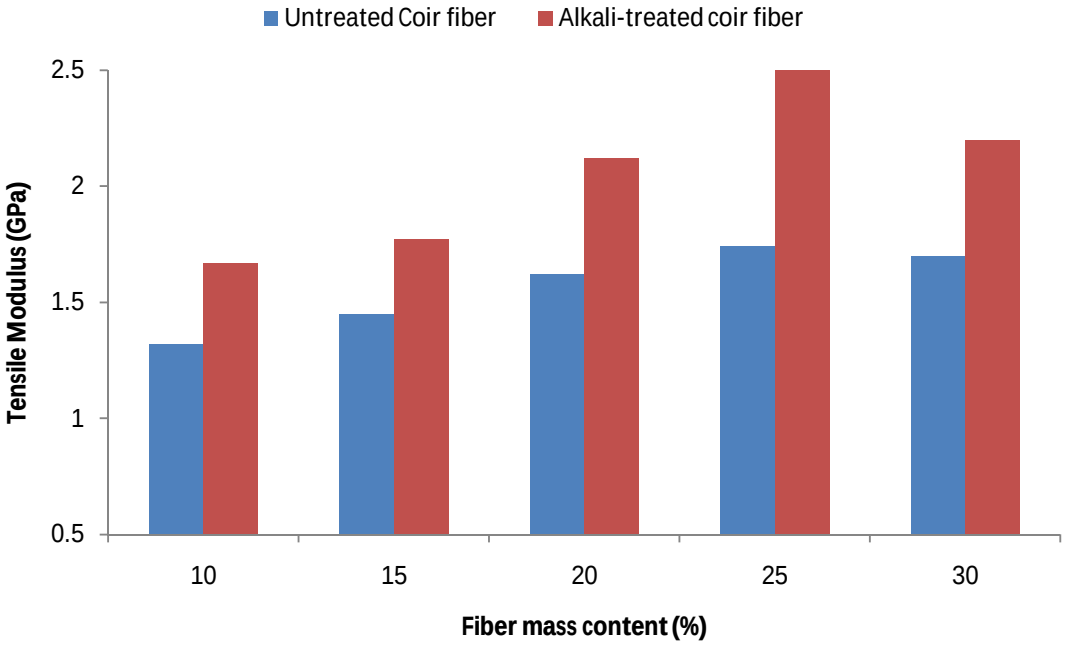


Fig 6. Tensile modulus of untreated and 5N72 treated Coir fiber/PBS biocomposites

E. Effect of fiber surface treatments on tensile strength of Ramie/PLA composites

Tao Yu et al. [5] analyzed the effect of surface treatments on Ramie fiber/PLA composites. It was found that tensile strength and stiffness of PLA was increased with addition of ramie fiber. Table 1 shows that the maximum tensile strength was 66.8 MPa achieved under the NaOH treated fiber condition. It is due to strong adhesion between alkaline treated ramie fiber and PLA matrix which results effective stress transfer between fiber and matrix.

©IJRASET (UGC Approved Journal): All Rights are Reserved

Samples	Tensile Strength (MPa)	Elongation at break (%)
Neat PLA	45.2 ± 1.5	1.2 ± 0.2
Untreated PLA/Ramie composite	52.5 ± 0.8	3.2 ± 0.2
PLA/Ramie composite treated by NaOH	66.8 ± 1.7	4.8 ± 0.2
PLA/Ramie composite treated by 3-aminopropyltriethoxysilane	59.3 ± 1.2	4.1 ± 0.2
PLA/Ramie composite treated by Gamma-glycidoxypropyltrimethoxysilane	64.2 ± 0.7	3.6 ± 0.1

Table 1. Mechanical properties of PLA and PLA-based composites

F. Effect of fiber surface treatments on tensile properties of Jute/PBS composites

Lifang Liu et al. [6] investigate the effect of surface treatments and fiber content on tensile properties of Jute/PBS composites. It was found that fiber surface modification is necessary to develop high strength biocomposites. Fig 7 and 8 represents that the increase of fiber mass content from 0 wt% to 20 wt% will result the increase of tensile strength and modulus but with 30 wt% they are decreased. This positive result up to 20 wt% jute fiber content was due to uniform stress distribution from PBS matrix to dispersed fiber phase and negative is due to agglomeration of fibers within the matrix which result non uniform stress distribution.The biocomposites of jute fiber treated by 2% NaOH, 2 + 5% NaOH, coupling agent with the 20 wt% fiber content exhibit 10%, 16.3%, and 21.7% enhancement in tensile strength, 22.5%, 41.1%, 49.6% in tensile modulus compared to the untreated jute fiber composites respectively.

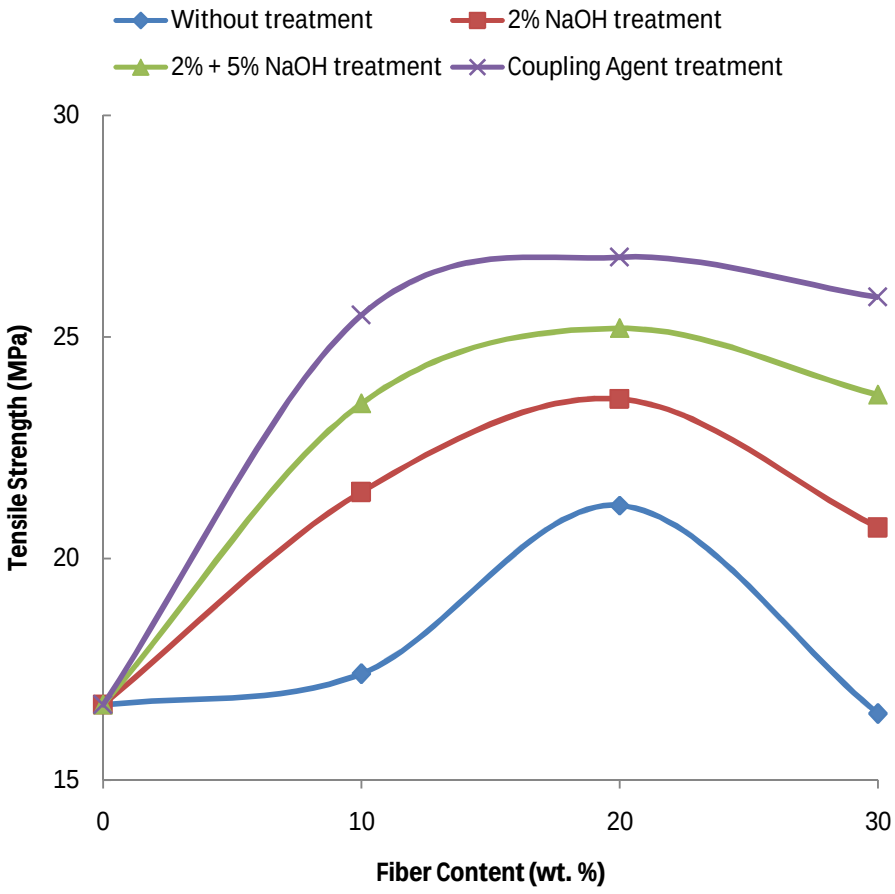


Fig 7. Effect of surface modifications on tensile strength of Jute/PBS biocomposites with different fiber content

©IJRASET (UGC Approved Journal): All Rights are Reserved

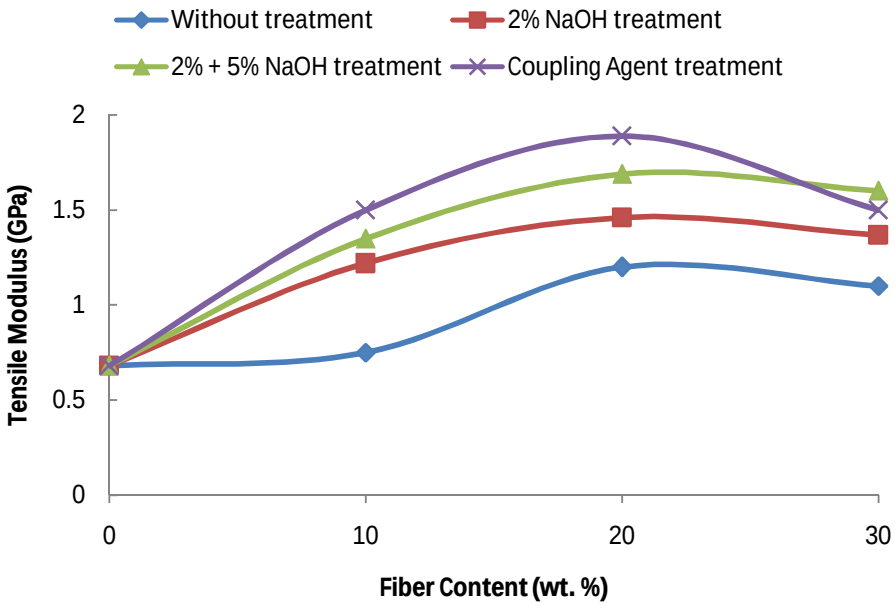


Fig8. Effect of surface modifications on tensile modulus of Jute/PBS biocomposites with different fiber content

III. EFFECT OF FIBER SURFACE TREATMENTS ON FLEXURAL PROPERTIES OF BIOCOMPOSITES

A. Effect of surface treatments on flexural properties of Jute/PLA composites

Bhanu K. Goriparthi et al. [1] investigates the effect of surface treatments on Jute fiber/PLA composites. Fig 9 and 10 shows that the modification of jute fiber surface resulted in enhancement of flexural strength and modulus by 24% and 41% respectively in silane 2(tri-methoxy methyl silane) treated composite due to the strong fiber-matrix adhesion. Out of the two silane, Silane 2 is more effective in fiber-matrix adhesion process which may be due to the strong chemical bonding between organo functional group and PLA matrix compared to the hydrogen bond formed in silane 1 treatment.

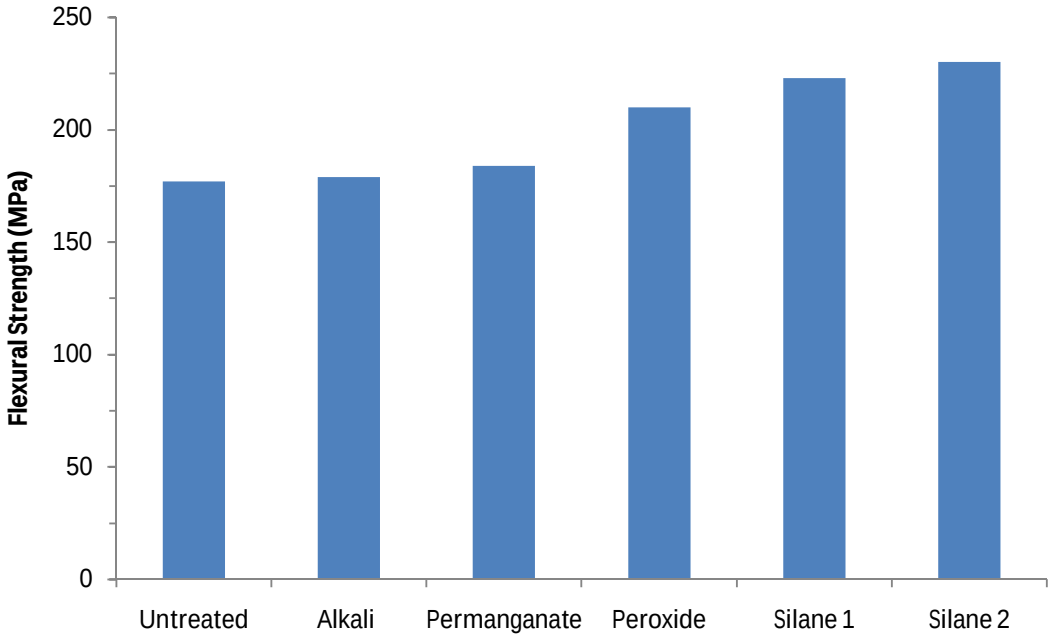


Fig 9. Variations of flexural strength with jute fiber treatments

©IJRASET (UGC Approved Journal): All Rights are Reserved

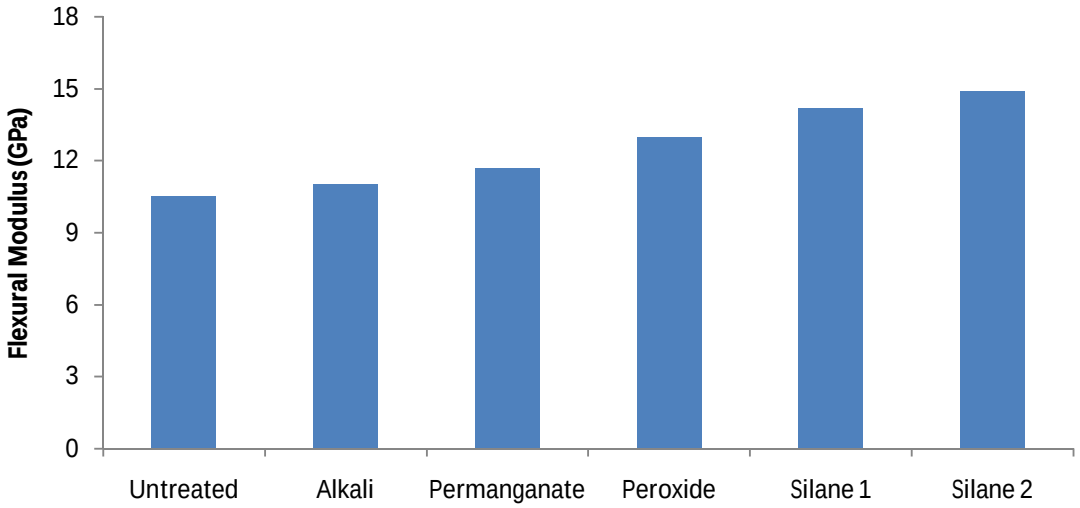


Fig 10. Variations of flexural modulus with jute fiber treatments

B. Effect of alkalization on flexural properties of Coir/PBS composites

Tran Huu Nam et al. [4] studied the effect of alkaline treatment and fiber mass content on flexural properties of Coir/PBS composites. It can be concluded from fig 11 and 12 that flexural properties are gradually increased with increasing fiber mass content from 0% to 25%. But beyond addition of fiber, they are decreased because of improper wetting. The alkali treated Coir/PBS composites with 25% mass content exhibited increase in flexural strength by 6% and flexural modulus by 16.7% compared to untreated composite. This reflects the contribution of sodium hydroxide in terms of change of fiber properties and enhancement of fiber-matrix adhesion.

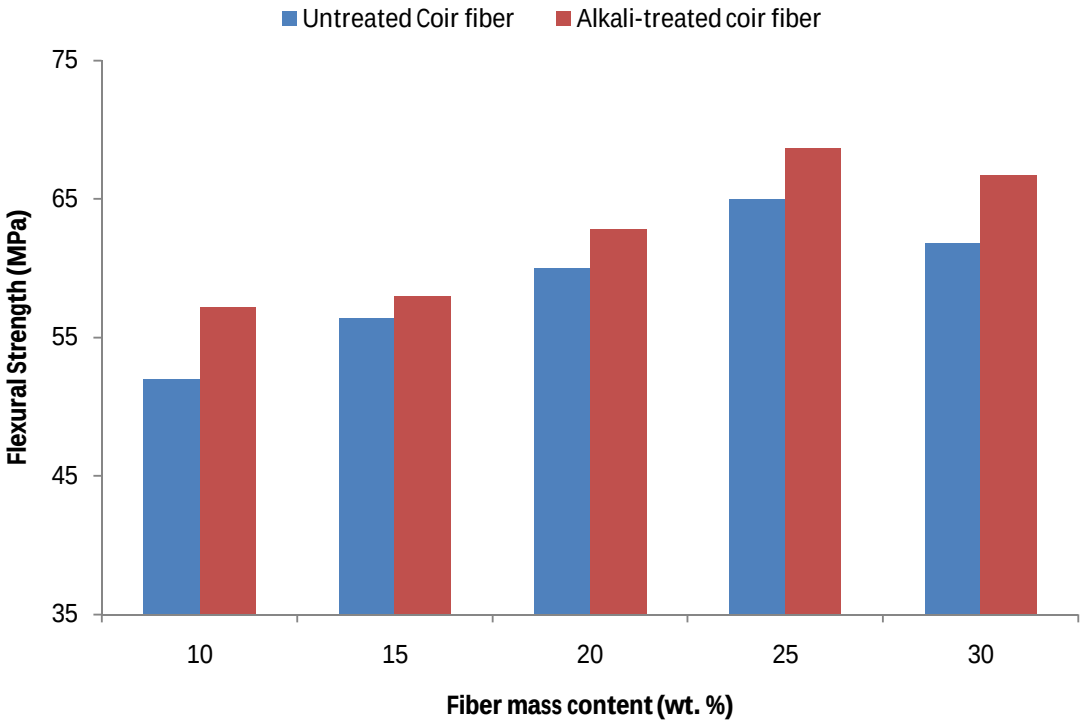


Fig 11. Flexural strength of untreated and 5N72 treated Coir fiber/PBS biocomposites

©IJRASET (UGC Approved Journal): All Rights are Reserved

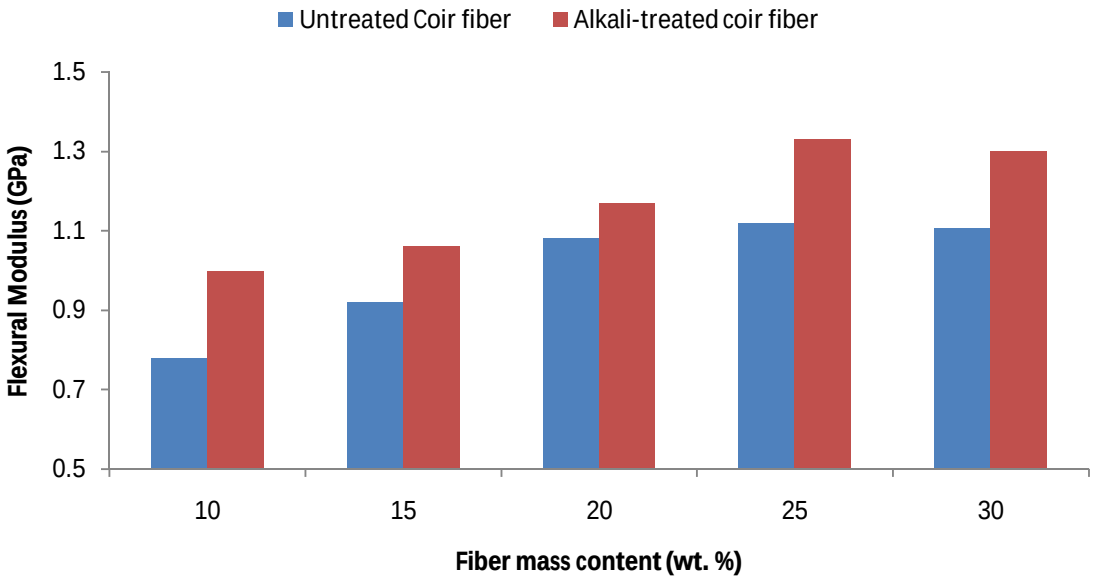


Fig 12. Flexural modulus of untreated and 5N72 treated Coir fiber/PBS biocomposites

C. Effect of surface treatments on flexural properties of Kenaf/PLA composites

Masud S. Huda et al. [7] investigates the effect of kenaf fiber surface treatments on flexural properties of Kenaf/PLA composites. It concluded from fig 13 & 14 that the introduction of kenaf fiber (untreated or treated) in PLA matrix will lead to significantly improvement in flexural modulus but flexural strength was decreases. It may be due to poor adhesion between the kenaf fiber and PLA. The flexural properties of surface-treated kenaf fiber composites show an evident increase compare to untreated fiber composite. It may be attributed to an increase in nucleation density. It was found that FIBNASI composite shows the best flexural modulus (80% improvement) compare to untreated fiber composite. The order of improvement in flexural properties compared to untreated fiber composite is: PLA/FIBNASI> PLA/FIBSI> PLA/FIBNA> PLA/FIB.

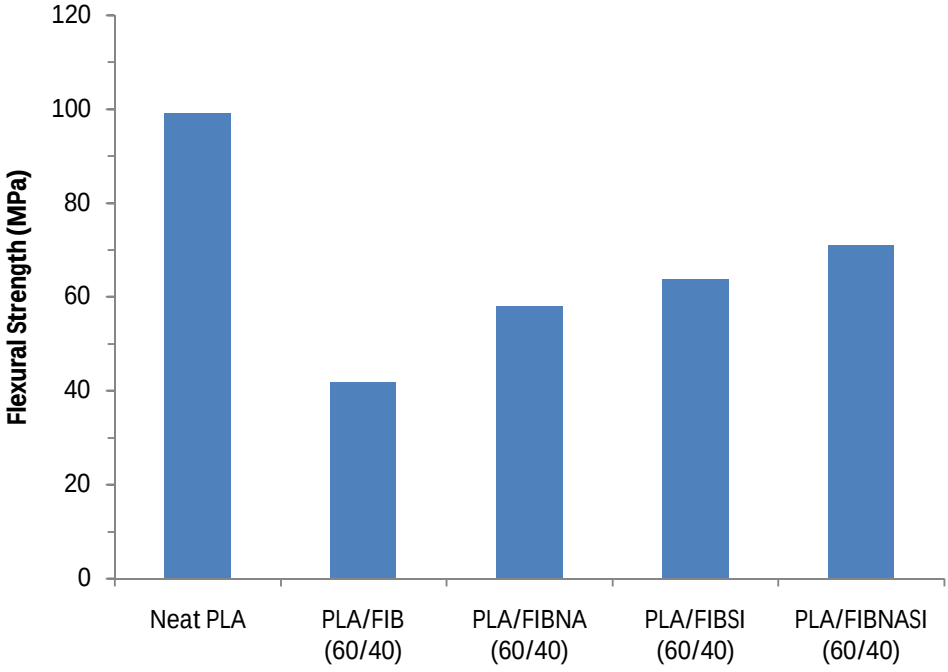


Fig 13. Flexural strength of PLA and surface treated kenaf/PLA biocomposites

©IJRASET (UGC Approved Journal): All Rights are Reserved

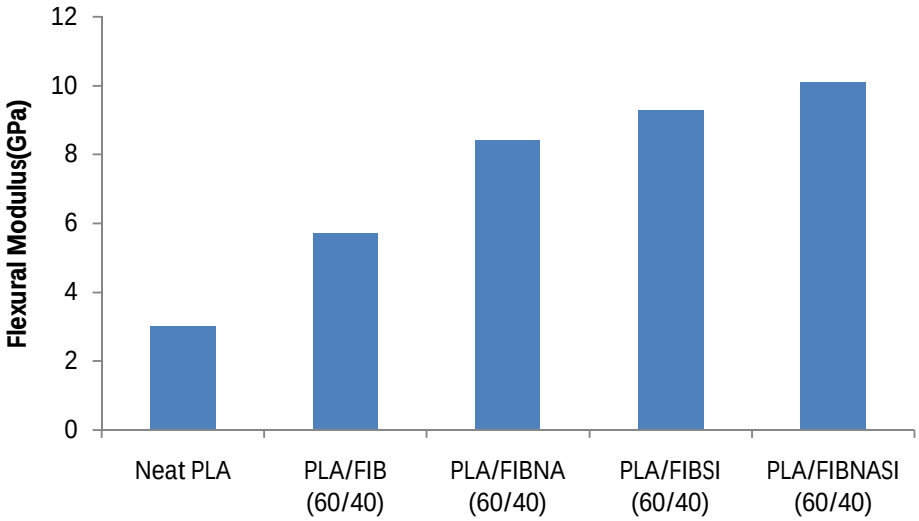


Fig 14. Flexural modulus of PLA and surface treated kenaf/PLA biocomposites

D. Effect of fiber surface treatments on flexural strength of non woven hemp fiber/PLA composites

Geeta Mehta et al. [3] investigate the effect of various surface treatments on flexural strength of non woven hemp fiber/PLA composites. Figure 15 clearly shows that the flexural strength and modulus of elasticity of alkali treated, silane treated, and UPE-MEKP treated biocomposites lie in the same range. The bending strength and modulus of elasticity of acrylonitrile-treated fiber based composites were 7% and 35% higher than those of untreated fiber composite

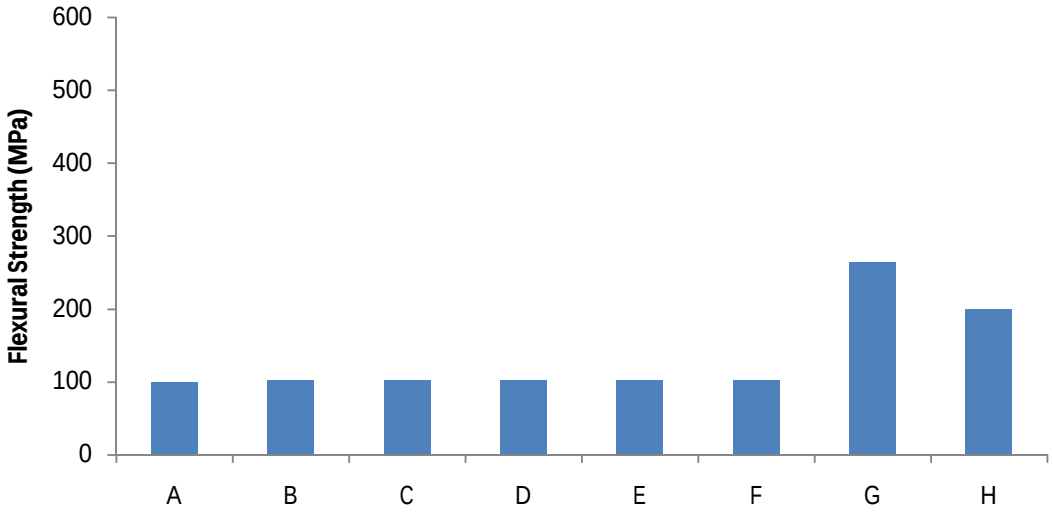


Fig 15. Comparison of flexural strength of surface-treated composites: A, UPE control; B, untreated hemp mat (30% vol.)-UPE; F, acrylonitrile treated hemp mat (30% vol.)-UPE; G, E-glass mat-UPE; H, E-glass mat-hemp mat-UPE.

E. Effect of fiber surface treatments on flexural strength of Ramie/PLA composites

Tao Yu et al. [5] conducted experiment to analyze the effect of fiber surface treatments on flexural strength of Ramie/PLA composites. Figure 16 depicts that the bending strength of composite is increased after surface treatment of ramie fiber. The maximum flexural strength of Ramie/PLA composite was achieved with incorporation of alkaline treated ramie fiber.

©IJRASET (UGC Approved Journal): All Rights are Reserved

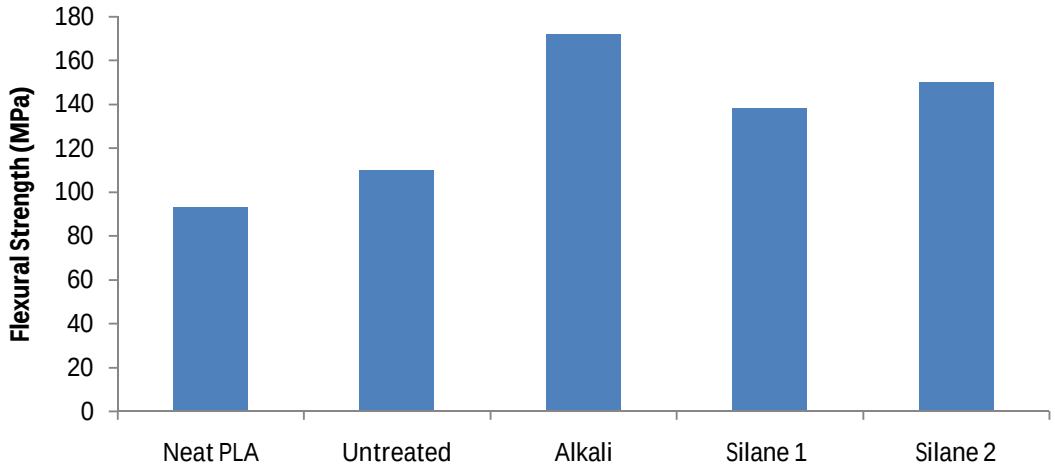


Fig 16. Flexural strength of PLA and PLA based composites

IV. EFFECT OF FIBER SURFACE TREATMENTS ON IMPACT STRENGTH OF BIOCOMPOSITES

A. Effect of surface treatments on impact strength of Jute/PLA composites

Bhanu K. Goriparthi et al. [1] conducted the experiment to analyze the effect of various surface treatments on impact strength of Jute fiber/PLA composite. It was concluded from fig 17 that izod impact strength of treated composites was lower than untreated composite which may be attributed to less fiber pullout due to better adhesion between fiber and the matrix. Debonding, fiber pullout and fracture of fibers are the energy absorption mechanisms during impact. Higher energy required to pull out fibers from matrix than fiber fracture and debonding which results untreated jute fiber composite have better impact strength than treated composites.

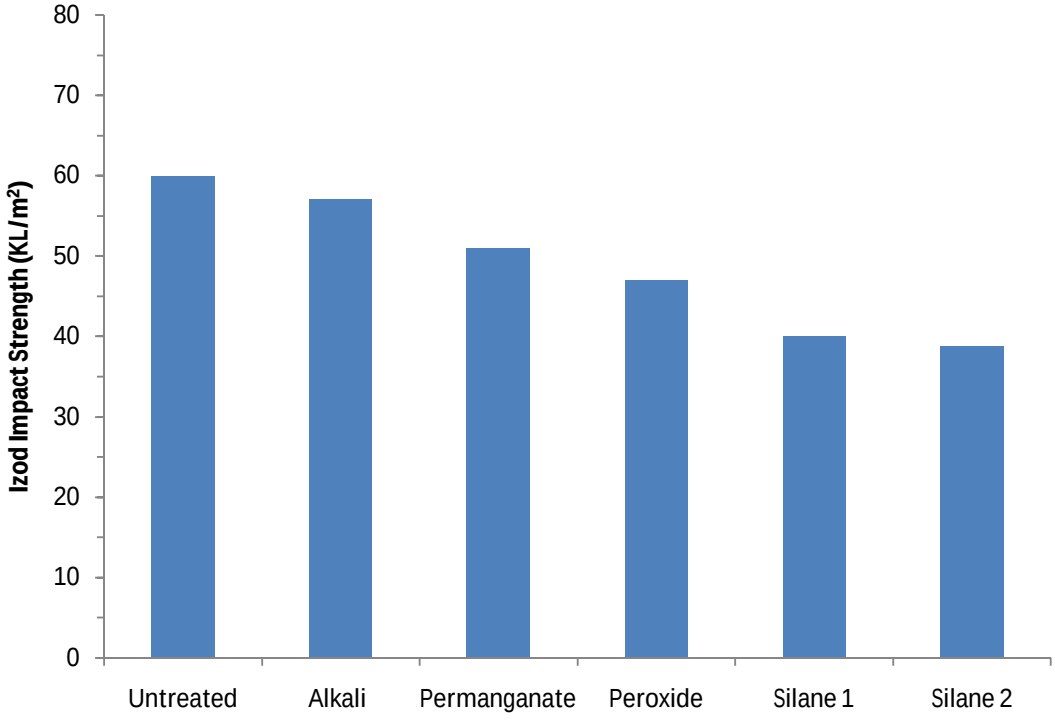


Fig 17. Variation of notched izod impact strength with fiber treatments

©IJRASET (UGC Approved Journal): All Rights are Reserved

B. Effect of surface treatments on impact strength of Ramie/PLA composites

Hae Young Choi et al. [2] studied the effect of various surface treatments on Ramie/PLA composites. Fig 18 depicts that surface treatments enhanced the impact strength, and FIBNAPO composite perform superior impact performance. For the FIBNA, FIBNASI, and FIBNAPO composites, the impact strength increased by approximately 52, 56, and 65% respectively compared to neat PLA. The excellent behaviour of peroxide treated composite is due to the fact that the stiff behaviour of ramie fiber is changed to flexible nature as well as improvement in surface adhesion characteristics by producing a rough surface morphology.

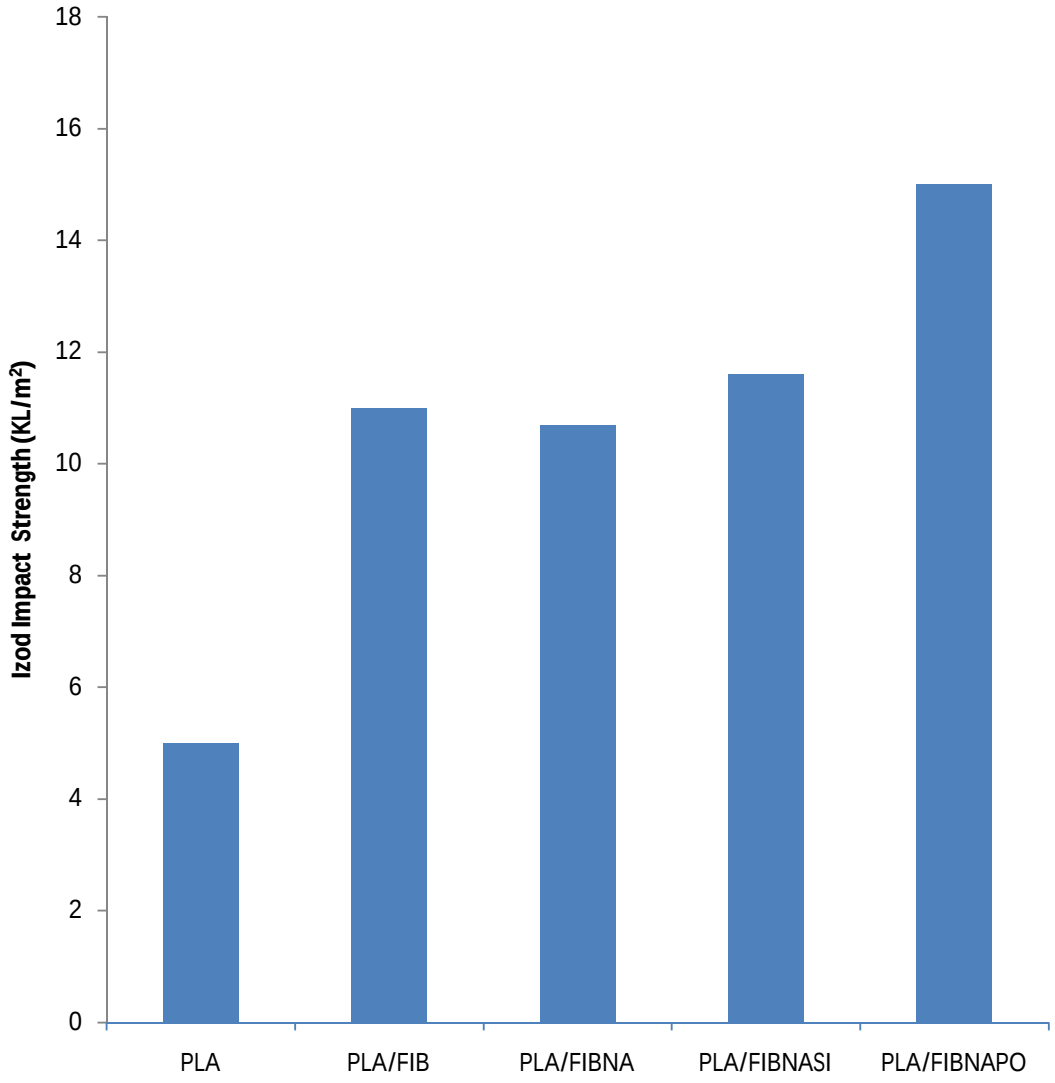


Fig 18. Notched Izod impact strength of the PLA and chemically treated fiber-reinforced composites

C. Effect of surface treatments on impact strength of Kenaf/PLA composites

Masud S. Huda et al. [7] conducted experiments to analyze the effects of various surface treatments on impact strength of Kenaf/PLA composites. Fig 19 reveals that the surface treatment enhanced the impact strength of Kenaf/PLA composite. It was found that FIBNA/PLA composite present an evident increase of 50% impact strength compared to untreated fiber composite. This excellent behaviour of alkaline treated kenaf fiber composite attributed to fact that alkali treatment improves the fiber surface adhesion characteristics by removing natural and artificial impurities, thereby producing a rough surface morphology. In contrast to FIBNA, FIBSI composites possessed decrease in impact strength compared to untreated fiber composite.

©IJRASET (UGC Approved Journal): All Rights are Reserved

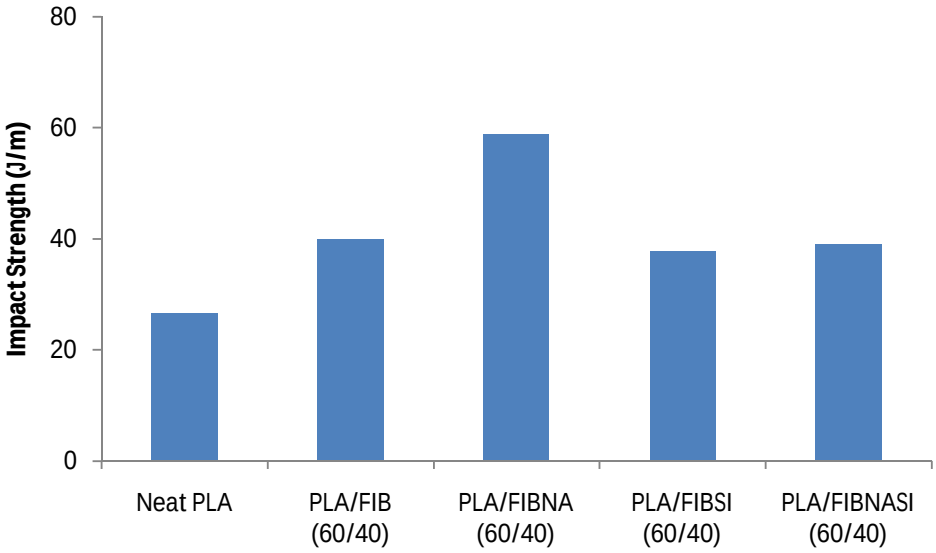


Fig 19. Notched Izod impact properties of PLA and its composites

D. Effect of fiber surface treatments on impact strength of Ramie/PLA composites

Tao Yu et al. [5] investigate the effect of various surface treatments on impact strength of Ramie/PLA composites. It was concluded that incorporation of untreated or treated ramie fibers in PLA matrix will leads to increases the impact strength of resulting composites. The reason behind this significant improvement is the ramie can increase the amount of energy required to pull out fiber from resin. Figure 20 clearly reveals that surface treated ramie fiber/PLA composites have higher impact strength compared to untreated ramie fiber/PLA composites. The maximum impact strength was achieved with alkali treated composites and it is due to strong interfacial adhesion characteristics by removing natural and artificial impurities.

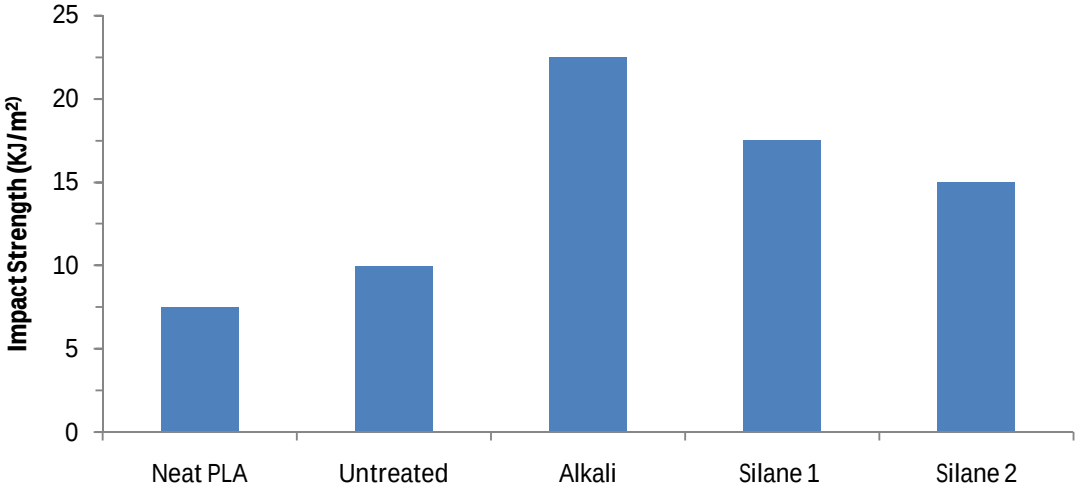


Fig 20. Impact strength of PLA and PLA-based composites

E. Effect of fiber surface treatments on impact strength of non woven hemp fiber/PLA composites

Geeta Mehta et al. [3] performed experiment to analyze the effect of various surface treatments on impact strength of non woven hemp fiber/PLA composites. It was concluded from fig 21 that there was an increment of 82% in impact strength of untreated hemp fiber based composites, 49% for alkali-treated fibers, 94% for silane treated fibers, 120% for UPE-MEKP treated fibers, and 180% for acrylonitrile treated hemp fiber/PLA composites as compared with neat resin.

©IJRASET (UGC Approved Journal): All Rights are Reserved

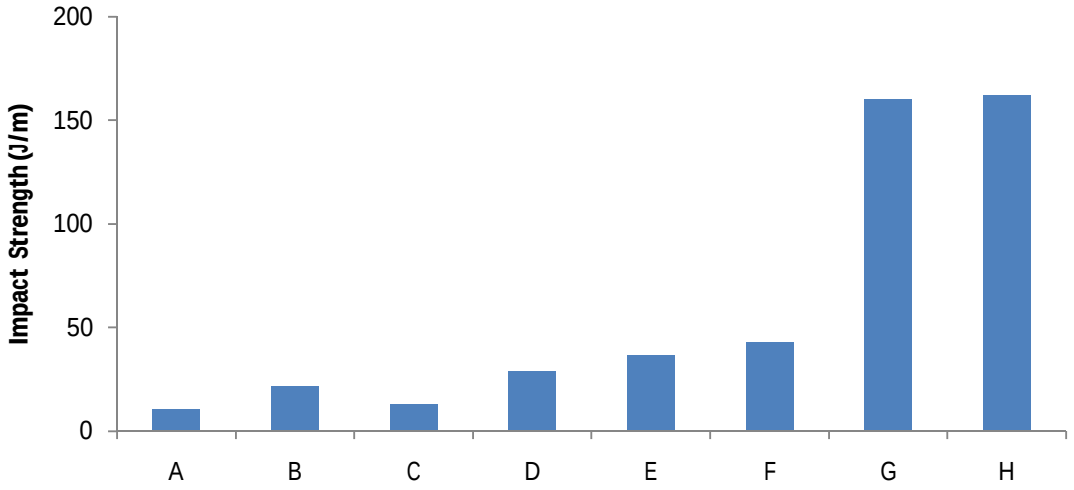


Fig 21. Comparison of impact strength of surface-treated composites: A, UPE control; B, untreated hemp mat (30% vol.)-UPE; F, acrylonitrile treated hemp mat (30% vol.)-UPE; G, E-glass mat-UPE; H, E-glass mat-hemp mat-UPE.

V. CONCLUSIONS

This paper presents the effect of fiber surface treatments on the mechanical properties of biocomposites. The conclusions from this study summarized as follows:

A. Surface treated Jute fiber/PLA biocomposites have better tensile and flexural properties but lower impact strength compared to untreated fiber composites.

B. Silane 2 (tri-methoxy methyl silane) is more effective than Silane 1(3-amino propyl tri-methoxy silane) for improvement in mechanical properties of biocomposites which may be attributed to the strong bond formed between organo functional group of silane 2 and matrix, compared to the hydrogen bond formed by nitrogen to the matrix in case of silane 1.

C. The impact strength of Ramie/PLA composites were increased by peroxide treatment of ramie fibers. This significant improvement is due to the improved interfacial adhesion between ramie fibers and PLA by morphological changes to the fiber surface

D. treatment of coir fibers have increased the mechanical interlocking between the fiber and PBS matrix which results significant improvement in their tensile strength and modulus

E. Fiber mass content in polymer composites positively affects the mechanical properties of the composites up to an optimum limit. In the case of Coir/PBS biocomposites, mean mechanical strength and modulus was increased with increasing fiber mass content up to 25%

F. In the case of Ramie/PLA biocomposites, alkali is an effective surface treatment approach for improvement in flexural strength and impact strength due to the enhanced interfacial adhesion between the PLA matrix and the ramie fibers

G. surface treatment of hemp fibers with alkali, silane, UPE, and acrylonitrile will result strong adhesion between hemp fibers and UPE matrix which leads to comparable performance than glass fiber based composites.

REFERENCES

[1] Bhanu K. Goriparthi, K.N.S. Suman, Nalluri Mohan Rao. Effects of fiber surface treatments on mechanical and abrasive wear performance of polylactide/jute composites. Composites Part A 2012;43:1800-1808.

[2] Hae Young Choi, Jung Soon Lee. Effect of surface treatment of ramie fibers in a ramie/polylactic acid composite. Fibers and Polymers 2012;Vol.13:217-223

[3] Geeta Mehta, Lawrence T. Drzal, Amar K. Mohanty, Manjusri Misra. Effect of fiber surface treatment on the properties of biocomposites from nonwoven industrial hemp fiber mats and unsaturated polyester resin. Journal of Applied Polymer Science 2006; Vol. 99:1055-1068

[4] Tran Huu Nam, Shinji Ogihara, Nguyen Huy Tung, Satoshi Kobayashi. Effect of alkali treatment on interfacial and mechanical properties of coir fiber reinforced poly butylenes succinate biodegradable composites. Composites Part B 2011;42:1648-1656

[5] Tao Yu, Jie Ren, Shumao Li, Hua Yuan, Yan Li. Effect of fiber surface treatments on the properties of polylactic acid/ramie composites. Composites Part A 2010;41:499-505.

[6] Lifang Liu, Jianyong Yu, Longdi Cheng, Weiwei Qu. Mechanical properties of polybutylene succinate (PBS) biocomposites reinforced with surface modified jute fibre. Composites Part A 2009;40:669-674.

©IJRASET (UGC Approved Journal): All Rights are Reserved

[7] Masud S. Huda, Lawrence T. Drzal, Amar K. Mohanty, Manjusri Misra. Effect of fiber surface treatments on the properties of laminated biocomposites from polylactic acid and kenaf fibers. Composites Science and Technology 2008;68:424-432.
[8] Hong CK, Hwang I, Kim N, Park DH, Hwang BS, Nah C. Mechanical properties of silanized jute-polypropylene composites. J Ind Eng Chem 2008;14:1471-147
[9] Abdelmouleh M, Boufi S, Belgacem MN, Duarte AP, Salah AB, Gandini A. Modification of cellulosic fibers with functionalized silanes: development of surface properties. Int J Adhes Adhes 2004;24:43-54
[10] Yu T, Ren J, Li S, Yuan H, Li Y. Effect of fiber surface treatment on the properties of polylactic acid/ramie composites. Composites Part A: Applied Science and Manufacturing 2010;41:499-505.

©IJRASET (UGC Approved Journal): All Rights are Reserved

View publication stats

ResearchGate

See discussions, stats, and author profiles for this publication at: https://www.researchgate.net/publication/328806382

Enhanced thermoelectric performance in p-type ZrCoSb based half-Heusler alloys employing nanostructuring and compositional modulation

Article · November 2018

DOI: 10.1016/j.jmat.2018.11.003

CITATIONS
0

READS
46

7 authors, including:



Nagendra Singh Chauhan
National Physical Laboratory - India
19 PUBLICATIONS **83** CITATIONS
SEE PROFILE



S. Bathula
National Physical Laboratory - India
65 PUBLICATIONS **614** CITATIONS
SEE PROFILE



Avinash Vishwakarma
National Physical Laboratory - India
7 PUBLICATIONS **15** CITATIONS
SEE PROFILE



Ruchi Bhardwaj
National Physical Laboratory - India
13 PUBLICATIONS **17** CITATIONS
SEE PROFILE

Some of the authors of this publication are also working on these related projects:

Half-Heusler Thermoelectric Materials View project

Development of micro and nanophosphor's for energy saving near UV based white LED View project

All content following this page was uploaded by Nagendra Singh Chauhan on 28 November 2018.

The user has requested enhancement of the downloaded file.

Journal of Materiomics xxx (xxxx) xxx

Contents lists available at ScienceDirect

Journal of Materiomics

journal homepage: www.journals.elsevier.com/journal-of-materiomics/

Enhanced thermoelectric performance in p-type ZrCoSb based half-Heusler alloys employing nanostructuring and compositional modulation

Nagendra S. Chauhan [a, b], Sivaiah Bathula [a, b, *], Avinash Vishwakarma [a, b], Ruchi Bhardwaj [a, b], Kishor Kumar Johari [a, b], Bhasker Gahtori [a, b], Ajay Dhar [a, b, **]

[a] Academy of Scientific & Innovative Research (AcSIR), CSIR-National Physical Laboratory, New Delhi 110012, India
[b] Division of Advanced Materials and Devices Metrology, CSIR-National Physical Laboratory, Dr. K. S. Krishnan Marg, New Delhi 110012, India

ARTICLE INFO

Article history:
Received 30 July 2018
Received in revised form
31 October 2018
Accepted 1 November 2018
Available online xxx

Keywords:
Half Heuslers
Iso-electronic
Waste heat recovery
Mid-temperature
Efficiency
Compositional modulation

ABSTRACT

ZrCoSb based half-Heusler (HH) alloys have been widely studied as a p-type thermoelectric (TE) material for power generation applications in the mid-temperature regime. However, their intrinsically high thermal conductivity has been found to be detrimental for the improvement in their thermoelectric figure-of-merit (ZT), which presently is far below unity. In the current work, a state-of-the-art *ZT* ~1.1 at 873 K was realized in an optimized composition of nanostructured $Zr_{1-x}Hf_xCoSb_{0.9}Sn_{0.1}$ HH alloys by employing compositional modulation i.e. grain-by-grain compositional variations, which leads to a substantial increase in its power factor coupled with a concurrent decrease in its thermal conductivity. Significant reduction in the phonon mean-free-path is observed on Hf substitution, which is comparable to the average crystallite size (~25 nm), thus leading to a very low thermal conductivity of ~2.2 $W m^{-1}K^{-1}$ at 873 K, which is amongst the lowest reported in HH alloys. The TE device characteristics, estimated using cumulative temperature dependence model for quantitative evaluation of TE performance, yielded an output power density of ~10 Wcm^{-2} with a leg efficiency of ~10% in the optimized composition of nanostructured $Zr_{1-x}Hf_xCoSb_{0.9}Sn_{0.1}$ HH alloys, which is comparable to the reported efficiencies of other state-of-the-art TE materials.

© 2018 The Chinese Ceramic Society. Production and hosting by Elsevier B.V. This is an open access article under the CC BY-NC-ND license (http://creativecommons.org/licenses/by-nc-nd/4.0/).

1. Introduction

In energy production worldwide, approximately two-third of the energy remains unutilized and discharged in the form of waste heat [1]. Waste heat recovery using a thermoelectric (TE) materials is a promising avenue which provides a convenient means for reliable, sustainable and scalable power generation by harnessing the waste heat [2,3]. As energy materials, TE materials have been developed by various schemes which mutually aims to improve TE energy conversion efficiency by maximizing the Seebeck coefficient, (α), and balancing the competing requirements of high electrical conductivity, (σ) and low thermal conductivity, (κ) at the absolute temperature (T). The thermoelectric figure-of-merit (ZT), represents a useful metric which characterizes the energy conversion of a thermoelectric material and is given as [4,5] $ZT = \left(\frac{\alpha^2\sigma}{\kappa}\right)T$. The ZT of a material provides a qualitative measure of its TE performance, as the direct evaluation of efficiency and output power generation is rather tedious and time-consuming. However, numerical and analytical methods presents a possibility to theoretically estimate intrinsic efficiency and output power. In this context, the Cumulative Temperature Dependence (CTD) model, based on overall temperature dependence of materials properties at given temperature boundary conditions provide a reliable approximation of thermoelectric materials and devices performance [6,7]. Such an estimate provides valuable insights of material's TE conversion potential and various factors contributing towards inefficiencies in a TE device.

The half-Heusler (HH) class of thermoelectric materials with

* Corresponding author. Academy of Scientific & Innovative Research (AcSIR), CSIR-National Physical Laboratory, New Delhi-110012, India.
** Corresponding author. Corresponding author. Academy of Scientific & Innovative Research (AcSIR), CSIR-National Physical Laboratory, New Delhi-110012, India.
E-mail addresses: sivaiahb@nplindia.org (S. Bathula), adhar@nplindia.org (A. Dhar).

Peer review under responsibility of The Chinese Ceramic Society.

https://doi.org/10.1016/j.jmat.2018.11.003

2352-8478/© 2018 The Chinese Ceramic Society. Production and hosting by Elsevier B.V. This is an open access article under the CC BY-NC-ND license (http://creativecommons.org/licenses/by-nc-nd/4.0/).

Please cite this article as: Chauhan NS et al., Enhanced thermoelectric performance in p-type ZrCoSb based half-Heusler alloys employing nanostructuring and compositional modulation, Journal of Materiomics, https://doi.org/10.1016/j.jmat.2018.11.003

high mechanical strength, non-toxicity and high thermal stability have been widely explored as potential candidates for TE power generation in the mid-temperature regime [8–10]. There exist numerous possible combination by which HH [11,12] alloys can be formed, among which ZrNiSn [13–17] (n-type), TiNiSn [18,19] (n-type), ZrCoSb [20–22] (p-type), TiCoSb [23] (p-type) and NbFeSb [24] (p-type) have been widely studied. Although ZT > 1 has already been realized in n-type HHs, the p-type HH alloys are still being explored for replicating the superior performance of their electron-doped n-type counterparts. In this context, ZrCoSb based alloys have been widely studied by over-compensating hole-doping (via. proper substitution and doping at Zr, Co and/or Sb sites) [20,25,26] and have displayed compatibility with the n-type HH on secondary metrics such as thermal expansion coefficient and long-term thermal and mechanical stability. However, their high thermal conductivity (κ) has remained a major limitation, reduction of which has long remained the main focus for enhancing TE performance of HH alloys.

The enhancement of ZT in HH alloys employing elemental substitution of Ti, and/or Hf on Zr site [27–29], Co by Fe [30], Ir [28], or Rh [29], and Sb by Sn [25,27–29,31] has been previously reported. Despite employing several alloying strategies in HH alloys the highest ZT ≤ 0.8 has been achieved thus far in p-type ZrCoSb HH alloys [20,32,33]. It suggested that finer grain samples with average grain size less than 100 nm is desirable for further strengthening of the phonon scattering to achieve maximal reduction in thermal conductivity [33], while 10% Sn substitution at Sb site is optimal for attaining higher power factor [25]. In general, advanced material strategies include simultaneous integration of effective schemes together in a material [34]. While traditional approach of uniform doping or alloying have been widely studied for tuning the Fermi level and carrier concentration optimization, it was found to be detrimental to carrier mobility. Recently prospects of compositional modulation doping scheme was demonstrated as an advanced scheme for ZT enhancement by carrier mobility promotion [35,36]. Thus, subsuming nanostructuring paradigm in the compositionally modulated p-type ZrCoSb HH is a worthy prospect for realization of enhancing its TE performance.

In the current study, we report a state-of-the-art ZT ~1.1 at 873 K in an optimized composition of $Zr_{1-x}Hf_xCoSb_{0.9}Sn_{0.1}$ based p-type HH alloys synthesized employing high energy ball milling of pulverized arc-melted ingots followed by spark plasma sintering. This enhancement in ZT is due to the synergistic integration of nanostructuring and iso-electronic alloying for attaining compositional modulation i.e. grain-by-grain compositional variations, which leads to an enhanced scattering of heat-carrying phonons and the favourable tuning of electrical transport properties. In addition, the TE conversion characteristics of synthesized thermoelectric unicouple material was quantitatively estimated using the CTD model. The as-sintered samples were structurally characterised employing XRD, HR-TEM and FE-SEM, based on which the enhancement in their TE performance has been discussed.

2. Experimental details

High purity elemental Zr (foil, 99.97%), Hf (powder, 99.99%), Co (powder, 99.97%), Sb (shots, 99.999%) and Sn (shots, 99.999%) were weighed in stoichiometric amount according to their nominal compositions $Zr_{1-x}Hf_xCoSb_{0.9}Sn_{0.1}$ (where x = 0–0.5), and arc melted in argon atmosphere. The arc melted ingots (~5 g) were flipped and re-melted multiple times to ensure homogeneity. The ingots were then subsequently broken into small pieces and grounded to a fine powder using mortar and pestle and milled to finer grain size using high energy mechanical ball milling (HEBM, Fritsch, Pulverisette-4) at 300 rpm for 12 h with ball-to-powder weight ratio of 20:1. The grinding jars (250 ml) and balls (diameter: 5 mm) used in which are made of hardened stainless steel. The resulting nano-powders were loaded into the graphite die with an inner diameter of 12.7 mm and compacted by spark plasma sintering at 1473 K under 50 MPa in a vacuum to obtained bulk dense pellets. The density of the as-sintered samples measured using Archimedes method was found to be ~98.4% of the theoretical density.

The Seebeck coefficient (α) and electrical resistivity (σ) were measured simultaneously employing commercial equipment (ULVAC, ZEM3) over the temperature range of 323 K–873 K on samples of polished bars of about $3 \times 2 \times 10\ mm^3$. Thermal diffusivity (D) was measured in the range 323–873 K using a laser flash technique (Lineseis, LFA 1000) on disk-shaped specimens of diameter 12.7 mm and thickness of 2.0 mm sprayed with a layer of graphite in order to minimize errors due to emissivity. Specific heat (Cp) was measured using a differential scanning calorimetry (DSC) instrument. The accuracies in transport measurement are: ± 6% for thermal diffusivity, ± 7% for electrical conductivity, ± 7% for Seebeck coefficient, ± 10% for specific heat and ± 0.5% for density. The carrier concentration and mobility were determined using Hall Effect Measurement System (HEMS, Nano-magnetics), under a magnetic field of 0.5T. The constituent phases were determined by X-Ray Diffractometer (XRD; Rigaku Mini Flex II) using Cu Kα radiation (λ = 1.5406 Å). The morphology and elemental ratios of the samples are characterised by a field-emission scanning electron microscope (FE-SEM, Zeiss; Model: Supra 40VP), while microstructural analysis was carried out using High resolution transmission electron microscopy (HRTEM model: Tecnai G2F30 STWIN operated at the electron accelerating voltage of 300 kV).

3. Results and discussion

3.1. Phase composition and microstructure

Fig. 1(a) represents the crystal structure of the synthesized $Zr_{1-x}Hf_xCoSb_{0.9}Sn_{0.1}$ HH alloy, which consists of four inter-penetrating face centered cubic (FCC) sub-lattices where the Zr, Co and Sn/Sb atoms occupy the Wyckoff positions (0, 0, 0), (¼, ¼, ¼) and (½, ½, ½), while the fourth sub-lattice located at (¾, ¾, ¾) remains vacant and the Sb atom is partially replaced by Sn [25]. XRD pattern of the synthesized $Zr_{1-x}Hf_xCoSb_{0.9}Sn_{0.1}$ HH alloy for different compositions are shown in Fig. 1(b). The diffraction peaks of all compositions are well-indexed to the cubic half-Heusler $ZrCoSb_{0.9}Sn_{0.1}$ (PDF4+: 04-015-2508) with the space group $F\bar{4}3m$ [25] with no noticeable impurity phases. The estimated lattice parameters of all samples with different Hf/Zr ratios were plotted with respect to the Hf concentration in the $Zr_{1-x}Hf_xCoSb_{0.9}Sn_{0.1}$ HH alloy and are shown in Fig. 1(c). The lattice parameter was found to linearly decrease with increasing Hf content, following the Vegard's law suggesting complete incorporation of Hf in the HH matrix. The average crystallite size, as determined using Williamson Hall method [37] by employing the XRD data (Fig. 1(b)), was found to be around ~20 nm (Table 1) for all the synthesized HH alloys.

The FE-SEM images of a typical synthesized $Zr_{0.8}Hf_{0.2}CoSb_{0.9}Sn_{0.1}$ HH alloy is shown in Fig. 2(a–c), which reveals a densely packed microstructure, as an outcome of rapid heating rates attained by spark plasma sintering, which prevents grain growth and result in high densification. The equiaxed microstructure at low (Fig. 2(b) and higher (Fig. 2(c)) magnification exhibits nano-grained microstructure with the fine crystallites ~ 10–30 nm, which are in close agreement to that estimated using the XRD data (Fig. 1(b)). Additionally, an equiaxed microstructure at low and higher magnification of another synthesized

Please cite this article as: Chauhan NS et al., Enhanced thermoelectric performance in p-type ZrCoSb based half-Heusler alloys employing nanostructuring and compositional modulation, Journal of Materiomics, https://doi.org/10.1016/j.jmat.2018.11.003

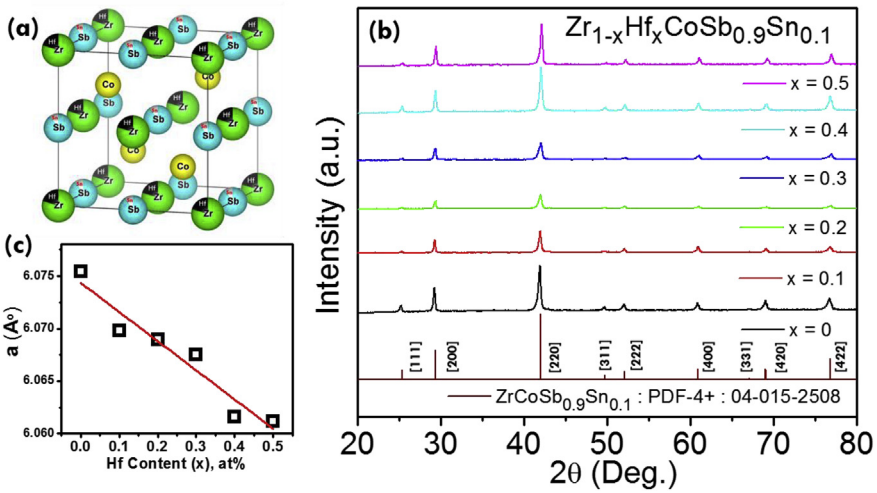


Fig. 1. Structural parameters of the synthesized $Zr_{1-x}Hf_xCoSb_{0.9}Sn_{0.1}$ (x = 0–0.5) half-Heusler alloys (a) Atomic Structure, (b) XRD patterns for different compositions, and (c) Lattice constant variation with composition.

Table 1
Room temperature physical parameters of half-Heusler $Zr_{1-x}Hf_xCoSb_{0.9}Sn_{0.1}$ (x = 0–0.5).

Parameters		x = 0	x = 0.1	x = 0.2	x = 0.3	x = 0.4	x = 0.5
Hall Coefficient R_H ($m^3\ C^{-1}$)		1.6×10^{-8}	8.3×10^{-8}	9.4×10^{-8}	1.1×10^{-8}	9.7×10^{-8}	8.6×10^{-8}
Carrier Concentration n (cm^{-3})		3.9×10^{20}	7.5×10^{19}	6.6×10^{19}	5.4×10^{19}	6.4×10^{19}	7.3×10^{19}
Hall Mobility μ ($cm^2\ V^{-1}\ s^{-1}$)		15	73	94	125	115	112
Effective Mass		$3.68m_e$	$1.33m_e$	$1.23m_e$	$1.08m_e$	$1.14m_e$	$1.17m_e$
Average Carrier MFP (Å)		26.6	15.8	19.4	24.0	23.4	23.7
Average Phonon MFP (nm)	323K	27.3	15.5	11.3	9.5	8.2	7.6
	873K	14.0	9.3	6.7	5.3	5.4	6.2
Average Crystallite Size (nm)		22	20	22	21	22	23
E_F (meV)		52.9	48.9	48.5	47.9	51.3	54.2

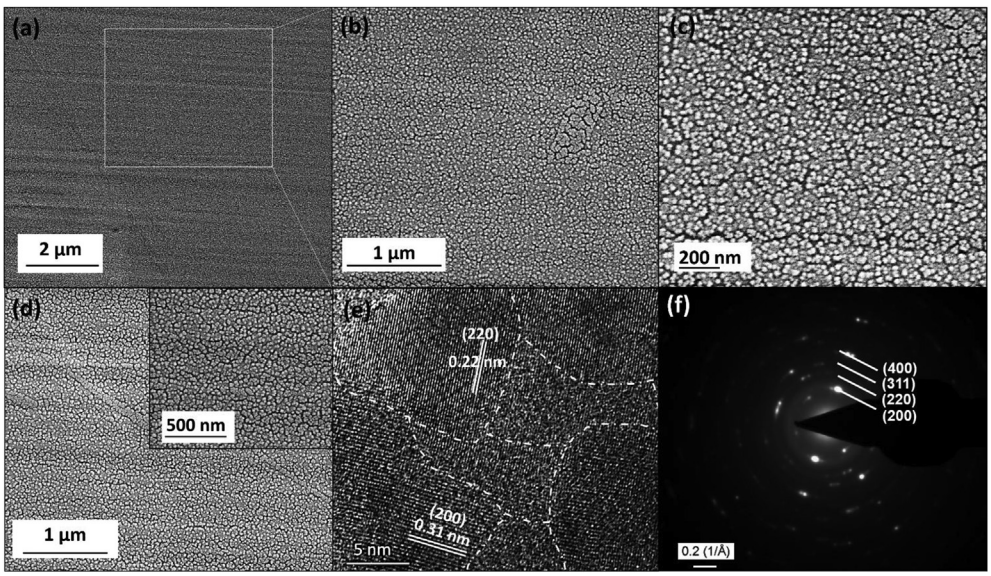


Fig. 2. FE-SEM image of typical $Zr_{0.8}Hf_{0.2}CoSb_{0.9}Sn_{0.1}$ half-Heusler alloy at (a) Low-magnification showing dense microstructure and at (b–c) high magnification indicating nanostructured morphology; (d) FE-SEM image of $Zr_{0.7}Hf_{0.3}CoSb_{0.9}Sn_{0.1}$ half-Heusler alloy at low and high magnification. HR-TEM micrographs showing (e) lattice scale image of nanostructured $Zr_{0.8}Hf_{0.2}CoSb_{0.9}Sn_{0.1}$, exhibiting the presence of different orientations of the crystallographic planes and their interface boundaries image, and its corresponding (f) Selected area electron diffraction pattern (SAED) confirming polycrystalline half-Heusler phase.

Please cite this article as: Chauhan NS et al., Enhanced thermoelectric performance in p-type ZrCoSb based half-Heusler alloys employing nanostructuring and compositional modulation, Journal of Materiomics, https://doi.org/10.1016/j.jmat.2018.11.003

HH alloys ($Zr_{0.7}Hf_{0.3}CoSb_{0.9}Sn_{0.1}$) is shown in Fig. 2(d), which also confirms the presence of nanosized grains.

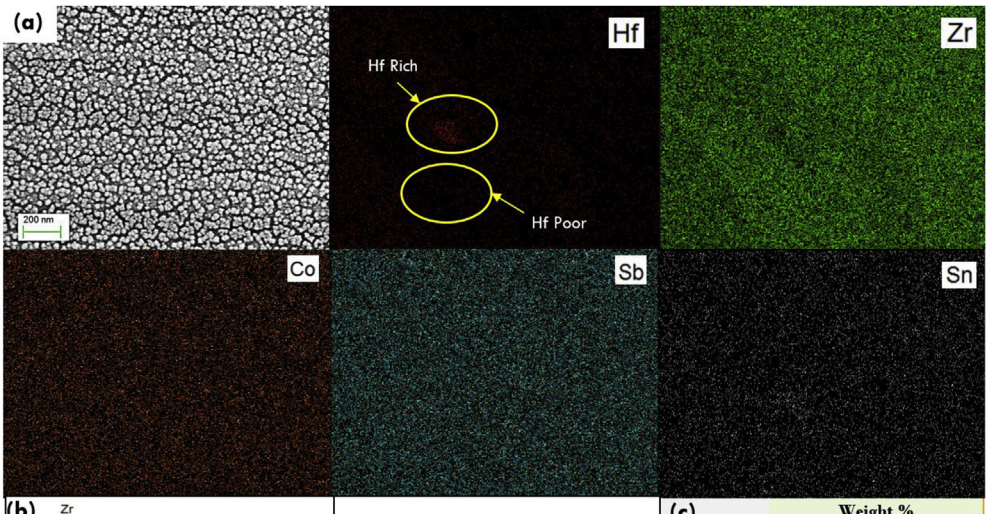
To further investigate the microscopic features in the representative $Zr_{0.8}Hf_{0.2}CoSb_{0.9}Sn_{0.1}$ HH alloy, HR-TEM analysis was performed in real and reciprocal space. Fig. 2(e), presents the obtained lattice scale image of nanostructured $Zr_{0.8}Hf_{0.2}CoSb_{0.9}Sn_{0.1}$ for a single particle. The image indicates the presence highly crystalline nanograins having different orientations of the crystallographic planes and their interface boundaries, which reveals the polycrystalline nature of individual particles. It can be seen that particles consist of grains up to 20 nm in size, similar to the size of the obtained nanostructured powder after ball milling, indicating insignificant grain growth during spark plasma sintering. This also agrees fairly well with the size calculated from the XRD spectra (Fig. 1(b)). A corresponding selected area electron diffraction pattern (SAED) recorded for Fig. 2(e), is shown in Fig. 2(f), which also reveals the presence of atomic planes of HH (hkl: 200, 220, 311 and 400) in the reciprocal space.

Overall, the low magnification FESEM micrographs (Fig. 2(a) – (d)) suggests that the synthesized HH samples are quite dense without any evidence of porosity or cracks, which is also supported by the high magnification HR-TEM lattice image (Fig. 2(e)) and the measured density of the synthesized HH sample (~98.4% of the theoretical density). This is primarily due to the sintering employing SPS, which is known not only to result in dense samples but also maintain the nanoscale features post-sintering.

Furthermore, the microstructure at higher magnification of the representative HH alloy ($Zr_{0.8}Hf_{0.2}CoSb_{0.9}Sn_{0.1}$) alongwith its elemental mapping is shown in Fig. 3 (a). The microstructure exhibited nanostructured morphology whose elemental mapping, clearly indicates the signatures of the constituent elements with Hf-rich and Hf-deficient regions heterogeneously distributed within the HH matrix (marked as region 1 & 2 in the figure). The variation in the stoichiometry in these two region was examined using energy-dispersive x-ray spectroscopy (EDX) and the resulting spectrum is shown in Fig. 3 (b), and quantitatively tabulated in Fig. 3(c). These observations quantitatively confirm the grain-by-grain compositional variations and presence of Hf-rich and Hf-deficient regions, heterogeneously distributed throughout the sample. Such compositionally modulated samples, although single-phase, behave similar to phase-separated composite material that exhibit grain-by-grain compositional variations, thus leading to an enhancement in the electrical transport properties, which is discussed in the forthcoming section.

3.2. Thermoelectric transport properties

The temperature dependence of TE transport properties of the synthesized $Zr_{1-x}Hf_xCoSb_{0.9}Sn_{0.1}$ HH alloys for different compositions are depicted in Fig. 4. All the samples exhibit a p-type degenerate semiconducting behaviour indicated by the positive values of α and decreasing σ with increasing temperature shown in Fig. 4(a, b). Furthermore, the σ increases with increasing content of Hf, while α initially increases up to a composition $x = 0.3$ in $Zr_{1-x}Hf_xCoSb_{0.9}Sn_{0.1}$ exhibiting a maximum value of ~255 μV/K at 873 K and decreases thereafter. The effect of Hf substitution on the electrical transport can be understood in terms of the Hall data, as shown in Table 1. The measured hall coefficient for the base composition $ZrCoSb_{0.9}Sn_{0.1}$ was found to be in similar order with high carrier concentrations (~10^{20}/cm^3) as reported previously for similar Sn content [31]. It is well known that any substitution, at such high levels of carrier concentration, tends to cause strong ionized impurity scattering of charge carriers, which severely limits the carrier mobility and electronic conductivity. However, it was previously reported [38,39] that very high carrier mobility can be attained via. modulating doping by minimizing the ionized impurity scattering. A typical modulation doped material contains heavily doped regions and undoped regions within the material,



(c)

Element	Weight % Region 1	Region 2
Zr	24.63	20.63
Hf	11.65	16.04
Co	27.04	26.63
Sb	35.29	35.20
Sn	1.39	1.50

Fig. 3. (a) FE-SEM image exhibiting the nano-sized grains alongwith elemental distribution of constituent elements and (b, c) EDS analysis; of the synthesized $Zr_{0.8}Hf_{0.2}CoSb_{0.9}Sn_{0.1}$ half-Heusler alloys.

Please cite this article as: Chauhan NS et al., Enhanced thermoelectric performance in p-type ZrCoSb based half-Heusler alloys employing nanostructuring and compositional modulation, Journal of Materiomics, https://doi.org/10.1016/j.jmat.2018.11.003

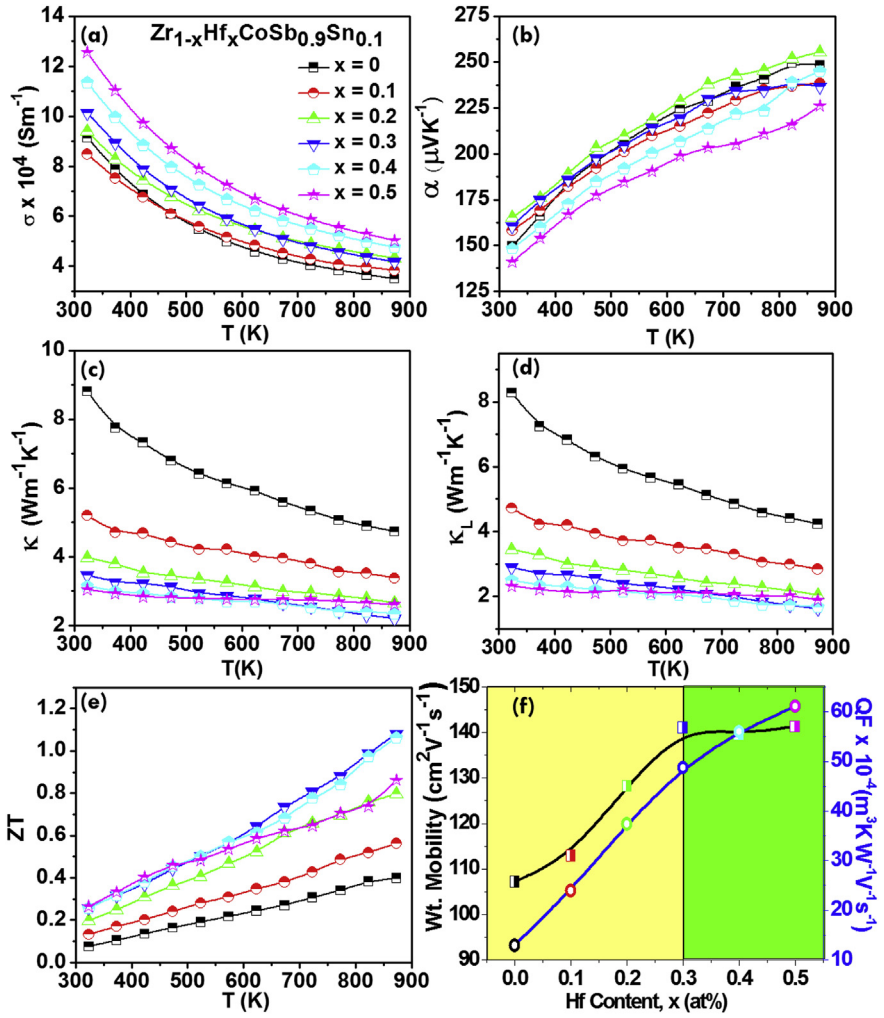


Fig. 4. Temperature dependence of thermoelectric transport properties of $Zr_{1-x}Hf_xCoSb_{0.9}Sn_{0.1}$ (x = 0–0.5) half-Heusler alloys (a) Electrical Conductivity; (b) Seebeck coefficient; (c) Total thermal conductivity; (d) Lattice thermal conductivity; (e) Thermoelectric figure of merit (ZT) and (f) Weighted mobility and Quality factor as a function of Hf concentration.

and remote doping is provided by heavily doped regions to the active undoped region. In our synthesized HH samples, it was observed (Fig. 3) that non-uniform distributions of Hf (dopant) atoms results in heavily doped Hf-rich regions and undoped Hf-deficient regions, heterogeneously distributed within the HH matrix.

It is apparent from Table 1 that with increasing Hf substitution the carrier concentration decreases drastically due to carrier scattering up to x = 0.3, and increases thereafter. While in contrast, the carrier mobility exhibits an increasing trend. The Hall data thus suggests the occurrence of a carrier filtering mechanism, which may be due to the grain-by-grain compositional variation in the synthesized HH alloys owing to the presence of Hf-rich and Hf-deficient regions within the HH matrix. As a result of this, a significant increase in the carrier mobility at lower Hf composition (x < 0.3) was observed, wherein the Hf-rich regions provide the high mobility carriers to the active undoped regions, resulting in an improved carrier mobility (Table 1). The compositional modulation approach thus mitigates the detrimental effects of Hf substitution on the carrier mobility, especially at high carrier concentrations.

As shown in Fig. 4(a), the σ of the all Hf substituted samples are higher than that of the pristine counterpart ($ZrCoSb_{0.9}Sn_{0.1}$), which suggest that despite a decrease in carrier concentration at lower concentration of Hf substitution, the increase in the carrier mobility results in an overall improvement of σ. However, the decrease in the carrier mobility at higher Hf content was subjugated by an increase in the carrier concentration. To further elucidate the electrical transport features of synthesized HH alloys, the carrier dependency of Fermi energy ($E_F = \frac{\pi^2 k_B^2 T}{3e\alpha}$), effective mass $\left(m^* = \frac{3eh^2\alpha}{8\pi^2 k_B^2 T}\left(\frac{3p}{\pi}\right)^{3/2}\right)$ and average carrier mean free path ($MFP = \sqrt{2E_F m^*}\frac{\mu}{e}$) were estimated using the experimental Seebeck coefficient data [40]. Table 1 show the calculated values of E_F, m^* and carrier MFP, whose variation trends are consistent with corresponding changes in α and σ observed in this study (Fig. 4(a and b)).

The temperature dependence of the total thermal conductivity (κ) and the lattice thermal conductivity ($κ_l$) of the synthesized HH samples is presented in Fig. 4(c & d), respectively. The $κ_l$ was obtained using $κ_l = κ - κ_e$, where the electronic thermal conductivity ($κ_e$) is calculated using the Wiedemann–Franz Law as $κ_e = L\sigma T$ (where L is the Lorenz number, estimated using the temperature dependent Seebeck coefficient data [41]. A value of κ ~2.2 W $m^{-1}K^{-1}$ at 873 K was observed in the optimized HH compositions $Zr_{1-x}Hf_xCoSb_{0.9}Sn_{0.1}$ (x = 0.3–0.4), which is amongst the lowest reported in p-type HH alloys thus far [21,32,33]. On comparing Fig. 4(c and d) it can be inferred that the major contribution comes to the κ originates from $κ_l$. The FE-SEM image

Please cite this article as: Chauhan NS et al., Enhanced thermoelectric performance in p-type ZrCoSb based half-Heusler alloys employing nanostructuring and compositional modulation, Journal of Materiomics, https://doi.org/10.1016/j.jmat.2018.11.003

(Fig. 4(a)) indicates that the synthesized HH alloys comprise of nanoscale crystallites (~10–30 nm) with a high density of nanocrystallite boundaries, which scatter heat-carrying phonons thereby leading to a substantial reduction in κ_l, which majorly contributes to the reduction in κ of the HH alloys. The nanostructuring contributes effectively in reducing the κ_l of pristine as well as the Hf-substituted HH samples, although this contribution is much higher at lower temperatures. Further, mass fluctuations owing to a large atomic mass difference between Zr and Hf also contribute towards lowering of the κ.

To further understand the phonon dynamics, the average phonon mean free path (MFP) was estimated using $l = 3\kappa_l/C_v u$ [42,43] where C_v , u and l represents the specific heat at constant volume, average phonon velocity and mean free path, respectively. The estimated average phonon MFP (shown in Table 1) which is substantially lowered than those reported earlier for similar HH compositions [44–47]. Table 1 also indicates that the phonon MFP decreases substantially with increasing Hf substitution although the crystallite size varies marginally. This suggest that Hf-substitution additionally contributes towards reduction in the phonon MFP, by creating defect scattering for phonons due to mass fluctuation and strain field fluctuation. Additionally, has also been reported earlier that in HH alloys most of the heat is transported by phonons with MFP in the range ~0.6–30 nm [48] and the calculated phonon MFP of our synthesized HH samples (Table 1) lie in this phonon-scattering favourable range, which also explains the significantly low κ in our HH samples. Thus, the compositional modulation in the synthesized $Zr_{1-x}Hf_xCoSn_{0.9}Sn_{0.1}$ HH alloys demonstrates the effectiveness of Hf substitution and nanostructuring in suppressing the κ_l.

3.3. Thermoelectric performance and compatibility factor

As shown in Fig. 4(e), a maximum ZT of ~1.1 was achieved at 873 K in the optimized p-type HH composition of $Zr_{1-x}Hf_xCoSn_{0.9}Sn_{0.1}$ (at $x = 0.3$, 0.4), which is the state-of-the-art value for p-type HH alloys, higher than those previously reported for ZrCoSb [20,25,27,29,31–33,49] and comparable to TiCoSb [21,23,49] and FeNbSb [50–52] based HH alloys. Such enhancement corresponds to ~170% increase in ZT compared to base composition $ZrCoSb_{0.9}Sn_{0.1}$ and is also comparable to the other actively explored p-type TE materials [53–56]. This enhancement in ZT is due to the synergistic contribution of nanostructuring as well as substitutional alloying, however it is rather tedious to separate their individual contribution. Additionally, the weighted mobility, $\mu_w = \mu\,(m^*/m_e)^{3/2}$ and TE quality factor $QF = \mu(m^*/m_e)^{3/2}\kappa_l^{-1}$, which primarily determines the optimal electrical performance, was also estimated and is shown in Fig. 4(f). This figure indicates that both the weighted mobility and TE quality factor increase with increasing Hf content and suggests $Zr_{0.7}Hf_{0.3}CoSn_{0.9}Sn_{0.1}$ as the optimized HH composition at which ZT exhibits a maxima.

The relationship between ZT and energy conversion efficiency (η_{max}) based on cumulative temperature dependence (CTD) of the thermoelectric transport properties formulated by Kim et al. [6,7] was used for reliable prediction of the TE performance of the synthesized HH alloys. The engineering figure-of-merit $(ZT)_{eng}$, as direct indicators, which exhibit linear correlations to efficiency is shown in Fig. 5(a). In all the Hf-substituted samples, an improvement in $(ZT)_{eng}$ was observed when compared with pristine $ZrCoSb_{0.9}Sn_{0.1}$ sample. The output power density (P_d) at the maximum efficiency estimated using the CTD model is expressed as [57] $P_d = \frac{(PF)_{eng}\,(T_H - T_C)^2}{4L}$. Where, L is the length of the TE material, T_h is the temperature at the hot junction and T_c the temperature at the cold junction. Considering, $T_H = 323$ K and leg length = 2 mm, a cubic-shaped TE leg is assumed for comparison with the output power prediction reported previously [6,7] for state-of-the-art p-type TE material (including SnSe, $MnSi_{1.78}$, $Pb_{0.98}Te_{0.75}Se_{0.25}K_{0.02}$). The calculated P_d as shown in Fig. 5(b), indicates enhancement in P_d of all the Hf-substituted samples, reaching a maximum of 10 Wcm^{-2}. The output power density is dependent on the TE leg's dimensions as well as the material properties whereas the efficiency is determined only by the material's characteristics.

Conventionally, the maximum efficiency of a TE device is

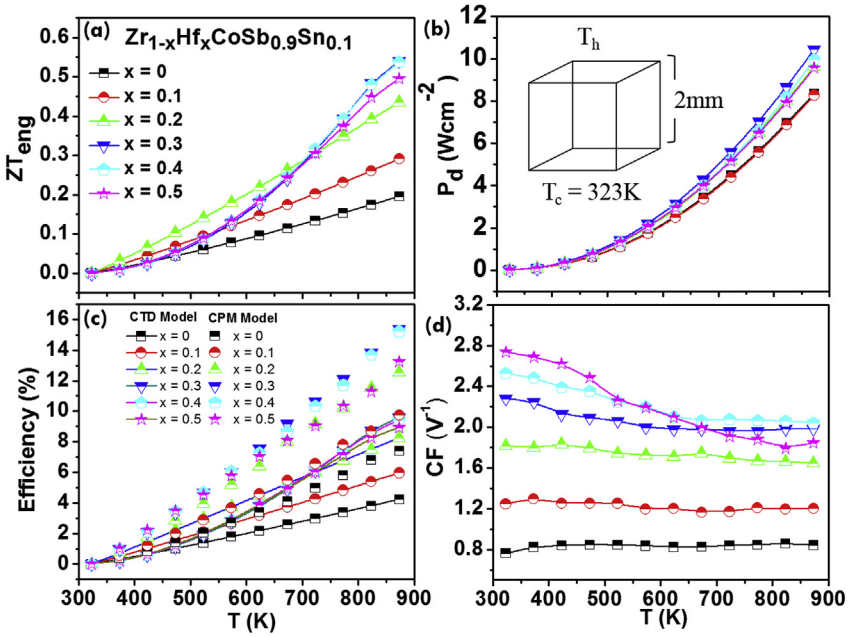


Fig. 5. Theoretically estimated TE device parameters of $Zr_{1-x}Hf_xCoSb_{0.9}Sn_{0.1}$ ($x = 0$–0.5) half-Heusler alloys (a) Engineering Thermoelectric figure of Merit; (b) Output Power Density; (c) Thermoelectric efficiency and (d) Compatibility factor.

Please cite this article as: Chauhan NS et al., Enhanced thermoelectric performance in p-type ZrCoSb based half-Heusler alloys employing nanostructuring and compositional modulation, Journal of Materiomics, https://doi.org/10.1016/j.jmat.2018.11.003

generally derived based on a constant property model (CPM) [6]. Fig. 5 (c) shows the efficiency prediction using CPM and CTD model with the temperature boundary condition that T_h increases while T_c is kept constant at 323 K [6]. It is reported that the calculation by CPM model overestimates the efficiency which is found to be almost twice of the efficiency calculated using the CTD model [6]. As shown in Fig. 5(c), maximum efficiency of ~10% for p-type was obtained using CTD model which represents significant TE conversion which is comparable to those reported earlier [6,7] for state-of-the-art p-type TE material (including SnSe, $MnSi_{1.78}$, $Pb_{0.98}Te_{0.75}Se_{0.25}K_{0.02}$) by the CTD model. As explicit indicators of TE performance, the output power density and efficiency provide a viewpoint for the applicability of the synthesized materials in TE devices, however, due to the device related issues such as, contact resistance and heat losses, the actual TE performance, is expected to be lower than the theoretical estimates.

The efficacy of segmentation, proposed for increasing the TE efficiency, is estimated using TE compatibility factor (CF) given as [58], $CF = \frac{\sqrt{1+ZT}-1}{\alpha T}$. From the applicability viewpoint, difference in compatibility factors for the two TE materials should be less than a factor of 2. Fig. 5(d) shows the calculated CF of synthesized TE materials, which increases with increasing temperature and is significantly enhanced compared to the pristine $ZrCoSb_{0.9}Sn_{0.1}$, while being comparable to the other state-of-the-art p-type TE materials such as TAGS, PbTe, $CeFe_4Sb_{12}$, SnTe etc. [59]. Thus, the synthesized p-type HH alloys could be a suitable TE material for segmentation with various TE materials for achieving highly efficient TE based power generation in the mid-temperature regime.

4. Conclusion

A state-of-the-art ZT ~1.1 at 873 K was achieved by integrating alloying and nanostructuring to attain compositional modulation i.e. grain-by-grain compositional variations in p-type ZrCoSb-based HH alloys. The HH alloys were synthesized using high-energy ball-milling of the arc-melted ingots, followed by the spark plasma sintering of the resulting HH alloy nano-powders. The efficacy of Hf-substitution and nanostructuring has been experimentally realized to attain a very low thermal conductivity, which enhances the ZT in ZrCoSb-based Half-Heusler TE alloys, making them promising candidates for mid-temperature power generation applications. The fundamental understanding of cumulative temperature dependence on thermoelectric characteristics of the materials is also presented using CTD model to enable better understanding of rational materials selection and device engineering to achieve higher thermoelectric conversion efficiency.

Conflicts of interest

Authors declare that there are no conflicts of interest.

Acknowledgements

The authors acknowledge the Board of Research in Nuclear Sciences, India for the financial support under the Scheme: 37(3)/14/22/2016-BRNS with BSC. Nagendra S. Chauhan acknowledges CSIR- Senior Research Fellowship. (Grant No : 31/001(0430)/2014-EMR-1)The technical support rendered by Dr. Vidya Nand Singh, Mr. Radhey Shyam, and Mr. Naval Kishor Upadhyay is also gratefully acknowledged.

Appendix A. Supplementary data

Supplementary data to this article can be found online at https://doi.org/10.1016/j.jmat.2018.11.003.

References

[1] Gingerich DB, Mauter MS. Quantity, quality, and availability of waste heat from United States thermal power generation. Environ Sci Technol 2015;49:8297–306.
[2] Bell LE. Cooling, heating, generating power, and recovering waste heat with thermoelectric systems. Science 2008;321:1457–61.
[3] LeBlanc S. Thermoelectric generators: linking material properties and systems engineering for waste heat recovery applications. Sustainable Materials and Technologies 2014;1:26–35.
[4] Snyder GJ, Toberer ES. Complex thermoelectric materials. Nat Mater 2008;7:105–14.
[5] Zebarjadi M, Esfarjani K, Dresselhaus M, Ren Z, Chen G. Perspectives on thermoelectrics: from fundamentals to device applications. Energy Environ Sci 2012;5:5147–62.
[6] Kim HS, Liu W, Chen G, Chu C-W, Ren Z. Relationship between thermoelectric figure of merit and energy conversion efficiency. Proc Natl Acad Sci Unit States Am 2015;112:8205–10.
[7] Kim HS, Liu W, Ren Z. The bridge between the materials and devices of thermoelectric power generators. Energy Environ Sci 2017;10:69–85.
[8] Zhu T, Fu C, Xie H, Liu Y, Zhao X. High efficiency half-heusler thermoelectric materials for energy harvesting. Advanced Energy Materials 2015;5.
[9] Chen S, Ren Z. Recent progress of half-Heusler for moderate temperature thermoelectric applications. Mater Today 2013;16:387–95.
[10] Poon SJ, Wu D, Zhu S, Xie W, Tritt TM, Thomas P, Venkatasubramanian R. Half-Heusler phases and nanocomposites as emerging high-ZT thermoelectric materials. J Mater Res 2011;26:2795–802.
[11] Graf T, Felser C, Parkin SS. Simple rules for the understanding of Heusler compounds. Prog Solid State Chem 2011;39:1–50.
[12] Bos J-WG, Downie RA. Half-Heusler thermoelectrics: a complex class of materials. J Phys Condens Matter 2014;26:433201.
[13] Chauhan NS, Bathula S, Vishwakarma A, Bhardwaj R, Gahtori B, Kumar A, Dhar A. Vanadium doping induced resonant energy levels for the enhancement of thermoelectric performance in Hf-free ZrNiSn half-heusler alloys. ACS Appl Energy Mater 2018;1(2):757–64.
[14] Chen S, Lukas KC, Liu W, Opeil CP, Chen G, Ren Z. Effect of Hf concentration on thermoelectric properties of nanostructured N-type half-heusler materials HfxZr1−xNiSn0. 99Sb0. 01. Advanced Energy Materials 2013;3:1210–4.
[15] Bhardwaj A, Chauhan N, Sancheti B, Pandey G, Senguttuvan T, Misra D. Panoscopically optimized thermoelectric performance of a half-Heusler/full-Heusler based in situ bulk composite Zr 0.7 Hf 0.3 Ni 1+ x Sn: an energy and time efficient way. Phys Chem Chem Phys 2015;17:30090–101.
[16] Chauhan NS, Bathula S, Vishwakarma A, Bhardwaj R, Gahtori B, Srivastava AK, Saravanan M, Dhar A. A nanocomposite approach for enhancement of thermoelectric performance in Hafnium-free Half-Heuslers. Materialia 2018;1:168–74.
[17] Chauhan NS, Bathula S, Vishwakarma A, Bhardwaj R, Johari KK, Gahtori B, Saravanan M, Dhar A. Compositional tuning of ZrNiSn half-Heusler alloys: thermoelectric characteristics and performance analysis. J Phys Chem Solid 2018;123:105–12.
[18] Bhattacharya S, Pope A, Littleton IV R, Tritt TM, Ponnambalam V, Xia Y, Poon S. Effect of Sb doping on the thermoelectric properties of Ti-based half-Heusler compounds, TiNiSn 1− x Sb x. Appl Phys Lett 2000;77:2476–8.
[19] Misra D, Rajput A, Bhardwaj A, Chauhan N, Singh S. Enhanced power factor and reduced thermal conductivity of a half-Heusler derivative Ti9Ni7Sn8: a bulk nanocomposite thermoelectric material. Appl Phys Lett 2015;106:103901.
[20] Chauhan NS, Bhardwaj A, Senguttuvan T, Pant R, Mallik R, Misra D. A synergistic combination of atomic scale structural engineering and panoscopic approach in p-type ZrCoSb-based half-Heusler thermoelectric materials for achieving high ZT. J Mater Chem C 2016;4:5766–78.
[21] Yan X, Liu W, Chen S, Wang H, Zhang Q, Chen G, Ren Z. Thermoelectric property study of nanostructured p-type half-heuslers (Hf, Zr, Ti) CoSb0. 8Sn0. 2. Advanced Energy Materials 2013;3:1195–200.
[22] Chauhan NS, Bathula S, Vishwakarma A, Bhardwaj R, Johari KK, Gahtori B, Dhar A. Facile fabrication of p-and n-type half-Heusler alloys with enhanced thermoelectric performance and low specific contact resistance employing spark plasma sintering. Mater Lett 2018;228:250–3.
[23] Yan X, Liu W, Wang H, Chen S, Shiomi J, Esfarjani K, Wang H, Wang D, Chen G, Ren Z. Stronger phonon scattering by larger differences in atomic mass and size in p-type half-Heuslers Hf 1− x Ti x CoSb 0.8 Sn 0.2. Energy Environ Sci 2012;5:7543–8.
[24] Joshi G, He R, Engber M, Samsonidze G, Pantha T, Dahal E, Dahal K, Yang J, Lan Y, Kozinsky B. NbFeSb-based p-type half-Heuslers for power generation applications. Energy Environ Sci 2014;7:4070–6.
[25] Sekimoto T, Kurosaki K, Muta H, Yamanaka S. High-thermoelectric figure of merit realized in p-type half-Heusler compounds: ZrCoSnxSb1-x. Jpn J Appl Phys 2007;46:L673.
[26] Rausch E, Balke B, Ouardi S, Felser C. Enhanced thermoelectric performance in the p-type half-Heusler (Ti/Zr/Hf) CoSb 0.8 Sn 0.2 system via phase separation. Phys Chem Chem Phys 2014;16:25258–62.
[27] Culp SR, Simonson J, Poon SJ, Ponnambalam V, Edwards J, Tritt TM. (Zr, Hf) Co

(Sb, Sn) half-Heusler phases as high-temperature (> 700° C) p-type thermoelectric materials. Appl Phys Lett 2008;93, 022105.
[28] Takas NJ, Shabetai MR, Poudeu PF. Effect of Sn doping on the thermoelectric performance of the complex p-type Zr0. 5Hf0. 5Co0. 3Ir0. 7Sb1−ySn y half-heusler system. Sci Adv Mater 2011;3:571−6.
[29] Maji P, Takas NJ, Misra DK, Gabrisch H, Stokes K, Poudeu PF. Effects of Rh on the thermoelectric performance of the p-type Zr 0.5 Hf 0.5 Co 1− xRhxSb 0.99 Sn 0.01 half-Heusler alloys. J Solid State Chem 2010;183:1120−6.
[30] Hsu C-C, Ma H-K. Microstructure and thermoelectric properties in Fe-doped ZrCoSb half-Heusler compounds. Mater Sci Eng, B 2015;198:80−5.
[31] Yuan B, Wang B, Huang L, Lei X, Zhao L, Wang C, Zhang Q. Effects of Sb substitution by Sn on the thermoelectric properties of ZrCoSb. J Electron Mater 2017;46:3076−82.
[32] He R, Kim HS, Lan Y, Wang D, Chen S, Ren Z. Investigating the thermoelectric properties of p-type half-Heusler Hf x (ZrTi) 1− x CoSb 0.8 Sn 0.2 by reducing Hf concentration for power generation. RSC Adv 2014;4:64711−6.
[33] Yan X, Joshi G, Liu W, Lan Y, Wang H, Lee S, Simonson J, Poon S, Tritt T, Chen G. Enhanced thermoelectric figure of merit of p-type half-Heuslers. Nano Lett 2010;11:556−60.
[34] Zhou X, Yan Y, Lu X, Zhu H, Han X, Chen G, Ren Z. Routes for high-performance thermoelectric materials, Materials Today 2018.
[35] Berry T, Fu C, Auffermann G, Fecher GH, Schnelle W, Serrano-Sanchez F, Yue Y, Liang H, Felser C. Enhancing thermoelectric performance of TiNiSn half-heusler compounds via modulation doping. Chem Mater 2017;29:7042−8.
[36] Wang J, Zhang B-Y, Kang H-J, Li Y, Yaer X, Li J-F, Tan Q, Zhang S, Fan G-H, Liu C-Y. Record high thermoelectric performance in bulk SrTiO3 via nano-scale modulation doping. Nanomater Energy 2017;35:387−95.
[37] Williamson G, Hall W. X-ray line broadening from filed aluminium and wolfram. Acta Metall 1953;1:22−31.
[38] Yu B, Zebarjadi M, Wang H, Lukas K, Wang H, Wang D, Opeil C, Dresselhaus M, Chen G, Ren Z. Enhancement of thermoelectric properties by modulation-doping in silicon germanium alloy nanocomposites. Nano Lett 2012;12:2077−82.
[39] Pei Y-L, Wu H, Wu D, Zheng F, He J. High thermoelectric performance realized in a BiCuSeO system by improving Carrier mobility through 3D modulation doping. J Am Chem Soc 2014;136:13902−8.
[40] Zhu T, Gao H, Chen Y, Zhao X. Ioffe−Regel limit and lattice thermal conductivity reduction of high performance (AgSbTe 2) 15 (GeTe) 85 thermoelectric materials. J Mater Chem 2014;2:3251−6.
[41] Kim H-S, Gibbs ZM, Tang Y, Wang H, Snyder GJ. Characterization of Lorenz number with Seebeck coefficient measurement. Apl Mater 2015;3, 041506.
[42] Cahill DG, Braun PV, Chen G, Clarke DR, Fan S, Goodson KE, Keblinski P, King WP, Mahan GD, Majumdar A. Nanoscale thermal transport. II. 2003−2012. Appl Phys Rev 2014;1, 011305.
[43] Kittel C. Interpretation of the thermal conductivity of glasses. Phys Rev 1949;75:972.
[44] Zhu T, Fu C, Xie H, Liu Y, Feng B, Xie J, Zhao X. Lattice thermal conductivity and spectral phonon scattering in FeVSb-based half-Heusler compounds. EPL (Europhysics Letters) 2013;104:46003.
[45] Hermet P, Jund P. Lattice thermal conductivity of NiTiSn half-Heusler thermoelectric materials from first-principles calculations. J Alloy Comp 2016;688:248−52.
[46] Sharp J, Poon S, Goldsmid H. Boundary scattering and the thermoelectric figure of merit. Phys Status Solidi 2001;187:507−16.
[47] Bhattacharya S, Skove M, Russell M, Tritt T, Xia Y, Ponnambalam V, Poon S, Thadhani N. Effect of boundary scattering on the thermal conductivity of TiNiSn-based half-Heusler alloys. Phys Rev B 2008;77:184203.
[48] Fu C, Liu Y, Xie H, Liu X, Zhao X, Jeffrey Snyder G, Xie J, Zhu T. Electron and phonon transport in Co-doped FeV0. 6Nb0. 4Sb half-Heusler thermoelectric materials. J Appl Phys 2013;114:134905.
[49] Rausch E, Balke B, Stahlhofen JM, Ouardi S, Burkhardt U, Felser C. Fine tuning of thermoelectric performance in phase-separated half-Heusler compounds. J Mater Chem C 2015;3:10409−14.
[50] Fu C, Zhu T, Liu Y, Xie H, Zhao X. Band engineering of high performance p-type FeNbSb based half-Heusler thermoelectric materials for figure of merit zT> 1. Energy Environ Sci 2015;8:216−20.
[51] Fu C, Zhu T, Pei Y, Xie H, Wang H, Snyder GJ, Liu Y, Liu Y, Zhao X. High band degeneracy contributes to high thermoelectric performance in p-type half-heusler compounds. Advanced Energy Materials 2014;4.
[52] Yu J, Fu C, Liu Y, Xia K, Aydemir U, Chasapis TC, Snyder GJ, Zhao X, Zhu T. Unique role of refractory Ta alloying in enhancing the figure of merit of NbFeSb thermoelectric materials. Advanced Energy Materials 2018;8:1701313.
[53] Bathula S, Jayasimhadri M, Gahtori B, Singh NK, Tyagi K, Srivastava A, Dhar A. The role of nanoscale defect features in enhancing the thermoelectric performance of p-type nanostructured SiGe alloys. Nanoscale 2015;7:12474−83.
[54] Prasad KS, Rao A, Tyagi K, Chauhan NS, Gahtori B, Bathula S, Dhar A. Enhanced thermoelectric performance of Pb doped Cu2SnSe3 synthesized employing spark plasma sintering. Phys B Condens Matter 2017;512:39−44.
[55] Prasad KS, Rao A, Chauhan NS, Bhardwaj R, Vishwakarma A, Tyagi K. Thermoelectric properties of p-type sb-doped Cu2SnSe3 near room and mid temperature applications. Appl Phys A 2018;124:98.
[56] Upadhyay NK, Kumaraswamidhas L, Gahtori B, Bathula S, Muthiah S, Shyam R, Chauhan NS, Bhardwaj R, Dhar A. Enhancement in thermoelectric performance of bulk CrSi 2 dispersed with nanostructured SiGe nanoinclusions. J Alloy Comp 2018;765:412−7.
[57] He R, Kraemer D, Mao J, Zeng L, Jie Q, Lan Y, Li C, Shuai J, Kim HS, Liu Y. Achieving high power factor and output power density in p-type half-Heuslers Nb1-xTixFeSb. Proc Natl Acad Sci Unit States Am 2016;113:13576−81.
[58] Snyder GJ, Ursell TS. Thermoelectric efficiency and compatibility. Phys Rev Lett 2003;91:148301.
[59] Snyder GJ, Caillat T. Using the compatibility factor to design high efficiency segmented thermoelectric generators. In: MRS Online Proceedings Library Archive; 2003. p. 793.



Mr. Nagendra Singh Chauhan is a CSIR-Senior Research Fellow at CSIR-National Physical Laboratory, New Delhi, India registered for Ph.D at the Academy of Scientific and Innovative Research (AcSIR), India. He received his M.Tech (Material Science & Technology) degree from Maulana Azad National Institute of Technology, India and his B.E (Mechanical) degree from Savitribai Phule Pune University, India. His current research interests focuses on advanced energy materials and devices for power generation.



Dr. Bathula Sivaiah is a Ph.D (Applied Physics) from Delhi Technological University, India and is currently working as Senior Scientist at CSIR-National Physical Laboratory, India. He received his M.Tech (Materials and Metallurgical Engineering) from Indian Institute of Technology (IIT), Kanpur, and B.Tech (Materials and Metallurgical Engineering) from National Institute of Technology (NIT), Warangal. He is also a Faculty at the Academy of Scientific and Innovative Research (AcSIR), India. He has published more than 50 research papers in scientific journals and presented his research work in more than 10 national and international conferences.



Mr. Avinash Vishwakarma is a Junior Research Fellow at CSIR-National Physical Laboratory, New Delhi, India registered for Ph.D at the Academy of Scientific and Innovative Research (AcSIR), India. He received his Master and Bachelor degree in Science from Banaras Hindu University, India. His current research interest focuses on half-Heusler thermoelectric materials.



Ms. Ruchi Bhardwaj is a Junior Research Fellow at CSIR-National Physical Laboratory, New Delhi, India registered for Ph.D at the Academy of Scientific and Innovative Research (AcSIR), India. She received her M.Sc. degree in Physics from Chaudhary Charan Singh University, Campus, Meerut in 2014. Her current area of research is on thermoelectric materials and has published several research papers in prestigious journals.



Mr. Kishor Kumar Johari is a CSIR-Junior Research Fellow at CSIR-National Physical Laboratory, New Delhi, India registered for Ph.D at the Academy of Scientific and Innovative Research (AcSIR), India. He received his Master and Bachelor degree in Science from M.J.P. Rohilkhand University, Bareilly India. His current research interest lies is in understanding the thermoelectric behaviour of half-Heusler based alloys.

Please cite this article as: Chauhan NS et al., Enhanced thermoelectric performance in p-type ZrCoSb based half-Heusler alloys employing nanostructuring and compositional modulation, Journal of Materiomics, https://doi.org/10.1016/j.jmat.2018.11.003



Dr. Bhasker Gahtori received his Ph.D. degree from Jamia Millia Islamia University, New Delhi in 2010 and is presently working as Scientist in Materials Physics and Engineering Division at CSIR-National Physical Laboratory, India. His current research is focused on Thermoelectric and Magnetic materials. He has published more than 30 research papers in scientific journals and presented his research work in more than 10 national and international conferences.



Prof. Ajay Dhar is an Associate Director (Student Affairs) at Academy of Scientific and Innovative Research (AcSIR), India. He holds Masters Degrees in Science and Philosophy and a doctorate from University of Delhi, India. He was a Chief Scientist & Head (Advance Material & Devices Division) at the CSIR-National Physical Laboratory, New Delhi, India. Dr. Dhar was earlier a post-doctoral fellow and later a visiting faculty at Queen's University, Canada. His current research interests among other include the development of cost-effective and non-toxic materials for efficient thermoelectric devices and rare-earth free permanent magnets.

Please cite this article as: Chauhan NS et al., Enhanced thermoelectric performance in p-type ZrCoSb based half-Heusler alloys employing nanostructuring and compositional modulation, Journal of Materiomics, https://doi.org/10.1016/j.jmat.2018.11.003

View publication stats

Purdue University
Purdue e-Pubs

International Refrigeration and Air Conditioning Conference

School of Mechanical Engineering

July 2018

Experimental Study of a Low-Temperature Compressor-Ejector Refrigeration System

Samsher Gautam
Delhi Technological University, India, samsher@dce.ac.in

Apoorva Roy
Delhi Technological University, India, apoorvar6@gmail.com

Bhuvan Aggarwal
Delhi Technological University, India, bhuvan_aggarwal@yahoo.com

Follow this and additional works at: https://docs.lib.purdue.edu/iracc

Gautam, Samsher; Roy, Apoorva; and Aggarwal, Bhuvan, "Experimental Study of a Low-Temperature Compressor-Ejector Refrigeration System" (2018). *International Refrigeration and Air Conditioning Conference.* Paper 2074.
https://docs.lib.purdue.edu/iracc/2074

This document has been made available through Purdue e-Pubs, a service of the Purdue University Libraries. Please contact epubs@purdue.edu for additional information.
Complete proceedings may be acquired in print and on CD-ROM directly from the Ray W. Herrick Laboratories at https://engineering.purdue.edu/Herrick/Events/orderlit.html

Experimental Study of a Low-Temperature Compressor-Ejector Refrigeration System

Dmytro BUYADGIE[3], Pavlo NESTEROV[2,3], Olexiy BUYADGIE[1,2*], Oleksii DRAKHNIA[3,4]

[1]Wilson Engineering Technologies, Inc
3330, Vincent Rd, Ste I, Pleasant Hill, CA 94523
Tel: (925) 3935413
e-mail: buyadgie@wilsonet.org

[2]V.S. Martynovsky Institute of Refrigeration, Cryogenic Technologies and Eco Energetics
1/3, Dvoryanskaya str, 65026, Odessa, Ukraine
Tel: +380674828353
e-mail: buyadgie@wilson-ukraine.com

[3]Wilson, Ejector Technology Lab
15/13, Mikhailivska str, Odessa, Ukraine
Tel: +380487348010
e-mail: buyadgie@wilson-ukraine.com

[4]Interdisciplinary School of Engineering Sciences, Department of Energy and Environmental Engineering, Kyushu University
Kasuga, Fukuoka Prefecture, Japan
drakhnia@kyudai.jp

* Corresponding Author

ABSTRACT

The paper presents the results of a theoretical and experimental study of the low-temperature compressor-ejector refrigeration machines, which led to an increase in the efficiency of refrigeration equipment by 20-60% under conditions of an extreme rise in the ambient temperatures. Such conditions take the character not sporadic, but rather long, which in practice disables a large fleet of refrigeration equipment and causes significant losses. The proposed schematic solutions allow the ejector to be paired with the compressor, regardless of the mode of operation with a positive effect. The use of this scheme makes it possible to increase the effective refrigerating coefficient simultaneously both by reducing the power consumption and by increasing the cooling capacity.

1. INTRODUCTION

The role of the refrigeration economy in the conditions of the civilizational boom is growing at the highest rates, its contribution now reaches about 15% of the world energy balance and continues to increase. It is necessary to find ways to reduce energy intensity with simultaneous increase of the reliability of refrigeration equipment. While radically new solutions are being

sought for creating new types of cold generators, it is necessary to find reserves when carrying out cycles of already operating equipment that has a sufficiently long service life, taking into account skilled and timely maintenance.

The relief of compressor operating conditions at peak times due to the ejector booster stage has found its application, however, the efficiency of this solution was small, because for the operation of the ejector, a part of the working steam compressed by the compressor was used (Alyokhin, et.al., 1991, Badylkes & Danilov, 1961).

Partly the role of this stage was performed by an ejector whose main purpose was to replace the throttling with a more reversible process of expansion in the ejector nozzle with the performance of external work, with a small preload of the steam before sucking into the compressor (Elbel, et.al., 2008).

This gives a stable overall increase in efficiency of 4-6%. More should not be expected for most refrigerants, because the work of expanding the liquid, even taking into account its effervescence in the nozzle, gives insignificant work. More significant results can be obtained when the compressor is operating on CO2 as the isoenthalps in the two-phase region on the T-S diagram of this substance are very flat.

It is more efficient to use the exergy of ballast steam separated after throttling to intermediate pressure. At the same time, losses from throttling are reduced, steam is compressed in front of the compressor, ballast steam is not circulated through the evaporator, which also reduces hydraulic losses in the machine, which represents the very long channels with many turns. Therefore, this method is the most promising in the sphere of application of the ejector booster stage.

2. CALCULATION AND THEORETICAL ANALYSIS OF A NEW SCHEME FOR THE INCLUSION OF A BOOSTER STAGE

Schematic of the compressor-ejector refrigeration machine is shown in Fig. 1. The corresponding cycle in the diagram is shown in Fig. 2.

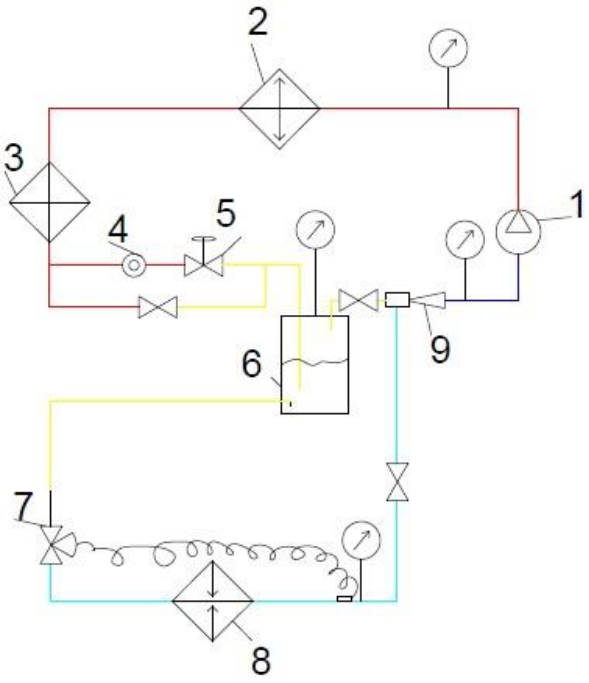


Figure 1: Schematics of an experimental test rig with ejector: 1- compressor; 2- capacitor; 3 - dehumidifier filter; 4 – flow meter; 5 - control valve; 6- liquid separator; 7 - throttling valve; 8 - evaporator; 9 - ejector.

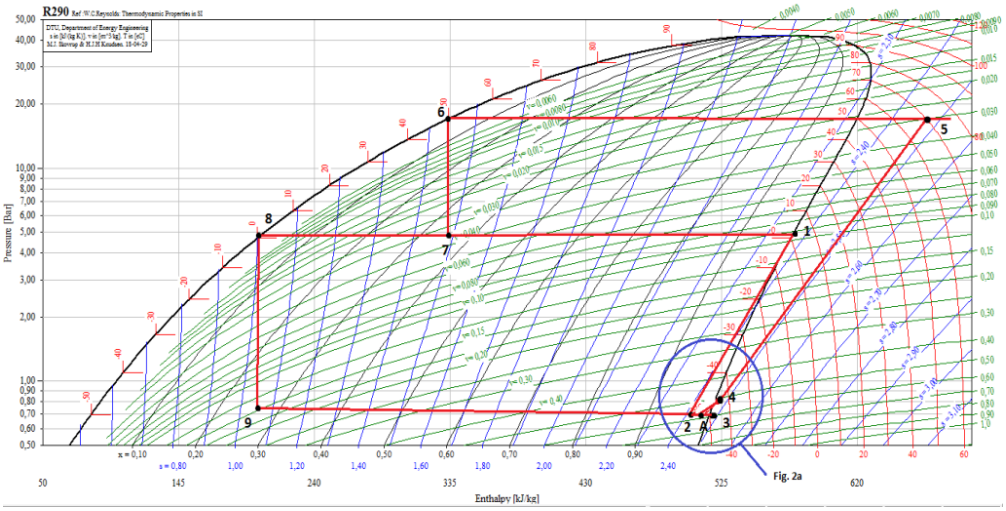


Figure 2: Cycle of vapor-compression machine with booster ejector

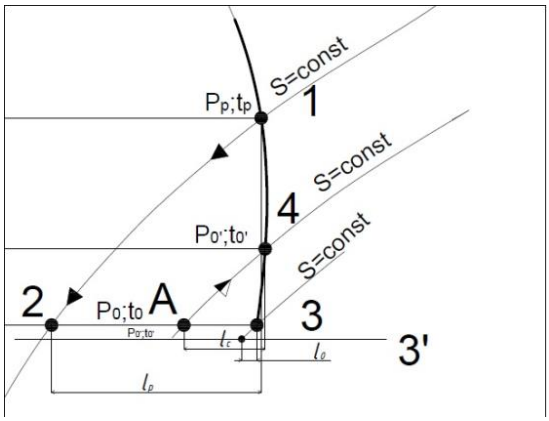


Figure 2a: Processes in the ejector on the h/lgP diagram

In this case, the ejection coefficient is set in advance by the ratio of the steam flow from the evaporator to the flow rate of the ballast steam.

$$U = \left(G_{eva} + G_m\right)\left(1 - x\right)/G_m \quad (1)$$

$$G_m = \left(G_{eva} + G_m\right)x \quad (2)$$

$$U = 1/x - 1 \quad (3)$$

The actual range of variation in the ejection coefficient lies in the range 0.7-5.5. The more gently the line of constant enthalpy passes through the beginning of the throttling, the greater the ballast steam consumption, so the pressure beyond the ejector can be increased. In this sense, the CO_2 benefits among other refrigerants, which coincides with the conclusions of S.Elbel and P.Hrnyak. In this case, the specific cooling capacity of the cycle falls, which adversely affects the operation of the compressor. Therefore, there is an optimal ratio of liquid and steam after the first throttling, where the compressor-ejector refrigeration machine produces the best result. Figure 3 shows the dependence of entrainment ratio from mixture dryness.

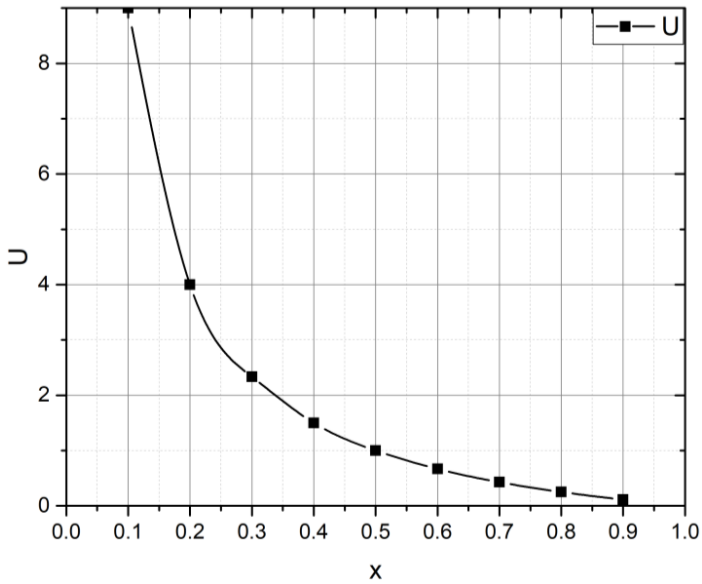


Figure 3: Dependence of U from dryness of vapor-liquid mixture after first throttling.

As it can be seen from the cycle, the main operating parameter is the intermediate pressure to which the condensate expands in the first throttle valve. If the intermediate pressure is high, the specific energy of the working flow will also be high. But the working steam flow will not be sufficient to ensure that the entire volume of the low-pressure steam is compressed to a value to significantly affect the energy and volumetric characteristics of the compressor. The reverse picture is observed if the intermediate pressure is excessively low. Therefore, the task of optimizing the cycle is complicated by the fact that the compressor pressure is affected both by the value of the intermediate pressure after the first throttling and by the value of the vapor compression pressure in the ejector. The ejector stage is calculated from the joint solution of the equation to determine the achievable entrainment ratio, the compressor feed rate, the power consumption and the resulting cooling capacity. In this case, the entrainment ratio is set in advance by the ratio of the steam flow from the evaporator to the ballast steam flow.
The operating modes of the ejector are determined by the expansion of the working flow at supersonic speed as the ratio of the pressure behind the nozzle to the pressure of the entrained flow is less than the critical

$$P_{eva} / P_p < \Pi^* \tag{4}$$

$$\Pi^* = \left(2/\left(k+1\right)\right)^{k/(k-1)} \tag{5}$$

The value of Π* lies in the range of 0.5-0.6.
The compression ratio in the booster ejector is low, lies in the range of 1.05-1.15, so the speed of the ejected vapor does not reach the speed of sound in the mixing chamber, i.e. the realization of limiting regimes is not observed at mixing.
To calculate the achievable pressure behind the ejector and the geometry of the flow section of the ejector, the following algorithm was proposed, eq. 6-16 (Sokolov and Zinger, 1989).

$$\frac{\Delta P_{out}}{P_{eva}} = \frac{k_p}{2\left(k_p+1\right)} \frac{1}{\Pi_{p.n.}} \frac{\varphi_1^2 \varphi_2^2 \lambda_{p.n.}^2}{\left[\left(1/\varphi_3 - 0.5\right) v_c / v_p \left(1+U\right)^2 - \left(\varphi_2\varphi_4 - 0.5\right) v_n / v_p n U^3\right]} \tag{6}$$

$$\frac{f_3}{f_*} = \frac{-b + \sqrt{b^2 - 4ac}}{2a} \tag{7}$$

$$a = \varphi_1 \varphi_2 q_{p.n.} \tag{8}$$

$$b = -\left\{\varphi_1\varphi_2 + 2\varepsilon_{p.n.}\left[\left(1/\varphi_3 - 0.5\right) v_c / v_p \left(1+U\right)^2 - \left(\varphi_2\varphi_4 - 0.5\right) v_n / v_p U^2\right]\right\} \tag{9}$$

$$c = 2\varepsilon_{p.n.} / q_{p.n.} \left(1/\varphi_3 - 0.5\right) v_c / v_p \left(1+U\right)^2 \tag{10}$$

$$\frac{\Delta P_c}{P_n} = \frac{0.5 k_p \varepsilon_{p*} \Pi_{p*} v_n / v_p}{\varphi_4^2 \Pi_{p.n.} \left(f_3 / f_{p*} - 1/q_{p1}\right)^2} U^2 \tag{11}$$

$$\frac{\Delta P_d}{\Delta P_k} = \left(\frac{1+U}{U}\right)^2 \frac{v_c}{v_n} \tag{12}$$

$$\frac{\Delta P_d}{\Delta P_k} = \left(\frac{1+U}{U}\right)^2 \frac{v_c}{v_n} \tag{13}$$

$$v_c / v_p = P_p T_c / \left(P_c / T_p\right) \tag{14}$$

$$v_n / v_p = P_p T_n / \left(P_n / T_p\right) \tag{15}$$

$$T_c = \left(T_p + U T_n\right) / \left(1+U\right) \tag{16}$$

The results of this calculation were used in the calculation of the CFD model of the ejector in the ANSYS program, on the basis of which the drawings of the ejector's geometry profile were produced.

The CFD model of the low-pressure ejector differs in that the high-speed core of the working flow occupies a small space, area ratio is in most cases greater than 20, and the difference in velocities in the flow core and on the boundary layers is much greater than in the high-pressure ejector, Fig. 4,5.

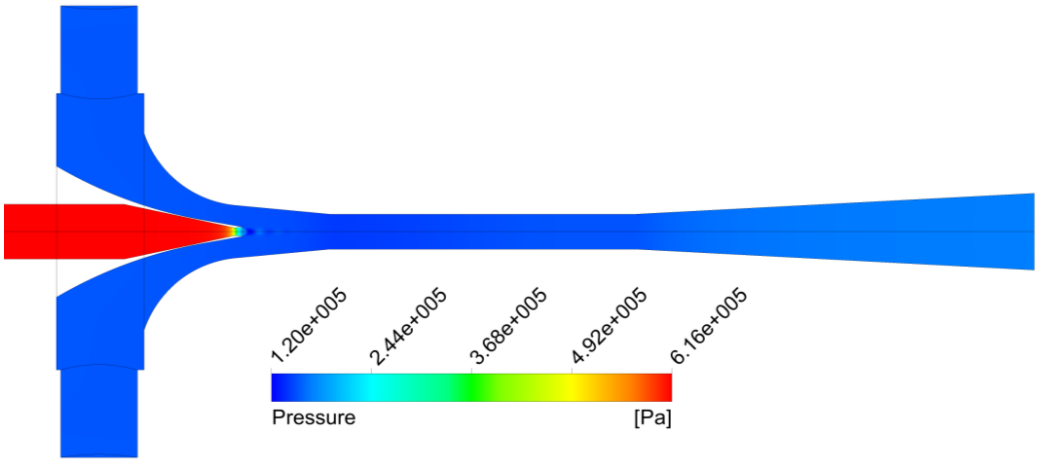


Figure 4: Pressure profile of booster ejector.

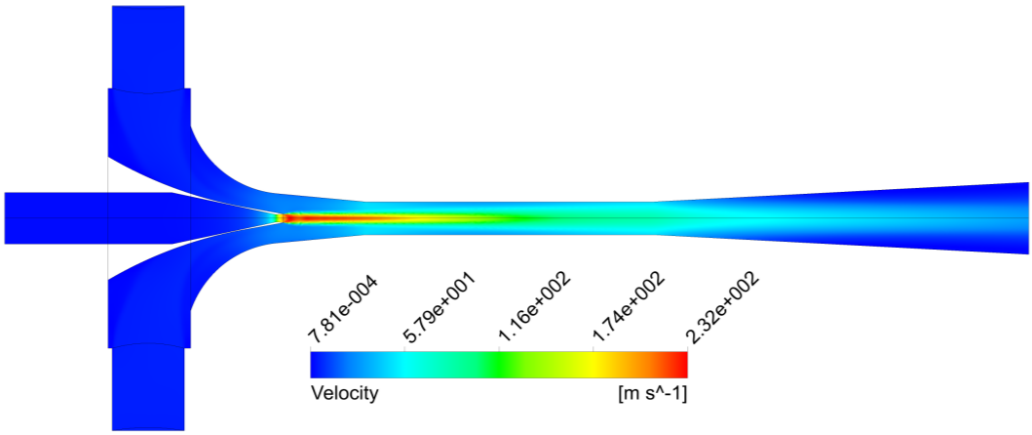


Figure 5: Velocity profile of booster ejector.

The results of calculating the achievable pressure and the effective refrigerating coefficient of the compressor in different modes for R-290, R-134a, R-404 are shown in Table 1. It can be seen from the table that the most important application of the ejector step affected the compressor operating on propane.

3. EXPERIMENTAL STUDY OF A COMPRESSOR-EJECTOR REFRIGERATION SYSTEM

For experimental studies, a test bench was installed on the basis of the hermetic compressor Embraco NE6210E with a cylinder capacity of V_h = 8.77 cm^3. The load on the evaporator was simulated by 5 air heaters of 200 W each, which made it possible to vary the cooling capacity over a wide range of values. The temperature of the outside air was changing by heating the air with a dryer.

Table 1: Entrainment ratios and pressures after first throttling

P_{cond} (MPa)	P_{eva} (MPa)	P_p (MPa)	P_{out} (MPa)	t_{cond} (°C)	t_{eva} (°C)	U
R134a						
1,36	0,15	0,6	0,168	55	-20	3
1,36	0,15	0,33	0,165	55	-20	1,857
1,36	0,15	0,246	0,163	55	-20	1,5
R-507a						
2,64	0,314	0,96	0,346	55	-20	1,5
2,64	0,314	0,85	0,343	55	-20	1,326
2,64	0,314	0,566	0,335	55	-20	1
R-290						
1,9	0,244	0,636	0,271	55	-20	1,857
1,9	0,244	0,474	0,269	55	-20	1,5
1,9	0,244	0,354	0,261	55	-20	1,222

Figure 6 shows schematics of the test rig with control measurement points

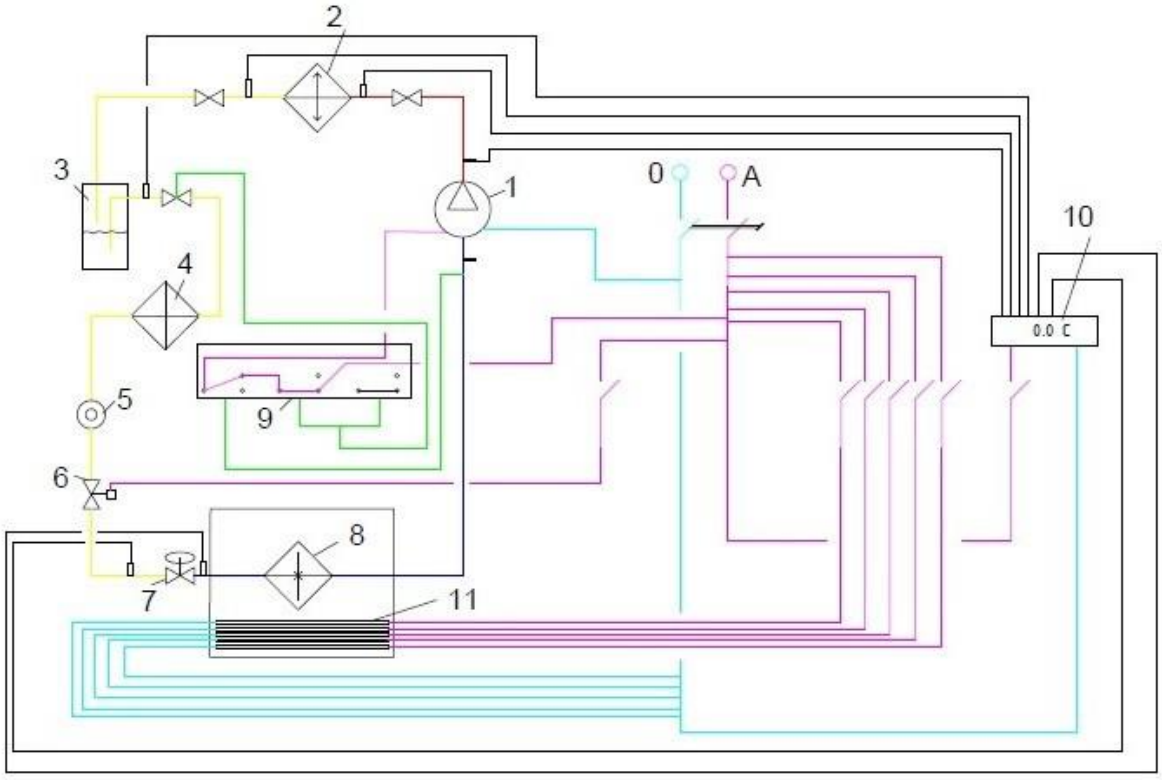


Figure 6: Test rig schematics

In the experimental bench, temperatures at the nodal points of the cycle were measured with the help of calibrated NTC thermistor, pressure was measured using standard manometers. The

refrigerant flow was determined by the method of thermal balances, the rotameters and the liquid separator was used as a measuring vessel, and therefore the measurement results were within the permissible error of the measurements. Photo of experimental setup is shown on Fig. 7



Figure 7: Test unit photos.

The first series of experiments allowed to determine the efficiency of the compressor-ejector system, which indicates the optimal values of the intermediate pressure and pressure behind the ejector.

The tests were carried out at 3 evaporation temperatures (-40°C, -30°C and -20°C) and a total condensation temperature of 50°C.

The next stage of the tests was carried out with the ejector turned on. For each mode, a design ejector was installed and readings were taken at various intermediate pressures, which were set with the help of a throttling valve. At each point, the cooling capacity and the electric power consumed by the compressor were determined. The obtained data were plotted with the calculated curves of the effective cooling coefficient versus the compressor suction pressure ratio to evaporation pressure. Measurements were made at the onset of steady-state conditions, when the pulsations of the suction pressure ceased.

When the intermediate pressure was higher than the calculated pressure, the flow rate of the working steam through the nozzle decreased, the pressure behind the ejector was below the design pressure, moreover, there was a separation of the flow from the walls, both in the nozzle and in the diffuser, which requires reducing the cone angle to 1.20 on side.

When the pressure was lowered after the first throttling, the steam flow rate through the nozzle exceeded the calculated value, so part of the ballast vapor was retained in the liquid separator and had to be throttled in the second throttle valve, which also led to a decrease in the refrigerating coefficient and the pressure behind the ejector. The highest values were achieved at the calculated parameters of the first throttling. In this case, the maximum achievable pressure increase in the ejector was observed and, accordingly, the maximum effective cooling coefficient.

Tests have shown that the maximum increase in the refrigerating coefficient is observed at the highest compression ratios in the compressor, which is explained by a sharp drop in the compressor's volumetric characteristics and its productivity. At the same time, the power of the compressor decreases not very fast. The discrepancies between the calculated and experimental values lie within the permissible errors, do not exceed 8-10% in the field of design parameters and 15-25% in the non-calculated regions where the ejector is unstable. Since the evaporation temperature is a stable parameter under real operating conditions, it makes sense to install 3 ejectors in the system: one for the maximum condensation temperature, the other for the average summer maximum, and the third for the off-season. In winter, the installation can work without the ejector, although the option of installing the 4th ejector on the average winter minimum is also considered. Even if the increase in the refrigeration ratio is 10-15%, in general, the electricity consumption for obtaining the cold will be reduced to such a level that it is possible to release more than one large power plant from the load.

6. CONCLUSIONS

1. The use of a new compressor-ejector schematics in refrigeration technology leads to a reduction in electricity consumption by 10-40% and a corresponding reduction in greenhouse gas emissions.
2. Experimental studies of a low-pressure ejector have shown its reliability, efficiency and stable operation under design conditions and in the vicinity of a change in the intermediate pressure of 10-25%.
3. The CFD model of a low-pressure ejector has higher impact losses than high-pressure one due to higher differences in the rates of mixing flows.
4. The mixing process in low-pressure ejectors is more irreversible, so a higher growth of the entropy of the mixture is observed compared to high-pressure ejectors.

NOMENCLATURE

G_m	motive vapour mass flow	kg/s
G_{eva}	evaporator mass flow	kg/s
U	entrainment ratio	(–)
x	dryness degree of vapour-liquid mixture after first throttling	(–)
P	pressure	MPa
T	temperature	°C
k	adiabatic index	(–)
$\varphi_1,\varphi_2,\varphi_3,\varphi_4$	velocity coefficients	(–)
Π	relative pressure	(–)
λ	relative velocity	(–)
ν	specific volume	m^3/kg
ε	relative density	(–)

Subscript

cond	condensation
eva,n	evaporation
p	pressure after first throttling

out	ejector outlet pressure
c	compression pressure
d	diffuser
*	critical parameter

REFERENCES

Alyokhin N.B., Buiadji D.I., Tichonov V.I. (1991). Microelectronic control system of long-distance refrigerated truck. *Proc. 18 International Congress of Refrigeration* (2020 – 2023), Montreal, Canada.

Badylkes, I.S, Danilov R.L. (1961). *Cooling systems using steam-jet devices as a booster compressors*. Moscow, Energia.

Elbel, Stefan and Hrnjak, Predrag (2008) Ejector Refrigeration: An Overview of Historical and Present Developments with an Emphasis on Air-Conditioning Applications. *Proceedings of the International Refrigeration and Air Conditioning Conference*. Paper 884

Sokolov, E. Y., & Zinger, N. M. (1989). *Jet Devices* (3rd ed.). Moscow: Energoatom Publiching House.

Buyadgie, Dmytro; Sechenyh, Vitaliy; and Nichenko, Sergii, "Booster Vapor-Compression Refrigerating Systems" (2010). *Proceedings of the International Refrigeration and Air Conditioning Conference.* Paper 1062. http://docs.lib.purdue.edu/iracc/1062

Buyadgie, O., *The Thermotransformation Processes Efficiency Enhancement in The Self-Contained Ejector Refrigerating Machines*, PhD Thesis, The Odessa National Academy of Food Technologies, V.S. Martynovsky Institute of Refrigeration, Cryogenic Technologies and Eco-Energetics, Odessa, Ukraine, 2016.

Buyadgie D.I., Buyadgie O.D. The Intallation to Produce Heat or Cold (Variants) (in Ukrainian), Patent for an Invention: UA 103365 F25B 1/02 F25B 1/06. № a 2011 10382, applied for 26.08.2011, published on 10.10.2013, Bul. №19.

Journal of Pharmacognosy and Phytochemistry

Available online at www.phytojournal.com

E-ISSN: 2278-4136
P-ISSN: 2349-8234
JPP 2018; 7(4): 1542-1545
Received: 15-05-2018
Accepted: 20-06-2018

Rupanjali Pathak
Food Processing Laboratory, University School of Biotechnology, GGS Indraprastha University, Sector 16C Dwarka Delhi, India

Vandana Thakur
Food Processing Laboratory, University School of Biotechnology, GGS Indraprastha University, Sector 16C Dwarka Delhi, India

Rajinder Kumar Gupta
Department of Applied Chemistry, Delhi Technological University, Shahbad Daulatpur, Bawana Road, Delhi, India

Correspondence
Rajinder Kumar Gupta
Department of Applied Chemistry, Delhi Technological University, Shahbad Daulatpur, Bawana Road, Delhi, India
Email: rkg67ap@yahoo.com

Formulation & analysis of papaya fortified biscuits

Rupanjali Pathak, Vandana Thakur and Rajinder Kumar Gupta

Abstract
Biscuits are popularly worldwide known for its taste, flavor and health benefits. A formulation of biscuits with *Carica papaya* pulp extract powder was prepared for enhancing multiple health benefits and also for increasing beneficial usage of biscuits as nutraceutical, especially seeing the enzyme action i.e. papain. The Chemical composition analysis where it was tested for different parameters like ash and moisture analysis, protein, carbohydrate content and antioxidant profile (DPPH, contents of flavonoids of control and fortified biscuits). Sensory Analysis was conducted by applying hedonic scale test by applying the method of 9 point hedonic scale. In analysis the result appeared that the antioxidant activity was significantly improved. This was clearly demonstrated by the fact that increases in flavonoid contents can also be observed in the fortified cookies. Hence, it was tested that by fortifying biscuits with papaya powder or juice could enhance the nutritional quality of biscuits without getting the parameters such as rheological, sensorial and antioxidant properties being affected along with receiving the benefits of digestive enzyme papain acting as a functional food.

Keywords: rheology, sensory, biscuits, textural characteristics, chemical tests

1. Introduction
Biscuits constitute a major component of human snacks in most part of the world. (Hasker *et al*. 2016) [1]. It is an unleavened crusty baked, sweet edible item made from wheat flour, shortening (hydrogenated fat) & sugar, and is normally produced light by mixing with baking powder (cereal flour mixed with sodium carbonate, sodium bi-phosphate) (Lakshmi M *et al*.) [2]. Wheat flour is the major constituent and acts as the basic ingredient for biscuit production because of its gluten proteins, which are found to be absent in flour of other cereals. (Ortolan and Steel *et al*.) [3]. Gluten protein supports to provide elasticity to the dough during the process of baking and provides high organoleptic quality of the end product. (Wang *et al*. 2017) [4].
The Baking industry holds a major portion in food industries and it has been growing at an average rate of 15% during the past 3 years. Therefore, various cereals based preparations, blending and mixing with different compounds to improve the nutritional standard of Indian diet is very important (Bassey, FI *et al*. 2013) [5]. Supplementary foods should be such, if taken in small quantity, could provide the necessary amount of nutrients. They should be made in the form of ready to eat snacks, drinks, etc. Biscuit has been good for a long time as a processed food (Ahmad S and Ahmed M, 2014) [6]. The primary objective is to develop healthy and nutritional biscuits fortified with papaya pulp powder. Papaya is an ingredient for different uses, all over the world and has been utilized in a variety of products after processing such as fruit juices, jams, and ice cream, dried fruit. The chemical compositions of papaya fruit are water 88.8%, carbohydrate 9.8%, fiber 0.8%, protein 0.6%, ash 0.6% and fat 0.1%. From 100 grams of papaya high amount of calories approximately 39 calories can be achieved. Papaya is a very good source of vitamin A. (Sujatha Y and Bera S, 2014) [7]

2. Materials and Methods
2.1 Reagents
All analytical grade reagents and solvents used were procured from Fluka (Fluka, Switzerland) and Sigma-Aldrich (Sigma- Aldrich, St. Louis, MO, USA) and purchased from Rankem (RFCL Ltd, India).

2.2 Main Ingredients
All the ingredients- The papayas, Atta (whole wheat flour) and Maida (refined flour) were procured from the local market of North Delhi (India). Fresh papaya was washed, peeled and grated. The grated papaya pieces were kept in the hot air oven dryer. Drying was carried out overnight at 50°C.

After the papaya pieces were dried to snapping stage, drying was complete. The papaya pieces were ground in a mixer–grinder and the powder papaya obtained was sealed in polyethylene (PE) bags.
The papaya powder was stored in the refrigerator along with atta and maida until usage.

2.3 Formulation of Biscuits
Biscuits were prepared in two different formulations. In one formulation papaya pulp powder was used and a control was also prepared in which no papaya was added. The formulation of biscuits was also done by adding papaya pulp powder and atta and a small amount of maida flour to add gluten to the mixture.

Table 1: Different concentration for formulation of biscuits

Biscuits code	Atta	Maida	Papaya pulp powder
C1	300	90	10
C2	300	100	-nil-

2.4 Determination of nutritional constituents
For nutritional analysis the formulated bars were crushed in mortar and pestle.
Moisture and total ash content were determined by AACC methods (AACC, 2000) [8]. The protein content was determined by the IS: 7219: 1973 standard. The total dietary fibre content was determined by the methods of (Lee *et al*. 1992 [9] and Prosky *et al*.1998) [10].

2.5 Estimation of Vitamin A and C Content
2, 6-Dichlorophenol indophenol method is used to estimate the total vitamin C content. (Ranganna, 1999) [11] Estimation of vitamin A content was done by the method of FRAC/SOP/INST/097 adopted by FICCI Research & Analysis Centre.

2.6 Phytochemical Analysis
2.6.1 Estimation of Total Phenolics Content
Estimation of total phenolic content was done by using the Folin Ciocalteu Assay (Siddiqui *et al*. 2017) [13].

2.6.2 Determination of Total Flavonoids
Total flavonoids were estimated using aluminum chloride colorimetric method. (Chang *et al*. 2002) [14]

2.7 Antioxidant Activity
DPPH radical scavenging Assay
DPPH radical scavenging activity was analyzed by the method of Blois, 1958 [15] with significant modification as described in paper.

2.8 Papain Activity test
Papain activity was measured using the method followed by (Trivedi *et al*, 2013) [16]

2.9 Microbial Analysis
Total plate count agar Media was prepared and autoclaved at 121° C for 15 mins at 5 psi. Meanwhile 10gm sample was crushed and dissolved in 90ml saline water. Further dilutions were made 10^{-9} concentration. Further 1ml of sample from the concentration of 10^{-3} and $10^{-6}$was plated and incubated in bacteriological incubator for 24 hours at 37 ℃. There after results were recorded according the number of microbial colonies appeared on the plate. (FSSAI Manual. 2015) [17].

3. Results and Discussion
3.1 Phytochemical estimation of papaya pulp powder
The phytochemical compounds that are found by testing of methanolic extract of papaya pulp powder fortified biscuits revealed the presence of phenolics, antioxidants and flavonoids.

3.2 Total phenolic content
The Total phenolic content was estimated colorimetrically by Folin Ciocalteu (FC) method and the result was expressed in terms of Gallic Acid Equivalent (GAE) which can be observed in table 2.
The determination of total phenolic contents was calculated by using the linear equation based on the calibration curve of Gallic acid:
$y = 0.0172x - 0.0404$, $R^2 = 0.9904$
Where y is the absorbance of sample and x is the amount of Gallic Acid Equivalent in µg.

Table 2: Total phenolic content of the Biscuits

Sample	GAE equivalents (µg GAE/mg sample)
Biscuit sample with papaya pulp powder	1.705

3.3 Total Flavonoid Content
By using the aluminium chloride method the results of total flavonoids were estimatedand it was expressed in terms of Catechin equivalents (CE) which is shown in table 3.
By using the following linear equation the total flavonoid content of the extract was calculated $y = 0.0045x - 0.0138$, $R^2 = 0.9976$
Table: Cathechin equivalent for biscuits made from papaya pulp (µg CE mg sample)

Table 3: Total flavonoid content of the biscuits

Sample	CE equivalents (µg CE/ mg sample)
Biscuit sample with papaya pulp powder	1.017

3.4 Determination of antibacterial activity
The total microbial count was found to be too less to count. From this we can say that if the biscuits are stored in proper packaging and away from moisture it could be safe for consumption after 15 days.

3.5 Determination of Vitamin Content
The results found after the vitamin content estimation, test was done are shown below:

Table 4: Total vitamin content of the Biscuits

Parameters	Results	Test method
Vitamin C mg/100g	5.88	IS:5838:1970
Vitamin A mcg/100g	235.26	FRAC/SOP/INST/097

3.6 Results of Protein Content
The total protein content in the biscuit sample was estimated by IS: 7219:1973 method and was estimated to be 6.96 g/100g.

3.7 Determination of Dietary Fibre
The dietary fiber in food sample was estimated by AOAC 985.29 method and was found to be 3.35g/100g.

3.8 Antioxidant Activity
The antioxidant activity was done by DPPH radical scavenging activity.

Table 5: Total antioxidant inhibition

Sample	% Inhibition
Papaya pulp fortified biscuits	90.8471

Papaya fruit contains 84.04% of the antioxidant and in comparison it was clearly found that the biscuits are highly enriched with antioxidants after baking.

Papain Activity Test: Papain activity test showed a positive result as the liquid coagulates. This showed that the biscuit sample contains papain but in very less amount due to baking process.

3.9 Sensory Evaluation of formulating Biscuits

The sensory qualities, particularly the flavor attributes, are essential to be measured subjectively (S Ranganna, 1986) [11]. The main objective behind the sensory analysis is to check the overall acceptability of the formulated biscuits. The samples were characterized for color, flavor, crisp and general acceptability. This was done by 9 point hedonic scale method. 9 represents like extremely 1 means dislike extremely as mentioned in a paper by author Ihekoronye and Ngoddy (1985) [18].

Table 6: Sensory Analysis chart

Sample code	Crispy	Taste	General acceptability
C1	7	7	7
Control	7	8	7

4. Nutritional analysis of formulated biscuits

Papaya pulp powder was used for the formulation of biscuits. After the sensory evaluation it was found that the taste and overall acceptability of the formulated biscuits was almost same to the controlled one.

The moisture content of biscuits is very low due to which they are less susceptible to spoilage and have a longer shelf life as compared to other bakery products. As soon as it was put under the convection water evaporates easily.

The moisture content was found to be 2.26% as it contained a high amount of fat in it, the ash content was found out to be 1.1%.

Table 7: Nutritional Analysis done for biscuits

S. No.	Parameters	Results (mg/100gm)*
1.	Calcium (Ca)	24.88
2.	Iron (Fe)	35.27
3.	Potassium (K)	199.14
4.	Magnesium (Mg)	37.72
5.	Sodium (Na)	351.42
6.	Zinc (Zn)	0.90

*Method: FRAC/SOP/INST/242

During investigation it was observed that the moisture content, fat and protein content of biscuits were found to increase with fortification of the biscuits with papaya powder. The composition along with the ingredients such as papaya powder, wheat flour and refined wheat flour is presented in Table1. Inside the oven keeping the temperature of 165 °C it was baked for 15mins. The moisture content found in the Papaya powder fortified biscuits sample was 1.36% higher than the control biscuits, which was due to the addition of papaya pulp powder. The protein content of Papaya pulp fortified biscuits sample was higher than those of control biscuits. The fat content of the fortified biscuits was also higher due to the incorporation of more butter. The data indicate that the fiber content of the biscuits was high.

It was found that papaya pulp fortified biscuits have higher amount of sodium, vitamin A and iron (as shown in Table). The concept behind this is the stability of each micronutrient during processing that involved different steps, including mixing, forming and baking. However, it was found that some of the micronutrients are stable in case of fortified biscuits.

The concentration of vitamin A in the fortified biscuits was found to be 235.26 mg/100g, and it is comparatively low in sweet potato fortified wheat biscuits (Herawati D *et al*. 2015) [19].

The effect of the papain enzyme found in papaya can be retained, though in a less amount through these biscuits.

5. Conclusion

Biscuit manufacture is no longer considered a craft, but a fully-fledged technology, developed after a full understanding of the various processes involved with the help of basic principles of science and engineering. All over the world, manufacturing equipment has been replaced by new and advanced automatic machines with high outputs. In some of the foreign country biscuit manufacturing has been computerized (Aziah AN *et al*. 2012) [20]. Irrespective of rural or urban area, it is the choice of consumer and hence the biscuit is the largest consumed processed product in India (Umadevi L and Uma N, 2014) [21]. The fortification process helps food to enrich their quality along with a great value of micro and macronutrients. The main view behind this fortification process is so to gain the essential nutrients directly without consuming the raw. Wu *et al*. 2016 [22], indicated that the rich amount of polyphenols (good sources of antioxidants) is found in the flesh and peel of white papaya, which is found to be effective in inhibiting the growth of melanoma cells. Red papaya is rich in nutrients such as proteins, vitamins and flavonoids, antioxidant and has radical scavenging activity (Septembre-Malaterre A *et al*. 2016) [23]. The basic objective of this study was to assist with or to evaluate total phenolic content, antioxidant capacity, flavonoid in the biscuit part fortified with semi ripe papaya. And the results showed that even after baking the nutrients can be retained to some extent.

Hope food processing technology will gain much benefit in near future through this process and help mankind to gain health benefits.

6. References

1. E Hasker Leelavathi K, Radhai Sri, Sangamithra. Effect of Differently Treated Soya Bean Flour on Quality of Biscuits. International Journal of Research in Advent Technology. 2016; 4(4):9637.
2. Lakshmi M, Majumdar SD, Ravi U. Development and Analysis of Composite Flour Bread. Journal of Food Science and Technology. 2018; 52(7):4156-4165.
3. Ortolan F, Steel CJ. Protein Characteristics that Affect the Quality of Vital Wheat Gluten to be used in Baking: A Review. Comprehensive Reviews in Food Science and Food Safety. 2017; 16:369-381.
4. Wang K, Lu F, Li Z, Zhao L, Han C. Recent developments in gluten-free bread baking approaches: a review. Food Sci. Technology, Suppl. 1 Campinas. 2017; 37:1-9
5. Bassey FI, Mcwatters KH, Edem CA, Iwegbue CMA. Formulation and nutritional evaluation of weaning food processed from cooking banana, supplemented with cowpea and peanut. Food Science & Nutrition. 2013; 1(5):384-391.

6. Ahmad S, Ahmed M. A Review on Biscuit, a largest consumed, processed product in India. Its fortification and Nutritional Improvement, IJSIT International Journal of Science Inventions Today, 2014, 3(2).
7. Sujatha Y, Bera S. Optimization of Ingredients in Papaya Fruit Bar. Journal of Biolife. 2014; 2(1):377-380.
8. AACC. Approved Methods of the American Association of Cereal Chemists. Am. Assoc. Cereal Chem. Inc., St. Paul, Minnesota.
9. Lee SC, Prosky L, DeVries JW. Determination of total, soluble, and insoluble, dietary fiber in foods-enzymatic10 gravimetric method, MES-TRIS buffer: Collaborative study. J Assoc. Off. Anal. Chem. 1992; 75:395-416.
10. Prosky L, Asp NG, Schweizer TF, De Vries JW, Furda I. Determination of insoluble, soluble, and total dietary fiber in foods and food products: Inter laboratory study. J Assoc. Off. Anal. Chem. 1988; 71:1017-1023.
11. Ranganna S. Handbook of analysis and quality control for fruits and vegetable products. McGraw Hill Education (India) Private Limited, 1999.
12. Siddiqui N, Rauf (Unani) A, Latif A. Spectrophotometric determination of the total phenolic content, spectral and fluorescence study of the herbal Unani drug Gul-e-Zoofa (*Nepetabracteata* Benth). Journal of Taibah University Medical Sciences. 2017; 12(4):360-363.
13. Chang CC, Yang MH, Wen HM, Chern JC. Estimation of total flavonoid content in propolis by two complementary colorimetric methods. Journal of Food and Drug Analysis. 2002; 10:178-182.
14. Blois MS. Antioxidant determinations by the use of a stable free radical. Nature. 1958; 26:1199-1200.
15. Trivedi V, Rathore RPS, Kamble PR, Goyal M, Singh N. Pepsin, Papain and Hyaluronidase Enzyme Analysis: A Review. IJRPS. 2013; 3(1):01-18.
16. FSSAI (Food Safety & Standards Authority of India), Manual of Methods and Analysis of Foods- Beverages (Coffee, Tea, Cocoa, Chicory), Sugar and Sugar Products & Confectionary Products, Ministry Of Health and Family Welfare, Government Of India, New Delhi, India, 2015.
17. Ihekoronye AI, Ngoddy PO. Integrated Food Science and Technology for the Tropics. Macmillan Publishers, London, 1985, 18.
18. Herawati D, Simanjuntak F, Syamsir E, Lioe HN, Briawan D. Physicochemical properties of sweet potato cookies fortified with some nutrients. International Food Research Journal, 2015; 22(2):684-690.
19. Aziah AN, Mohamad ANY, Ho LH. Physicochemical and organoleptic properties of cookies incorporated with legume flour. International Food Research Journal, 2012; 19(4):1539-1543.
20. Umadevi L, Uma N. Retention and Dropout Status at Secondary level of schooling in urban and rural areas of Andhra Pradesh: An overview. The J Res. Angrau. 2014; 42(1):33-39.
21. Wu LC, Hsu HW, Chen YC, Chiu CC, Lin YI, Ho JA. Antioxidant and antiproliferative activities of red pitaya. Food Chemistry. 2006; 95(2):319-327.
22. Septembre-Malaterre A, Stanislas G, Douraguia E, Gonthier MP. Evaluation of nutritional and antioxidant properties of the tropical fruits, banana, litchi, mango, papaya, passion fruit and pineapple cultivated in Réunion French Island. Food Chemistry. 2016; 212:225-233.

Genre Classification using Feature Extraction and Deep Learning Techniques

Akshi Kumar

Department of Computer Science and Engineering
Delhi Technological University
Delhi, India
akshikumar@dce.ac.in

Arjun Rajpal, Dushyant Rathore

Computer Science and Engineering
Delhi Technological University
Delhi, India
rajpal.arjun@yahoo.in, dushyant.bgs@gmail.com

***Abstract*— Music genre refers to categorisation of music on the basis of interaction between artists, market forces, and culture. It helps to organize music into collections by indicating similarities between compositions or musicians. Automatic genre classification is non-trivial as it is difficult to distinguish between different genres. Many times the boundaries are not clearly defined and genres are overlapping. In this paper we present a novel approach to classify a list of songs present on Spotify into mainly four genres - Christian, Metal, Country, Rap. Two different kinds of data - lyrics and album artwork are used for the classification process. Two Natural Language Processing techniques namely Bag-Of-Words and Term Frequency-Inverse Document Frequency (TFIDF) are used to process the lyrical data. We apply machine learning algorithms like Random Forest, Support Vector Machine (SVM), Naive Bayes, Linear Support Vector Classifier (Linear SVC) and eXtreme Gradient Boosting (XGBoost) on lyrical data and Deep Convolutional Neural Network (CNN) on the album artwork to predict the genre. On application of machine learning algorithms on lyrical data obtained from Bag-Of-Words a mean precision of 75.96% and a mean f-score of 75.92% is achieved. On application of the same set of algorithms on lyrical data obtained from TFIDF a mean precision of 76.85% and a mean f-score of 77.38% is achieved. In both cases XGBoost outperforms all the other algorithms giving a maximum precision of 79.30% and 80.16% and a maximum f-score of 79.6% and 84.09% for Bag-Of-Words and TFIDF respectively. On application of deep neural network on album artwork, a precision of 82.46% and a f-score of 81.84% is achieved.**

***Keywords* —- Album Artwork; Bag-of-Words; Convolutional Neural Network (CNN); Genre Classification; Lyrics; Term Frequency-Inverse Document Frequency (TFIDF)**

I. INTRODUCTION

Genre classification involves designating objects to a group on the basis of similarities in subject, style, purpose or format. It has been used in music for information management and topic classification. However, the notion of genre is not well-defined for text. There exists some controversy over the constitution of genre among the classification community. Many times, it is possible that a song may belong to more than one genre.

Genre classification by lyrics is a classic example of a Natural Language Processing (NLP) problem [1]. In NLP, the aim is to extract meaning from the text and assign labels to it; here this equates to the genre classification of the lyrical text.

At present, digital music services like Spotify, etc., classify music into sub-genres using song metadata like the digital signatures for some factors such as acoustics, dance ability and emotional tone [2], [3]. The digital music services ignore lyrics as it is difficult to collect large scale lyrical data [4]. However, genre is closely related to lyrics. Genre of the song can be recovered from word frequencies in lyrics.

We try to explore the field of genre classification by applying and comparing the performances of machine learning models like Naive Bayes, Support Vector Machines, XGBoost, etc. on the lyrical data obtained using feature extraction techniques such as Bag-of-Words and TFIDF [5]. In addition to this, we present a relatively new technique of automatic genre classification through application of convolutional neural networks on the album artwork. In recent years, the use of deep learning methods such as Convolutional Neural Networks (CNNs) has led to significant performance improvements and breakthroughs in the field of image classification. While linear and kernel models rely on good hand-selected features these deep learning architectures circumvent this by letting models learn important features themselves.

The rest of the paper is structured as follows. Sections II and III present a literature survey along with the experimental design. Section IV consists of the description of the proposed architecture and machine learning models. Section V gives the research results and visualizations. Finally, section VI presents the conclusion and discusses the future scope of the research.

II. LITERATURE SURVEY

Initial works on automatic genre classification almost exclusively dealt with rhythm and harmony of musical content. In [6], [7], rhythmic content, timbre texture and pitch content were used to evaluate genre.

Later works recognized the importance of lyrics in automatic genre classification. Bag-Of-Words technique established the role of lyrics in genre classification.

In [8], [9], combination of both rhythm based and lyric based classification techniques were used. However only

978-1-5386-6113-0/18/$31.00 ©2018 IEEE

Bag-Of-Words technique was used for textual analysis.

No paper has used more than one method of textual analysis. In this paper, we have used both TFIDF and Bag-Of-Words as NLP techniques and have compared their performances for different machine learning models.

Since the use of album artwork for image classification has not been undertaken previously, we try to explore the field of genre classification using convolutional neural networks on the album art to predict the genres.

We also perform a comparative analysis of the performances of the image data with lyrical data in automatic genre classification.

III. EXPERIMENTAL DESIGN

A. Data Sources and Data Preprocessing

The initial lyrical data is taken from Kaggle [10] and LyricsFreak. The album artwork and genre labels for each song are downloaded using the Spotify API. The final dataset consists of 10,000 songs belonging to the genres - Christian, Metal, Country, and Rap. These four genres are chosen since they are more popular and can be easily differentiated by themes, feature sets, etc. The final dataset is split into 70/30 for training and testing purposes.

Since the Spotify API returns a list of micro-genres for a particular song/artist, one challenge is to determine which broad genre a particular song belongs to. Thus, to determine the target genre, we check if the broad genre (Christian, Metal, Country, and Rap) is a substring of the micro-genres generated for that song by Spotify. After this, the broad genre with the maximum number of instances is selected and used as the target genre for that particular song. Table I describes the attributes present in the dataset.

The lyrical data in the Kaggle dataset is minimally structured and cleaned. To clean it we perform word tokenization and then remove the delimiters, followed by removal of non-alphabetic characters and stop words. Finally, the structured lyrical data is formed by removing the words not present in the English dictionary.

The album artwork needed for genre classification is obtained by using song name and artist name from Kaggle dataset. These details act as inputs to the search function of Spotipy (Spotify's Web API Wrapper for Python) which returns the url address of the album artwork for each song.

B. Lyrical Data

Using the structured/cleaned lyrics available from the preprocessing step, we create two kinds of textual representation structures -

- **Bag-Of-Words** - A vector of length n is used to represent a song. n denotes the count of unique words present in the lyrics of all the cleaned songs. Each feature x(i) in the vector corresponds to the number of times the word i appears in the specific song.
- **TFIDF (Term Frequency-Inverse Document Frequency)** - It is an extension of Bag-Of-Words technique. Each feature x(i) in the vector corresponds to the TFIDF score for the word i in the specified song.

C. Image Data

The album art shown in Fig 1 is resized into a 50*50 gray-scale pixel image. The image is then converted to a feature vector of 2500 pixel values for each song using image matrix transformation techniques. This feature vector is then used as input to our Convolutional Neural Network model.

A Convolutional Neural Network (CNN) [11] is a type of multilayer neural network. It comprises of multiple convolutional layers (often with a sub sampling step) followed by multiple fully connected layers. CNN's architecture makes use of the 2D structure of the input (image, speech, etc.). This is achieved with the help of local connections and tied weights followed by some form of pooling resulting in translation invariant features. CNNs are easier to train and have fewer parameters as compared to fully connected networks having the same number of hidden units.

TABLE I
DATASET ATTRIBUTE DESCRIPTION

Attribute	Description
song	Denotes the name of the song
artist	Name of the artist
lyrics_link	LyricsFreak link containing the lyrics of the song
lyrics	Lyrics of the song
album_uri	Unique album uri on Spotify
artist_uri	Unique artist uri on Spotify
genres	List of micro-genres returned by the Spotify API
album_art	Link containing the album art
target	Target genre for the song obtained by applying the preprocessing step



Fig. 1. Example Metal Song Artwork

IV. PROPOSED ARCHITECTURE

A. Model One : Lyrical Data

*1) **Bag of Words**:* It is an algorithm that counts the number of times a word appears in a document. These word counts help to compare documents and gauge their similarities for applications like topic modeling, document classification and search. It lists the words along with their

word counts per document. E.g.: If there are two sentences –

1) Sam likes to read comics. Maria likes comics too.
2) Sam also likes to read thriller novels.

We create a corpus of all the unique/distinct words present in both the sentences as follows: ['Sam', 'likes', 'also', 'to', 'read', 'Maria', 'comics', 'thriller', 'novels', 'too']. Finally, they represent each sentence as feature vectors of length n (size of the corpus) where feature x(i) in the vector represents the number of times the word i (of the corpus) appears in the specific sentence.

$$BOW1 = [1; 2; 0; 1; 1; 1; 2; 0; 0; 1]$$

$$BOW2 = [1; 1; 1; 1; 1; 0; 0; 1; 1; 0]$$

*2) **TFIDF**:* TFIDF stands for Term Frequency-Inverse Document Frequency. TFIDF weight is a statistical measure used to evaluate the importance of a word to a document in a corpus. It is often used in text mining and information retrieval. The importance of a word increases in direct proportion to the number of times it appears in the document. However, it is neutralized by the frequency of that word in the corpus. It is defined as:

$$tfidf(t, d) = tf(t, d) * idf(t) \quad (1)$$

where: TFIDF(t,d) is TFIDF score of term t in document d, TF(t,d) is number of times the term t appears in document d, and IDF(t) is IDF score of term t.
IDF(t) is defined as:

$$IDF(t) = log((1 + n_d)/(1 + DF(d, t))) + 1 \quad (2)$$

where: n_d is the number of documents, and DF(d,t) is number of documents which have the term t.

We apply L2-Normalization because in the TF (Term Frequency), they represent each term as the number of times it appeared in the document. However, a major problem with this representation is that it creates a bias towards long documents, as a given term has more chances to appear in the longer document, thus making them appear more important than they actually are.

The modified formula for $TFIDF(t_i, d)$ with L2-Normalization is defined as:

$$TFIDF(t_i, d)' = \frac{TFIDF(t_i, d)}{\sqrt[2]{\sum_{i=1}^{m}(TFIDF(t_i, d))^2}} \quad (3)$$

where: m is the no. of unique words in the corpus and TFIDF(t_i ,d) represents the TFIDF score for i^{th} word in the corpus for document d.

After preprocessing the lyrical data using Bag-Of-Words and TFIDF techniques, we apply the following machine learning models with their default parameters —

- **Naive Bayes** : This technique uses Bayes Theorem and probability theory to categorize the sample. The Bayes Theorem is used to get the probabilities and the algorithm returns the category with the highest probability for that sample. The probability of the feature is calculated using the prior knowledge of the related features. The posterior probability P(t|x) is calculated using the following formula:

$$P(t|x) = (P(t) * P(x|t))/(P(x)) \quad (4)$$

where: $P(t|x)$ is the posterior probability of target class, given predictor (x), P(t) is the prior probability of target class, $P(x|t)$ is the likelihood which is the probability of predictor given target class, and P(x) is the prior probability of predictor.
- **Linear SVC** : This is an implementation of Support Vector Classification where the kernel is linear. It works better for a large sample. It gives more choices of penalties and loss functions.
- **Support Vector Machine (SVM)** : These are supervised learning models and their associated learning algorithms. They help in analyzing the data used for classification and regression analysis. In SVM model, the examples are represented as points in space such that different categories are separated by wide gaps. The new examples are mapped in this space. Depending on the side of the gap in which they fall, they are classified into a particular category.
- **Random Forest** : This method is used for regression and classification. It is an ensemble learning model. In this multitude decision trees are constructed during training time. The mode of the classes is outputted and the mean prediction of individual trees is calculated. The use of random decision forests corrects the habit of decision trees to over-fit to the training set.
- **XG Boost (eXtreme Gradient Boosting)** : This refers to Gradient Boosting decision tree which enhances both speed and performance. In this approach new models are created. These models predict the errors of the previous models. These are then added together to arrive at the final prediction. While adding new models XG Boost makes use of gradient descent algorithm to minimize loss.

B. Model Two : Image Data

As described earlier each album art is transformed to a 50x50 gray-scale image. This image is finally converted to a feature vector using image matrix transformation techniques available in Numpy library in python. The converted album arts of the training set are passed into a Convolutional Neural Network (CNN) for classification.

Our convolutional neural network model as shown in Fig 2 consists of 4 convolutional layers having "ReLU" activation function and MaxPool layers. The number of filters for these convolutional layers are 32, 64, 32 and 128 respectively. In addition to the convolutional layers, we make use of a fully connected layer having a "ReLU" activation function and 1024 output units. Finally the output units

from this fully connected layer are fed into another fully connected layer having 4 output units denoting the target genre classes. The parameter values of our Convolutional Neural Network model are shown in Table II.

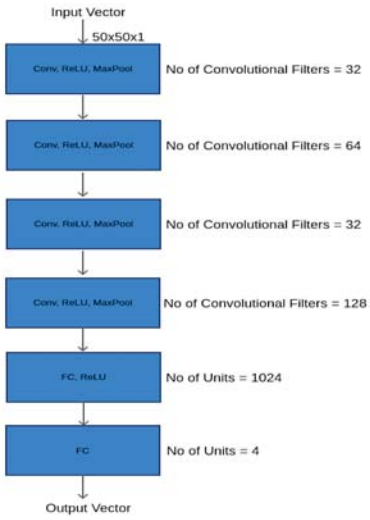


Fig. 2. CNN Architecture

TABLE II
PARAMETER VALUES FOR THE CONVOLUTIONAL NEURAL NETWORK MODEL

Parameter	Values
Epochs	15
Activation function for input and hidden layers	ReLU
Activation function for output layer	Softmax
Loss	categorical_crossentropy
Optimizer	Adam Optimizer (learning rate=0.001, beta1=0.9, beta2=0.999, epsilon=1e-08, use_locking=False)
Dropout	0.8

V. RESEARCH RESULTS

A. Model One : Lyrical Data

On application of the above-mentioned machine learning algorithms, we obtain the precision and f-score of each of Bag-of-words and TFIDF model as shown in Table III and Table IV. As one can make out from Table III and Fig 3 and Table IV and Fig 4, the TFIDF textual analysis model outperforms the Bag-Of-Words model in 4 of the 5 machine learning models in terms of both precision and f-score. On further observation, we find that XGBoost algorithm gives the maximum precision of 79.3% and maximum f-score of 79.6% in Bag-of-words and maximum precision of 80.16% and maximum f-score of 84.09% in TFIDF analysis models. This supports the established domination of the XGBoost algorithm in the field of applied machine learning for structured data.

TABLE III
PRECISION SCORE FOR GENRE CLASSIFICATION

Classifiers	Bag-of-words %	TFIDF %
Naive Bayes	75.0	68.5
Linear_SVC	70.7	79.2
SVM	77.1	77.4
Random Forest	77.7	79.0
XGBoost	79.3	80.16

TABLE IV
F-SCORE FOR GENRE CLASSIFICATION

Classifiers	Bag-of-words %	TFIDF %
Naive Bayes	75.8	66.7
Linear_SVC	70.1	78.2
SVM	76.3	78.4
Random Forest	77.8	79.5
XGBoost	79.6	84.09

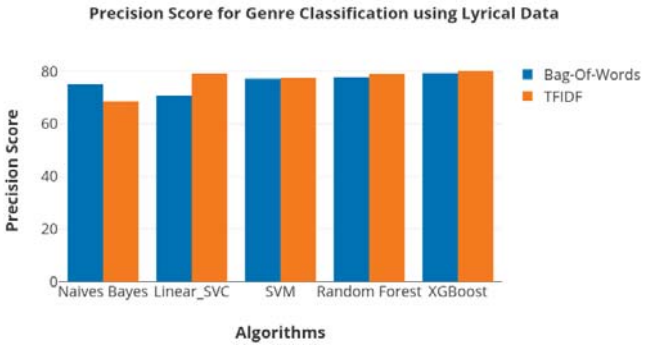


Fig. 3. Precision Score for different models

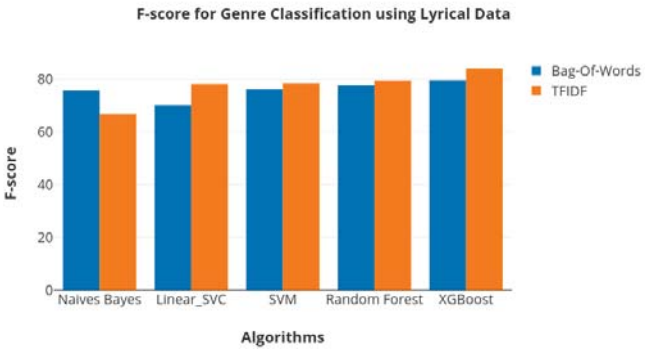


Fig. 4. F-score for different models

B. Model Two : Image Data

On application of our Convolutional Neural Network model, we obtain a precision of 82.46% and f-score of 81.84%. Variation in accuracy, validation accuracy and log loss with change in epochs is shown in Fig 5 and Fig 6. It is evident from the figures that the model accuracy increases and the log loss decreases with the subsequent epochs.

The normalized and un-normalized confusion matrix for the predictions made by our model are shown in Fig 7 & Fig 8 respectively.

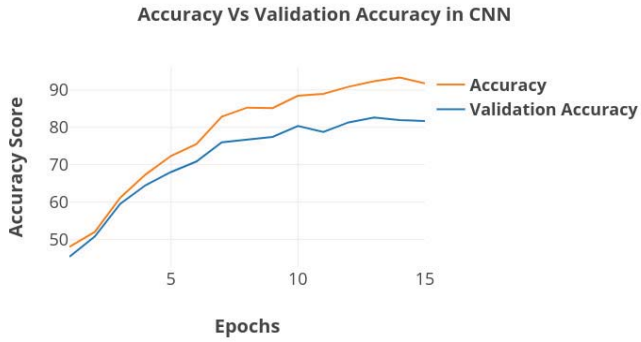


Fig. 5. Accuracy Vs Validation Accuracy in CNN

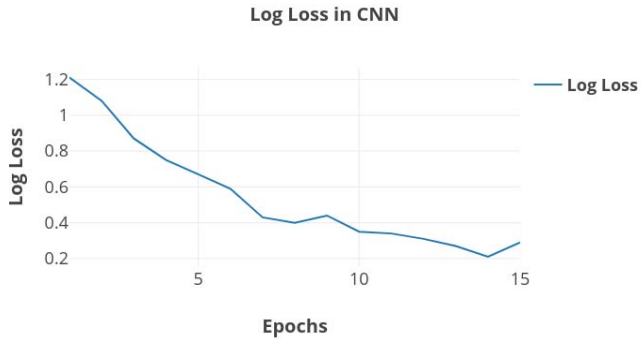


Fig. 6. Log Loss in CNN

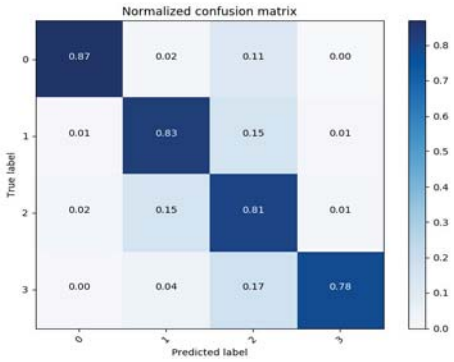


Fig. 7. Normalized Confusion Matrix

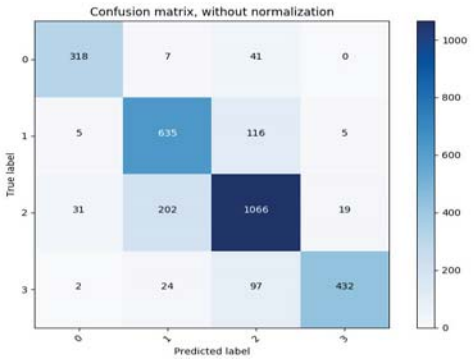


Fig. 8. Un-normalized Confusion Matrix

VI. CONCLUSIONS

While performing automatic genre classification on songs, it is found that both lyrics and album artwork have a deep influence on determining the genre of a particular song. It is also discovered that since TFIDF, unlike Bag-Of-Words, not only takes into account the frequency of a particular word in a particular song but also considers its frequency in the entire corpus and assigns terms weights to each word, so it outperforms the Bag-Of-Words technique in case of lyrical data. Also, it is observed that there is a huge possibility for more exploration of album artwork in regards to genre and other information about the song.

For future work, we plan to explore more sophisticated natural language processing techniques like word2vec, doc2vec and semantic analysis [12] for rigorous cleaning of the lyrical data. Along with it, classifying the songs in an even wider range of genres by using other features like beats per minute, tone patterns, etc can also have a significant effect on the domain. Finally, applying a suitable optimization technique like Particle Swarm Optimization with an objective of maximizing both precision and f-score in case of both lyrical data and album artwork can also lead to significant improvements in the results.

REFERENCES

[1] Mahedero et al., "Natural language processing of lyrics," in Proceedings of the 13th Annual ACM International conference on Multimedia, MULTIMEDIA'05, November 06 - 11, 2005, Hilton, Singapore, doi:10.1145/1101149.1101255.

[2] T. Dammann and K. Haugh, "Genre Classification of Spotify Songs using Lyrics, Audio Previews, and Album Artwork".

[3] Teh Chao Ying, S. Doraisamy and Lili Nurliyana Abdullah, "Genre and mood classification using lyric features," in Proceedings of 2012 International Conference on Information Retrieval & Knowledge Management, March 13 - 15, 2012, Kuala Lumpur, Malaysia, pp. 260-263, doi:10.1109/InfRKM.2012.6204985.

[4] D. Liang, H. Gu, and B. O'Connor., "Music Genre Classification with the Million Song Dataset".

[5] X. Hu, J.S. Downie, & A.F. Ehmann, "Lyric Text Mining in Music Mood Classification.," in Proceedings of 10th International Conference on Music Information Retrieval, ISMIR 2009, October 26 - 30, 2009, Kobe, Japan, pp. 411-416.

[6] G. Tzanetakis and P. Cook, ”Musical genre classification of audio signals,” IEEE Transactions on Speech and Audio Processing, vol. 10, no. 5, pp. 293-302, July 2002.
[7] N. Scaringella, G. Zoia and D. Mlynek, ”Automatic genre classification of music content: a survey,” IEEE Signal Processing Magazine, vol. 23, no. 2, pp. 133-141, March 2006.
[8] R. Neumayer and A. Rauber, ”Integration of Text and Audio Features for Genre Classification in Music Information Retrieval.,” in Proceedings of 29th European Conference on IR Research, ECIR 2007, April 2-5, 2007, Rome, Italy, pp. 724-727, doi:10.1007/978-3-540-71496-5_78.
[9] R. Mayer and A. Rauber, ”Building ensembles of audio and lyrics features to improve musical genre classification,” in Proceedings of 2010 International Conference on Distributed Frameworks for Multimedia Applications, Yogyakarta, 2010, pp.1-6.
[10] S. Kuznetsov, ”55000+ Song Lyrics, Kaggle,” 2016, URL: https://www.kaggle.com/mousehead/songlyrics.
[11] K. O’Shea and R. Nash, “An Introduction to Convolutional Neural Networks,” arXiv:1511.08458 [cs.NE], November. 2015
[12] B. Logan, A. Kositsky and P. Moreno, ”Semantic analysis of song lyrics,” 2004 IEEE International Conference on Multimedia and Expo (ICME) (IEEE Cat. No.04TH8763), Taipei, 2004, pp. 827-830 Vol.2. doi: 10.1109/ICME.2004.1394328

arXiv:1811.12748v1 [cs.CV] 30 Nov 2018

Improving Landmark Recognition using Saliency detection and Feature classification

Akash Kumar*, Sagnik Bhowmick*, N. Jayanthi, and S. Indu

Delhi Technological University, New Delhi
{akash_bt2k15, sagnikbhomic_2k15ec133, njayanthi, s.indu}@dtu.ac.in

Abstract. Image Landmark Recognition has been one of the most sought-after classification challenges in the field of vision and perception. After so many years of generic classification of buildings and monuments from images, people are now focussing upon fine-grained problems - recognizing the category of each building or monument. We proposed an ensemble network for the purpose of classification of Indian Landmark Images. To this end, our method gives robust classification by ensembling the predictions from Graph-Based Visual Saliency (GBVS) network alongwith supervised feature-based classification algorithms such as kNN and Random Forest. The final architecture is an adaptive learning of all the mentioned networks. The proposed network produces a reliable score to eliminate false category cases. Evaluation of our model was done on a new dataset, which involves challenges such as landmark clutter, variable scaling, partial occlusion, etc.

Keywords: Landmark Recognition · Transfer Learning · Graph-based Visual Saliency.

[1]

1 Introduction

United Nation Educational, Scientific and Cultural Organization (UNESCO) World Heritage Center recognizes over 1500 monuments and landmarks as World heritage sites. Apart from this, there are over 10K monuments and landmarks spread over the globe which serves as a local tourist attraction and have a huge contribution in the history and culture of the location. However, it is impossible for humans to individually recognize and classify all monuments according to history and architecture. Technology like Computer Vision and Deep Learning plays a pivotal role to overcome this challenge.

Many Convolutional Neural Network(CNN) based deep learning frameworks shows to be handy in such a scenario, where classes have different features. Every landmark architecture style has distinguishable features from other forms of architecture. These features play a pivotal role in the recognition of such

[1] * Equal Contribution

landmark architectures. India, one of the most diverse country in the world, is a house to varied architectures. We propose a framework to classify these landmarks based on the era they were constructed. These varied architectural features make classication of Indian monuments a dreadful task. Moreover, these historic buildings are useful references for architects designing contemporary architecture, thus information about the architectural styles of these monuments seems necessary.

In this paper, we employ CNN to address the problem of Landmark Recognition. Our main contributions are:

1. We proposed an end-to-end architecture to classify Indian monuments in the image. Experiments show that our model surpass the existing baseline on the dataset.
2. We employ convolutional architectures to learn the intra-class variations between different landmarks. The final the averageprediction is ensemble of three networks consisting of salient regions detection, kNN and Random Forest supervised classification algorithms.

2 Related Work

There are several recent papers to address the problem of Landmark Recognition [1], [2], [3], most of them are based on deep learning except [8], which classify landmarks using visual features such as HoG [12], SIFT [1] and SURF [11]. While landmark recognition can be considered as descriptor matching, our work relates to some [2] in that we learn to employ a visual saliency algorithm to focus on the most noticeable region and extract those features to classify them.

Landmark Recognition using CNN presents a competitive research as there is so much little intra-class variations [16]. [3] employed a multi-scale feature embedding to generate condition viewpoint invariant features for specific place recognition. [13] uses local binary patterns and Gray-level co-occurrence matrix to match the pairs using pixel-wise information. [14] devised an architecture using visual descriptors and Bag-of-Words for Image-based Monument Classification. [2] uses AlexNet to extract features and classify landmarks using supervised feature learning. Many works has been done on specific place recognition but the area of using fine-grained features to recognize Indian Landmarks has not been explored yet.

3 Problem Formulation

Landmark Recognition in Indian scenario is very different from the European and American counter-part, due to its extreme varieties within each region and diversified architecture. Approaches like bag of words, HoG and SIFT are constrained to database size. Other approaches based on deep learning framework [9] face challenges in identifying diverse image in same class (refer fig.1). Among all these methods, we need a more robust and dynamic framework that can learn

these intra-class variations. Hence, our architecture focusses on these explicit and implicit features of the images.



Fig. 1. Same class had varied architecture style

4 Dataset

The manually collected Indian monument dataset consist of monument images majorly of 4 classes based on architecture types, i.e. Buddhist, Dravidian, Kalinga and Mughal architectures.

Table 1. Categorical distribution of data among 4 classes

Class Label	Train Set	Validation Set	Test Set
I. Buddhist	647	81	81
II. Dravidian	657	83	82
III. Kalinga	881	111	110
IV. Mughal	624	79	78

The total 3514 dataset images has been divided in ratio 80:10:10 of Training:Validation:Testing images respectively. Overview of the dataset is shown in the diagram below Fig. 2.

5 Proposed Approaches

In this section, we discuss about the proposed framework that is used for landmark classification. We devised two architectures to solve the problems of monument classification. These methods are described as follows:



Fig. 2. Dataset Overview

5.1 Graph-based Visual Saliency (GBVS)

Image Saliency is what stands out and how fast you are able to quickly focus on the most relevant parts of what you see. Now, in the case of landmarks the less salient region is common backgrounds, that's of blue sky. The architectural design of the monuments is what differentiates between the classes. GBVS[14] [17] firstly finds feature maps and then apply non-linear Activation maps to highlight "significant" locations in the image. We used GBVS to detect 5 important locations per training image. Those images were used for multi-stage training. It helped to improve our accuracy by 3-4%. Example of salient region detected using GBVS algorithm is shown in Fig. 3.

5.2 Supervised Feature Classification

In this approach, we used *fc* layer features of ImageNet models to train supervised machine learning models such as kNN and Random Forest Classification. Among all the ImageNet models, Inception ResNet V2 performed best for landmark classification. Therefore, we extracted the representation from Inception Net of dimension 2048×1.

5.3 Ensemble Model Architecture

Our final architecture comprises of Averaging based Ensemble [10] methods. Test image is passed firstly from GBVS algorithm to create a batch of 5 images. The batch prediction is done using Inception ResNet V2 [4]. Similarly, the test image is also passed through Inception ResNet model for feature extraction. These features were used to learn and predict classes using kNN and Random Forest Classifiers. The final prediction is done using averaging of predictions from the three models described above. Ensemble learning boosted the accuracy

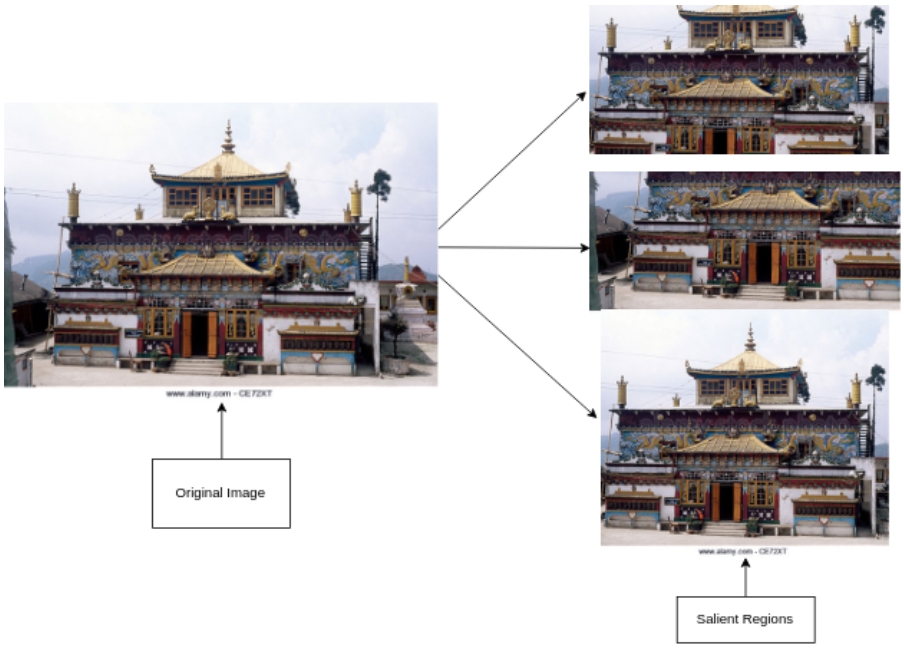


Fig. 3. Salient Region Detection using Graph-based Visual Saliency

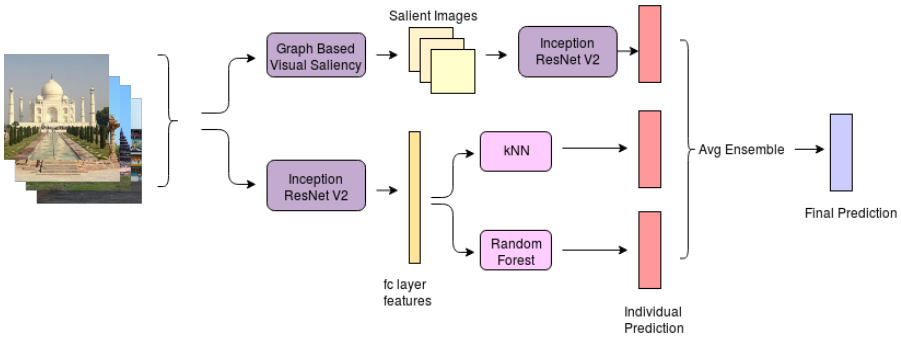


Fig. 4. Proposed Architecture

by approximately 2-3%. The final architecture is diagramatically explained in Fig. 4.

6 Experiments

Improved Feature Learning using Multi-stage Training We trained our model firstly on original images that were resized to 416 × 416 and then on high salient regions extracted using Graph-based Visual Saliency Algorithm. We used ImageNet pretrained weights to train Inception ResNet V2 [4] architecture on original and salient images. The salient images helped us to learn discriminative features between various classes. Original images assisted in learning of global spatial features.

Parameters In our model, we used ADAM (lr= 0.0001) [7] optimizer and ReLU[6] activation function. The model was trained for 7 epochs using the pre-trained ImageNet weights as initialization for Transfer Learning.

7 Results

The experimental results on the landmarks dataset are presented in Table 2. The scores obtained are from different architectures trained on salient crops and original images during Multi-stage Training.

Table 2. Accuracy during Multi-Stage Training on Inception V3 and Inception ResNet V2 models

Model Architecture	**Data Subset**	**Train**	**Validation**	**Test**
Inception V3 [5]	Original Images	90.1	77.23	75.42
	Original + Salient	91.81	80.3	78.91
Inception Resnet V2 [4]	Original Images	91.76	77	76.35
	Original + Salient	92.29	81	80

Table-3 compares the accuracy scores for all the models on train, validation and testing dataset. The final prediction is done by average ensembling of three models to get the final architecture with low variance and low bias.

Table 4 compares the results on the existing dataset with our new proposed approach. It is clear that our approach the outperforms the existing models by 8%.

8 Conclusion and Future Work

The paper presented two approaches on which extensive experiments were done to classify Indian architectural styles. Landmark Recognition problem presents

Table 3. Evaluation comparison (in %) of different models

Model Architecture	**Train**	**Validation**	**Test**
GBVS + InceptionResNetV2	92.61	89.65	86.18
InceptionResnetV2 + kNN	93.62	90.72	86.94
InceptionResNetV2 + Random Forest	91.58	89.8	88
Average Ensemble	**94.58**	**93.8**	**90.08**

Table 4. Comparison of our best model with competing methods[9]

Framework	**Test**
SIFT + BoVW	51%
Gabor Transform + Radon Barcode	70%
Radon Barcode	75%
CNN	82%
Our Method (Average Ensemble)	**90%**

some noteworthy solutions as there are no training data available for less popular landmarks. Our solution focusses on the most noticeable region of the image to classify landmarks accurately. Our approach targets the fine-grained features as well as on the global features of monuments. Previous works lack the attention mechanism to differentiate models on the basis of fine-grained features. Our model outperforms the existing approach by 8%.

In future, the authors aim to improve the model accuracy by using DELF features and Visual Attention mechanism to further improve the accuracy of the model as well as learn more substantial features.

References

1. D. G. Lowe, Distinctive image features from scale-invariant keypoints, International Journal of Computer Vision, vol. 60, no. 2, pp. 91110, 2004. https://doi.org/10.1023/B:VISI.0000029664.99615.94
2. P. Shukla, B. Rautela and A. Mittal, "A Computer Vision Framework for Automatic Description of Indian Monuments," 2017 13th International Conference on Signal-Image Technology & Internet-Based Systems (SITIS), Jaipur, 2017, pp. 116-122. https://doi.org/10.1109/SITIS.2017.29
3. Z. Chen, A. Jacobson, N. Sunderhauf, B. Upcroft, L. Liu, C. Shen, I. Reid, M. Milford, Deep Learning Features at Scale for Visual Place Recognition, 2017 IEEE International Conference on Robotics and Automation (ICRA), Singapore. https://doi.org/10.1109/ICRA.2017.7989366
4. Szegedy, Christian et al. Inception-v4, Inception-ResNet and the Impact of Residual Connections on Learning. AAAI (2017).
5. C. Szegedy, V. Vanhoucke, S. Ioffe, J. Shlens and Z. Wojna, "Rethinking the Inception Architecture for Computer Vision," 2016 IEEE Conference on Computer Vision and Pattern Recognition (CVPR), Las Vegas, NV, United States, 2016, pp. 2818-2826.https://doi.org/10.1109/CVPR.2016.308

6. Vinod Nair and Geoffrey E. Hinton. Rectified Linear Units Improve Restricted Boltzmann Machines. In Proceedings of the 27th International Conference on International Conference on Machine Learning. ICML10. Haifa, Israel: Omnipress, 2010, pp.807814. ISBN : 978-1-60558-907-7. URL : http://dl.acm.org/citation.cfm?id=3104322.3104425.
7. Diederik P. Kingma and Jimmy Ba. Adam: A Method for Stochastic Optimization. In: CoRR abs/1412.6980 (2014). arXiv: 1412.6980. URL:http://arxiv.org/abs/1412.6980.
8. G. Amato and F. Falchi and P. Bolettieri, "Recognizing Landmarks Using Automated Classification Techniques: Evaluation of Various Visual Features,". 2010 Second International Conferences on Advances in Multimedia. 78-83 https://doi.org/10.1109/MMEDIA.2010.20
9. Sharma S., Aggarwal P., Bhattacharyya A.N., Indu S. (2018) Classification of Indian Monuments into Architectural Styles. NCVPRIPG 2017. Communications in Computer and Information Science, vol 841. Springer, Singapore. https://doi.org/10.1007/978-981-13-0020-2_47
10. Sainin, Mohd & Alfred, Rayner & Adnan, Fairuz & Ahmad, Faudziah. (2018). Combining Sampling and Ensemble Classifier for Multiclass Imbalance Data Learning. 262-272. https://doi.org/10.1007/978-981-10-8276-4_25.
11. Bay, Herbert and Ess, Andreas and Tuytelaars, Tinne and Van Gool, Luc, "Speeded-Up Robust Features (SURF),". Comput. Vis. Image Underst. Journal. June, 2008. Vol. 110. 346–359. https://doi.org/10.1016/j.cviu.2007.09.014
12. Dalal, Navneet and Triggs, Bill, "Histograms of Oriented Gradients for Human Detection,". Proceedings of the 2005 IEEE Computer Society Conference on Computer Vision and Pattern Recognition (CVPR'05) - Volume 1 - Volume 01. 886–893. https://doi.org/10.1109/CVPR.2005.177
13. A. Saini, T. Gupta, R. Kumar, A. K. Gupta, M. Panwar and A. Mittal, "Image based Indian monument recognition using convoluted neural networks," 2017 International Conference on Big Data, IoT and Data Science (BID), Pune, 2017, pp. 138-142. https://doi.org/10.1109/BID.2017.8336587
14. TRIANTAFYLLIDIS, Georgios; KALLIATAKIS, Gregory. Image based Monument Recognition using Graph based Visual Saliency. ELCVIA Electronic Letters on Computer Vision and Image Analysis, [S.l.], v. 12, n. 2, p. 88-97, apr. 2013. ISSN 1577-5097. https://doi.org/10.5565/rev/elcvia.524
15. B. Ghildiyal, A. Singh and H. S. Bhadauria, "Image-based monument classification using bag-of-word architecture," 2017 3rd International Conference on Advances in Computing,Communication & Automation (ICACCA) (Fall), Dehradun, 2017, pp. 1-5. https://doi.org/10.1109/ICACCAF.2017.8344728
16. Google AI Blog:Google-Landmarks: A New Dataset and Challenge for Landmark Recognition, `https://ai.googleblog.com/2018/03/google-landmarks-new-dataset-and.html`.
17. Harel, Jonathan and Koch, Christof and Perona, Pietro (2007) Graph-Based Visual Saliency. In: Advances in Neural Information Processing Systems 19 (NIPS 2006). Advances in Neural Information Processing Systems. No.19. MIT Press , Cambridge, MA, pp. 545-552. ISBN 0-262-19568-2.

I.J. Wireless and Microwave Technologies, **2018, 2, 15-26**
Published Online March 2018 in MECS(http://www.mecs-press.net)
DOI: 10.5815/ijwmt.2018.02.02

***Available online at** http://www.mecs-press.net/ijwmt*

Intelligent Software Defined Atmospheric Effect Processing for 5th Generation (5G) Millimeter Wave (MMWave) Communication System

S. K. Agrawal[a, *], Kapil Sharma[b]

[a,b] *Computer Engineering Department, Delhi Technological University (DTU), Formerly : Delhi College of Enginering (DCE), Delhi, India*

Received: 06 July 2017; Accepted: 17 January 2018; Published: 08 March 2018

Abstract

In this paper, we present atmospheric effect on 5th Generation (5G) millimeter wave (MMWave) communication system. Atmospheric effects for Delhi (India) based 5G communication system is calculated as per Delhi atmospheric conditions. Atmospheric impairments are major cause of degrading mmWave signal power while mmWave propagation in wireless channel. Due to Atmospheric impairments attenuation takes place and major impairments are like water vapour, oxygen, rain and fog for Delhi (India). 5G mmWave attenuation calculations are performed for the mmWave band frequencies 28 GHz, 37 GHz and 39 GHz. In this paper intelligent adaptive transmitter based on trend of the atmospheric conditions tunes to machine learning (ML) based derivation of channel capacity. The ML based transmitter is a supervised ML device and it has provision of self teaching learning machine based on data. Results are graphed for the mentioned frequencies and also intelligently software defined (SD) Shannon channel capacity calculated for Delhi (India) based 5G mmWave communication system under different atmospheric conditions.

Index Terms: Millimeter Wave (mmWave), 5th Generation (5G), Software Defined (SD).

© 2018 Published by MECS Publisher. Selection and/or peer review under responsibility of the Research Association of Modern Education and Computer Science

1. Introduction

The Worldwide continuous demand of data on wireless communication system having user ubiquitous access requires high speed data rate and high bandwidth to full the requirement seamlessly. Around 3GHz

* Corresponding author. Tel.: +919910741162
E-mail address: sachin.ecin@gmail.com

several research has been done to justify and provide the efficient data bandwidth and data rates; however this is not sufficient for upcoming years [1-7].

There is demand and need to fulfill this high speed data rate and high bandwidth along efficient frequency spectrum with intelligence in the system. 5th generation (5G) millimeter wave (MMWave) communication system is an emerging technology which will provide efficient mmWave spectrum utilization to provide high speed data rate and high bandwidth. MMWave frequencies bands are capable to provide the high speed data rate and high bandwidth by fulfilling the spectrum shortage. 5G MMWave communication system requires efficient spectrum handling by considering various MMWave propagation channel characteristics for the entire MMWave range. MMWave frequencies range from 30 to 300 GHz and provide a large spectrum. It forms the base for the 5G MMWave communication system. In this paper, we propose a feature for an intelligent ML based adaptive transmitter for 5G wireless system [5-13].

2. 5G MMWave Frequency Spectrum

High speed data rate and high bandwidth can be achieved under 5G communication system by having MMWave frequency spectrum. Several MMWave frequencies are proposed globally for 5G MMWave communication system. 5G MMWave frequency spectrum offers high speed data rate and high bandwidth. 5G communication system research is under development with MMWave frequencies. Recently; The United States Federal Communications Commission (FCC) authorizes and proposes broadband device operations in the following MMWave bands [13-16]:

- 27.5-28.35 GHz band (28 GHz band)
- 37-38.6 GHz band (37 GHz band)
- 38.6-40 GHz band (39 GHz band)

FCC proposed MMWave bands are considering:

- High speed
- Low latency
- High capacity
- Advance user experience

3. Atmospheric Gaseous Attenuation

MMWave frequency link suffers with atmospheric attenuation and this MMWave attenuation takes place due to atmospheric gaseous absorption. The impact of atmospheric gases on the propagation of MMWave comes in form of:

- Signal attenuation
- Phase shift and
- Angle of arrival variations

Atmospheric attenuation takes place majorly due to atmospheric water vapor and atmospheric oxygen, scattering and scintillation. For certain MMWave frequencies losses are high because of the resonance gas molecules. Atmospheric water vapour attenuation is high as compare to oxygen particles due to atmospheric absorption and scattering [16-19].

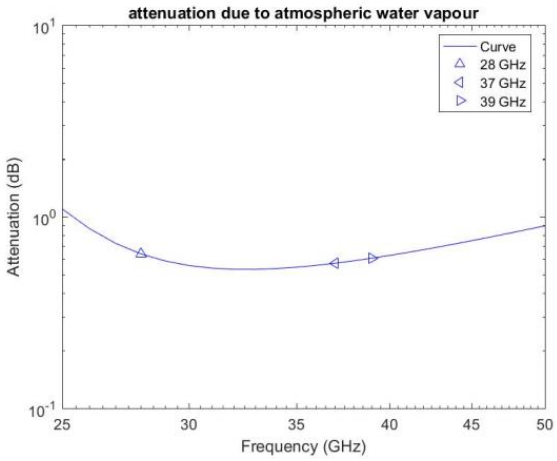


Fig.1. Atmospheric Water Vapor Attenuation for 5G mmWave Wireless Communication System

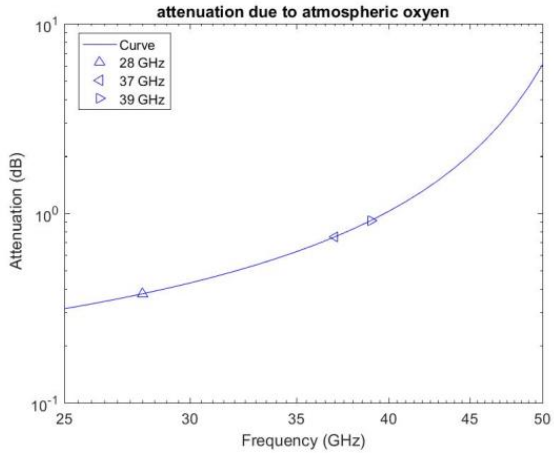


Fig.2. Atmospheric Oxygen Attenuation for 5G mmWave Wireless Communication System

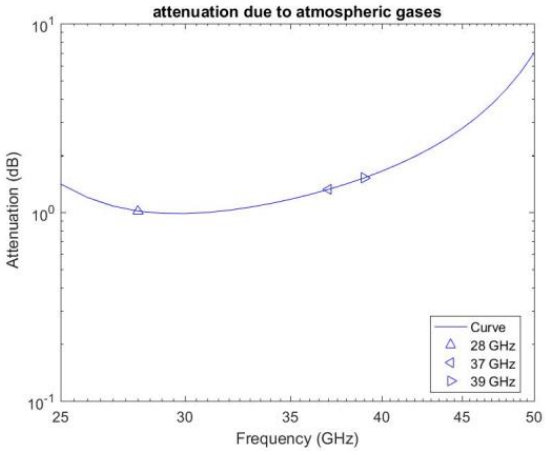


Fig.3. Atmospheric Gaseous Attenuation for 5G mmWave Wireless Communication System

To calculate 5G MMWave communication system; atmospheric attenuation here we are using ITU-R recommended method for calculating atmospheric water vapor attenuation and atmospheric oxygen attenuation. This model comprises various parameters like; Frequency, Path-elevation angle, Height above mean sea level, Water vapor density and etc. The atmospheric gaseous attenuation is calculated by having equi probable summation of the atmospheric water vapor attenuation and oxygen attenuation [16-21].

Atmospheric water vapor specific attenuation is given by following equation (1):

$$\gamma_w(f) = F(f) \tag{1}$$

In equation (1) 'rho' is the water vapour concentration in g/m^3 and 'f' is the frequency in GHz. For Delhi rho changes from 6-10 g/m^3. The total MMWave atmospheric water vapour attenuation is shown by the following equation (2)

$$A_{watervapour} = \frac{h_w \gamma_w}{\sin\theta} \quad .....\theta > 10^{\circ} \tag{2a}$$

$$A_{watervapour} = \frac{\gamma_w \sqrt{R_e h_w}}{\cos\theta} F(\tan(\theta)\sqrt{R_e / h_w})..\theta \le 10^{\circ} \tag{2b}$$

The details about above equations and related functions are explained the cited reference. As per equations (1) and (2) attenuation due to the MMWave water vapour has been plotted with mmWave frequencies in the Fig. (1). In this Fig. (1) logarithmic scale has been used with the MMWave frequency range 10 GHz to 1000 GHz. Rho = 8 for Delhi and as per plot in the Fig. (1) atmospheric water vapor shows high value attenuation due to resonances at 22 GHz. The variation of atmospheric attenuation due to the water vapour along with MMWave frequencies is shown in the Fig. (1). Due to high MMWave resonance frequency absorption mmWave attenuation takes place [16-21].

Atmospheric oxygen specific attenuation is given by the following equation (3)

$$\gamma_o(f) = F(f) \tag{3}$$

Atmospheric oxygen specific attenuation is given by the following equation (3) having MMWave frequency in GHz. The total attenuation in dB is given by the equation (4):

$$A_{oxygen} = \frac{h_o \gamma_o}{\sin\theta} \quad .....\theta > 10 \tag{4a}$$

$$A_{oxygen} = \frac{\gamma_o \sqrt{R_e h_o}}{\cos\theta} F(\tan(\theta)\sqrt{R_e / h_o})..\theta \le 10 \tag{4b}$$

As per equations (3) and (4) attenuation due to the MMWave oxygen has been plotted with mmWave frequencies in the Fig. (2). In this Fig. (2) logarithmic scale has been used with the MMWave frequency range 10 GHz to 1000 GHz. Atmospheric oxygen shows high attenuation due to strong bands of resonances at 57-60 GHz. Fig. (2) shows graph of Delhi atmospheric attenuation due to oxygen. 5G MMWave communication

system; MMWave transmission windows are at 35 GHz and 94 GHz. These windows are having minimal attenuation and surrounded by the attenuation peaks.

5G MMWave communication system; total gaseous atmospheric attenuation is calculated by having equi-probability summing. The total MMWave atmospheric losses for 5G MMWave is calculated by having sum of equation (2) and (4).

$$A_{gas} = A_{water} + A_{oxygen} \tag{5}$$

As per equations (2) and (4) summation to the equation (5) the total atmospheric attenuation due to the MMWave water vapor and oxygen has been plotted with mmWave frequencies in the Fig. (3). In this Fig. (3) logarithmic scale has been used with the MMWave frequency range 10 GHz to 1000 GHz. This plot provides all peaks in a single graph to decide transmission window easily.

It is easy to design and select MMWave frequency for Delhi based 5G MMWave communication system. The minimal attenuation area in Fig. (3) shows the space for transmission with minimal attenuation due to atmosphere. Table (1) depicts the attenuation due to water vapor, oxygen and total gaseous attenuation for the mmWave frequencies as per table (1):

Table 1. Atmospheric Gaseous Attenuation Values for 5G mmWave Wireless Communication System

Attenuation dB	28GHz	37GHz	39GHz
water	0.63	0.646	0.53
Oxygen	0.016	0.646	0.019
Gaseous / Total	0.646	0.646	0.549

4. Atmospheric Rain & Fog Attenuation

Atmospheric attenuation has one of the major factor due to rain and rain drops play major role for atmospheric attenuation. Rain drops acts as a poor dielectric and absorbs the MMWave power and dissipates the MMWave signal power by scattering or heat loss. Here we are using modified ITU-R rain attenuation model to calculate MMWave rain attenuation majorly based on rain rate. Atmospheric specific attenuation for 5G MMWave communication link is given equation (6) in db/km [19-23]:

$$\Gamma_R = kR^a \tag{6}$$

In equation (6) R is the rain rate in mm/hr and k and alpha are frequency and polarization dependent coefficients which are detailed in the prior literature. Total rain attenuation rain A exceeded for 0.01% of an year in dB is shown by equation (7)

$$A_{rain} = \gamma_R L_s r_{0.01} \tag{7}$$

Fig. (4), (5), (6) and (7) show the summary of the rain attenuation graphs for the coefficients k, alpha, specific attenuation and total rain attenuation graph of Delhi atmospheric rain attenuation. 5G MMWave communication system; attenuation due to rain for the frequencies 28GHz, 37 GHz and 39GHz are marked the figures. It is clear from the plot that rain attenuation keeps increasing with frequency.

MMWave 5G MMWave communication system also suffers with the fog attenuation. in the presence of fog goes through significant amount of attenuation. Atmospheric fog attenuation has dependent parameters like amount of water, temperature, fog particle average size, water distribution and etc. Attenuation due to fog is given by equation (8)

$$A_{fog} = L_s \gamma_c$$
$$A_{fog} = L_s K_l M \tag{8}$$

In Delhi; MMWave 5G MMWave communication system will suffer fog attenuation in the month of December and January. Fig. (8) plots the attenuation due to fog for different temperatures. It is clear that the fog attenuation is significant value for the frequencies 28GHz, 37 GHz and 39GHz. Plot also shows fog attenuation also depends on the varying temperatures.

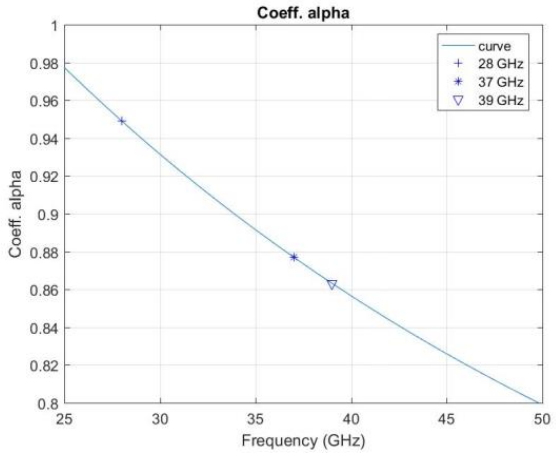


Fig.4. Atmospheric Rain Attenuation Coefficient Alpha for 5G mmWave Wireless Communication System

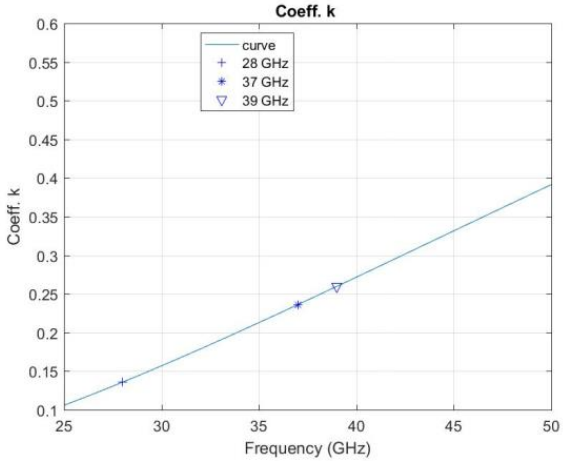


Fig.5. Atmospheric Rain Attenuation Coefficient k for 5G mmWave Wireless Communication System

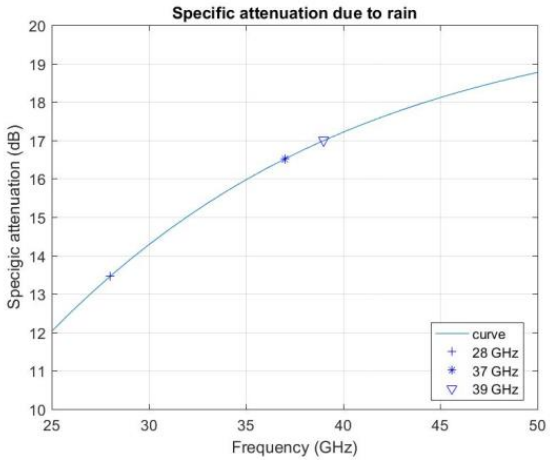


Fig.6. Atmospheric Rain Attenuation Specific for 5G mmWave Wireless Communication System

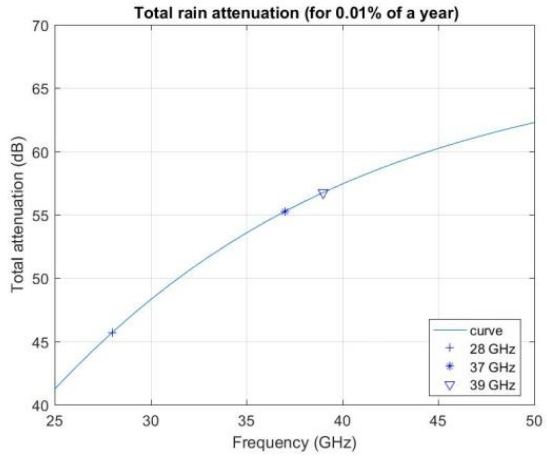


Fig.7. Atmospheric Rain Attenuation for 5G mmWave Wireless Communication System

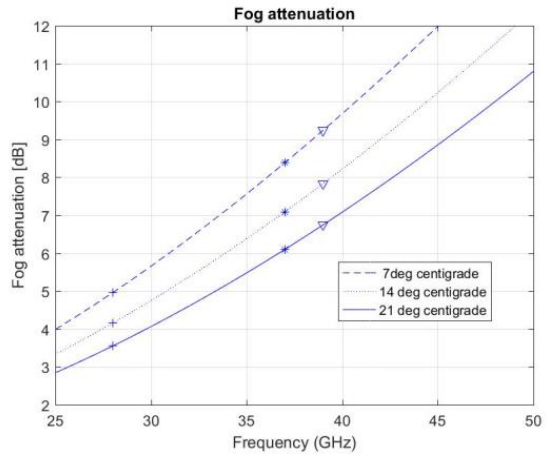


Fig.8. Atmospheric Fog Attenuation for 5G mmWave Wireless Communication System

5. Software Defined Channel Capacity

Software Defined MMWave facilitates transmission power control in a real manner. 5G millimeter wave communication system transmitter and receivers can be controlled by artificial intelligent (AI) software defined (SD) mmwave communication system. AI based software defined MMWave facilitates methods to control the transceiver as per atmospheric attenuation [19-23].

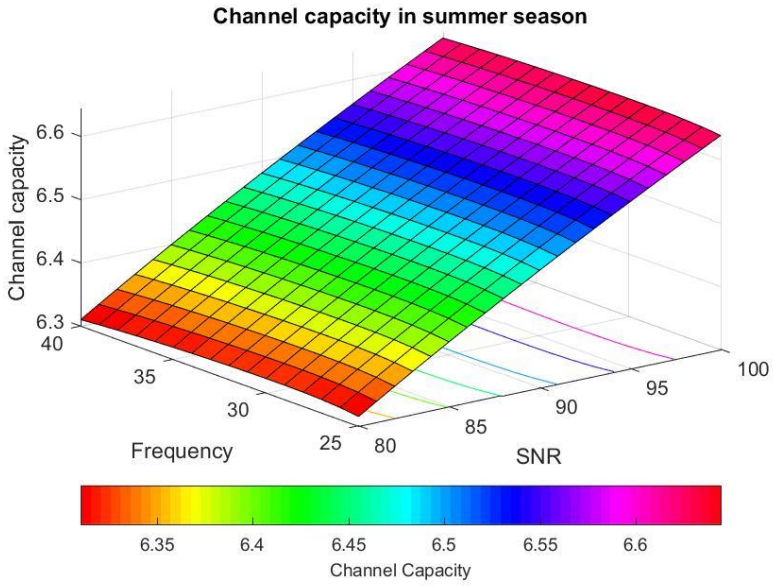


Fig.9. Channel Capacity in Summer Season for 5G mmWave Wireless Communication System

In this paper intelligent adaptive transmitter based on trend of the atmospheric conditions tunes to machine learning (ML) based derivation of channel capacity. The ML based transmitter is a supervised ML device and it has provision of self teaching learning machine based on data. Here intelligent an adaptive transmitter which is having machine learning (ML) based on previous trends of the attenuations decides the optimal channel capacity. Its intelligence is based on the various type of attenuations as per various conditions as described. The decision-directed adaptive receiver has the same structure as the gremlin receiver, but uses its own decisions . The adaptive ML based transmitter is useful to intelligently provide the required channel capacity. It intelligently regulates the demand and need of channel capacity in 5G millimeter wave communication system in Delhi. Shannon channel capacity in the presence of continuous additive white Gaussian noise channel is given by equation (9) [19-26].

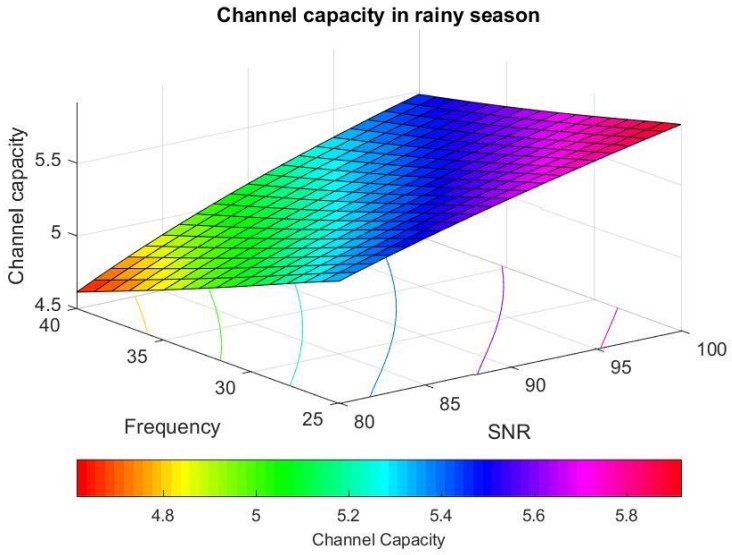


Fig.10. Channel Capacity in Rainy Season for 5G mmWave Wireless Communication System

$$\frac{C}{B} = \log 2(1+\frac{S}{N}) \tag{9}$$

The received signal-to-noise power ratio (S/N) in dB due to water vapor, oxygen, rain and fog are classified using machine learning (ML) for various seasons. Delhi summer season includes atmospheric attenuation due to atmospheric water vapor and oxygen. For this city rainy season includes atmospheric attenuation due to atmospheric water vapor, rain and oxygen. Further, in winter season fog play one of the role for attenuation and winter season includes atmospheric attenuation due to atmospheric water vapor, fog and oxygen.

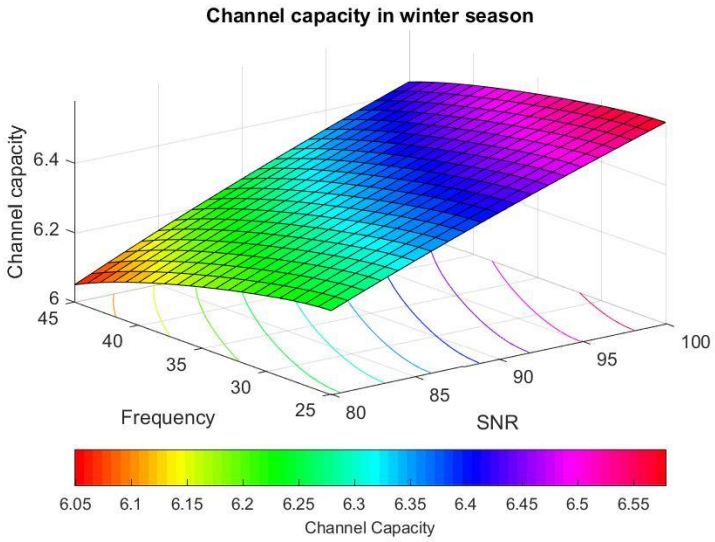


Fig.11. Channel Capacity in Winter Season for 5G mmWave Wireless Communication System

In Delhi; MMWave 5G MMWave communication system software defined channel capacity are shown for summer, rain and winter in Fig. (9), (10) and (11). These plots are shown with channel capacity as per atmosphere and shown for the frequencies 28GHz, 37 GHz and 39GHz. By using AI based software controlled transmitter and or receivers the channel capacity can be controlled intelligently.

6. Conclusions

This paper presented atmospheric attenuation calculation for various atmosphere attenuation causes for 5G millimeter wave propagation attenuation at the frequencies 28 GHz, 37 GHz and 39 GHz for Delhi (India) . It is shown in the paper that the atmospheric attenuation due to water vapor, oxygen, rain and fog varies and depends on the millimeter wave frequencies. This research also signifies the reason of the selection of the frequencies 28 GHz, 37 GHz and 39 GHz for 5G Millimeter Wave (mmWave) Communication System. These frequencies 28 GHz, 37 GHz and 39 GHz for 5G Millimeter Wave (mmWave) Communication System shows minimal attenuation.

Software Defined MMWave facilitates transmission power control in a real manner. 5G millimeter wave communication system transmitter and receivers can be controlled by the software defined mmwave communication system. Software Defined MMWave facilitates methods to control the transceiver as per atmospheric attenuation and demand and need of channel capacity in 5G millimeter wave communication system. Here intelligent an adaptive transmitter which is having machine learning (ML) based on previous trends of the attenuations decides the optimal channel capacity. Its intelligence is based on the various type of attenuations as per various conditions as described. The decision-directed adaptive receiver has the same structure as the gremlin receiver, but uses its own decisions. The adaptive ML based transmitter is useful to intelligently provide the required channel capacity.

This research paper is useful for transmission link budget for 5G Millimeter Wave (mmWave) Communication system for instant installation. Future work involves the identifying the various other dynamic atmospheric attenuation causes for the atmospheric attenuation for 5G Millimeter Wave (mmWave) Communication.

Acknowledgements

This paper is specifically meant for educational purpose for completing Ph.D. degree with Delhi Technological University (DTU), Delhi India. This paper is prepared for submission to under Ph.D. progress. The authors are very much thankful to Samsung Research Institute Noida, India and Delhi Technological University (DTU) earlier recognized as Delhi-College of Engineering (DCE), New Delhi, India.

References

[1] Ghosh, Amitabha. "Can mmwave wireless technology meet the future capacity crunch?." Presentation at IEEE ICC (2013).

[2] Bergren, Steven. "Design Considerations for a 5G Network Architecture." arXiv preprint arXiv:1705.02902 (2017).

[3] Agrawal, S. K., and Kapil Sharma. "5G millimeter wave (mmWave) communications." Computing for Sustainable Global Development (INDIACom), 2016 3rd International Conference on. IEEE, 2016.

[4] Sun, Shu, et al. "Investigation of prediction accuracy, sensitivity, and parameter stability of large-scale propagation path loss models for 5G wireless communications." IEEE Transactions on Vehicular Technology 65.5 (2016): 2843-2860.

[5] Agrawal, S. K., and Kapil Sharma. "5G Millimeter Wave (mmWave) Communication System with Software Defined Radio (SDR)." International Conference on Recent Trends in Engineering & Science (ICRTES-16), 29th-30th September. 2016.

[6] Zhouye Pi et al., "An Introduction to Millimeter- Wave Mobile Broadband Systems, " IEEE Communications Magazine, vol.49, no.6, pp.101- 107, Jun. 2011.

[7] Andrews J.G. et al., "What Will 5G Be?, " IEEE JSAC Special Issue On 5G Wireless Communication Systems, May 2014.

[8] Yang L-L, Hanzo L. Software-defined-radio-assisted adaptive broadband frequency hopping multicarrier DSCDMA. IEEE Commun Mag 2002;40(3):174–83.

[9] Scudder, II. J., Adaptive communication receivers. IEEE Trans. Inform. Theory, 1965, 2, 167-174

[10] X. Wang, X. Li, and V. C. M. Leung, "Artificial Intelligence-Based Techniques for Emerging Heterogeneous Network: State of the Arts, Opportunities, and Challenges," IEEE Access, vol. 3, 2015, pp. 1379–91.

[11] G. Huang, G.-B. Huang, S. Song, and K. You, ``Trends in extreme learning machines: A review," Neural Netw., vol. 61, pp. 32_48, Jan. 2015.

[12] Theodore S. Rappaport et al., "Millimeter Wave Mobile Communications for 5G Cellular: It Will Work!, " IEEE Access, vol.1, pp.335-349, May 2013.

[13] FCC, "Millimeter wave Propagation: Spectrum management Implications," office of Eng. and Tech., Bulletin no. 70, July, 1997.

[14] FCC "Report And Order And Further Notice Of Proposed Rulemaking" , FCC 16-89, July, 2016

[15] Evaluating Compliance with FCC Guidelines for Human Exposure to Radiofrequency Electromagnetic Fields, Federal Communication Commission, OET Bulletin 65, Edition 97-01.

[16] ITU Recommendation ITU-R RPN.618-4, 1996

[17] International Telecommunication Union, "Water Vapour: Surface Density and Total Columnar Content," Recommendation ITU-R P.836-3, Electronic Publication, Geneva, Switzerland, November 2001.

[18] Recommendation, "Attenuation by atmospheric gases," in ITU-R P.676-8, 10 2009.

[19] S. K. Agrawal and P. Garg, "Calculation of Channel Capacity Considering the Effect of Different Seasons for Higher Altitude Platform System", Wireless Personal Communications, Springer, Wireless Personal Communications: vol. pp-719-729, Issue 4 2010.

[20] S. K. Agrawal and P. Garg, "Calculation of the Channel Capacity in the Presence of Vegetation and Urban-site Environment for Higher Altitude Platform Communication System", to Wireless Personal Communications", IET Microwaves, Antenna & Propagation, IET Microw. Antennas Propag., Vol. 3, Iss. 4, pp. 703–713, 2009.

[21] Agrawal, S. K., and Kapil Sharma. " Software Defined Radio Based Channel Capacity In 5G Millimeter Wave Communication System" International Virtual Conference on Computer Science, Engineering and Technology (25th - 28th December, 2016), Indore - India.

[22] S. K. Agrawal and K. Sharma, "5G Millimeter Wave (mmWave) Communication System with Software Defined Radio (SDR)", International Journal for Innovative Research in Science & Technology, Volume 2, Issue 9, September 2016

[23] Dissanayake, A., Allnutt, J., & Haidara, F. (1997). A prediction model that combines rain attenuation and other propagation impairments along earth-satellite paths. In Proceedings of IEEE Transactions on Antenna and Propagation (Vol. 45, pp. 1546–1558), Oct. 1997.

[24] Blum, Avrim L., and Pat Langley. "Selection of relevant features and examples in machine learning." Artificial intelligence 97.1-2 (1997): 245-271.

[25] Kotsiantis, Sotiris B., I. Zaharakis, and P. Pintelas. "Supervised machine learning: A review of classification techniques." Emerging artificial intelligence applications in computer engineering 160 (2007): 3-24.

[26] J. Mitola. III, "Technical Challenges in the Globalization of Software Radio,'' IEEE Commun. Mag., Feb. 1999, pp. 84–89.

Authors' Profiles



Mr. S. K. Agrawal's educational and professional interest include 5G, Antenna, Beam, RF, Wireless communication, Networking, Channel Capacity, MIMO, Physical Layer, Machine Learning (ML), Artificial Intelligence (AI) and related technologies. He has published various research papers in international conferences and journals in the domain of wireless communications and intelligent solutions along with best paper award. He has invented several novel features which are protected as several national and international patents. He is member of TPCs (international conferences/ journal), Member of Indian Science Congress Association (ISCA), Member of International Computer Science and Engineering Society (ICSES), International Association of Engineers (IAENG), IAENG Society of Artificial Intelligence (AI) and etc.

S. K. Agrawal has reviewed various international research papers for conferences and journals in the domain of mobile communications. He is currently working for Research / Inventions / Patents in Samsung R&D, Noida India. He has extensive experience in research and intellectual property (IP) domain. Agrawal is currently pursuing Ph.D. in Artificial Intelligent (AI) wireless solutions from Delhi Technological University (DTU), formerly known as Delhi College of Engineering (DCE) Delhi. He is having Masters degree in Signal processing (SP) from Netaji Subhas Institute of Technology (Formerly: Delhi Institute of Technology), University of Delhi, India. He has worked as a researcher at Telecommunications Research Centre (TRC), University of Limerick (UL) Ireland and Indian Institute of Technology (IIT) Delhi. He has also worked with Computer Patent Annuities (CPA) Global, National Atmospheric Research Laboratory (NARL), Department of Space, (Govt. of India) India and ASC Zee Networks, DTH R&D India.



Dr. Kapil Sharma was born in Haryana, India. In 2011,he has completed Doctors Degree in Computer Science and Engineering under the Faculty of Engineering and Technology at the M. D. University, Rohtak (Haryana), India. He has obtained his Bachelor of Engineering and Master of Technology Degrees in Computer Science & Engineering and Information Technology from M. D. University, Rohtak and IASE, Rajasthan, India in 2000 and 2005 respectively. He has published various research papers in international conferences and journals in the domain of mobile communications along with several national and international patents.

He is head of department of IT department and also Associate Professor in Department of Computer Engineering; Delhi Technological University. He previously worked as Assistant Professor with School of Information Communication & Technology; Department of Computer Science & Engineering; Greater Noida, Gautam Budh Nagar and as Reader and Head with Department of Information Technology; Guru Premsukh Memorial College of Engineering 245, Budhpur Villege, G.T Karnal Road; Delhi.

How to cite this paper: S. K. Agrawal, Kapil Sharma," Intelligent Software Defined Atmospheric Effect Processing for 5th Generation (5G) Millimeter Wave (MMWave) Communication System", International Journal of Wireless and Microwave Technologies(IJWMT), Vol.8, No.2, pp. 15-26, 2018.DOI: 10.5815/ijwmt.2018.02.02

RESEARCHERID
THOMSON REUTERS

[Tripathi, 8(4): October-December 2018]

ISSN 2277 – 5528
Impact Factor- 5.085

INTERNATIONAL JOURNAL OF ENGINEERING SCIENCES &MANAGEMENT

OPPORTUNITIES AND CHALLENGES OF USING HYBRID VEHICLES IN INDIA

Akshit Tripathi[*1] & Dr J.P. Kesari[2]

[*1]B.Tech passed out 2018, Department of Mechanical Engineering, Delhi Technological University (Formerly DCE), Bawana Road, New Delhi-110042

[2]Associate Professor, Department of Mechanical Engineering, Delhi Technological University (Formerly DCE), Bawana Road, New Delhi-110042

ABSTRACT

A hybrid electric vehicle (HEV) is a sort of vehicle which joins a customary internal combustion engine (ICE) impetus framework with an electric drive framework. The nearness of the electric power train is proposed to accomplish either preferable mileage over a traditional vehicle, or better execution. An assortment of kinds of HEV exists, and how much they work as EVs shifts also. Current HEVs make utilization of proficiency enhancing innovations. A few assortments of HEVs utilize their internal combustion engine to produce power by turning an electrical generator (this blend is known as an engine generator), to either revive their batteries or to specifically control the electric drive engines. Numerous HEVs lessen sit emanations by closing down the ICE out of gear and restarting it when required; this is known as a begin stop framework. In this paper, the various types of vitality sources are said and disclosed how they're used to control a vehicle or should be possible later on.

Keywords *Steering mountins . brackets , Casting*

I. INTRODUCTION

Energy crisis and cost consideration

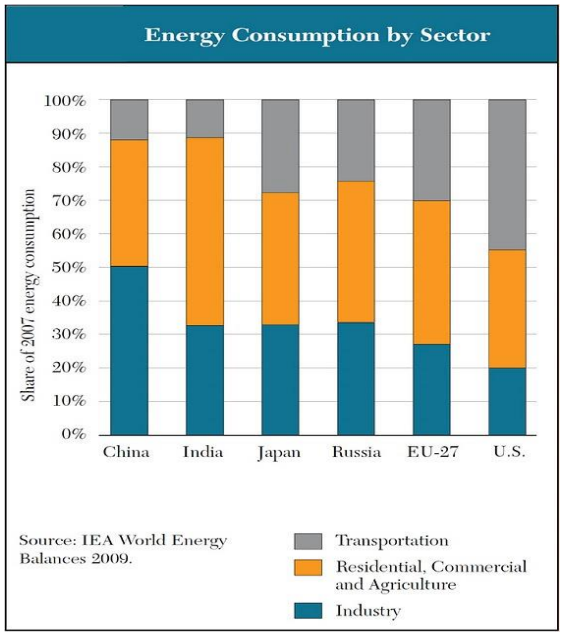
As we rely on coal, oil and gas (the fossil fuels) for over 70% of our current energy needs, there exists a concern to conserve these resources. On top of this energy demand is expected to grow by almost half over the next two decades. In light of this it is causing some dread that our vitality assets are beginning to run out, with crushing results for the worldwide economy and personal satisfaction which could without a doubt be awful to the general population. Energy crisis is the result of using excessive non renewable resources and use of limited renewable resources. Attributable to unreasonable reliance on non-renewable energy sources notwithstanding for the following two decades, petroleum derivatives are subjected to consumption which is presently a noteworthy worry for the forthcoming age.

The whole globe today is currently centering to move their aggregate power age to inexhaustible power as it is inferable from usage of spotless, substitute and reusable vitality sources. “Denmark has just produced 140% of its electricity needs with renewable wind power and The Scottish Government aims to generate 50% of Scotland’s electrical power from renewable energy by 2015, and 100% by 2020” as stated by The United States Energy Information Administration (EIA) which provides a hope for improvement in India. The population of India is rapidly increasing day by day and over 80,000 villages in the country are not electrified. Vitality security keeps on being one of the greatest difficulties in India. The greater part of the introduced limits in India are controlled by the coal based power age which is related with nearby and worldwide natural contamination with resultant effect on air, water, land and biodiversity. Consequently it opens the entryway for an immense venture on the use of the inexhaustible assets. Because of the huge significance of vitality preservation, there is a need to center around mechanical alternatives for enhancing vitality productivity in numerous segments, for example, the modern, control age and business structures.

Non Conventional to Conventional Transition

As India remains very nearly a noteworthy change, conveying new work chances to its 1.3 billion individuals, satisfactory vitality supply will assume a major part. A nation that is uncommonly rich in bio-assorted variety, with types of uncommon greenery is undermined today by finished misuse of assets. "An examination has featured that in Delhi, 96 for every penny of the day's contamination levels surpass the national guidelines". Bengaluru, Mumbai, Pune, Kolkata and Hyderabad are excessively are battling with poor air quality on most days with contamination levels transcending allowable cutoff points – 72 for every penny, 33 for each penny, 57 for each penny and 45 for every penny, individually. Considerably littler urban areas like Kanpur, Haridwar, Agra, Surat and Varanasi are contaminating step by step and the circumstance is deteriorating with every day passing. Along these lines, it's not just the activity to tackle the option or sustainable assets for control age however to control this condition as well.

In India, not long ago the CNG driven vehicles were exempted from the odd-even govern in Delhi and Supreme court requested to boycott all the oil or diesel vehicles presently running. In this way it was a noteworthy advance in controlling the disturbing state in the capital. India will confront generous increment in vitality request in the following couple of years, with expanded industrialization and higher interest for power. Power is basic in managing monetary exercises and producing work openings. The Government needs to reassess how India delivers and devours vitality and together with partners work towards a lower-carbon future. Therefore it requires the presentation of the Hybrid Vehicles which can demonstrate compelling by giving less destructive outflows and better fuel proficiency sooner rather than later.



II. REVIEW OF LITERATURE

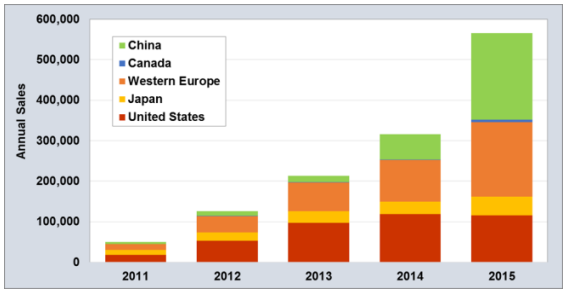
2.1 Hybrid Vehicles in the World

Because of the vast acknowledgment of electric vehicles, numerous automakers are beginning to investigate this market with unmistakable fascination, as these vehicles are giving clean outflows and better fuel effectiveness around the world.

"The world's top of the line battery electric and module half breed vehicles incorporate Tesla's Model S, Nissan's Leaf and Toyota's Prius Plug-in Hybrid. California-based Tesla Motors was among the main carmakers to collect electric vehicles only. In July 2014, Tesla and Panasonic made ready for the development and activity of the world's

biggest battery processing plant in the United States. In the principal quarter of 2017, Tesla conveyed around 25,000 vehicles around the world, which later turned out to be super hit.

China is positioned as the biggest market for every single electric vehicle. The developing interest for electric autos in business sectors, for example, China, the United States and Norway is frequently empowered by government motivating forces including sponsorships, exceptions from tolls and stopping expenses" as specified by statista.



2.2 Development in India

In August 2017, the Minister of State for Power and Renewable Energy, Piyush Goyal demonstrated that the Niti Aayog was planning with different government services to make an arrangement to guarantee that lone electric vehicles are at a bargain in the nation by 2030. Over the span of his announcements, the clergyman likewise showed that hybrid vehicles were a superfluous redirection on the grounds that while they decrease fuel utilization, the advantages are peripheral and the innovation is dated. Despite the fact that the 2030 date was along these lines pulled back, it appears that the Indian government is awakening to the potential advantages of electric vehicles. Indeed, even the financial aspects are noteworthy – changing to an electric armada would likewise enable India to lessen its reliance upon oil imports, and spare the nation a brain boggling $330 billion by not obtaining 876 million metric huge amounts of oil. Nonetheless, regardless of these numbers, the market has been ease back to embrace electric vehicles. A report by showcase knowledge firm BIS Research demonstrates that the moderate rate of appropriation is an aftereffect of the cost of possession being at a 45 percent premium over regular cars. The report additionally recognizes absence of framework, government support, and motivations as being boundaries to the offer of more electric vehicles in a market that it distinguishes as to a great degree promising.

2.3 Challenges and the opportunities

There are certain signs for the electric vehicle division in India. The previously mentioned articulation from the pastor of state demonstrates that the administration is currently working towards empowering the reception of electric vehicles in the Indian market. In 2015, the legislature had propelled a plan named Faster Adoption and Manufacturing of (Hybrid and) Electric Vehicles (FAME) under the National Electric Mobility Mission (NEMM) to advance the offers of fuel-productive autos. Under this plan, the legislature is wanting to dole out concede up to $16 million to urban communities with a populace of in excess of a million, for acquiring electric vehicles in FY 2018. Producers, for example, Hyundai, Mahindra and Mahindra, Nissan, Maruti, Toyota and Tata are starting to demonstrate an enthusiasm for the market, and a large number of electric vehicle models – 25, as indicated by the BIS Research report – are probably going to be propelled by them by 2021. Be that as it may, for the area to achieve a minimum amount and start supplanting the 230 million vehicles on Indian streets, the Indian government must make more solid strides.

It can take a gander at governments in the APAC locale, chiefly China, Japan and South Korea, for motivation. The improvement of electric vehicles in these business sectors has earned enormous consideration. This is because of the aggregate exertion of governments and makers to start changes that advance the offer of these vehicles and make them more prudent to utilize. Their endeavors have prompted the division demonstrating a maintained increment in showcase volume, and the monetary markers appear to point to a time of touchy development. As indicated by the BIS Research report, the area will demonstrate an anticipated CAGR of 29.5 percent in the vicinity of 2016 and

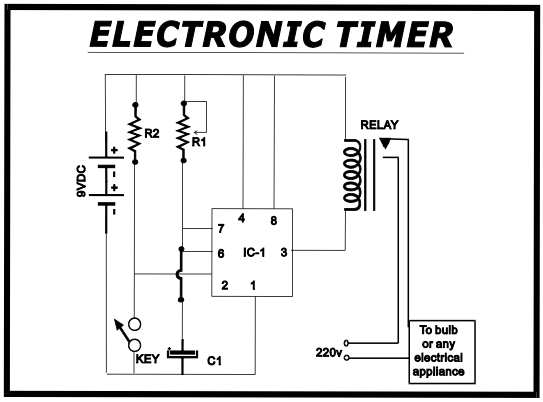
2026. Trend-setters, business people, and controllers must cooperate to develop new plans of action for effective selection. There should streamline of hardware, a more brilliant circulation of monetary motivations, and a deliberate push to build up a powerful foundation around electric vehicles. Once these components are set up, the market can move to decrease the cost of electric vehicle possession and help achieve a change in outlook in how individuals in India see and utilize transportation.

III. PROJECT DESCRIPTION

Materials Used

Resistors(100K variable resistance), Capacitors,9V DC Battery, DC motor, Solar Panel, semiconductors, LED, Shock absorbers, sound and wind system.

Circuit Diagram

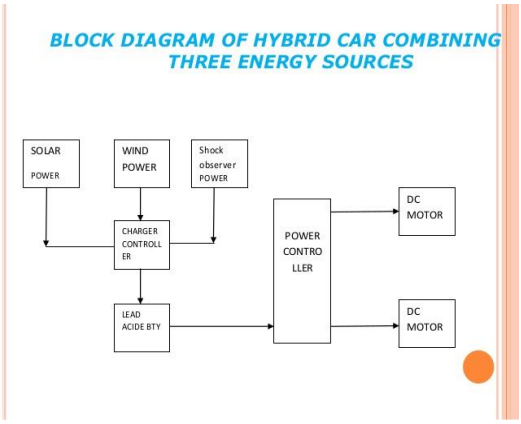


How it works?

An ordinary car safeguard hoses suspension development to create a controlled activity that keeps the tire solidly out and about. This is finished by changing over the dynamic vitality into warm vitality, which is then consumed by the stun's oil. The Power-Generating Shock Absorber (PGSA) changes over this motor vitality into power rather than warm using a Linear Motion Electromagnetic System (LMES). The LMES utilizes a thick perpetual magnet stack installed in the primary cylinder, a switchable arrangement of stator loop windings, a rectifier, and an electronic control framework to deal with the shifting electrical yield and hosing load. The base shaft of the PGSA mounts to the moving suspension part and powers the magnet stack to respond inside the annular cluster of stator windings, creating substituting current power. That power is then changed over into coordinate current through a full-wave rectifier and put away in the vehicle's batteries. The power created by each PGSA would then be able to be joined with power from other power age frameworks (solar, wind and noise) and put away in the vehicle's batteries.

The circuit involves the inverter unit. The 6V DC of the battery is changed over into AC by control transistor T-1 (NPN). The yield of the transistor is sustained to the inverter transformer. Capacitor and Resistor arrange utilized for swaying. Accordingly, inverter transformer (here utilized 6-0-6 transformer) ventures up 6v DC to 160V AC, which is adequate for working a tube light. In the circuit every one of the segments ought to be mounted on PCB with the exception of X-1 stage down transformer. It is utilized to charge the battery and turn off transistor T-1 by applying reverse predisposition to its base when 230V AC mains supply is accessible. Diode D-2 and D-4 gives negative supply to the base of T-1 to make it turn around one-sided. Capacitor C-2 smooths this negative supply. At the point when the supply comes up short, T-1 leads through LC organize. The biasing voltage can be differing by R-3. The yield from its authority is nourished to the essential of inverter transformer. The progression up yield is accessible at auxiliary of is transformer to gleam the tube light.

ISSN 2277 – 5528
Impact Factor- 5.085



IV. SCOPE FOR FUTURE EXPERIMENT ACTION

Since oil is restricted and will some time or another come up short on supply. In the self-assertive year 2037, an expected one billion oil energized vehicles will be on the world's streets. Fuel will turn out to be restrictively costly. The world needs answers for the "400 million generally futile autos". So year 2037 "gas runs out year" implies, oil will never again be utilized for individual portability. A market may create for sunlight based fueled EVs of the extent of a bike or golf truck. Since mixture innovation applies to overwhelming vehicles, crossover transports and half breed trains will be huger. Producers of hybrid cars are endeavoring anticipating expanding the proficiency of hybrid motors, ideally having the capacity to drive these vehicles up to 70 miles to the gallon. General Motors is as of now hoping to build up their new half and half to that 70 mile stamp in 2010, and might have the capacity to push that number even higher. If hybrids can utilize Lith-Ion batteries, at that point cars can quicken speedier to higher rates, be considerably more productive, and would have the capacity to extend the separation between fill-ups. Not exclusively would those points of interest be accessible, new hybrids would be considerably more reasonable to buyers, and ideally would tackle a great deal of issues. Particularly since, the way things are, the greater part of the battery packs utilized as a part of current mixtures could be substantially more proficient than they are. Hybrid cars are now amazingly proficient; however there is dependably opportunity to get better. 90% of the hybrid cars available today could without much of a stretch be more proficient, albeit, Zero Emissions won't be conceivable, seeing as how cross breeds still require gas So, despite the fact that the mixture you need may not be accessible yet, there is trust regardless. For whatever length of time that purchasers will purchase hybrids now, these advances will be more reasonable, and soon you could be making the most of your own one of a kind Volkswagen Beetle Hybrid with near zero emanations and a lot of space for that strolling stick you simply needed to carry outdoors with you.

V. RESULTS AND CONCLUSION

Hybrid cars are unquestionably more ecologically agreeable than inward ignition vehicles. Batteries are being designed to have a long life. At the point when the hybrid vehicles turned out to be more across the board, battery reusing will turn out to be monetarily conceivable. Examination into other vitality sources, for example, power modules and inexhaustible fills make the future look more splendid for hybrid vehicles.

Based on the research, the following conclusions can be drawn:-

5.1 Lithium-particle battery innovation has been growing quickly, particularly at the cell level, yet costs are still high, and the potential for sensational decreases seems restricted. Amassed battery packs right now cost about Rs72,250 to Rs1,10,500 per kWh of usable vitality (Rs40,625 to Rs55,250/kWh of nameplate vitality). A PHEV-10 will require about 2.0 kWh and a HEV around 8 kWh even after the batteries have experienced expected corruption over the long run. Expenses are relied upon to decay by around 35 percent by 2020 yet more gradually from there on. Projections of future battery pack costs are dubious, as they rely

upon the rate of enhancements in battery innovation and assembling strategies, potential achievements in new innovation, conceivable unwinding of battery assurance parameters as experience is picked up, and the level of generation, among different components. Additionally investigate is expected to lessen costs and accomplish leaps forward in battery innovation.Costs to a vehicle maker for a HEV worked in 2030 are

5.2 probably going to be about Rs9,10,000 to Rs11,70,000 in excess of an equal customary vehicle, including a Rs6,00,000 to Rs9,10,000 battery pack. The incremental expense of a HEV would be about Rs3,00,500 to Rs3,90,300, including a Rs1,20,500 to $1,80,300 battery pack. Likewise, a few homes will require electrical framework overhauls, which may cost more than Rs60,000. In examination, the incremental expense of a HEV may be Rs18,000.

5.3 HEV are probably not going to accomplish cost-adequacy before 2040 at fuel costs underneath Rs240.00 per gallon, however PHEV-10s may arrive before 2030. PHEVs will recover a portion of their incremental expense, on the grounds that a mile driven on power will be less expensive than a mile on gas, yet it is probably going to be quite a few years previously lifetime fuel investment funds begin to adjust the higher originally cost of the vehicles. Endowments of tens to many billions of dollars will be required for the change to cost-viability. Higher oil costs or quick decreases in battery expenses could diminish the time and appropriations required to achieve cost-adequacy.

5.4 At the most extreme Commonsense rate, upwards of 40 million HEVs could be out and about by 2030, yet different variables (e.g., high expenses of batteries, unassuming fuel reserve funds, restricted accessibility of spots to connect, rivalry from different vehicles, and purchaser protection from connecting for all intents and purposes each day) are probably going to keep the number lower. The Greatest Down to earth rate relies upon quick mechanical advancement, expanded government support, and shopper acknowledgment. A more practical entrance rate would result in 13 million HEVs by 2030 out of around 300 million vehicles out and about, which still expect that current levels of government support will proceed for quite a few years.

5.5 HEVs will have little effect on oil utilization before 2030 on the grounds that there won't be sufficient of them in the armada. More generous decreases could be accomplished by 2050. PHEV-10s will lessen oil utilization just marginally more than can be accomplished by HEVs. A PHEV-10 is relied upon to use around 20 percent less fuel than an identical HEV, sparing around 70 gallons in 15,000 miles. Forty million PHEV-10s would spare a sum of about 0.2 million barrels of oil for every day. The current light-obligation vehicle armada utilizes around 9 million barrels for each day. PHEV-40s will expend around 55 percent less gas than proportional HEVs, sparing in excess of 200 gallons of gas for every year per vehicle.

5.6 HEVs will discharge less carbon dioxide than non-half breed vehicles, yet spare minimal with respect to HEVs subsequent to representing emanations at the producing stations that supply the electric power.

No significant issues are probably going to be experienced for quite a few years in providing the ability to charge HEVs, as long as most vehicles are charged around evening time. Age and transmission of power amid off-crest hours ought to be sufficient for a huge number of HEVs, albeit a few conveyance circuits may require updating on the off chance that they are to serve groups of HEVs. Urging HEV proprietors to charge their vehicles amid off-top hours will require both rate plans that remunerate time-proper charging and hardware that can screen—or even control—time of utilization. A portfolio way to deal with research, improvement, exhibition, and, maybe, showcase change bolster is fundamental. It isn't clear what innovation or mix of advancements—batteries, hydrogen, or biofuels—will be best in decreasing the country's oil reliance to levels that might be vital over the long haul. It is clear, in any case, that a portfolio approach will empower the best decrease in oil utilize. Expanding the proficiency of ordinary vehicles (counting HEVs) past the current administrative system could diminish gas utilization by around 40 percent in 2050, contrasted with the Reference Case. Including biofuels would decrease it another 20 percent. On the off chance that HEVs are likewise included at the Greatest Reasonable rate, gas utilization would be lessened an extra 7 percent, while HEVs could decrease utilization by 23 percent.

REFERENCES

1. *Schmidt, R. (2008, May). Information technology energy usage and our planet. In Thermal and Thermomechanical Phenomena in Electronic Systems, 2008. ITHERM 2008. 11th Intersociety Conference on (pp. 1255-1275). IEEE.*
2. *Information available at : Sources of greenhouse gas emissions (http://www.epa.gov/climatechange/ghgemissions/sources/transportation.html)*
3. *Transport energy and CO2: Moving toward sustainability, 2009 International energy agency publications*
4. *Olivier JGJ, Berdowski JJM (2001) in The Climate System, eds Berdowski J, Guicherit R, Heij BJ (Balkema/Swets & Zeitlinger, Lisse, The Netherlands), pp 33–78.*
5. *Ismet Ugursal, V. "Energy consumption, associated questions and some answers." Applied Energy (2013).*
6. *Lukic SM, Emadi A. 'Effects of drivetrain hybridization on fuel economy and dynamic performance of parallel hybrid electric vehicles." Vehicular Tech- nology, IEEE Transactions on 2004; 53(2):385–9.*
7. *Ahmad Pesaran, Jeff Gonder Keyser, M., Ultracapacitor applications and evaluation for hybrid electrcic vehicles, In: 7th annual advanced capacitor world summit conference, National Renewable Energy Laboratory (NREL): Hotel Torrey Pines La Jolla, CA; 2009.*
8. *International Energy Outlook 2014, US Energy Information Administration online publication.*
9. *Budget of the United States Government Fiscal Year 2008, DC, US Office of Management and Budget, 2008, Washington, February*
10. *Tie, S. F., & Tan, C. W. (2013). A review of energy sources and energy management system in electric vehicles. Renewable and Sustainable Energy Reviews, 20, 82-102.*
11. *Xin, L Williamson., SS. Assessment of efficiency improvement techniques for future power electronics intensive hybrid electric vehicle drive trains, In: Electrical power conference, EPC 2007. IEEE Canada. 2007.; 2007.*
12. *Emadi A, Young Joo L, Rajashekara K. Power Electronics and motor drives in electric, hybrid electric, and plug-In hybrid electric vehicles. Industrial Electronics, IEEE Transactions on 2008;55(6):2237–45.*
13. *Chan CC. The state of the art of electric, hybrid, and fuel cell vehicles. Proceedings of the IEEE 2007; 95(4):704–18.*
14. *Momoh, OD and Omoigui., MO. An overview of hybrid electric vehicle technology, In: Vehicle Power and Propulsion Conference, 2009. VPPC '09. IEEE;. 2009.*
15. *Energy Use in Cars 4: Regenerative braking systems.2010; Available from: /http://c21.phas.ubc.ca/article/energy-use-cars-4-regenerative-braking-systems#footnoteref1_w7bmpniS.*
16. *Bin Wang RGW, Cai Qun Ying, Sun Han Wen. Experimental research on regenerative braking of wheel-hub motor. Advanced materials research. Manufacturing Science and Technology 2012:1879–83.*
17. *Valente S, Ferreira H. Braking energy regeneration using hydraulic systems. Portugal: Polytechnic Institute of Porto (IPP); 2008 p. 8.*
18. *MAZDA Global Site. 2011[cited 5 December 2011]; Available from: /http://www.mazda.com/*
19. *Anup Bandivadekar, K.B., Lynette Cheah, Christopher Evans, Tiffany Groode, John Heywood, Emmanuel Kasseris, Matthew Kromer, Malcolm Weiss ,On the road in 2035: reducing transportation's petroleum consumption and GHG emissions, , Massachusetts Institute of Technology; 2008.*
20. *Baglione ML. Development of system analysis methodologies and tools for modeling and optimizing vehicle system efficiency, In: Mechanical engineering. Michigan: University of Michigan; 2007 p. 207.*
21. *Jiang Hong DWZ, Wang Guang Pin, Sui Ni. Simulation of a regenerative braking system producing controlled braking force. Advanced materials research. Manufacturing Science and Technology 2011:5729–37.*

22. *Chan CC, Chau KT. An overview of power electronics in electric vehicles. Industrial Electronics, IEEE Transactions on 1997; 44(1):3–13.*
23. *Stabler, F., Automotive thermoelectric generator design issues, In: DOE thermoelectric applications workshop, Future Tech LLC,; 2009.*
24. *Fleurial J-P. Design and discovery of highly efficient thermoelectric materials. National Aeronautics and Space Administration; 1993.*
25. *Crane, DT. Progress towards maximizing the performance of a thermo- electric power generator, In: Proceeding of the 25th International Conference on Thermoelectrics, Vienna, Austria: BSST LLC; 2006.*
26. *Graham, R. (2001). Comparing the benefits and impacts of hybrid electric vehicle options. Electric Power Research Institute (EPRI), Palo Alto, CA, Report, 1000349.*
27. *California Air Resources Board, "California Exhaust Emission Standards and Test Procedures for 2005 and Subsequent Model Zero-Emission Vehicles, and 2002 and Subsequent Model Hybrid Electric Vehicles, in the Passenger Car, Light-Duty Truck and Medium-Duty Vehicle Classes," California EPA, 2003.*
28. *Kubik, M. (2006). Consumer views on transportation and energy. National Renewable Energy Laboratory.*

Journal of Physics: Conference Series

PAPER • **OPEN ACCESS**

Machine Learning from Theory to Algorithms: An Overview

To cite this article: Jafar Alzubi *et al* 2018 *J. Phys.: Conf. Ser.* **1142** 012012

View the article online for updates and enhancements.



IOP ebooks™

Bringing you innovative digital publishing with leading voices to create your essential collection of books in STEM research.

Start exploring the collection - download the first chapter of every title for free.

This content was downloaded from IP address 14.139.251.107 on 07/12/2018 at 05:58

Machine Learning from Theory to Algorithms: An Overview

Jafar Alzubi[1], Anand Nayyar[2], Akshi Kumar[3]

[1]School of Engineering, Al-Balqa Applied University, Jordan

[2]Graduate School, Duy Tan University, Da Nang, Viet Nam

[3]Department of CSE, Delhi Technological University, Delhi, India

j.zubi@bau.edu.jo, anandnayyar@duytan.edu.vn, akshikumar@dce.ac.in

Abstract. The current SMAC (Social, Mobile, Analytic, Cloud) technology trend paves the way to a future in which intelligent machines, networked processes and big data are brought together. This virtual world has generated vast amount of data which is accelerating the adoption of machine learning solutions& practices. Machine Learning enables computers to imitate and adapt human-like behaviour. Using machine learning, each interaction, each action performed, becomes something the system can learn and use as experience for the next time. This work is an overview of this data analytics method which enables computers to learn and do what comes naturally to humans, i.e. learn from experience. It includes the preliminaries of machine learning, the definition, nomenclature and applications' describing it's what, how and why. The technology roadmap of machine learning is discussed to understand and verify its potential as a market & industry practice. The primary intent of this work is to give insight into why machine learning is the future.

Keywords: Machine Learning, Supervised Learning, Unsupervised Learning, Algorithms, Instant Learning, Ensemble Learning

1. Introduction

Learning as a generic process is about acquiring new, or modifying existing, behaviors, values, knowledge, skills, or preferences. Behaviorism, Cognitivism, Constructivism, Experientialism and Social Learning define the theory of personal learning, i.e. how humans learn. Machines rely on data contrary to what comes naturally to humans: learning from experience. At the very fundamental level machine learning (ML) is a category of artificial intelligence that enables computers to think and learn on their own. It is all about making computers modify their actions in order to improve the actions to attain more accuracy, where accuracy is measured in terms of the number of times times the chosen actions results into correct ones.

Researchers have formally defined ML across pertinent literature. The term was coined by Arthur Samuel in 1959, who defined ML as a field of study that provides learning capability to computers without being explicitly programmed [1].More recently, Tom Mitchell gave a "well-posed" definition that has proven more useful to engineering set-up: "A computer program is said to learn from experience E with respect to some task T and some performance measure P, if its performance on T, as measured by P, improves with experience E [2]"

Content from this work may be used under the terms of the Creative Commons Attribution 3.0 licence. Any further distribution of this work must maintain attribution to the author(s) and the title of the work, journal citation and DOI.
Published under licence by IOP Publishing Ltd

Machine learning is a multi-disciplinary field having a wide-range of research domains reinforcing its existence. These are as shown in the following figure 1.

The simulation of ML models is significantly related to Computational Statistics whose main aim is to focus on making predictions via computers. It is also co-related to Mathematical Optimization which relates models, applications and frameworks to the field of statistics.

Real world problems have high complexity which make them excellent candidates for application of ML. Machine learning can be applied to various areas of computing to design and program explicit algorithms with high performance output, for example, email spam filtering, fraud detection on social network, online stock trading, face & shape detection, medical diagnosis, traffic prediction, character recognition and product recommendation amongst others. The self-driving Google cars, Netflix showcasing the movies and shows a person might like, online recommendation engines—like friend suggestions on Facebook, "more items to consider" and "get yourself a little something" on Amazon, and credit card fraud detection, are all real-world examples of application of machine learning.

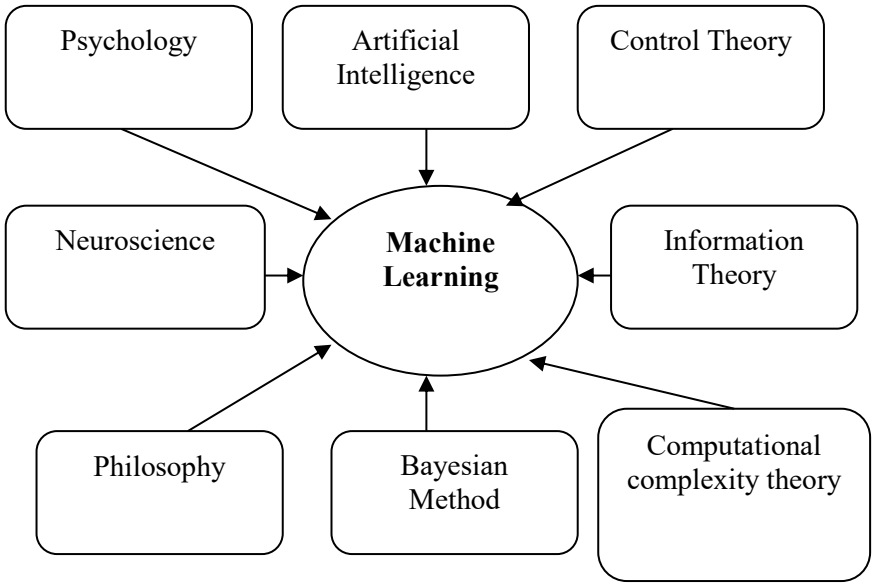


Fig.1. The Multi-disciplinary ML

The main objective of this work is to give an overview of development of Machine Learning to the present day, various machine learning algorithms, applications and challenges.

This paper presents an overview of machine learning, its origin and development through the decades to the present age. The study is organized as follows: Section 2 explains the problems in data science for which ML approaches offer a solution. Section 3 gives the evolution of ML to the present day. Section 4 describes the generic model of machine learning followed by the explanation of the machine learning process in section 5. Section 6 and 7 explain the various machine learning paradigms and algorithms respectively while section 8 presents a brief summary of the challenges faced by ML and its future scope as a discussion followed by conclusion of the study in section 9.

2. Data Science problems and Machine Learning

Machine learning is required to make the computers sophisticatedly perform the task without any intervention of human beings on the basis of learning and constantly increasing experience to understand the problem complexity and need for adaptability.

- *Tasks performed by Human Beings:* There are lots of tasks performed on day to day basis by human beings, but the main concern is that to perform the tasks perfectly and to perform under well-defined program. Examples: Cooking, Driving, Speech Recognition.
- *Tasks beyond Human Capabilities:* Another category of tasks includes which can be done by machine learning in effective manner is analysis of large and complex data sets like Remote Sensing, Weather forecasting, Ecommerce, Web search etc. With large amounts of data, it becomes really complex for human beings to predict meaningful data.

Machine learning has proven capabilities to inherently solve the problems of data science. Hayashi and Chikio [3] define data science as, "a concept to unify statistics, data analysis, machine learning and their related methods in order to understand and analyze actual phenomena" with data". Before taking to problem solving, the problem must be categorized suitably so that the most appropriate machine learning algorithm can be applied to it. Any problem in data science can be grouped in one of the following five categories as shown in Figure 2.

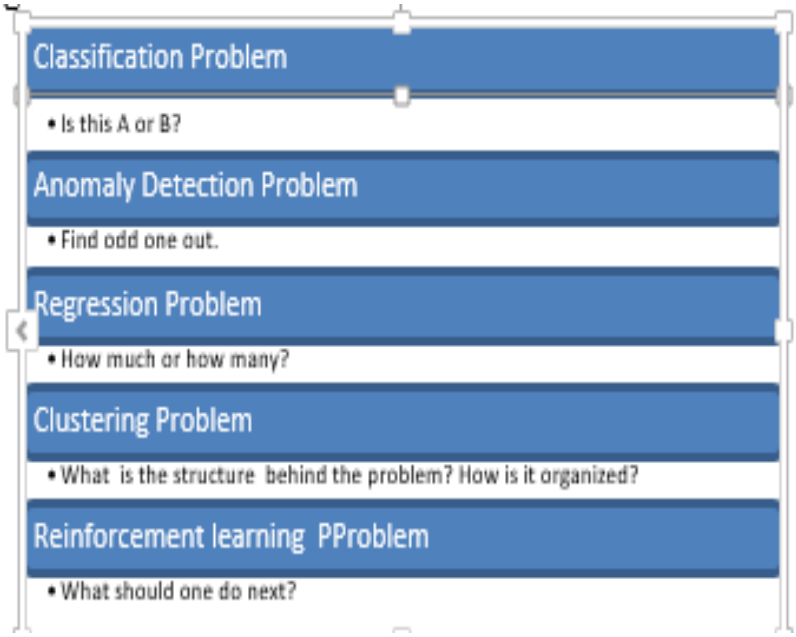


Fig 2. Types of Problems

Thus depending on the type of problem, an appropriate machine learning approach can be applied. The various categories are explained below:

- *Classification Problem*- A problem in which the output can be only one of a fixed number of output classes known apriori like Yes/No, True/False, is called a classification problem. Depending on the number of output classes, the problem can be a binary or multi-class classification problem.
- *Anomaly Detection Problem*- Problems which analyze a certain pattern and detects changes or anomalies in the pattern fall under this category. For example, credit card companies use anomaly detection algorithms to find deviation from the usual transaction behavior of their client and raises alerts whenever there is an unusual transaction. Such problems deal with finding out the outliers.

- *Regression Problem*- Regression algorithms are used to deal with problems with continuous and numeric output. These are usually used for problems that deal with questions like, 'how much' or 'how many'.
- *Clustering Problem*- Clustering falls under the category of unsupervised learning algorithms. These algorithms try to learn structures within the data and attempt to make clusters based on the similarity in the structure of data. The different classes or clusters are then labeled. The algorithm, when trained, puts new unseen data in one of the clusters.
- *Reinforcement Problem*-Reinforcement algorithms are used when a decision is to be made based on past experiences of learning. The machine agent learns the behaviour using trial and error sort of interaction with the continuously changing environment. It provides a way to program agents using the concept of rewards and penalties without specifying how the task is to be accomplished. Game playing programs and programs for temperature control are some popular examples using reinforcement learning.

3. Development of Machine Learning

The words, Artificial Intelligence and Machine Learning are not new. They have been researched, utilized, applied and re-invented by computer scientists, engineers, researchers, students and industry professionals for more than 60 years. The mathematical foundation of machine learning lies in algebra, statistics, and probability. Serious development of Machine Learning and Artificial Intelligence began in 1950's and 1960's with the contributions of researchers like Alan Turing, John McCarthy, Arthur Samuels, Alan Newell and Frank Rosenblatt. Samuel proposed the first working machine learning model on Optimizing Checkers Program. Rosenblatt created Perceptron, a popular machine learning algorithm based on biological neurons which laid the foundation of Artificial Neural Network [4, 5, 6]. The following table 1 depicts the illustrious, expansive and practical development of machine learning.

Table 1. Development of ML

1950	Alan Turning created "Turning Test" to check a machine's intelligence. In order to pass the Turning Test, the machine should be able to convince humans that there they are actually talking to a human and not a machine.
1952	Samuel created a highly capable learning algorithm than can play the game of Checkers with itself and get self-trained.
1956	Martin Minsky and John McCarty with Claude Shannon and Nathan Rochester organized a conference in Dartmouth in 1956 where actually Artificial Intelligence was born.
1958	Frank Rosenblatt created Perceptron, which laid the foundation stone for the development of Artificial Neural Network (ANN).
1967	The Nearest Neighbor Algorithm was proposed which could be used for "Pattern Recognition".
1979	Stanford University students developed "Stanford Cart", a sophisticated robot that could navigate around a room and avoid obstacles in its path.
1981	Explanation Based Learning (EBL) was proposed by Gerald Dejong, whereby, a computer can analyze the training data and create rules for discarding useless data [7]
1985	NetTalk was invented by Terry Sejnowski, [8] which learnt to pronounce English words in the same manner that children learn.
1990s	The focus of Machine Learning shifted from Knowledge-driven to Data Driven. Machine Learning was implemented to analyze large chunks of data and derive conclusions from it [9]
1997:	IBM invented the Deep Blue computer which was able to beat World Chess Champion Gary Kasparov.
2006	The term "Deep Learning" was coined by Geoffery Hinton which referred to a new architecture of neural networks that used multiple layers of neurons for learning.
2011	IBM's Watson, built to answer questions posed in a natural language, defeats a Human Competitor at Jeopardy Game.
2012	Jeff Dean from Google, developed GoogleBrain, which isa Deep Neural Network to detect patterns in Videos and Images.
2014	Facebook invented the "DeepFace" algorithm based on Deep Neural Networks capable of

	recognizing human faces in photos.
2015	Amazon proposed its own Machine Learning Platform. Microsoft created "Distributed Machine Learning Toolkit" for efficient distribution of machine learning problems to multiple computers to work parallel to find a solution [10,11]. Elon Musk and Sam Altman, created a non-profit organization- OoeaAI, with the objective of using Artificial Intelligence to serve human beings.
2016	Google proposed DeepMind which is regarded as the most complex Board Game. Google AlphaGo program becomes the first Computer Go program to beat a professional human player. It is based on the combination of machine learning and tree searching techniques [12].
2017	Google proposed Google Lens, Google Clicks, Google Home Mini and Google Nexus based phones which use Machine Learning and Deep Learning Algorithms. Nvidia proposed NVIDIA GPUs- The Engine of Deep Learning. Apple proposed Home Pod which is a Machine Learning Interactive device.

4. The Generic Model of ML

ML is used to solve various problems that require learning on the part of the machine. A learning problem has three features:

- Task classes (The task to be learnt)
- Performance measure to be improved
- The process of gaining experience

For example, in a game of checkers, the learning problem can be defined as:

- Task T: Playing the game
- Performance Measure P: number of games won against the opponent.
- Experience E: practicing via playing games against itself and consistently improving the performance.

The generic model of machine learning consists of six components independent of the algorithm adopted. The following figure 3 depicts these primary components.

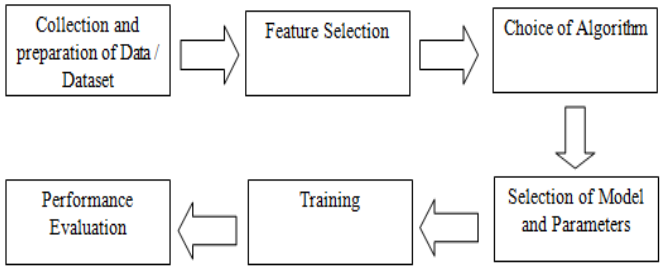


Fig 3. Components of a Generic ML model

Each component of the model has a specific task to accomplish as described next.

i. **Collection and Preparation of Data**: The primary task of in the machine learning process is to collect and prepare data in a format that can be given as input to the algorithm. A large amount may be available for any problem. Web data is usually unstructured and contains a lot of noise, i.e., irrelevant data as well as redundant data. Hence the data needs to be cleaned and pre-processed to a structured format.

ii. **Feature Selection**: The data obtained from the above step may contain numerous features, not all of which would be relevant to the learning process. These features need to be removed and a subset of the most important features needs to be obtained.

iii. **Choice of Algorithm**: Not all machine learning algorithms are meant for all problems. Certain algorithms are more suited to a particular class problem as explained in the previous section. Selecting the best machine learning algorithm for the problem at hand is imperative in getting the best possible results. The various ML algorithms are discussed in Section 6.
iv. **Selection of Models and Parameters**: Most of machine learning algorithms require some initial manual intervention for setting the most appropriate values of various parameters.
v. **Training**: After selecting the appropriate algorithm and suitable parameter values, the model needs to be trained using a part of the dataset as training data.
vi. **Performance Evaluation**: Before real-time implementation of the system, the model must be tested against unseen data to evaluate how much has been learnt using various performance parameters like accuracy, precision and recall.

5. Machine Learning Paradigms

Depending on how an algorithm is being trained and on the basis of availability of the output while training, machine learning paradigms can be classified into ten categories. These include: supervised learning, semi-supervised learning, unsupervised learning, reinforcement learning, evolutionary learning, ensemble learning, artificial neural network, Instance-based learning, dimensionality reduction algorithms and hybrid learning [4, 5, 6, 13,14,15,16 17]. Each of these paradigms is explained in the following sub-sections.

5.1. Supervised Learning

Under supervised learning, a set of examples or training modules are provided with the correct outputs and on the basis of these training sets, the algorithm learns to respond more accurately by comparing its output with those that are given as input. Supervised learning is also known as learning via examples or learning from exemplars. The following figure 4 explains the concept.

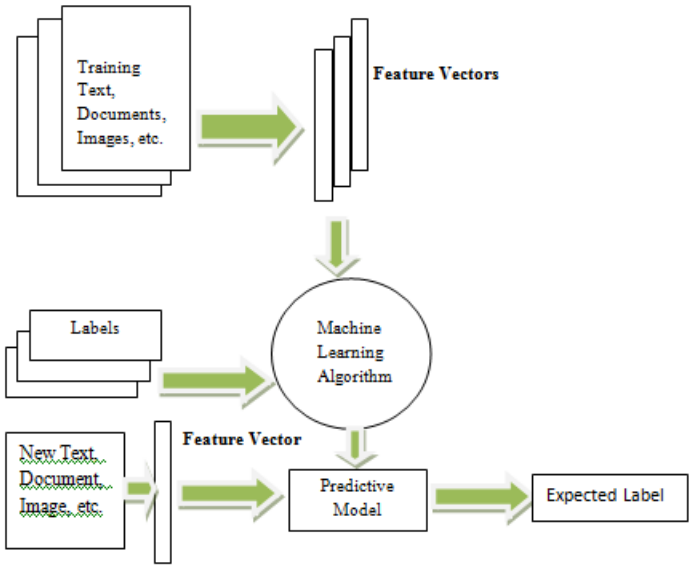


Fig. 4. Supervised Learning [4]

Supervised learning finds applications in prediction based on historical data. For example: to predict the Iris species given a set of its flower measurements or a recognition system that determines whether an object is a galaxy, a quasar or a star given a colored image of an object through a telescope, or given an e-commerce surfing history of a person, recommendation of the products by e-commerce websites

[4]. Supervised learning tasks can be further categorized as classification tasks and regression tasks. In case of classification, the output labels are discrete whereas they are continuous in case of regression.

5.2. Unsupervised Learning

The unsupervised learning approach is all about recognizing unidentified existing patterns from the data in order to derive rules from them. This technique is appropriate in a situation when the categories of data are unknown. Here, the training data is not labeled. Unsupervised learning is regarded as a statistic based approach for learning and thus refers to the problem of finding hidden structure in unlabeled data. Figure 5 explicates the concept.

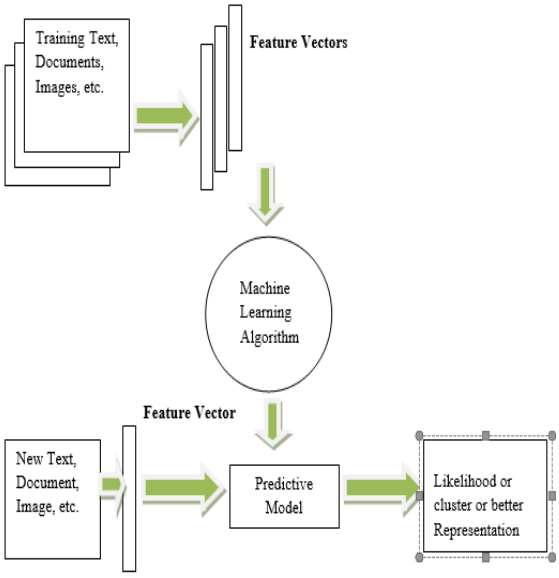


Fig 5. Unsupervised Learning

5.3. Reinforcement Learning

Reinforcement learning is regarded as an intermediate type of learning as the algorithm is only provided with a response that tells whether the output is correct or not. The algorithm has to explore and rule out various possibilities to get the correct output. It is regarded as learning with a Critic as the algorithm doesn't propose any sort of suggestions or solutions to the problem.

5.4. Evolutionary Learning

It is inspired by biological organisms who adapt to their environment. The algorithm understands the behavior and adapts to the inputs and rules out unlikely solutions. It is based on the idea of fitness to propose the best solution to the problem.

5.5. Semi-Supervised Learning

These algorithms provide a technique that harnesses the power of both - supervised learning and unsupervised learning. In the previous two types output labels areeither provided for all the observations or no labels are provided. There might be situations when some observations are provided with labels but majority of observations are unlabeled due to high cost of labeling and lack of skilled human expertise. In such situations, semi-supervised algorithms are best suited for model building. Semi supervised learning can be used with problems like classification, regression and prediction [4, 13,18].

It may further be categorized as Generative Models, Self-Training and Transductive SVM.

5.6. Ensemble Learning

It is a machine learning model in which numerous learners (individual models) are trained to solve a common problem. Unlike other machine learning techniques which learn a single hypothesis from the training data, ensemble learning tries to learn by constructing a set of hypotheses from the training data and by combining them to make a prediction model [15,19] in order to decrease bias(boosting), variance (bagging), or improve predictions(stacking). Ensemble learning can be further divided into two groups:

- Sequential ensemble approaches- These are the methods in which the base learners are constructed sequentially (AdaBoost). This method exploits the dependence between the base learners.
- Parallel ensemble approaches- In these, the base learners are independent of each other, so this relationship is exploited by constructing the base learners in parallel (e.g. Random Forest)
    - *Bagging:* It stands for bootstrap aggregation. It implements homogenous learners on sample populations and takes the mean of all predictions [4, 15,16]. For example, M different trees can be trained on dissimilar subsets of data and compute the ensemble as:

$$f(x) = 1/M \sum_{m=1}^{M} f_m(x)$$

    - *Boosting:* It is an iterative technique that adjusts the observation's weight on the basis of last classification. It tries to fit a sequence of weak learner models that performs a little better than just random predicting e.g. small decision trees [4,16]. AdaBoost stands for adaptive boosting and is the most widely used boosting algorithm.

5.7. Artificial Neural Network

Artificial neural networks (ANNs) are encouraged by the biological neural network. A neural network is an interconnection of neuron cells that help the electric impulses to propagate through the brain. The basic unit of learning in a neural network is a neuron, which is a nerve cell. A neuron consists of four parts, namely dendrites (receptor), soma (processor of electric signal), nucleus (core of the neuron) and axon (the transmitting end of the neuron). Analogical to a biological neural network, an ANN works on three layers: input layer, hidden layer and output layer. This type of network has weighted interconnections and learns by adjusting the weights of interconnections in order to perform parallel distributed processing. The Perceptron learning algorithm, Back-propagation algorithm, Hopfield Networks, Radial Basis Function Network (RBFN) are some popular algorithms.

Based on learning behavior, ANN can be further classified as:

- *Supervised Neural Network* – The inputs and the outputs are presented to the network as training data. The network is trained with this data by adjusting the weights to get accurate results. When it is fully trained, it is presented with unseen data to predict the output.
- *Unsupervised Neural Network*- In unsupervised neural network, the network is not provided with any output. It tries to find some structure or correlation among the input data and group those data together in a group or class. When new data is presented to it as input, it identifies its features and classifies it in one of the groups based on similarities.
- *Reinforcement Neural Network*- As humans interact with their environment and learn from mistakes, a reinforcement neural network also learns from its past decisions by way of penalties for wrong decisions and rewards for good decisions. The connection weights producing correct output are strengthened, while those producing incorrect responses are weakened.

5.8. Instance based learning

Unlike other machine learning methods where clear definition of the target function are provided from the training data, this lerning method does not describe any target function in the beginning. Rather it simply stores the training instance and generalizing is postponed until a new instance is classified. Hence it is also known as lazy learner. Such methods build up a database of training instances and whenever new data is presented as input it compares that data with other instances in the database using a similarity measure to find the nearest match and make the prediction [4]. The lazy learner estimates the target function differently and locally for every new instance to be classified instead of estimating it globally for the whole instance space hence it is faster to train but, takes time in making prediction [16]. K-Means, k-medians, hierarchical clustering and expectation maximization are some popular instance-based algorithms.

5.9. Dimensionality reduction algorithms

During the past few decades, intelligent machine learning models have been adopted in numerous complex and data intensive applications like climatology, biology, astronomy, medical, economy and finance. However, existing ML based systems are not sufficiently efficient and extensible enough to deal with massive and voluminous data. High dimensionality of data has proved to be a curse for data processing. Another challenge is sparsity of data. Global optimum is costly to find for such data. A dimensionality reduction algorithm helps in reducing the computational cost by reducing the number of dimensions of the data. It does so by reducing the redundant and irrelevant data and cleaning the data so as to improve the accuracy of results. Dimensionality reduction works in an unsupervised manner to search and exploit the implicit structure in the data [4, 5]. There are many algorithms for dimensionality reduction that can be adapted with classification and regression algorithms like Multidimensional scaling (MDS), Principal component analysis (PCA), Linear Discriminant Analysis (LDA), Principal component regression (PCR), and Linear Discriminant Analysis (LDA).

5.10. Hybrid Learning

Though ensemble learning appeared as a relief to researchers dealing with the common problems of computational complexity, over fitting and sticking to local minima in classification algorithms, researchers have found problems with ensemble learning. Complicated ensemble of multiple classifiers makes it difficult to implement and difficult to analyze the results. Instead of improving accuracy of the model, ensembles may tend to increase error at the level of individual base learner. Ensembles may result in poor accuracy as a result of selection of poor classifiers in combination. Recent approach to deal with such problems is hybridization i.e. creating ensemble of heterogeneous models. In this, more than one method is combined for example, combining clustering and decision tree or clustering and association mining etc.

Out of all the above-mentioned learning paradigms, the supervised learning is by far the most popular with researchers and practitioners.

6. Machine Learning Algorithms

In this section, we focus on some popular machine learning algorithms from the different paradigms [4, 5, 6, 16] explained in the preceding section. Although the number of algorithms falling within each paradigm are numerous and reported across pertinent literature, in this study we consider only few of these. The following table 2 briefly explains few of these algorithms.

These algorithms have a wide domain of practical applications, some of which are described in the next section.

Table 2. ML Algorithms

Paradigm	Algorithm	Description
Supervised Learning	Decision Tree	Decision Tree is a technique for approximating discrete valued target function which represents the learnt function in the form of a decision tree [10]. A decision tree classifies instances by sorting them from root to some leaf nodes on the basis of feature values. Each node represents some decision (test condition) on attribute of the instance whereas every branch represents a possible value for that feature. Classification of an instance starts at the root node called the decision node. Based on the value of node, the tree traverse down along the edge which corresponds to the value of the output of feature test. This process continues in the sub-tree headed by the new node at the end of the previous edge. Finally, the leaf node signifies the classification categories or the final decision. While using a decision tree, focus is on how to decide which attribute is the best classifier at each node level. Statistical measure like information gain, Gini index, Chi-square and entropy are calculated for each node to calculate the worth of that node [10]. Several algorithms are used to implement decision trees. The most popular ones are: Classification and Regression Tree (CART), Iterative Dichotomiser 3 (ID3), Automatic Interaction Detection (CHAID), Chi-Squared C4.5 and C5.0 and M5
	Naïve Bayes	Naïve Bayes classifies using Bayes' Theorem of probability. Bayes' theorem calculates the posterior probability of an event (A) given some prior probability of event B represented by P(A/B) as follows: $$\mathrm{P(A/B)} = \frac{P(B/A)P(A)}{P(B)}$$ Where, • A and B are events. • P(A) and P(B) are the probabilities of observing A and B independent of each other. • P(A/B) is the conditional probability, i.e. Probability of observing A, given B is true. • P(B/A) is the probability of observing B, given A is True. Naïve Bayes' classifiers fall under the category of simple probabilistic classifiers based on the concept of Bayes' Theorem having strong independence assumptions among the features.

		It is particularly suited when the dimensionality of the inputs is high [4,5].
	Support Vector Machines	SVMs can be used for classification as well as regression problems. It is a supervised learning algorithm. It works on the concept of margin calculation. In this algorithm, each data item is plotted as a point in n-dimensional space (where n is the number of features we have in our dataset). The value of each feature is the value of the corresponding coordinate. It classifies the data into different classes by finding a line (hyper plane) which separates the training datasets into classes. It works by maximizing the distances between the nearest data point (in both classes) and the hyper plane that we can call as margin.
	Regression Analysis	Regression analysis is a predictive modelling technique which investigates the relationship between a dependent (target) and independent variable(s) (predictor). It is an important tool for analysing and modelling of data. In this method, we try to fit the line/curve to the data points so as to minimize the differences between distances of data points from the curve or line. There are various kinds of regression analysis like linear, logistic and polynomial.
Unsupervised Learning	K-Means Clustering	K-means is a popular unsupervised machine learning algorithm for cluster analysis. Its goal is to partition 'n' observations into 'k' clusters in which each observation belongs to the cluster having the nearest mean, serving as a prototype of the cluster. The mean of the observations in a particular cluster defines the center of the cluster.
Instance based Learning	K-nearest Neighbours	It is a non-parametric method used for classification and regression. Given N training vectors, KNN algorithm identifies the k-nearest neighbours of an unknown feature vector whose class is to be identified.
Ensemble Learning	Random Forest	It is an ensemble learning method used in classification and regression. It uses bagging approach to create a bunch of decision trees with random subset of data. The output of all decision trees in the random forest is combined to make the final decision trees. There are two stages in Random Forest Algorithm, one is to create random forest, and the other is to make a prediction from the random forest classifier created in the first stage.

Dimensionality Reduction	Principal Component Algorithm	It is primarily used for reducing dimensionality of data set. It helps in reducing the number of features of the data set or the number of independent variables in the data set. It uses orthogonal transformation to convert correlated variables into a set of linearly uncorrelated variables called principal components.

7. Applications of Machine Learning

Machine learning problems range from game playing to self-driven vehicles. Table 3 enlists some popular real-life applications of ML.

Table 3. Applications of ML

Application	Description
Playing Checkers Game	A computer program learns to play checkers game, improvises its performance as determined by its ability to win at various class of tasks involving the game, through experience obtained by playing games against itself.
Speech Recognition	The most sophisticated speech recognition systems these days deploy machine learning algorithms in some forms. Example: SPHINX system [20] learns speaker-specific sounds and words from speech signals. Various Neural Network learning methodologies for interpreting hidden Markov Models are highly effective for automatically customizing speakers, dictionary, noise etc.
Autonomous Vehicles	Machine learning models are these days being applied to drive autonomous vehicles like Cars, Drones etc. Example: Google Driver Less Cars, Tesla Cars. Machine learning techniques are also highly effective in controlling sensor-based applications.
Filtering Emails (Spam Emails)	Machine learning can be applied to filter spam emails. The machine learning based model will simply memorize all the emails classified as spam emails by user. When new email arrives in inbox, the machine learning based model will search, compare and based on the previous spam emails. If new email matches any one of them, it will be marked as spam; else it will be moved to user's inbox.
Robotics and Artificial Intelligence	Machine learning is regarded as improved approach to problem solving. Using base knowledge and training data with machine learning models, learning can be improved which will take robotics and AI to next generation levels.
Web and Social Media	• Naïve Bayes classifiers have been successfully applied in the field of text mining, may it be spam filtering or classifying the web page, an email or any document. • Facebook uses Naïve Bayes' to analyze status update expressing positive and negative emotions. • Document Categorization: Google uses Naïve Bayes algorithm for document categorization. • K-means clustering is used by search engines like Google, Yahoo to cluster web pages by similarity. • Apriori is used by websites such as Amazon or Flipkart to recommend which items are purchased together frequently. • Another common application of Apriori is the Google auto-complete. When a person types a word, Google search engine looks for other associated words that go together with the word earlier typed word. • Sentiment analysis on social networking sites is a typical text classification problem solved using application of variety of ML algorithms [21, 22, 23,24]
Medical Field	TRISS: Trauma & Injury Severity Score, which is widely used to predict mortality in injured patients, was originally developed by Boyd et al. using logistic regression. Many other medical scales used to assess severity of a patient have been developed using logistic regression.
Bayesian Methods	Bayes' Theorem is one of the most popular methods for calculating conditional probabilities given the set of hypothesis. It can be used to solve complex data science and analytics problems by integrating with various Machine Learning models and algorithms. Some examples real world problems that can be solved using Bayesian methods are: • Suggestions on Netflix • Auto-correction

	• Credit card fraud detection • Google page ranking • Facial recognition • Climate modeling forecast • Stock trading systems

8. Analysis and Discussion

Given the wide range of applicability of ML, it faces a number of challenges. Some of them are as follows:

- The machine learning algorithms require large volumes of data to be accurate and efficient which is still not available to researchers. Tech giants like Facebook and Google have had access to such enormous data which is why they are leading in the field of Artificial Intelligence. It becomes even more difficult to get this data in the fields like banking and healthcare where sparse digital data is available making it tough to make accurate predictions.
- Spam Detection: Given email in an inbox, the intelligent systems developed so far are still not able to correctly detect the spam mail. It ends up in sending spam in inbox and non-spam mails to spam directory.
- Machine learning algorithms have not yet been successful in identifying the objects and images. This field is still an open research field for machine learning. Though we have mentioned a few challenges in machine learning, there are many more fields which still challenging for deep learning algorithms i.e. speech understanding, credit card fraud detection, face detection, digit recognition given a zip code, and product recommendation etc.

Machine learning algorithms are in continuous development and will definitely become more widespread in the years to come. They are useful in many different applications; there is significant brainpower and funding behind pushing the boundaries towards innovation [25]. Some open areas of application include:

- Deep learning, e.g. for predicting stock market trends, designing circuits, identifying illnesses, designing voice-controlled devices, and much more (save special attention for Generative Adversarial Neural Networks)
- Data mining and big data analytics, e.g. for predicting business market trends
- Natural language processing, e.g. in search engines
- Hardware accelerators for new AI architectures, e.g. from AMD and Intel
- Simulation environments for evaluation and testing, e.g. for self-driving cars and virtual reality
- Healthcare machine learning (medical imaging, working with clinical data, making sense of genomic data of huge populations)
- HCI (Human Computer Interaction), keep advancing better interfaces and usability between different devices with the rise of cloud computing and IoT

Given the current rate of advancement in the field, it has a bright future. Applications of machine learning have the potential to expand dramatically in the near future.

9. Machine Learning in Future

In near future machine learning is expected to be a part of almost every software application. There are some of the future predictions of machine learning applications: As machine learning helps computers understand the context and semantics of sentences using Natural Language Processing, so we do not have to wait long for a time when computers will learn to talk like humans. In the near future we can expect machine learning tools and techniques to connect to the internet and continuously retain on the most relevant information. This will help algorithms in constant retaining of algorithms and there will be no need to train the systems time and again. Personalization could be enhanced and recommendations could be improved leading to more beneficial and successful experiences.

10. Conclusion

Digitalization and the Internet revolution have led to a mounting volume of structured and unstructured data which needs to be utilized for analytics. Machine learning as a key technology driver encompasses the intelligent power to harness the knowledge from the available data. Moreover, the adoption of machine learning solutions for complex real-life problems by both researchers & practitioners has made this field a dynamic area of research with an active participation across industries & countries. In this paper, a comprehensive review of Machine Learning process and algorithms is presented. The purpose is clearly to understand the role, advantage and scope of Machine learning as a technology-based solution.

References

[1] Samuel AL. Some studies in machine learning using the game of checkers. IBM Journal of research and development. 1959 Jul;3(3):210-29.
[2] Mitchell, T. (1997). Machine Learning. McGraw Hill. p. 2. ISBN 978-0-07-042807-2.
[3] Hayashi, Chikio (1998-01-01). "What is Data Science? Fundamental Concepts and a Heuristic Example". Data Science, Classification, and Related Methods. Studies in Classification, Data Analysis, and Knowledge Organization. Springer Japan. pp. 40–51. doi:10.1007/978-4-431-65950-1_3. ISBN 9784431702085
[4] Sandhya N. dhage, Charanjeet Kaur Raina, "A review on Machine Learning Techniques", March 16 Volume 4 Issue 3 , International Journal on Recent and Innovation Trends in Computing and Communication (IJRITCC), ISSN: 2321-8169, PP: 395 – 399
[5] AyonDey , "Machine Learning Algorithms: A Review", (IJCSIT) International Journal of Computer Science
[6] A report by Royal Society, April 2017, "Machine learning: the power and promise of computers that learn by example ", ISBN: 978-1-78252-259-1.and Information Technologies, Vol. 7 (3) , 2016, 1174-1179
[7] Minton S, Zweben M. Learning, Planning, and Scheduling: An Overview. InMachine Learning Methods for Planning 1993 (pp. 1-29).
[8] Sejnowski T. Net talk: A parallel network that learns to read aloud. Complex Systems. 1987;1:145-68.
[9] Han J, Cai Y, Cercone N. Data-driven discovery of quantitative rules in relational databases. IEEE Transactions on Knowledge & Data Engineering. 1993 Feb 1(1):29-40.
[10] Shokri R, Stronati M, Song C, Shmatikov V. Membership inference attacks against machine learning models. InSecurity and Privacy (SP), 2017 IEEE Symposium on 2017 May 22 (pp. 3-18). IEEE.
[11] Li M, Andersen DG, Park JW, Smola AJ, Ahmed A, Josifovski V, Long J, Shekita EJ, Su BY. Scaling Distributed Machine Learning with the Parameter Server. InOSDI 2014 Oct 6 (Vol. 14, pp. 583-598).
[12] Chen JX. The evolution of computing: AlphaGo. Computing in Science & Engineering. 2016 Jul;18(4):4-7.
[13] Al-Jarrah OY, Yoo PD, Muhaidat S, Karagiannidis GK, Taha K. Efficient machine learning for big data: A review. Big Data Res. 2015; 2(3):87–93.
[14] A.Khan,B.Baharudin,Lan Hong Lee, " A Review of Machine Learning Algorithms for Text Documents Classification", Journal Of Advances in Information Technology, Vol. 1 , No. 1, Feb.2010.
[15] Zhou ZH. (2009) Ensemble Learning. In: Li S.Z., Jain A. (eds) Encyclopedia of Biometrics. Springer, Boston, MA
[16] Tom M. Mitchell , "Machine Learning ", WCB McGraw-Hill, 2013, ISBN-13:978-1-25-909695-2, ISBN-10: 1-25-909695-5.

[17] Tang W, Zhang T, Sazonov E. The application of machine learning in monitoring physical activity with shoe sensors. Cyber-Physical Systems: Integrated Computing and Engineering Design. 2013 Sep 26:187.
[18] Zhu X. Semi-supervised learning literature survey. Computer Science, University of Wisconsin-Madison. 2006;2(3):4.
[19] Witten IH, Frank E, Hall MA, Pal CJ. Data Mining: Practical machine learning tools and techniques. Morgan Kaufmann; 2016 Oct 1.
[20] Lee KF, Hon HW, Hwang MY, Mahajan S, Reddy R "The SPHINX speech recognition system", International Conference on Acoustics, Speech, and Signal Processing (ICASSP '89), Vol. 1, pp. 445 - 448, May, 1989
[21] KumarA., Sharma A., "Systematic Literature Review on Opinion Mining of Big Data for Government Intelligence." Webology, Vol.14, No. 2, December 2017.
[22] Kumar A., Jaiswal A., "Empirical Study of Twitter and Tumblr for Sentiment Analysis using Soft Computing Techniques" International Conference on Soft Computing and Applications (ICSCA 2017), World Congress on Engineering and Computer Science 2017, vol. 1, ISBN: 978-988-14047-5-6, pp. 1-5, Oct 2017.
[23] Kumar A., Abraham A. "Opinion Mining to Assist User Acceptance Testing for Open-Beta Versions", Journal of Information Assurance and Security, Vol.12, Issue 4, pp. 146-153, 2017, ISSN:1554-1010.
[24] Pazzani MJ, Billsus D. Content-based recommendation systems. InThe adaptive web 2007 (pp. 325-341). Springer, Berlin, Heidelberg.
[25] Bhatia MPS, Kumar A., "Information Retrieval & Machine Learning: Supporting Technologies for Web Mining Research & Practice", Webology, Vol. 5, No. 2.

ADVANCED FUNCTIONAL MATERIALS

www.afm-journal.de

Mixed Dimensional 2D/3D Hybrid Perovskite Absorbers: The Future of Perovskite Solar Cells?

*Anurag Krishna, Sébastien Gottis, Mohammad Khaja Nazeeruddin, and Frédéric Sauvage**

The cost-effective processability and high efficiency of the organic–inorganic metal halide perovskite solar cells (PSCs) have shown tremendous potential to intervene positively in the generation of clean energy. However, prior to an industrial scale-up process, there are certain critical issues such as the lack of stability against over moisture, light, and heat, which have to be resolved. One of the several proposed strategies to improve the stability that has lately emerged is the development of lower-dimensional (2D) perovskite structures derived from the Ruddlesden–Popper (RP) phases. The excellent stability under ambient conditions shown by 2D RP phase perovskites has made the scalability expectations burgeon since it is one of the most credible paths toward stable PSCs. In this review, the 2D/3D mixed system for photovoltaics (PVs) is elaborately discussed with the focus on the crystal structure, optoelectronic properties, charge carrier dynamics, and their impact on the photovoltaic performances. Finally, some of the further challenges are highlighted while outlining the perspectives of 2D/3D perovskites for high-efficiency stable solar cells.

1. Introduction

Organic–inorganic metal halide perovskite solar cells (PSCs) have rapidly emerged as one of the hottest topics in material sciences during the last few years owing to their low-cost, solution processed devices, and exceptional optoelectronic properties.[1–4] Hybrid perovskites are represented by the formula ABX_3, wherein the organic cation A is larger than the metal cation B, and X is a halide anion[5] (**Figure 1**a). The most commonly studied compositions are the methylammonium (MA) lead tri-iodide ($CH_3NH_3PbI_3$ or $MAPbI_3$), the other halide variants such as $CH_3NH_3PbBr_3$ and mixed halides, $CH_3NH_3PbI_{3-x}Cl_x$ and $CH_3NH_3PbI_{3-x}Br_x$. The 3D perovskite $CH_3NH_3PbI_3$ has emerged as the archetypical material of interest, combining direct bandgap with high molar extinction coefficient (≈10^4–10^5 M^{-1} cm^{-1}),[6] low trap densities,[7] low exciton binding energies (≈10–50 meV)[8] which cause long-range free-carrier diffusion lengths (≈100 nm–1 µm),[9,10] The growth of perovskite photovoltaics (PV) is unprecedented since, in only a very few years, the power conversion efficiency (PCE) raised from 3.8% back in 2009[11] to 22.7% in 2017.[12] The key ingredient driving the efficiency enhancement has been the association of the perovskite to the solid hole transporting materials (HTM) based on the so-called doped Spiro-OMeTAD and mesoporous TiO_2 scaffold to separate charges more efficiently. The easily tunable bandgap[13] of perovskites, through a careful control in the absorber's stoichiometry, in particular within $CH_3NH_3PbI_{3-x}H_x$ solid solution (H = Br or Cl), makes this family of materials themselves extremely attractive and also as a 2- or 4-terminals top cell of Si modules to give a new impetus on the power conversion efficiency limit of Si, e.g., achieve new record breaking of as high as 30% low-cost modules,[14,15] Before bringing PSCs to a pilot and consequently to production lines, two major issues require to be addressed: i) Pb toxicity which implies careful encapsulation of modules to avoid lead dissemination into the external environment in case of device failure and ii) enhancing significantly the device stability to comply with the standard IEC61646 accelerated ageing protocol.

The scientific and technical challenges related to the device stability enhancement efforts stem from i) an inadequate materials interplay between the 3D methylammonium lead halide compositions which are prone to thermal, moisture and light-induced degradation,[16–20] ii) Spiro-OMeTAD which losses its conductivity under air and moisture exposure[21] whereas it is often combined to a hydrophilic dopant such as LiTFSI or tert-butylpyridine,[21,22] *and* iii) gold back-contact which tends to diffuse throughout the HTM to the perovskite.[23,24] The sensitiveness to water ingress results from the weak electrostatic attraction between cationic and anionic species within the inorganic layers which can easily accommodate water molecules. This dissociates the perovskite back into the initial ammonium salt and lead halide precursor.[25] In addition, depending on the

Dr. A. Krishna, Dr. S. Gottis, Dr. F. Sauvage
Laboratoire de Réactivité et Chimie des Solides (LRCS)
UMR CNRS 7314 - Institut de Chimie de Picardie FR 3085
Université de Picardie Jules Verne
33 rue Saint Leu, FR-80039 Amiens Cedex, France
E-mail: frederic.sauvage@u-picardie.fr
Dr. M. K. Nazeeruddin
Group for Molecular Engineering of Functional Materials
Ecole Polytechnique Fédérale de Lausanne
CH-1951Sion, Switzerland

The ORCID identification number(s) for the author(s) of this article can be found under https://doi.org/10.1002/adfm.201806482.

DOI: 10.1002/adfm.201806482

 © 2018 WILEY-VCH Verlag GmbH & Co. KGaA, Weinheim

external conditions in terms of temperature and humidity level, the perovskite can produce gases even at moderate temperatures (≈85 °C), causing thermal decomposition, layers cracking, and interfacial deterioration issues which cause irreversible performance fading.[26] Finally, under light exposure, $MAPbI_3$ can sustain internal ionic migration, which further adds to performance decline.[27]

Two strategies have emerged to stabilize the perovskite, one of them being the incorporation of triple/quadruple cations within the A-site[28–31] and other being the development of lower dimensional perovskites.[32,33] The lower-dimensional 2D perovskites composed of alternating organic and inorganic layers called Ruddlesden–Popper (RP) phases having general formula $A_2A'_{n-1}B_nX_{3n+1}$.[34] 3D to 2D structural transition is controlled by the size of the organic cation, in particular when it exceeds the critical size of Goldschmidt's tolerance factor (TF).[34] The advantages of the layered 2D structure are multiple, e.g., 2D perovskites are thermally more robust, larger cations hamper internal ionic motion and can bring to the absorber the much needed hydrophobic character through adequate organic moieties leading to an improved stability.[35] However, these appealing features are overshadowed by more common optoelectronic properties such as a wider optical bandgap of at least 2.5 eV which restricts photons conversion to less than 500 nm[36,37] and by a larger exciton binding energy of ≈300 meV[36] (10–50 meV for 3D counterpart) which penalizes output photovoltage, therefore the power conversion efficiencies. The current record showed a noncertified PCE of 12.5% under standard AM 1.5G conditions with 60% of PCE retention over 2250 h stability under light, heat, and humidity stress.[38] This progress was achieved by mixing 3D with 2D Ruddlesden–Popper perovskites.

The 2D expectations are flourishing since currently, it is one of the most credible paths toward stable PSCs. The cons of 2D perovskites aforementioned can be alleviated by mixing 2D with the conventional 3D lead halide perovskite. Indeed, 2D/3D engineering aims to combine both advantages, namely the outstanding optoelectronic properties of the 3D perovskite and the high robustness of the 2D Ruddlesden–Popper phase. The 2D/3D mixed system for photovoltaics is elaborately discussed with the focus on the crystal structure, optoelectronic properties, charge carrier dynamics, and their impact on the photovoltaic performances. Finally, some of the key challenges which remain to be addressed are herein highlighted while giving the outline on the perspectives of 2D/3D perovskites for high-efficiency stable solar cells.

2. 2D Perovskites

Goldschmidt's TF is used as a general abacus to account for the distortion in the perovskite crystal structure for predicting 3D to 2D transition.[34] The TF simply depends on ionic radii of the A, B, and X sites of the perovskite structure as given below

$$t_G = \frac{r_A + r_X}{\sqrt{2}(r_B + r_X)} \quad (1)$$

where r_A, r_B, and r_X are the ionic radii of A, B and X elements, atoms, or units. The majority of the archetypical 3D perovskites, e.g., $MAPbI_3$ or $FAPbI_3$ have values in the range $0.8 < t_G < 1$ (Figure 1b). The deviation of the tolerance factor from the above range leads to the crystal structure distortions that result



Anurag Krishna is currently a Postdoctoral Fellow at the Laboratoire de Reactivite et Chimie des Solides, Centre National de la Recherche Scientifique (CNRS) UMR7314, Amiens, France. He received his B.E. in Polymer Science and Chemical Technology from Delhi College of Engineering at the University of Delhi in 2012. He completed his Ph.D. in February 2017 at Nanyang Technological University (NTU) on hole transporting materials for perovskite solar cells under the supervision of Associate Professors Andrew Grimsdale and Cesare Soci. Currently, his research focuses on novel organic semiconductors for organic/hybrid optoelectronics application.



Sébastien Gottis is currently an Assistant Professor in the Photochemistry and Photovoltaic systems group at Laboratoire de Réactivité et Chimie des Solides, UMR7314. He obtained his Ph.D. in 2008 in the group of Robert Deschenaux in Neuchâtel (Switzerland). After much experience with organic material science on organometallics phosphorylated dendrimers for catalysis in Laboratoire de Chimie de Coordination (LCC)-Toulouse, organic electrodes for batteries in Laboratoire de Réactivité et Chimie des Solides (LRCS)-Amiens and conducting polymers for fuel cells in Lawrence Berkeley National Lab (LBNL)-University of Berkeley, he joined the photovoltaic and photoelectrochemistry group at LRCS to research the stability of halide perovskite and hole transporting materials for solar cells.



Frédéric Sauvage is a CNRS researcher and heads the group "Photochemistry and Photovoltaic Systems" at Laboratoire de Réactivité et Chimie des Solides, UMR7314. His research focuses on new concepts and stability of dye-sensitized solar cells and perovskite solar cells, photocatalysis, and molecular bifunctional materials combining sunlight conversion and energy storage.

© 2018 WILEY-VCH Verlag GmbH & Co. KGaA, Weinheim

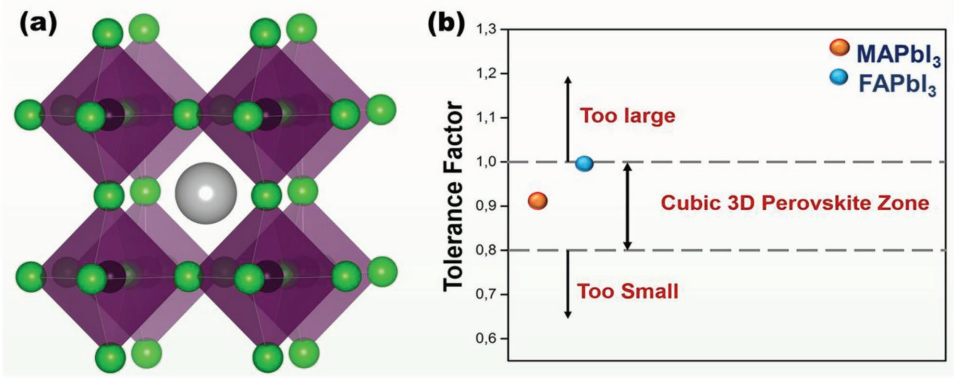


Figure 1. a) Crystal structure of cubic perovskite with generic chemical formula ABX_3. b) Tolerance factor for the formation of the ideal cubic perovskite structures.

in edge-shared and face-shared octahedra, instead of the pristine corner-shared structure of the classical ABX_3 perovskite.

When the A-site cation has a too large size to be well accommodated within the octahedral cage of the original 3D perovskite, the initial tetragonal structure becomes energetically stabilized through a phase transition toward a layered Ruddlesden–Popper structure of generic formulae $A'A_{n-1}B_nX_{3n+1}$.[39] By misuse of language, this phase is often termed 2D "perovskite" in analogy with the perovskite-like building motifs. During the past 3 years, 2D perovskites have attracted interests to overcome stability issues of the 3D counterparts despite their optoelectronic property limitations in terms of larger exciton binding energy, indirect and larger bandgap structure.[40]

2.1. Structure and Photophysical Properties of 2D Perovskites

The so-called 2D perovskites were discovered by Ruddlesden and Popper back in 1957[39] through the first compound of composition K_2NiF_4. The 2D perovskites integrated into photovoltaic applications are composed of alternating organic and inorganic sheets along [001] direction leading to the formation of a layered structure.[41] The organic layer can be composed of either a single or a double level of organic sheets depending upon the type of ammonium cation. The simplest 2D materials, namely $(NH_3\text{-R-}NH_3)MX_4$ and $(R\text{-}NH_3)_2MX_4$, are depicted in **Figure 2**a, where $R\text{-}NH_3^+$ and $NH_3^+\text{-R-}NH_3^+$ may be an aliphatic or aromatic ammonium cation(s).[42] In $(R\text{-}NH_3)_2MX_4$ the inorganic sheet interacts with the organic layer via hydrogen-ionic bonding. The tail of the organic moieties stabilizes the overall structure through Van der Waals interactions. This is in contrast with $(NH_3\text{-R-}NH_3)MX_4$ where the hydrogen atoms of the organic part bond to the inorganic sheets at both ends, thereby removing the van der Waals gap between the layers.[42]

These alternating layers of organic and inorganic units confer to the 2D perovskite appealing properties. One such feature is the dielectric confinement effect along [001] direction. This stems from the periodic changing of a low dielectric constant layer related to the organic sheet and a higher dielectric constant characteristic of the inorganic layer.[43] Also, the bandgap of organic material is generally higher than the inorganic counterpart. This gives rise to a fascinating multiple-pseudo quantum-well structure (Figure 2b) in which the inorganic layers serve as the potential wells and the organic layers as the potential barriers. This unique property makes these 2D perovskites one strong candidate for light emission applications.[44–46] In addition, organic moieties confer hydrophobicity to the perovskite structure which in turn improves their chemical stability compared to 3D counterparts. However, the wider bandgap of pure 2D perovskites (>2.3 eV) renders them less desirable for photovoltaic application. One first approach led by Karunadasa et al.[35] to overcome with the higher bandgap value consists of mixing together 2D perovskite with conventional 3D perovskite within a single absorber layer to decrease

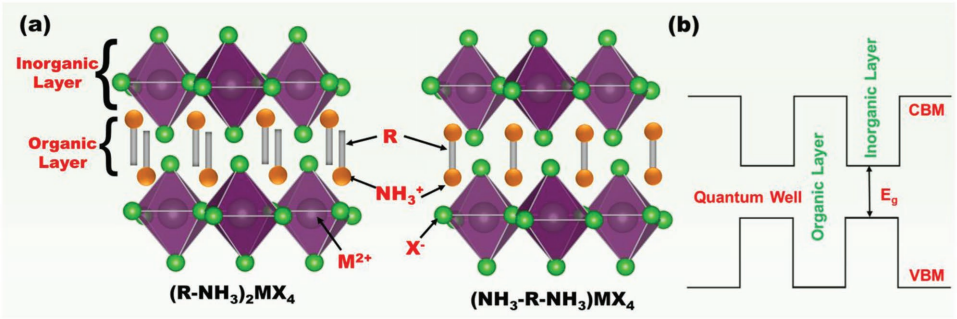


Figure 2. a) Typical structures of the 2D layered hybrid organic–inorganic perovskite for $n = 1$ with mono and disubstituted amines. b) Band alignment of 2D perovskite with multiple quantum wells.

© 2018 WILEY-VCH Verlag GmbH & Co. KGaA, Weinheim

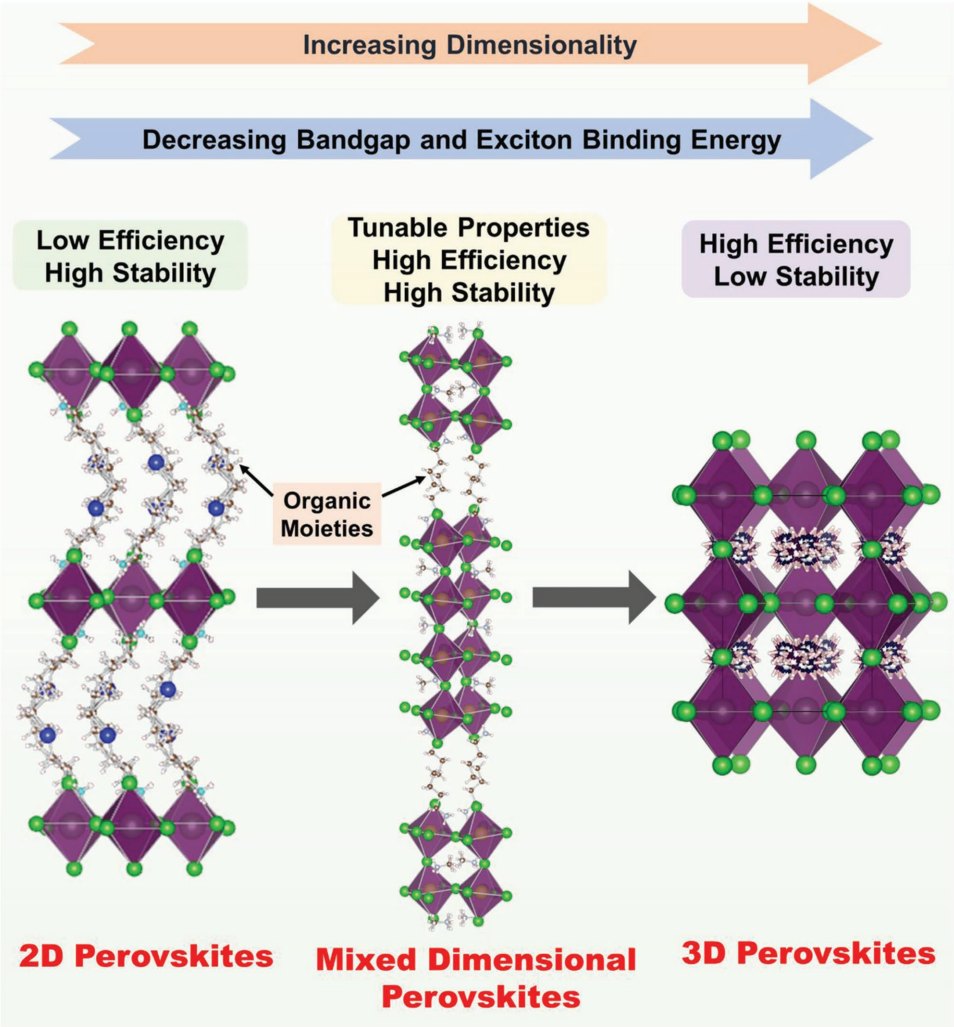


Figure 3. Illustration of the 2D crystalline structure, mixed-dimensional 2D/3D perovskites, and 3D perovskites. Adapted with permission.[52] Copyright 2016, Wiley-VCH.

both optical bandgap and exciton binding energy together with enhancing the charge collection efficiency (**Figure 3**).

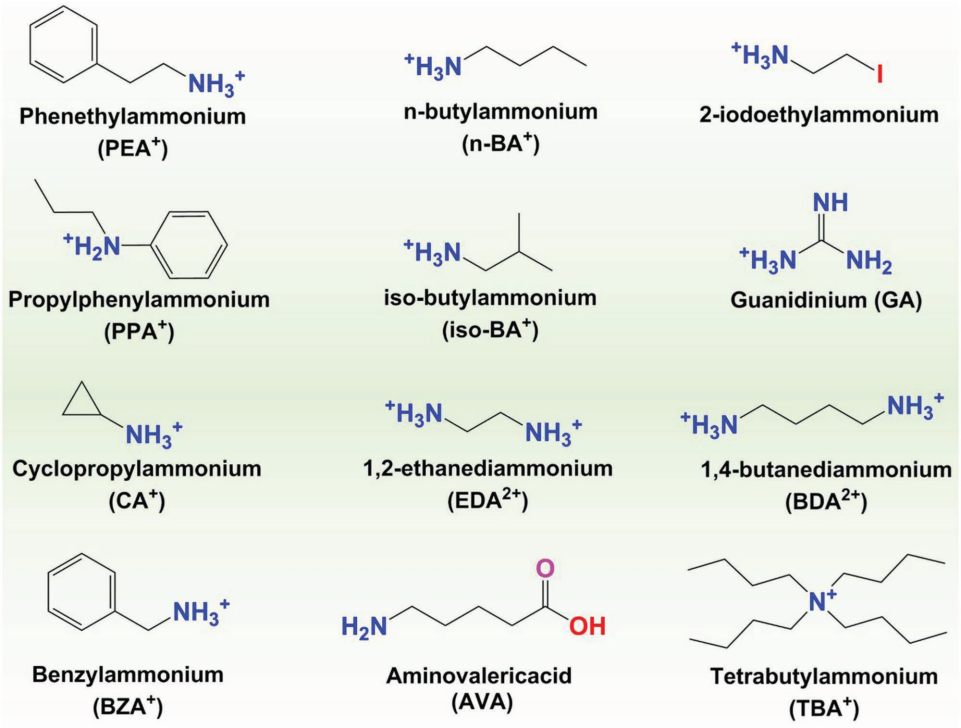
3. Mixed Dimensional (2D/3D) Perovskites for Photovoltaics

Compared to the benchmark 3D perovskites (e.g., $MAPbI_3$) that have been extensively studied since the seminal paper back in 2009,[11,47,48] much less effort has been devoted on mixed-dimensional perovskites although mixed-dimensional absorbers still exhibit well-tunable optical properties and offer improved stability under ambient conditions.[38] **Scheme 1** shows the chemical structure of the organic moieties that are commonly used at A-site.

3.1. 2D/3D Ruddlesden–Popper Lead (Pb) Based PSCs

In 2014, Karunadasa et al. were the first to introduce mixed-dimensional perovskite as an absorber layer for PSCs.[35] In this work, larger phenylethylammonium (PEA) and MA cations were mixed to obtain a Ruddlesden–Popper structure of composition $(PEA)_2(MA)_2[Pb_3I_{10}]$ ($(PEA)_2(MA)_{n-1}[Pb_nI_{3n+1}]$ for $n = 3$). This 2D perovskite exhibits a wider bandgap of 2.10 eV compared to 1.63 eV for the 3D $MAPbI_3$. The crystal structure of $(PEA)_2(MA)_2[Pb_3I_{10}]$ is shown in **Figure 4**a, where the 3D perovskite layer is separated by PEA chain to form a layered structure.[35] The PSCs were fabricated in a planar configuration using a compact TiO_2 layer and spiro-OMeTAD serving as an electron transporting material (ETM) and HTM, respectively. The back contact is ensured by a thin evaporated layer of gold on top of the HTM. Although the overall PCE remained comparatively modest, $\eta = 4.73\%$ under standard AM 1.5G conditions, interestingly a rather high open circuit voltage (V_{OC}) of 1.18 V was achieved. In addition, the authors demonstrated an enhanced structural robustness, exhibiting stability over 46 d of air exposure at a relative humidity level (RH) of 52%. For comparison, under same aging conditions, $MAPbI_3$ was completely degraded turning from brown to yellow after 46 d. Unfortunately, these results based on X-ray diffraction and UV–vis absorption spectroscopy were not supported by device performance evolution.

© 2018 WILEY-VCH Verlag GmbH & Co. KGaA, Weinheim



Scheme 1. Chemical structure of the ammonium cations reported in 2D/3D perovskite solar cells.

Further to this work, Sargent et al. investigated both stability and power conversion performances of the higher members of mixed dimensional $(PEA)_2(MA)_{n-1}[Pb_nI_{3n+1}]$ perovskites with $n = 6$, 10, 40, 60, and ∞.[49] In this work, ab initio density function theory (DFT) calculations on PEA-based perovskites suggest that bulkier organic moieties strengthen the Van der waals interactions between the inorganic layers. This leads to increased formation energy and improvement in the stability of the perovskites (Figure 4b). DFT calculations showed that the removal of phenylethylammonium iodide (PEAI) from $(PEA)_2(MA)_{n-1}[Pb_nI_{3n+1}]$ has an additional energy barrier of 0.36 eV compared to methylammonium iodide (MAI) counterpart, thus potentially an important means in the material's decomposition rate. The stability of the perovskite films was studied by UV–vis spectroscopy, X-ray diffraction (XRD), and time-resolved photoluminescence (TR-PL) techniques. These experimental techniques unraveled as expected the improved stability of the quasi-2D perovskites ($n = 10$, 40, 60) compared to the 3D equivalents on the one hand, and on the other hand they demonstrated that perovskites with lower n values (i.e., closer to 2D) are the most stable (Figure 4b). However, the devices with $n < 40$ show inferior performances owing to a lower carrier mobility leading to charge accumulation and thus an increase in radiative recombination losses. In the case of perovskites with $n < 10$, the lower performances were originating from a wider bandgap and poorer carrier transport. The best performing device was obtained with perovskite $n = 60$ which exhibited a power conversion efficiency of 15.3% under AM 1.5G conditions without hysteresis from backward versus forward scan. Unfortunately, these performances declined to 11.3% PCE after 60 d of storage under a low humidity atmosphere. This study put forward that high members of Ruddlesden–Popper phases with a dimensionality approaching to 3D have relatively poor stability as compared to lower members. This is the first study suggesting that a tradeoff "n" value exists between a high power conversion efficiency and more stable devices, thus prompting i) the optimization of 2D/3D mixed dimensional perovskites and ii) the exploration of other type of organic moieties to further prolong the device stability.

To continue this momentum given to the elaboration of 2D/3D mixed perovskites, Kanatzidis et al. introduced n-butylammonium (BA) cation within a series of homologous perovskites of general formula $(BA)_2(MA)_{n-1}Pb_nI_{3n+1}$, where $n = 1$, 2, 3, and 4.[50] This work gave major insights into the crystal structure versus optical properties relationship. One important key to address concern the film's texturation within 2D materials along the [001] direction perpendicular to the substrate's plane, an experimental observation also sometimes pointed out in the case of single-layer halide perovskites.[51] This preferential orientation is obtained because this direction corresponds to the denser atomic plane of the 2D perovskite. This was demonstrated in the case of $(BA)_2PbI_4$ for which X-ray diffraction patterns were showing exclusively the family of (00l) diffraction planes (**Figure 5**a). Such preferential orientation has also been noticed in powder suggesting a highly anisotropic growth of the particles along this direction. Regrettably, this growth orientation is harmful to the device performances as the carrier transport is expected to be the fastest within the plane and poorer perpendicular, thus penalizing a quantitative charge collection efficiency to be obtained. One interesting solution was already proposed. Indeed, the authors already found that the degree of texturation is a function of the n value. For example with low n value, more particularly for $n = 3$

© 2018 WILEY-VCH Verlag GmbH & Co. KGaA, Weinheim

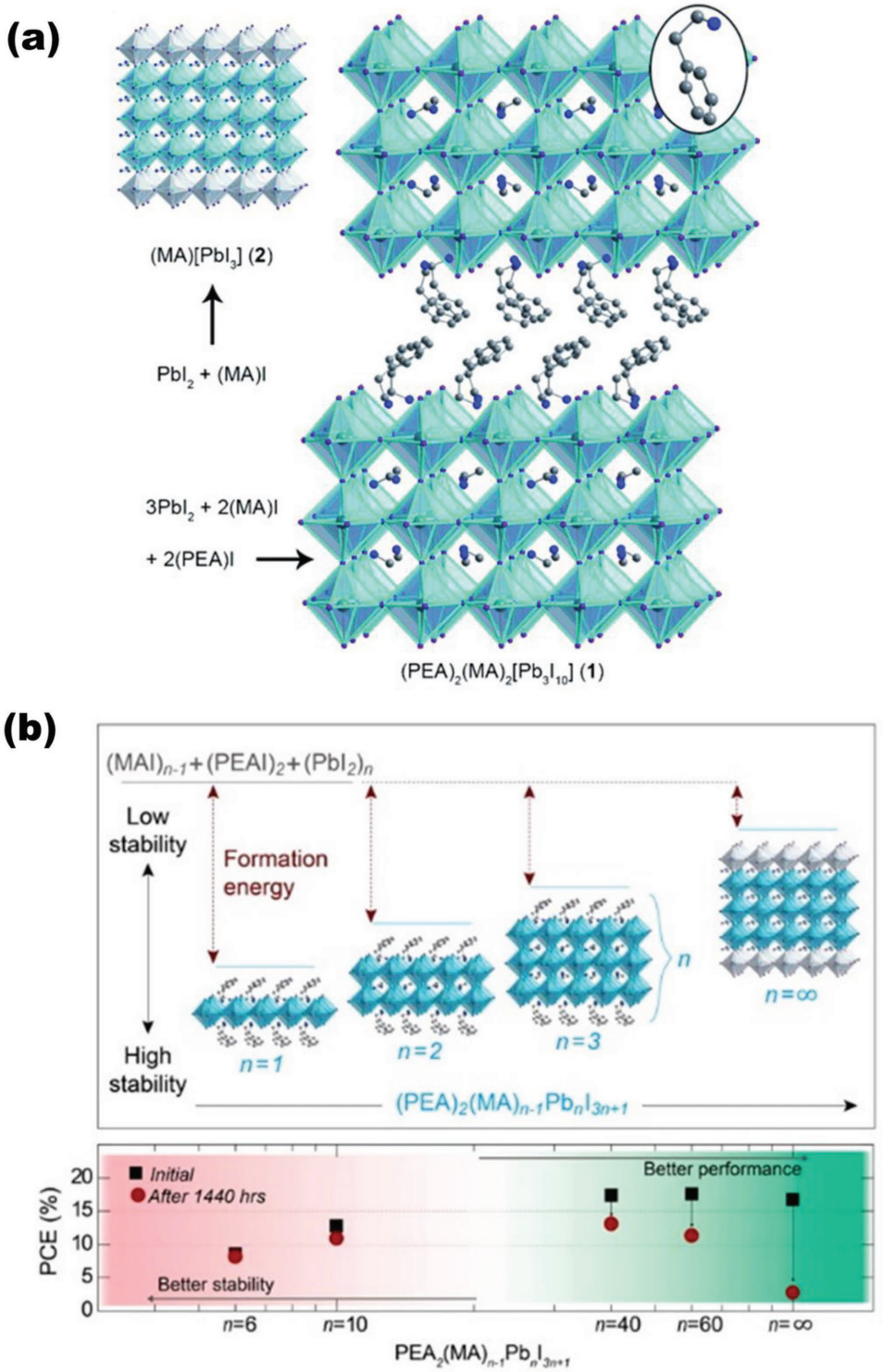


Figure 4. a) Crystal structures of 2D/3D perovskite, $(PEA)_2(MA)_2[Pb_3I_{10}]$ and 3D perovskite, $MAPbI_3$. Reproduced with permission.[35] Copyright 2014, Wiley-VCH. b) Unit cell structure of $(PEA)_2(MA)_{n-1}Pb_nI_{3n+1}$ perovskites and device performance with different *n* values. Reproduced with permission.[49] Copyright 2016, American Chemical Society.

and 4, another preferential growth along (111) and (202) becomes prominent, thus corresponding a diagonal vertical growth of the perovskites (Figure 5b). One possible explanation would be that as the number of layers (*n*) increases, MA^+, which has a tendency to expand the perovskite growth out of the plane layer dominates BA^+ which has a tendency to grow within the

© 2018 WILEY-VCH Verlag GmbH & Co. KGaA, Weinheim

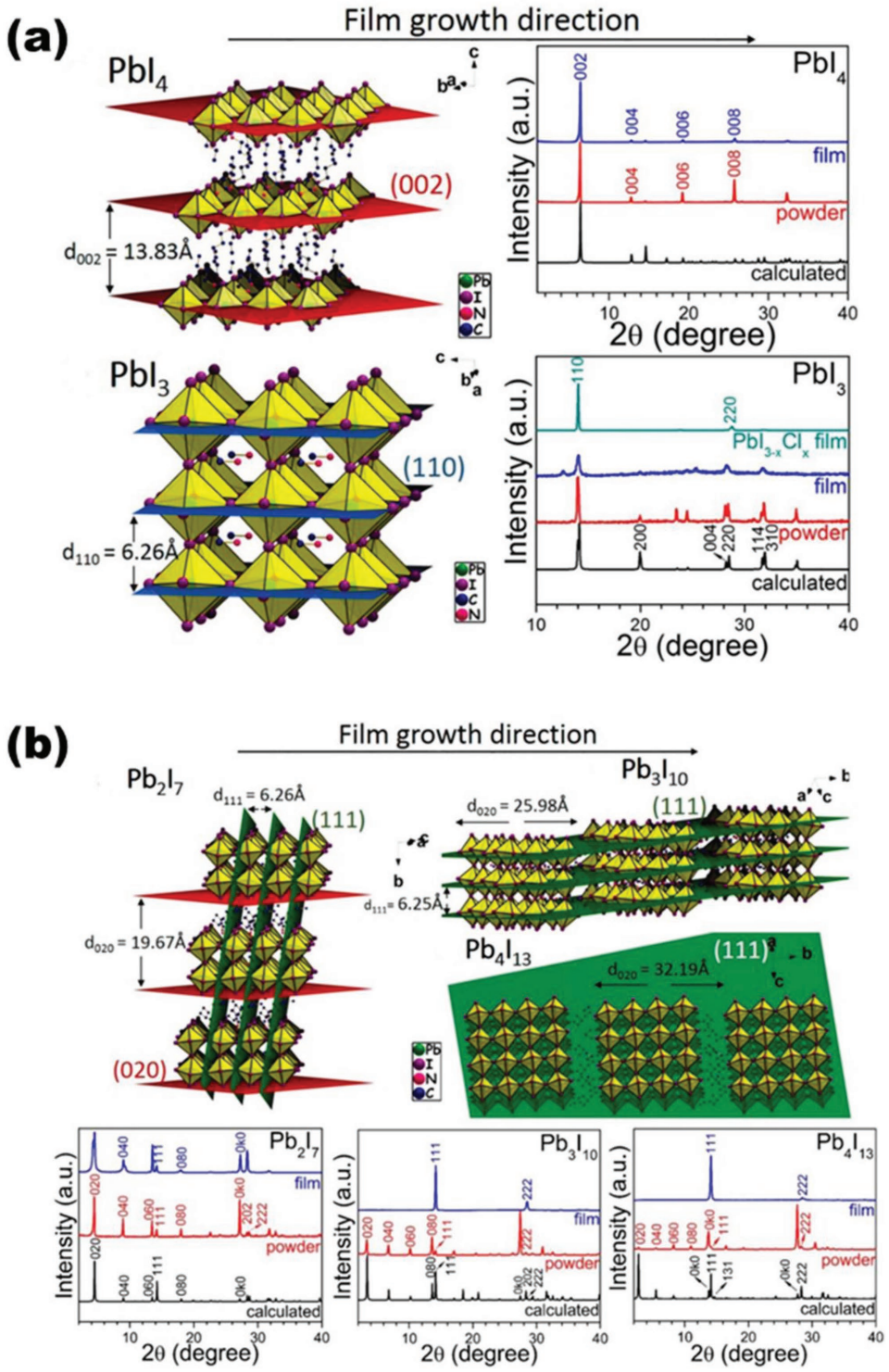


Figure 5. a) X-ray diffraction patterns of thin films versus bulk materials of BA_2PbI_4 and $MAPbI_3$ perovskites, with the illustration of the crystal structure along the preferential orientation. b) X-ray diffraction patterns of thin films versus bulk materials of $(BA)_2(MA)Pb_2I_7$, $(BA)_2(MA)_2Pb_3I_{10}$, and $(BA)_2(MA)_3Pb_4I_{13}$ perovskites, with the illustration of the crystal structure along the preferential orientation. Reproduced with permission.[50] Copyright 2015, American Chemical Society.

planar layer. The perpendicular growth of the perovskites to the substrate leads to a uniform, dense and well-packed film with an excellent surface coverage. Promoting vertical growth during the film deposition/crystallization offers a way to improve the electron collection along Pb-I-Pb pathway without perceptively affecting the hole transfer dynamic to the HTM.

© 2018 WILEY-VCH Verlag GmbH & Co. KGaA, Weinheim

Increasing the number of inorganic layers affords a narrowing of the bandgap value from 2.24 eV for $n = 1$ to 1.60 eV for $n = 4$. Interestingly, in addition to the redshifted absorption edge, one can observe the onset of a sharp absorption band after the absorption edge. This is ascribed to long-lived excitonic states which are harmful for the device operation. It is the result of a greater exciton binding energy which is penalizing the charge separation process and contributes to the overall energy losses within the device. This phenomenon is predominant for $n = 1$ compounds while they tend to disappear with the number of the inorganic slabs until $n = 4$ at which this phenomenon almost vanished. In this case, the photovoltaic devices were fabricated with a scaffold of mesoporous TiO_2 as ETM and spiro-OMeTAD as HTM. The best PCE of 4.02% was obtained by using $(BA)_2(MA)_2Pb_3I_{10}$ with an open-circuit voltage (V_{OC}) of 0.929 V and a short-circuit current density (J_{SC}) of 9.42 mA cm^{-2}. Although these characteristics are lagging far behind the 3D standards, $(BA)_2(MA)_2Pb_3I_{10}$ films show much longer term stability and resistance against moisture. The absorber structure can be preserved over 2 months under 40% relative humidity. This work is probably one of the most convincing toward the development of stable lead halide absorbers based on the mixed 2D/3D perovskite structure. The comparatively lower PCEs stem from the difficulties to efficiently collect the electrons as a result of the poor out-of-plane charge transport caused by the alternation of the insulating BA^+ units.

To try addressing this important issue, Mhaisalkar and co-workers proposed a two-step dipping approach leading to $(IC_2H_4NH_3)_2(CH_3NH_3)_{n-1}Pb_nI_{3n+1}$.[52] First, a pure 2D perovskite ($n = 1$) was spin coated using a precursor solution containing a stoichiometric ratio between lead iodide (PbI_2) and iodoethylammonium iodide ($IC_2H_4NH_3I$). Subsequently, the substrate was immersed into a solution containing MAI for a different time from 1 to 5 min to increase the stacking order and hence to convert it into a mixed-dimensional perovskite. With this methodology, the dipping time was highlighted to be crucial in controlling both the dimensionality and the orientation of the layered perovskite with respect to the substrate, i.e., the higher the dipping time, the higher the dimensionality as deduced from both absorption and PL spectra. In addition, the samples dipped for 4 and 5 min showed different crystal orientation than shorter dipping time with a preferential growth along (110) and (002) directions. This indicates that some crystals are oriented along the *c*-axis being close to perpendicular to the substrate's plane. These perovskites obtained within 5 min of dipping time exhibited good air stability, improved robustness under a relative humidity of 70–80% with and without encapsulation. Because of this improved orientation to enhance the charge collection efficiency, the authors achieved a remarkable power conversion efficiency of over 9% (J_{SC} = 14.88 mA cm^{-2}, V_{oc} = 0.883 V, and fill factor (FF) = 0.69) under AM 1.5G conditions.

In 2016, Mohite and co-workers reported a new efficient approach called hot-casting (HC) to improve both the stability and efficiency of 2D/3D structures. The HC technique, in which the substrate (fluorine doped tin oxide (FTO)/poly(3,4-ethylenedioxythiophene) polystyrene sulfonate [PEDOT:PSS]) is heated to ≈150 °C prior to the spin coating of the perovskite, produces higher quality thin films with preferential out of the plane alignment $(BA)_2(MA)_3Pb_4I_{13}$.[38] Following this methodology, the film's texture is modified with the occurrence of a preferential crystal growth along (111) and (202) planes. Such an orientation is beneficial toward the enhancement of the charge collection efficiency (**Figure 6**a–c). This translates first into a significant improvement in the device PCE reaching 12.5% (Figure 6d). The advantage of incorporating the 2D material in terms of stability is also demonstrated in this work, unencapsulated devices made of mixed-dimensional perovskite retain over 60% of their initial efficiency for over 2250 h under continuous incident light exposure at room temperature. This work also reported enhanced tolerance to 65% relative humidity compared to 3D perovskites (Figure 6e–h). Although such stability remains still far from IEC61646 specification, the device life-in-service can be markedly prolonged by a careful device encapsulation at end of fabrication. With this means, stability can be significantly enhanced not only under constant white light stress but also under a humid atmosphere. Very recently, the same group reported a fifth member $(BA)_2(MA)_4Pb_5I_{16}$ of $(BA)_2(MA)_{n-1}Pb_nI_{3n+1}$ family.[53] PSCs fabricated with HC method gave a PCE of 8.7% with an open-circuit photovoltage of 1.0 V. The main intent of this work was not to optimize the device performances but rather to investigate both physical and stability aspects of higher members of RP phase. The $(BA)_2(MA)_4Pb_5I_{16}$ film shows a partial degradation in presence of moisture which leads to the formation of $(BA)_2(MA)_2Pb_3I_{10}$ on one hand and $MAPbI_3.H_2O$ on the other hand. $MAPbI_3.H_2O$ is discarded from bulk material, an $n = 3$ RP perovskite "skin" develops, effectively protecting the material from further degradation. This very recent study calls for further investigations on higher "*n*" members of RP structure.

Chen et al. reported an RP perovskite based on a short branched iso-butylamine (iso-BA+) chain as the organic spacer leading to $(iso\text{-}BA)_2(MA)_{n-1}Pb_nI_{3n+1}$ composition.[54] The $n = 4$ compound, i.e., $(iso\text{-}BA)_2(MA)_3Pb_4I_{13}$, showed very interesting features such as an increase in optical absorption and crystallinity in comparison to the $(n\text{-}BA)_2(MA)_3Pb_4I_{13}$ counterpart. In addition, including a short branching of butylamine at the A site helps to bring the inorganic layers perpendicular to the substrate's surface and therefore the out-of-plane crystal orientation by chemical means. The out of the plane crystal orientation of $(iso\text{-}BA)_2(MA)_3Pb_4I_{13}$ film was notably enhanced as confirmed by grazing-incidence wide-angle X-ray scattering (GIWAXS), which dramatically improves charge transport toward their collection. Interestingly, the authors compared the carrier transport dynamic of *n*-BA with that of iso-BA by time-resolved terahertz spectroscopy (TRTS). The samples were measured at two different tilted angles (0° and 30°). The results demonstrated clearly that out-of-plane carrier mobility is significantly enhanced by almost two orders of magnitude by the inclusion of a short branching of BA at the A site. The authors measured by TRTS a carrier mobility of 1.35 cm^2 V^{-1} s^{-1} compared to less than 0.01 cm^2 V^{-1} s^{-1} for the *n*-BA counterpart. This greater mobility obtained with $(iso\text{-}BA)_2(MA)_3Pb_4I_{13}$ film, which would translate in the device performance by an enhancement of charge collection efficiency, stems in part or in whole from a textural effect of the film showing the out-of-plane orientation of the absorber. The $(iso\text{-}BA)_2(MA)_3Pb_4I_{13}$-based inverted planar solar cell of $ITO/C_{60}/(iso\text{-}BA)_2(MA)_3Pb_4I_{13}$/spiro-OMeTAD/Au fabricated at room-temperature exhibited a PCE of 8.82%. This is three times greater than the performances obtained within the

© 2018 WILEY-VCH Verlag GmbH & Co. KGaA, Weinheim

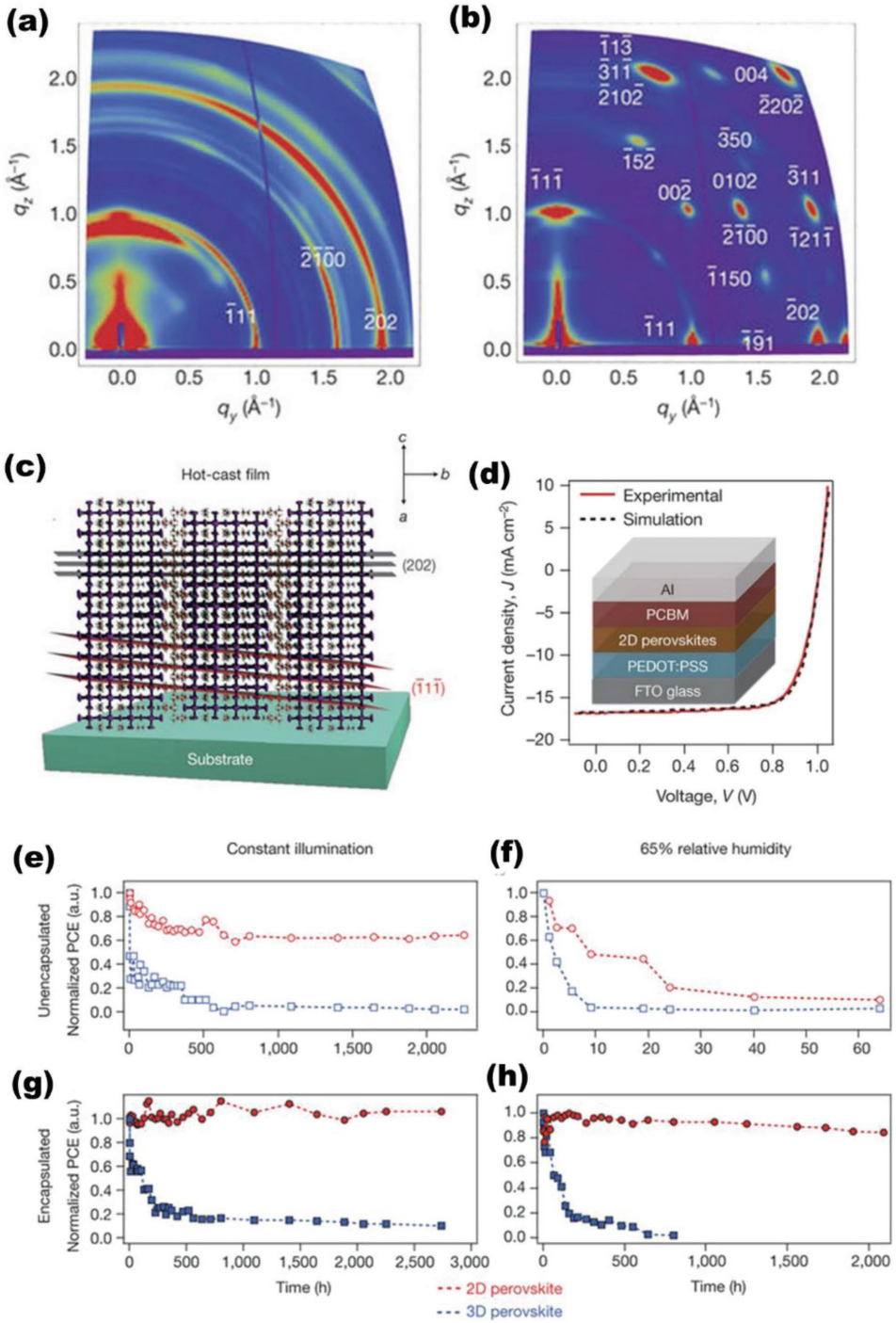


Figure 6. a) GIWAXS maps for polycrystalline room-temperature-cast and b) hot-cast, near single- crystalline $(BA)_2(MA)_3Pb_4I_{13}$ perovskite films with Miller index of the most prominent peaks shown in white. Color scale is proportional to X-ray scattering intensity. c) Schematic representation of the (101) orientation, along with the (111) and (202) planes of a 2D perovskite crystal, consistent with the GIWAXS data. d) Experimental (red line) and simulated (black dashed line) current density–voltage (*J*–*V*) curves under an AM 1.5G solar simulator for planar devices using 2D $(BA)_2(MA)_3Pb_4I_{13}$ perovskites as the absorbing layer at an optimized thickness (230 nm). The inset shows the device architecture. Stability measurements on planar solar cells (e) and (g) under constant light illumination (AM 1.5 G), (f) and (h) under 65% humidity environment; (e) and (f) are not encapsulated whereas (g) and (h) are encapsulated. Reproduced with permission.[38] Copyright 2016, Nature Publishing Group.

same configuration with $(n\text{-BA})_2(MA)_3Pb_4I_{13}$. This again stresses that 2D/3D performance optimization requires a careful control of the film's texture. This work stands as the first example demonstrating that the out-of-plane texturing in the film growth can be achieved by introducing molecularly engineered organic cations. By combining this synthetic approach with the HC

 © 2018 WILEY-VCH Verlag GmbH & Co. KGaA, Weinheim

methodology, the performances were further improved to a PCE of 10.63% in a planar configuration. Note that with this configuration and elaboration procedure, an important hysteresis has been reported, probably as a result of charge accumulation and poor extraction at the C_{60}/perovskite interface. The improved robustness of (iso-BA)$_2$(MA)$_3$Pb$_4$I$_{13}$ absorber is verified without any encapsulation against moisture and oxygen exposure. Thus, the optical properties of the absorber did not show any degradation even after continuous exposure for >840 h in an environmental chamber at 20 °C with an RH of 60%.

Following the same strategy to achieve out-of-plane film's texturation, Chen et al. reported a series of low bandgap absorbers lying between 1.82 and 1.51 eV using BA and formamidinium (FA) cations, i.e., $(BA)_2(FA)_{n-1}Pb_nI_{3n+1}$ (n = 1–5).[55] As in the previous cases, a strong preferential out-of-plane orientation of the film is achieved for $(BA)_2(FA)_2Pb_3I_{10}$ as a result from the introduction of butylammonium in the A site and the addition of thiourea in the precursor. In good agreement with previous other works, the authors also pointed out the beneficial effect of this film's texturation to improve the charge collection efficiency. In the following planar inverted configuration, i.e., ITO/PEDOT: PSS/$(BA)_2(FA)_2Pb_3I_{10}$/PC61BM/bathocuproine (BCP)/Ag, the authors reached at best a power conversion efficiency of 6.88% under standard conditions with n = 4 composition. Stability enhancement is also demonstrated on non-encapsulated devices with PCE retention of ≈80% over 600 h aging in air under a relative humidity of (25 ± 5)%.

As aforementioned, the interaction between the organic and the inorganic layers can potentially influence the film's texturation and also contribute to the optoelectronic properties (i.e., bandgap value, exciton binding energy, etc.).[56] Most of the current work is focusing on mixed dimensional perovskites using monoammonium cations such as BA and PEA which interacts on one side of the inorganic layer. This creates consequently a Van der waals gap between the organic and inorganic layers which makes the perovskite unstable. Multiammonium cation can overcome this lack of stability as they can electrostatically bind with the two adjacent inorganic layers,[57] leading to the more robust structure. A new series of RP phase perovskites containing polyethyleneimine (PEI) cations $(PEI)_2(MA)_{n-1}Pb_nI_{3n+1}$ with n = 3, 4, 5, and 7) were reported by Zhou and co-workers.[58] The advantage of PEI cation lies in their multiple amines which afford to obtain a tighter stacking of adjacent inorganic layers, thus increasing the structural stability and also enhancing the charge transport. The charge transport within the layers and the quality of perovskite films containing PEI were improved by enhancing the electronic integration in the adjacent layers[59] as compared to those using small-molecule BA and PEA. The PCE obtained is 8.77% under standard AM 1.5G conditions in an inverted configuration with a V_{OC} and J_{SC} value of 1.0 V and 11.7 mA cm^{-2}, respectively. Simultaneous to this work, Jiang et al. reported a new layered hybrid perovskite film (EDA)(MA)$_2$[Pb$_3$I$_{10}$] which incorporated ethylenediamine (EDA) cations.[60] PSCs fabricated using this perovskite (EDA)(MA)$_2$[Pb$_3$I$_{10}$]) in mesoporous configuration yielded a PCE of 11.58%, FF of 56%, a J_{SC} of 16.57 mA cm^{-2} and a V_{OC} of 1.24 V. It was demonstrated that 2D perovskite films based on EDA yielded to a dense and a compact microstructure while 3D perovskites film consisted of independent microsized grains. The external dense layer of (EDA)(MA)$_2$[Pb$_3$I$_{10}$] protects the inner layer from degradation. Therefore, the stability of such a device showed higher resistance against humidity compared to 3D PSCs. Very recently Ma et al. reported a series of perovskite (PDA)$(MA)_{n-1}Pb_nI3_{n+1}$ (n = 2, 3, and 4) by incorporating propane-1,3-diammonium (PDA) cations.[61] A reduced interlayer distance around 2 Å was observed in PDA-based 2D perovskites, which is shorter than the more traditionally used BA-based 2D perovskites with a distance about 7 Å. This special structure suppressed the quantum confinement effect, leading to efficient charge separation and fast carrier mobilities. As a result, the solar cells fabricated using PDA$MA_3Pb_4I_{13}$ with the configuration of ITO/PEDOT: PSS/perovskites/C_{60}/BCP/Ag achieve a PCE of 13.0%. Furthermore, PDA-based 2D PSC retains 99% of its initial efficiency after 100 h when kept in dark under continuous heating at 70 °C and 85% RH. These results reveal the excellent performances of the 2D perovskite with short interlayer distance and provide an alternative approach for improving the efficiency and stability of 2D perovskites.

3.2. Halide Substitution in 2D/3D Ruddlesden–Popper Perovskites

Iodide is the most commonly used halide in these 2D phases. Their richness in composition affords broadly tunable optoelectronic properties that still prompt for further exploration. For instance, in analogy to the 3D counterpart, substitution of iodide with bromide widens the bandgap value. Although this substitution limits the absorption capability from blue to orange, in turn, it affords not only to increase the photovoltage output by limiting energy losses in the charge transfer processes, but it also enhances the device stability as demonstrated by Cai et al. and Edri et al.,[62,63] Etgar and co-workers replaced iodide with bromide within a higher member of RP phases $(PEA)_2(MA)_{n-1}Pb_nBr_{3n+1}$ (n = 40, 50, 60).[64] They demonstrated in their work the possibility to obtain very high photovoltage reaching as high as 1.46 V for an absorber having ≈2.25 eV bandgap value. The authors obtained a power conversion efficiency of 8.5% (J_{SC} = 9 mA cm^{-2}, V_{OC} = 1.46 V, and FF = 65%) under AM 1.5G conditions using a mesoporous configuration. One possible explanation lies in the lower carrier mobility in quasi-2D perovskites, improved charge extraction and lower recombination rate as supported by both ab initio calculations and charge extraction measurements. Unfortunately, no information related to the stability of these absorbers are mentioned. Still based on bromide, the same group continued to explore various organic long cations such as benzylammonium (BA), PEA, and propylphenylammonium (PPA).[65] Interestingly, the authors highlighted that the exciton binding energy was not influenced by the type of the A site (i.e., 310–320 meV for n = 1 for all organic moieties). This experimental work associated to DFT calculations including spin–orbit coupling showed in the case of BA that holes are entirely delocalized over the whole molecule by contrast to PEA and PPA in which hole carriers are more localized within the phenyl ring. Such a modification of carrier distribution is influencing the holes conductivity for which one can anticipate better photovoltaic properties with BA than PEA and PPA. In addition, the energy onset for the

© 2018 WILEY-VCH Verlag GmbH & Co. KGaA, Weinheim

nonzero electronic conductivity is lowest for BA. These calculations provide further insight in consistency with experimental evidences showing best power conversion efficiencies on BA (PCE = 9.5%), compared to PEA (PCE = 8.6%) and PPA (PCE = 7.1%) in mesoporous configuration. The devices with these quasi 2D perovskites were also more stable than 3D perovskite devices under ambient air.

3.3. 2D/3D Heterostructure and Bilayer Lead Based PSCs

Another approach to improve device stability has been explored where the 2D perovskite is combined with the 3D counterpart to form a 2D/3D heterostructure or 2D/3D bilayered structure. Docampo et al. were the first to propose the two layers approach in 2D/3D perovskite solar cells.[66] In their configuration, a thin layer of 2D perovskite $(PEA)_2(MA)_4Pb_5I_{16}$ is sheltering the standard 3D $MAPbI_3$. The subsequent spin-coating deposition, first $MAPbI_3$ followed by $(PEA)_2(MA)_4Pb_5I_{16}$ also leads to a mutual effect which translates into a reorganization/reorientation of the $MAPbI_3$ underlayer. With this configuration, devices reached a PCE of 14.94% (J_{SC} = 18.63 mA cm^{-2}, V_{OC} = 1.08 V, and FF = 0.73), whereas pure methyl ammonium lead iodide (MAPI)-based devices showed a PCE of 13.61% (J_{SC} = 19.82 mA cm^{-2}, V_{OC} = 1.08 V, FF = 0.70). The increase in V_{OC} and FF is due to reduced recombination losses. Such a two layers configuration improves the device stability on the one hand and provides an additional moisture barrier from the under-3D layer.

Ma et al. reported a similar bilayer configuration obtained by depositing a thin layer of cyclopropylammonium iodide over the 3D $MAPbI_xCl_{3-x}$ perovskite.[67] The thin layer of 2D CA_2PbI_4 perovskite increases the moisture resistance of the perovskite films while maintaining excellent optoelectronic properties. Compared with 3D perovskites, 2D/3D perovskite showed significant improvement in moisture stability of films and unsealed devices in a high humidity of 63 ± 5%. The 2D/3D perovskite film did not undergo any degradation even after 40 d, while the 3D perovskite degraded completely under the same conditions only after 8 d. The 2D/3D perovskite devices maintained 54% of the original efficiency after 220 h of aging, whereas the 3D perovskite device completely degraded within 50 h only. More interestingly, 2D/3D hybrid perovskite achieved comparable device performances (PCE = 13.86%, J_{SC} = 19.29 mA cm^{-2}, V_{OC} = 0.92 V, FF = 77.26%) as compared to 3D perovskites (PCE = 13.12%, J_{SC} = 18.50 mA cm^{-2}, V_{OC} = 0.92 V, FF = 76.55%).

Most of the work on 2D/3D mixed dimensional perovskites are focusing on MA cation within the A site. Lately, this understanding has been extended to FA as well as to Cs^{2+} cation with the final aim to replace toxic lead as well as to maximize the device stability. For instance, Jen and co-workers fabricated mixed-cation $FA_xPEA_{1-x}PbI_3$ perovskites by changing the molar ratio (x) between formamidinium iodide (FAI) and PEAI.[68] The larger PEA cation was self-assembled on both lattice surface and grain boundaries to form a quasi-3D perovskite structure and served as a molecular lock to tighten the $FAPbI_3$ domains. Thus, the free enthalpy to turn from the black phase to the yellow phase is raised in energy, thus offering more robust phase stability. In addition, the optical absorbance of $FA_xPEA_{1-x}PbI_3$ films with n of 20–60 was increased in comparison to that of the pristine $FAPbI_3$, thus suggesting a role played by PEA^+ in enhancing the film's crystallinity without modifying the bandgap value ($E_g \approx 1.52$ eV) for $n \geq 10$. The improved crystallinity is demonstrated by the narrowing in the full width at half maximum of the related diffraction peaks in the XRD diffraction pattern. After evaluation of the effect of n value on the power conversion efficiency, n = 40 composition afforded to obtain the best performances, namely PCE = 17.7% (J_{SC} = 22.08 mA cm^{-2}), V_{OC} = 1.04 V, FF = 77.14%) using the following inverted configuration ITO/NiO_x/$FA_xPEA_{1-x}PbI_3$/phenyl-C61-butyric acid methyl ester (PCBM)/C_{60}/Ag.

Snaith et al. introduced BA cation into a mixed-anion iodide/bromide $FA_{0.83}Cs_{0.17}Pb(I_{0.6}Br_{0.4})_3$ 3D perovskite.[69] By modifying the BA content, platelet-like particles are orientated perpendicularly to the substrate plane. These platelets are embedded between 3D perovskite grains to form a heterostructure. 2D-XRD, scanning electron microscopy (SEM), and TR-PL confirmed the presence of this heterostructure within the perovskite film. This particular heterostructure seems responsible for improved crystallinity and passivating surface defects, controlling nonradiative recombination. It leads to a combination of the beneficial effect for the device operating, namely an attenuation in the well-known current–voltage hysteresis, improved PCE and stability. Solar cells with an optimal butylammonium content exhibit an average power conversion efficiency of 17.5% (±1.3%) with a 1.61 eV bandgap perovskite $[BA_{0.09}(FA_{0.83}Cs_{0.17})_{0.91}Pb(I_{0.6}Br_{0.4})_3]$ and 15.8% (±0.8%) with a 1.72 eV bandgap perovskite $[BA_{0.05}(FA_{0.83}Cs_{0.17})_{0.91}Pb(I_{0.8}Br_{0.2})_3]$. The performances maintained 80% of their "post burn-in" efficiency after 1000 h exposure to air and closed to 4000 h when encapsulated. Since one degradation path of the perovskite proceeds via active defects,[70] therefore defect passivation positively impact on the long-term stability of the device.

Along such line, Nazeeruddin et al. were the first to achieve 1-year stable solar cell by engineering a multidimensional junction made of 2D/3D perovskite $(HOOC(CH_2)_4NH_3)_2PbI_4$/$CH_3NH_3PbI_3$.[71] The 2D/3D composite was formed by mixing at different molar ratios (0%, 3%, 5%, 10%, 20%, and 50%) (aminovaleric acid iodide ($COOH(CH_2)_4NH_3I$), AVAI:PbI_2) and (CH_3NH_3I:PbI_2) precursors. In the perovskite formed with 3% AVAI, very sharp spectroscopic Raman bands were experienced, suggesting a more ordered crystal packing of the 2D/3D film compared to the pure 3D phase. Interestingly, for this composition, the family of X-ray diffraction peaks (00l) decreases in intensity in favor of the (hh0) planes, thus indicating preferential orientation in the film. 2D RP only appears for AVAI content greater than 10%. This suggests that the perovskite film formed with 3% AVAI is highly heterogeneous, likely constituted by a very thin layer of 2D perovskite forming on top of the highly textured tetragonal 3D perovskite; PSCs were fabricated with this 2D/3D perovskite using two configurations viz. with a mesoporous scaffold and a fully printable HTM-free configuration, where the HTM and gold were substituted with a carbon matrix (**Figure 7**a). Both small area cells (0.64 cm^2) and larger area 10 × 10 cm^2 solar modules were fabricated. The absorbers with 3% AVAI showed the best PCE of reaching 14.6% on small devices (Figure 7b). Stability was improved compared to the standard 3D $MAPbI_3$. PCE retention was maintained up to 60% of the initial value after 300 h of continuous illumination under Ar at 45 °C. (Figure 7c). For printable HTM-free architecture, the small cell

© 2018 WILEY-VCH Verlag GmbH & Co. KGaA, Weinheim

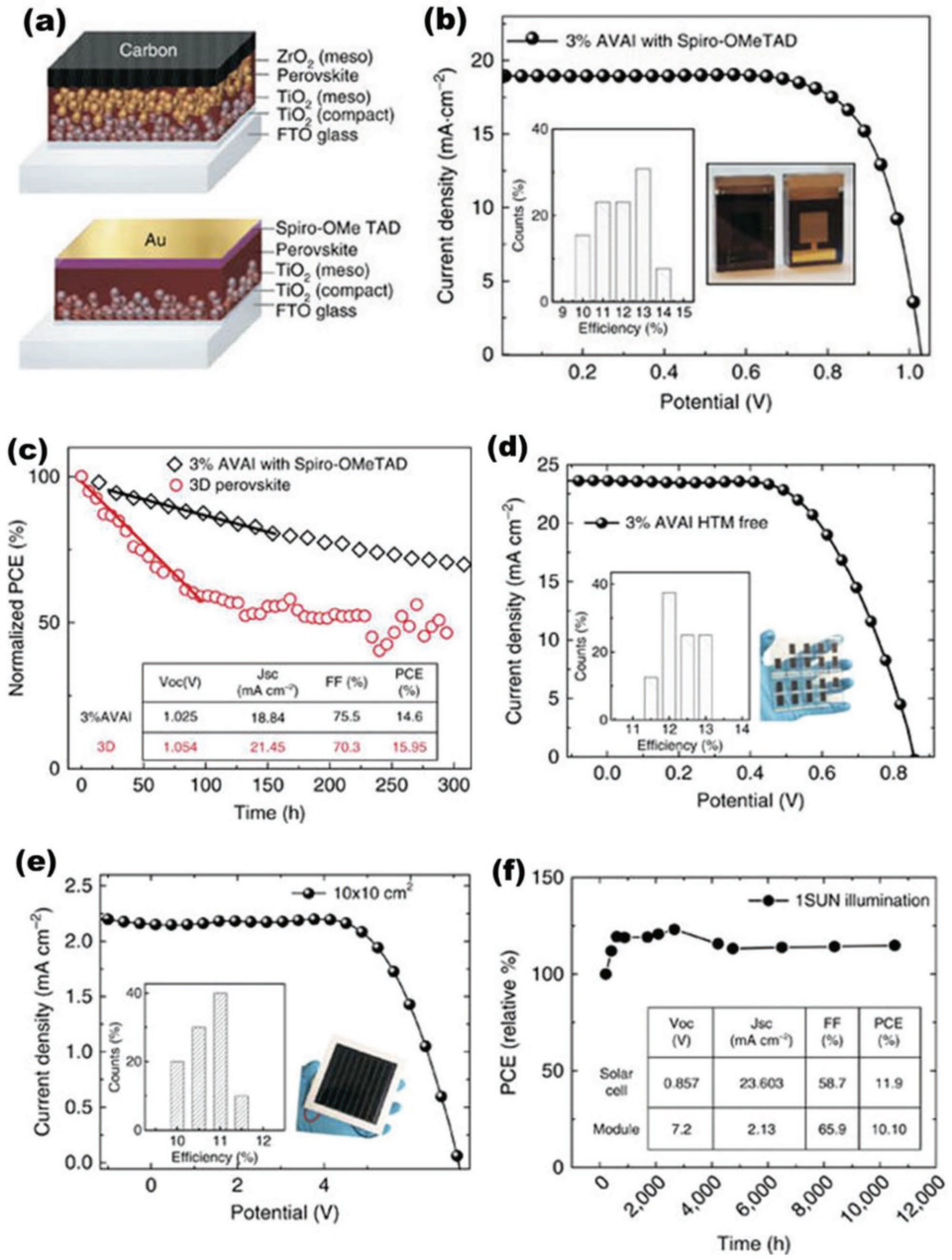


Figure 7. a) Device scheme of the hole transporting material (HTM)-free solar cell and of the standard HTM-based solar cell. b) Current density–voltage (*J*–*V*) curve using the 2D/3D perovskite with 3% $HOOC(CH_2)_4NH_3I$, AVAI hereafter, in a standard mesoporous configuration, using spiro-OMeTAD)/Au (devise statistics and picture of the cell in the inset). c) Stability curve of the Spiro-OMeTAD/Au cell comparing standard 3D with the mixed 2D/3D perovskite at maximum power point under AM 1.5G illumination, argon atmosphere and stabilized temperature of 45 °C. Solid line represents the linear fit. In the inset the champion device parameters are listed. d) (*J*–*V*) curve using the 2D/3D perovskite with 3% AVAI in HTM-free solar cell measured under air mass (AM) 1.5G illumination (device statistics and picture in the inset). e) (*J*–*V*) curve using the 2D/3D perovskite with 3% AVAI in an HTM-free 10×10 cm^2 module (device statistics and picture in the inset). f) Typical module stability test under 1 sun AM 1.5 G conditions at a stabilized temperature of 55 °C and at short circuit conditions. Stability measurements were done according to the standard aging conditions. Reproduced under the terms of the Creative Commons Attribution 4.0 International License (CC BY 4.0).[71] Copyright 2017, the authors, published by Nature Publishing Group.

and the 100 cm^2 module delivered a PCE of 12.71% and 11.2%, respectively (Figure 7d,e). The module retained outstanding air-stability by maintaining a PCE of 11.2% over 10 000 h (≈1 year) without any losses at a stabilized temperature of 55 °C under AM 1.5G conditions and at short-circuit conditions (Figure 7f).

Poli et al. incorporated a large amphiphilic tetrabutylammonium (TBA^+) cation into the 3D $MAPbI_3$ perovskite leading to the formation of $(TBA)_n(MA)_{1-n}PbX_3$ where X is I^- or Cl^-.[72] TBA^+ is an interesting cation as it confers more hydrophobicity to the hybrid perovskites. As for optimization, TBA^+ was added into different molar ratio along the precursor solution

© 2018 WILEY-VCH Verlag GmbH & Co. KGaA, Weinheim

containing MAI. The structural analysis employing XRD suggested the coexistence of two distinct phases: a 3D perovskite layer and a 2D layered perovskite. Because of its large ionic radii (494 pm),[73] TBA^+ may segregate toward the surface of the 3D perovskite grains, thus forming a shell of 2D sheets and intralayers at the perovskite/Spiro-OMeTAD interface. Interestingly, although it may be process dependent, the films containing TBA^+ are exhibiting better surface coverage with only fewer pinholes compared to the reference $MAPbI_3$ films. Mixed 2D/3D structures showed very comparable photovoltaic performances than the standard 3D $MAPbX_3$, with PCE of 9.95% (V_{OC} = 0.85 V, J_{SC} = 20.82 mA cm^{-2}, FF = 0.56) for 1 mol% of TBA^+. The advantage of the TBA^+ is again nested in the stability improvement. Indeed, higher contact angles with water were measured for mixed cation films confirming the greater hydrophobic character of this absorber. When aged in darkness under ambient conditions (40 ± 20% relative humidity), the PCE for the TBA-based device was found very stable for over 1000 h.

A new family of layered perovskites based on guanidinium cation as a spacer has been reported by Kanatzidis et al. leading to the formula $(C(NH_2)_3)(CH_3NH_3)_nPb_nI_{3n+1}$ (n = 1–3).[74] These perovskites contain Alternating Cations in the Interlayer space (ACI) which leads to different stacking motif and higher crystal symmetry compared to the related RP phases. These materials are optically interesting as they exhibit a narrower bandgap than RP structures while they monotonically decrease with the n value: E_g = 2.27, 1.99, and 1.73 eV for n = 1, 2, and 3, respectively. Theoretical calculations suggested that these new perovskites have small exciton binding energy which is beneficial for charge transport. The solar cells fabricated using $(C(NH_2)_3)(CH_3NH_3)_3Pb_3I_{10}$ as an absorber showed a PCE of 7.26% in a planar configuration with an impressive FF of ≈80%, moderate J_{SC} = 9.36 mA cm^{-2} and V_{OC} = 0.974 V. Despite the PCE value and further information related to their photophysical properties, this work reveals the superior optoelectronic properties of the 2D ACI perovskites compared to RP phases which establish a high credibility of this new class of materials for the application.

Ran et al. designed a 2D-3D perovskite with a stacking layer by in situ growing 2D PEA_2PbI_4 capping layers on top of the 3D perovskite $Cs_{0.05}(FA_{0.83}MA_{0.17})_{0.95}Pb(I_{0.83}Br_{0.17})_3$ film.[75] This architecture drastically improves the device stability without compromising the device performance. The capping layer based on 2D perovskite induces a larger Fermi-level splitting and reduces recombination losses as deduced by time-resolved photoluminescence study. This contributes to generate a higher V_{OC} (1.11 V) and high power conversion efficiency of 18.51% (FF = 0.73, J_{SC} = 22.89 mA cm^{-2}) compared to 17.02% for the 3D counterpart. The downward shift of the quasi-Fermi level calculated by kelvin probe force microscope (KPFM) method also explains the origin of the V_{OC} enhancement. The improved stability of this structure is demonstrated by 90% retention of the PCE after 1000 h exposure in a humid environment (RH 60% ± 10%).

With a similar approach, Lin et al.[76] tailored a 2D/3D stacking structure by a reaction between n-butylamine (BA) with the surface of 3D perovskite. The introduction of a thin 2D perovskite layer on the surface and/or at the grain boundaries of 3D perovskites affords to enhance the stability of the devices against thermal stress. In addition, the thin 2D layers also play the role of defects passivation which translates into a reduction in density for intrabandgap trap states. The devices fabricated in ITO/poly(triarylamine) (PTAA)/Perovskite/PCBM/C_{60}/BCP/Cu configuration showed PCE as high as of 19.56% under standard AM 1.5G conditions. The stability of nonencapsulated devices was evaluated at an elevated temperature of 95 °C. The control $MAPbI_3$ devices showed a PCE retention of 69.8% after continuous heating for 100 h compared to as high as 96.5% for the perovskite treated with BA.

Very recently, Ye et al. fabricated a bilayer structure of $2D[(AVAI)_2PbI_4]/3D(MAPbI_3)$ by utilizing an in situ growth route via flash annealing.[77] The $MAPbI_3$ was spin coated then rapidly (3, 5, and 10 s) annealed at 300 °C. Subsequently, the 5-aminovaleric acid iodide ($HOOC(CH_2)_4NH_3I$, AVAI) solution in isopropanol was spun coated on the 3D perovskite. The high temperature (300 °C) flash-annealing process led to removal surface MAI from Pb-I framework in 3D perovskite, which subsequently interacts with the AVAI molecules to yield a better interface between the 3D and 2D phases. Authors suggest that the deposition of the AVAI solution results in the formation of 2D perovskite, possibly into an $(AVA)_2PbI_4$ structure at the surface, forming the 2D@3D perovskites. The amine and carboxyl functional groups of AVAI can interact with the 3D perovskite through hydrogen-to-halogen bonding, allowing better 2D/3D interfaces and hence lower recombination at the 2D/3D interface. The devices fabricated with 2D@3D perovskite annealed for 5 s showed a high PCE of 18.0% (J_{sc} = 22.3 mA cm^{-2}, V_{oc} = 1.06 V, FF = 76%) and enhanced device stability (retaining 72% of their initial efficiency after 20 d at 40% RH) as compared with their 3D counterparts, $MAPbI_3$ (PCE = 17.3%, retained 40% of their initial efficiency after 20 d). This bilayered 2D@3D perovskite fabrication approach provides a simple and universal solution for efficient and ambient-air-stable perovskite film and device fabrication.

Hu et al. fabricated 2D/3D heterostructure by combining high-performance lead-based 3D perovskite $MAPbI_3$ with moisture resistant bismuth-based quasi-2D perovskite $MA_3Bi_2I_9$.[78] For a content of up to 9.2% of 2D in 3D, the authors demonstrated that the hydrophobic platelets are formed vertically in the film mesostructure playing the role of defect passivation of $MAPbI_3$ grain boundaries. This led to a reduction in nonradiative recombination dynamic. The device fabricated with 9.2% 2D in 3D achieved the best performances in terms of power conversion efficiency attaining 18.97% under AM 1.5G condition compared to 16.83% for the 3D $MAPbI_3$. The beneficial effect of the 2D on stability is demonstrated in this study. The authors reported 72.3% PCE retention subsequently to 1000 h exposure in ambient conditions.

3.4. 2D/3D Lead (Pb) Free Based PSCs

The state of the art related to high-performance PSCs is systematically involving lead (Pb) as the divalent cation. Its use has a major concern for environmental toxicity and has stringent disposal regulations at a different level depending on geography. The chemical decomposition of 3D $MAPbI_3$ or $FAPbI_3$ proceeds

© 2018 WILEY-VCH Verlag GmbH & Co. KGaA, Weinheim

through the release of Pb^{2+} which has a large solubility in water (K_s: 1×10^{-8}) and accumulates inside the human body without natural elimination.[79] Consequently, alternative divalent metal cations such as Sn^{2+}, Ge^{2+}, and Bi^{3+} have been explored, unfortunately without triumphal results, as they suffer from lower power conversion performances and/or extremely poor stability. Tin lags far behind lead because the Sn^{2+} valence state is particularly unstable conversely to the tetravalent state. Its introduction causes a perceptible bandgap narrowing, E_g = 1.55 eV for $MAPbI_3$ versus 1.20 eV for $MASnI_3$.[80]

Recently, few groups have focused on the introduction of Sn in 2D/3D RP phase to narrow the bandgap of the absorber for improving the device performance while maintaining at least their better stability. Kanatzidis et al. were the first to elaborate PSCs based on tin Ruddlesden–Popper $(BA)_2(MA)_{n-1}Sn_nI_{3n+1}$ perovskites (n = 1–5).[81] To improve both processability and repeatability, triethylphosphine was used as an antioxidant into the precursor solution to avoid Sn^{2+} oxidation to Sn^{4+}. High-quality perovskite films were obtained with a bandgap of 1.83 eV for n = 1 down to 1.2 eV for $n = \infty$, which verifies the lower bandgap value of Pb^{2+} counterpart. The excitonic peak contributing to internal energy losses for exciton dissociation was only observed for $(BA)_2SnI_4$ composition. It disappears in the other member of this family, conversely to Pb^{2+} counterpart in which an excitonic band was systematically perceived regardless of the "n" value. Consequently, the introduction of tin within the structural can be seeming as a chemical mean to lower energy losses by favoring the exciton dissociation. In their work, the authors also pointed out the film texturation depends on the solvent characteristics. For instance, using dimethylsulfoxide, the perovskite layers were oriented parallel to the substrate by contrast to the *N,N*-dimethylformamide for which this latter becomes oriented perpendicular to the substrate.[81] Nevertheless, the power conversion efficiency of the devices remained modest, a PCE = 1.94% for n = 3 and PCE = 2.5% for n = 4 using an inverted configuration were reported. Nevertheless, as one could anticipate based on the acquired knowledge of lead-based materials, the 2D/3D perovskites made of tin are exhibiting improved stability than pure 3D $MASnI_3$. The encapsulated devices retained more than 90% of their initial PCE after 1 month storage at ambient conditions owing to the hydrophobic character of the long BA chains.

Soon after, Liao et al. reported the Sn-based mixed dimensional perovskites $(PEA)_2(FA)_{n-1}Sn_nI_{3n+1}$.[82] The orientation of the crystals to improve the charge collection was controlled by optimizing the PEA/FA ratio. At a PEA ratio of 20 mol%, the inorganic layers were mainly oriented perpendicular to the substrate. Moreover, first principle calculations showed that $(PEA)_2(FA)_{n-1}Sn_nI_{3n+1}$ would possess a higher energetical stability with respect to the oxidation disproportionation mechanism. The best power conversion performances were obtained with $PEA_2FA_8Sn_9I_{28}$ (n = 9) composition with a PCE = 5.94% using an inverted configuration. Unencapsulated devices were found to be stable up to 100 h under ambient conditions. The improved stability was ascribed to PEA moieties at the grain boundaries and to pinhole-free films that can effectively hamper oxygen/moisture penetration into the film.

Following this work, Shao et al. reported higher members of $(PEA)_2(FA)_{n-1}Sn_nI_{3n+1}$ (n = 12, 16, 25, 50) by adding the lower amount of PEA cation into the 3D $FASnI_3$ perovskite.[83] In contrast to Pb-based materials, the hot casting method used for the growth/crystallization of Sn-based materials yielded lower quality films. One possible explanation put forward by the authors is that more Sn vacancies are formed owing to the higher temperature of deposition. The 2D perovskite acts as a seed layer to induce large-scale crystallization and orientation of 3D $FASnI_3$. Planar configuration made of 2D/3D $(PEA)_2(FA)_{n-1}Sn_nI_{3n+1}$ perovskite were fabricated, leading to a maximum of 9% PCE (J_{SC} = 24.1 mA cm^{-2}, V_{OC} = 0.458 V, FF = 0.71) for n = 50 composition. For comparison, the authors reported for the 3D analog a lower PCE of 6%. The authors also stressed as commonly accepted now that devices based on the 2D/3D perovskites are more stable. After 76 h of air exposure, the device made of pure 3D perovskite completely degraded by contrast to the 2D/3D mixture which maintained 59% of their initial PCE.

Very recently, Ran et al.[75] developed a so-called bilateral interfacial engineering strategy to fabricate 2D/3D bulk heterojunction Sn-based perovskite solar cells through a planar ITO/LiF/PEDOT:PSS/$(PEA,FA)SnI_3$/C_{60}/BCP/Ag configuration. Large PEA^+ organic cations and LiF were evaporated at the bilateral interfaces of an $FASnI_3$ film. The presence of PEAI improved the V_{oc} and FF of the device as a result from a better covering film. The role played by LiF into this 2D–3D (PEA,FA)SnI_3 bulk heterojunction structure, has two functions: i) lower the working function of PEDOT:PSS and ii) facilitate the hole extraction at the ITO/PEDOT:PSS interface. This strategy afforded a PCE of 6.98% with a V_{OC} of 0.47 V and an FF of 0.74. The stability test of the unencapsulated device stored in a N_2 atmosphere enabled showing stability enhancement of a $(PEA,FA)SnI_3$-based PSC device compared to $FASnI_3$-based devices. **Table 1** summaries the photovoltaic parameters of recently reported mixed dimensional 2D/3D perovskite solar cells.

4. Photophysics of 2D/3D Mixed Dimensional Perovskites

4.1. Charge Carrier Dynamics: Electron–Hole Diffusion Length, Charge Carrier Mobility, and Recombination Dynamics

Herz and co-workers probed the charge carrier dynamics of mixed MA–PEA 2D perovskites by TR-PL and time-resolved terahertz (TR-THz) spectroscopies.[84] The charge-carrier mobility decreased with increasing PEA content from 25 cm^2 V^{-1} s^{-1} for $MAPbI_3$ to 1 cm^2 V^{-1} s^{-1} for $(PEA)_2PbI_4$ and remained between 6 and 11 cm^2 V^{-1} s^{-1} for mixed MA-PEA perovskites. The composition having 40% PEA displays the lowest carrier mobility of 6 cm^2 V^{-1} s^{-1}. This lower value was ascribed to the lack of preferential layer alignment with respect to the THz electric field rather than intrinsic material properties. For instance, the sample including 50% PEA showed improved texturation while it exhibited the highest charge-carrier mobility value within all mixed MA-PEA 2D perovskites (11 cm^2 V^{-1} s^{-1}). For PEA content greater than 50%, the effect of exciton binding energy increases outweighed the benefits of the improved film's orientation upon the conducting glass substrate. As a consequence

© 2018 WILEY-VCH Verlag GmbH & Co. KGaA, Weinheim

Table 1. Summary of photovoltaic parameters of recently reported mixed dimensional 2D/3D perovskite solar cells.

Perovskite	E_g [eV]	Device architecture	V_{OC} [V]	J_{SC} [mA cm^{-2}]	FF [%]	PCE [%]	Ref.
$(PEA)_2(MA)_2Pb_3I_{10}$	2.1	FTO/c-TiO_2/perovskite/spiro-OMeTAD/Au	1.18	6.72	60	4.73	[35]
$(BA)_2(MA)_2Pb_3I_{10}$	1.85	FTO/mp-TiO_2/perovskite/spiro-OMeTAD/Au	0.93	9.42	46	4.02	[50]
$(BA)_2(MA)_3Pb_4I_{13}$	1.60	FTO/mp-TiO_2/perovskite/spiro-OMeTAD/Au	0.87	9.09	30	2.39	[50]
$(IC_2H_4NH_3)_2(MA)_{n-1}Pb_nI_{3n+1}$	1.63	FTO/mp-TiO_2/perovskite/spiro-OMeTAD/Au	0.893	14.33	63	9.03	[52]
$(AVA)_x(MA)_{1-x}PbI_3$	–	FTO/mp-TiO_2/mp-ZrO_2/perovskite/carbon	0.85	21.78	64	11.86	[71]
$(PEA)_2(MA)_{49}Pb_{50}Br_{151}$	–	FTO/mp-TiO_2/perovskite/spiro-OMeTAD/Au	1.46	9.0	65	8.5	[64]
$(PPA)_2(MA)_{49}Pb_{50}Br_{151}$	–	FTO/mp-TiO_2/perovskite/spiro-OMeTAD/Au	1.24	9.5	60	7.1	[65]
$(BZA)_2(MA)_{49}Pb_{50}Br_{151}$	–	FTO/mp-TiO_2/perovskite/spiro-OMeTAD/Au	1.35	11.5	63	9.5	[65]
(EDA) $(MA)_2[Pb_3I_{10}]$	1.67	FTO/mp-TiO_2/perovskite/spiro-OMeTAD/Au	1.24	16.57	56	11.58	[60]
$GAMA_3Pb_3I_{10}$	1.79	FTO/PEDOT:PSS/perovskite/PCBM/Al	0.97	9.35	80	7.26	[74]
$(PEI)_2(MA)_6Pb_7I_{22}$	1.62	ITO/PEDOT:PSS/perovskite/PCBM/LiF/Ag	1.1	13.12	65	9.39	[58]
$(BA)_2(MA)_3Pb_4I_{13}$ (HC)	–	FTO/PEDOT:PSS/perovskite/PCBM/Al	1.01	16.76	74	12.51	[38]
(iso-BA)$_2$(MA)$_3$Pb$_4$I$_{13}$ (HC)	1.74	ITO/C_{60}/perovskite/spiro-OMeTAD/Au	1.20	16.54	53	10.63	[54]
$(BA)_2(MA)_3Sn_4I_{13}$	1.42	FTO/m-TiO_2/perovskite/PTAA:TPFB/Au	0.23	24.1	46	2.53	[81]
$PEA_2FA_8Sn_9I_{28}$	1.40	ITO/NiO_x/perovskite/PCBM/Al	0.59	14.44	69	5.94	[82]
$(PEA)_2(FA)_{n-1}Sn_nI_{3n+1}$	–	ITO/PEDOT:PSS/perovskite/C_{60}/BCP/Al	0.458	22.5	58	9.0	[83]

of lower mobility/higher exciton binding energy, the charge carrier diffusion length decreases dramatically with the inclusion of PEA, from 2.2 µm for $MAPbI_3$ to only 60 nm for $(PEA)_2PbI_4$. However, mixing MA and PEA is beneficial for this aspect since the authors reported that including 50% PEA attains a maximum of 2.5 µm of electron diffusion length. This result, which one can consider counter-intuitive, was explained on the basis of a complex interplay between many factors such as subtle excitonic effects and low monomolecular recombination due to effective trap passivation. The relatively high carrier mobility was a result of enhanced ordering of layers in the direction of the electrical field used as a probe.

In another work, Liu et al. studied the charge carrier dynamics of $(BA)_2(MA)_{n-1}Pb_nI_{3n+1}$ perovskite using ultrafast transient absorption (TAS) and TR-PL spectroscopies.[85] Surprisingly, it was found that the multiple perovskite phases are coexisting with various n values in the final film (although prepared as $n = 4$). More interestingly, the direction of growth for these perovskites was naturally aligned in the order of n along the growth direction perpendicular to the substrate. This kind of sequential distribution in the order of their n values are inducing electron and hole transfer occurring in the opposite direction. Furthermore, driven by the built-in band alignment between the different adjacent perovskite phases, on a film of ≈360 nm thickness, this leads to consecutive fast internal electron transfers within a half-time of ≈477 ps from small-n to larger-n phases and hole transfer with a time of ≈987 ps in opposite direction. This unique self-charge separation property of the 2D perovskite films is particularly fascinating as it can facilitate their applications in photovoltaics and other related photonic devices. Xing et al.[86] in good consistency with the results reported by Liu et al.[85] observed the efficient photon-induced charge transfer processes taking place within the 2D layer phases from low n value to the adjacent thicker layer larger n phases. These authors found that such charge transfer processes are taking place at the sub-picosecond time scale (≈0.5 ps). This ultrafast process can potentially suppress most of the carrier recombination pathways and could lead to the exciton localization at those thick quantum wells ($n > 5$). The excitonic recombination in those thick multiple quantum-wells should take place at much higher decay rate and more efficiently than bimolecular recombination in 3D perovskites. In thick 2D perovskite films, the timescale related to internal charge transfer processes is dominated by the geometry of the perovskite particles forming the film, where the mixture phases are spatially well separated. In this scenario, internal charge transfer observed in thick 2D films is within hundreds of ps timescale.

The charge carrier dynamics in $(PEA)_2(MA)_{n-1}Pb_nI_{3n+1}$ perovskite were investigated by Shang et al. by combining TAS, low-temperature PL, and KPFM.[87] This study unraveled that the multiple phases of perovskites were naturally arranged in the increasing order of n (from small to large) along the direction normal to the substrate and that different n perovskites also distribute within the same planes, parallel to the substrate. The electrons are transferred from small n-value of perovskite phases toward large n-perovskite phases. The holes are transferred in the opposite direction. The typical time scales were within 30 ps from room temperature to 80 K. Blancon et al. observed a unique phenomenon in RP thin films where photogenerated electrons and holes are strongly bounded by coulombic interactions or excitons.[88] This finding is also counter-intuitive if we consider classical quantum-confined systems. In their work, the existence of the edge states at the interface of perovskite layers was shown. These edge states provide a direct pathway for dissociating excitons into longer-lived free-carriers that can significantly improve the performance of optoelectronic devices (**Figure 8**)

© 2018 WILEY-VCH Verlag GmbH & Co. KGaA, Weinheim

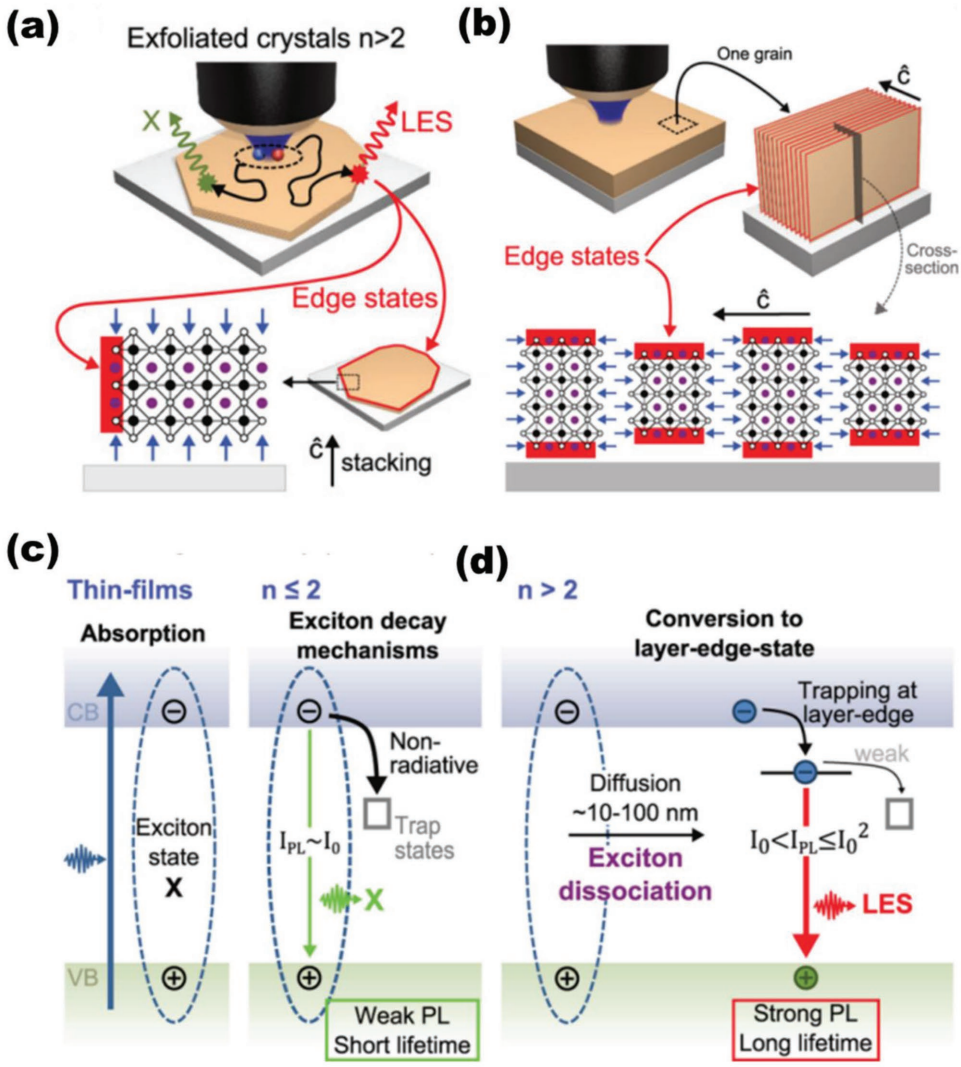


Figure 8. a) Schematics of the photoabsorption and PL processes in 2D perovskite exfoliated crystals with $n > 2$. b) Schematics of the photoabsorption and PL processes in a 2D perovskite thin film with $n > 2$. c) Summary of the main photoemission mechanisms in thin films. Reproduced with permission.[88] Copyright 2017, American Association for the Advancement of Science.

4.2. Electron–Phonon Coupling

Electron–phonon coupling (EPC) plays sometimes a significant role in the geminate recombination dynamics responsible for nonradiative recombination. Although EPC effect is now well-established for 3D perovskites,[89] a better understanding of this effect in 2D perovskites is needed for the complete comprehension of this complex family of materials. The first work comes from Straus et al. who monitored the EPC in 2D perovskites by the temperature evolution of the PL linewidth.[90] In a typical $(PEA)_2PbI_4$ thin layer, the excitonic absorption, and PL spectra exhibited splitted photonic side bands corresponding to various phonon resonance. The energy spacing between those side bands can be used as a fingerprint to identify the coupled phonon modes in 2D perovskites. It was also highlighted that the existence of phonon coupling is located in both the organic and inorganic components of the 2D perovskites. Following this first work, Guo et al. investigated the EPC in atomically thin $(BA)_2(MA)_{n-1}Pb_nI_{3n+1}$ 2D perovskites by time-resolved and temperature dependent PL spectroscopy.[91] The power law dependence of scattering rate T_γ ($\gamma > 0$), which indicates that phonons were the main sources of scattering, was used to study the type of EPC. The exponent γ depends on the dominating phonon scattering mechanism. For a 2D semiconductor, scattering by acoustic phonons via a deformation potential mechanism leads to $\gamma_{ac} = 1$. The fitted exponent γ was 1.9 and 1.6 for interband and intraband scattering, respectively. This result tends to suggest that optical phonons are also contributing alongside to acoustic phonon scattering. For 2D-layered semiconductors, two types of optical phonons can contribute to scattering of carriers and excitons: 1) in-plane polar optical phonons through Frölich interaction and 2) out-of-plane homopolar (nonpolar) phonons via deformation potential. To decipher the contribution from the polar and homopolar optical

© 2018 WILEY-VCH Verlag GmbH & Co. KGaA, Weinheim

phonons, the temperature dependence of the two scattering mechanisms was considered. It was found that homopolar phonon scattering was the other contributor as part from acoustic phonon scattering. Further investigation showed that the unconventional EPC to organic cations in 2D perovskites facilitated the white-light emission in solution-processed $(PEA)_2PbCl_4$ perovskites at room temperature.[92] The $(PEA)_2PbCl_4$ exhibited a remarkably high color rendering index of 84 together with excellent photostability, making this material ideal for natural white light-emitting diode (LED) applications. This work highlights that the organic framework is not acting merely as an inert spacer. This latter is of critical importance to select an appropriate combination between the inorganic and organic components.

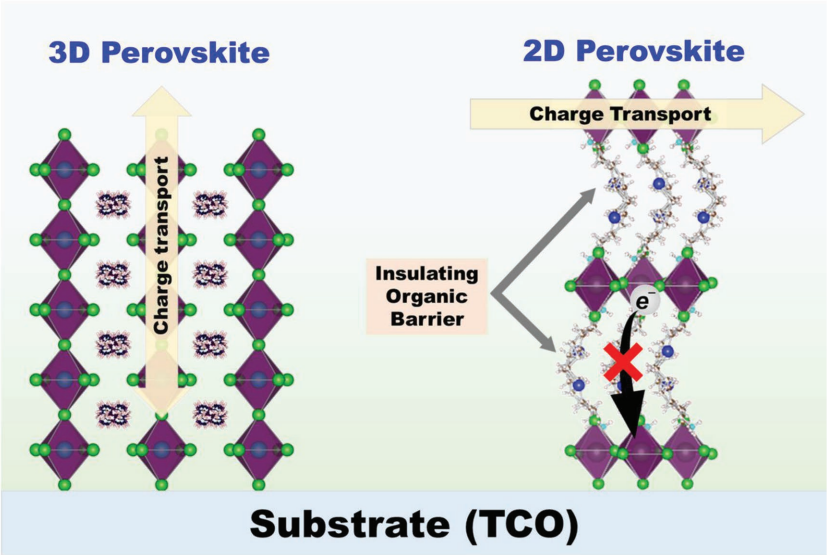


Figure 9. Illustration of charge transport in 3D and 2D perovskites.

5. Key Challenges in 2D/3D Mixed Dimensional Perovskites

Investigations on low dimensional hybrid perovskites give an important scientific and technological credit to continue scrutinizing this class of absorbers with final aim to bring 2D perovskite solar cells to the level of 3D perovskite in terms of PCEs and Si modules in terms of stability. Relating the stability of perovskite to the standard of silicon is particularly relevant as one mainstream of perovskite market would be in 2T or 4T tandem with silicon to improve the performances of this latter. However, before this, there are few key challenges which need to be tackled as discussed in following.

5.1. Anisotropic Charge Transport and Preferential Film Growth

As discussed in the earlier sections, typically 2D perovskites grow preferentially with inorganic layers parallel to the substrate for energetical reasons. This preferential growth, which is often encountered in layered compounds regardless of their chemical constitution, applications etc., leads to highly anisotropic charge transport properties, i.e., high conduction within the inorganic planes and poor across the layers as the organic part behaves as an insulator for the carrier conduction (**Figure 9**). For PV applications, this anisotropy combined with the preferential growth along the stacking planes is particularly detrimental to the device performance as it penalizes the charge collection efficiency. By contrast, 2D perovskites can be found very suitable for optoelectronic devices where charge transport needs to be parallel to the substrate. For example, Kagan et al. reported a 2D perovskite-based field-effect transistor with a mobility of 0.61 $cm^2\ V^{-1}\ S^{-1}$. This value is comparable to the mobility reported in amorphous Si devices.[93] The hot casting method was introduced by Tsai et al.[38] to grow films with texturation perpendicular to the plane of the substrate. As a result, power conversion efficiencies were significantly ameliorated, in the case of absorbers relying on lead, validating the key role of the film texturation on the performances. Nevertheless, this strategy may suffer from a lack of reproducibility and difficulties for upscaling to practical modules. Few organic cations[54] and solvents[81] have shown some promise for bringing the inorganic planes perpendicular to the substrate, albeit no concrete method has been established yet. It is, therefore, crucial to bring focus to well-reproducible and upscalable methods to overcome with the poor charge transport in these perovskites.

5.2. Large Exciton Binding Energy and Wider Bandgap

Larger exciton binding energies (0.1–0.5 eV) and wider bandgap value ($E_g > 2$ eV) are two major disadvantages of the 2D class of perovskites. For realizing high-efficiency devices approaching the Shockley–Queisser limit, it is crucial to reduce all energy losses and hence the exciton binding energy. Thanks to recent and current investigations, it is now well established that the bandgap value and exciton binding energy can be decreased by increasing the perovskite dimensionality. Higher member of Ruddlesden–Popper phase still required to be explored and processed to achieve this goal. Replacing Pb^{2+} to Sn^{2+} can lead to a reduction in the bandgap value and exciton binding energy. However, the poor stability of Sn^{2+} and related devices prompt the exploration of other divalent cations.

6. Conclusions and Outlook

Mixed dimensional 2D/3D hybrid perovskites are now emerging as one of the most credible approaches to improving the stability of PSCs while maintaining high efficiencies of the 3D perovskite. This review summarizes the latest research progress in this direction. It provides to the reader access to the most important highlights and the key challenges/issues which need to be addressed in order to make this technology entering

© 2018 WILEY-VCH Verlag GmbH & Co. KGaA, Weinheim

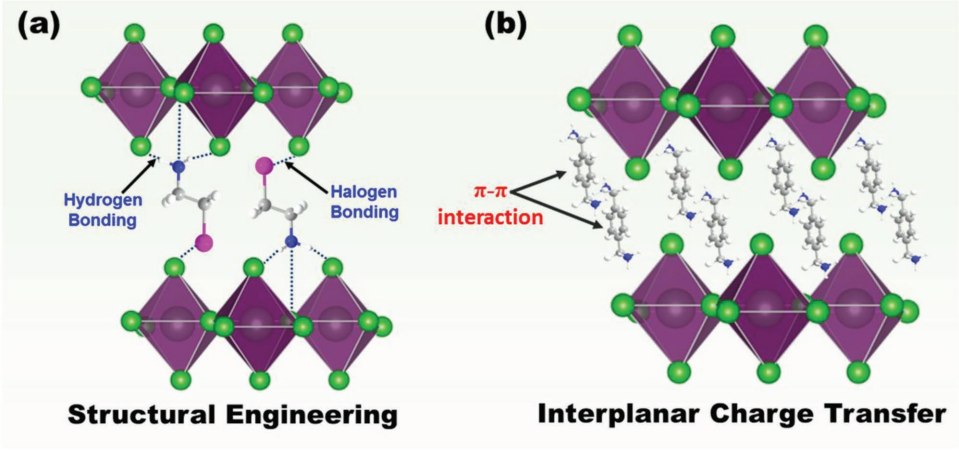


Figure 10. Illustration of a) halogen/hydrogen bonding using bifunctional organic cation and b) interplanar charge transfer using aromatic ammonium cation.

the market. One critical concern in this type of technology is a delicate balance between hydrophobicity and charge transport properties. One elegant approach in terms of materials science is the introduction of hydrophobic organic spacers in the A site which helps to improve both air and moisture stability of perovskite-based PV technology. However, such a bulky introduction between the inorganic layers weaken both electronic and optical performances of the absorber. One force of perovskite is the chemical richness of this family of materials. Further exploration of this very rich family will enable to circumscribe an acceptable trade-off between high efficiency/poor stability (3D) and high stability/lower efficiencies (2D). This will require to introduce an optimized organic spacer (possibly different organic moieties), fine-tuning of chemical composition and optimize film processing to obtain a well-oriented film for quantitative charge collection efficiency, high quality, defect-free grains optimized at both the nanoscopic and mesoscopic levels within the film. The main part of 2D/3D mixed dimensional perovskite has been focusing on PEA and BA cation. Few recent publications report the use of iso-BA, TBA and $IC_2H_4NH_3$ cations which allows out of the plane film growth leading to enhanced charge transport and power conversion efficiencies. In particular, an aromatic cation with the ability of π–π stacking and bifunctional ammonium cations as shown in **Figure 10** can lead to improvement in the electron transport by enhancing the electronic coupling between the quantum wells. Furthermore, doping of organic moieties which can reduce dielectric constant and lower the potential barriers for charge transport. Modeling and theoretical calculation of various cations could give major insights in designing these future materials. It has been demonstrated that the members of RP phase with higher n have lower bandgap and exciton binding energy. A possible route to explore should be given to this class of materials to meet both scientific and technological objectives.

Toward high power conversion performances and high stability to pass IEC61646 accelerating aging protocol, new

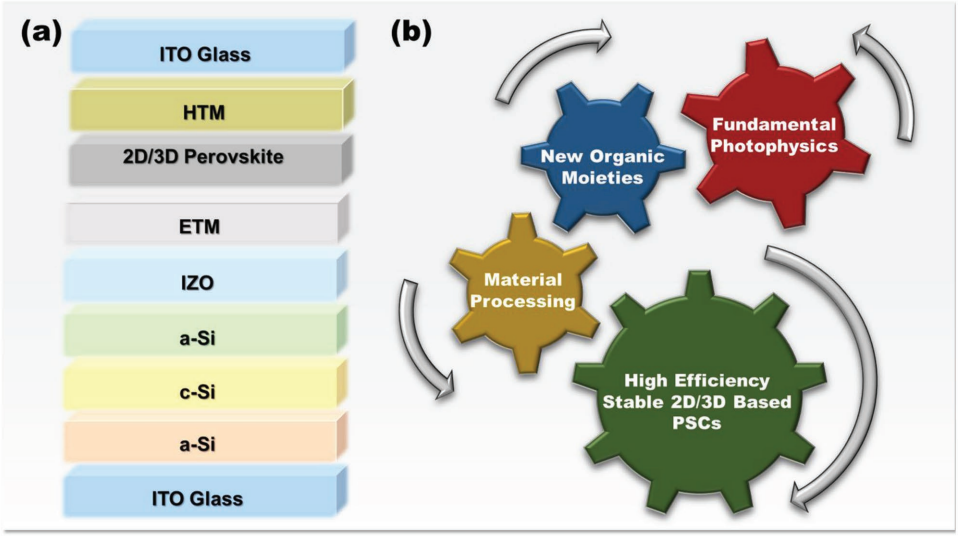


Figure 11. a) Scheme of tandem cell using Si and 2D/3D perovskites b) showing a pathway for achieving high-performance 2D/3D devices.

© 2018 WILEY-VCH Verlag GmbH & Co. KGaA, Weinheim

robust HTM with working function well adapted to the optoelectronic properties of the mixed 2D/3D perovskites is a need. The HTM-free carbon based 2D/3D perovskites devices have shown stability over 1 year in ambient conditions and prompt further investigations as most HTM were explored with conventional 3D perovskites and spiro-OMeTAD is generally used as a benchmark polymer.

The incorporation of perovskite absorber materials into multijunction cells could potentially allow going well beyond silicon-based technology by reaching higher performances in terms of spectra response and therefore PCE without excessive additional cost.[15] As discussed in this review, 2D/3D perovskites have been shown to offer a more promising pathway toward chemical/photochemical stability compared their 3D counterpart while gathering a significant chemistry richness and all properties of the 3D in terms of bandgap tuning through the number of layers (n), the stoichiometry and type of divalent cation and halide,[38,71] A bandgap as low as 1.8 eV has been achieved by means of tin cation and bromide, thus can be put on top of silicon solar cells to broaden spectra response and thus reach above 30% PCEs (**Figure 11**a).[94]

At last, understanding the fundamental photophysics of this almost infinite chemical platform and the chemical/photophysical interplay between 2D and 3D materials at the nanoscale is imperative to maximize both stability and performances of this fast raising technology. As we have included in this review, some work already started toward this direction using a pool of insightful techniques amongst ultrafast time-resolved spectroscopic techniques, high-resolution transmission electron microscopy, X-ray diffraction, etc. This mutual effort by the chemical and physical community will undoubtedly enable to inscribe the 2D/3D perovskites as the future not only for perovskite-based solar but also possibly for LEDs application or heterogeneous photocatalysis for chemistry and fuel production from sunlight.

Conflict of Interest

The authors declare no conflict of interest.

Keywords

2D perovskites, 3D perovskites, charge transport, interfacial engineering, stability

Received: September 12, 2018
Revised: November 21, 2018
Published online:

[1] H. S. Kim, C. R. Lee, J. H. Im, K. B. Lee, T. Moehl, A. Marchioro, S. J. Moon, R. Humphry-Baker, J. H. Yum, J. E. Moser, M. Grätzel, N. G. Park, *Sci. Rep.* **2012**, *2*, 1.
[2] M. M. Lee, J. Teuscher, T. Miyasaka, T. N. Murakami, H. J. Snaith, *Science* **2012**, *338*, 643.
[3] B. Saparov, D. B. Mitzi, *Chem. Rev.* **2016**, *116*, 4558.
[4] T. Salim, S. Sun, Y. Abe, A. Krishna, A. C. Grimsdale, Y. M. Lam, *J. Mater. Chem. A* **2015**, *3*, 8943.
[5] A. F. Wells, *Structural Inorganic Chemistry*, Clarendon Press, Oxford, **1984**.
[6] S. De Wolf, J. Holovsky, S. J. Moon, P. Löper, B. Niesen, M. Ledinsky, F. J. Haug, J. H. Yum, C. Ballif, *J. Phys. Chem. Lett.* **2014**, *5*, 1035.
[7] P. Docampo, S. Guldin, T. Leijtens, N. K. Noel, U. Steiner, H. J. Snaith, *Adv. Mater.* **2014**, *26*, 4013.
[8] T. C. Sum, N. Mathews, G. Xing, S. S. Lim, W. K. Chong, D. Giovanni, H. A. Dewi, *Acc. Chem. Res.* **2016**, *49*, 294.
[9] G. Xing, N. Mathews, S. Sun, S. S. Lim, Y. M. Lam, M. Graťzel, S. Mhaisalkar, T. C. Sum, *Science* **2013**, *342*, 344.
[10] S. D. Stranks, G. E. Eperon, G. Grancini, C. Menelaou, M. J. P. Alcocer, T. Leijtens, L. M. Herz, A. Petrozza, H. J. Snaith, *Science* **2013**, *342*, 341.
[11] A. Kojima, K. Teshima, Y. Shirai, T. Miyasaka, *J. Am. Chem. Soc.* **2009**, *131*, 6050.
[12] NREL Efficiency Chart, https://www.nrel.gov/pv/assets/pdfs/pv-efficiencies-07-17-2018.pdf (accessed: July 2018).
[13] J. H. Noh, S. H. Im, J. H. Heo, T. N. Mandal, S. I. Seok, *Nano Lett.* **2013**, *13*, 1764.
[14] N. N. Lal, T. P. White, K. R. Catchpole, *IEEE J. Photovoltaics* **2014**, *4*, 1380.
[15] G. E. Eperon, M. T. Hörantner, H. J. Snaith, *Nat. Rev. Chem.* **2017**, *1*, 0095.
[16] G. Niu, X. Guo, L. Wang, *J. Mater. Chem. A* **2015**, *3*, 8970.
[17] J. A. Christians, P. A. Miranda Herrera, P. V. Kamat, *J. Am. Chem. Soc.* **2015**, *137*, 1530.
[18] J. S. Manser, M. I. Saidaminov, J. A. Christians, O. M. Bakr, P. V Kamat, *Acc. Chem. Res.* **2016**, *49*, 330.
[19] J. Yang, B. D. Siempelkamp, D. Liu, T. L. Kelly, *ACS Nano* **2015**, *9*, 1955.
[20] D. A. Egger, L. Kronik, A. M. Rappe, *Angew. Chem., Int. Ed.* **2015**, *54*, 12437.
[21] Z. Hawash, L. K. Ono, S. R. Raga, M. V. Lee, Y. Qi, *Chem. Mater.* **2015**, *27*, 562.
[22] S. N. Habisreutinger, T. Leijtens, G. E. Eperon, S. D. Stranks, R. J. Nicholas, H. J. Snaith, *Nano Lett.* **2014**, *14*, 5561.
[23] S. Cacovich, L. Ciná, F. Matteocci, G. Divitini, P. A. Midgley, A. Di Carlo, C. Ducati, *Nanoscale* **2017**, *9*, 4700.
[24] K. Domanski, J. P. Correa-Baena, N. Mine, M. K. Nazeeruddin, A. Abate, M. Saliba, W. Tress, A. Hagfeldt, M. Grätzel, *ACS Nano* **2016**, *10*, 6306.
[25] G. Niu, W. Li, F. Meng, L. Wang, H. Dong, Y. Qiu, *J. Mater. Chem. A* **2014**, *2*, 705.
[26] S. Kim, S. Bae, S. Lee, K. Cho, K. D. Lee, S. Park, G. Kwon, S. Ahn, H. Lee, Y. Kang, S. Lee, D. Kim, *Sci. Rep.* **2017**, *7*, 1200.
[27] Y. Yuan, J. Huang, *Acc. Chem. Res.* **2016**, *49*, 286.
[28] M. Saliba, T. Matsui, K. Domanski, J. Seo, A. Ummadisingu, S. M. Zakeeruddin, J.-P. Correa-Baena, W. Tress, A. Abate, A. Hagfeldt, M. Grätzel, *Science* **2016**, *354*, 206.
[29] M. Saliba, T. Matsui, J.-Y. Seo, K. Domanski, J.-P. Correa-Baena, M. K. Nazeeruddin, S. M. Zakeeruddin, W. Tress, A. Abate, A. Hagfeldt, M. Grätzel, *Energy Environ. Sci.* **2016**, *9*, 1989.
[30] L. K. Ono, E. J. Juarez-Perez, Y. Qi, *ACS Appl. Mater. Interfaces* **2017**, *9*, 30197.
[31] T. Bu, X. Liu, Y. Zhou, J. Yi, X. Huang, L. Luo, J. Xiao, Z. Ku, Y. Peng, F. Huang, Y.-B. Cheng, J. Zhong, *Energy Environ. Sci.* **2017**, *10*, 2509.
[32] L. Chao, Z. Wang, Y. Xia, Y. Chen, W. Huang, *J. Energy Chem.* **2017**, *27*, 1091.
[33] Y. Chen, Y. Sun, J. Peng, J. Tang, K. Zheng, Z. Liang, *Adv. Mater.* **2017**, *30*, 1703487.
[34] V. M. Goldschmidt, *Die Naturwiss.* **1926**, *14*, 477.
[35] I. C. Smith, E. T. Hoke, D. Solis-Ibarra, M. D. McGehee, H. I. Karunadasa, *Angew. Chem.* **2014**, *126*, 11414.

 © 2018 WILEY-VCH Verlag GmbH & Co. KGaA, Weinheim

[36] A. H. Slavney, R. W. Smaha, I. C. Smith, A. Jaffe, D. Umeyama, H. I. Karunadasa, *Inorg. Chem.* **2017**, *56*, 46.
[37] R. K. Misra, B. Cohen, L. Iagher, L. Etgar, *ChemSusChem* **2017**,*10*, 3712.
[38] H. Tsai, W. Nie, J.-C. Blancon, C. C. Stoumpos, R. Asadpour, B. Harutyunyan, A. J. Neukirch, R. Verduzco, J. J. Crochet, S. Tretiak, L. Pedesseau, J. Even, M. A. Alam, G. Gupta, J. Lou, P. M. Ajayan, M. J. Bedzyk, M. G. Kanatzidis, A. D. Mohite, *Nature* **2016**, *536*, 312.
[39] B. V. Beznosikov, K. S. Aleksandrov, *Crystallogr. Rep.* **2000**, *45*, 792.
[40] D. A. Egger, A. M. Rappe, L. Kronik, *Acc. Chem. Res.* **2016**, *49*, 573.
[41] S. N. Ruddlesden, P. Popper, *Acta Crystallogr.* **1958**, *11*, 54.
[42] Z. Cheng, J. Lin, *CrystEngComm* **2010**, *12*, 2646.
[43] T. Ishihara, X. Hong, J. Ding, A. V. Nurmikko, *Surf. Sci.* **1992**, *267*, 323.
[44] M. Era, S. Morimoto, T. Tsutsui, S. Saito, *Appl. Phys. Lett.* **1994**, *65*, 676.
[45] T. Hattori, T. Taira, M. Era, T. Tsutsui, S. Saito, *Chem. Phys. Lett.* **1996**, *254*, 103.
[46] J. Jagielski, S. Kumar, W.-Y. Yu, C.-J. Shih, *J. Mater. Chem. C* **2017**, *5*, 5610.
[47] M. A. Green, A. Ho-Baillie, H. J. Snaith, *Nat. Photonics* **2014**, *8*, 506.
[48] S. I. Seok, M. Grätzel, N.-G. Park, *Small* **2018**, *14*, 1704177.
[49] L. N. Quan, M. Yuan, R. Comin, O. Voznyy, E. M. Beauregard, S. Hoogland, A. Buin, A. R. Kirmani, K. Zhao, A. Amassian, D. H. Kim, E. H. Sargent, *J. Am. Chem. Soc.* **2016**, *138*, 2649.
[50] D. H. Cao, C. C. Stoumpos, O. K. Farha, J. T. Hupp, M. G. Kanatzidis, *J. Am. Chem. Soc.* **2015**, *137*, 7843.
[51] D. B. Mitzi, *J. Mater. Chem.* **2004**, *14*, 2355.
[52] T. M. Koh, V. Shanmugam, J. Schlipf, L. Oesinghaus, P. Müller-Buschbaum, N. Ramakrishnan, V. Swamy, N. Mathews, P. P. Boix, S. G. Mhaisalkar, *Adv. Mater.* **2016**, *28*, 3653.
[53] C. C. Stoumpos, C. M. M. Soe, H. Tsai, W. Nie, J. C. Blancon, D. H. Cao, F. Liu, B. Traoré, C. Katan, J. Even, A. D. Mohite, M. G. Kanatzidis, *Chemistry* **2017**, *2*, 427.
[54] Y. Chen, Y. Sun, J. Peng, W. Zhang, X. Su, K. Zheng, T. Pullerits, Z. Liang, *Adv. Energy Mater.7*, **2017**, 1700162.
[55] J. Yan, W. Fu, X. Zhang, J. Chen, W. Yang, W. Qiu, G. Wu, F. Liu, P. Heremans, H. Chen, *Mater. Chem. Front.* **2017**, *2*, 121.
[56] S. Sourisseau, N. Louvain, W. Bi, N. Mercier, D. Rondeau, F. Boucher, J. Y. Buzaré, C. Legein, *Chem. Mater.* **2007**, *19*, 600.
[57] E. R. Dohner, A. Jaffe, L. R. Bradshaw, H. I. Karunadasa, *J. Am. Chem. Soc.* **2014**, *136*, 13154.
[58] K. Yao, X. Wang, Y. X. Xu, F. Li, L. Zhou, *Chem. Mater.* **2016**, *28*, 3131.
[59] N. Mercier, *Chem. Commun.* **2004**, *33*, 844.
[60] W. Jiang, J. Ying, W. Zhou, K. Shen, X. Liu, X. Gao, F. Guo, Y. Gao, T. Yang, *Chem. Phys. Lett.* **2016**, *658*, 71.
[61] C. Ma, D. Shen, T. W. Ng, M. F. Lo, C. S. Lee, *Adv. Mater.* **2018**, *30*, 2.
[62] B. Cai, Y. Xing, Z. Yang, W.-H. Zhang, J. Qiu, *Energy Environ. Sci.* **2013**, *6*, 1480.
[63] E. Edri, S. Kirmayer, D. Cahen, G. Hodes, *J. Phys. Chem. Lett.* **2013**, *4*, 897.
[64] B.-E. Cohen, M. Wierzbowska, L. Etgar, *Adv. Funct. Mater.* **2017**, *27*, 1604733.
[65] B. El Cohen, M. Wierzbowska, L. Etgar, *Sustainable Energy Fuels* **2017**, *1*, 1935.
[66] Y. Hu, J. Schlipf, M. Wussler, M. L. Petrus, W. Jaegermann, T. Bein, P. Müller-Buschbaum, P. Docampo, *ACS Nano* **2016**, *10*, 5999.
[67] C. Ma, C. Leng, Y. Ji, X. Wei, K. Sun, L. Tang, J. Yang, W. Luo, C. Li, Y. Deng, S. Feng, J. Shen, S. Lu, C. Du, H. Shi, *Nanoscale* **2016**, *8*, 18309.
[68] N. Li, Z. Zhu, C. C. Chueh, H. Liu, B. Peng, A. Petrone, X. Li, L. Wang, A. K. Y. Jen, *Adv. Energy Mater.* **2017**, *7*, 1.
[69] Z. Wang, Q. Lin, F. P. Chmiel, N. Sakai, L. M. Herz, H. J. Snaith, *Nat. Energy* **2017**, *2*, 1.
[70] J. M. Azpiroz, E. Mosconi, J. Bisquert, F. De Angelis, *Energy Environ. Sci.* **2015**, *8*, 2118.
[71] G. Grancini, C. Roldán-Carmona, I. Zimmermann, E. Mosconi, X. Lee, D. Martineau, S. Narbey, F. Oswald, F. De Angelis, M. Graetzel, M. K. Nazeeruddin, *Nat. Commun.* **2017**, *8*, 15684.
[72] I. Poli, S. Eslava, P. Cameron, *J. Mater. Chem. A* **2017**, *5*, 22325.
[73] J. S. Banait, K. S. Sidhu, J. S. Walia, *Can. J. Chem.* **1984**, *62*, 303.
[74] C. M. M. Soe, C. C. Stoumpos, M. Kepenekian, B. Traoré, H. Tsai, W. Nie, B. Wang, C. Katan, R. Seshadri, A. D. Mohite, J. Even, T. J. Marks, M. G. Kanatzidis, *J. Am. Chem. Soc.* **2017**, *139*, 16297.
[75] C. Ran, J. Xi, W. Gao, F. Yuan, T. Lei, B. Jiao, X. Hou, Z. Wu, *ACS Energy Lett.* **2018**, *3*, 713.
[76] Y. Lin, Y. Bai, Y. Fang, Z. Chen, S. Yang, X. Zheng, S. Tang, Y. Liu, J. Zhao, J. Huang, *J. Phys. Chem. Lett.* **2018**, *9*, 654.
[77] T. Ye, A. Bruno, G. Han, T. M. Koh, J. Li, N. F. Jamaludin, C. Soci, S. G. Mhaisalkar, W. L. Leong, *Adv. Funct. Mater.* **2018**, *1*, 1801654.
[78] Y. Hu, T. Qiu, F. Bai, W. Ruan, S. Zhang, *Adv. Energy Mater.* **2018**, *8*, 1.
[79] Z. Shi, J. Guo, Y. Chen, Q. Li, Y. Pan, H. Zhang, Y. Xia, W. Huang, *Adv. Mater.* **2017**, *29*, 1605005.
[80] F. Hao, C. C. Stoumpos, D. H. Cao, R. P. H. Chang, M. G. Kanatzidis, *Nat. Photonics* **2014**, *8*, 489.
[81] D. H. Cao, C. C. Stoumpos, T. Yokoyama, J. L. Logsdon, T.-B. Song, O. K. Farha, M. R. Wasielewski, J. T. Hupp, M. G. Kanatzidis, *ACS Energy Lett.* **2017**, *2*, 982.
[82] Y. Liao, H. Liu, W. Zhou, D. Yang, Y. Shang, Z. Shi, B. Li, X. Jiang, L. Zhang, L. N. Quan, R. Quintero-Bermudez, B. R. Sutherland, Q. Mi, E. H. Sargent, Z. Ning, *J. Am. Chem. Soc.* **2017**, *139*, 6693.
[83] S. Shao, J. Liu, G. Portale, H. Fang, G. R. Blake, G. H. Brink, L. J. A. Koster, M. A. Loi, **2017**, *8*, 1702019.
[84] R. L. Milot, R. J. Sutton, G. E. Eperon, A. A. Haghighirad, J. Martinez Hardigree, L. Miranda, H. J. Snaith, M. B. Johnston, L. M. Herz, *Nano Lett.* **2016**, *16*, 7001.
[85] J. Liu, J. Leng, K. Wu, J. Zhang, S. Jin, *J. Am. Chem. Soc.* **2017**, *139*, 1432.
[86] G. Xing, B. Wu, X. Wu, M. Li, B. Du, Q. Wei, J. Guo, E. K. L. Yeow, T. C. Sum, W. Huang, *Nat. Commun.* **2017**, *8*, 14558.
[87] Q. Shang, Y. Wang, Y. Zhong, Y. Mi, L. Qin, Y. Zhao, X. Qiu, X. Liu, Q. Zhang, *J. Phys. Chem. Lett.* **2017**, *8*, 4431.
[88] J.-C. Blancon, H. Tsai, W. Nie, C. C. Stoumpos, L. Pedesseau, C. Katan, M. Kepenekian, C. M. M. Soe, K. Appavoo, M. Y. Sfeir, S. Tretiak, P. M. Ajayan, M. G. Kanatzidis, J. Even, J. J. Crochet, A. D. Mohite, *Science* **2017**, *355*, 1288.
[89] A. D. Wright, C. Verdi, R. L. Milot, G. E. Eperon, M. A. Pérez-Osorio, H. J. Snaith, F. Giustino, M. B. Johnston, L. M. Herz, *Nat. Commun.* **2016**, *7*, 11755.
[90] D. B. Straus, S. Hurtado Parra, N. Iotov, J. Gebhardt, A. M. Rappe, J. E. Subotnik, J. M. Kikkawa, C. R. Kagan, *J. Am. Chem. Soc.* **2016**, *138*, 13798.
[91] Z. Guo, X. Wu, T. Zhu, X. Zhu, L. Huang, *ACS Nano* **2016**, *10*, 9992.
[92] K. Thirumal, W. K. Chong, W. Xie, R. Ganguly, S. K. Muduli, M. Sherburne, M. Asta, S. Mhaisalkar, T. C. Sum, H. Sen Soo, N. Mathews, *Chem. Mater.* **2017**, *29*, 3947.
[93] C. R. Kagan, D. B. Mitzi, C. D. Dimitrakopoulos, *Science* **1999**, *286*, 945.
[94] H. Chung, X. Sun, A. D. Mohite, R. Singh, L. Kumar, M. A. Alam, P. Bermel, *Opt. Express* **2017**, *25*, A311.

© 2018 WILEY-VCH Verlag GmbH & Co. KGaA, Weinheim

Volume 6 Issue 4 (2018) 312-317 ISSN 2347-3258
International Journal of Advance Research and Innovation

Modelling and Optimization of Process Parameters affecting machining involved in Electric Discharge Machining by GA-ANN

Shadab Ahmad, Praveen, Prateek, Prateek Kalyani, Ranganath M S, R S Mishra, Md Jamil Akhtar
Department of Mechanical, Production & Industrial and Automobiles Engineering, Delhi Technological University, Delhi-110042, India

Article Info:
Article history
Received 7 October 2018
Received in revised form:
28 October 2018
Accepted 2 November 2018
Available online 15 December 2018

Keywords: Electric discharge machine, optimization, Artificial neural networks

Abstract
Electric Discharge Machining process is one of the earliest and most extensively used unconventional machining process. It is a non-contact machining process that uses a series of electric discharges to remove material from an electrically conductive workpieces. The EDM process parameter are pulse on time, duty factor, peak current, peak voltage, flushing pressure. This study is aimed to do a comprehensive study of the EDM, develop a model that can predict the machining characteristic and then optimize the output parameters. Artificial Neural Network processes the information by transferring the data between its basic building block i.e. Artificial Neuron. Genetic algorithm is a metaheuristic technique used to find the best fit and approximate solutions to optimization and search problems. In this project we proposed a GA-ANN hybrid model. Also comparison is studied the experimental values and ANN predicted values. GA-ANN model concludes that the error calculated in experimental values V/S ANN-GA predicted values is very less compared to experimental values V/S ANN predicted values.

1. Introduction

Electrical Discharge Machining (EDM) is one of the earliest and most extensively used machining process. It is a thermal metal erosion process that uses series of electrical discharges to remove material from an electrically conductive workpiece. Unlike the traditional machining processes such as drilling, milling, turning etc. there is no contact between the workpiece and the tool in the EDM process, i.e. instead of using mechanical forces to fracture the material, a series of electrical pulses is used to erode it. The electrical discharges occurring due to the pulsating voltage applied across the electrodes results in melting of the workpiece which is then flushed by the surrounding dielectric.

During the EDM process a gap of about 40 µm is maintained between the electrodes using a servo mechanism and a pulsating direct current supply is connected across them. As shown in Fig. 1 which describes the general schematic diagram of Electro Discharge Machining, the electrodes are immersed in a dielectric material such as hydrocarbon oil, deionized water, cutting oils etc. When a gap voltage ($V_g \approx 200V$) is applied across the electrodes, due to the resulting high electric field between the electrodes, breakdown of the in between dielectric material takes place and a plasma channel is developed after a certain delay time. Once the plasma channel is set up, discharge current starts flowing in the circuit, the voltage across the electrodes falls to a lower value ($V_d \approx 25V$), during this pulse on time (ton), the temperature of the plasma reaches as high as 40,000K and a melt pool of the molten electrodes is produced [1]. Due to such a high temperature vaporization of the electrodes as well as the dielectric takes place, the gases formed confines the plasma channel in a bubble and the pressure within this gas bubble can be as high as 14 bars. This high pressure results in superheating of the molten metal. When the applied voltage turns off during the pulse off time (t_{off}), the gas bubble implodes violently flushing the molten metal out of the melt pool, and a crater about 100 µm wide is left out. The voltage and pulse waveforms measured at the gap in a typical EDM operation is shown in Fig. 2. This process is repeated many times throughout the whole workpiece surface during the machining process, to remove the desired amount of material from the workpiece. A more detailed description of the material erosion mechanism is given in section 2.1.2.

2. Types of Edm Processes

The most common types of EDM are:-

1. Die Sinking EDM:- The die-sinker EDM uses a shaped tool electrode and workpiece which are immersed in a dielectric fluid, when the voltage is applied across the electrodes, erosion of workpiece takes place and the tool the tool shape is replicated on it.

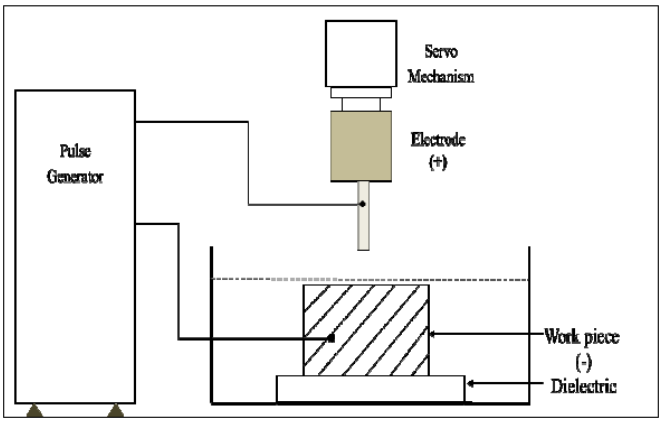


Fig. 1: Schematic Diagram of an EDM machine [2]

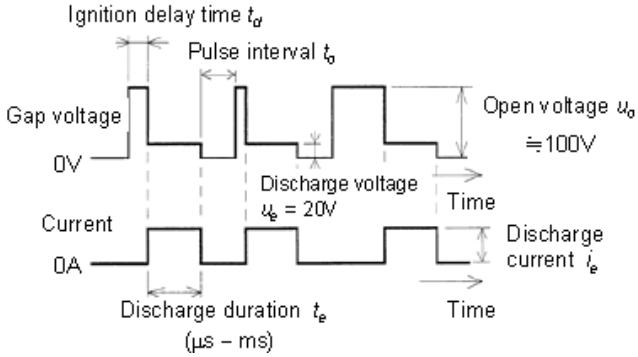


Fig. 2: Voltage and Pulse waveforms of an EDM machine [3]

2. Wire EDM (WEDM):- The wire EDM uses a thin continuously travelling metallic wire usually made of copper, brass or tungsten and having a diameter of around 0.05-0.3mm. This wire is always kept in tension using a mechanical tensioning device and is fed through the workpiece which is submerged in a dielectric fluid. The metal ahead of the wire gets eroded, and the wire is controlled numerically to produce desired shapes and cavities without the requirement of pre-shaped electrodes. De-ionized water is mostly used as the dielectric fluid in case of WEDM, due to its low viscosity and fast cooling rate [4].

Using wire EDM hard conductive materials can be machined easily to produce complex and precision components. The WEDM can produce surface finish as fine as 0.04-0.25 µRa, and the residual stresses in the EDMed surface is very low. Typical cutting rates of

***Corresponding Author,**
E-mailaddress: shadab.gkp09@gmail.com, kakodiapraveen@gmail.com
All rights reserved: http://www.ijari.org

WEDM are 300 mm^2/min for a 50 mm thick D2 tool steel and 750 mm^2/min for a 150 mm thick aluminium plate. Fig. 3 shows the schematic diagram of the wire EDM process.

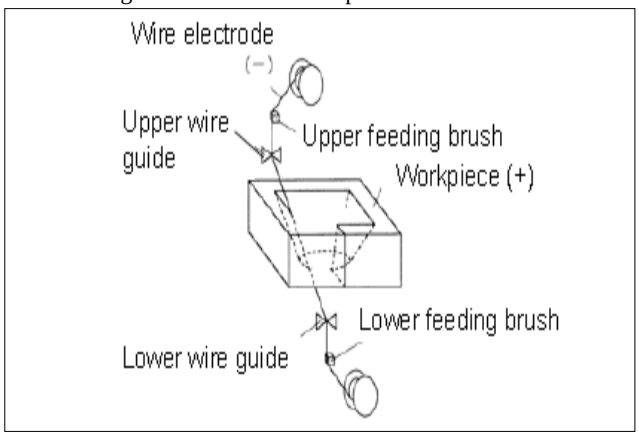


Fig. 3: Schematic Diagram of Wire EDM [6]

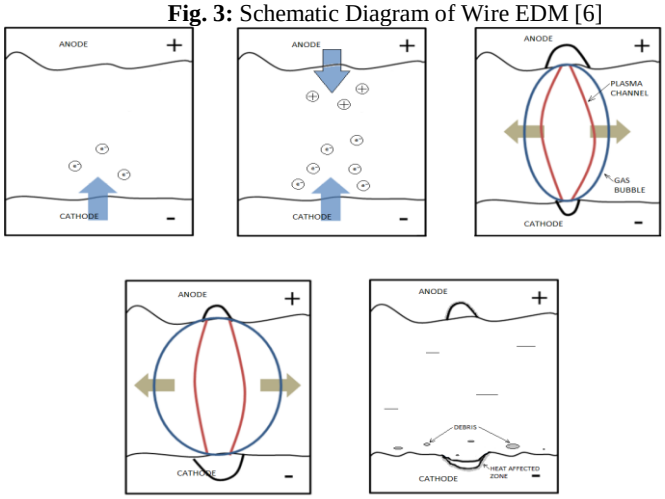


Fig.4: Diagrammatic Representation of EDM metal erosion mechanism

Pandey and Jilani [10-12] presented a thermo-mathematical model describing the EDM process. For a disc shaped heat source and a semi-infinite workpiece, the cylindrical heat conduction equation was solved numerically with appropriate initial and boundary conditions, taking into account the effect of plasma channel widening [11]. Consideration of the plasma channel expansion improves the consistency between the theoretically predicted values and the experimental outcomes. Thickness of the heat affected zones were also predicted with reasonable accuracy [10]. The effect of non-rectangular pulses on the material removal and the relative electrode wear was studied and the optimum current pulse form in terms of the relative electrode wear was found out [12]. F S Van Dijck et al. [13] calculated the exact solution of a two dimensional transient heat conduction equation for a semi-infinite body subjected to a time dependent uniform heat flux. Plasma channel widening is taken into account to improve the accuracy of the model. Pandit and Rajurkar [14] developed a hybrid thermal model of transient temperature distribution in the EDM process using Data Dependent Systems (DDS) and the heat conduction equation. A complex and stochastic process such as EDM can be modeled using DDS directly from the experimental data, and any other knowledge about the system is not required in this approach. A first order DDS model of the machined surface generated after EDM process is combined with the heat conduction equation using some realistic assumptions. The model used a circular heat source and semi infinite workpiece assumption and the results matched well with the experimental results. A. Erden et al. [15] examined 8 different Mathematical models of EDM process and compared their predictions with experimental outcomes. He concluded that the point heat source model used by Zingerman and Carslaw gave satisfactory result with low computation time but the predicted crater shape was in accurate while the model developed by Pandey and Jilani [10], gave the best results among 2D models in terms of crater volume and computing time.

An extensive research on the EDM process was carried out at the Texas A&M University, and a series of three papers was released afterwards. The first paper by DiBitonto et al. [1] proposed a simple cathode erosion model of the EDM process. Several simplifying assumptions were used, that apply to a cathode erosion model with reasonable accuracy, such as a point heat source model; a constant fraction of the total power is lost to the cathode independent of current and pulse time; average thermo physical properties of the cathode material apply to the range of solid to liquid etc. The model predicted the pulse time with an average of 16% error for steel, when the model was tuned to a single experimental point of 12.8A current. They also presented a dimensionless universal model of the EDM process, that included two dimensionless parameters g (optimum pulse time factor) and j (erodibility). At last the Compton's energy balance for gas discharges was modified for EDM process. In the second paper Mukund R. Patel et al. [16] proposed an anode erosion model, in which all the simplifying assumptions similar to the above paper were used. The plasma radius expansion at the Anode was also taken into consideration and a Gaussian heat flux distribution was used. The model is able to show the rapid melting of the anode material and its successive resolidification at longer pulse times and predict the erosion rate curves qualitatively correct. Also the plasma flushing efficiency predicted by this model is within experimental uncertainty compared to the experimental data of the AGIE EDM technologies. The third paper by Phillip T. Eubank et al. [17] presents a variable mass cylindrical plasma model for the sparks created in a liquid dielectric by the electrical discharge during EDM process. The theoretical model is formulated by solving three differential equations i.e. a fluid mechanics equation, an energy balance equation, and a radiation balance equation combined with a plasma equation of state. Numerical solutions of these equations are developed yielding temperature, plasma radius, mass and pressure as a function of pulse times for fixed current, electrode gap and the power fraction remaining in the plasma. These three papers although based on comprehensive research used oversimplifying assumptions and are unable to give satisfactory results for small discharge energies.

The material removal rate during an EDM process is affected by various process parameters, out of which the pulse waveform is among the most influential factor. A. Erden et al. [18] studied the effect of different energy pulse forms on the MRR and relative electrode wear. He concluded that the commonly used rectangular pulses are not the optimum pulse forms and more general pulse shapes offer better MRR and lower REW. Out of these pulses he advocated for trapezoidal, because they can be achieved cheaply and the trapezoidal pulses with negative slopes gives high MRR in comparison to the rectangular pulses although REW is also high while positive slopes give less MRR as well as less REW.

Singh and Ghosh [8] proposed that the electrostatic forces acting on the metal surface are responsible for metal removal in case of short pulses (discharge duration < 5µs), while melting is the dominant factor for metal removal in case of long discharge durations (discharge duration > 100 µs). They estimated the electrostatic forces acting on the surface of the metal and the stress distribution within the metal due to the electrostatic forces. The model explains that crater depth is independent of the discharge duration (t_d), for small values of t_d and increases for medium discharge duration.

3.Numerical/Computational Models

Equations governing the EDM process are hard to model and solve using analytical techniques, hence a large number of researchers have heeled toward the use of numerical methods. Numerous papers are present devoted to the numerical modeling of the EDM process [3,19-25]. All the different factors that influence the EDM performance are tried to be incorporated in these computational models, to improve the model accuracy.

P. Shankar et al. [25] used finite element method to solve equations governing the temperature and current simultaneously. In the model discharge process and heat transfer within the electrodes and dielectric were accounted. The variations in the material properties with change in temperature was used in the model. The electrode

region was divided into a 2D mesh using an automatic mesh generation program and the Glaerkin's method was used to solve the partial differential equations. The spark profile, energy distribution between the electrodes, MRR and REW was calculated and compared with the experimental results. Discrepancies were found between the experimental and theoretically predicted MRR and REW values, because of the assumption made while formulating the model.

Marafona and Chousal [24] proposed a Joule heating based model, in which heat dissipated by the cylindrical heat source is governed by Joule heating effect. ABAQUS software was used to develop a FEM model, and the results were compared with Ref. [1]. The two results followed the same pattern but appreciable discrepancy was present between the two models. A user subroutine was used by Y.B. Guo et al. [22] to develop Gaussian heat flux distribution in a multiscale diesinker EDM model of ASP2023 tool steel.

The finite element computational packages (such as ANSYS, ABAQUS, HYPERMESH etc.) provide an interactive tool to researchers using which they can model complex processes, which will otherwise be very hard or even impossible to model using analytical methods. H. K. Kansal et al. [26] used the finite element method to develop a model of the powder mixed EDM (PWEDM) process. Critical features such as change in material properties with temperature, heat distribution between the electrodes, size and shape of heat source, pulse on/off time, phase change of material, material ejection efficiency were considered in the model, and the effect of different process parameters on the temperature distribution was analyzed. Their model predicted MRR values with good accuracy, compared to the experimental results. They also concluded that the PMEDM model produced craters which are smaller and shallow craters. Borja Izquierdo et al. [27] developed a finite element model addressing the successive discharges that takes place in a real EDM process in spite of the single discharge model used by most of the researchers.

4. ANN Models

Artificial neural networks are intelligent tools which can be used to model complex nonlinear relationships between variables by mimicking the working process a nervous system [31]. An artificial neural network consists of a network of artificial neurons that can learn the complicated relationship between the input variable such as various process parameters like discharge voltage, current, machining time, pulse on time etc. and the corresponding output variable i.e. surface roughness, MRR etc. A set of experiments is designed and fed to appropriate ANN model, which models the interrelation between the input and output variables and then can be used to predict the outcome of an out of set machining parameter set The data set provided to the ANN model is divided into two sets, namely, training and testing data sets. The training data set is used to train the neural network while testing data set is used to check the accuracy of the model's prediction. A number of researchers [32-41] used ANN to create a model of the EDM process, to predict the effect of various process parameters [34,37,39] and for the process optimization [32,35,38,41].

Assarzadeh and Ghoreishi [35] used a 3-6-4-2 neural network trained to model the EDM process of BD3 steel material machined using copper electrode. Here 3-6-4-2 denotes that the neural network had 4 layers, one input layer with 3 neurons, two hidden layers with 6 and 4 neurons respectively and one output layer with 2 neurons. The machining was carried out 96 times using different input parameters out of which 82 sets were used for training and the rest for testing. The trained network predicted the MRR and Ra values for the testing data set with 5.31% and 4.89% mean error.

The selection of optimum network topology is a rigorous process and there is no general method available for its prediction, hence usually the trial and error approach is used for its selection. Panda and Bhoi [38] provided a detailed comparison of the performance of ANN models having different number of hidden layers and the number of neurons in each layer, that was used for the prediction of metal removal rate corresponding to input parameters. The network was trained using Levenberg Marquardt Backpropagation algorithm. The 3-7-1 network was found to give the most accurate results. Tsai and Wang [33] compared six different neural networks and a neuro-fuzzy network in terms of the error in their predicted outputs. The neuro-fuzzy system was found optimal for the given experimental data set.

A genetic algorithm is a robust heuristic global optimization tool that can be used to calculate global maxima in a multimodal search space. GA's are coupled with neural networks in two different ways.

Genetic Algorithms are used to optimize the EDM process by selecting the machining input parameters corresponding to the optimum output characteristic, such as high MRR, or low Ra etc. using a trained neural network[33,38,43,44].

A hybrid approach has been adapted by some researchers in which GA is used to optimize the network weights in order to improve the network predictions [33,37].

4.1 Experimental Data

The experimental data presented in table 1 has been used to develop a Hybrid GA-ANN based model that can predict the machining characteristic using the set of machining inputs and its output. The experiments were performed on ELECTRONICA-ELECTRAPLUS PS 50ZNC (die sinking type) EDM machine in the LML company in Kanpur (U.P). This data has been used with due permission from the original experimenter.

Set of experiment were designed using a L27 orthogonal array with 5 input parameters and one output parameter. The selected input parameters are Gap Voltage, Pulse Current, Pulse On Time, Pulse Off time, and Flushing pressure, and the corresponding measure output is the Material Removal Rate (MRR). This set of experiments is used to develop a neural network model which can accurately predict interpolate machining output for off sample data points, i.e. set of machining inputs which area are not present in the experimental set.

Table 1: Experimental Set of Data

Exp.No	Gap voltage (V)	Pulse current (A)	Pulse off time (µs)	Pulse on time (µs)	Flushing pressure (kg/cm^2)	MRR (gm/min)
1	50	9	15	90	0.25	0.092805
2	50	9	15	90	0.50	0.095663
3	50	9	15	90	0.75	0.099430
4	50	12	45	120	0.25	0.138074
5	50	12	45	120	0.50	0.141079
6	50	12	45	120	0.75	0.137190
7	50	15	90	150	0.25	0.158560
8	50	15	90	150	0.50	0.145560
9	50	15	90	150	0.75	0.160241
10	60	9	45	150	0.25	0.065670
11	60	9	45	150	0.50	0.065600
12	60	9	45	150	0.75	0.065480
13	60	12	90	90	0.25	0.065408
14	60	12	90	90	0.50	0.144221
15	60	12	90	90	0.75	0.150787
16	60	15	15	120	0.25	0.154021
17	60	15	15	120	0.50	0.175421
18	60	15	15	120	0.75	0.176577
19	70	9	90	120	0.25	0.074460
20	70	9	90	120	0.50	0.069428
21	70	9	90	120	0.75	0.071915
22	70	12	15	150	0.25	0.094715
23	70	12	15	150	0.50	0.096211
24	70	12	15	150	0.75	0.098076
25	70	15	45	90	0.25	0.180139
26	70	15	45	90	0.50	0.171739
27	70	15	45	90	0.50	0.180506

ensured then using the validation points, and then the model is used to predict the outcome at the set of input parameters corresponding to the testing data points, which were not fed to the neural network during the training process. The corresponding regression plot is shown in figure 5. The comparison between the experimental

outcomes and the network predicted values is shown in figure 6. The total correlation coefficient is found to be equal to 0.9987 for the ANN model.

Table-2: Parameter values of Feed-forward Backpropagation neural network

Topology of the Neural Network	Feed-forward
Learning Algorithm	Scaled Conjugate Gradient
Number of hidden layers	1
Number of neurons in hidden layer	10
Iterations	2000
Max-validation checks	20
Performance function	Mean Square Error
Number of weight elements	71
Training Divide Function	Random
Training ratio	0.7
Validation ratio	0.15
Testing ratio	0.15

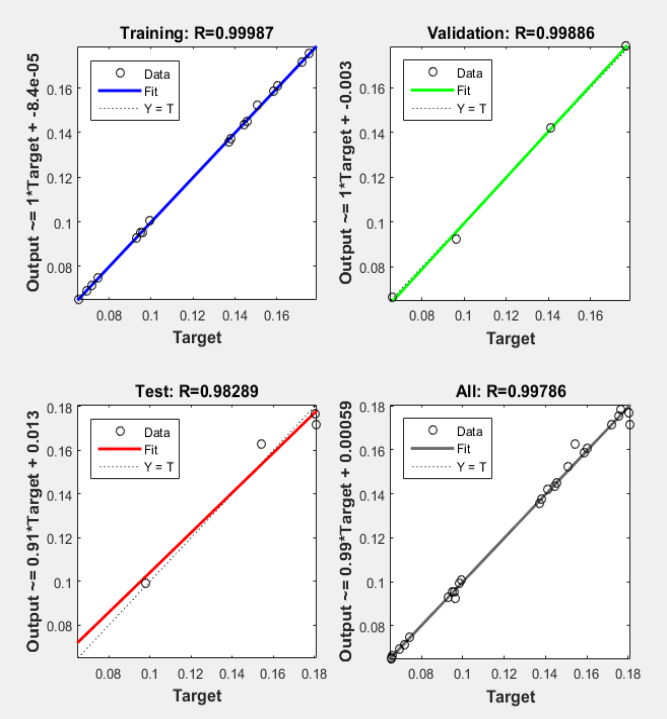


Fig.5: Regression curve of ANN model

4.2 GA-ANN model

A hybrid GA-ANN model was then developed afterwards using the same parameter settings selected for the ANN model as shown in Table 2. Table 3 shows the various parameters selected for the Genetic algorithm program that is used as a training algorithm in this model. The corresponding regression curve is shown in Fig. 16, and the Fig. 17 shows the comparison between the GA-ANN model predicted values and the experimental values.

Total Correlation coefficient of 1 is obtained using the hybrid model. As it can be seen from the figures 7 and 8, significant improvement in the network predictions are obtained on using the hybrid training algorithm. Figure 8 compares the errors between the predicted and the actual values for the two models.

From the figure 9, the maximum error in case of the ANN model that was around 17.52% reduces to 7.5% in case of the GA-ANN model which means is 43% decrease in the maximum error. It shows that the developed GA-ANN model is better than the simple ANN model.

Optimum Machining output Prediction :- The developed hybrid GA-ANN model is then used to calculate the optimum machining characteristics and the corresponding set of input parameters. The control of the developed model was passed to a genetic algorithm which generates a population of set of input parameters in the form of chromosomes. The fitness function was selected as the MRR. These chromosomes are then evolved to the optimum MRR value by using the genetic operators. The result of which is shown in Table 4. The maximum MRR value obtained in the experimental data set is 0.180506 gm/cc, while the optimum value of MRR obtained is 0.2184 gm/cc which is a 21% increase in the material removal rate.

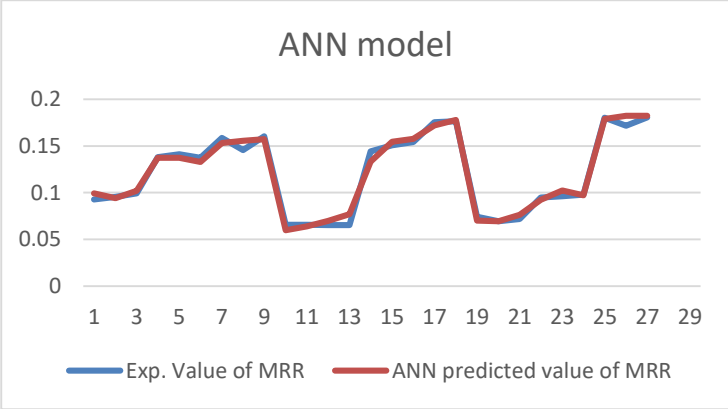


Fig.6: Comparison between the ANN predicted and experimental outcomes for the ANN model

Table-3: Parameter values of the Genetic Algorithm

Population Size	200
Population Type	Double Vector
Selection Function	Stochastic Uniform
Crossover Method	Scattered Crossover
Mutation Method	Gaussian
Mutation Probability	0.01
Stopping Criterion	Tolerance Value
Tolerance Value	10^{-15}

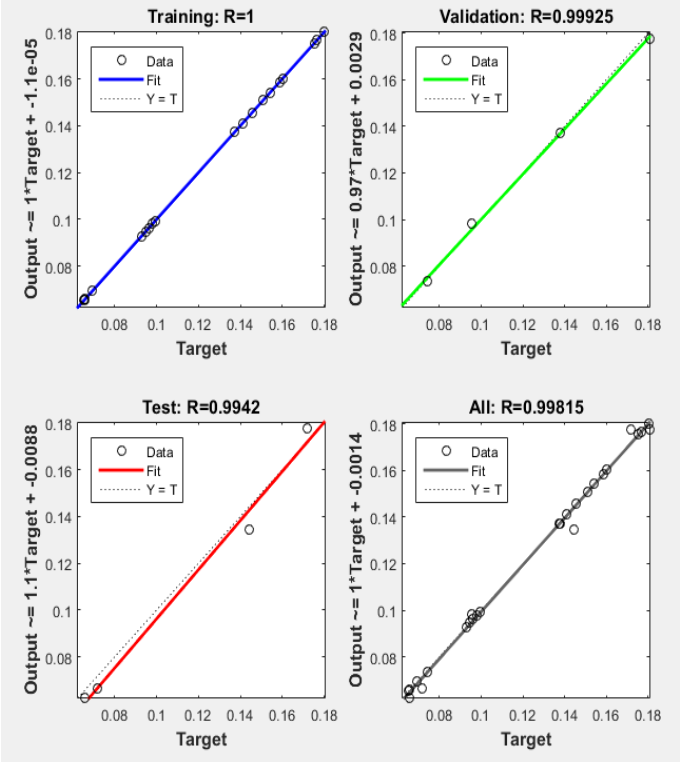


Fig. 7: Regression curve of ANN model

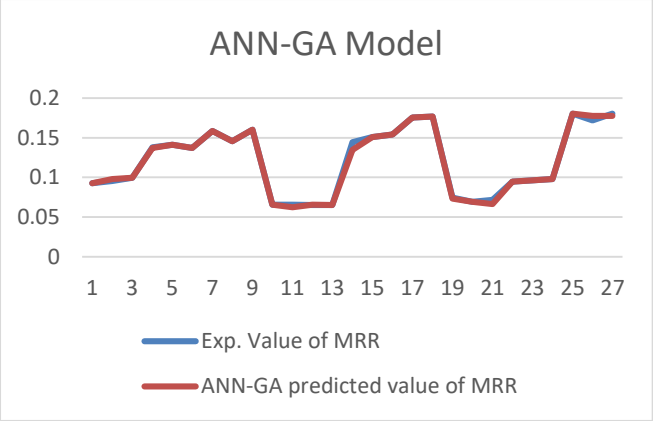


Fig.8: Comparison between the ANN predicted and experimental outcomes for the GA-ANN model

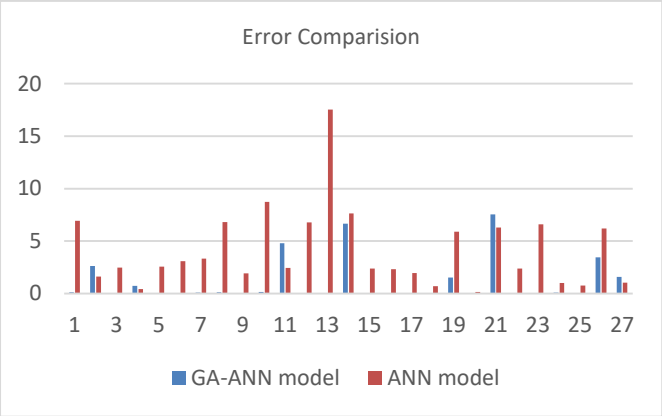


Fig. 9: Error Histogram of the GA-ANN & ANN model

Table-4: Optimum Machining Characteristics.

Machining parameters for achieving Maximum MRR	
Gap Voltage	56.907
Pulse Current	15.00
Pulse off time	44.99
Pulse on time	123.67
Flushing Pressure	0.5069
MRR	0.2184

Conclusions

- A large number of different techniques and methods are used for EDM process modeling, e.g. mathematical models, analytical models, numerical/computational models and AI based models.
- None of these models are perfect and certain disadvantages are present with all these models.
- The mathematical models are found to give satisfactory results only, due to complexity of the process and the large assumptions made to simplify the model.
- Numerical models are very accurate in their predictions and can incorporate most of the factors in the model.
- Analytical models require expensive experimentation, valid in the experimental range and have limited accuracy.
- The AI models are widely by researchers recently and have good generalization capability and quite accurate in their predictions.
- The Hybrid GA-ANN model gave better results in comparison to the simple ANN model, and using it a 47% decrease in the maximum prediction error is noticed.
- A 21% increase in the MRR is got when this model is used to predict the optimum machining characteristic.

References

[1]. DD DiBitonto, PT Eubank, MR Patel, MA Barrufet. Theoretical Models of the Electrical Discharge Machining Process, IA Simple Cathode Erosion Model. Journal of Applied Physics, 66(9), 1989, 4095-4103.
[2]. A Deshmukh. Modeling of Anode Crater Formation in Micro-Electrical Discharge Machining. MSc. Thesis, University of Nebraska-Lincoln, December 2013.
[3]. M Kunieda, B Lauwers, KP Rajurkar, BM Schumacher. Advancing EDM Through Fundamental Insight into the Process. CIRP Annals – Manufacturing Technology, 54(2), 2005, 64-87.
[4]. KH Ho, ST Newman, SRahimifard, RD Allen. State of the art in Wire Electrical Discharge Machining (WEDM). International Journal of Machine Tools & Manufacture, 44(12-13), 2004, 1247-1259.
[5]. MP Jahan, ABMAli Asad, M Rahman, YS Wong, T Masaki. µ-Electro Discharge Machining (EDM). Micro-Manufacturing, John Wiley & Sons, Inc. DOI: 10.1002/978111801570.ch10.
[6]. BE Stucker, WLBradley, S Norasettekul, PT Eubank. The production of electrical discharge machining electrodes using SLS: Preliminary results. Solid Freeform Fabr Symp, 1996, 278–286.
[7]. KH Ho, ST Newman. State of the art Electrical Discharge Machining (EDM). International Journal of Machine Tools & Manufacture, 43(13), 2003, 1287-1300.
[8]. A Singh, A Ghosh. A Thermo-Electric Model of Material Removal during Electric Discharge Machining. International Journal of Machine Tools & Manufacture, 39(4), 1999, 669-680.
[9]. K Ojha, RK Garg, KK Singh. MRR Improvement in Sinking Electrical Discharge Machining: A Review. Journal of Minerals and Materials Characterization & Engineering, 9(8), 2010, 709-739.
[10]. PC Pandey ST Jilani. Plasma Channel Growth and the Resolidified Layer in EDM. Precision Engineering, 8(2), 1986, 104-110.
[11]. ST Jilani, PC Pandey. Analysis and Modeling of EDM Parameters. Precision Engineering, 4(4), 1982, 215-221.
[12]. ST Jilani, PC Pandey. An Analysis of Surface Erosion in Electrical Discharge Machining. Wear, 84, 1983,275-284.
[13]. FS Van Dijck, WL Dutré. Heat Conduction Model for the Calculation of the Volume of Molten Metal in Electric Discharge. Journal Physics D:Applied Physics, 7(6), 1973, 899-910.
[14]. SM Pandit, KP Rajurkar. A Stochastic Approach to Thermal Modeling Applied to Electro-Discharge Machining. Journal of Heat Transfer, 105(3), 1983, 555-562.
[15]. A Erden, F Arinc, M Kögmen. Comparison of Mathematical Models for Electric Discharge Machining. Journal of Materials Processing and Manufacturing Science, 4, 1995, 163-175.
[16]. MR Patel, MA Burrufet, PT Eubank, DD DiBitonto. Theoretical Models of the Electrical Discharge Machining Process. II. The Anode Erosion Model. Journal of Applied Physics, 66(9), 1989, 4104-4111.
[17]. PT Eubank, MR Patel, MA Barrufet, B Bozkurt. Theoretical Models of the Electrical Discharge Machining. III. The Variable Mass Cylindrical Plasma Model. Journal of Applied Physics, 73(11), 1993, 7900-7909.
[18]. A Erden, B Kaftanoglu. Thermo-Mathematical Modeling and Optimization of Energy Pulse Forms in Electric Discharge Machining(EDM). International Journal of Machine Tool Design and Research, 21(1), 1981, 11-22.
[19]. C Mascaraque-Ramirez, P Franco. Numerical Modeling of Surface Quality in EDM Processes. Procedia Engineering, 132, 2015, 671-678.
[20]. Y Zhang, Y Liu, Y Shen, Z Li, R Ji, F Wang. A New Method of Investigation the Characteristic of the Heat Flux of EDM Plasma. Procedia CIRP, 6, 2013, 450.
[21]. M Shabgard, R Ahmadi, M Seyedzavvar, SNB Oliaei. Mathematical and Numerical Modelling of the Effect of Input-parameters on the Flushing Efficiency of Plasma Channel in EDM Process. International Journal of Machine Tools and Manufacture, 65, 2013, 79-87.
[22]. YB Guo, A Klink, F Klocke. Multiscale Modeling of Sinking - EDM with Gaussian Heat Flux via User Subroutine, Procedia CIRP, 6, 2013, 438-443.

[23]. NB Salah, F Ghanem, KB Atig. Numerical Study of Thermal Aspects of Electric Discharge Machining Process. International Journal of Machine Tools and Manufacture, 46(7-8), 2006, 908-911.
[24]. J Marafona, JAG Chousal. A Finite Element Model of EDM based on the Joule Effect. International Journal of Machine Tools and Manufacture, 46(6), 2006, 595-602.
[25]. P Shankar, VK Jain, T Sundararajan. Analysis of Spark Profiles during EDM Process. Machining Science and Technology, 1(2), 1997, 195-217.
[26]. HK Kansal, S Singh, P Kumar. Numerical Simulation of powder mixed electric discharge machining (PWEDM) using Finite Element Method. Mathematical and Computer Modeling, 47(11-12), 2008, 1217-1237.
[27]. B Izquierdo, JA Sanchez, N Ortega, S Plaza, I Pombo. Insight into fundamental aspect of the EDM process using Multidischarge numerical solution. International Journal of Advanced Manufacturing Technology, 52(1), 2011, 195-206.
[28]. E Aliakbari, H Baseri. Optimization of machining parameters in rotary EDM process by using Taguchi method. International Journal of Advanced Manufacturing Technology, 62(9), 2012, 1041-1053.
[29]. ML Jeswani. Roughness and Wear Characteristics of Spark Eroded Surfaces. Wear, 51, 1978, 227-236.
[30]. ML Jeswani. Dimensional Analysis of Tool Wear in Electrical Discharge Machining. Wear, 55(1), 1979, 153-161.
[31]. RM Singari, GS Bajwa, Prateek, Praveen, P Kalyani, S Ahmad. Modeling of Surface Roughness of during Conventional Turning using a Hybrid GA-ANN based model. IOSR Journal of Mechanical and Civil Engineering, 13(5) Version IV, 2016, 1-8.
[32]. K Wang, HL Gelgele, Y Wang, Q Yuan, M Fang. A Hybrid Intelligent Method for modelling the EDM process. International Journal of Machine Tools & Manufacture, 43(10), 2003,995-999.
[33]. KM Tsai, PJ Wang. Comparisons of Neural Network Models on Material Removal Rate in Electrical Discharge Machining. Journal of International Processing Technology, 117, 2001,111-124.
[34]. GKM Rao, G Rangajanardhaa, DH Rao, MS Rao. Development of Hybrid Model and Optimization of Surface Roughness in Electric Discharge Machining using Artificial Neural Network and Genetic Algorithm. Journal of Materials Processing Technology, 209, 2009, 1512-1520.
[35]. S Assarzadeh, M Ghoreishi. Neural-network-based Modeling and Optimization of the Electro-Discharge Machining Process. International Journal of Advance Manufacturing Technology, 39, 2008, 488-500.
[36]. KM Tsai, PJ Wang. Prediction on Surface Finish in Electrical Discharge Machining based Upon Neural Network Models. International Journal of Machine Tools & Manufacture, 41, 2001, 1385-1403.
[37]. AP Markopoulos, DE Manolakos, NM Vaxevanidls. Artificial Neural Network Models for the Prediction of Surface Roughness in Electrical Discharge Machining. Journal of Intelligent Manufacturing, 19(3), 2008, 283-292.
[38]. DK Panda, RK Bhoi. Artificial Neural Network Prediction of Material Removal Rate in Electro-Discharge Machining. Materials and Manufacturing Processes, 20(4), 2005, 645-672.
[39]. MAR Khan, MM Rahman, K Kadirgama. Neural Network Modeling and Analysis for Surface Characteristics in Electrical Discharge Machining. Procedia Engineering, 90, 2014, 631-636.
[40]. R Karthikeyan, PRL Narayanan, RS Naagarazan. Mathematical Modeling for Electric Discharge Machining of Aluminium-Silicon Carbide Particulate Composites. Journal of Material Processing Technology, 87, 1999, 59-63.
[41]. KP Somashekhar, N Ramachandran, J Mathew. Optimization of Material Removal Rate in Micro-EDM Using Artificial Neural Network and Genetic Algorithms. Materials and Manufacturing Processes, 25(6), 2010, 467-475.
[42]. U Caydas, A Hascalik, S Akici. An adaptive neuro-fuzy inference system (ANFIS) model for wire-EDM. Expert Systems with Applications, 3(2), 2009, 6135.
[43]. CC Kao, AJ Shih, SF Miller. Fuzzy Logic Control of Microhole Electrical Discharge Machining. Journal of Manufacturing Science & Engineering, 130(6), 2008, 064502.
[44]. TJ Ross. Fuzzy Logic with Engg. Applications, 2nd Ed., John Wiley and Sons Ltd.
[45]. O Yilmaz, O Eyercioglu, NNZ Gindy. A user friendly fuzy based system for the selection of electro-discharge machining process parameters. Journal of Materials Processing Technology, 172(3), 2006, 363-371.
[46]. S Singhal, RM Singari, R Batra, S Nanda. Effective utilization of Fuzzy system and Fuzzy logic in manufacturing: A Review. Proceedings of the 2016 Int. Conf. on Industrial Engg. & Operations Management, 3, 2016.
[47]. CL Lin, JL Lin, TC Ko. Optimization of the EDM process based on the Orthogonal Array with Fuzzy Logic and Grey Relational Analysis. International Journal of Advanced Manufacturing Technology, 19(4), 2002, 271.
[48]. CC Kao, AJ Shih, SF Miller. Fuzzy Logic Control of Microhole Electrical Discharge Machining. Journal of Manufacturing Science & Engineering, 130(6), 2008, 064502.

Multilingual Author Profiling from SMS

Deepanshu Gaur[1], Meghna Ayyar[2], Ashutosh Kumar Singh[3], and Rajiv Ratn Shah[4]

[1] Maharaja Agrasen Institute of Technology,New Delhi 110086, INDIA
deepanshugaur1998@gmail.com
[2] Indraprastha Institute of Information Technology, Delhi 110020, INDIA
leomi7ayyar@gmail.com
[3] Delhi Technological University, Delhi 110042, INDIA
ashu0788@gmail.com
[4] Indraprastha Institute of Information Technology, Delhi 110020, INDIA
rajivratn@iiitd.ac.in

Abstract. This paper presents our solution for the Author Profiling task in the FIRE challenge 2018. This task mainly focuses on finding the age and gender of people from South Asian countries such as India, Pakistan, Nepal, and Bangladesh from their short messaging services (SMS). Since most of these people use a combination of languages such as Hindi, English and Roman Urdu (i.e., multilingual text) on social media platforms such as WhatsApp, Facebook, and Twitter, they also follow the same practice in SMS while communicating. Thus, we aim to perform author profiling by identifying gender and age of people by analyzing their multilingual SMS. In this paper, we classify the gender of a person into male or female categories. Moreover, we classify age into the following three age groups: (i) 15-19, (ii) 20-24, and (iii) above 25. After preprocessing steps including tokenization and normalization, we provide the results of an experiment with several machine learning models like SVM, Random Forest, and Naive Bayes. Experimental results show that Naive Bayes provides competitive results when used with bilingual dictionary for translation and count vectorizer for feature extraction.

Keywords: Multilingual Corpus · Naive Bayes · SMS · Author Profiling

1 Introduction

The ubiquitous availability of smartphones and affordable network infrastructure has helped social media in increasing its popularity dramatically, clearly seen in Fig.1 taken from [26]. Often people share their thoughts, ideas, opinion, feedback, and sentiments on social media platforms such as blogging websites, Twitter, WhatsApp, YouTube, and Facebook. Social media has helped in bridging the gap between different communities. Often many people use multilingual text on social media because (i) they feel more comfortable to express themselves in local languages, (ii) they have some affinity towards their native languages, (iii) they want to increase their reachability to even those people who cannot understand

CEUR-WS.org/Vol-2266/T4-8.pdf

English well, and (iv) probably, they themselves might not be very good at expressing their thoughts via English. Social media platforms understand this need for using multilingual text in communication. Thus, they allow users to choose their preferred language from a list of languages that are used around the world.

Authorship Profiling(AP) task, which is predicting the authorship of a text only by extracting the linguistic and stylistic features, has a number of potential applications. For instance, it has been a pertinent task to the intelligence and security agencies that monitor author information. Moreover, author details can be of utmost importance in cyber forensics for identifying fake profiles, fraud messages and social harassment etc. For companies focused on marketing, this information will be definitely helpful in providing clear understanding of the target audience, solely by using blogs and reviews as a source.

Much work has been done on author profiling in languages such as English and other European languages like German, French, Spanish etc. However, a very limited research attention has been paid to South Asian languages such as Roman Urdu, Hindi etc. For example, in Hindi we say "आपसे मिलकर अच्छा लगा" which we can write using the English script as "Aapse milkar acha laga" which translates to "Nice to meet you". While, in Urdu [15], we say "آپ سے ملکر خوشی ہوئی!" which we can write with the English alphabets (Roman Urdu) as "Aapse milkar Khushi hui" which translates to "Pleased to meet you". Translations like these coupled with analysis of the patterns seen in the common text can prove beneficial in profiling the South Asian users too.

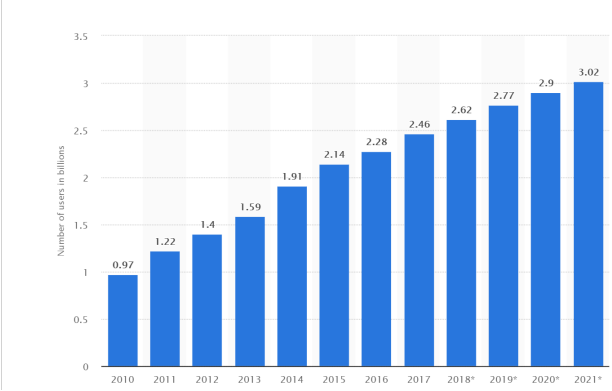


Fig. 1. Increasing number of social media users

The article [26] shows a worldwide increase in the number of people who use mobiles and smartphones to connect to the social media platforms. The following statistics reported in the article [1] is very interesting but at the same time very disturbing too. A huge number of user profiles on Facebook are reported fake. This necessitates that, appropriate action should be taken to address the increasing number of the fake profile. It is therefore essential to develop auto-

matic tools and techniques for the detection of fake profiles from different types of texts like Facebook posts/comments, SMS texts, Twitter tweets, blogs posts etc. AP is one technique that acts as a starting step for the detection of fake user profiles.

The rest of the paper is organized as follows. Sections 2 and 3 describe related work and methodology, respectively. Evaluation is presented in Section 4. Finally, Section 5 concludes the paper.

2 Related Work

The findings of Martine et al. [13] suggested that in author profiling tasks done before, the texts used were mostly monolingual as is the case provided by BNC [4], where they used only parts of the British National Corpus for their work. Pardo et al. [18] provided an overview about author profiling, its uses, and how the traits apart from gender and age, like personality type etc. could also be used as author aspects. There has been a growing interest in including a multitude of dialects and languages for author profiling, with PAN including different languages in their shared tasks. Different dialects that were explored are Portuguese varieties Zampieri et al. [28, 29], Castro et al. [2], English varieties Lui, Cook [10], Romanian dialects Ciobanu, Dinu [3] and Chinese varieties Xu et al. [27].

For features to be used for the task, simple n-gram models or using word n-grams have been observed to be effective in getting better results than character n-grams as proved by Maharajan et al. [11]. The major drawbacks of Maharajan et al. [11] approach was that they analyzed only monolingual text. Estival et al. [5] showed how author profiling tasks could be implemented for texts pertaining to emails also. But both these studies did not include the use of multilingual text, which is the most preferred way of communication among most of the people. Rangel et al. [16] pointed out that stylistic features could be useful in learning demographic traits. However, this suffered from a shortcoming that the results of stylistic features did not generalize for other traits like gender and thus have been ranked lower in preference while performing classification of gender for profiling. Many papers Zampieri et al. [28, 29], Castro et al. [2], Lui, Cook [10], Ciobanu, Dinu [3], Xu et al. [27] have focused so far on using monolingual text only, which encouraged us and many others to pursue further research in multilingual author profiling.

Gonzalez et al. [7] showed that POS and n-grams have been useful for the extraction of stylistic features. Unlike the previously mentioned papers, Gonzalez et al. [7] have used multilingual text for their study. Multilingual author profiling done by Bayot, Goncalves [1] have shown that word vectors outperform TF-IDF when used with SVM and obtained best results on a dataset containing both Spanish and English text.

Research in the area of author profiling for less explored languages played a huge role in motivating different researchers to pursue their study further in such languages and one such study Kapociute et al. [9] on the Lithuanian literary

texts shed light on some results that were significant. They found that it was easy to determine gender and age when using literary texts than with parliamentary scripts. Rangel et al. [17] on PAN-AP 2016 task focused on cross-genre evaluation. The participants for the task were given different genres for training, early bird and testing, and the subcorpus for this contained three different languages, English, Spanish and Dutch. The final result was that most of the teams had scored below the baseline for Dutch but were significantly better for English and Spanish. This points to the fact that the profiling task itself heavily depends on the nature of the language being considered. For the social media corpus that was provided in the same task, they concluded that there is no such impact of the cross-genre evaluation on language such as English. However, for a language such as Spanish, there is a much greater impact on doing this joint evaluation for age identification task but not so much for gender classification. Another study by Rangel et al. [12] on cross-genre evaluation described some notable approaches in the field of cross-genre in author profiling. The results obtained varied for different languages with different models.

Most of the studies in the field of author profiling Zampieri et al. [28, 29], Castro et al. [2], Lui, Cook [10], Ciobanu, Dinu [3], Xu et al. [27] has been restricted to the European languages, Middle East, Japanese, and Chinese. However, a limited work has been done on South Asian languages such as Roman Urdu, Hindi, and other regional languages of the South Asian countries.

3 Methodology

The problem at hand is to use multilingual text collected from SMS to perform author profiling by classifying gender and age traits. The following sections describe in detail the various steps that have been performed to achieve the results. Section 3.2 describes the pre-processing steps, followed by the Section 3.3 which discusses feature extraction techniques applied. Finally, Section 3.4 deals with model selection to achieve the best results.

3.1 System Architecture

The complete architecture of the proposed system has been summarized in Fig. 2. The pipeline starts with the collection of data and its subsequent preprocessing. This is followed by the process of feature extraction which has been described in detail in Section 3.3. Once the features were extracted as vectors, we experimented with various models and selected the one which performs best by employing cross validation and then testing the model by predicting labels on the unseen data.

3.2 Data Preprocessing

Since the data given to us is raw, noisy and also prone to more errors, it cannot be directly used for analysis. It is necessary to perform some preprocessing to

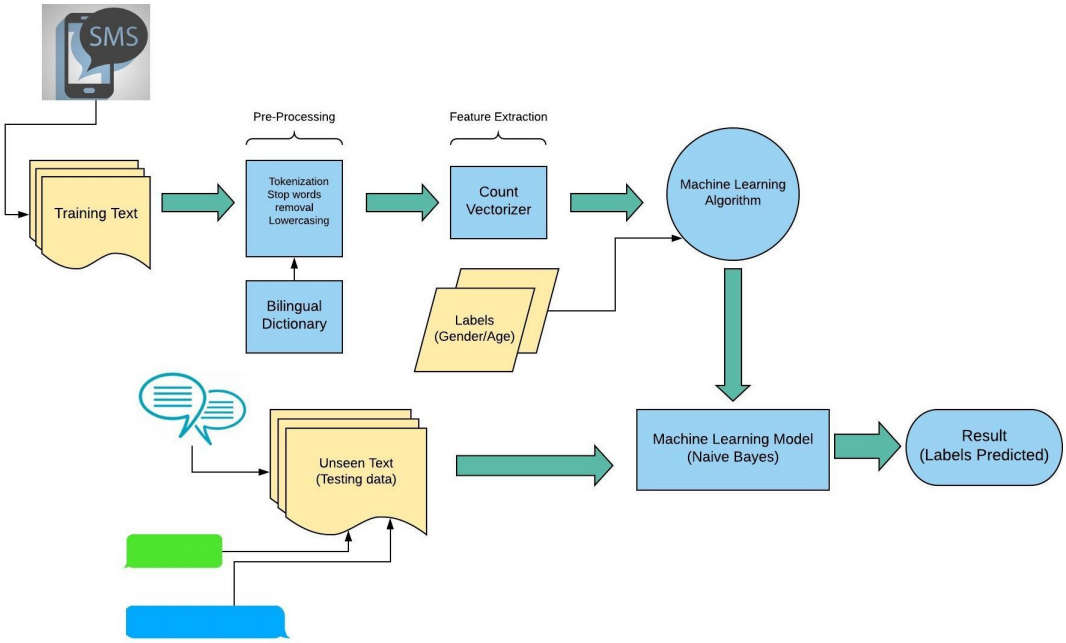


Fig. 2. System architecture of our proposed solution

make the data more suitable so that we can extract some information from it by feeding it to our model. The following preprocessing steps were performed:

1. **Tokenization:** Tokenization refers to the breaking down of the given text into individual words and symbols called as tokens. The words, phrases, symbols, and other characters present in a text are the basic characteristics of a document or in our case the SMS. Hence we use the NLTK library's word tokenizer to perform tokenization of the corpus. Consider an example for a tokenization of a text like "Natural language processing is fun" will give out different tokens such as 'Natural', 'language', 'processing', 'is' and 'fun'. People may use word tokenization or sentence tokenization depending upon their needs.
2. **Normalization:** Normalization is another type of preprocessing step which is performed to transform the data into a consistent form. It involves a number of techniques that ensure that the text is converted into a canonical form. We perform the following steps to normalize our corpus:
   - **Stopwords removal:** Many words like *the, is, are etc.* occur frequently in all the text. They do not convey any new meaning and are essentially used just to join words and sentences. They are not necessary to derive information from the text and hence are removed from our corpus by using the stopwords package from the NLTK library.

- **Punctuation removal:** Punctuation marks, similar to stopwords do not convey special meaning. Hence they are also discarded from the texts using NLTK library.
- **Text case conversion** We convert all the text to lower case before storing (using .lower() method in python). Capital letter and small letters of the same alphabets convey similar meaning and hence the conversion is necessary to ensure that they both are not treated as separate entities of the text under consideration. For instance, if we consider a text like "Apple is Red" since the previous text will also convey the same meaning as "apple is red" we may change the case of all the words to lower/upper so as to normalize the data.

3.3 Text Feature Extraction

After creating tokens, extracting features is an important task that needs to be performed before using our model so that we can predict from texts. Each token after creating vectors will act as a feature for our model.

For extracting relevant features from the text we have used two major feature extraction techniques namely TF-IDF [25] and count vectorizer [24]. TF-IDF gives a numerical value to the importance of each word in a particular text whereas count vectorizer gives us a document-term matrix which is then used as a feature for each document or in other words it counts the number of time a word is appearing in a text. The theory behind using count vectorizer is that the more frequent a word or token is the more central or important it might be to the text we used. It is an effective way to determine significant words in a text based on the number of times they are used. It is observed that word vectors perform the best in each of the classification tasks that we were given. Thus, we choose count vectorizer as our final text feature extraction technique.

3.4 Model Selection

We are given the task of classifying the author's gender and age from his/her text and thus this task falls into the category of supervised learning. For gender identification, we have binary classification task of predicting labels as either male or female. For the age identification, we have a multi-classification task whose goal is to predict age among three classes: 15-19, 20-24, 25 and above.

We use cross-validation with a ratio of 80:20 for the training and testing dataset. While considering different models a cheat sheet [23] provided by scikit learn is also considered. After analyzing the problem we conclude that the model to be used must fall into the category of supervised learning thus we choose models that are part of the same. Since the dataset given to us is not large we select Random Forest, Linear Support Vector Machines (SVM) and Logistic Regression. Also considering a fact that dataset given to us is in the form of text we opt for Naïve Bayes model as well. Following models from Scikit-Learn [19] library are selected :

1. Random Forest
2. Linear Support Vector Machines (SVM)
3. Naive Bayes
4. Logistic Regression

4 Evaluation

Section 4.1 gives a description of the data while Section 4.2 provides insight into the experimental setup used. Section 4.3 describes the evaluation metrics used and Section 4.4 gives details about the results[5] obtained and also provides some analysis of the same.

4.1 Dataset Description

Our dataset contains the multilingual text of Roman Urdu and English in different text files. We classify gender as one of the two given classes, male or female and similarly, for age, we used three categories: 15-19, 20-24, 25 and above.

Table 1. Description of training dataset

FileName	Gender	Age Group
author_id_001	male	25 and above
author_id_002	female	15-19
author_id_003	male	20-24
author_id_004	female	25 and above
author_id_005	male	15-19

There are 350 text files and each contains a SMS written in Roman Urdu or English. Some of the messages from the dataset looks something like : "Abhi tak to ni hai", "Check kr rahe hain ameer sahab" and "Aa ni rahe?". A separate CSV file is also provided which contains all the text files. The details have been summarized in the Table 1. Apart from the training corpus, we are also provided with the testing corpus to evaluate our final results that contained 150 text files. The task is, therefore, to predict the gender and age corresponding to AuthorId and also predict the gender and age individually.

4.2 Experimental Setup

This section describes the approaches and resources employed for model selection to obtain best results for the task.

[5] Source code is made available in downloads folder in repository at `https://bitbucket.org/deep1998/author-profiling-on-sms/downloads/`

1. **Resources Employed:** We use a bilingual dictionary [14] that contains 7189 commonly used words in Hindi and Urdu which can be used to translate Roman Urdu words into English.
2. **Model Selection Results:** Different models like SVM, Random Forest and Naive Bayes are tested on the data with different parameter combinations and the results are summarized in Table 2. The random forest model performed lower (accuracy=0.78 for gender and 0.55 for age) as compared to Naive Bayes in terms of accuracy with parameters : n_estimators=1000(for gender),n_estimators=1000(for age), criterion='gini', max _depth=None, min_samples _split=5, min_samples_leaf=1(for gender) and min_samples_leaf=1 (for age).

Table 2. Accuracy results of different models on the holdout set

Model	Gender	Age
Random Forest	0.78	0.55
SVM	0.70	0.52
Naive Bayes	**0.87**	**0.60**
Logistic regression	0.82	0.54

Next, we use SVM, which performs badly on the dataset and rank lowest on gender with accuracy = 0.70 with parameters C=1.0, kernel='rbf', degree=3, gamma='auto', coef0=0.0, shrinking=True, probability=False. Accuracy is 0.52 for age and thus perform badly as well on age classification task. Finally, we use logistic regression model with parameters: penalty='l2', dual=False, tol=0.0001, C=1.0(for gender), C=1.0(for age), fit _intercept=True, intercept _scaling=1 which gets an accuracy of 0.82 for gender and a value of 0.54 for age and both values are close to the results obtained by Naive Bayes model. Out of all the models used we get best results with the Naive Bayes classifier(accuracy of 0.87 and 0.60 for gender and age respectively), which is used with the parameters: alpha=1.0, fit_prior=True, class_prior=None. For both age and gender classification task we use the same Naive Bayes classification model to evaluate the performance.

4.3 Evaluation Measures

Accuracy [8] has been used as the metric for evaluating classification models in our experiments. Formally, accuracy has the following definition which says accuracy is the ratio between a total number of correct predictions N_c upon total number of predictions N_t :

$$\text{Accuracy} = \frac{N_c}{N_t}$$

4.4 Result and Analysis

We tested the accuracy of our Naive Bayes classifier for both the tasks on both the datasets : (i) Official dataset given for training (ii) Official test dataset (only for testing). The accuracy for the gender classification task was 0.87 and the accuracy for the age classification task was 0.60 on the training dataset(Table 2). The accuracy on the test dataset for the gender classification task was 0.75 and for the age classification task was 0.64 and jointly for both the accuracy was found to be 0.47(see Table 3).

Table 3. Accuracy on the official test corpus using Naive Bayes technique

Naive Bayes Model	
Task	Accuracy
Gender	**0.75**
Age	0.64
Jointly	0.47

The model performed its best on the gender classification task achieving competitive accuracy and gave a bit lower accuracy for the age classification task. By comparing the test results with training results, we found that the results were better on test dataset for age classification task than on training dataset which might signify that the model might generalize well for the age classification task as it performs well on unseen data. In contrast, this also points out that for gender classification the model could be overfitting on the training dataset which has lead to a drop in the accuracy of the testing dataset.

Table 4 summarizes the final results of other teams that participated in the FIRE'18 task. We were ranked 4th in the competition with a joint accuracy of 0.47. Highest accuracy was achieved by the first team whose joint accuracy was 0.57. The lowest joint accuracy achieved in the competition was 0.23. The baseline scores for joint accuracy was 0.32 and our results like above this base limit, showing that the model makes progress from the current state of the art and perform efficiently.

5 Conclusion and Future Work

To conclude our study, we say that we have presented our approach to an intriguing task of FIRE'18, the Multilingual Author Profiling on SMS. Previous research work [21, 20, 22] have also been taken into consideration while deciding the best approach for the task. Detailed preprocessing techniques with their proper methodologies as well as other approaches such as using bilingual dictionaries have been discussed in a lucid manner. Lastly, we have presented the results achieved on the official FIRE 18-Multilingual Author Profiling on SMS test set. The best results for the gender and age classification tasks using accuracy as

Table 4. Final results of all teams in the competition

Teams	Gender	Age	Joint
Sharmila Devi et al.	0.87	0.65	0.57
D. Thenmozhi et al.	0.85	0.63	0.52
Ali Nemati	0.83	0.60	0.49
Deepanshu Gaur et al.	***0.75***	***0.64***	***0.47***
Dijana Kosmajac et al.	0.74	0.59	0.43
Òscar Garibo	0.77	0.57	0.43
Ramsha Imran et al.	0.73	0.53	0.38
Asmara Safdar et al.	0.69	0.53	0.35
Abdul Sittar et al.	0.55	0.37	0.23

an evaluation measure were achieved with values 0.75 and 0.64 respectively and for jointly value was 0.47. The results of the competition made our team stand at fourth position globally in terms of joint accuracy, **second** in age classification and fourth for gender classification in the FIRE'18.

We conclude from our study that, to identify age and gender from a multilingual corpus, using a bilingual dictionary can be an efficient method to translate Roman Urdu to English as supported by Fatima et al. [6]. Though using dictionary is an efficient way but some drawbacks of using dictionary has also been observed. For instance, if words in the dictionary are not translated properly it may affect the results. Moreover, different writing styles in messages nowadays can cause a problem in understanding meaning of the sentences and may affect the results. For example, people may write the word *Please* as *Plz* or *Pls* and word like *Good* as *gud* and in many other ways as well.

We aim to extend the model by making it more efficient by using different techniques we did not explore such as using other features like POS or n-grams, combined with the ones we already tried. So far the text contained two languages but in the future, it would be beneficial to include more South Asian languages as they are relatively less explored and contain potential to be very useful.

References

1. Bayot, R., Gonçalves, T.: Multilingual author profiling using word embedding averages and svms. In: Software, Knowledge, Information Management & Applications (SKIMA), 2016 10th International Conference on. pp. 382–386. IEEE (2016)
2. Castro, D.W., Souza, E., Vitório, D., Santos, D., Oliveira, A.L.: Smoothed n-gram based models for tweet language identification: A case study of the brazilian and european portuguese national varieties. Applied Soft Computing **61**, 1160–1172 (2017)
3. Ciobanu, A.M., Dinu, L.P.: A computational perspective on the romanian dialects. In: LREC (2016)
4. Corpus, B.N.: Bnc home page, `http://www.natcorp.ox.ac.uk/`
5. Estival, D., Gaustad, T., Pham, S.B., Radford, W., Hutchinson, B.: Author profiling for english emails. In: Proceedings of the 10th Conference of the Pacific Association for Computational Linguistics. pp. 263–272 (2007)

6. Fatima, M., Hasan, K., Anwar, S., Nawab, R.M.A.: Multilingual author profiling on facebook. Information Processing & Management **53**(4), 886–904 (2017)
7. González-Gallardo, C.E., Torres-Moreno, J.M., Rendón, A.M., Sierra, G.: Efficient social network multilingual classification using character, pos n-grams and dynamic normalization. arXiv preprint arXiv:1702.06467 (2017)
8. Google: Machine learning crash course, `https://developers.google.com/machine-learning/crash-course/classification/accuracy`
9. Kapočiūtė-Dzikienė, J., Utka, A., Šarkutė, L.: Authorship attribution and author profiling of lithuanian literary texts. In: The 5th Workshop on Balto-Slavic Natural Language Processing. pp. 96–105 (2015)
10. Lui, M., Cook, P.: Classifying english documents by national dialect. In: Proceedings of the Australasian Language Technology Association Workshop 2013 (ALTA 2013). pp. 5–15 (2013)
11. Maharjan, S., Shrestha, P., Solorio, T.: A simple approach to author profiling in mapreduce. In: CLEF (Working Notes). pp. 1121–1128 (2014)
12. Markov, I., Gómez-Adorno, H., Sidorov, G., Gelbukh, A.F.: Adapting cross-genre author profiling to language and corpus. In: CLEF (2016)
13. Martinc, M., Škrjanec, I., Zupan, K., Pollak, S.: Pan 2017: Author profiling-gender and language variety prediction. Cappellato et al.[13] (2017)
14. Mathur, P., Shah, R., Sawhney, R., Mahata, D.: Detecting offensive tweets in hindi-english code-switched language. In: Proceedings of the Sixth International Workshop on Natural Language Processing for Social Media. pp. 18–26. Association for Computational Linguistics (2018), `http://aclweb.org/anthology/W18-3504`
15. Omniglot: Omniglot urdu phrases, `https://www.omniglot.com/language/phrases/urdu.php`
16. Rangel, F., Rosso, P.: Use of language and author profiling: Identification of gender and age. Natural Language Processing and Cognitive Science **177** (2013)
17. Rangel, F., Rosso, P., Verhoeven, B., Daelemans, W., Potthast, M., Stein, B.: Overview of the 4th author profiling task at pan 2016: cross-genre evaluations. In: Working Notes Papers of the CLEF 2016 Evaluation Labs. CEUR Workshop Proceedings/Balog, Krisztian [edit.]; et al. pp. 750–784 (2016)
18. Rangel Pardo, F.M., Celli, F., Rosso, P., Potthast, M., Stein, B., Daelemans, W.: Overview of the 3rd author profiling task at pan 2015. In: CLEF 2015 Evaluation Labs and Workshop Working Notes Papers. pp. 1–8 (2015)
19. Scikit: Scikit learn home page, `http://scikit-learn.org/stable/`
20. Shah, R., Zimmermann, R.: Multimodal analysis of user-generated multimedia content. Springer (2017)
21. Shaikh, A.D., Jain, M., Rawat, M., Shah, R.R., Kumar, M.: Improving accuracy of sms based faq retrieval system. In: Multilingual Information Access in South Asian Languages, pp. 142–156. Springer (2013)
22. Shaikh, A.D., Shah, R.R., Shaikh, R.: Sms based faq retrieval for hindi, english and malayalam. In: Post-Proceedings of the 4th and 5th Workshops of the Forum for Information Retrieval Evaluation. p. 9. ACM (2013)
23. sklearn: cheat-sheet, `http://scikit-learn.org/stable/tutorial/machine_learning_map/index.html`
24. sklearn: Count-vectorizer, `http://scikit-learn.org/stable/modules/generated/sklearn.feature_extraction.text.CountVectorizer.html`
25. sklearn: tf-idf, `http://scikit-learn.org/stable/modules/generated/sklearn.feature_extraction.text.TfidfVectorizer.html`
26. Statista: Statistics page, `https://www.statista.com/statistics/278414/number-of-worldwide-social-network-users/`

27. Xu, F., Wang, M., Li, M.: Sentence-level dialects identification in the greater china region. arXiv preprint arXiv:1701.01908 (2017)
28. Zampieri, M., Gebre, B.G.: Automatic identification of language varieties: The case of portuguese. In: KONVENS2012-The 11th Conference on Natural Language Processing. pp. 233–237. Österreichischen Gesellschaft für Artificial Intelligende (ÖGAI) (2012)
29. Zampieri, M., Malmasi, S., Sulea, O.M., Dinu, L.P.: A computational approach to the study of portuguese newspapers published in macau. In: Proceedings of Workshop on Natural Language Processing Meets Journalism (NLPMJ). pp. 47–51 (2016)

New approach for maximizing generation and optimal utilization of available space for solar PV system

Anirudh Dube, M. Rizwan, and Majid Jamil

Citation: Journal of Renewable and Sustainable Energy **10**, 063703 (2018); doi: 10.1063/1.5007780
View online: https://doi.org/10.1063/1.5007780
View Table of Contents: http://aip.scitation.org/toc/rse/10/6
Published by the American Institute of Physics

Articles you may be interested in

Intelligent model for solar energy forecasting and its implementation for solar photovoltaic applications
Journal of Renewable and Sustainable Energy **10**, 063702 (2018); 10.1063/1.5027824

Improvement of energy forecasting model to safeguard energy security in India
Journal of Renewable and Sustainable Energy **10**, 065907 (2018); 10.1063/1.5053109

Thermo-economic evaluations of dual pressure organic Rankine cycle (DPORC) driven by geothermal heat source
Journal of Renewable and Sustainable Energy **10**, 063901 (2018); 10.1063/1.5034062

A review of algorithms for control and optimization for energy management of hybrid renewable energy systems
Journal of Renewable and Sustainable Energy **10**, 053502 (2018); 10.1063/1.5032146

Comparisons of dynamical characteristics of a 5 MW floating wind turbine supported by a spar-buoy and a semi-submersible using model testing methods
Journal of Renewable and Sustainable Energy **10**, 053311 (2018); 10.1063/1.5048384

Operating performance analysis on wind turbines with the speed regulating differential mechanism
Journal of Renewable and Sustainable Energy **10**, 063301 (2018); 10.1063/1.5046784



New approach for maximizing generation and optimal utilization of available space for solar PV system

Anirudh Dube,[1] M. Rizwan,[2,a)] and Majid Jamil[1]
[1]*Department of Electrical Engineering, Jamia Millia Islamia, New Delhi 110025, India*
[2]*Department of Electrical Engineering, Delhi Technological University, Delhi 110042, India*

(Received 2 October 2017; accepted 24 November 2018; published online 17 December 2018)

To accomplish an enormous demand of power with solar energy, a cost effective and optimum system has to be developed which works in synchronisation with the existing grid. The Government in developing countries like India is providing momentous opportunities and marvellous schemes to promote renewable energy sources like solar for generating power. This paper aims to analyse the generation of power from solar photovoltaic (PV) systems economically and efficiently as it is always a challenge for the design engineer to develop an economical and efficient solar PV system. Apart from technical issues, structural aspects also affect the power generation from PV modules. This paper proposes an innovative design of non-movable tracking system that enhances the power generation of PV modules by just providing two grooves in the mounting structure in place of the tracking system. A formula for the optimum space calculation for PV installation is also proposed in this paper. A comparative analysis of total annual energy generated by the hardware setup and the results obtained using software of the rooftop solar PV system has also been analysed for practical consideration. To verify the results, first, the system has been simulated using the PVSYST software considering all practical and existing realistic losses like PV loss due to irradiance and temperature, array soil loss, module quality loss, array mismatch loss, ohmic wiring loss, and inverter loss which formulate a bonafide case of consideration and then hardware implementation of the proposed system. The hardware and software results have been compared to analyse the proposed topologies adopted to address the aforesaid problems. *Published by AIP Publishing*. https://doi.org/10.1063/1.5007780

I. INTRODUCTION

Solar photovoltaic (PV) systems nowadays are a key focus area of discussion all over the world. If there is a talk about solar, it is all about the credentials or number, whether for units generated or for targets to be achieved. A steep fall in solar photovoltaic module prices lures many investors to get associated with it and become renewable energy producers. The cost of solar photovoltaic modules, a key component in setting up solar plants, has a share of almost 60% of the total cost of any solar project considering that the land is available for the installation of solar PV systems. The decrease in the solar PV module cost and enticing government policies for solar PV power plants help promoters to invest in this emerging field. But the two major challenges for implementing the solar PV system, i.e., generation of energy and area/space requirement for setting up the solar PV system, make investors think about the investment risk and the perceived uncertainty.[1–4] Hence, to overcome these challenges, there is a need to estimate solar energy at a particular area with all the expected losses.[5–7] The energy produced by a solar PV system depends on various factors such as electrical and geographical configurations, weather conditions of the site, local horizon, and near-field shading. Some researchers[8–11] have worked on evaluating the yield from the solar PV systems considering the

a)Author to whom correspondence should be addressed: rizwan@dce.ac.in. Mobile: +91-9891558821.

variation in different environmental and technical parameters. A trend has been observed in previous research studies wherein the key focus areas of research were Maximum Power Point Tracking (MPPT) algorithms, DC-DC converters, DC-AC converters, etc. To improve the efficiency of the solar PV system, researchers have worked and developed novel MPPT algorithms,[12–18] DC-DC converter topologies,[19–22] inverters and control structures with modifications like transformerless,[23–27] and further stages of the grid connected PV system.[28–31] With the advancement in the topologies, the system efficiency as well as complexity has emerged. With the complexity, the cost of the system has also evolved. Perez-Gallardo *et al.*[32] proposed an integrated framework that manages simultaneously technical, economic, and environmental criteria for the grid connected PV system. A few researchers have focused on the levelized cost of PV energy (LCOE),[33–36] while some have focused on optimal sizing of the solar PV system.[37,38] A techno-economic variable and environmental parameter based design process for photovoltaic based different configurations has been proposed by Rawat *et al.*,[39] Karimi *et al.*,[40] and Obi and Bass,[41] wherein the various issues and challenges of the grid connected solar photovoltaic system were discussed. So, it can be concluded that many advancements in the technology used for the solar PV system and the challenges and issues pertaining to the PV system have been studied by researchers and technocrats. But it is observed that a very limited work has been done on area optimization and the module mounting structure and its placement. A few papers propose the tracking system either single axis or dual axis, but it enhances the cost as well as complexity which affects the system efficiency and increases the maintenance cost.

This paper focuses on two main challenges in the current scenario that is area optimization and boosting energy generation from the PV system, within the existing practice system by simple modifications with no additional cost and less maintenance. PVSYST software has been used to obtain the results. This paper will be of great help for the technocrats in this field to design the cost effective PV system with optimum utilization of area. This paper is organised as follows: in Sec. I, the introduction describing the work done in the related field is presented. In Sec. II of this paper, grid connected PV systems in India are discussed, for emphasizing the importance of the solar PV system in Indian context. In Sec. III, the proposed methodology, results, and discussion are presented in detail. A conclusion followed by the reference is discussed in the end.

II. GRID CONNECTED PV SYSTEM IN INDIA

India imports about 75% crude oil at present and a steep increase in this figure is expected in the near future, because of the growing economy and rapid developments. 18% of the world's population resides in India but uses only 6% of world's primary energy, in spite of being the third largest democracy. Nearly 240 million people are still living in India without electricity. The Government of India has already initiated many plans to provide power to such areas and citizens of India. Solar photovoltaic being a free source of energy and available easily everywhere in India has groomed a lot with several government schemes such as JNNSM (Jawaharlal Nehru National Solar Mission), state government policies, and NSM (National Solar Mission). With these schemes, the Government of India has two main aims, first to provide power to all and second to generate power with less carbon content emission in the environment. With the successful implementation of the above said schemes in India, the current status of installed renewable energy in India is shown in Fig. 1.

Figure 1 shows the installed capacity of renewable energy in India till July, 2018.[42] The total renewable energy used to generate power is approximately 71 GW, and this figure is expected to raise four folds till the end of year 2022. With the initiatives of the Government of India and technology development, the projected generation till 2022 is shown in Fig. 2(a) and the expected percentage share of each renewable energy source in India in 2022 is shown in Fig. 2(b).

The region-wise data to be projected by the year 2022 are shown in Fig. 3. Figure 3 shows that the main focus of solar energy is in Northern and Western regions due to ample and high irradiance of sun.

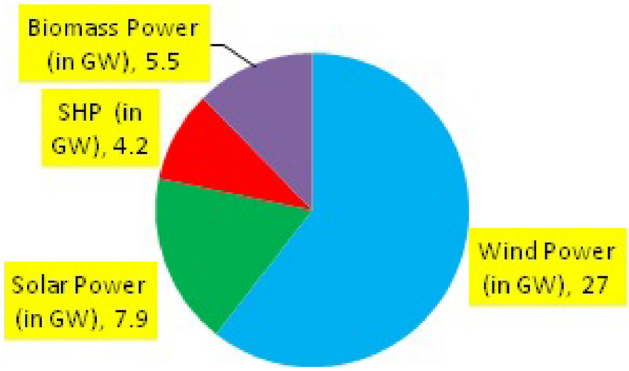


FIG. 1. India's renewable energy installed capacity till July, 2018 (71 GW).

The figure illustrates the growth and development in the field of renewable energies and enhances the dependency of power on renewable energy particularly on solar energy.

However, the safety for installation of solar PV systems is equally important and needs special focus while designing. Few international organizations such as IEEE, International Electro technical Commission (IEC), and National Electric Code (NEC) have prepared and published standards for grid connected as well as standalone PV systems. Standards are also available for solar batteries, modules, and inverters. IEEE 1547-2003 series, IEEE 519-1981, IEEE 1526-2003, IEEE 1562-2007, IEEE 1106-Series, IEEE 1361-2003/14, ANSI/IEEE 937-Series, IEEE 1262-1995, and IEEE 1513-2001 are the few standards available and should be considered while designing the solar PV system.

III. PROPOSED MODEL, RESULTS, AND DISCUSSION

Optimum utilization of space, minimization of losses, and generating power economically from PV solar systems are some of the issues that require attention of scientists and researchers. Many researchers have come up with the new topologies for DC-DC converters as well as for inverters so that the losses can be reduced and the generation can be enhanced. But in practical scenario apart from technical features, optimum space utilization for PV system installation is one of the main criteria for all designers. Within the limited area, how maximum energy can be generated is the key concern of the research. Research studies have been performed on the tracking system to grab maximum solar irradiance by the PV modules. Trackers like single axis, dual axis, and seasonal tracking are commercially available but have disadvantage in terms of initial investment as well as maintenance. To overcome these problems and to grab the maximum irradiance, this paper has proposed the module tilt angle (MTA) technique, which is discussed in detail below. Optimum module placement (OMP) is another expected solution to address the problem of space utilization optimally by the designers. This study shows that by taking few simple steps during the installation process, the system may be made more efficient and technically viable.

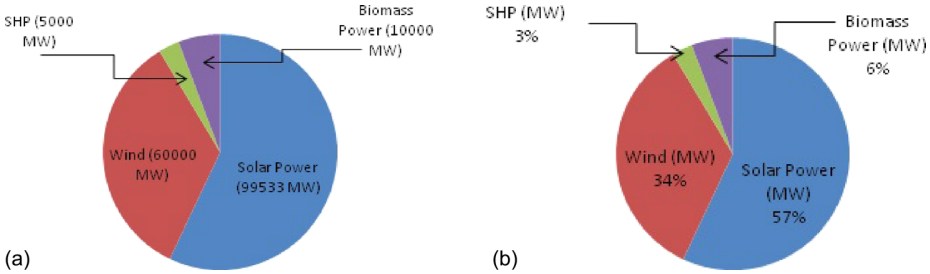


FIG. 2. Projected renewable energy in India by the year 2022.

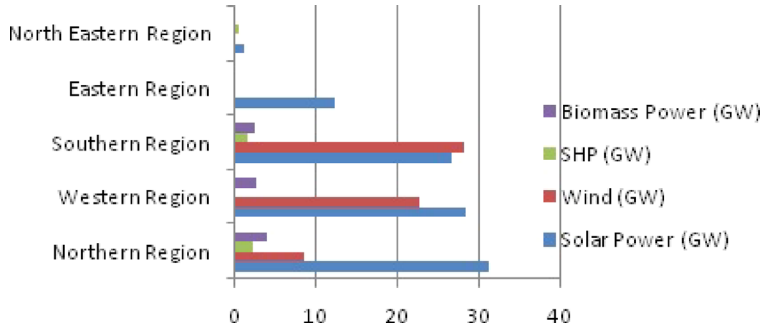


FIG. 3. Regionwise distribution of renewable energy by the year 2022 in India.

A. Module Tilt Angle (MTA)

A normal practice in designing the solar PV system is to take the tilt angle of the module approximately the same as that of the latitude of the area or site. Designers preferred single axis or dual axis trackers to track more energy and thus increase the solar power generation. But the placement of trackers also causes problem. First, it adds an additional cost to the project for the tracking system, and second, it requires maintenance. Although manufacturers are working for maintenance free trackers, that too enhances the total project cost. So, to analyze this problem and its possible solution, the results from the PVSYST report have been investigated. A 10 kW PV system considering site at New Delhi, India, is simulated using PVSYST software after incorporating all possible losses. The data for the same are shown in Table I. After careful examination of the generation pattern throughout the year, some interesting facts are observed.

In present status, two tilt angles are considered, one at 30° which is approximately the same as that of the latitude of New Delhi and the other at zero degree keeping sun perpendicular to the horizontal surface. Thus, the graph is plotted between the irradiance received (in kWh/m^2) and months of the year as shown in Fig. 4. It is found that from the months of April to August, the irradiance received is more if the module is at zero degree or can say, flat or horizontal to ground, whereas in the rest of months, generation is more at 30° tilted module. Thus, if a provision is provided in the mounting structure with just two grooves, one with the

TABLE I. Comparison analysis of irradiance with different configurations.

	Irradiance		
Months	Irradiance received with 30° tilt as per PVSYST data (in kWh/m^2)	Irradiance received with 0° tilt as per PVSYST data (in kWh/m^2)	Irradiance received with the proposed configuration as per PVSYST data (in kWh/m^2)
January	167.9	118.0	167.9
February	177.3	137.0	177.3
March	214.6	188.0	214.6
April	206.3	207.0	207.0
May	199.8	222.0	222.0
June	171.0	197.0	197.0
July	149.0	167.0	167.0
August	151.8	160.0	160.0
September	182.3	171.0	182.3
October	205.8	165.0	205.8
November	184.6	129.0	184.6
December	174.2	115.0	174.2
Total	2184.4	1976.0	2259.7

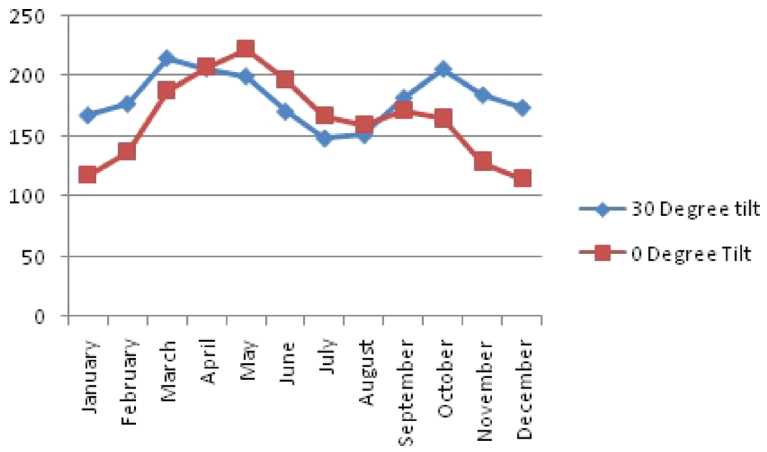


FIG. 4. Irradiance received (in kWh/m^2) with two different tilt angles as per PVSYST data.

same angle as that of the latitude and the other at zero degree or horizontal to the surface, then the irradiance and further the generation of the PV system can be enhanced without a tracking system. Table I shows the improvement in irradiance received from the PV system by the proposed method as per PVSYST, which further leads to the enhancement of generation of solar energy.

The report of energy generated from the 10 kW solar PV system by PVSYST software has been examined and subsequently verified by comparing the results with the hardware setup which is installed at the rooftop. Figure 5 shows the experimental setup for the 10 kW system, and the comparative results obtained from the hardware and software are tabulated in Table II. This comparison is provided to analyze the error difference in software and hardware results.

However, the difference between the hardware and software results mentioned in this paper may be due to other environmental factors such as smog and heat. During the analysis of the energy generated from the hardware setup, the pollution level was very high in Delhi especially during November to February, and hence, the smog was too high in Delhi. This is the reason for higher differences in the result obtained using software and hardware during these months.

A simple modification can generate 3%–5% more energy/year from the solar PV system with no extra financial burden on the project. Generally, the PV system is considered for a period of 25 years. Hence, around 2000 more units can be generated with a small change in the structure.

A groove has to be provided in the mounting structure with two slots out of which one is at a defined tilt angle according to the area specific and other with parallel to the ground or surface where it is mounted. From the results obtained and as shown in Table I, it can be concluded that during April to August, the module can be placed at the parallel position (to the surface) and in

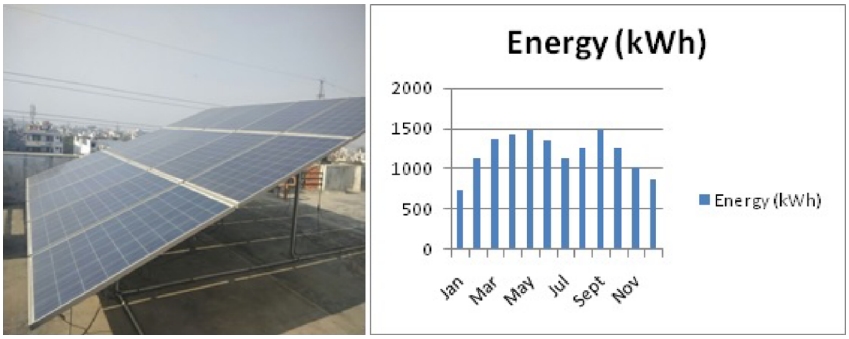


FIG. 5. Hardware implementation of the 10 kW rooftop solar PV system.

TABLE II. Comparison analysis of hardware and software results for energy injected into the grid.

	Energy	
Months	Energy injected into the grid with 30° tilt from PVSYST data (in kWh)	Energy injected into the grid with 30° tilt from the hardware setup (in kWh)
January	1376	750
February	1420	1125
March	1662	1375
April	1551	1425
May	1478	1475
June	1263	1354
July	1124	1125
August	1153	1250
September	1375	1477
October	1581	1250
November	1455	1027
December	1418	876
Total	16 856	14 509

remaining months of the year, panels may be placed at 30° or latitude angle of the area. This paper focuses on the only two grooves which need to be changed only twice in a year. So, it is a convenient method and requires no additional cost or manpower. The regular maintenance staff is able to implement the same. However, end users of this method may utilize other grooves for more conversion affording the labour and maintenance cost.

Figure 6 shows the comparison of irradiance received per month by using the existing and proposed structure.

A simple modification can generate 3%–5% more energy/year from the solar PV system with no extra financial burden on the project. Generally, the PV system is considered for a period of 25 years. Hence, approximately 2000 more units from only the 10 kW system can be generated with a small change in the structure in the lifespan of the PV module. Also, such a designed mounting structure does not require any maintenance and can easily be manhandled too.

B. Optimum Module Placement (OMP)

In designing the solar PV system, optimum utilization of space is another important aspect. The area can be optimized by placing the modules in the suitable orientation. Mainly two orientations, that is, vertical and landscape, are present, and the designer has to choose either of the two orientations. However, there are no such guidelines available. The designer may consider

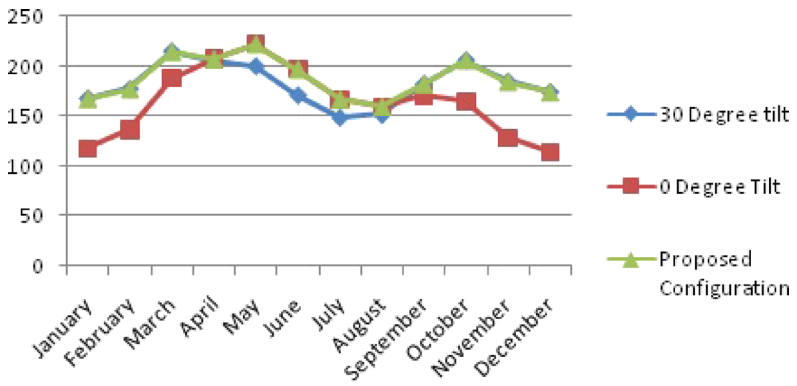


FIG. 6. Comparative analysis of irradiance received (in kWh/m^2) with different tilt angles as per PVSYST data.

any orientation based on the land size and shape. This paper presents a study that proposes the best possible way to place modules so that maximum generation may be achieved from limited land space. Second, the number of modules in series-parallel combination to form the array depends on the current and voltage calculation. But no such methods are accessible which enlighten the module combination in an array. Combination of modules to form an array is always a big question for a design engineer as the entire shadow calculations or the distance between the rows entirely depend on the array size which significantly impacts the design calculation of the PV system. This study considers different combinations along with the shadow calculation and area requirement, which helps the designer to design solar PV systems with optimum utilization of space. Before calculating the area required, the calculation of the PV array row spacing is an important task. The exact PV array row spacing or interrow space calculations are presented here.

Many solar PV designers use the formula given in Eq. (1) for calculating the inter-row distance which is correct but does not provide the exact calculation

$$Shadow\ Length = w \times \left(\cos\beta + \frac{\sin\beta}{\tan\alpha}\right), \tag{1}$$

where $\alpha = 90^\circ - (\phi + 23.45)$, w is the width of the module, φ is the latitude of the area, and β is the tilt angle of the module.

This paper proposes generalized Eq. (2) for calculating the shadow length or inter-row area

$$Shadow\,Length\,(D) = \left(w \times \frac{\sin\beta \times \cos(180^\circ - \theta)}{\tan\alpha}\right), \tag{2}$$

where w is the width of the module, β is the tilt angle, and θ is the azimuth angle at December 21. December 21 is taken because the sun altitude angle is maximum on this day, and thus, the shadow length is maximum. A is the altitude angle of the area on December 21. Figure 7 illustrates the above shadow length calculation more evidently.

This paper considers the site at Delhi. Hence, the value of the azimuth angle (θ) and altitude angle (α) is taken to be 143.5° and 28°, respectively.

The following parameter calculations are considered for designing the test system:

1. Thermal parameters

$$\text{Thermal loss factor U} = \text{U}_\text{c} + \text{U}_\text{v} \times \text{Wind velocity},$$

where U_c is the constant loss factor (whose value is taken to be 29 W/m^2k) and U_v is the wind loss factor which is considered to be 0 W/m^2k m s. The design of the module mounting structure is considered as the free mounted module with air circulation.

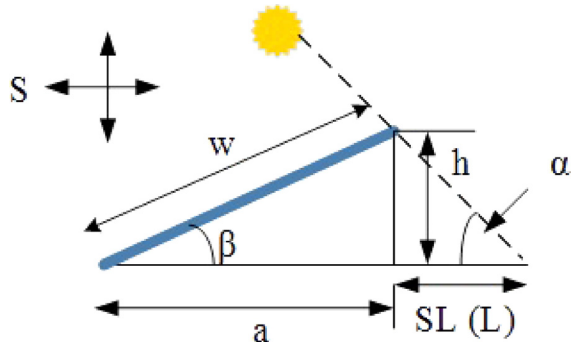


FIG. 7. Shadow length calculation.

2. Ohmic losses

The 10 kW system has two strings of 20 modules each. Each module rating is considered to be 250 W_p. V_{mpp} (voltage at the maximum power point) and I_{mpp} (current at the maximum power point) of each module are 30.8 V and 8.12 A, respectively. Hence, the cross-sectional area of the wire is calculated as

$$A_{DC} = \left(\frac{2 \times L_{DC} \times I_{DC} \times \rho}{Loss \times V_{mpstring}}\right). \tag{3}$$

Due to less loss, we preferred to take copper wire at the DC side. Hence, here also the corresponding values of constants are taken considering copper wire. Also, we have considered 0.5% of voltage drop. $V_{mpstring}$ is the voltage of the whole string at MPP. Here, V_{mpp} per module is 30.8 V. Hence, $V_{mpstring} = 30.8 \times 20 = 616$ V as 20 modules are in a string. The unit of ρ is Ω/m mm^2. Using Eq. (3), the cross-section of the wire with ohmic losses can be calculated from the array to array junction box (AJB) and from AJB to the inverter for the DC side. For the AC side, the standard equations are used to calculate the losses.

3. Module quality or mismatch loss

The module quality or mismatch loss entirely depends on the manufactures of the module. The datasheet of the module can be helpful for the same. But the proposed study has considered the standard or average module mismatch loss as 1.5%. Also, the power loss at MPP is taken to be 2%, and loss when running at fixed voltage is considered to be 4%.

4. Soiling loss

If the soil or any other dust particle is spread over the modules, then the efficiency of the modules gets decreased and it will not generate the expected energy. This loss entirely depends on the area. In India, Rajasthan has a sandy area, and so, the soiling loss is more in that area. In areas like Delhi, the soiling losses are considerably less. This paper has considered an average of 2% per year as soiling loss. This loss can be reduced if a proper module cleaning schedule is planned and executed for the PV plant.

The total optimized précised area (OPA) required after calculating the inter-row spacing or shadow calculation is proposed as

$$OPA\,(\text{in m}^2) = \left\lfloor \left\{ w\cos\beta + \left(\frac{w\sin\beta \times \cos(180^o - \vartheta)}{\tan\alpha}\right)\right\} \times n_r \right\rfloor \times \left[n_h \times l + (n_h - 1) \times d_m + d_a \times (n_a - 1)\right], \tag{4}$$

where n_r is the number of rows; n_h is the total number of modules connected horizontally; l is the length of each module (in m); d_m is the distance between the modules for air circulation (in m); d_a is the distance between the arrays (in m); and n_a is the number of array tables. Using the proposed formula, the optimized area is calculated for the test system of 10 kW at Delhi, India. The dimensions of the module considered for the test system and the two different module orientations are shown in Fig. 8.

The test system is of 10 kW with each module having a rating of 250 Wp. Thus, totally, 40 such modules are required for the proposed system. These 40 numbers of modules have been placed with different positions and configurations so that the area requirement can be analyzed with the same number and dimensions of modules. The calculation of the area is tabularized in Table III with two different orientations, i.e., landscape orientation and vertical orientation. Considering these two orientations, different module placements have been studied to find out the optimum area requirement for setting up the solar PV plant. Figures 9 and 10 show different arrangement of modules with landscape and vertical orientation, respectively, which are tabulated in Table III.

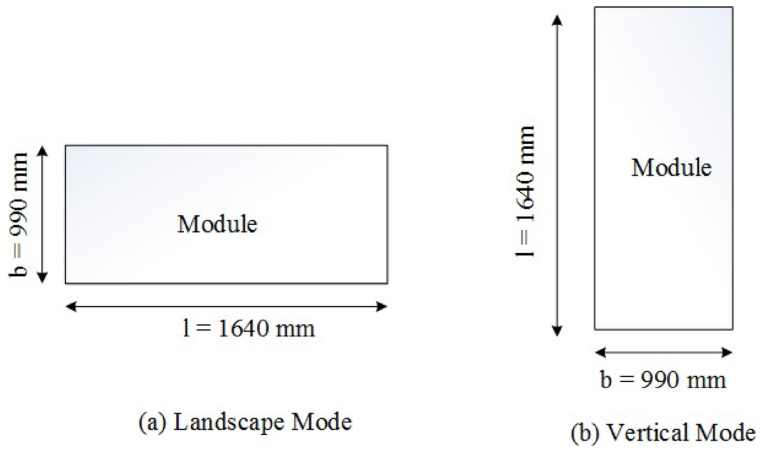


FIG. 8. Dimension and orientation of the module for the test system.

TABLE III. Area required with different module configurations and orientations.

	Landscape orientation of the module			Vertical orientation of the module		
Case No.	Array size ($n_r \times n_c$)	Level multiplier	Area required (in m^2)	Array size ($n_r \times n_c$)	Level multiplier	Area required (in m^2)
1	10 × 4	1 × 1	153.51	10 × 4	1 × 1	185.14
2	10 × 2	2 × 1	140.23	10 × 2	2 × 1	160.47
3	5 × 2	4 × 1	141.62	5 × 2	4 × 1	161.44
4	10 × 2	1 × 2	122.68	10 × 2	1 × 2	134.06
5	5 × 2	2 × 2	125.16	5 × 2	2 × 2	135.70
6	5 × 2	1 × 4	115.29	5 × 2	1 × 4	121.83

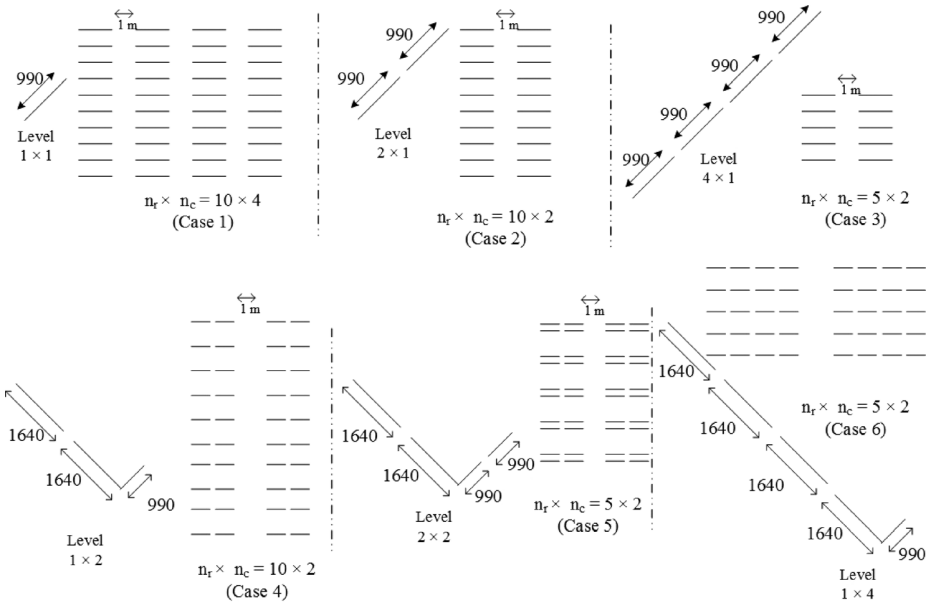


FIG. 9. Different configurations in landscape orientation of the module.

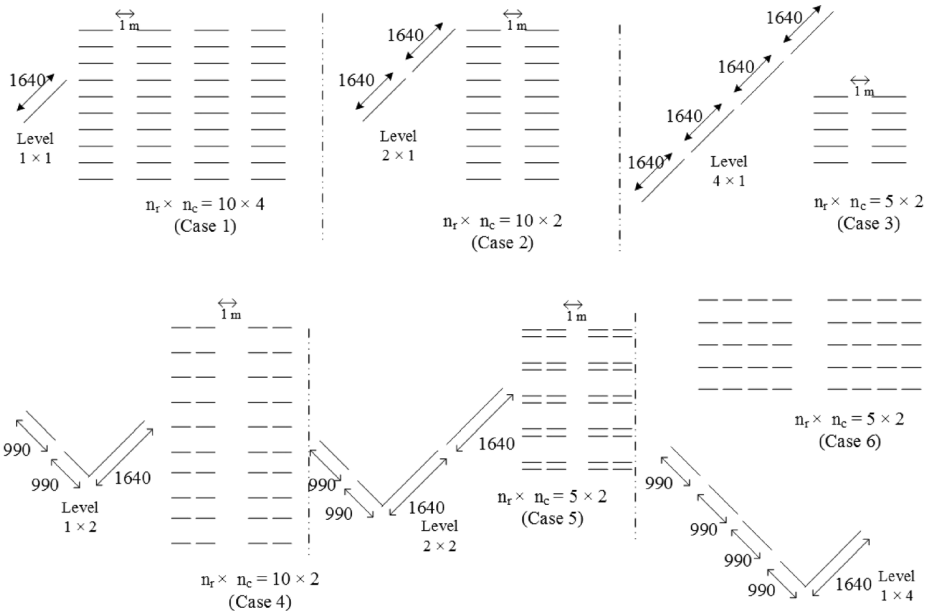


FIG. 10. Different configurations in vertical orientation of the module.

The results shown in Table III are illustrated graphically in Fig. 11. Figure 11 shows the area requirement with different orientations and placements of modules.

It has been observed from Fig. 11 that area requirement varies with the orientation and placement of the PV modules. If the modules are placed in the vertical orientation, they would acquire more space as compared to horizontal orientation. Table III describes the area requirement with different module configurations and orientations, wherein 40 modules each of 250 Wp are used to form a 10 kWPV system. Column 2 in Table III is the matrix or array in which the number of solar PV modules placed in a rowwise and columnwise manner is mentioned. The third column, i.e., level multiplier, is the row or column-wise level incremental of the PV modules, vertically or horizontally in an array. The fourth column endows with the area requirement on the particular array configuration. Two configurations, i.e., Landscape orientation and vertical orientation of the PV modules, are considered for the study of area requirement of the PV system. It has been observed that the area requirement is different for different

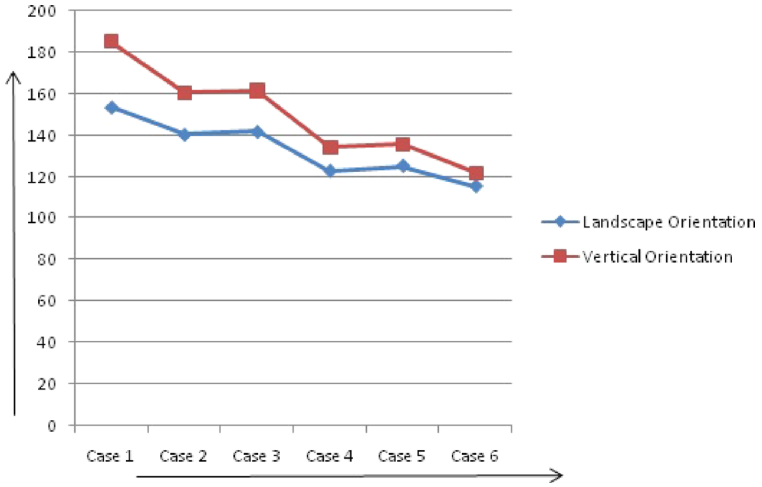


FIG. 11. Area required (in m^2) with different module orientations.

configurations of modules. With the same number and dimension of modules, the space requirement varies from 185.14 m^2 to 115.29 m^2 to form a 10 kW solar PV system. The difference between these area requirements is nearly 38%, which means without compromising the output generation from the PV system, the area requirement may be optimized to the minimum possible extend. In this paper, Eq. (4) is proposed to find out the optimized précised area requirement for setting up the solar PV system, and subsequently, the placement of the modules can be executed on the field. This would help in calculating the optimize area requirement and can utilize the available space more optimally.

IV. CONCLUSIONS

Due to rapid urbanization, availability of land or space for installing power plants is becoming a major concern these days. A solar PV system is a good option that may use rooftop of buildings, wall fencings, and other available waste space for installing solar PV systems. Even such spaces also require the use of optimal space to generate maximum power. In this paper, efforts have been made to maximize power generation from solar PV modules with minimum space requirements. Here, in this study, a test system of 10 kWp comprising 40 numbers of modules each of 250 Wp has been simulated using PVSYST software for analysis of solar energy at various angles of inclination of the solar module, and then, the results are successfully compared with the hardware setup. By assessing real time losses, considering the specific geographical location and appropriate shading calculations, the results obtained are nearly precise for generation of solar energy. In this study, two models have been proposed, i.e., Module Tilt Angle (MTA) and Optimum Module Placement (OMP). In the MTA technique, by simple modification in the module mounting structure for varying module tilt angles, energy generation is increased by 3%–5%. Further, in the MTA module, different case studies have been conducted with two different orientations of the module, and based on their results, a formula for calculating space requirements has been derived. It is observed that with the same dimensions and number of modules, the area requirements has reduced from 185.14 m^2 to 115.29 m^2 depending upon the arrangement and orientation of modules. Thus, the optimum area required from the proposed formula leads to a saving of 38% in space requirement.

APPENDIX: SPV SYSTEM COMPONENT DATASHEET

1. Solar PV module datasheet

Make: Waaree; Model: WS-250; $I_{sc} = 8.96$ A; $V_{oc} = 37.20$ V; $I_{mpp} = 8.12$ A; $V_{mpp} = 30.80$ V; Module efficiency (η) = 15.40%; Number of cells per module = 60.

2. Inverter datasheet

Make: Refusol; Minimum MPP Voltage = 380 V; Nominal MPP = 590V; Max. MPP voltage = 850 V; Absolute max. PV voltage = 1000 V; efficiency (η) = 97.80%.

[1]D. Easan, J. Thomas, J. Dirk, and M. Robert, "Photovoltaic investment risk and uncertainty," IEEE J. Photovoltaics **4**(1), 278–284 (2014).
[2]V. Rai and B. Sigrin, "Diffusion of environmentally-friendly energy technologies: Buy versus lease differences in residential PV markets," Environ. Res. Lett. **8**(1), 014022 (2013).
[3]A. Audenaert, L. De Boeck, S. De Cleyn, S. Lizin, and J.-F. Adam, "Aneconomic evaluation of photovoltaic grid connected systems (PVGCS)in Flanders for companies: Ageneric model," Renewable Energy **35**(12), 2674–2682 (2010).
[4]E. Drury, P. Denholm, and R. Margolis, "The impact of different economic performance metrics on the perceived value of solar photovoltaics," Technical Report of National Renewable Energy Laboratory, USA, No. NREL/TP-6A20-52197, 2011.
[5]M. Rizwan, M. Jamil, S. Kirmani, and D. P. Kothari, "Fuzzy logic based modeling and estimation of global solar energy using meteorological parameters," Energy **70**(1), 685–691 (2014).
[6]M. S. Wong, R. Zhu, Z. Liu, L. Lu, J. Peng, Z. Tang, C. H. Lo, and W. K. Chan, "Estimation of Hong Kong's solar energy potential using GIS and remote sensing technologies," Renewable Energy **99**, 325–335 (2016).

[7]S. Kaplanis and E. Kaplani, "Stochastic prediction of hourly global solar radiation for Patra Greece," Appl. Energy **87**(12), 3748–3758 (2010).
[8]J. Munoz and O. Perpinan, "A simple model for the prediction of yearly energy yields for grid-connected PV systems starting from monthly meteorological data," Renewable Energy **97**, 680–688 (2016).
[9]I. B. Efstratios, A. R. Iason, and A. P. Stavros, "An explicit PV string model based on the Lambert function and simplified MPP expressions for operation under partial shading," IEEE Trans. Sustainable Energy **5**(1), 301–312 (2014).
[10]E. F. Fernandez, D. L. Talavera, F. M. Almonacid, and G. P. Smestad, "Investigating the impact of weather variables on the energy yield andcost of energy of grid-connected solar concentrator systems," Energy **106**(1), 790–801 (2016).
[11]D. Bub, M. Strobel, and M. Koentopp, "Influence of technological changes on the energy yield of PV modules: An outdoor study," Energy Procedia **55**, 38–46 (2014).
[12]D. Enrico, L. Alessandro, M. Davide, and V. Giuseppe, "Direct MPPT algorithm for PV sources with only voltage measurements," IEEE Trans. Power Electron. **30**(12), 6742–6750 (2015).
[13]S. Elmetennani, T. M. Laleg-Kirati, M. Djemai, and M. Tadjine, "New MPPT algorithm for PV applications based on hybrid dynamical approach," J. Process Control **48**, 14–24 (2016).
[14]T. Kok Soon and M. Saad, "Modified incremental conductance algorithm for photovoltaic system under partial shading conditions and load variation," IEEE Trans. Ind. Electron. **61**(10), 5384–5392 (2014).
[15]A. E. Mohammed, Z. Bashar, and J. A. David, "Assessment of the incremental conductance maximum power point tracking algorithm," IEEE Trans. Sustainable Energy **4**(1), 108–117 (2013).
[16]M. A. G. de Brito, L. Galotto, Jr., L. P. Sampaio, G. de Azevedo e Melo, and C. A. Alberto Canesin, "Evaluation of the main MPPT techniques for photovoltaic applications," IEEE Trans. Ind. Electron. **60**(3), 1156–1167 (2013).
[17]K. Eftichios and B. Frede, "Overview of maximum power point tracking techniques for photovoltaic energy production systems," Electr. Power Compon. Syst. **43**(12), 1329–1351 (2015).
[18]S. Bidyadhar and P. Raseswari, "A comparative study on maximum power point tracking techniques for photovoltaic power systems," IEEE Trans. Sustainable Energy **4**(1), 89–98 (2013).
[19]M. Schuck and R. C. N. Pilawa-Podgurski, "Ripple minimization through harmonic elimination in asymmetric interleaved multiphase DC–DC converters," IEEE Trans. Power Electron. **30**(12), 7202–7214 (2015).
[20]F. L. Tofoli, D. de Castro Pereira, W. J. de Paula, and D. de Sousa Oliveira, Jr., "Survey on non-isolated high-voltage step-updc–dc topologies based on the boost converter," IET Power Electron. **8**(10), 2044–2057 (2015).
[21]L. Nousiainen, J. Puukko, A. Maki, T. Messo, J. Huusari, J. Jokipii, J. Viinamaki, D. T. S. Lobera, S. Valkealahti, and T. Suntio, "Photovoltaic generator as an input source for power electronic converters," IEEE Trans. Power Electron. **28**(6), 3028–3038 (2013).
[22]C. N.-M. Man, H. Breuninger, S. Pettersson, G. Escobar, L. A. Serpa, and A. Coccia, "Practical design and implementation procedure of aninterleaved boost converter using SiCdiodes for PV applications," IEEE Trans. Power Electron. **27**(6), 2835–2845 (2012).
[23]M. Islam, S. Mekhilef, and M. Hasan, "Single phase transformerless inverter topologies for grid-tied photovoltaic system: A review," Renewable Sustainable Energy Rev. **45**, 69–86 (2015).
[24]W. Li, Y. Gu, H. Luo, W. Cui, X. He, and C. Xia, "Topology "Review and derivation methodology of single-phase transformerless photovoltaic inverters for leakage current suppression," IEEE Trans. Ind. Electron. **62**(7), 4537–4551 (2015).
[25]M. Islam and S. Mekhilef, "An improved transformerless grid connected photovoltaic inverter with reduced leakage current," Energy Convers. Manage. **88**, 854–862 (2014).
[26]F. Spertino and G. Graditi, "Power conditioning units in grid-connected photovoltaic systems: A comparison with different technologies and wide range of power ratings," Sol. Energy **108**, 219–229 (2014).
[27]L. Hassaine, E. OLias, J. Quintero, and V. Salas, "Overview of power inverter topologies and control structures for grid connected photovoltaic systems," Renewable Sustainable Energy Rev. **30**, 796–807 (2014).
[28]C. Jain and B. Singh, "Single-phase single-stage multifunctional grid interfaced solar photo-voltaic system under abnormal grid conditions," IET Gener. Transm. Distrib. **9**(10), 886–894 (2015).
[29]Y. Yang and F. Blaabjerg, "Overview of single-phase grid-connected photovoltaic systems," Electr. Power Compon. Syst. **43**(12), 1352–1363 (2015).
[30]B. N. Alajmi, K. H. Ahmed, G. P. Adam, and B. W. Williams, "Single-phase single-stage transformer lessgrid-connected PV system," IEEE Trans. Power Electron. **28**(6), 2664–2676 (2013).
[31]A. K. Barnes, J. C. Balda, and C. M. Stewart, "Selection of converter topologies for distributed energy resources," in *2012 Twenty-Seventh Annual IEEE Applied Power Electronics Conference and Exposition (APEC)*, USA (2012), pp. 1418–1423.
[32]J. R. Perez-Gallardo, C. Azzaro-Pantel, S. Astier, S. Domenech, and A. Aguilar-Lasserre, "Ecodesign of photovoltaic grid-connected systems," Renewable Energy **64**, 82–97 (2014).
[33]M. H. Kang and A. Rohatgi, "Quantitative analysis of the levelized cost of electricity of commercial scale photovoltaics systems in the US," Sol. Energy Mater. Sol. Cells **154**, 71–77 (2016).
[34]A. S. Mundada, K. K. Shah, and J. M. Pearce, "Levelized cost of electricity for solar photovoltaic, battery and cogen hybrid systems," Renewable Sustainable Energy Rev. **57**, 692–703 (2016).
[35]M. Said, M. EL-Shimy, and M. A. Abdelraheem, "Photovoltaics energy: Improved modelling and analysis of the levelized cost of energy (LCOE) and grid parity – Egypt case study," Sustainable Energy Technol. Assess. **9**, 37–48 (2015).
[36]K. Branker, M. J. M. Pathak, and J. M. Pearce, "A review of solar photovoltaic levelized cost of electricity," Renewable Sustainable Energy Rev. **15**, 4470–4482 (2011).
[37]R. K. Jones, A. Baras, A. Al-Saeeri, A. Al Qahtani, A. O. Al Amoudi, Y. Al Shaya, M. Alodan, and S. A. Al-Hsaien, "Optimized cleaning cost and schedule based on observed soiling conditions for photovoltaic plants in central Saudi Arabia," IEEE J. Photovoltaics **6**(3), 730–738 (2016).
[38]G. Notton, V. Lazarov, and L. Stoyanov, "Optimal sizing of a grid-connected PV system for various PV module technologies and inclinations, inverter efficiency characteristics and locations," Renewable Energy **35**(2), 541–554 (2010).

[39]R. Rawat, S. C. Kaushik, and R. Lamba, "A review on modelling, design methodology and size optimization of photovoltaic based water pumping, standalone and grid connected system," Renewable Sustainable Energy Rev. **57**, 1506–1519 (2016).
[40]M. Karimi, H. Mokhlis, K. Naidu, S. Uddin, and A. H. A. Bakar, "Photovoltaic penetration issues and impacts in distribution network—A review," Renewable Sustainable Energy Rev. **53**, 594–605 (2016).
[41]M. Obi and R. Bass, "Trends and challenges of grid-connected photovoltaic systems—A review," Renewable Sustainable Energy Rev. **58**, 1082–1094 (2016).
[42]See http://www.mnre.gov.in for Ministry of New and Renewable Energy, Government of India.

Volume 6 Issue 4 (2018) 296-311 ISSN 2347-3258
International Journal of Advance Research and Innovation

Optimization of two-stage cascade refrigeration systems using HFO refrigerants in the high-temperature circuit and HFC-134a in low-temperature circuit

Radhey Shyam Mishra
Department of Mechanical, Production & Industrial and Automobiles Engineering, Delhi Technological University, Delhi-110042, India

Article Info:
Article history
Received 7 October 2018
Received in revised form:
28 October 2018
Accepted 2 November 2018
Available online 15 December 2018

Keywords: Thermodynamic Modelling, Energy-Exergy-Analysis Exergy Destruction Ratio, Entropy Generation Principle

Abstract
The eco-friendly refrigeration technologies which are receiving more and more attention in the days by day of for solving energy and environmental problems. In this paper, it is suggested to phase out presently most used refrigerant R-134a considering global warming and to use natural refrigerants such as ammonia, carbon dioxide and hydro carbons in two stage cascade vapour compression refrigeration system for sustainable environment. Thermal model was developed for single stage and also two stage cascade refrigeration systems using HFO-1234yf for low temperature applications in the range of 100℃ to -51.5℃ and HFO-1234ze for high temperature applications in the range of 100℃ to -30.5℃. Numerical computation was carried out by using R1234ze in the temperature range of 60℃to -30℃in the high temperature circuit and R1234yf in the range of 20℃to -50℃for low temperature range. The developed model can also predicts the thermal performances of using nine eco-friendly refrigerants in low temperature circuit and R1234ze n low temperature applications. The ecofriendly refrigerants HFO can replace R134a without minor modifications. However up to temperature -50℃in the low temperature evaporator circuit with temperature overlapping (Approach=10ºC) and condenser temperature of 55℃with cascade evaporator temperature of 0℃ , the combination of R1234ze in high temperature circuit and R1234yf in low temperature circuit gives best results for replacing R134a and for -100℃of low temperature evaporator circuit and 55℃of high temperature condenser and -30℃ cascade evaporator with temperature overlapping (Approach=10ºC) the combination of R1234ze – and R245fa gives better thermodynamic performances as compared to R-1234yf and R245fa. The optimum values for system-6 (using R1234ze in high temperature circuit and HFC-134a in low temperature circuit , the optimum second law efficiency (exergetic efficiency) obtained at low temperature evaporator is at -78℃to -80℃respectively and no optimum was found using HFO-1234yf in high temperature circuit and HFC-134a in low temperature circuit.

1. Introduction

Refrigerant selection based on a simple approach of 'zero ODP' required high cost to both global warming and energy efficiency. The alarming increase in atmospheric concentration of HFC-134a suggested careful considerations of not overusing any single compound for substituting ODSs. The use of refrigeration will continue to expand worldwide, especially in developing countries, because it is vital to life. However, the environmental impacts, both on the ozone layer and on global warming are important. The refrigeration sector has already helped to mitigate global warming by applying the Montreal Protocol, for improved refrigeration technologies. The chemical industry is promoting new refrigerant it calls 'hydro fluoro-olefins'(i.e. HFOs). Chemically, HFOs are HFCs. The refrigeration industry has been working for the past few decades to find replacement refrigerants for the ozone-depleting chlorofluorocarbons (CFCs) and hydrochlorofluorocarbons (HCFCs) being phased out as a result of the Montreal Protocol. The solution for most refrigerant producers has been the commercialization of hydrofluorocarbon (HFC) refrigerants. The new HFC refrigerants, HFC-134a being the most widely used at this time, have zero ozone depletion potential and thus are not affected by the current regulatory phase out as a result of the Montreal Protocol[1].Further environmental regulations may ultimately cause global phase out of certain HFC refrigerants. Currently, the refrigeration industry is facing regulations relating to global warming potential for refrigerants used in mobile air-conditioning. Therefore, there is a great current need to identify new refrigerants with reduced global warming potential for the mobile air-conditioning market. Should the regulations be more broadly applied in the future, for instance for stationary air conditioning and refrigeration systems, an even greater need will be felt for refrigerants that can be used in all areas of the refrigeration and air-conditioning industry. Currently, proposed replacement refrigerants for HFC-134a include HFC-152a, pure hydrocarbons such as butane or propane, or "natural" refrigerants such as CO2. Many of these suggested replacements are toxic, flammable, and/or have low energy efficiency. New replacements are also being proposed for R1234yf and R1234ze among others. As these replacements are found, new uses of such alternative refrigerants are being sought in order to take advantage of their low or zero ozone depletion potential and lower global warming potential because GWP is a measure of a greenhouse gas when it is released into the atmosphere and benchmarked against CO2 which has a GWP equal to one so-called 'natural' or 'stable' gases such as carbon dioxide, methane and butane, do not break down in the atmosphere and are non-flammable

***Corresponding Author,**
E-mailaddress: rsmishra@dtu.ac.in
All rights reserved: http://www.ijari.org

2.Ecofriendly low GWO & zero ODP hydro-fluoro-olefin (HFO-1234yf)

DuPont and Honeywell [2] jointly identified HFO-1234yf ($CF_3CF=CH_2$) as a single substance as the preferred low GWP refrigerant which offers thermal performance.HFO-1234yf is the leading alternative refrigerant to replace R-134a has excellent environmental properties, very low GWP of four, zero ODP, for favourable life cycle climate performance (LCCP) (Spatz et.al, 2008)[3], Atmospheric chemistry determined low toxicity similar to R-134a due to system performances are very similar to R-134a. Excellent COP and Capacity, no glide temperature.The only problem is HFOs are mildly flammable .HFO-1234yf has recently been approved as a class–A2L refrigerant by American Society of Heating, Refrigerating and Air Conditioning Engineers (ASHRAE). Despite carbon dioxide's appeal as a ''natural refrigerant'' and favourable findings in some reported bench and vehicle tests, as a single compound refrigerant, HFO-1234yf offers similar thermos-physical properties to R-134a, thus minimizing equipment changes and has met criteria for stability and compatibility. The Society of Automotive Engineers (SAE) validated that HFO-1234yf as safe for use in automotive applications. The critical temperature, critical density and critical pressure were measured by the visual observation

of the meniscus disappearance and were determined to be 367.85 K, 478 kg/m3, and 3382 kPa, respectively (Tanaka and Higashi 2010)[4]. After independent review of all toxicology test results, DuPont and Honeywell have concluded that HFO1234yf is safe to commercialize for use in refrigeration and air conditioning systems.Furthermore, industry risk assessments of various potential exposure scenarios have also concluded HFO-1234yf is safe for use in MAC applications. HFO-1234yf flammability characteristics are much more favourable than those of hydrocarbon gases. It is far less dangerousthanotherhydro-carbonrefrigerants.HFO-1234yf offers equivalent or lower toxicity as compared to R-134a or R-12 in terms of both human health effects and ecological effects. HFO-1234yf met all key technical customer criteria to be adopted for MAC. Various LCCP evaluations done showing LCCP benefit of HFO-1234yf compared to HFC-134a and CO2 (Spatzet al. 2008) [3].HFO-1234yf is not yet a proven entity and even though it may not be commercialized for at least a year or two, it is nevertheless promoted by the chemical industry as the alternative to HFC-134a, The currently available, safe, environmentally friendly, efficient and low GWP, non-fluorocarbon alternatives such as CO2 in refrigeration and air conditioning systems or the commercialization of hydrocarbon (SAE International 2008) (Table 1) because CO2 manufacturers also argue that, CO2 is proven, safe, natural and sustainable for environmental point of view (Spatz Mark 2009)[3] as compared to HFO-1234yf. The Greenpeace Germany had raised flammability , stating that ‘‘the HFO-1234yf will be an alternative for replacing R134a. The Thermodynamic properties of several fluorinated propene isomers, namely: R-1225ye (E), R-1225ye (Z), R-1225zc, R-1234ye (E), R-1234yf, R-1234ze (E), R-1234ze (Z), and R-1243zf for the naming convention for the fluorinated propene series) (Steven Brown et al. 2010)[5].Hydro-Fluro-Olefin (HFO)-1234yf in direct expansion systems (‘‘secondary loop’’) systems employing an intermediate heat transfer fluid. According to DuPont and Honeywell’s R1234yf is a near drop in replacement to HFC-134a . because R744 on the other hand, operates at higher pressure so requires a new re system design with new components and tooling. So selection of proper refrigerant is very important. One can select the refrigerant as per the application, the environmental and physiological properties and performance parameters. Tetra fluoropropene (HFO-1234ze) is a hydro-fluoro-olefin. It was developed as a "fourth generation" refrigerant to replace R-134a and as a blowing agent for foam and aerosol applications.[2] The use of R-134a is being phased out because of its high global-warming potential. HFO-1234ze has zero ozone-depletion potential (ODP=0) and a very low global-warming potential (GWP <1), even lower than CO2

3.Cascade two stages vapour compression refrigeration systems using ecofriendly refrigerants

A cascade refrigeration system having at least two refrigeration loops, each circulating a refrigerant therethrough, comprising (a) first refrigeration loop, including:

(a) a first expansion device for reducing the pressure and temperature of a first refrigerant liquid

(b) an evaporator having an inlet and an outlet, wherein the first refrigerant liquid from the first expansion device enters the evaporator through the evaporator inlet and is evaporated in the evaporator to form a first refrigerant vapor, thereby producing cooling, and circulates to the outlet;

(c) a first compressor having an inlet and an outlet, wherein the first refrigerant vapor from the evaporator circulates to the inlet of the first compressor and is compressed, thereby increasing the pressure and the temperature of the first refrigerant vapor, and the compressed first refrigerant vapor circulates to the outlet of the first compressor; a cascade heat exchanger system comprising: (i) a first cascade heat exchanger having: (A) a first inlet and a first outlet, wherein the first refrigerant vapor from the evaporator circulates from the first inlet to the first outlet and is condensed in the first heat exchanger to form a first refrigerant liquid, thereby rejecting heat, and (B) a second inlet and a second outlet, wherein a heat transfer fluid circulates from the second inlet to the second outlet, wherein the heat rejected by the first refrigerant vapour as it is condensed is absorbed by the heat transfer fluid, (ii) a second cascade heat exchanger having: (A) a first inlet and a first outlet, wherein the heat transfer fluid from the first cascade heat exchanger circulates from the first inlet to the first outlet and rejects the heat absorbed in the first cascade heat exchanger, and (B) a second inlet and a second outlet, wherein a second refrigerant liquid circulates from the second inlet to the second outlet and absorbs the heat rejected by the heat transfer fluid and forms a second refrigerant vapor; a second compressor having an inlet and an outlet, wherein the second refrigerant vapor from the second cascade heat exchanger is drawn into the compressor and is compressed, thereby increasing the pressure and temperature of the second refrigerant vapor; a condenser having an inlet and an outlet for circulating the second refrigerant vapor therethrough and for condensing the second refrigerant vapor from the compressor to form a second refrigerant liquid, wherein the second refrigerant liquid exits the condenser through the outlet; and (g) a second expansion device for reducing the pressure and temperature of the second refrigerant liquid exiting the condenser and entering the second inlet of the second cascade heat exchanger.A method of exchanging heat between at least two refrigeration loops, comprising: (a) absorbing heat from a body to be cooled in a first refrigeration loop and rejecting this heat to a second refrigeration loop; and (b) absorbing the heat from the first refrigeration loop in the second refrigeration loop and rejecting this heat to ambient, wherein the refrigerant in at least one of the refrigeration loops comprises a fluoro-olefin.

4. Results and Discussion

The input data for computing thermal performance of single stage and two tages cascade refrigeration system is given as.

4.1 For two stages cascade refrigeration System-1, System-2, System-3

High temperature condenser temperature (T_Cond_HTC) =50˚C, High temperature evaporator temperature (T_Eva_HTC)=0˚C, Low temperature Evaporator temperature (T_Eva_LTC)=-50˚C, Approach (Temperature overlapping)=10˚C,
Efficiency of Compressor_HTC=0.80,
Efficiency of Compressor_LTC=0.80

4.2 For twostages cascade refrigeration system-4

High temperature condenser temperature (T_Cond_HTC) =55˚C, High temperature Evaporator temperature (T_Eva_HTC) =0˚C, Low temperature evaporator temperature(T_Eva_LTC)= - 50˚C, Approach (Temperature overlapping)=10˚C,
Efficiency of Compressor_HTC=0.80,
Efficiency of Compressor_LTC=0.80

4.3 For cascade refrigeration System-5 & system-6

High temperature condenser temperature (T_Cond_HTC) =55˚C, High temperature Evaporator temperature(T_Eva_HTC) =-30˚C, Low temperature Evaporator temperature(T_Eva_LTC)=-100˚C, Approach (Temperature overlapping)=10oC,
Efficiency of Compressor_HTC=0.80,
Efficiency of Compressor_LTC=0.80

4.4 For vapour compression refrigerationsystem-7

High temperature condenser temperature (T_Cond_)=55˚C,
Evaporator temperature (T_Eva)_= -30˚C,
Efficiency of Compressor=0.80,

The two stages cascade system of consisting of the first refrigerant comprises HFO- 1234yf wherein the second refrigerant comprises HFO-1234ze.Table-1 shows the properties of HFO-1234yf and R-134a

Table 1(a): Physical properties comparison of R1234yf and R134a [3]

Properties	HFO-1234 yf	R-134a
Boiling Point (˚C)	-29	-26
Critical Point ((˚C)	95	102
Vapour Press (25 (˚C) MPa	0.677	0.665
Liquid Density (kg/m3) (25 (˚C)	1,094	1,207
Vapour Density (kg/m3)(25 (˚C)	37.6	32.4

As pure substance R1234ze is seen as the R134a replacement for high temperature application. However, its volumetric refrigerating capacity is below that of R134a and R1234yf. Its boiling point is also higher than that of R134a Similarly to R134a, R1234ze is a medium pressure refrigerant with a slightly higher critical and boiling temperatures and lower critical pressure. Some of the properties of R1234ze in comparison to R134a are listed in the Table 1(b).

Table 1 (b) : Physical properties comparison of R1234ze and R134a [6]

Physical properties	R1234ze	R134a
Molecular weight, kg/mol	114	102
Boiling point at 101.3 kPa, °C	-18,95	-26,06
Critical temperature, °C	109,4	101,1
Critical pressure, bar	36,4	40,6
Latent heat of vaporization at 30 °C, kJ/kg	162,9	173,1
Critical density, kg/m3	489	515,3

The performance of vapour compression system using following eco-friendly refrigerants have been computed and results of thermal model are shown in Table-1, 2, 3, 4, 5, 6 for system 1,2,3,4, 5 and 6 respectively. Thermal performance of System-3 with variation of HTC condenser temperature of two stage cascade vapour compression refrigeration system using HFO-1234yf in high temperature circuit and HFC-134a in low temperature circuit.

Table-2(a): Variation of Thermal performance with variation of HTC condenser temperature of two stage cascade vapour compression refrigeration system using HFO-1234ze in high temperature circuit and HFO-1234yf in low temperature circuit for T_Cond=50°C with subcooling of 5°C, $T_{_Eva_HTC}$= 0°C, $T_{_Eva_LTC}$=-50°C, $Q_{_Eva_LTC}$=35 "kW"

Effect of Temperature Overlapping (Approach)	COP	System EDR	Exergetic Efficiency	$EDR_{_Rational}$	Exergy of Fuel (kW)	Exergy of Product kW)	COP_HTC	COP_LTC
0	1.402	1.121	0.4715	0.5285	25.08	11.83	3.737	2.844
2	1.356	1.193	0.4561	0.5439	25.93	11.83	3.737	2.698
4	1.312	1.267	0.4412	0.5588	26.81	11.83	3.737	2.562
6	1.269	1.344	0.4267	0.5733	27.72	11.83	3.737	2.435
8	1.227	1.423	0.4127	0.5873	28.66	11.83	3.737	2.316
10	1.187	1.506	0.3991	0.6009	29.64	11.83	3.737	2.204
12	1.147	1.592	0.3858	0.6142	30.66	11.83	3.737	2.098

Table-2(b): Variation of Thermal performance with variation of HTC condenser temperature of two stage cascade vapour compression refrigeration system using HFO-1234ze in high temperature circuit and HFO-1234yf in low temperature circuit for T_Cond=50°C with subcooling of 5°C, $T_{_Eva_HTC}$= 0°C, $T_{_Eva_LTC}$=-50°C, $Q_{_Eva_LTC}$=35 "kW"

Effect of Temperature Overlapping (Approach)	COP	W_{Comp_HTC}	W_{Comp_LTC}	Mass flow rate in HTC circuit (kg/sec)	Mass flow rate in LTC circuit (kg/sec)	$Q_{_Cond_HTC}$ (kW)	$Q_{_Cond_Cascade}$(kW)	$Q_{_Eva_LTC}$(kW)
0	1.402	12.72	12.37	0.3924	0.2695	60.25	47.53	35.167
2	1.356	12.9	13.04	0.3979	0.2749	61.1	48.2	35.167
4	1.312	13.08	13.73	0.4036	0.2805	61.98	48.89	35.167
6	1.269	13.27	14.44	0.4096	0.2864	62.89	49.61	35.167
8	1.227	13.47	15.19	0.4157	0.2927	63.83	50.35	35.167
10	1.187	13.68	15.96	0.4221	0.2992	64.81	51.13	35.167
12	1.147	13.89	16.76	0.4287	0.3061	65.82	51.93	35.167

Table-2(c): Variation of Thermal performance with variation of HTC condenser temperature of two stage cascade vapour compression refrigeration system using HFO-1234ze in high temperature circuit and HFO-1234yf in low temperature circuit for T_Cond=50°C with subcooling of 5°C, $T_{_Eva_HTC}$= 0°C, $T_{_Eva_LTC}$=-50°C, $Q_{_Eva_LTC}$=35 "kW"

LTC Refrigerants	COP	System EDR	Exergetic Efficiency	$EDR_{_Rational}$	Exergy of Fuel (kW)	Exergy of Product (kW)	COP_HTC	COP_LTC
R-134a	1.219	1.438	0.4101	0.5899	28.84	11.83	3.737	2.294
R-1234yf	1.181	1.506	0.3991	0.6009	29.64	11.83	3.737	2.204
R717	1.206	1.466	0.4055	0.5945	29.17	11.83	3.737	2.256
R141b	1.289	1.307	0.4334	0.5666	27.29	11.83	3.737	2.493
R-404a	1.151	1.584	0.3870	0.6130	30.57	11.83	3.737	2.107
R-410a	1.214	1.45	0.4081	0.5919	28.98	11.83	3.737	2.278
R-407c	1.094	1.717	0.3680	0.6320	32.14	11.83	3.737	1.961
R-152a	1.246	1.386	0.4192	0.5808	28.22	11.83	3.737	2.370
R-227ea	1.131	1.629	0.3804	0.6196	31.09	11.83	3.737	2.056
R-236fa	1.188	1.503	0.3995	0.6005	29.6	11.83	3.737	2.207
R-245fa	1.239	1.40	0.4166	0.5834	28.39	11.83	3.737	2.349
R-32	1.203	1.471	0.4047	0.5953	29.22	11.83	3.737	2.250
R-600a	1.215	1.447	0.4087	0.5923	28.94	11.83	3.737	2.282
R-600	1.243	1.392	0.4180	0.5820	28.3	11.83	3.737	2.360
R-290	1.218	1.442	0.4096	0.5904	28.88	11.83	3.737	2.290
R-123	1.259	1.361	0.4235	0.5735	27.93	11.83	3.737	2.408
R-125	1.13	1.632	0.380	0.620	31.13	11.83	3.737	2.052
R-507a	1.168	1.546	0.3928	0.6072	30.11	11.83	3.737	2.153

Table-2(d): Variation of Thermal performance with variation of HTC condenser temperature of two stage cascade vapour compression refrigeration system using HFO-1234ze in high temperature circuit and HFO-1234yf in low temperature circuit for T_Cond=50ºC with subcooling of 5ºC, $T_{_Eva_HTC}$= 0ºC, $T_{_Eva_LTC}$=-50ºC, $Q_{_Eva_LTC}$=35 "kW"

LTC Refrigerants	COP	W_{Comp_HTC} (kW)	W_{Comp_LTC} (kW)	Mass flow rate in HTC circuit (kg/sec)	Mass flow rate in LTC circuit (kg/sec)	$Q_Cond_{_HTC}$ (kW)	$Q_Cond_{_Cascade}$ (kW)	$Q_Eva_{_LTC}$ (kW)
R-134a	1.219	13.51	15.33	0.4169	0.2282	64.01	50.5	35.167
R-1234yf	1.181	13.68	15.96	0.4221	0.2992	64.81	51.13	35.167
R717	1.206	13.58	15.59	0.4194	0.03072	64.34	50.75	35.167
R141b	1.289	13.18	14.10	0.4068	0.1819	62.45	49.27	35.167
R-404a	1.151	13.88	16.69	0.4281	0.2867	65.73	51.86	35.167
R-410a	1.214	13.54	15.44	0.4128	0.188	64.15	50.81	35.167
R-407c	1.094	14.21	17.93	0.4384	0.2109	67.31	53.10	35.167
R-152a	1.246	13.38	14.84	0.4128	0.1390	63.38	50.0	35.167
R-227ea	1.131	13.99	17.10	0.4315	0.433	66.26	52.27	35.167
R-236fa	1.188	13.67	15.93	0.4218	0.3118	64.77	51.10	35.167
R-245fa	1.239	13.42	14.91	0.4139	0.2556	63.55	50.14	35.167
R-32	1.203	13.59	15.63	0.4194	0.1258	64.39	50.80	35.167
R-600a	1.215	13.53	15.41	0.4175	0.1342	64.11	50.57	35.167
R-600	1.243	13.40	14.9	0.4133	0.1206	63.46	50.07	35.167
R-290	1.218	13.52	15.36	0.4171	0.121	64.04	50.53	35.167

Table-2(e): Variation of Thermal performance with variation of HTC condenser temperature of two stage cascade vapour compression refrigeration system using HFO-1234ze in high temperature circuit and HFO-1234yf in low temperature circuit for T_Cond=50ºC with subcooling of 5ºC, $T_{_Eva_HTC}$= 0ºC, $T_{_Eva_LTC}$=-50ºC, $Q_{_Eva_LTC}$=35 "kW"

HTC Refrigerants	COP	System EDR	Exergetic Efficiency	$EDR_{_Rational}$	Exergy of Fuel (kW)	Exergy of Product (kW)	COP_HTC	COP_LTC
R1234ze	1.187	1.506	0.3991	0.6009	29.64	11.83	3.737	2.204
R717	1.228	1.422	0.4129	0.5871	28.64	11.83	4.030	2.204
R152a	1.217	1.442	0.4095	0.5905	28.89	11.83	3.955	2.204
R290	1.178	1.523	0.3963	0.6037	29.84	11.83	3.682	2.204
R600	1.217	1.442	0.4095	0.5905	28.89	11.83	3.955	2.204
R600a	1.196	1.486	0.4022	0.5978	29.41	11.83	3.801	2.204
R134a	1.190	1.498	0.4003	0.5997	29.55	11.83	3.762	2.204
R1234yf	1.160	1.564	0.390	0.610	30.32	11.83	3.559	2.204

Table-2(f): Variation of Thermal performance with variation of HTC condenser temperature of two stage cascade vapour compression refrigeration system using HFO-1234ze in high temperature circuit and HFO-1234yf in low temperature circuit for T_Cond=50ºC with subcooling of 5ºC, $T_{_Eva_HTC}$= 0ºC, $T_{_Eva_LTC}$=-50ºC, $Q_{_Eva_LTC}$=35 "kW"

HTC Refrigerants	COP	W_{Comp_HTC} (kW)	W_{Comp_LTC} (kW)	Mass flow rate in HTC circuit (kg/sec)	Mass flow rate in LTC circuit (kg/sec)	$Q_Cond_{_HTC}$ (kW)	$Q_Cond_{_Cascade}$ (kW)	$Q_{_EVA_LTC}$ (kW)
R1234ze	1.187	13.89	16.76	0.4287	0.3061	65.82	51.93	35.167
R717	1.228	12.89	16.76	0.04964	0.3061	64.81	51.93	35.167
R152a	1.217	13.13	16.76	0.2305	0.3061	65.06	51.93	35.167
R290	1.178	14.10	16.76	0.2058	0.3061	66.03	51.93	35.167
R600	1.217	13.13	16.76	0.1887	0.3061	65.06	51.93	35.167
R600a	1.196	13.66	16.76	0.2187	0.3061	65.59	51.93	35.167
R134a	1.190	13.8	16.76	0.3856	0.3061	65.73	51.93	35.167
R1234yf	1.160	14.59	16.76	0.5086	0.3061	66.52	51.93	35.167

Table-2(g): Variation of Thermal performance with variation of HTC condenser temperature of two stage cascade vapour compression refrigeration system using HFO-1234ze in high temperature circuit and HFO-1234yf in low temperature circuit for T_Cond=50ºC with subcooling of 5ºC, $T_{_Eva_HTC}$= 0ºC, $T_{_Eva_LTC}$=-50ºC, $Q_{_Eva_LTC}$=35 "kW"

T_Cond (ºC)	COP	EDR	Exergetic Efficiency	Rational EDR	Exergy of Fuel (kW)	Exergy of Product (kW)	COP_HTC	COP_LTC
60	1.024	1.905	0.3443	0.6557	34.35	11.83	2.779	2.204
55	1.104	1.694	0.3712	0.6288	31.86	11.83	3.215	2.204
50	1.187	1.506	0.3991	0.6009	29.64	11.83	3.737	2.204
45	1.273	1.336	0.4280	0.5720	27.63	11.83	4.379	2.204
40	1.363	1.182	0.4583	0.5417	25.81	11.83	5.192	2.204
35	1.458	1.039	0.4903	0.5097	24.12	11.83	6.264	2.204

30	1.559	0.9070	0.5244	0.4756	22.56	11.83	7.75	2.204
25	1.667	0.7832	0.5608	0.4392	21.09	11.83	9.962	2.204

Table-2(h): Variation of Thermal performance with variation of HTC condenser temperature of two stage cascade vapour compression refrigeration system using HFO-1234ze in high temperature circuit and HFO-1234yf in low temperature circuit for T_Cond=50ºC with subcooling of 5ºC, $T_{_Eva_HTC}$= 0ºC, $T_{_Eva_LTC}$=-50ºC, $Q_{_Eva_LTC}$=35 "kW"

T_Cond (ºC)	COP	$W_{_c_HTC}$ (kW)	$W_{_c_LTC}$ (kW)	Mass flow rate (kg/sec) of R-1234ze	Mass flow rate (kg/sec) of R-1234yf	$Q_{_Cond_HTC}$ (kW)	$Q_{_Cond_Cascade}$ (kW)	$Q_{_EVA_LTC}$ (kW)
60	1.024	18.68	16.76	0.4892	0.3061	70.61	51.93	35.167
55	1.104	16.15	16.76	0.4587	0.3061	68.08	51.93	35.167
50	1.187	13.89	16.76	0.4287	0.3061	65.82	51.93	35.167
45	1.273	11.86	16.76	0.4042	0.3061	63.79	51.93	35.167
40	1.363	10.0	16.76	0.3827	0.3061	61.93	51.93	35.167
35	1.458	8.29	16.76	0.3636	0.3061	60.22	51.93	35.167
30	1.559	6.701	16.76	0.3464	0.3061	58.63	51.93	35.167
25	1.667	5.212	16.76	0.3310	0.3061	57.14	51.93	35.167

Table-2(i): Variation of Thermal performance with variation of cascade evaporator temperature of two stage cascade vapour compression refrigeration system using HFO-1234ze in high temperature circuit and HFO-1234yf in low temperature circuit for T_Cond=50ºC with subcooling of 5ºC, $T_{_Eva_HTC}$= 0ºC, $T_{_Eva_LTC}$=-50ºC, $Q_{_Eva_LTC}$=35 "kW"

T_Eva (ºC)	COP	EDR	Exergetic Efficiency	EDR	Exergy of Fuel (kW)	Exergy of Product (kW)	COP_HTC	COP_LTC
20	1.049	1.836	0.3527	0.6473	33.54	11.83	8.032	1.356
15	1.099	1.706	0.3696	0.6304	32.0	11.83	6.415	1.533
10	1.139	1.611	0.383	0.6170	30.88	11.83	5.264	1.729
5	1.168	1.546	0.3928	0.6072	30.11	11.83	4.404	1.951
4	1.173	1.536	0.3944	0.6056	29.99	11.83	4.257	1.998
3	1.177	1.527	0.3958	0.6042	29.89	11.83	4.118	2.048
2	1.180	1.519	0.3970	0.6030	29.79	11.83	3.985	2.098
1	1.184	1.512	0.3981	0.6019	29.71	11.83	3.858	2.15
0	1.187	1.506	0.3991	0.6009	29.64	11.83	3.737	2.204
-1	1.189	1.501	0.3999	0.6001	29.58	11.83	3.622	2.259
-2	1.191	1.497	0.4005	0.5995	29.53	11.83	3.511	2.316
-3	1.193	1.493	0.4011	0.5989	29.49	11.83	3.405	2.374
-4	1.193	1.491	0.4015	0.5985	29.46	11.83	3.304	2.435
-5	1.194	1.489	0.4017	0.5983	29.44	11.83	3.206	2.497
-6	1.195	1.489	0.4018	0.5991	29.43	11.83	3.113	2.562
-7	1.195	1.489	0.4018	0.5982	29.44	11.83	3.023	2.629
-8	1.194	1.490	0.4016	0.5984	29.45	11.83	2.937	2.698
-9	1.193	1.492	0.4014	0.5986	29.47	11.83	2.854	2.77
-10	1.192	1.494	0.4009	0.5991	29.5	11.83	2.744	2.844
-15	1.180	1.519	0.3969	0.6031	29.8	11.83	2.416	3.261
-20	1.159	1.585	0.3899	0.6101	30.33	11.83	2.116	3.777

Table-2(j): Variation of Thermal performance with variation of cascade evaporator temperature of two stage cascade vapour compression refrigeration system using HFO-1234ze in high temperature circuit and HFO-1234yf in low temperature circuit for T_Cond=50ºC with subcooling of 5ºC, $T_{_Eva_HTC}$= 0ºC, $T_{_Eva_LTC}$=-50ºC, $Q_{_Eva_LTC}$=35 "kW"

T_Eva (ºC)	COP	$W_{_Comp_HTC}$ (kW)	$W_{_Comp_LTC}$ (kW)	Mass flow rate (kg/sec) of R-1234ze	Mass flow rate (kg/sec) of R-1234yf	$Q_{_Cond_HTC}$ (kW)	$Q_{_Cond_Cascade}$ (kW)	$Q_{_EVA_LTC}$ (kW)
20	1.049	7.772	27.26	0.4638	0.4018	70.19	62.42	35.167
15	1.099	9.237	24.09	0.4513	0.3719	68.49	59.26	35.167
10	1.139	10.73	21.34	0.4416	0.3467	67.24	56.51	35.167
5	1.168	12.28	18.92	0.4342	0.3349	66.37	54.09	35.167
4	1.173	12.60	18.47	0.4329	0.3210	66.24	53.64	35.167
3	1.177	12.92	18.03	0.4318	0.3171	66.11	53.20	35.167
2	1.180	13.24	17.60	4307	0.3133	66.01	52.76	35.167
1	1.184	13.57	17.17	0.4297	0.3096	65.91	52.34	35.167
0	1.187	13.89	16.76	0.4287	0.3061	65.82	51.93	35.167
-1	1.189	14.23	16.36	0.4278	0.3026	65.75	51.52	35.167
-2	1.191	14.56	15.96	0.4270	0.2992	65.69	51.13	35.167
-3	1.193	14.91	15.57	0.4262	0.2959	65.64	50.74	35.167
-4	1.193	15.24	15.19	0.4255	0.2927	65.60	50.35	35.167
-5	1.194	15.59	14.81	0.4248	0.2895	65.57	49.98	35.167
-6	1.195	15.94	14.44	0.4242	0.2864	65.55	49.61	35.167
-7	1.195	16.29	14.08	0.4237	0.2834	65.54	49.25	35.167
-8	1.194	16.65	13.73	0.4232	0.2805	65.54	48.89	35.167

-9	1.193	17.01	13.38	0.4227	0.2777	65.55	48.55	35.167
-10	1.192	17.37	13.04	0.4223	0.2749	65.58	48.20	35.167
-15	1.180	19.27	11.40	0.4210	0.2618	65.84	46.57	35.167
-20	1.159	21.29	9.887	0.4207	0.2901	66.35	45.05	35.167

Table-3(a): Variation of Thermal performance with variation of LTC evaporator temperature of two stage cascade vapour compression refrigeration system using HFO-1234ze in high temperature circuit and HFC-134a in low temperature circuit for T_Cond=50°C with subcooling of 5°C, $T_{_Eva_HTC}$= -10°C, $T_{_Eva_LTC}$=-50°C, $Q_{_Eva_LTC}$=35 "kW"

T_Cond (°C)	COP	EDR	Exergetic Efficiency	Rational EDR	Exergy of Fuel (kW)	Exergy of Product (kW)	COP_HTC	$COP_{_LTC}$
25	1.724	0.7246	0.5798	0.4202	20.4	11.83	9.962	2.294
30	1.61	0.8470	0.5414	0.4586	21.84	11.83	7.75	2.294
35	1.503	0.9777	0.5056	0.4944	23.39	11.83	6.264	2.294
40	1.404	1.118	0.4721	0.5279	25.05	11.83	5.192	2.294
45	1.309	1.271	0.4403	0.5597	26.86	11.83	4.379	2.294
50	1.219	1.438	0.4101	0.5899	28.84	11.83	3.737	2.294
55	1.133	1.624	0.3811	0.6189	31.03	11.83	3.215	2.294
60	1.05	1.832	0.3531	0.6469	33.50	11.83	2.779	2.294

Table-3(b): Variation of Thermal performance with variation of LTC evaporator temperature of two stage cascade vapour compression refrigeration system using HFO-1234ze in high temperature circuit and HFC-134a in low temperature circuit for T_Cond=50°C with subcooling of 5°C, $T_{_Eva_HTC}$= 0°C, $T_{_Eva_LTC}$=-50°C, $Q_{_Eva_LTC}$=35 "kW"

T_Cond (°C)	COP	$W_{_Comp_HTC}$ (kW)	$W_{_Comp_LTC}$ (kW)	Mass flow rate (kg/sec) of R-1234ze	Mass flow rate (kg/sec) of R-1234yf	$Q_Cond_{_HTC}$ (kW)	$Q_Cond_{_Cascade}$ (kW)	$Q_{_EVA_LTC}$ (kW)
25	1.724	5.069	15.33	0.3219	0.2282	55.56	50.5	35.167
30	1.61	6.516	15.33	0.3369	0.2282	57.01	50.5	35.167
35	1.503	8.062	15.33	0.3535	0.2282	58.56	50.5	35.167
40	1.404	9.726	15.33	0.3721	0.2282	60.22	50.5	35.167
45	1.309	11.53	15.33	0.3931	0.2282	62.03	50.5	35.167
50	1.219	13.51	15.33	0.4169	0.2282	64.01	50.5	35.167
55	1.133	15.71	15.33	0.4441	0.2282	66.20	50.5	35.167
60	1.05	18.17	15.33	0.4758	0.2282	68.66	50.5	35.167

Table-3(c): Variation of Thermal performance with variation of LTC evaporator temperature of two stage cascade vapour compression refrigeration system using HFO-1234ze in high temperature circuit and HFC-134a in low temperature circuit for T_Cond=50°C with subcooling of 5°C, $T_{_Eva_HTC}$= -10°C, $T_{_Eva_LTC}$=-50°C, $Q_{_Eva_LTC}$=35 "kW"

T_Eva (°C)	COP	EDR	Exergetic Efficiency	Rational EDR	Exergy of Fuel (kW)	Exergy of Product (kW)	COP_HTC	$COP_{_LTC}$
-50	1.219	1.438	0.4101	0.5899	28.84	11.83	3.737	2.294
-45	1.331	1.446	0.4088	0.5912	26.41	10.8	3.737	2.622
-40	1.454	1.465	0.4057	0.5943	24.18	9.811	3.737	3.017
-35	1.589	1.497	0.4005	0.5995	24.14	8.866	3.737	3.503
-30	1.737	1.544	0.3931	0.6069	20.25	7.96	3.737	4.112
-25	1.90	1.611	0.383	0.6170	18.51	7.09	3.737	4.899
-20	2.081	1.702	0.3701	0.6699	16.9	6.255	3.737	5.951

Table-3(d): Variation of Thermal performance with variation of LTC evaporator temperature of two stage cascade vapour compression refrigeration system using HFO-1234ze in high temperature circuit and HFC-134a in low temperature circuit for T_Cond=50°C with subcooling of 5°C, $T_{_Eva_HTC}$= 0°C, $T_{_Eva_LTC}$=-50°C, $Q_{_Eva_LTC}$=35 "kW"

T_Eva (°C)	COP	$W_{_Comp_HTC}$ (kW)	$W_{_Comp_LTC}$ (kW)	Mass flow rate (kg/sec) of R-1234ze	Mass flow rate (kg/sec) of R-134a	$Q_Cond_{_HTC}$ (kW)	$Q_Cond_{_Cascade}$ (kW)	$Q_EVA_{_LTC}$ (kW)
-50	1.219	13.51	15.33	0.4169	0.2282	64.01	50.5	35.167
-45	1.331	13.0	13.41	0.4031	0.2236	61.58	48.54	35.167
-40	1.454	12.53	11.66	0.3885	0.2192	59.36	46.82	35.167
-35	1.589	12.1	10.04	0.3732	0.2149	57.3	45.21	35.167
-30	1.737	11.7	8.552	0.3609	0.2109	55.42	43.72	35.167
-25	1.90	11.33	7.179	0.3449	0.2070	53.68	42.35	35.167
-20	2.081	10.99	5.91	0.3391	0.2033	52.07	41.08	35.167

Table-3(e): Variation of Thermal performance with variation of cascade evaporator temperature of two stage cascade vapour compression refrigeration system using HFO-1234ze in high temperature circuit and HFO-134a in low temperature circuit for T_Cond=50°C with subcooling of 5°C, $T_{_Eva_HTC}$= 0°C, $T_{_Eva_LTC}$=-50°C, $Q_{_Eva_LTC}$=35 "kW"

T_Eva (°C)	COP	$W_{_Comp_HTC}$ (kW)	$W_{_Comp_LTC}$ (kW)	Mass flow rate (kg/sec) of R-1234ze	Mass flow rate (kg/sec) of R-1234yf	$Q_{_Cond_HTC}$ (kW)	$Q_{_Cond_Cascade}$ (kW)	$Q_{_EVA_LTC}$ (kW)
20	1.134	7.327	23.64	0.4372	0.2793	66.17	58.85	35.167
15	1.169	8.801	21.29	0.430	0.2642	65.26	56.56	35.167
10	1.194	10.31	19.13	0.4243	0.2508	64.61	54.30	35.167
5	1.211	11.88	17.15	0.420	0.2389	64.2	52.32	35.167
4	1.214	12.2	16.78	0.4193	0.2367	64.14	51.94	35.167
3	1.216	12.52	16.41	0.4186	0.2345	64.10	51.57	35.167
2	1.217	12.85	16.04	0.4180	0.2324	64.06	51.21	35.167
1	1.218	13.18	15.68	0.4174	0.2303	64.03	50.85	35.167
0	1.219	13.51	15.33	0.4169	0.2282	64.01	50.5	35.167
-1	1.22	13.85	14.98	0.4164	0.2262	64.0	50.15	35.167
-2	1.22	14.19	14.64	0.4159	0.2242	63.99	49.8	35.167
-3	1.22	14.53	14.30	0.4155	0.2223	63.99	49.47	35.167
-4	1.219	14.87	13.97	0.4152	0.2204	64.01	49.13	35.167
-5	1.219	15.22	13.64	0.4148	0.2185	64.03	48.8	35.167
-6	1.217	15.57	13.31	0.4145	0.2167	64.05	48.48	35.167
-7	1.216	15.93	12.99	0.4143	0.2149	64.09	48.16	35.167
-8	1.214	16.29	12.68	0.4141	0.2132	64.14	47.84	35.167
-9	1.212	16.65	12.37	0.4139	0.2114	64.19	47.53	35.167
-10	1.209	17.02	12.06	0.4137	0.2097	64.25	47.23	35.167
-15	1.192	18.93	10.58	0.4135	0.2017	64.67	45.74	35.167
-20	1.167	20.96	9.176	0.4141	0.1943	65.30	44.34	35.167

Table-3(f): Variation of Thermal performance with variation of cascade evaporator temperature of two stage cascade vapour compression refrigeration system using HFO-1234ze in high temperature circuit and HFO-134a in low temperature circuit for T_Cond=50°C with subcooling of 5°C, $T_{_Eva_HTC}$= 0°C, $T_{_Eva_LTC}$=-50°C, $Q_{_Eva_LTC}$=35 "kW"

T_Eva (°C)	COP	EDR	Exergetic Efficiency	Rational EDR	Exergy of Fuel (kW)	Exergy of Product (kW)	COP_ HTC	$COP_{_LTC}$
20	1.134	1.621	0.3815	0.6185	31.01	11.83	8.032	1.485
15	1.169	1.544	0.3930	0.6070	30.09	11.83	6.415	1.652
10	1.194	1.489	0.4017	0.5983	29.44	11.83	5.264	1.838
5	1.211	1.455	0.4074	0.5936	29.03	11.83	4.408	2.05
4	1.214	1.45	0.4082	0.5918	28.98	11.83	4.257	2.096
3	1.216	1.446	0.4088	0.5912	28.93	11.83	4.118	2.144
2	1.217	1.443	0.4094	0.5906	28.89	11.83	3.985	2.192
1	1.218	1.44	0.4098	0.5902	28.86	11.83	3.858	2.242
0	1.219	1.438	0.4101	0.5899	28.84	11.83	3.737	2.294
-1	1.22	1.437	0.4103	0.5897	28.83	11.83	3.622	2.347
-2	1.22	1.437	0.4103	0.5897	28.82	11.83	3.511	2.402
-3	1.22	1.437	0.4103	0.5897	28.83	11.83	3.405	2.459
-4	1.219	1.438	0.4101	0.5899	28.84	11.83	3.304	2.518
-5	1.219	1.440	0.4098	0.5902	28.86	11.83	3.206	2.579
-6	1.217	1.442	0.4094	0.5906	28.89	11.83	3.113	2.641
-7	1.216	1.445	0.4089	0.5911	28.92	11.83	3.023	2.706
-8	1.214	1.449	0.4083	0.5917	28.97	11.83	2.937	2.774
-9	1.212	1.454	0.4075	0.5925	29.02	11.83	2.854	2.844
-10	1.209	1.459	0.4067	0.5933	29.08	11.83	2.774	2.916
-15	1.192	1.495	0.4009	0.5991	29.51	11.83	2.416	3.325
-20	1.167	1.548	0.3925	0.6075	30.13	11.83	2.116	3.832

Table-3(g): Variation of Thermal performance with variation of HTC condenser temperature of two stage cascade vapour compression refrigeration system using HFO-1234ze in high temperature circuit and HFO-134a in low temperature circuit for T_Cond=50°C with subcooling of 5°C, $T_{_Eva_HTC}$= 0°C, $T_{_Eva_LTC}$=-50°C, $Q_{_Eva_LTC}$=35 "kW"

Effect of Temperature Overlapping (Approach)	COP	EDR	Exergetic Efficiency	Rational EDR	Exergy of Fuel (kW)	Exergy of Product (kW)	COP_HTC	$COP_{_LTC}$
0	1.424	1.088	0.4789	0.5211	24.7	11.83	3.737	2,916
2	1.36	1.154	0.4642	0.5358	25.48	11.83	3.737	2.774
4	1.338	1.222	0.450	0.550	26.29	11.83	3.737	2.641
6	1.297	1.295	0.4362	0.5638	27.11	11.83	3.737	2.518
8	1.258	1.364	0.4229	0.5771	27.96	11.83	3.737	2.402
10	1.219	1.438	0.4101	0.5899	28.84	11.83	3.737	2.294

12	1.182	1.515	0.3977	0.6023	29.74	11.83	3.737	2.192

Table-3(h): Variation of Thermal performance with variation of HTC condenser temperature of two stage cascade vapour compression refrigeration system using HFO-1234ze in high temperature circuit and HFO-134a in low temperature circuit for T_Cond=50ºC with subcooling of 5ºC, $T_{_Eva_HTC}$= 0ºC, $T_{_Eva_LTC}$=-50ºC, $Q_{_Eva_LTC}$=35 "kW"

Effect of Temperature Overlapping (Approach)	COP	W_{Comp_HTC}	W_{Comp_LTC}	Mass flow rate in HTC circuit (kg/sec)	Mass flow rate in LTC circuit (kg/sec)	$Q_{_Cond_HTC}$ (kW)	$Q_{_Cond_Cascade}$(kW)	$Q_{_Cond_LTC}$(kW)
0	1.424	12.64	12.06	0.3899	0.2097	59.86	47.23	35.167
2	1.36	12.8	12.68	0.3950	0.2132	60.85	47.84	35.167
4	1.338	12.97	13.31	0.4002	0.2167	61.45	48.48	35.167
6	1.297	13.15	13.97	0.4056	0.2204	62.28	49.13	35.167
8	1.258	13.33	14.64	0.4112	0.2242	63.13	49.80	35.167
10	1.219	13.51	15.33	0.4169	0.2282	64.01	50.50	35.167
12	1.182	13.7	16.04	0.4228	0.2324	64.91	51.21	35.167

Table-4(a): Variation of Thermal performance with variation of HTC condenser temperature of two stage cascade vapourcompression refrigeration system using HFO-1234yf in high temperature circuit and HFO-134a in low temperature circuit for T_Cond=50ºC with subcooling of 5ºC, $T_{_Eva_HTC}$= 0ºC, $T_{_Eva_LTC}$=-50ºC, $Q_{_Eva_LTC}$=35 "kW"

Effect of Temperature Overlapping (Approach)	COP	EDR	Exergetic Efficiency	Rational EDR	Exergy of Fuel (kW)	Exergy of Product (kW)	COP_HTC	$COP_{_LTC}$
0	1.388	1.141	0.4670	0.5330	25.33	11.83	3.559	2.916
2	1.346	1.204	0.4528	0.5472	26.12	11.83	3.559	2.774
4	1.306	1.227	0.4391	0.5609	26.94	11.83	3.559	2.641
6	1.266	1.348	0.4259	0.5741	27.77	11.83	3.559	2.518
8	1.228	1.421	0.4131	0.5869	28.63	11.83	3.559	2.402
10	1.191	1.496	0.4007	0.5993	29.52	11.83	3.559	2.294
12	1.156	1.573	0.3887	0.6113	30.43	11.83	3.559	2.192

Table-4(b): Variation of Thermal performance with variation of HTC condenser temperature of two stage cascade vapour compression refrigeration system using HFO-1234yf in high temperature circuit and HFO-134a in low temperature circuit forT_Cond=50ºC with subcooling of 5ºC, $T_{_Eva_HTC}$= 0ºC, $T_{_Eva_LTC}$=-50ºC, $Q_{_Eva_LTC}$=35 "kW"

Effect Temperature Overlapping (Approach)	COP	$W_{_Comp_HTC}$ (kW)	$W_{_Comp_LTC}$ (kW)	Mass flow rate (kg/sec) of R-1234ze	Mass flow rate (kg/sec) of R1234yf	$Q_Cond_{_HTC}$ (kW)	$Q_Cond_{_Cascade}$ (kW)	$Q_{_EVA_LTC}$ (kW)
0	1.388	13.27	12.06	0.4626	0.2097	60.50	47.23	35.167
2	1.346	13.44	12.66	0.4686	0.2132	61.29	47.84	35.167
4	1.306	13.62	13.31	0.4748	0.2167	62.10	48.48	35.167
6	1.266	13.81	13.97	0.4813	0.2204	62.94	49.13	35.167
8	1.228	13.99	14.64	0.4878	0.2242	63.80	49.8	35.167
10	1.191	14.19	15.33	0.4948	0.2282	64.68	50.5	35.167
12	1.156	14.39	16.04	0.5016	0.2304	65.60	51.27	35.167

Table-4(c): Variation of Thermal performance with variation of cascade evaporator temperature of two stage cascade vapour compression refrigeration system using HFO-1234yf in high temperature circuit and HFO-134a in low temperature circuit for T_Cond=50ºC with subcooling of 5ºC, $T_{_Eva_HTC}$= -10ºC, $T_{_Eva_LTC}$=-50ºC, $Q_{_Eva_LTC}$=35 "kW"

T_Eva (ºC)	COP	EDR	Exergetic Efficiency	EDR	Exergy of Fuel (kW)	Exergy of Product (kW)	COP_HTC	COP_LTC
20	1.125	1.642	0.3784	0.6216	31.25	11.83	7.768	1.485
15	1.156	1.572	0.3887	0.6113	30.42	11.83	5.264	1.838
10	1.177	1.526	0.3959	0.6041	29.87	11.83	5.054	1.652
5	1.189	1.501	0.3999	0.6001	29.58	11.83	4.211	2.050
4	1.190	1.498	0.4003	0.5997	29.55	11.83	4.068	2.096
3	1.191	1.496	0.4006	0.5994	29.52	11.83	3.931	2.144
2	1.192*	1.495	0.4008	0.5992	29.51	11.83	3.801	2.192
1	1.192*	1.495	0.4008	0.5992	29.51	11.83	3.677	2.242
0	1.191	1.496	0.4007	0.5993	29.52	11.83	3.559	2.324

-1	1.191	1.497	0.4005	0.5995	29.53	11.83	3.446	2.347
-2	1.190	1.499	0.4001	0.5999	29.56	11.83	3.338	2.402
-3	1.188	1.502	0.3997	0.6003	29.59	11.83	3.235	2.459
-4	1.187	1.506	0.3991	0.6009	29.64	11.83	3.135	2.518
-5	1.184	1.510	0.3984	0.6016	29.69	11.83	3.04	2.579
-6	1.182	1.515	0.3975	0.6025	29.75	11.83	2.949	2.641
-7	1.179	1.521	0.3966	0.6034	29.82	11.83	2.862	2.706
-8	1.176	1.528	0.3955	0.6045	29.90	11.83	2.778	2.774
-9	1.173	1.536	0.3944	0.6056	29.99	11.83	2.697	2.844
-10	1.169	1.544	0.3931	0.6069	30.09	11.83	2.619	2.916
-15	1.145	1.597	0.3850	0.6150	30.72	11.83	2.271	3.325
-20	1.113	1.670	0.3745	0.6255	31.58	11.83	1.979	3.832

Table-4(d): Variation of Thermal performance with variation of cascade evaporator temperature of two stage cascade vapour compression refrigeration system using HFO-1234yf in high temperature circuit and HFO-134a in low temperature circuit for T_Cond=50ºC with subcooling of 5ºC, $T_{_Eva_HTC}$= -10ºC, $T_{_Eva_LTC}$=-50ºC, $Q_{_Eva_LTC}$=35 "kW"

T_Eva (ºC)	COP	$W_{_Comp_HTC}$ (kW)	$W_{_Comp_LTC}$ (kW)	Mass flow rate (kg/sec) of R-1234ze	Mass flow rate (kg/sec) of R-1234yf	$Q_{_Cond_HTC}$ (kW)	$Q_{_Cond_Cascade}$ (kW)	$Q_{_EVA_LTC}$ (kW)
20	1.125	7.575	23.68	0.5130	0.2793	66.42	58.85	35.167
15	1.156	9.132	21.29	0.5057	0.2642	66.59	56.46	35.167
10	1.177	10.74	19.13	0.5004	0.2508	65.04	54.30	35.167
5	1.189	12.42	17.15	0.4968	0.2389	64.74	52.32	35.167
4	1.190	12.77	16.78	0.4962	0.2367	64.71	51.94	35.167
3	1.191	13.12	14.14	0.4957	0.2345	64.69	51.57	35.167
2	1.192	14.92	14.64	0.4941	0.2242	64.73	49.3	35.167
1	1.192	13.83	15.68	0.4949	0.2303	64.68	50.85	35.167
0	1.191	14.19	15.33	0.4946	0.2282	64.68	50.5	35.167
-1	1.191	14.55	14.98	0.4943	0.2262	64.70	50.15	35.167
-2	1.190	14.92	14.64	0.4941	0.2242	64.73	49.8	35.167
-3	1.188	14.29	14.3	0.4940	0.2223	64.76	49.47	35.167
-4	1.187	15.67	13.97	0.4938	0.2204	64.8	49.13	35.167
-5	1.184	16.05	13.64	0.4938	0.2185	64.86	48.8	35.167
-6	1.182	16.44	13.31	0.4938	0.2204	64.92	48.43	35.167
-7	1.179	16.83	12.99	0.4938	0.2167	64.99	48.16	35.167
-8	1.176	17.22	12.68	0.4939	0.2132	65.07	47.84	35.167
-9	1.173	17.62	12.37	0.494	0.2114	65.16	47.53	35.167
-10	1.169	18.03	12.06	0.4342	0.2097	65.26	47.23	35.167
-15	1.145	20.14	10.58	0.4958	0.2017	65.88	45.74	35.167
-20	1.113	22.41	9.176	0.4986	0.1943	66.75	44.34	35.167

Table-4(e): Variation of Thermal performance with variation of LTC evaporator temperature of two stage cascade vapour compression refrigeration system using HFO-1234yf in high temperature circuit and HFC-134a in low temperature circuit for T_Cond=50ºC with subcooling of 5ºC, $T_{_Eva_HTC}$= 0ºC, $T_{_Eva_LTC}$=-50ºC, $Q_{_Eva_LTC}$=35 "kW"

T_Cond (ºC)	COP	EDR	Exergetic Efficiency	Rational EDR	Exergy of Fuel (kW)	Exergy of Product (kW)	COP_HTC	$COP_{_LTC}$
25	1.716	0.7325	0.5772	0.4338	20.49	11.83	9.783	2.294
30	1.599	0.8592	0.5379	0.4621	21.99	11.83	7.581	2.294
35	1.49	0.9961	0.5010	0.4990	23.61	11.83	6.099	2.294
40	1.386	1.141	0.4661	0.5339	25.38	11.83	5.026	2.294
45	1.287	1.311	0.4328	0.5672	27.33	11.83	4.208	2.294
50	1.191	1.496	0.4007	0.5993	29.52	11.83	3.559	2.294
55	1.099	1.706	0.3695	0.6305	32.01	11.83	3.027	2.294
60	1.007	1.952	0.3388	0.6612	34.91	11.83	2.579	2.294

Table-4(f): Variation of Thermal performance with variation of LTC evaporator temperature of two stage cascade vapour compression refrigeration system using HFO-1234yf in high temperature circuit and HFC-134a in low temperature circuit for T_Cond=50ºC with subcooling of 5ºC, $T_{_Eva_HTC}$= 0ºC, $T_{_Eva_LTC}$=-50ºC, $Q_{_Eva_LTC}$=35 "kW"

T_Cond (°C)	COP	W_Comp_HTC (kW)	W_Comp_LTC (kW)	Mass flow rate (kg/sec) of R-1234yf	Mass flow rate (kg/sec) of R-134a	Q_Cond _HTC (kW)	Q_Cond _Cascade (kW)	Q_EVA _LTC (kW)
25	1.716	5.162	15.33	0.3669	0.2282	55.56	50.5	35.167
30	1.599	6.661	15.33	0.3862	0.2282	57.16	50.5	35.167
35	1.49	8.28	15.33	0.4079	0.2282	58.78	50.5	35.167
40	1.386	10.05	15.33	0.4327	0.2282	60.54	50.5	35.167
45	1.287	12.0	15.33	0.4612	0.2282	62.5	50.5	35.167
50	1.191	14.19	15.33	0.4946	0.2282	64.68	50.5	35.167
55	1.099	16.68	15.33	0.5341	0.2282	67.18	50.5	35.167
60	1.007	19.58	15.33	0.5818	0.2282	70.08	50.5	35.167

Table4(g): Variation of Thermal performance with variation of LTC evaporator temperature of two stage cascade vapour compression refrigeration system using HFO-1234yf in high temperature circuit and HFC-134a in low temperature circuit for T_Cond=50°C with subcooling of 5°C, T_Eva_HTC= -10°C, T_Eva_LTC=-50°C, Q_Eva_LTC=35 "kW"

T_Eva (°C)	COP	EDR	Exergetic Efficiency	Rational EDR	Exergy of Fuel (kW)	Exergy of Product (kW)	COP_HTC	COP_LTC
-50	1.191	1.496	0.4007	0.5993	29.52	11.83	3.559	2.294
-45	1.299	1.507	0.3990	0.6010	27.06	10.8	3.559	2.622
-40	1.417	1.529	0.3954	0.6046	24.81	9.811	3.559	3.017
-35	1.546	1.565	0.3898	0.6102	22.74	8.866	3.559	3.503
-30	1.688	1.618	0.3820	0.6170	20.84	7.96	3.559	4.112
-25	1.843	1.691	0.3717	0.6283	19.08	7.09	3.559	4.899
-20	2.015	1.789	0.3584	0.3416	17.45	6.255	3.559	5.951

Table-4(h): Variation of Thermal performance with variation of LTC evaporator temperature of two stage cascade vapour compression refrigeration system using HFO-1234yf in high temperature circuit and HFC-134a in low temperature circuit for T_Cond=50°C with subcooling of 5°C, T_Eva_HTC= 0°C, T_Eva_LTC=-50°C, Q_Eva_LTC=35 "kW"

T_Eva (°C)	COP	W_Comp_HTC (kW)	W_Comp_LTC (kW)	Mass flow rate (kg/sec) of R-1234yf	Mass flow rate (kg/sec) of R-134a	Q_Cond _HTC (kW)	Q_Cond _Cascade (kW)	Q_EVA_LTC (kW)
-50	1.191	14.19	15.33	0.4946	0.2282	64.68	50.5	35.167
-45	1.299	13.65	13.41	0.4758	0.2236	62.23	48.58	35.167
-40	1.417	13.16	11.66	11.660.4585	0.2192	59.98	46.82	35.167
-35	1.546	12.7	10.04	0.4428	0.2149	57.91	45.21	35.167
-30	1.688	12.28	8.552	0.4282	0.2109	56.0	43.72	35.167
-25	1.843	11.9	7.179	0.4148	0.2070	54.24	42.35	35.167
-20	2.015	11.54	5.91	0.4023	0.2033	52.62	41.08	35.167

System-4:Table-5(a): Variation of Thermal performance with variation of LTC evaporator temperature of two stage cascade vapour compression refrigeration system using HFO-1234ze in high temperature circuit and HFC-134a in low temperature circuit for T_Cond=55°C with subcooling of 5°C, T_Eva_HTC= -30°C, T_Eva_LTC=-100°C, Q_Eva_LTC=70 "kW"

T_Eva (°C)	COP	EDR	Exergetic Efficiency	Rational EDR	Exergy of Fuel (kW)	Exergy of Product (kW)	COP_HTC	COP_LTC
R134a	0.4791	1.889	0.3461	0.6539	146.10	50.58	1.448	1.211
R245fa	0.4852	1.852	0.3506	0.6494	144.3	50.58	1.448	1.234
R143a	0.4719	1.933	0.3409	0.6561	148.3	50.58	1.448	1.184
R227ea	0.4517	2.064	0.3264	0.6736	155.0	50.58	1.448	1.110
R123	0.4880	1.836	0.3526	1.448	143.0	50.58	1.448	1.245

Table-5(a): Variation of Thermal performance with variation of HTC condenser temperature of two stage cascade vapour compression refrigeration system using HFO-1234ze in high temperature circuit and following refrigerants in low temperature circuit for T_Cond=55°C with subcooling of 5°C, T_Eva_HTC= -30°C, T_Eva_LTC=-100°C, Q_Eva_LTC=35 "kW"

LTC Refrigerants	COP	System EDR	Exergetic Efficiency	EDR_Rational	Exergy of Fuel (kW)	Exergy of Product (kW)	COP_HTC	COP_LTC
R-134a	0.4791	1.889	0.3461	0.6539	73.41	25.41	1.448	1.211
R141b	0.5026	1.754	0.3632	0.6368	69.97	25.41	1.448	1.302
R-404a	0.4608	2.003	0.3330	0.6670	65.93	25.41	1.448	1.143
R-410a	0.4757	1.910	0.3437	0.6563	73.93	25.41	1.448	1.198
R-407c	0.4115	2.363	0.2973	0.7027	85.47	25.41	1.448	0.972
R-227ea	0.4517	2.064	0.3264	0.6736	77.85	25.41	1.448	1.10
R-236fa	0.4729	1.927	0.3417	0.6583	74.37	25.41	1.448	1.187
R-245fa	0.4852	1.852	0.3506	0.6494	72.48	25.41	1.448	1.234
R-32	0.4531	2.054	0.3234	0.6766	77.61	25.41	1.448	1.115
R-600a	0.4834	1.863	0.3493	0.6507	72.75	25.41	1.448	1.227
R-600	0.4906	1.821	0.3545	0.6455	71.68	25.41	1.448	1.255
R-290	0.4829	1.866	0.3489	0.6511	72.82	25.41	1.448	1.225
R-123	0.4880	1.836	0.3526	0.6474	72.06	25.41	1.448	1.245
R-125	0.4583	2.020	0.3312	0.6688	76.73	25.41	1.448	1.134

R-507a	0.4678	1.939	0.3380	0.6620	75.18	25.41	1.448	1.168

Table-5(b): Variation of Thermal performance with variation of HTC condenser temperature of two stage cascade vapour compression refrigeration system using HFO-1234ze in high temperature circuit and following refrigerants in low temperature circuit for T_Cond=55ºC with subcooling of 5ºC, $T_{_Eva_HTC}$=-30ºC, $T_{_Eva_LTC}$=-100ºC, $Q_{_Eva_LTC}$=35 "kW"

LTC Refrigerants	COP	$W_{_Comp_HTC}$ (kW)	$W_{_Comp_LTC}$ (kW)	Mass flow rate (kg/sec) of R-1234ze	Mass flow rate (kg/sec) of LTC refrigerants	$Q_Cond_{_HTC}$ (kW)	$Q_Cond_{_Cascade}$ (kW)	$Q_{_EVA_LTC}$ (kW)
R-134a	0.4791	44.36	29.05	0.6939	0.2158	108.6	64.22	35.167
R141b	0.5026	42.95	27.01	0.6720	0.1807	105.1	62.18	35.167
R-404a	0.4608	45.55	30.77	0.7125	0.2642	111.5	65.93	35.167
R-410a	0.4757	44.57	29.37	0.6973	0..1715	109.1	64.52	35.167
R-407c	0.4115	49.29	36.18	0.7710	0.1971	120.6	71.35	35.167
R-227ea	0.4517	46.17	31.68	0.7223	0.4154	113.0	66.84	35.167
R-236fa	0.4729	44.75	29.62	0.7001	0.3020	109.5	64.78	35.167
R-245fa	0.4852	43.98	28.5	0.6880	0.2188	107.6	63.67	35.167
R-32	0.4531	46.08	31.53	0.7208	0.1163	112.8	66.70	35.167
R-600a	0.4834	44.08	28.66	0.6897	0.1264	107.9	63.83	35.167
R-600	0.4906	43.66	28.03	0.6829	0.1191	106.9	63.2	35.167
R-290	0.4829	44.12	28.7	0.6902	0.1152	106.0	63.87	35.167
R-123	0.4880	43.81	26.25	0.6854	0.2418	107.2	63.42	35.167
R-125	0.4583	45.72	31.01	0.7152	0.3415	111.90	66.18	35.167
R-507a	0.4678	45.08	30.10	0.7053	0.2701	110.3	65.26	35.167

Table-5(c): Variation of Thermal performance with variation of LTC evaporator temperature of two stage cascade vapour compression refrigeration system using HFO-1234ze in high temperature circuit and HFC-134a in low temperature circuit for T_Cond=55ºC with subcooling of 5ºC, $T_{_Eva_HTC}$= -30ºC, $T_{_Eva_LTC}$=-100ºC, $Q_{_Eva_LTC}$=35 "kW"

T_Eva (ºC)	COP	EDR	Exergetic Efficiency	Rational EDR	Exergy of Fuel (kW)	Exergy of Product (kW)	COP_HTC	$COP_{_LTC}$
-100	0.4791	1.889	0.3464	0.6536	73.41	25.54	1.448	1.211
-95	0.5197	1.854	0.3504	0.6496	67.66	23.71	1.448	1.371
-90	0.5625	1.829	0.3535	0.6465	62.52	22.10	1.448	1.556
-85	0.6075	1.813	0.3554	0.6446	57.89	20.58	1.448	1.77
-84	0.6167	1.811	0.3557	0.6443	57.02	20.28	1.448	1.81
-83	0.6261	1.81	0.3559	0.6441	56.17	19.99	1.448	1.885
-82	0.6356	1.809	0.3560	0.6440	55.33	19.70	1.448	1.916
-81	0.6451	1.808	0.3561	0.6439	54.51	19.42	1.448	1.969
-80	0.6547(opt)	1.807(opt)	0.3562(opt)	0.6438(opt)	53.71(opt)	19.13	1.448	2.201(opt)
-79	0.6645(opt)	1.807(optimum)	0.3562(opt)	0.6438(opt)	52.92(opt)	18.85	1.448	2.077(opt)
-78	0.6743	1.807(opt)	0.3562(opt)	0.6438	52.15(opt)	18.58	1.448	2.134(opt)
-77	0.6842	1.808	0.3561	0.6439	51.4	18.30	1.448	2.194
-76	0.6943	1.809	0.3559	0.6441	50.65	18.03	1.448	2.256
-75	0.7044	1.811	0.3557	0.6443	49.93	17.76	1.448	2.32
-70	0.7585	1.825	0.3540	0.6460	46.49	16.46	1.448	2.679
-65	0.8113	1.849	0.3510	0.6490	43.35	15.22	1.448	3.12
-60	0.8688	1.894	0.3567	0.6433	40.48	14.03	1.448	3.674

Table-5(d): Variation of Thermal performance with variation of LTC evaporator temperature of two stage cascade vapour compression refrigeration system using HFO-1234ze in high temperature circuit and HFC-134a in low temperature circuit for T_Cond=55ºC with subcooling of 5ºC, $T_{_Eva_HTC}$= -30ºC, $T_{_Eva_LTC}$=-100ºC, $Q_{_Eva_LTC}$=35 "kW"

T_Eva (ºC)	COP	$W_{_Comp_HTC}$ (kW)	$W_{_Comp_LTC}$ (kW)	Mass flow rate (kg/sec) of R-1234yf	Mass flow rate(kg/sec)of R-134a	$Q_Cond_{_HTC}$(kW)	$Q_Cond_{_Cascade}$ (kW)	$Q_EVA_{_LTC}$ (kW)
-100	0.4791	44.36	29.05	0.6939	0.2158	108.60	64.22	35.167
-95	0.5197	42.01	25.65	0.6572	0.2118	102.80	60.82	35.167
-90	0.5625	39.91	22.61	0.6243	0.2080	97.69	57.78	35.167
-85	0.6075	38.02	19.87	0.6075	0.2043	93.06	55.04	35.167
-84	0.6167	37.66	19.36	0.5892	0.2036	92.19	54.52	35.167
-83	0.6261	37.32	18.85	0.5838	0.2029	91.34	54.02	35.167
-82	0.6356	36.97	18.36	0.5784	0.2021	90.05	53.53	35.167
-81	0.6451	36.64	17.87	0.5732	0.2014	89.68	53.04	35.167
-80	0.6547	36.31	17.40	0.5681	0.2007	88.88	52.57	35.167
-79	0.6645	35.99	16.93	0.5630	0.20	88.09	52.10	35.167
-78	0.6743	35.68	16.48	0.5581	0.1993	87.32	51.64	35.167

-77	0.6842	35.37	16.03	0.5533	0.1986	86.56	51.2	35.167
-76	0.6943	35.06	15.59	0.5485	0.1979	85.82	50.76	35.167
-75	0.7044	34.77	15.16	0.5439	0.1972	85.09	50.33	35.167
-70	0.7585	33.36	13.13	0.5219	0.1938	81.65	48.29	35.167
-65	0.8113	32.08	11.27	0.5018	0.1906	78.52	46.44	35.167
-60	0.8688	30.91	9.573	0.4835	0.1874	75.65	44.74	35.167

Table-5(e): Performance of Two stages Cascade Vapour compression Refrigeration System with HFO R1234ze in high temperature circuit and HFO1234ze Refrigerantin the low temperature circuit $T_{_Cond_HTC}$=55ºC, $T_{_Eva_HTC}$= -30ºC ,Approach (Temperature$_{_Overlapping}$) = 10ºC , $T_{_Eva_LTC}$= -50ºC , Compressor $_{_Efficiency_HTC}$= 0.80, Compressor $_{_Efficiency_LTC}$=0.80,Eva=35.167 "KW"

T_Eva_HTC (ºC)	First law Efficiency (COP)	System Exergy Destruction Ratio based on output	Second Law Efficiency/ Exergetic Efficiency	High Temperature Circuit $COP_{_HTC}$	Low Temperature Circuit $COP_{_LTC}$	Exergy of fuel (kW)	Exergy of product (kW)
20	0.3958	2.497	0.2860	6.446	0.4871	88.86	25.41
15	0.4171	2.318	0.3034	5.287	0.5385	84.81	25.41
10	0.4358	2.176	0.3149	4.421	0.5928	80.70	25.41
5	0.4516	2.064	0.3263	3.75	0.6504	77.87	25.41
0	0.4646	1.979	0.3357	3.215	0.7120	75.69	25.41
-5	0.4746	1.916	0.3429	2.78	0.7781	74.10	25.41
-10	0.4895	1.874	0.3479	2.42	0.8496	73.03	25.41
-15	0.4854	1.851	0.3507	2.42	0.9273	72.44	25.41
-20	0.4863	1.846	0.3514	1.86	1.012	72.32	25.41
-25	0.4841	1.859	0.3493	1.639	1.106	72.64	25.41
-30	0.4791	1.889	0.3461	1.448	1.211	73.41	25.41

Table-5(f): Performance of Two stages Cascade Vapour compression Refrigeration System with HFO R1234yf in high temperature circuit and HFO1234ze Refrigerant in the low temperature circuit $T_{_Cond_HTC}$=55ºC, $T_{_Eva_HTC}$= -30ºC ,Approach (Temperature$_{_Overlapping}$) = 10ºC , $T_{_Eva_LTC}$= -100ºC , Compressor $_{_Efficiency_HTC}$= 0.80, Compressor $_{_Efficiency_LTC}$=0.80,Eva=35.167 "KW"

T_Eva_HTC (ºC)	First law Efficiency (COP)	$W_{_Comp_HTC}$ (kW)	$W_{_Comp_LTC}$ (kW)	Mass flow rate (kg/sec) of R-1234yf	Mass flow rate (kg/sec) of R-134a	$Q_{_Cond_HTC}$ (kW)	$Q_{Cond\ Cascade}$ (kW)	$Q_{_Eva_LTC}$ (kW)
20	0.3958	16.66	72.2	0.8444	0.3706	124.4	107.4	35.167
15	0.4171	19.0	66.31	0.8111	0.3446	119.5	100.5	35.167
10	0.4358	21.38	59.33	0.7839	0.3222	115.9	94.49	35.167
5	0.4516	23.8	54.07	0.7618	0.3026	113.0	89.23	35.167
0	0.4646	26.3	49.39	0.7437	0.2858	110.9	84.56	35.167
-5	0.4746	28.9	45.19	0.7291	0.2708	109.3	80.36	35.167
-10	0.4895	31.64	41.39	0.7175	0.2574	108.2	76.56	35.167
-15	0.4854	34.52	37.92	0.7074	0.2454	107.6	73.09	35.167
-20	0.4863	37.68	34.74	0.7015	0.2345	107.6	69.9	35.167
-25	0.4841	40.85	31.79	0.6967	0.2247	107.8	66.96	35.167
-30	0.4791	44.36	29.05	0.6939	0.2158	108.6	64.22	35.167

Table-5(g): Performance of Two stages Cascade Vapour compression Refrigeration System with HFO R1234ze in high temperature circuit and HFO1234ze Refrigerantin the low temperature circuit $T_{_Cond_HTC}$=55ºC, $T_{_Eva_HTC}$= -30ºC ,Approach (Temperature$_{_Overlapping}$) = 10ºC , $T_{_Eva_LTC}$= -100ºC , Compressor $_{_Efficiency_HTC}$= 0.80, Compressor $_{_Efficiency_LTC}$=0.80, Q_Eva=35.167 "KW"

Temperature Overlapping (ºC)	First law Efficiency (COP)	System Exergy Destruction Ratio based on output	Second Law Efficiency/ Exergetic Efficiency	High Temperature Circuit $COP_{_HTC}$	Low Temperature Circuit $COP_{_LTC}$	Exergy of fuel (W)	Exergy of product (W)
0	0.5410	1.558	0.3909	1.448	1.461	65.0	25.41
2	0.5280	1.621	0.3815	1.448	1.405	66.6	25.41
4	0.5153	1.686	0.3734	1.448	1.353	68.24	25.41
6	0.5030	1.752	0.3634	1.448	1.303	69.92	25.41
8	0.4909	1.819	0.3547	1.448	1.256	71.64	25.41
10	0.4791	1.889	0.3461	1.448	1.211	73.41	25.41
12	0.4675	1.96	0.3378	1.448	1.167	75.12	25.41

Table-5(h): Performance of Two stages Cascade Vapour

compression Refrigeration System with HFO R1234ze in high temperature circuit and HFC 134a Refrigerant in the low temperature circuit $T_{_Cond_HTC}$=55ºC, $T_{_Eva_HTC}$= -30ºC ,Approach (Temperature$_{_Overlapping}$) = 10ºC , $T_{_Eva_LTC}$= -100ºC , Compressor $_{_Efficiency_HTC}$= 0.80, Compressor $_{_Efficiency_LTC}$=0.80,Eva=35.167 "KW"

Temperature Overlapping (ºC)	First law Efficiency (COP)	W_{Comp_HTC} (kW)	W_{Comp_LTC} (kW)	Mass flow rate (kg/sec) of R-1234yf	Mass flow rate (kg/sec) of R-134a	Q_{Cond_HTC} (kW)	$Q_{Cond\ Cascade}$ (kW)	Q_{Eva_LTC} (kW)
0	0.5410	40.92	24.08	0.6402	0.20	100.2	59.24	35.167
2	0.5280	41.58	25.02	0.6504	0.2029	101.8	60.19	35.167
4	0.5153	42.25	25.99	0.6609	0.2060	103.4	61.16	35.167
6	0.5030	42.93	26.96	0.6716	0.2091	105.10	62.15	35.167
8	0.4909	43.64	28.0	0.6826	0.2134	106.8	63.17	35.167
10	0.4791	44.36	29.05	0.6939	0.2158	108.6	64.22	35.167
12	0.4675	45.10	30.12	0.7056	0.2192	110.4	65.29	35.167

Table-6(a): Variation of Thermal performance with variation of LTC evaporator temperature of two stage cascade vapour compression refrigeration system using HFO-1234yf in high temperature circuit and HFC-134a in low temperature circuit for T_{Cond}=55ºC with subcooling of 5ºC, T_{Eva_HTC}= -30ºC, T_{Eva_LTC}=-100ºC, Q_{Eva_LTC}=35 "kW"

T_Eva (ºC)	COP	EDR	Exergetic Efficiency	Rational EDR	Exergy of Fuel (kW)	Exergy of Product(kW)	COP_HTC	COP_{LTC}
-100	0.4548	2.043	0.3286	0.6714	77.33	25.41	3.027	0.7120
-95	0.5002	1.966	0.3372	0.6628	70.31	23.71	3.027	0.7972
-90	0.5490	1.899	0.3450	0.6550	64.04	22.10	3.027	0.8922
-85	0.6014	1.842	0.3519	0.6481	58.47	20.58	3.027	0.9985
-84	0.6124	1.832	0.3532	0.6468	57.43	20.28	3.027	1.021
-83	0.6235	1.822	0.3544	0.6456	56.4	19.99	3.027	1.045
-82	0.6347	1.812	0.3556	0.6444	55.4	19.7	3.027	1.068
-81	0.6482	1.803	0.3567	0.6433	54.42	19.42	3.027	1.093
-80	0.6578	1.794	0.3579	0.6421	53.46	19.13	3.027	1.118
-79	0.6695	1.786	0.3589	0.6411	52.52	18.85	3.027	1.144
-78	0.6815	1.778	0.360	0.640	51.6	18.58	3.027	1.170
-77	0.6936	1.77	0.3609	0.6391	50.7	18.30	3.027	1.197
-76	0.7059	1.763	0.3619	0.6381	49.82	18.03	3.027	1.225
-75	0.7183	1.756	0.3628	0.6372	48.96	17.76	3.027	1.253
-74	0.7310	1.750	0.3637	0.6363	48.11	17.50	3.027	1.282
-73	0.7438	1.744	0.3645	0.6355	47.28	17.23	3.027	1.312
-72	0.7569	1.738	0.3653	0.6347	46.46	16.97	3.027	1.343
-71	0.7701	1.732	0.3660	0.6340	45.87	16.71	3.027	1.374
-70	0.7835	1.727	0.3667	0.6333	44.88	16.46	3.027	1.406
-65	0.8536	1.707	0.3694	0.6306	41.2	15.22	3.027	1.582
-60	0.9292	1.697	0.3708	0.6292	37.85	14.03	3.027	1.784

Table-6(b): Variation of Thermal performance with variation of LTC evaporator temperature of two stage cascade vapour compression refrigeration system using HFO-1234yf in high temperature circuit and HFC-134a in low temperature circuit for T_{Cond}=55ºC with subcooling of 5ºC, T_{Eva_HTC}= -30ºC, T_{Eva_LTC}=-100ºC, Q_{Eva_LTC}=35 "kW"

T_Eva (ºC)	COP	W_{Comp_HTC} (kW)	W_{Comp_LTC} (kW)	Mass flow rate (kg/sec) of R-1234yf	Mass flow rate (kg/sec) of R-134a	Q_{Cond_HTC} (kW)	$Q_{Cond_Cascade}$(kW)	Q_EVA_{LTC} (kW)
-100	0.4548	27.93	49.30	0.8944	0.2858	112.50	84.56	35.167
-95	0.5002	26.19	44.11	0.8386	0.2789	105.50	79.26	35.167
-90	0.5490	24.64	39.42	0.7889	0.2724	99.22	74.59	35.167
-85	0.6014	23.25	35.22	0.7446	0.2661	93.64	70.39	35.167
-84	0.6124	22.99	34.43	0.7362	0.2648	92.60	69.60	35.167
-83	0.6235	22.74	33.67	0.7281	0.2636	91.57	68.83	35.167
-82	0.6347	22.49	32.91	0.7201	0.2624	90.57	68.08	35.167
-81	0.6482	22.25	32.18	0.7123	0.2612	89.59	67.34	35.167
-80	0.6578	22.01	31.46	0.7047	0.260	88.63	66.62	35.167
-79	0.6695	21.78	30.75	0.6972	0.2588	87.69	65.92	35.167
-78	0.6815	21.55	30.06	0.6899	0.2577	86.77	65.22	35.167
-77	0.6936	21.32	29.38	0.6936	0.2565	85.87	64.55	35.167
-76	0.7059	21.10	28.72	0.6557	0.2553	84.99	63.88	35.167
-75	0.7183	20.89	28.07	0.6689	0.2542	84.12	63.23	35.167
-74	0.7310	20.68	27.43	0.6621	0.2530	83.28	62.6	35.167
-73	0.7438	20.47	26.8	0.6555	0.2519	82.44	61.97	35.167
-72	0.7569	20.27	26.19	0.6491	0.2508	81.63	61.36	35.167
-71	0.7701	20.07	25.59	0.6427	0.2497	80.83	60.76	35.167
-70	0.7835	19.88	25.01	0.6385	0.2486	80.05	60.17	35.167
-65	0.8536	18.96	22.23	0.6072	0.2432	76.36	57.40	35.167
-60	0.9292	18.13	19.72	0.5805	0.2380	73.01	54.88	35.167

Table-6(c): Performance of Two stages Cascade Vapour compression Refrigeration System with HFO R1234ze in high temperature circuit and HFO1234yf Refrigerantin the low temperature circuit T_{Cond_HTC}=55ºC, T_{Eva_HTC}= -30ºC ,Approach (Temperature$_{Overlapping}$) = 10ºC , T_{Eva_LTC}= -50ºC , Compressor _Efficiency$_{HTC}$= 0.80, Compressor _Efficiency$_{LTC}$=0.80,Eva=35.167 "KW"

T_Eva_HTC (ºC)	First law Efficiency (COP)	System Exergy Destruction Ratio based on output	Second Law Efficiency/ Exergetic Efficiency	High Temperature Circuit $COP_{_HTC}$	Low Temperature Circuit $COP_{_LTC}$	Exergy of fuel (W)	Exergy of product (W)
20	0.3969	2.526	0.2837	6.179	0.4871	89.58	25.41
15	0.4127	2.354	0.2982	5.047	0.5385	85.22	25.41
10	0.4298	2.22	0.3106	4.201	0.5928	81.82	25.41
5	0.4439	2.118	0.3207	3.547	0.6504	79.22	25.41
0	0.4548	2.043	0.3286	3.027	0.712	77.33	25.41
-5	0.4624	1.993	0.3341	2.604	0.7781	76.05	25.41
-10	0.4668	1.965	0.3373	2.255	0.8496	75.34	25.41
-15	0.4678	1.958	0.3380	1.962	0.9273	75.17	25.41
-20	0.4656	1.972	0.3364	1.714	1.012	75.52	25.41
-25	0.4603	2.007	0.3326	1.501	1.106	76.4	25.41
-30	0.4520	2.062	0.3266	1.317	1.211	77.8	25.41

Table-6(d): Performance of Two stages Cascade Vapour compression Refrigeration System with HFO R1234yf in high temperature circuit and HFO1234yf Refrigerant in the low temperature circuit $T_{_Cond_HTC}$=55ºC, $T_{_Eva_HTC}$= -30ºC ,Approach (Temperature$_{_Overlapping}$) = 10ºC, $T_{_Eva_LTC}$= -100ºC, Compressor Efficiency$_{_HTC}$= 0.80, Compressor $_Efficiency_{_LTC}$=0.80,Eva=35.167 "KW"

T_Eva_HTC (ºC)	First law Efficiency (COP)	$W_{_Comp_HTC}$ (kW)	$W_{_Comp_LTC}$ (kW)	Mass flow rate (kg/sec) of R-1234yf	Mass flow rate (kg/sec) of R-134a	$Q_Cond_{_HTC}$ (kW)	$Q_Cond_{Cascade}$ (kW)	$Q_Eva_{_LTC}$ (kW)
20	0.3969	17.38	72.20	1.002	0.3706	124.7	107.4	35.167
15	0.4127	19.91	65.71	0.9654	0.3445	120.9	100.5	35.167
10	0.4298	22.49	59.33	0.9361	0.3222	117.0	94.49	35.167
5	0.4439	25.16	54.07	0.9128	0.3028	114.4	89.23	35.167
0	0.4548	27.93	49.39	0.8944	0.2858	112.5	84.56	35.167
-5	0.4624	30.85	45.19	0.8803	0.2708	111.2	80.35	35.167
-10	0.4668	33.93	41.39	0.870	0.2574	110.5	76.56	35.167
-15	0.4678	37.25	37.92	0.8629	0.2454	110.3	73.09	35.167
-20	0.4656	40.79	34.74	0.8590	0.2345	110.7	69.9	35.167
-25	0.4603	44.61	31.79	0.8580	0.2247	111.6	66.96	35.167
-30	0.4520	48.76	29.05	0.8598	0.2158	113.0	64.22	35.167

Table-6(e): Performance of Two stages Cascade Vapour compression Refrigeration System with HFO R1234ze in high temperature circuit and HFO1234yf Refrigerantin the low temperature circuit $T_{_Cond_HTC}$=55ºC, $T_{_Eva_HTC}$=-30ºC, Approach (Temperature$_{_Overlapping}$)= 10ºC, $T_{_Eva_LTC}$= -100ºC, Compressor $_Efficiency_{_HTC}$=0.80, Compressor $_Efficiency_{_LTC}$=0.80, Eva=35.167 "kW"

Temperature Overlapping (ºC)	First law Efficiency (COP)	System Exergy Destruction Ratio based on output	Second Law Efficiency/ Exergetic Efficiency	High Temperature Circuit $COP_{_HTC}$	Low Temperature Circuit $COP_{_LTC}$	Exergy of fuel (W)	Exergy of product (W)
0	0.5093	1.718	0.3680	1.317	1.461	69.05	26.41
2	0.4993	1.783	0.3593	1.317	1.405	70.02	26.41
4	0.4856	1.85	0.3509	1.317	1.363	72.42	26.41
6	0.4741	1.919	0.3426	1.317	1.303	74.17	26.41
8	0.4630	1.989	0.3345	1.317	1.256	75.96	26.41
10	0.4548	2.043	0.3266	1.317	1.211	77.80	26.41
12	0.4413	2.136	0.3189	1.317	1.167	79.69	26.41

Table-6(f): Performance of Two stages Cascade Vapour compression Refrigeration System with HFO R1234yf in high temperature circuit and HFC 134a Refrigerant in the low temperature circuit $T_{_Cond_HTC}$=55ºC, $T_{_Eva_HTC}$= -30ºC ,Approach (Temperature$_{_Overlapping}$) = 10ºC , $T_{_Eva_LTC}$= -100ºC , Compressor $_Efficiency_{_HTC}$= 0.80, Compressor $_Efficiency_{_LTC}$=0.80,Eva=35.167 "KW"

Temperature Overlapping (ºC)	First law Efficiency (COP)	$W_{_Comp_HTC}$ (kW)	$W_{_Comp_LTC}$ (kW)	Mass flow rate (kg/sec) of R-1234yf	Mass flow rate (kg/sec) of R-134a	$Q_Cond_{_HTC}$ (kW)	$Q_Cond_{Cascade}$ (kW)	$Q_Eva_{_HTC}$ (kW)
0	0.5093	44.98	26.06	0.7932	0.200	104.2	59.24	35.167
2	0.4993	45.70	25.02	0.8059	0.2029	105.9	60.19	35.167
4	0.4856	46.43	26.99	0.8189	0.2060	107.6	61.16	35.167
6	0.4741	47.19	26.98	0.8322	0.2091	109.3	62.15	35.167
8	0.4630	47.97	28.0	0.8458	0.2124	111.1	63.17	35.167
10	0.4548	48.75	29.05	0.8598	0.2158	113.0	64.22	35.167

12	0.4413	49.57	30.12	0.8742	0.2192	114.9	65.29	35.167

Table7: Thermal Performance of Vapour compression Refrigeration System with following Refrigerants in the low temperature circuit T_{Cond}=55ºC, $T_{Evaporator}$= -30ºC , Compressor _Efficiency_ = 0.80, Q_Eva=70 "KW"

Refrigerants In VCR	First law Efficiency (COP)	System Exergy Destruction Ratio based on output	Second Law Efficiency/ Exergetic Efficiency	Rational EDR	Exergy of product (W)	Exergy of fuel (W)
R1234ze	1.448	2.052	0.3277	0.6723	15.84	53.14
R1234yf	1.317	2.354	0.2981	0.7019	15.84	48.36
R134a	1.508	1.930	0.3413	0.6787	15.84	46.43
R290	1.475	1.995	0.3339	0.6661	15.84	47.45
R152a	1,67	1.646	0.3779	0.6221	15.84	41.93
R717	1.718	1.572	0.3887	0.6113	15.84	40.76
R-600a	1.501	1.944	0.3396	0.6604	15.84	46.65
R-600	1.623	1.723	0.3693	0.3307	15.84	43.19
R123	1.722	1.566	0.3931	0.6069	15.84	40.65
R410a	1.409	2.137	0.3186	0.6814	15.84	49.70
R404a	1.173	2.767	0.2654	0.7346	15.84	59.69
R125	1.003	3.4	0.3541	0.6459	15.84	71.04
R407c	1.301	2.393	0.2944	0.7056	15.84	53.82

Table-8(a): Optimum Results for two stage cascade system (system-6) using HFO-1234ze in high temperature circuit using condenser temperature of 55 ºC and HFC-134a in low temperature circuit using low temperature circuit evaporator temperature of (-100ºC) at Optimum LTC evaporator temperature= -78 ºC, -79 ºC & -80ºC.

Optimum Parameters	Optimum Temperature =- 78 ºC	Optimum Temperature = -79 ºC	Optimum Temperature = -80 ºC
First law efficiency (COP_System)	0.6743	0.6645	0.6547
Exergy Destruction Ratio (EDR)	1.807	1.807	1.807
Exergy of Fuel (kW)	52.15	52.92	53.71
Exergy of Product (kW)	18.58	18.85	19.13
Total work done by HTC compressor (kW)	35.68	35.99	36.31
Total work done by LTC compressor (kW)	16.48	16.93	17.40
Mass flow rate in HTC compressor (Kg/sec)	0.5581	0.5630	0.5681
Mass flow rate in LTC compressor (Kg/sec)	0.1993	0.200	0.2007
Heating Load on cascade Condenser (KW)	51.64	52.10	52.57
Heating Load on HTC Condenser (KW)	87.32	88.09	88.88
Cooling Load on LTC Condenser (KW)	35.167	35.167	35.167
Second law efficiency (Exergetic _Efficiency)	0.3562	0.3562	0.3562
First law circuit efficiency (COP_HTC)	1.448	1.448	1.448
First law circuit efficiency (COP_LTC)	2.134	2.077	2.20

Table 8(b): Optimum Results for two stage cascade system (system-6) using HFO-1234ze in high temperature circuit using condenser temperature of 55 ºC and HFC-134a in low temperature circuit using low temperature circuit evaporator temperature of (-50ºC) at Optimum HTC evaporator temperature= -6 ºC and -7 ºC.

Optimum Parameters	Optimum emperature =-6 ºC	Optimum emperature =-7 ºC
First law efficiency (COP_System)	1.195	1.195
Exergy Destruction Ratio (EDR)	1.489	1.489
Exergy of Fuel (kW)	29.43	29.44
Exergy of Product (kW)	=11.83	11.83
Total work done by HTC compressor (kW)	15.71	16.06
Total work done by LTC compressor (kW)	13.73	13.38,
Mass flow rate in HTC compressor (Kg/sec)	0.4181	0.4176
Mass flow rate in LTC compressor (Kg/sec)	0.2805	0.2777
Heating Load on cascade Condenser (KW)	48.89	48.55
Heating Load on HTC Condenser (KW)	64.6	64.6
Cooling Load on LTC Condenser (KW)	35.167	35.167
Second law efficiency (Exergetic_Efficiency)	0.4018	0.4018
First law circuit efficiency (COP_HTC)	3.113	3.113
First law circuit efficiency (COP_LTC)	2.562	2.562

5.Conclusions

The following conclusions were drawn from present investigations.

(i) The Optimum Results for cascade refrigeration using R1234ze in high temperature circuit using high temperature condenser temperature (55 ^{o}C)and R134a in low temperature circuit (system-6) of -100^{o}C low temperature circuit evaporator , 10^{o}C of temperature overlapping (Approach) and 80% high temperature circuit compressor efficiency and also 80% of low temperature circuit compressor efficiency the optimum evaporator temperature high temperature circuit (HTC) to be -78 ^{o}C , -79 ^{o}C & -80 ^{o}C respectively and no optimum was found using HFO-1234yf in high temperature circuit and HFC-134a in low temperature circuit.

(ii)The Optimum Results for cascade refrigeration using R1234ze in high temperature circuit and R1234yf in low temperature circuit (system-1) using50^{o}C of high temperature circuit condenser temperature & -50^{o}C low temperature circuit evaporator , 10^{o}C of temperature overlapping (Approach) and 80% high temperature circuit compressor efficiency and also 80% of low temperature circuit compressor efficiency the optimum evaporator temperature high temperature circuit (HTC)to be -6 ^{o}C and -7 ^{o}C respectively

(iii)Up to temperature -50 ^{o}C in the low temperature evaporator circuit with temperature overlapping (Approach=10^{o}C) and condenser temperature of 50 ^{o}C with cascade evaporator of 0^{o}C , the combination of R1234ze in high temperature circuit and R1234yf in low temperature circuit gives best results for replacing R134a.

iv) For -100^{o}C of low temperature evaporator circuit and 50^{o}C of high temperature condenser and -30^{o}C cascade evaporator with temperature overlapping (Approach=10^{o}C) the combination of R1234ze – and R245fa gives better thermodynamic performances as compared to R-1234yf and R245fa

(v)The ecofriendly refrigerants HFO can replace R134a without minor modifications.

References

[1] C Tanga. Refrigeration drives sustainable development, state of the art, 20th anniversary of the Montreal Protocol, 10th anniversary of the Kyoto Protocol, International Institute of Refrigeration (IIR), 2007.

[2] Honeywell Spatz Mark, Honeywell Barbara Minor, DuPont, HFO1234yf—A low GWP refrigerant for MAC-SAE World Congress–Detroit, Michigan, 2008.

[3] Spatz, Mark and Minor, Barbara. HFO-1234yf Low GWP Refrigerant Update 7, 2008.

[4] K Tanaka, Y Higashi. Thermodynamic properties of HFO1234yf (2,3,3,3- tetrafluoropropene). Int. J. of Refrigeration 33(3), 2010, 474–479

[5]JS Brown, C Zilio, A Cavallini. Thermodynamic properties of eight fluorinated olefins. Int J Refrig 33, 2010, 235–241

[6] D Daniel. Selection of refrigerants on a per application basis: trends, Institute of Refrigeration ,inter governmental organization for the development of refrigeration, new refrigerants. Int J Refrig 31, 2007, 1121–1122

International Journal of Research in Engineering and Innovation (IJREI)
journal home page: http://www.ijrei.com
ISSN (Online): 2456-6934

Performance parameters optimization of cascade refrigeration system using ecofriendly refrigerants

R.S. Mishra

Department of Mechanical & Production Engineering, Delhi Technological University Delhi, India

Abstract

The present paper presents optimum thermodynamic performance of three cascade vapour compression refrigeration systems. The numerical thermal model have been developed for two stages cascade refrigeration systems and thermodynamic performances in terms of and first law efficiency, second law efficiency system exergy destruction ratio , first law efficiency of lower temperature and high temperature circuit have been computed. The effect of low temperature evaporator on the system first and second law performances and system exergy destruction ratio it was found that as low temperature evaporator temperature is decreasing , the first law and second law efficiencies are increasing and exergy destruction ratio is decreasing .The optimum performance parameters obtained from thermal model have been presented.
© 2018 ijrei.com. All rights reserved
Keywords: Optimal two stages cascade refrigeration systems, HFO Refrigerants, Thermal modelling

1. Introduction

The refrigeration industry has been working for the past few decades to find replacement refrigerants for the ozone-depleting chlorofluorocarbons (CFCs) and hydrochlorofluorocarbons (HCFCs) being phased out as a result of the Montreal Protocol. The solution for most refrigerant producers has been the commercialization of hydrofluorocarbon (HFC) refrigerants. The new HFC refrigerants, HFC-134a being the most widely used at this time, have zero ozone depletion potential and thus are not affected by the current regulatory phase out as a result of the Montreal Protocol. The refrigeration industry has been working for the past few decades to find replacement refrigerants for the ozone-depleting chlorofluorocarbons (CFCs) and hydrochlorofluorocarbons (HCFCs) being phased out as a result of the Montreal Protocol.

Global warming potential (GWP) is an index for estimating relative global warming contribution due to atmospheric emission of a kilogram of a particular greenhouse gas compared to emission of a kilogram of carbon dioxide. GWP can be calculated for different time horizons showing the effect of atmospheric lifetime for a given gas. The GWP for the 100 year time horizon is commonly the value referenced.

The new ecofriendly refrigerant (hydrofluoroolefin) HFO-1234ze, has zero ozone-depletion potential and meets EU regulatory requirements for reducing the use of high global-warming-potential (GWP) substances such as R134a etc.. This fourth-generation technology is a direct replacement for hydrofluorocarbon R-134a in the low temperature applications as of today, HFOs found in a number of applications. In refrigeration and heat pump technology HFO-1234yf has been chosen to replace R134a. A number of the refrigerants have been suggested to substitute R134a. R-1234yf, for instance, has very low GWP of 4 and zero ODP. The Thermal performance of R-1234yf in R-134a system have similar coefficient of performance (COP), but R-1234yf provides much lower capacity. Energy conservation and environmental concerns are the main reasons for the development growth of new low GWP refrigerants. While the direct contribution of all the proposed refrigerants to global warming is lower than that of R134a.

2. Literature review

Zubair [1] evaluated the thermal performance of vapour compression system and experimental investigation and theoretical study of a different type of two-stage vapor compression cascade refrigeration system. Bansal P.K [2]

Corresponding author: R. S. Mishra
Email Address: hod.mechanical.rsm@dtu.ac.in

carried out the thermal analysis of cascade refrigeration system using R717in high temperature circuit and R744 refrigerant in the low temperature circuit. Bhattacharyya et al [3] carried out the thermal performance of a cascade heat pump system and developed thermal model which incorporated both internal and external irreversibility in the system. Agnew et al [4] also computed the first law performance of a cascade refrigeration systems. Mishra [5] studied thermal performances in terms of COP and exergetic efficiency and system exergy destruction ratio (EDR) for very low temperature application using ethane in the low temperature circuits and R1234ze and R1234yf in higher temperature circuit. Kilicarslan [6] carried out the experimental and theoretical studied of two-stage vapor compression cascade refrigeration system. Lee et al [7] studied thermal performances a cascade refrigeration system by using carbon dioxide in low temperature circuit and ammonia (R717) as refrigerant in high temperature circuit. Samant [8] designed & developed of two stage cascade refrigeration system using carbon dioxide (R744) in low temperature circuit and propane as HTC refrigerant. Mishra [5] studied thermal performances in terms of COP and exergetic efficiency and system exergy destruction ratio (EDR) for very low temperature application using R404a , in the low temperature circuits and R1234ze and R1234yf in higher temperature circuit and found that performance using R404a worked in low temperature circuit up to temperature -135ºC respectively. S. Fukuda [10] suggested the use of R1234ze (e) for heat pump application to replace R410a.

3. Utility of HFO Refrigerants in Two Stages Cascade Refrigeration Systems

In the two stages vapour compression cascade refrigeration systems 1,3,3,3-Tetrafluoropropene (HFO-1234ze) is known as hydro-fluoro-olefin was used in the high temperature circuit in the condenser temperature range of 40ºC to 60ºC and evaporator temperature range of -20ºC to 20ºC . The HFO R1234ze being a stable refrigerant very low global-warming potential (GWP < 7) for high temperature application used as a "fourth generation" refrigerant to replace R-134a.[1] For low temperature applications, ecofriendly refrigerants such as Carbon dioxide, propane, butane, R152a and HFO1234yf has seen as potential candidates to substitute R134a. Finally, HFO1234yf has been chosen due to its properties, which allow replacing R134a ecofriendly. The use of R-134a is being phased out because of its high global-warming potential. HFO-1234yf has zero ozone-depletion potential (ODP=0) and a very low global-warming potential (GWP < 5), are known for low-temperature refrigeration circuit. The refrigerant R152a is more efficient, where it leads to a system with better COP that alternative refrigerants. Similarly hydrocarbons reach similar or better efficiency.

4. Results & Discussions

The following assumptions have been taken for analyzing two stages cascade vapour compression system for low temperature applications. The cooling load is considered to be 35 kW‖ Temperature of condenser is to be 50ºC and temperature of R1234yf evaporator to be -50 ºC, The temperature of high temperature evaporator to be 0 ºC, The temperature overlapping in terms of approach (i.e.) temperature difference between cascade condenser using R1234yf and cascade evaporator using R1234ze is known as approach which is equal to 10ºC.

Input Data

Temperature of high temperature circuit condenser ($T_{_Cond_HTC}$)=50 ºC,
Temperature of high temperature circuit evaporator $T_{_Eva_HTC}$=0 ºC,
Temperature of low temperature circuit evaporator $T_{_Eva_LTC}$= - 50 ºC,
Temperature overlapping (Approach) =10ºC
Efficiency of Compressor_HTC=0.80,
Efficiency of Compressor_LTC=0.80

Table-1 shows the variation of Thermal performance with variation of HTC condenser temperature of two stage cascade vapour compression refrigeration system using HFO-1234ze in high temperature circuit and following refrigerants in low temperature circuitand it was found that R141(b) and R236fa gives better first law efficiency in terms of COP and second law efficiency in terms of exergetic efficiency.
Table-2(a) shows the effect of approaches (differences in temperature between cascade condenser and cascade evaporators in the various intermediate temperature circuits and low temperature circuit) on the first law and second law performances on the four stage cascade refrigeration systems. It was observed that as approach is decreasing the system first and second law efficiency is increasing and exergy destruction ratio is decreases and lowest COP was found by using R407c.

Table-1 Variation of Thermal performance with variation of HTC condenser temperature of two stage cascade vapour compression refrigeration system using HFO-1234ze in high temperature circuit and following refrigerants in low temperature circuit for $T_{_Cond}$=50ºC with subcooling of 5ºC, $T_{_Eva_HTC}$= 0ºC, $T_{_Eva_LTC}$=-50ºC, $Q_{_Eva_LTC}$=35 "kW"

LTC Refrigerants	COP	System EDR	Exergetic Efficiency	$EDR_{_Rational}$	Exergy of Fuel (kW)	Exergy of Product (kW)	COP_HTC	COP_LTC
R-134a	1.219	1.438	0.4101	0.5899	28.84	11.83	3.737	2.294
R-1234yf	1.181	1.506	0.3991	0.6009	29.64	11.83	3.737	2.204
R717	1.206	1.466	0.4055	0.5945	29.17	11.83	3.737	2.256

R141b	1.289	1.307	0.4334	0.5666	27.29	11.83	3.737	2.493
R-404a	1.151	1.584	0.3870	0.6130	30.57	11.83	3.737	2.107
R-410a	1.214	1.45	0.4081	0.5919	28.98	11.83	3.737	2.278
R-407c	1.094	1.717	0.3680	0.6320	32.14	11.83	3.737	1.961
R-152a	1.246	1.386	0.4192	0.5808	28.22	11.83	3.737	2.370
R-227ea	1.131	1.629	0.3804	0.6196	31.09	11.83	3.737	2.056
R-236fa	1.188	1.503	0.3995	0.6005	29.6	11.83	3.737	2.207
R-245fa	1.239	1.40	0.4166	0.5834	28.39	11.83	3.737	2.349
R-32	1.203	1.471	0.4047	0.5953	29.22	11.83	3.737	2.250
R-600a	1.215	1.447	0.4087	0.5923	28.94	11.83	3.737	2.282
R-600	1.243	1.392	0.4180	0.5820	28.3	11.83	3.737	2.360
R-290	1.218	1.442	0.4096	0.5904	28.88	11.83	3.737	2.290
R-123	1.259	1.361	0.4235	0.5735	27.93	11.83	3.737	2.408
R-125	1.13	1.632	0.380	0.620	31.13	11.83	3.737	2.052
R-507a	1.168	1.546	0.3928	0.6072	30.11	11.83	3.737	2.153

Table-2(a) shows as the variation of condenser temperature with thermal performance parameters. It was observed that as condenser temperature decreases overall COP of system (First law efficiency of system) increases and System EDR is decreases and also second law efficiency (exergetic efficiency) increases. While First law efficiency of hot fluid circuit is increases. There will not be effect on other circuit first law efficiencies. The exergetic efficiency and Overall COP of system using R1234ze is higher in the high temperature circuit while system EDR increases. As decreasing High temperature evaporator temperature, the first law efficiency (i.e. overall cop of system) and second law efficiency (i.e. exergetic efficiency of whole system) is is increasing up to maximum value at the evaporator temperature of 20°C and then decreases rapidly.

System-1: HFO-1234ze in HTC and HFO-1234yf in low temperature circuit

Table-2(a) Variation of Thermal performance with variation of HTC condenser temperature of two stage cascade vapour compression refrigeration system using HFO-1234ze in high temperature circuit and HFO-1234yf in low temperature circuit for $T_{_Cond}$=50°C with subcooling of 5°C, $T_{_Eva_HTC}$= -10°C, $T_{_Eva_LTC}$=-50°C, $Q_{_Eva_LTC}$=35 "kW"

Effect of Temperature Overlapping (Approach)	COP	System EDR	Exergetic Efficiency	$EDR_{_Rational}$	Exergy of Fuel (kW)	Exergy of Product (kW)	COP_HTC	COP_LTC
0	1.402	1.121	0.4715	0.5285	25.08	11.83	3.737	2.844
2	1.356	1.193	0.4561	0.5439	25.93	11.83	3.737	2.698
4	1.312	1.267	0.4412	0.5588	26.81	11.83	3.737	2.562
6	1.269	1.344	0.4267	0.5733	27.72	11.83	3.737	2.435
8	1.227	1.423	0.4127	0.5873	28.66	11.83	3.737	2.316
10	1.187	1.506	0.3991	0.6009	29.64	11.83	3.737	2.204
12	1.147	1.592	0.3858	0.6142	30.66	11.83	3.737	2.098

Table-2(b) Variation of Thermal performance with variation of HTC condenser temperature of two stage cascade vapour compression refrigeration system using HFO-1234ze in high temperature circuit and HFO-1234yf in low temperature circuit for $T_{_Cond}$=50°C with subcooling of 5°C, $T_{_Eva_HTC}$= -10°C, $T_{_Eva_LTC}$=-50°C, $Q_{_Eva_LTC}$=35 "kW"

HTC Refrigerants	COP	System EDR	Exergetic Efficiency	$EDR_{_Rational}$	Exergy of Fuel (kW)	Exergy of Product (kW)	COP_HTC	COP_LTC
R1234ze	1.187	1.506	0.3991	0.6009	29.64	11.83	3.737	2.204
R717	1.228	1.422	0.4129	0.5871	28.64	11.83	4.030	2.204
R152a	1.217	1.442	0.4095	0.5905	28.89	11.83	3.955	2.204
R290	1.178	1.523	0.3963	0.6037	29.84	11.83	3.682	2.204
R600	1.217	1.442	0.4095	0.5905	28.89	11.83	3.955	2.204
R600a	1.196	1.486	0.4022	0.5978	29.41	11.83	3.801	2.204
R134a	1.190	1.498	0.4003	0.5997	29.55	11.83	3.762	2.204
R1234yf	1.160	1.564	0.390	0.610	30.32	11.83	3.559	2.204

Table-2(d) .shows as the variation of high temperature evaporator with thermal performance parameters As decreasing High temperature evaporator temperature the system EDR first decreasing up to decreasing evaporator temperature and then further constant and then increasing and optimum becomes at evaporator temperature at 20°C in both cases using R1234ze in the high temperature circuit. However COP of hot fluid circuit is decreases and COP of low temperature fluid circuit is increases.

Table-2(c) Variation of Thermal performance with variation of HTC condenser temperature of two stage cascade vapour compression refrigeration system using HFO-1234ze in high temperature circuit and HFO-1234yf in low temperature circuit for T_Cond=50°C with subcooling of 5°C, $T_{_Eva_HTC}$= -10°C, $T_{_Eva_LTC}$=-50°C, $Q_{_Eva_LTC}$=35 "kW"

T_Cond (°C)	COP	EDR	Exergetic Efficiency	Rational EDR	Exergy of Fuel (kW)	Exergy of Product (kW)	COP_HTC	COP_LTC
60	1.024	1.905	0.3443	0.6557	34.35	11.83	2.779	2.204
55	1.104	1.694	0.3712	0.6288	31.86	11.83	3.215	2.204
50	1.187	1.506	0.3991	0.6009	29.64	11.83	3.737	2.204
45	1.273	1.336	0.4280	0.5720	27.63	11.83	4.379	2.204
40	1.363	1.182	0.4583	0.5417	25.81	11.83	5.192	2.204
35	1.458	1.039	0.4903	0.5097	24.12	11.83	6.264	2.204
30	1.559	0.9070	0.5244	0.4756	22.56	11.83	7.75	2.204
25	1.667	0.7832	0.5608	0.4392	21.09	11.83	9.962	2.204

Table-2(d) shows the variation of Thermal performance with variation of cascade evaporator temperature of two stage cascade vapour compression refrigeration system using HFO-1234ze in high temperature circuit and HFO-1234yf in low temperature circuit and it was observed that first law performance (COP) of system increases as temperature of HTC evaporator is increases and becomes a optimum values at -6°C and then and then decreases.

Table-2(d) Variation of Thermal performance with variation of cascade evaporator temperature of two stage cascade vapour compression refrigeration system using HFO-1234ze in high temperature circuit and HFO-1234yf in low temperature circuit for $T_{_Cond}$=50°C with subcooling of 5°C, $T_{_Eva_HTC}$= -10°C, $T_{_Eva_LTC}$=-50°C, $Q_{_Eva_LTC}$=35 "kW"

T_Eva (°C)	COP	EDR	Exergetic Efficiency	EDR	Exergy of Fuel (kW)	Exergy of Product (kW)	COP_HTC	COP_LTC
20	1.049	1.836	0.3527	0.6473	33.54	11.83	8.032	1.356
15	1.099	1.706	0.3696	0.6304	32.0	11.83	6.415	1.533
10	1.139	1.611	0.383	0.6170	30.88	11.83	5.264	1.729
5	1.168	1.546	0.3928	0.6072	30.11	11.83	4.404	1.951
4	1.173	1.536	0.3944	0.6056	29.99	11.83	4.257	1.998
3	1.177	1.527	0.3958	0.6042	29.89	11.83	4.118	2.048
2	1.180	1.519	0.3970	0.6030	29.79	11.83	3.985	2.098
1	1.184	1.512	0.3981	0.6019	29.71	11.83	3.858	2.15
0	1.187	1.506	0.3991	0.6009	29.64	11.83	3.737	2.204
-1	1.189	1.501	0.3999	0.6001	29.58	11.83	3.622	2.259
-2	1.191	1.497	0.4005	0.5995	29.53	11.83	3.511	2.316
-3	1.193	1.493	0.4011	0.5989	29.49	11.83	3.405	2.374
-4	1.193	1.491	0.4015	0.5985	29.46	11.83	3.304	2.435
-5	1.194	1.489	0.4017	0.5983	29.44	11.83	3.206	2.497
-6	1.195	1.489	0.4018	0.5991	29.43	11.83	3.113	2.562
-7	1.195	1.489	0.4018	0.5982	29.44	11.83	3.023	2.629
-8	1.194	1.490	0.4016	0.5984	29.45	11.83	2.937	2.698
-9	1.193	1.492	0.4014	0.5986	29.47	11.83	2.854	2.77
-10	1.192	1.494	0.4009	0.5991	29.5	11.83	2.744	2.844
-15	1.180	1.519	0.3969	0.6031	29.8	11.83	2.416	3.261
-20	1.159	1.585	0.3899	0.6101	30.33	11.83	2.116	3.777

Table-2(e) shows as the variation of low temperature evaporator with thermal performance parameters using R1234yf in thelow temperature circuit It was observed that As evaporator temperature decreases, the first law efficiency (overall COP) and second law efficiency (exergetic efficiency) of the system is increases and maximum efficiency is obtained at evaporator temperature of -50 °C and also cop of primary intermediate temperature circuit is decreases and secondary intermediate temperature circuit COP is increases.

Table-2(e) Variation of Thermal performance with variation of LTC evaporator temperature of two stage cascade vapour compression refrigeration system using HFO-1234ze in high temperature circuit and HFO-1234yf in low temperature circuit for $T_{_Cond}$=50°C with subcooling of 5°C, $T_{_Eva_HTC}$= -10°C, $T_{_Eva_LTC}$=-50°C, $Q_{_Eva_LTC}$=35 "kW"

T_Eva (°C)	COP	EDR	Exergetic Efficiency	Rational EDR	Exergy of Fuel (kW)	Exergy of Product (kW)	COP_HTC	COP_{LTC}
-50	1.187	1.506	0.3991	0.6009	29.64	11.83	3.737	2.204
-45	1.301	1.504	0.3993	0.6007	27.04	11.83	3.737	2.529

-40	1.426	1.515	0.3977	0.6023	24.67	11.83	3.737	2.921
-35	1.563	1.538	0.3939	0.6061	22.51	11.83	3.737	3.404
-30	1.713	1.578	0.3878	0.6122	20.52	11.83	3.737	4.011
-25	1.88	1.638	0.3790	0.6209	18.71	11.83	3.737	4.795
-20	2.064	1.724	0.3672	0.6328	17.04	11.83	3.737	5.845

The performance of two other cascade systems are given below. The system-2 consists of HFO-1234ze in HTC and HFC-134a in low temperature circuit while system-3 consists of HFO-1234yf in HTC and HFC-134a in low temperature circuit and performances are shown in Tables-3 & Tables 4 respectively. It was also shown from table-3(a) & table-4(a) respectively. For system-2 (Table-3 (a)) and system-3(Table-4 (a)) , as low temperature circuit evaporator temperature decreases from -20ºC to -50ºC, the first law efficiency (COP) of system is decreases and second law efficiency is increases and rational EDR and EDR system is also decreases. Similarly Table-3(b) shows the variation of Thermal performance with variation of HTC condenser temperature of two stage cascade vapour compression refrigeration system using HFO-1234ze in high temperature circuit and HFC-134a in low temperature circuit and Table-4(b) shows the variation of Thermal performance with variation of HTC evaporator temperature of two stage cascade vapour compression refrigeration system using HFO-1234yf in high temperature circuit and HFC-134a in low temperature circuit and it was found that as high temperature circuit condenser is increase, the first law efficiency in terms of COP is and second law efficiency in terms of exergetic efficiency and High temperature circuit first law efficiency (COP_HTC) are also decreases and exergy destruction ratio of system and rational EDR and exergy of fuel I.e. total power required to run both compressors in cascade system are also increases. Table-3(c) shows (system-3) the variation of Thermal performance with variation of cascade evaporator temperature of two stage cascade vapour compression refrigeration system using HFO-1234ze in high temperature circuit and HFC-134a in low temperature circuit and Table-4(c) shows the variation of Thermal performance with variation of cascade evaporator temperature of two stage cascade vapour compression refrigeration system using HFO-1234yf in high temperature circuit and HFC-134a in low temperature circuit and it was found that by increasing temperature of high temperature evaporator , the first law efficiency and second law efficiency in terms of exergetic efficiency increases and becomes optimum exergetic efficiency at temperature of -1ºC for system-2 and 1ºC for system-3 and then decreases.

System-2; HFO-1234ze in HTC and HFC-134a in low temperature circuit

Table-3(a) Variation of Thermal performance with variation of LTC evaporator temperature of two stage cascade vapour compression refrigeration system using HFO-1234ze in high temperature circuit and HFC-134a in low temperature circuit for T_Cond=50ºC with subcooling of 5ºC, $T_{_Eva_HTC}$= -10ºC, $T_{_Eva_LTC}$=-50ºC, $Q_{_Eva_LTC}$=35 "kW"

T_Eva (ºC)	COP	EDR	Exergetic Efficiency	Rational EDR	Exergy of Fuel (kW)	Exergy of Product (kW)	COP_HTC	$COP_{_LTC}$
-50	1.219	1.438	0.4101	0.5899	28.84	11.83	3.737	2.294
-45	1.331	1.446	0.4088	0.5912	26.41	10.8	3.737	2.622
-40	1.454	1.465	0.4057	0.5943	24.18	9.811	3.737	3.017
-35	1.589	1.497	0.4005	0.5995	24.14	8.866	3.737	3.503
-30	1.737	1.544	0.3931	0.6069	20.25	7.96	3.737	4.112
-25	1.90	1.611	0.383	0.6170	18.51	7.09	3.737	4.899
-20	2.081	1.702	0.3701	0.6699	16.9	6.255	3.737	5.951

Table-3(b) Variation of Thermal performance with variation of LTC evaporator temperature of two stage cascade vapour compression refrigeration system using HFO-1234ze in high temperature circuit and HFC-134a in low temperature circuit for $T_{_Cond}$=50ºC with subcooling of 5ºC, $T_{_Eva_HTC}$= -10ºC, $T_{_Eva_LTC}$=-50ºC, $Q_{_Eva_LTC}$=35 "kW"

$T_{_Cond}$ (ºC)	COP	EDR	Exergetic Efficiency	Rational EDR	Exergy of Fuel (kW)	Exergy of Product (kW)	COP_HTC	$COP_{_LTC}$
25	1.724	0.7246	0.5798	0.4202	20.4	11.83	9.962	2.294
30	1.61	0.8470	0.5414	0.4586	21.84	11.83	7.75	2.294
35	1.503	0.9777	0.5056	0.4944	23.39	11.83	6.264	2.294
40	1.404	1.118	0.4721	0.5279	25.05	11.83	5.192	2.294
45	1.309	1.271	0.4403	0.5597	26.86	11.83	4.379	2.294
50	1.219	1.438	0.4101	0.5899	28.84	11.83	3.737	2.294
55	1.133	1.624	0.3811	0.6189	31.03	11.83	3.215	2.294
60	1.05	1.832	0.3531	0.6469	33.50	11.83	2.779	2.294

Table-3(c) Variation of Thermal performance with variation of cascade evaporator temperature of two stage cascade vapour compression refrigeration system using HFO-1234ze in high temperature circuit and HFC-134a in low temperature circuit for T_Cond=50°C with subcooling of 5°C, $T_{_Eva_HTC}$= -10°C, $T_{_Eva_LTC}$=-50°C, $Q_{_Eva_LTC}$=35 "kW"

T_Eva (°C)	COP	EDR	Exergetic Efficiency	EDR	Exergy of Fuel (kW)	Exergy of Product (kW)	COP_HTC	COP_LTC
20	1.134	1.621	0.3815	0.6185	31.01	11.83	8.032	1.485
15	1.169	1.544	0.3930	0.6070	30.09	11.83	6.415	1.652
10	1.194	1.489	0.4017	0.5983	29.44	11.83	5.264	1.838
5	1.211	1.455	0.4074	0.5926	29.03	11.83	4.404	2.050
4	1.214	1.45	0.4082	0.5918	28.98	11.83	4.257	2.096
3	1.216	1.446	0.4088	0.5912	28.93	11.83	4.118	2.144
2	1.217	1.443	0.4094	0.5906	28.89	11.83	3.985	2.192
1	1.218	1.44	0.4098	0.5902	28.86	11.83	3.858	2.242
0	1.219	1.438	0.4101	0.5899	28.84	11.83	3.737	2.324
-1 (optimum)	1.22	1.437	0.4103	0.5897	28.83	11.83	3.622	2.347
-2(optimum)	1.22	1.437	0.4103	0.5897	28.82	11.83	3.511	2.402
-3	1.22	1.437	0.4103	0.5897	28.83	11.83	3.405	2.459
-4	1.219	1.438	0.4101	0.5899	28.84	11.83	3.304	2.518
-5	1.219	1.44	0.4098	0.5902	28.86	11.83	3.206	2.579
-6	1.217	1.442	0.4094	0.5906	28.89	11.83	3.113	2.641
-7	1.216	1.445	0.4089	0.5911	28.92	11.83	3.023	2.706
-8	1.214	1.454	0.4083	0.5917	28.97	11.83	2.937	2.774
-9	1.212	1.454	0.4075	0.5925	29.02	11.83	2.854	2.844
-10	1.209	1.459	0.4067	0.5933	29.08	11.83	2.774	2.916
-15	1.192	1.495	0.4009	0.5991	29.51	11.83	2.416	3.325
-20	1.167	1.548	0.3925	0.6075	30.13	11.83	2.116	3.832

System-3; HFO-1234yf in HTC and HFC-134a in low temperature circuit

Table-4(a) Variation of Thermal performance with variation of LTC evaporator temperature of two stage cascade vapour compression refrigeration system using HFO-1234yf in high temperature circuit and HFC-134a in low temperature circuit for T_Cond=50°C with subcooling of 5°C, $T_{_Eva_HTC}$= -10°C, $T_{_Eva_LTC}$=-50°C, $Q_{_Eva_LTC}$=35 "kW"

T_Eva (°C)	COP	EDR	Exergetic Efficiency	Rational EDR	Exergy of Fuel (kW)	Exergy of Product (kW)	COP_HTC	COP_{LTC}
-50	1.191	1.496	0.4007	0.5993	29.52	11.83	3.559	2.294
-45	1.299	1.507	0.3990	0.6010	27.06	10.8	3.559	2.622
-40	1.417	1.529	0.3954	0.6046	24.81	9.811	3.559	3.017
-35	1.546	1.565	0.3898	0.6102	22.74	8.866	3.559	3.503
-30	1.688	1.618	0.3820	0.6170	20.84	7.96	3.559	4.112
-25	1.843	1.691	0.3717	0.6283	19.08	7.09	3.559	4.899
-20	2.015	1.789	0.3584	0.3416	17.45	6.255	3.559	5.951

Table-4(b) Variation of Thermal performance with variation of LTC evaporator temperature of two stage cascade vapour compression refrigeration system using HFO-1234yf in high temperature circuit and HFC-134a in low temperature circuit for $T_{_Cond}$=50°C with subcooling of 5°C, $T_{_Eva_HTC}$= -10°C, $T_{_Eva_LTC}$=-50°C, $Q_{_Eva_LTC}$=35 "kW"

T_Eva (°C)	COP	EDR	Exergetic Efficiency	Rational EDR	Exergy of Fuel (kW)	Exergy of Product (kW)	COP_HTC	COP_{LTC}
25	1.716	0.7325	0.5772	0.4338	20.49	11.83	9.783	2.294
30	1.599	0.8592	0.5379	0.4621	21.99	11.83	7.581	2.294
35	1.49	0.9961	0.5010	0.4990	23.61	11.83	6.099	2.294
40	1.386	1.141	0.4661	0.5339	25.38	11.83	5.026	2.294
45	1.287	1.311	0.4328	0.5672	27.33	11.83	4.208	2.294
50	1.191	1.496	0.4007	0.5993	29.52	11.83	3.559	2.294
55	1.099	1.706	0.3695	0.6305	32.01	11.83	3.027	2.294
60	1.007	1.952	0.3388	0.6612	34.91	11.83	2.579	2.294

Table-4(c) Variation of Thermal performance with variation of cascade evaporator temperature of two stage cascade vapour compression refrigeration system using HFO-1234yf in high temperature circuit and HFO-134a in low temperature circuit for T_Cond=50°C with subcooling of 5°C, $T_{_Eva_HTC}$= -10°C, $T_{_Eva_LTC}$=-50°C, $Q_{_Eva_LTC}$=35 "kW"

T_Eva (°C)	COP	EDR	Exergetic Efficiency	EDR	Exergy of Fuel (kW)	Exergy of Product (kW)	COP_ HTC	COP_LTC
20	1.125	1.642	0.3784	0.6216	31.25	11.83	7.768	1.485
15	1.156	1.572	0.3887	0.6113	30.42	11.83	5.264	1.838
10	1.177	1.526	0.3959	0.6041	29.87	11.83	5.054	1.652
5	1.189	1.501	0.3999	0.6001	29.58	11.83	4.211	2.050
4	1.190	1.498	0.4003	0.5997	29.55	11.83	4.068	2.096
3	1.191	1.496	0.4006	0.5994	29.52	11.83	3.931	2.144
2(optimum)	1.192*	1.495	0.4008	0.5992	29.51	11.83	3.801	2.192
1(optimum)	1.192*	1.495	0.4008	0.5992	29.51	11.83	3.677	2.242
0	1.191	1.496	0.4007	0.5993	29.52	11.83	3.559	2.324
-1	1.191	1.497	0.4005	0.5995	29.53	11.83	3.446	2.347
-2	1.190	1.499	0.4001	0.5999	29.56	11.83	3.338	2.402
-3	1.188	1.502	0.3997	0.6003	29.59	11.83	3.235	2.459
-4	1.187	1.506	0.3991	0.6009	29.64	11.83	3.135	2.518
-5	1.184	1.510	0.3984	0.6016	29.69	11.83	3.04	2.579
-6	1.182	1.515	0.3975	0.6025	29.75	11.83	2.949	2.641
-7	1.179	1.521	0.3966	0.6034	29.82	11.83	2.862	2.706
-8	1.176	1.528	0.3955	0.6045	29.90	11.83	2.778	2.774
-9	1.173	1.536	0.3944	0.6056	29.99	11.83	2.697	2.844
-10	1.169	1.544	0.3931	0.6069	30.09	11.83	2.619	2.916
-15	1.145	1.597	0.3850	0.6150	30.72	11.83	2.271	3.325
-20	1.113	1.670	0.3745	0.6255	31.58	11.83	1.979	3.832

Table-5 and Table-6 shows the optimum value of parameters for three systems

Table- 5: Optimum parameters obtained for three systems

Parameters	System-1; using HFO-1234ze in HTC and HFO-1234yf in LTC	System-2: using HFO-1234ze in HTC and HFC-134a in LTC	System-3: using HFO-1234yf in HTC and HFC-134a in LTC
Optimum HTC evaporator temperature	-6 °C	-1 °C	1 °C
First law efficiency (COP_System)	1.195	1.22	1.192
Exergy Destruction Ratio (EDR)	1.489	1.437	1.495
Exergy of Fuel (kW)=	29.43	28.82	29.51
Exergy of Product (kW)=	11.83	11.83	11.83
Total work done by HTC compressor (kW)	15.71	13.85	13.83
Total work done by LTC compressor (kW)	13.73	14.48	15.68
Mass flow rate in HTC compressor (Kg/sec)	0.4181	0.4164	0.4949
Mass flow rate in LTC compressor (Kg/sec)	0.2805	0.2262	0.2303
Heating Load on cascade Condenser (KW)	48.89	50.15	50.15
Cooling Load on LTC Condenser (KW)	35.167	35.167	35.167
Heating Load on HTC Condenser (KW)	64.6	64.0	64.68
Second law efficiency (Exergetic _Efficiency)	0.4018	0.4103	0.4008
First law circuit efficiency (COP_HTC)	3.113	3.622	3.801
First law circuit efficiency (COP_LTC)	2.562,	2.347	2.192

Table 6: Optimum parameters obtained for three systems

Parameters	System-1; using HFO-1234ze in HTC and HFO-1234yf in LTC	System-2: using HFO-1234ze in HTC and HFC-134a in LTC	System-3: using HFO-1234yf in HTC and HFC-134a in LTC
Optimum HTC evaporator temperature	-7 °C	-2 °C	2 °C
First law efficiency (COP_System)	1.195	1.22	1.192
Exergy Destruction Ratio (EDR)	1.489	1.437	1.495
Exergy of Fuel (kW)	29.44	28.82	29.51
Exergy of Product (kW)	11.83,	11.83	11.83
Total work done by HTC compressor (kW)	16.06	13.85	13.83

Total work done by LTC compressor (kW)	13.38,	14.48	15.68
Mass flow rate in HTC compressor (Kg/sec)	0.4176	0.4164	0.4949
Mass flow rate in LTC compressor (Kg/sec)	0.2777	0.2262	0.2303
Heating Load on cascade Condenser (KW)	48.55	50.15	50.15
Cooling Load on LTC Condenser (KW)	35.167	35.167	35.167
Heating Load on HTC Condenser (KW)	64.6	64.0	64.68
Second law efficiency (Exergetic _Efficiency)	0.4018,	0.4103	0.4008
First law circuit efficiency (COP_HTC)	3.113,	3.622	3.801
First law circuit efficiency (COP_LTC)	2.562,	2.347	2.192

5. Conclusions and Recommendation

The following optimum values of parameters were obtained during numerical investigations for system-1.

(i) The optimum temperature of high temperature evaporator for system-1 was found between -6ºC to -7ºC, for sytem-2: was found between -1ºC to -2ºC and for system-3: was found between 1ºC to 2ºC of temperature. The other value of performance parameters for three cascade systems are given in Table-5 & 6 respectively.

(ii) The volumetric refrigerating capacity of HFO R1234ze is below that of R134a and It\s boiling point is also higher than that of R134a in the high temperature circuit of cascade refrigeration system in the range of HTC Circuit from 60ºC to -20ºC is suitable for replacing R134a.

(iii) HFO R1234yf is suitable for replacing R134a. in the low temperature circuit of cascade refrigeration system in the range of LTC Circuit from -20ºC to -50ºC.

(iv) Increasing evaporator temperature overall first law efficiency in terms of COP is increases.

References

[1] S. M. Zubair, [1999]Performance evaluation of Vapour Compression System, International Journal of Refrigeration, 22, , 235-243.

[2] P. K. Bansal, [2008] Thermodynamic analysis of an R744–R717 cascade refrigeration system, international journal of refrigeration Vol-31 , page-45-54.

[3] Souvik Bhattacharyya, [2007] Exergy maximization of cascade refrigeration cycles and its numerical verification for a trans critical CO2-C3H8 system, International Journal of Refrigeration, Vol-30, ,page. 624- 632.

[4] B. Agnew, et.a.,[2004] A finite time analysis of a cascade refrigeration system using alternative refrigerants, Applied Thermal Engineering, Vol-24 , page. 2557–2565.

[5] R.S. Mishra[2014] Use of Hydrocarbons in Low Temperature Circuit in Terms of First Law and Second Law Efficiency of Four Stage Cascade Refrigeration of Semen Preservation" International Journal of Advance Research and Innovation, ISSN 2347 - 3258 , Volume 2, Issue 4, page-725-731.

[6] A. Kilicarslan, [2004] An experimental investigation of a different type vapor compression cascade refrigeration system, Applied Thermal Engineering, Vol-24, page. 2611– 2626.

[7] F. Lee. [2002] Monte, Calculation of thermodynamic properties of R407C and R410A by the Martin–Hou equation of state — part II: technical interpretation, International Journal of Refrigeration, 25, , 314–329.

[8] Samant Maji, [2006]Design and Development of two stage cascade refrigeration system, Mechanical Engineering Department, IIT Delhi,

[9] R.S. Mishra[2014] Performance Optimization of Four Stage Cascade Refrigeration Systems using Energy-Exergy Analysis in the R1234ze & R1234yf in High Temperature Circuitand Ecofriendly Refrigerants in Intermediate Ciircuits and Ethane in the Low Temperature Circuit for Food, Pharmaceutical, Chemical Industries" International Journal of Advance Research and Innovation, ISSN 2347 - 3258 , Volume 2, Issue 4 , page- 701-709

[10] DuPont, "DuPont [2012]Fluorochemicals Affirms Confidence that HFO-1234yf Can Be Safely Used as an Automotive Refrigerant," 18 Oct 2012. [Online]. Available: goo.gl/cyyoS.

[11] Honeywell, "Honeywell Solstice[2015]Lower-Global-Warming refrigerants approved by leading global compressor suppliers," 18 June 2015. [Online]. Available: bit.ly/1LedeT.

[12] S. Fukuda, C. Kondou, N. Takata and S. Koyama, [2014] "Low GWP refrigerants R1234ze(E) and R1234ze(Z) for high temperature heat pumps," International Journal of Refrigeration, vol. 40, pp. 161-173.

Cite this article as: R.S. Mishra, Performance parameters optimization of cascade refrigeration system using ecofriendly refrigerants, *International journal of research in engineering and innovation (IJREI)*, vol 2, issue 6 (2018), 602-609.

raiden11@IECSIL-FIRE-2018 : Named Entity Recognition For Indian Languages

Ayush Gupta[1], Meghna Ayyar[2], Ashutosh Kumar Singh[3], and Rajiv Ratn Shah[4]

[1] Delhi Technological University, Delhi 110042, INDIA
gupta.ayush11786@gmail.com
[2] Indraprastha Institute of Information Technology, Delhi 110020, INDIA
leomi7ayyar@gmail.com
[3] Delhi Technological University, Delhi 110042, INDIA
ashu0788@gmail.com
[4] Indraprastha Institute of Information Technology, Delhi 110020, INDIA
rajivratn@iiitd.ac.in

Abstract. This paper presents our solution for the Named Entity Recognition (NER) task for the Information Extractor for Conversational Systems in Indian Languages challenge (IECSIL) [5] of the FIRE 2018 conference. A subset of the Information Extraction (IE) task, NER is a key to extract information and semantics of the text from unstructured data. The objective of NER is the identification and classification of every word or token in a document into predefined categories such as names of person, location, organization, etc. For this challenge the dataset provided by IECSIL [4] comprised of multilingual text of various Indian languages like Hindi, Tamil, Malayalam, Telugu, and Kannada. We mainly focus on the identification and classification of named entities belonging to nine categories like Name, Location, Datenum, etc. We tried linear models like Naive Bayes and SVM, and also a simple Neural Network to solve this problem. The best results are achieved by the simple neural network with an accuracy of 90.33% for all languages combined. This indicates that different advanced neural networks could be possible solutions to further improve this accuracy.

Keywords: Named Entity Recognition · Information Extraction · Word Embeddings · Neural Networks.

1 Introduction

The sheer volume of unstructured data available on the Web, in the form of blogs, articles, emails, social media posts, documents et cetera is so large that the task of deriving information from them demands an approach that does not involve the manual annotation of this data. The data is heterogeneous, which makes annotation by a human nearly impossible. Therefore, we would like to develop a computer annotation approach to structure the data and make the information from it easily extractable. Information extraction from unstructured data and

CEUR-WS.org/Vol-2266/T3-8.pdf

text is an NLP technique that deals with this problem and entity recognition is one small subtask in the direction of solving it.

NER tasks traditionally require large amounts of knowledge in the form of feature engineering and lexicons to achieve high performance. Moreover, named entities are open class expressions that have a lot of varieties, where new expressions are being added constantly. NER deals with the location and identification of the named entities that are present in the sentences given in the textual input. It generally has pre-defined categories like names of people, places, organizations, terms specific to a particular topic or field, industrial product names et cetera which together comprise of the named entities [18]. NER is essential for various NLP tasks like Question Answering Systems [17], Information Retrieval [22], Machine Translation [3] etc. In addition to this, NER finds many applications in multiple industries such as news and media, search engines, content recommendations, customer support and also in academia.

Several techniques have been developed to recognize named entities for the English language and also for other foreign languages like Chinese, Japanese, Korean, Arabic, and Spanish. Many of these techniques use either rule-based technique shown by Kim and Woodland[13] or some form of statistical technique e.g. Malouf, Robert[16] used Hidden Markov Model to perform entity recognition. Both these approaches rely on the help of a language expert for the creation and validation of a large dataset which can then be used for further analysis. In contrast, for Indian languages, not much work has been reported because of insufficient resources due to which it has been difficult to employ statistical techniques for Indian languages. Moreover, due to the morphological nature of the Indian languages, it needs different methods than what has been employed for English to form a language model. For e.g. in the sentence *Peter likes Paris.*, NER needs to tag the entities *Peter* as <Name of a person> and *Paris* as <Name of place>. Here one rule to identify the nouns would be that nouns generally start with a capital letter. However, for Indian languages like Hindi, Tamil et cetera the nouns have a non-capitalized form and also incorporate a richer morphology as compared to English making it more challenging to perform NER [19].

The corpora provided as a part of the challenge consisted of pre-processed data for five Indian languages thereby, reducing the main difficulty of getting a validated and annotated dataset for the NER task. As an effort to perform entity recognition we have used some linear models as baselines, and have also used a neural network model to demonstrate that these techniques can be extended for the purpose of NER of Indian languages. The rest of the paper is organized as follows. The related work is presented in Section 2 while Section 3 describes the methodology followed in detail. Section 4 discusses the evaluation of the various models tried for the different languages in the corpora and Section 5 concludes the paper and presents some future work that can be pursued.

2 Related Work

Saha et al. [21] developed *A Hybrid Feature Set based Maximum Entropy (MaxEnt) Hindi Named Entity Recognition*. The four identified named entity (NE) by them were Person names (P), Location names (L), Organization names (O) and Date (D). MaxEnt, a supervised machine learning technique as given by Birthwick and Grishman [6] was applied to solve linguistic problems with the help of orthographic, collocation features and gazetteers lists. They used a 2-phase transliteration model to construct about 34 entities and subsequently employed a semi-automatic induction of context patterns used for classification. A 0.76 F-measure was achieved as a baseline result and 0.81 F-measure was achieved after adding gazetteer lists and context patterns into MaxEnt based NER system.

Saha et al. [20] implemented *Hybrid Approach for Named Entity Recognition in Indian Languages* for 5 Indian languages - Hindi, Bengali, Oriya, Telugu, and Urdu. They used two approaches i.e. the Linguistic approach where the typical rules were written by linguists and the Machine Learning (ML) approach – in which the system was trained using tags. They received poor accuracy for Oriya, Telugu and Urdu languages compared to the other two languages due to lack of Parts Of Speech (POS) information, morphological information, language-specific rules, and gazetteers lists.

CRF was introduced by Lafferty et al. [14] to build a probabilistic model for segmenting and labelling the sequence data. Ekbal et al. [7] have worked on *Named Entity Recognition in Bengali: A Conditional Random Field Approach* by using a CRF based approach to develop NER for Bengali. They achieved F-measure of 0.91 using CRF, more than the HMM result.

Gali et al. [8] discussed the ambiguities for Indian languages that deal with the linguistic issues like agglutinative nature and absence of capitalization, same meaning for common name and proper name, spelling variation, patterns, and suffixes. Using CRF's they performed statistical tagging, resolved capitalization etc. They achieved F - measures 0.41, 0.50, 0.39, 0.40, and 0.43 for Bengali, Hindi, Oriya, Telugu, and Urdu respectively.

Amarappa and Sathyanarayana [1] worked on *Named Entity Recognition and Classification (NERC) in Kannada language*, built a SEMI-Automatic Statistical Machine Learning NLP model based on noun taggers using HMM which was a challenging task. In addition, they extended their work in Amarappa and Sathyanarayana [2] to use a Multinomial Naïve Bayes (MNB) Classifier discussed by Kibriya et al. [12] to develop a novel model for NERC.

Malarkodi et al. [15] experimented with NER on Tamil database, which coped with real-time challenges using CRF's and could be applied for most of the Indian languages. Kaur and Gupta [11] built an NER for *Punjabi* language using rule-based and list look-up approaches. Punjabi is a language with high clung and inflections, which leads to linguistic problems. The rule-based approach trained the system to identify NE by writing rules manually for all NE features.

3 Methodology

The problem at hand is to use multilingual corpora to perform entity recognition task for five Indian languages. The following sections describe in detail the various steps that have been performed to achieve the results. Section 3.1 describes the system architecture followed by Section 3.2 which discusses feature extraction techniques applied. Finally, Section 3.3 deals with the description of the various models used in our approach.

3.1 System Architecture

The complete architecture of the proposed system has been summarized in Fig. 1. The pipeline of the system starts with the given dataset, as the input. We marked all the full-stops and punctuation marks as entities belonging to Other class and removed them. Then, we marked the numerical entities as all of them belong to Numbers or Datenum class. This reduced the dataset size and aided in feature extraction as we do not have word embeddings for numerical entities. As different languages can have different ways of writing digits, we have to modify the digit recognizer for each new language we add. This step is followed by the process of feature extraction which has been described in detail in Section 3.2. Once the features were extracted as vectors, we experimented with various models like Naive Bayes and SVM, selected the one which gave the best results in terms of accuracy by predicting the labels on unseen data. For each entity, we selected the class having the highest probability among all.

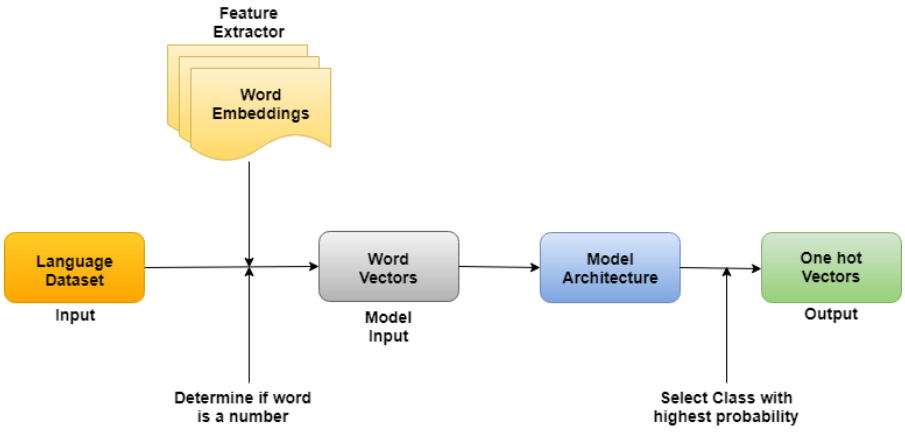


Fig. 1. System Architecture Diagram

3.2 Feature Extraction

An effective representation for sentences is to use the Bag of Words (BoW) model which can then be given as input to a linear classifier like Naive Bayes or Support Vector Machine (SVM). However just using BoW poses problems like large feature dimension and sparse vector representation to represent words. Word embeddings can capture the semantic relations amongst the words, unlike BoW. Hence, we used FastText, a fast word embedding/vector generator by Facebook [10] that provides a way to represent words using numbers. We used a pre-trained collection[5] of word vectors in 294 languages. These word vectors were trained using skip-gram model described by Bojanowski et al. [9] with default parameters. Each word vector consists of 300 decimal numbers representing unique features. Words which are semantically close in meaning appear together in the 300-dimensional graph. Word vectors were downloaded for all five Indian Languages and stored as binary files. Except for Number and Datenum, all other classes, as shown in Table 1, have more than 90% of their entities present in these vectors. Overall 95.83 % of the entities were present. Remaining entities were marked as unknown and a randomly generated sequence of decimals between -1 and 1 was used as their feature sets.

Table 1. Presence percent of training set entities in Facebook word embeddings (Org: Organization)

Language	**Event**	**Things**	**Org**	**Occupation**	**Name**	**Location**	**Other**	**Average Presence**
Hindi	99.69	99.33	99.23	99.48	94.96	98.91	96.38	98.28
Kannada	98.85	97.11	96.85	96.92	89.17	96.94	89.4	95.03
Malayalam	94.86	96.65	97.17	95.72	90.71	96.52	86.14	93.96
Tamil	98.34	98.3	97.95	96.93	91.72	95.13	93.05	95.91
Telugu	98.9	99.16	98.72	98.72	83.65	99.15	93.48	95.96
Class Avg.	98.12	98.11	98.00	97.55	90.04	97.33	91.69	**95.83**

3.3 Model Description

A simple and efficient baseline for our model is to use a linear classifier, e.g. a logistic regression or a SVM algorithm. However, these classifiers fail to capture the context of the statement while evaluating entity. Common examples are the words; *book, battle, address, bear etc.*, which can represent a verb as well as a noun depending on the context. Also, they cannot generalize well in case of imbalance in the class distribution in the dataset. To overcome this, we can apply a multi-layer neural network or a deep neural network which can capture the composite relation between the words.

[5] https://github.com/facebookresearch/fastText/blob/master/pre-trained-vectors.md

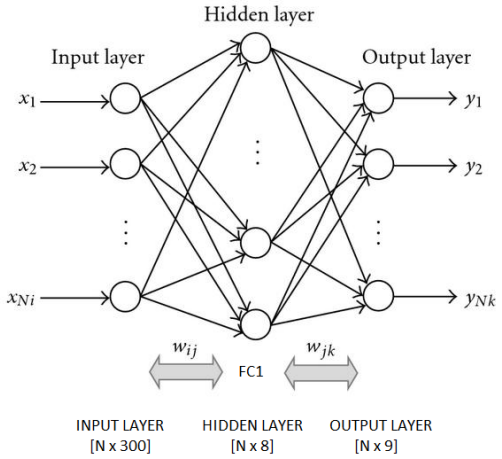


Fig. 2. Artificial Neural Network model diagram

Neural network algorithms tend to exploit patterns and structures in datasets to discover useful representations. So we chose to build a simple artificial neural network, with one fully connected hidden layer with 8 units using the TensorFlow library as shown in Fig. 2. The input layer consists of 300 nodes without any activation function while the following layers have a softmax activation function. The following equation describes the forward propagation in the first hidden layer of the neural network :

$$a_i^{l+1} = g\left(\sum_{j=1}^{300}\left(a_j^l * W_{ij}\right) + b^l\right) \tag{1}$$

Here a_i^{l+1} is the activation value of the ith node at the $(l+1)$th layer, W_{ij} is the weight from jth node of the lth layer to the ith node, b_l is the bias at the lth layer and g is the softmax activation function. In our case, we have used a basic neural network with one input layer of 300 units, one fully connected layer of size 8 followed by the output layer of size 9 units. So $l = 0$ for the first hidden layer.

Finally, the output layer takes the values from the hidden layer nodes as input, adds a bias value and returns a one hot vector as output which represents the predicted class of the entity. The number of training epochs was fixed to 20 as above this number we could not observe any improvement in the performance of the model in terms of accuracy. It takes about 2 hours to execute the model on each language.

4 Evaluation

Section 4.1 describes the data while Section 4.2 provides insight into the experimental setup used. Section 4.3 lists the evaluation metrics used. Section 4.4 presents the results obtained in detail while Section 4.5 presents Error Analysis.

4.1 Dataset Description

The corpora consisted of five Indian languages namely, Hindi, Kannada, Malayalam, Tamil, and Telugu. It was provided by ARNEKT Organization[6] for the purpose of this challenge. The dataset comprised of files for each language in which the sentences were separated by *newline string*. Most of the sentences provided were about 20 to 35 words long although some extended to above 100 words as well. The details about the entity categories and their distribution in the different languages are shown in Table 2. The entities were tagged into 9 separate classes namely number, event, Datenum, things, organization, occupation, name, location and other.

Table 2. Description of Dataset (Num: Numbers, Org: Organisation, Occ: Occupation, Loc: Location.)

Languages	Num	Event	Date/ Num	Things	Org	Occ	Name	Loc	Other
Hindi	37754	2932	2672	4048	12254	15732	88887	166547	1141207
Kannada	3948	523	1046	242	746	3081	15110	10473	262651
Malayalam	30553	837	1609	1999	4841	8037	59422	29371	701664
Tamil	77310	5112	15482	6183	9999	16507	118021	134262	1109354
Telugu	28618	729	2521	1069	2431	8437	60499	95756	577625

4.2 Experimental Setup

The dataset provided was properly annotated and hence did not need any kind of pre-processing except the removal of punctuation marks. By using the words vectors provided by Facebook, these words were then vectorized to a form that could be directly given as input for our models. The supervised dataset was divided into training and testing sets in the ratio 8:1.

[6] http://iecsil.arnekt.com

4.3 Evaluation Metrics

Accuracy has been used as the metric for evaluating classification models in our experiments. Accuracy is defined as the ratio between a total number of correct predictions N_c upon the total number of predictions N_t.

$$\text{Accuracy} = \frac{N_c}{N_t} \tag{2}$$

In addition to classification accuracy we have also used :

1. Recall (R) : Calculates the fraction of entities identified by the model and the total number of named entities actually present in the corpus. For instance let N_t be the total number of named entities present in the corpus and N_i be the number of entities identified by the model.

$$\text{Recall} = \frac{N_i}{N_t} \tag{3}$$

2. Precision (P): Calculates the fraction of the named entities that were correctly identified by the model. For instance let N_i be the total number of named entities actually present in the corpus that were correctly identified and N_e be the total number of named entities identified by the model.

$$\text{Precision} = \frac{N_p}{N_e} \tag{4}$$

3. F1-Score: F1 score is the harmonic mean of precision and recall. A perfect F1 score of 1 is reached when the model has perfect precision and recall and worst at 0.

$$\text{F1-Score} = 2*\frac{\text{R} * \text{P}}{\text{R} + \text{P}} \tag{5}$$

4.4 Results and Analysis

The model was initially tested on the basic implementations of Naive Bayes Classifier and Support Vector Machine(SVM). They yielded an overall accuracy of 81.42% and 86.50% respectively. The results for all the languages provided in the dataset have been listed in Table 3. It is evident from the reported figures that the artificial neural network performs better than the standard SVM and Naive Bayes models. We observe that the accuracy values of the neural network lies in the vicinity of 90% and are relatively close to each other. This is because our model is language independent and thus, it should yield similar values for any new language. We can also observe that Tamil has comparatively lower accuracy than other languages. This could be due to large word vectors corpus for Tamil as compared to other languages.

The detailed classification results of all 5 languages for each of the 9 classes on the FIRE 2018 dataset are presented in Table 4. Fig. 3 depicts a graph comparing recall values for all the languages. Similarly, Fig. 4 and Fig. 5 depict

Table 3. Accuracy results for entity recognition for various models

Language	ANN	SVM	Naive Bayes
Hindi	91.52	87.20	78.95
Kannada	**92.14**	**88.15**	**86.62**
Malayalam	90.27	86.80	84.40
Tamil	87.72	83.48	79.27
Telugu	90.02	86.87	77.90
Average	**90.33**	**86.50**	**81.42**

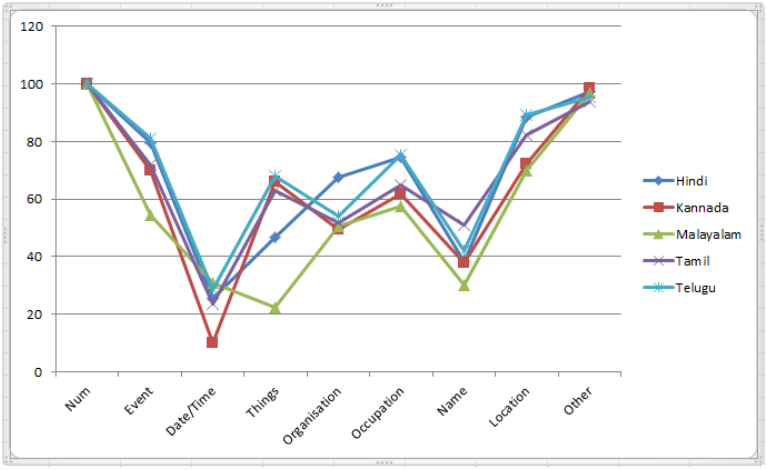


Fig. 3. Class wise Recall Values

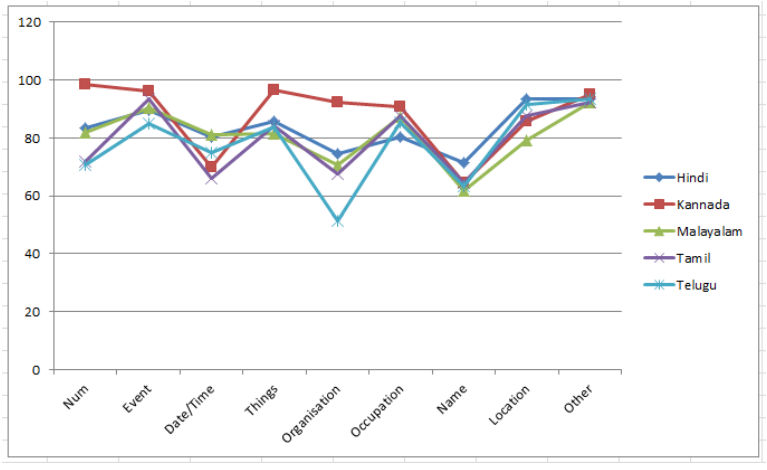


Fig. 4. Class wise Precision Values

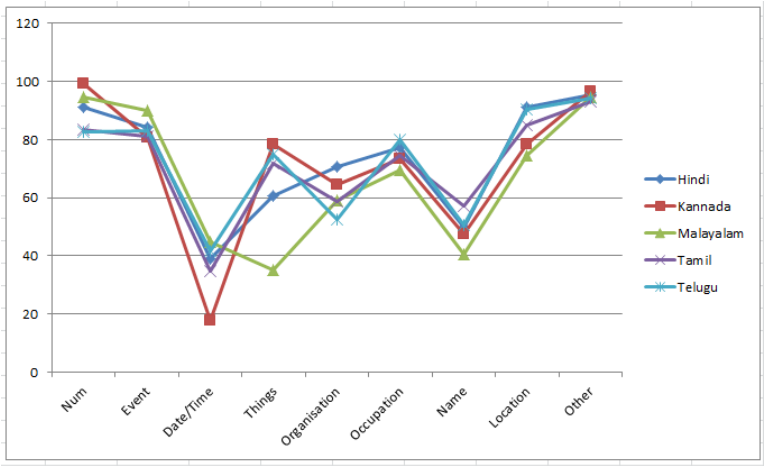


Fig. 5. Class wise F1-Score

graphs comparing precision values and F1-Score respectively. The recall rate of Number class is 100% for all the languages due to the digit recognizer. Many Datenum entities get tagged as Number entities thereby reducing the precision value of Number class and recall value of Datenum class. This points to the need to adopt a different strategy to recognize Datenum class.

Table 4. Class wise metrics for entity recognition for ANN model

		Num	**Event**	**Date/ Num**	**Things**	**Org**	**Occ**	**Name**	**Loc**	**Other**
Hindi	Recall	**100.0**	79.48	25.65	46.80	67.40	74.38	38.15	88.47	97.21
	Precision	83.62	89.71	80.40	85.77	74.41	80.39	71.27	**93.61**	93.33
	F1-Score	91.08	84.29	38.91	60.56	70.73	77.27	49.70	90.97	**95.23**
Kannada	Recall	**100.0**	69.73	10.11	66.11	49.32	61.63	37.72	72.04	98.46
	Precision	**98.56**	96.29	70.00	96.38	92.46	90.64	64.69	85.73	94.83
	F1-Score	**99.27**	80.88	17.66	78.43	64.33	73.37	47.68	78.29	96.61
Malayalam	Recall	**100.0**	54.65	30.88	22.47	50.72	57.57	30.00	69.98	96.91
	Precision	81.88	90.38	81.25	81.66	70.72	87.24	61.99	79.37	**92.35**
	F1-Score	**94.58**	90.03	44.80	35.25	59.07	69.37	40.43	74.38	94.58
Tamil	Recall	**100.0**	71.91	23.45	63.02	51.60	64.79	51.03	82.17	93.94
	Precision	71.70	**93.51**	65.88	84.05	67.68	87.84	64.66	87.58	92.49
	F1-Score	83.58	81.29	34.71	72.03	58.60	74.57	57.04	84.78	**93.20**
Telugu	Recall	**100.0**	81.15	28.70	67.93	53.96	75.34	41.91	89.34	95.28
	Precision	70.51	84.84	74.80	83.96	51.32	85.37	63.29	91.72	**93.32**
	F1-Score	82.71	82.96	41.68	75.10	52.61	80.04	50.43	90.51	**94.29**

4.5 Error Analysis

We did an error analysis to identify the incorrect predictions. In all the languages, several Name entities were misclassified as Other entities. This is because Name entities have relatively lower presence in the Word Embeddings leading to a random vector getting assigned to represent them during the feature extraction stage. One way to solve this would be the addition of a language-specific gazetteers list to separate out the Names beforehand. The model also misclassifies Things and Organization entities at times. This is due to the diverse nature of these entities and also because they are rarely repeated in the dataset. The classifier also experiences some problems while differentiating between Location and Name entities. Along with Number entities, Event and Occupation entities are also classified with high accuracy and very low misclassifications. This is because of the limited set of common Events and Occupations entities present in both the real world and consequently in the dataset.

5 Conclusion and Future Work

The increasing amount of unstructured data requires that we develop an approach to extract useful information in an efficient way. Information Extraction (IE) from data is an important area of research of which named entity recognition is a subset. In this paper, we have described the approach we adopted for developing models capable of performing the task of NER for IECSIL as a part of the FIRE 2018 challenge. The exact methods followed have been discussed in detail. We have provided the results obtained along with analysis about the entities for which the models performed well and reasons for such a behaviour. The highest accuracy for NER was 90.33% for all languages combined when we used our simple ANN model, which is an improvement to the baseline accuracy of 85.73%.

As an extension to the model presented, we can work on deeper models with a better-suited structure for handling textual data. Recurrent Neural Network (RNN), sometimes even addressed as Long short-term Memory (LSTM) is one such example. A further improvement to this model is RNN with added attention mechanism as demonstrated in Zhou, Peng et.al.[23], where they have shown that RNNs with attention mechanism perform well on NLP related problems. In addition to this, we can work towards adding language specific markers and special features like adding a Datenum recognizer that can reduce the misclassifications, enhance the model and increase its robustness.

References

1. Amarappa, S., Sathyanarayana, S.: Named entity recognition and classification in kannada language. International Journal of Electronics and Computer Science Engineering **2**(1), 281–289 (2013)

2. Amarappa, S., Sathyanarayana, S.: Kannada named entity recognition and classification (nerc) based on multinomial na\" ive bayes (mnb) classifier. arXiv preprint arXiv:1509.04385 (2015)
3. Babych, B., Hartley, A.: Improving machine translation quality with automatic named entity recognition. In: Proceedings of the 7th International EAMT workshop on MT and other Language Technology Tools, Improving MT through other Language Technology Tools: Resources and Tools for Building MT. pp. 1–8. Association for Computational Linguistics (2003)
4. Barathi Ganesh, H.B., Soman, K.P., Reshma, U., Mandar, K., Prachi, M., Gouri, K., Anitha, K., Anand Kumar, M.: Information extraction for conversational systems in indian languages - arnekt iecsil. In: Forum for Information Retrieval Evaluation (2018)
5. Barathi Ganesh, H.B., Soman, K.P., Reshma, U., Mandar, K., Prachi, M., Gouri, K., Anitha, K., Anand Kumar, M.: Overview of arnekt iecsil at fire-2018 track on information extraction for conversational systems in indian languages. In: FIRE (Working Notes) (2018)
6. Borthwick, A., Grishman, R.: A maximum entropy approach to named entity recognition. Ph.D. thesis, Citeseer (1999)
7. Ekbal, A., Haque, R., Bandyopadhyay, S.: Named entity recognition in bengali: A conditional random field approach. In: Proceedings of the Third International Joint Conference on Natural Language Processing: Volume-II (2008)
8. Gali, K., Surana, H., Vaidya, A., Shishtla, P., Sharma, D.M.: Aggregating machine learning and rule based heuristics for named entity recognition. In: Proceedings of the IJCNLP-08 Workshop on Named Entity Recognition for South and South East Asian Languages (2008)
9. Grave, E., Bojanowski, P., Gupta, P., Joulin, A., Mikolov, T.: Learning word vectors for 157 languages. arXiv preprint arXiv:1802.06893 (2018)
10. Grave, E., Mikolov, T., Joulin, A., Bojanowski, P.: Bag of tricks for efficient text classification. In: Proceedings of the 15th Conference of the European Chapter of the Association for Computational Linguistics, EACL. pp. 3–7 (2017)
11. Kaur, K., Gupta, V.: Name entity recognition for punjabi language. Machine translation **2**(3) (2012)
12. Kibriya, A.M., Frank, E., Pfahringer, B., Holmes, G.: Multinomial naive bayes for text categorization revisited. In: Australasian Joint Conference on Artificial Intelligence. pp. 488–499. Springer (2004)
13. Kim, J.H., Woodland, P.C.: A rule-based named entity recognition system for speech input. In: Sixth International Conference on Spoken Language Processing (2000)
14. Lafferty, J., McCallum, A., Pereira, F.C.: Conditional random fields: Probabilistic models for segmenting and labeling sequence data (2001)
15. Malarkodi, C., Pattabhi, R., Sobha, L.D.: Tamil ner–coping with real time challenges. In: 24th International Conference on Computational Linguistics. p. 23 (2012)
16. Malouf, R.: Markov models for language-independent named entity recognition, proceedings of the 6th conference on natural language learning. August **31**, 1–4 (2002)
17. Mollá, D., Van Zaanen, M., Smith, D., et al.: Named entity recognition for question answering (2006)
18. Nadeau, D., Sekine, S.: A survey of named entity recognition and classification. Lingvisticae Investigationes **30**(1), 3–26 (2007)

19. Pillai, A.S., Sobha, L.: Named entity recognition for indian languages: A survey. International Journal **3**(11) (2013)
20. Saha, S.K., Chatterji, S., Dandapat, S., Sarkar, S., Mitra, P.: A hybrid approach for named entity recognition in indian languages. In: Proceedings of the IJCNLP-08 Workshop on NER for South and South East Asian languages. pp. 17–24 (2008)
21. Saha, S.K., Sarkar, S., Mitra, P.: A hybrid feature set based maximum entropy hindi named entity recognition. In: Proceedings of the Third International Joint Conference on Natural Language Processing: Volume-I (2008)
22. Salomonsson, A.: Entity-based information retrieval. Department of Computer Science, Faculty of Engineering, LTH, Lund University (2012)
23. Zhou, P., Shi, W., Tian, J., Qi, Z., Li, B., Hao, H., Xu, B.: Attention-based bidirectional long short-term memory networks for relation classification. In: Proceedings of the 54th Annual Meeting of the Association for Computational Linguistics (Volume 2: Short Papers). vol. 2, pp. 207–212 (2016)

ResearchGate

See discussions, stats, and author profiles for this publication at: https://www.researchgate.net/publication/299597486

Stress variation due to change in centre distance of spur gears using finite element analysis

Conference Paper · December 2015

CITATIONS
0

READS
37

3 authors, including:



Akash Sharma
The University of Tokyo
2 PUBLICATIONS **0** CITATIONS
SEE PROFILE



Paras Kumar
Delhi Technological University
15 PUBLICATIONS **39** CITATIONS
SEE PROFILE

All content following this page was uploaded by Akash Sharma on 20 January 2018.

The user has requested enhancement of the downloaded file.

International Conference on Computer Aided Engineering (CAE-2015)
Department of Mechanical Engineering, GITAM University, School of Technology, Hyderabad, India

STRESS VARATION DUE TO CHANGE IN CENTRE DISTANCE OF SPUR GEARS USING FINITE ELEMENT ANALYSIS

Akash Sharma[1*], Harish Dakshana Moorthy[1], Paras Kumar[2]

[1]Student, Mechanical Engineering Department, Delhi Technological University, Delhi-110042, India
[2]Assistant Professor, Mechanical Engineering Department, Delhi Technological University, Delhi-110042, India

ABSTRACT

In this present work, the variation in contact and bending stresses due to the change in the centre distance between two spur gears has been analysed using ANSYS. The gears have been designed using AGMA standards and are made of structural steel. To analyse the stresses on the gear tooth during engagement, 20 different SolidWorks models have been created which covered the tooth engagement from the start to end. To analyse the contact problems in ANSYS, special contact elements need to be created during meshing to obtain accurate results. The contact element used in the present simulation is CONTA174, which is associated with the TARGE170 element on the target side.

The variation of transmitted force, contact stress and bending stress during one complete cycle of engagement has been successfully analysed with and without centre distance variation. The centre distance has been increased from 80 mm to 81mm due to 1mm radial displacement of pinion shaft. The ANSYS model has been validated with AGMA results for bending and contact stresses at pitch point. The value of contact stress decreases whereas the value of bending stress increases with the variation in centre distance. The value of contact stress reduces by 6.59% while the value of bending stress increases by 3.84% at the pitch point.

Keywords: AGMA, Contact Stress, FEM, Spur Gear, Centre distance variation, Pitting

1. INTRODUCTION

Pitting is a surface fatigue failure of the gear tooth in which there is fracture and dislodgment of small pieces of material from the surface. It occurs due to repeated loading of tooth surface with the contact stress exceeding the surface fatigue strength of the material. The pit itself causes stress concentration and soon the pitting spreads to adjacent region till the whole surface is covered. Subsequently, higher impact load resulting from pitting may cause fracture of already weakened tooth.

Contact stress analysis between two spur gear teeth has been considered in different contact positions, representing a pair of mating gears during rotation by Ali Raad Hassan [1]. The bending and contact stress variation on complete mesh cycle of a high contact ratio gear pair for identical load conditions has been determined using ANSYS Parametric Design language (APDL) by M. Rameshkumar [2]. Vladimir I. Medvedev et al. [3] analysed the contact pressure and tooth-to-tooth accuracy of transmission in gears with predesigned parabolic function of transmission errors and with localized contact using mathematical modeling. Surface contact stress and root bending stress of a pair of spur gears with machining errors, assembly errors and tooth modifications along with tooth contact pattern and root stains have been analysed by Shuting Li using Finite Element Method [4]. Through a series of experiments and numerical simulations, the effects of tooth profile modification and lead relieving on tooth engagements of a pair of spur gears and the effects of misalignment error of gear shafts on the plane of action, tooth lead crowing and transmitted torque on tooth mesh stiffness have also been studied [5]. The dynamic responses of the gear drives has been obtained under the conditions of both the initial speed and the sudden load being applied. Shaft misalignment and assembly deflection effects on the gear surface wear damage has been investigated using accurate non-linear finite element method to provide a quantitative understanding of gear tooth contact behaviour by K. Mao [6]. In 2006, Tengjiao Lin et al. [7] studied the influence of the backlash on impact characteristics of the meshing teeth. The effect of addendum on tooth load, load-sharing rate, tooth contact strength, bending strength and basic performance parameters of spur gears has been performed by Shuting Li [8]. The dynamic analysis to compare conventional spur gears with symmetric teeth and spur gears with asymmetric teeth and the

* shrama.akash3008@gmail.com

optimization of asymmetric tooth design in order to minimize dynamic loads has been performed by Fatih Karpat et al. [9]. A large rotational approach for dynamic contact problems with friction has been proposed by Lundvall et al. [10].

This paper outlines our recent work on Finite Element based models for contact problems as applied to spur gear drives. The gears that have been designed using AGMA standards have been simulated for the variation in the force and stresses along the line of action and compared to the case in which there is variation in centre distance. The stress analysis has been performed using 20 finite element models where each model represents a case of contact between a pair of teeth at a different position during the rotation. The domain in this study is the angular location of the point of contact on the arc of action from the beginning to the end of contact between this pair of teeth.

2. AGMA MODELLING

The various parameters used while designing the gear and pinion using AGMA standards are given in the Table 1 below:

Table 1: Gear Parameters

Parameters	Pinion	Gear
Module	2	2
Pitch diameter (mm)	54	106
Number of teeth	27	53
Outer Diameter(mm)	58	110
Face width (mm)	33	33
Pressure angle (degrees)	20	20
Contact Ratio	1.697	1.697
Material	EN19	EN19

2.1. AGMA Bending Equation

$$\sigma_b = W^t K_o K_v K_s \frac{P_d}{F} \frac{K_m K_B}{J} \quad (1)\ [11]$$

Where:

σ_b *is the Bending Stress*

W^t *is the tangential transmitted load in N*

K_o *is the overload factor*

K_v *is the dynamic factor*

K_s *is the size factor*

P_d *is the transverse diametric pitch*

K_m *is the load-distribution factor*

K_B *is the rim-thickness factor*

J *is the geometry factor for bending strength*

F *is the face width of the narrower member, in mm*

2.2. AGMA Contact Stress Equation

$$\sigma_c = C_p \sqrt{W^t K_o K_v K_s \frac{K_m}{d_p F} \frac{C_f}{I}} \quad (2)\ [11]$$

Where:

σ_c *is the Contact Stress*

C_p *is an elastic coefficient in* $\sqrt{N}/mm^2$

C_f *is the surface condition factor*

d_p *is the pitch diameter of the pinion in mm*

I *is the geometry factor for pitting resistance*

The values of the various parameters used in the above AGMA equations are given in Table 2:

Table 2: Values of various factors used in AGMA equations

Parameter	Value
Load Distribution Factor K_m	1
Overload Factor K_o	1
Dynamic Factor K_v	1
Size Factor K_s	1
Rim Thickness Factor K_B	1
Geometry Factor for Bending Strength J (Pinion)	0.37
Geometry Factor for Pitting Resistance I	0.1064
Elastic Coefficient C_p	191 $(MPa)^{1/2}$
Surface Condition Factor C_f	1

The bending stress and contact stress on the pinion at the pitch point has been calculated using AGMA equations and are shown in the Table 3:

Table 3: Calculated values of AGMA Bending and Contact Stress at the pitch point

Parameter	AGMA Theoretical Value
$\sigma_{Bending}$ Pinion	106.1 MPa
$\sigma_{Contact\ Stress}$ Pinion	704 MPa

3. GEOMETRICAL MODELLING

The angle of contact for a pinion teeth was calculated as follows:

Path of Contact =

$$\sqrt{R_a^2 - R^2\cos^2\phi} - \sqrt{r_a^2 - r^2\cos^2\phi} - (R + r)\sin\phi \quad (3)$$

Where:

r = *pitch circle radius of pinion*

R = *pitch circle radius of gear*

r_a = *addendum circle radius of pinion*
R_a = *addendum circle radius of gear*

$$\text{Arc of contact} = \frac{\text{Path of contact}}{\cos\phi} \quad (4)$$

The arc of contact was calculated as 23 degrees. To analyse the stresses on the teeth during the duration of its engagement, 20 model assemblies were created in SolidWorks which covered the tooth from the start to end of engagement by giving fixed rotation of 1.15 degrees for each case. The centre distance between the gear and the pinion shaft was later on increased by 1mm to study the variation in stress due to assembly errors. Twenty such models were developed after 1.132 degree rolling from the previous case.

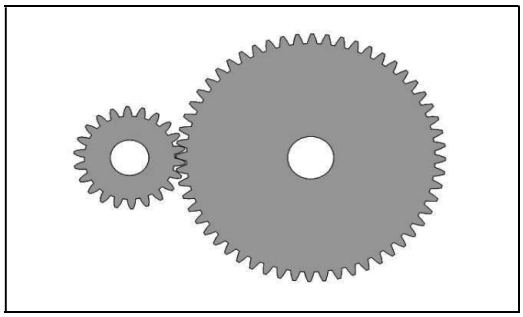


Fig. 1: SolidWorks model for the pinion and gear assembly

4. FINITE ELEMENT ANALYSIS

ANSYS Mechanical is the preferred solver due to its robustness, accuracy and computational turnaround time. The Static Structural component system was employed for running this analysis. Solver settings were modified to provide the most accurate results for gear simulation.

Contact problems are highly nonlinear and require significant computer resources to solve. In Finite Element Analysis (FEA) contact problem can be described by two bodies that get in contact because of the action of an external force. One of these bodies is defined as a contact body, and the other as a target body. In the case of a flexible-to-flexible body contact, the FEA procedure is complex and it needs to be analyzed carefully to obtain desired results. The contact forces that appear when the bodies are in contact prevent mutual penetration of bodies, the result of which is deformations around the contact patch.

The meshing has been improved by making use of the contact sizing to increase the number of elements. A highly refined mesh has been employed for the analysis with elements of edge length 0.5 mm.

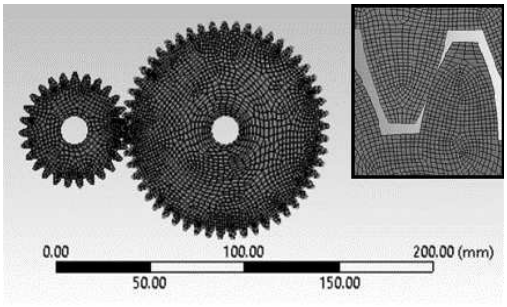


Fig. 2: Meshing of the gear and the pinion

5. RESULTS AND DISCUSSION

To verify that the chosen solver settings and boundary conditions applied on the model are correct, the case for the pinion and gear making contact at the pitch point was chosen as a test case where the bending and contact stresses were calculated using AGMA's equations and compared with the results obtained from the simulation performed using ANSYS.

Table 4: Comparison of calculated and FEA stress values at the pitch point

Parameter	AGMA Value (MPa)	FEA Value (MPa)	Difference (%)
$\sigma_{Bending}$ Pinion	106.1	103.98	1.97
$\sigma_{Contact\ Stress}$ Pinion	704	681.78	3.125

The results of the Finite Element analysis for the pitch point contact are presented in the following figures. The stress values at the pinion tooth have been indicated because the pinion is more prone to fatigue failure than the gear which has usually a higher factor of safety. Thus, the failure of the gear drive depends on the strength of the pinion.

The figure below shows the magnitude of the transmitted force at the pitch point and is along the line of action.

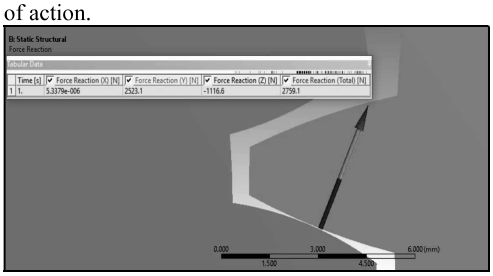


Fig. 3: Transmitted force from pinion to the gear when there is no centre distance variation

The magnitude of the bending stress at the pinion tooth evaluated using ANSYS is found out to be 103.98 MPa as compared to 106.1 MPa calculated using AGMA bending stress equation.

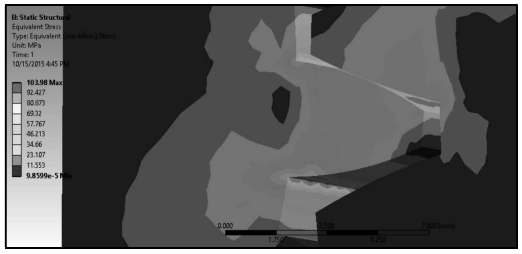


Fig 4: Bending stress on the pinion when there is no centre distance variation

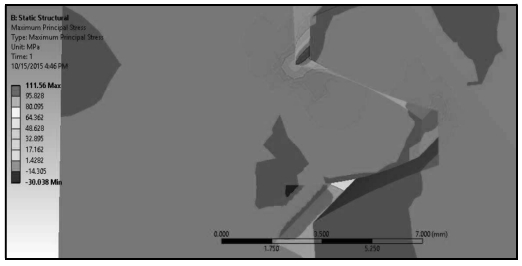


Fig 5: Maximum principal stress on the pinion when there is no centre distance variation

The magnitude of the bending stress and the maximum principal stress at the gear tooth when the centre distance is increased by 1mm are presented in the Figures 6 and 7 below.

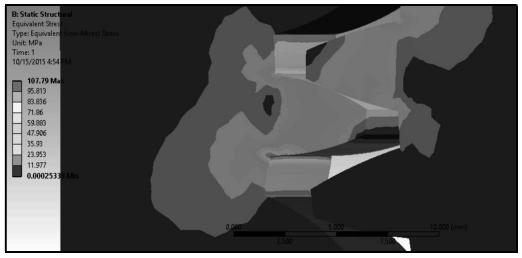


Fig 6: Bending stress on the pinion when there is centre distance variation of 1 mm

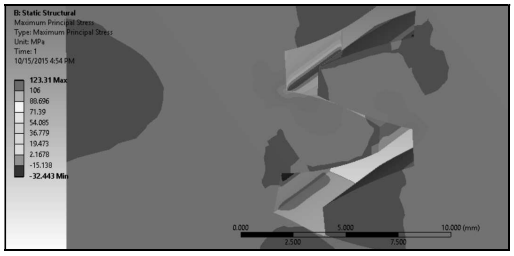


Fig 7: Maximum principal stress on the pinion when there is centre distance variation of 1 mm

From the distribution of contact pressure obtained through analysis in ANSYS, it can be seen that the contact stress is uniformly distributed throughout the face width of the pinion and the maximum value occurs along the contact patch indicated by the red region in the Figure 8.

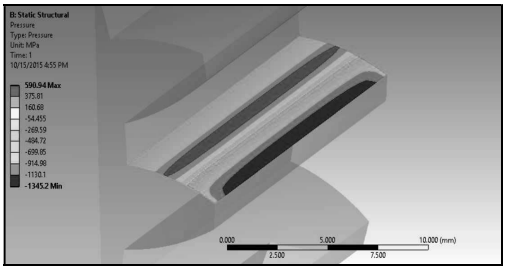


Fig 8: Contact pressure on the pinion when there is centre distance variation of 1 mm

After evaluating the results for each of case using ANSYS, scatter plots were have been created for both the cases, one in which there is variation in centre distance and the other in which there is no variation in centre distance, to get a better visualization of the variation in transmitted force and stress.

The Figure 9 shows the variation in transmitted force during one complete cycle of tooth engagement. It can be seen that the magnitude of transmitted force reduces to half in the case 1 to 7 and the case 14 to 20 since there is double tooth contact in the above cases of no centre distance variation. During the case 8 to 13, only a single tooth remains in contact and hence the transmitted force is higher. The single tooth remains in contact for a longer period of time when there is variation in centre distance as seen in the graph below.

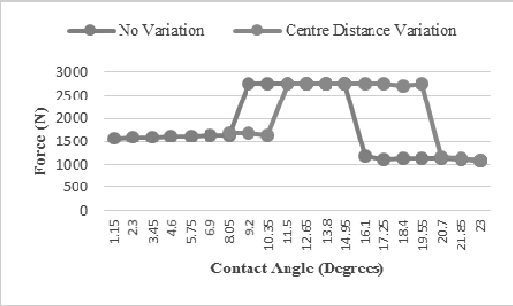


Fig 9: Variation in transmitted force for the duration of tooth engagement

The Bending stress rises sharply during the phase when the pinion undergoes single tooth contact (cases 7-13). The magnitude of bending stress (cases 10-17) are higher when there is centre distance variation and thus the chances of failure are also high.

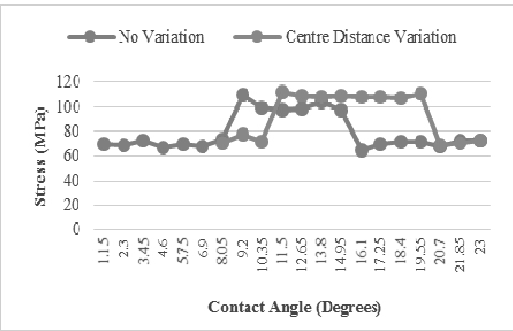


Fig 10: Variation in bending stress for the duration of tooth engagement

Similar variation is seen in the Maximum Principal stress. The magnitude of Maximum Principal Stress increases when there is centre distance variation as seen in the Figure 11.

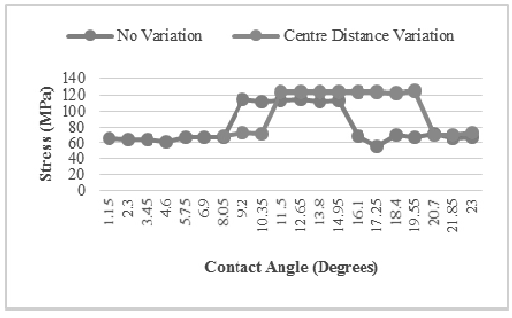


Fig 11: Variation in maximum principal stress for the duration of tooth engagement

As can be seen from Figures 9-11, the maximum and minimum values for the stresses change due to an increase in centre to centre distance. This change has been recorded as follows:

Table 5: Change in Maximum and Minimum stress values due to variation in centre distance

Parameters	**Change in Maximum value**	**Change in Minimum value**
Bending stress	1.552%	5.566%
Shear stress	3.500%	5.559%
Maximum Principal stress	8.590%	21.228%
Transmitted force	0.130%	-1.500%

6. CONCLUSION

In light of the above findings, the following conclusion can be drawn:

- The contact ratio for the gear pair has changed due to variation in centre to centre distance between the pinion and gear.
- Maximum and minimum values of Bending and Shear Stresses show a marked rise due to this increase in the centre distance.
- While the duration of engagement (in seconds) has decreased due to this increase in distance, the plot for stresses over the duration of engagement shows that single tooth contact duration has increased when there is centre distance variation.

7. REFERENCES

[1] Ali Raad Hassan,"Contact Stress Analysis of Spur Gear Teeth Pair", World Academy of Science, Engineering and Technology, Vol: 3 2009-10-20

[2] M. Rameshkumar, G. Venkatesan and P. Sivakumar, DRDO, "Finite Element Analysis of High Contact Ratio Gear", AGMA Technical Paper, 2010

[3] Vladimir I. Medvedev, Andrey E. Volkov, Marina A. Volosova, Oleg E. Zubelevich, "Mathematical model and algorithm for contact stress analysis of gears with multi-pair contact", Mechanism and Machine Theory, Pg. 156–171, 2015

[4] Shuting Li, "Finite element analyses for contact strength and bending strength of a pair of spur gears with machining errors, assembly errors and tooth modifications," Mechanism and Machine Theory, Pg. 88–114, 2007

[5] Shuting Li, "Effects of misalignment error, tooth modifications and transmitted torque on tooth

View Publication Stats

engagements of a pair of spur gears", Mechanism and Machine Theory, Pg. 698–726, 2007

[6] K. Mao, "Gear tooth contact analysis and its application in the reduction of fatigue wear", Wear, Volume 262, Issues 11–12, Pages 1281–1288, 10 May 2007

[7] Tengjiao Lin, H. Ou, Runfang Li, "A finite element method for 3D static and dynamic contact/impact analysis of gear drives", Computational Methods Applied Mechanical Engineering, Pg. 1716–1728, 2007

[8] Shuting Li, "Effect of addendum on contact strength, bending strength and basic performance parameters of a pair of spur gears", Mechanism and Machine Theory, Pg. 1557–158, 2008

[9] Fatih Karpat, Stephen Ekwaro-Osire, Kadir Cavdar, Fatih C. Babalik, "Dynamic analysis of involute spur gears with asymmetric teeth", International Journal of Mechanical Sciences, Volume 50, Issue 12, Pages 1598–1610, December 2008

[10] O. Lundvall, N. Stromberg, A. Klarbring, "A flexible multi-body approach for frictional contact in spur gears" Journal of Sound and Vibration, Volume 278, Issue 3, Pages 479–499, 6 December 2004

[11] Richard G. Budynas, J. Keith Nisbett, Shigley's Mechanical Engineering Design, 6th Edition, Tata McGraw Hill India, 2010

International Journal of Research in Engineering and Innovation (IJREI)
journal home page: http://www.ijrei.com
ISSN (Online): 2456-6934

Thermal performances (first law efficiency, exergy destruction ratio & exergetic efficiency) of cascade single effect ammonia-water (NH_3-H_20) vapour absorption refrigeration system coupled with vapour compression refrigeration using ecofriendly refrigerants in the low temperature cycle of VCRS system

R.S. Mishra

Department of Mechanical & Production Engineering, Delhi Technological University Delhi, India

Abstract

Solar thermal power energy and waste heat from different power plants have immense application potential for production of refrigeration through combined vapour compression–absorption refrigeration systems. The aim of this work is to develop an integrated solar refrigeration system where waste heat from different energy resources assists a combined vapour absorption compression system, and to analyze feasibility & practicality of that system of thermodynamically for improving its COP and exergetic efficiency by reduction of irreversibilities in terms of exergy destruction /losses occurred in the system components. The combined thermodynamic first law efficiency in terms of coefficient of performance (COP_Overall), second law efficiency in terms of exergetic efficiency and exergy destruction ratio based on exergy of product of a combined vapour absorption-compression system working with each of the following refrigerants in the cascaded vapour compression cycle R1234yf, R227ea, R236fa, R245fa, R143a,R134a, R32, R507 operating at - 223 K evaporator temperature with temperature overlapping (Approach means the difference between cascaded condenser temperature of vapour compression cycle and evaporator temperature of vapour absorption refrigeration cycle working at 13.5 bar of highest generator pressure and 1.75 bar as lowest evaporator pressure have been presented and it is found thatR141b and R245fa gives better performance
© 2019 ijrei.com. All rights reserved

Keywords: Low GWP Refrigerants, Energy-Exergy Analysis, Single effect VAR-Cascade VCR System,

1. Introduction

Vapor compression refrigeration system (VCRS) is widely used refrigeration system (about 80%) and requires a large amount of electrical energy for its operation. The advancement in refrigeration sector has a major impact on energy demand which approximates to 15% of the total energy consumption in the world. Many developing countries like India currently suffer from a major shortage of electricity. Around 55% of the total electrical capacity is generated using coal in India [1].
Solar thermal power energy and waste heat from different power plants have immense application potential for production of refrigeration through combined vapour compression absorption refrigeration systems. The aim of this work is to develop an integrated solar refrigeration system where waste heat from different energy resources assists a combined vapour absorption -compression system, and to analyze feasibility & practicality of that system of thermodynamically for improving its COP and exergetic efficiency by reduction of irreversibilities in terms of exergy destruction /losses occurred in the system components [2].
The combined refrigeration system consists of a conventional vapour compression refrigeration system cascaded with vapour absorption system. The LiBr–H_2O couples is used for the absorption refrigeration system and nine different refrigerants (i.e.R1234yf, R227ea, R236fa, R245fa , R141b,R134a, R32, R507, R717, are evaluated to find the best suitable ecofriendly) for cascaded vapour compression system and found that first law efficiency of combined cycle cascaded of evaporator of vapour absorption cycle with

Corresponding author: R. S. Mishra
Email Address: hod.mechanical.rsm@dtu.ac.in

condenser of vapour compression cycle found 55.36% enhancement in overall COP of combined cycle using double effect vapour absorption LiBr-H2O system and 80% enhancement in overall COP of combined cycle using double effect vapour absorption LiBr-H_2O system as compared to single effect LIBr-H_2O) system for -323 K of evaporator VCR temperature using R134a while 16% improvement in COP using triple effect VARS as compared to double effect VARS cascaded with VCRS. Similarly Second law efficiency of combined cycle cascaded of evaporator of vapour absorption cycle with condenser of vapour compression cycle found 11.29% enhancement in overall COP of combined cycle using double effect vapour absorption LiBr-H_2O system and 21.8% enhancement in overall COP of combined cycle using double effect vapour absorption LiBr-H_2O system as compared to single feect LIBr-H_2O) system for -323 K of evaporator VCR temperature using R134a while 9.44% improvement in COP using triple effect VARS as compared to double effect VARS cascaded with VCRS [3]

The present paper provided the best refrigerant for the novel combined vapour absorption refrigeration cycle/cascaded with vapour compression cycle to provide the highest thermodynamic efficiency for lowest degree of environmental damage.

2. Literature Review

Jain et al. [1] studied various integrated refrigeration systems and concluded that these systems are promising energy efficient and decarbonizing cooling technology in near future. Riiffit S.B., Shankland N [4] thermo-dynamically analyzed different types of integrated single-effect, double-effect series and the double-effect parallel continuous absorption systems and their integration with vapour-compression systems using various refrigerant/absorbent pairs and intermittent absorption system, the intermittent absorption/vapour recompression system and the combined intermittent absorption/vapour compression system.L. Kairouani, E. Nehdi [5] carried out thermodynamic analysis of novel combined refrigeration system using geothermal energy temperature source in the range 343–349 K supplied to a generator operating at 335 K.to supply vapour absorption system cascaded with conventional compression system using three working fluids (i.e.R717, R22, and R134a) and found that the COP can be improved by 37–54%, as compared with the conventional cycle, under the same operating conditions, (i.e. Vaporization temperature of 263 K and a condensation temperature of 308 K). Results of this studied show that the COP of a combined system is significantly higher than that of a single stage refrigeration system. For industrial refrigeration, the proposed system constitutes an alternative solution for reducing energy consumption and greenhouse gas emissions

3. Results and Discussions

Table-1 shows the variation of thermal performance parameters of single effect cascade vapour absorption refrigeration system using lithium bromide -water solution coupled with vapour compression refrigeration system. The evaporator of VARS is cascaded with condenser of vapour compression refrigeration systems using nine ecofriendly refrigerants. It is found that overall first law efficiency in terms of coefficient of performance (COP) of cascade refrigeration system using R245fa refrigerant is highest and lowest by using R227ea as shown in fig-1 .while exergy destruction of cascade system is lowest by using R141b and highest while using R227ea as shown in Fig-2. The cascade system exergetic efficiency is highest by using R141b and lowest by using R227ea as shown in Fig-3. The thermal performances using ecofriendly refrigerants in the low temperature circuit of vapour compression refrigeration system is shown in Table-1 and it is found that maximum coefficient of performance (COP)of vapour compression refrigeration system by using R141b and lower COP by using R227ea respectively as shown in Fig-4. Similarly exergy destruction of vapour compression refrigeration system is lowest by using R141b and highest while using R227ea as shown in Fig-5. The exergetic efficiency of vapour compression of refrigeration system is highest by using R141b and lowest by using R227ea as shown in Fig-6

Table 1: Thermal performances of single effect (NH_3-H_20) vapour absorption refrigeration system using vapour compression refrigeration system (T_Eva_VARS= -20°C, approach_VCRS=10°C, T_Eva_Ref= -50°C, compressor efficiency=0.80, generator heat exchanger effectiveness= 0.6894

Refrigerant	COP (Overall)	Overall Exergy Destruction ratio (EDR)	Overall Exergetic Efficiency	COP (VCRS)	VCRS Exergy destruction Ratio (EDR)	VCRS Exergetic Efficiency
R134a	0.4554	1.998	0.3335	1.485	1.002	0.4995
R1234yf	0.4463	2.152	0.3173	1.356	1.192	0.4561
R141b	0.4699	1.773	0.3607	1.719	0.7301	0.5780
R227ea	0.4331	2.394	0.2947	1.188	1.503	0.3996
R236fa	0.4474	2.133	0.3192	1.371	1.169	0.4610
R245fa	0.4596	1.930	0.3413	1.55	0.9188	0.5212
R32	0.4558	1.992	0.3342	1.491	0.9947	0.5013
R507a	0.4426	2.217	0.3109	1.387	1.275	0.4396

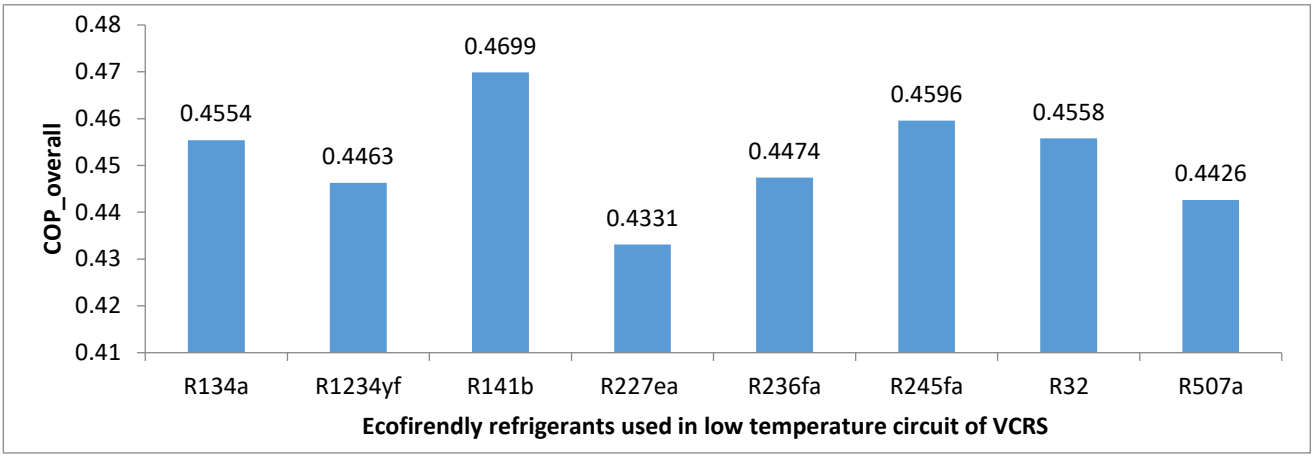


Figure 1: *Thermal performances in terms of first law efficiency (overall COP_Cascade) of cascade single effect ammonia-water(NH_3-H_20) vapour absorption refrigeration system coupled with vapour compression refrigeration using ecofriendly refrigerants in the low temperature cycle of VCRS system*

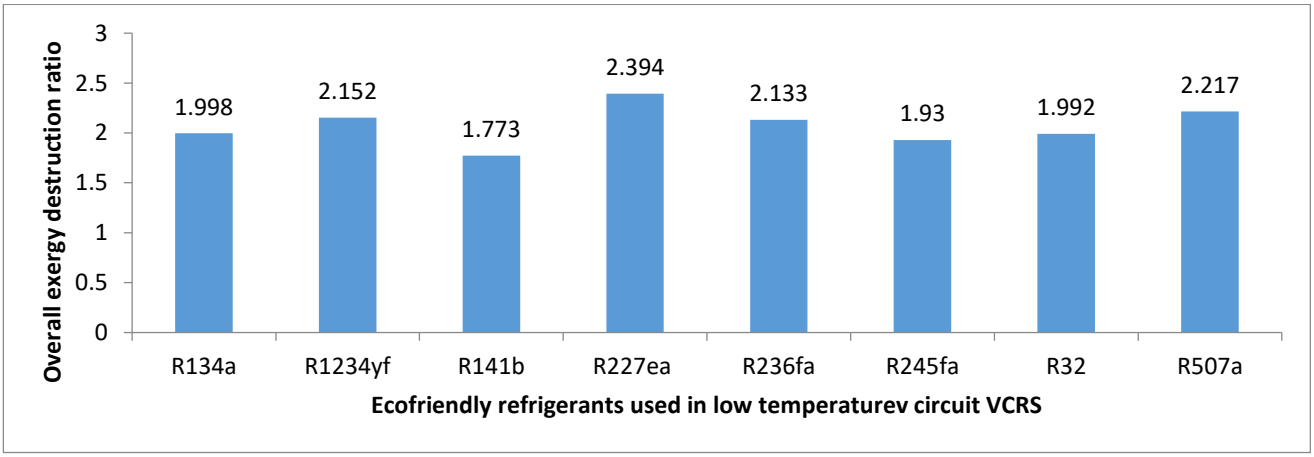


Figure 2: Thermal performances in terms of overall exergy destruction ratio (EDR_Overall) of cascade single effect ammonia-water (NH_3-H_20) with vapour absorption refrigeration system coupled with vapour compression refrigeration using ecofriendly refrigerants in the low temperature cycle of VCRS system

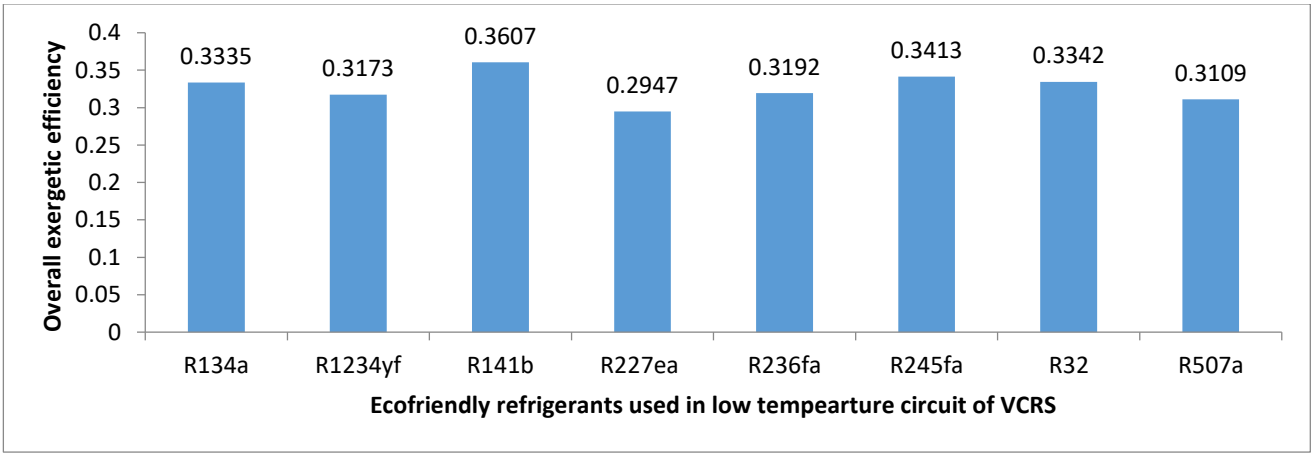


Figure 3: *Thermal performances in terms of overall exergetic efficiency of cascaded single effect ammonia-water (NH_3-H_20) with vapour absorption refrigeration system coupled with vapour compression refrigeration using ecofriendly refrigerants in the low temperature cycle of VCRS system*

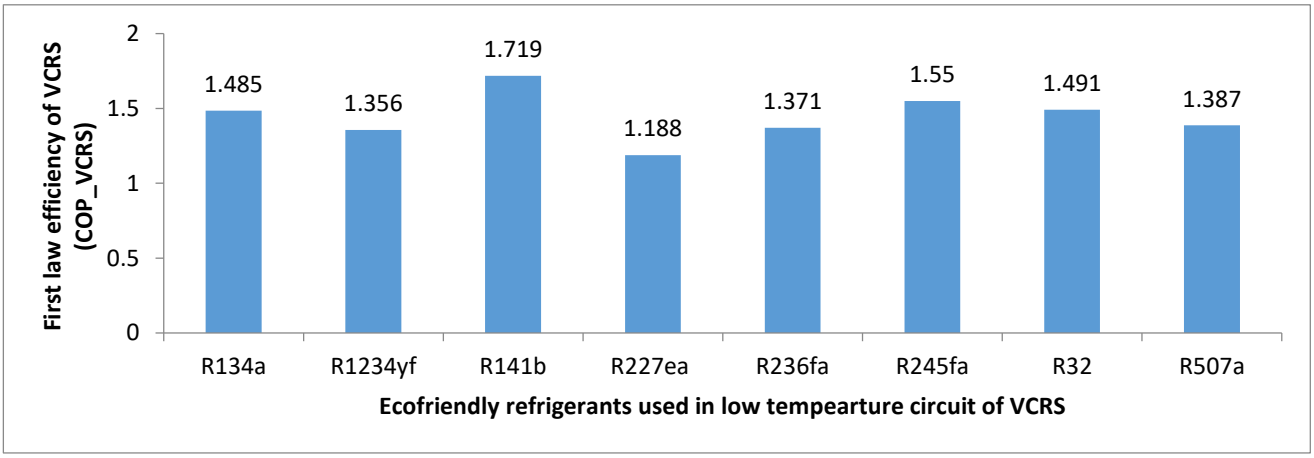


Figure 4: *Thermal performances in terms of first law efficiency of vapour compression refrigeration system (COP_VCRS) of cascaded with single effect ammonia-water (NH_3-H_20) vapour absorption refrigeration system coupled with vapour compression refrigeration using ecofriendly refrigerants in the low temperature cycle of VCRS system*

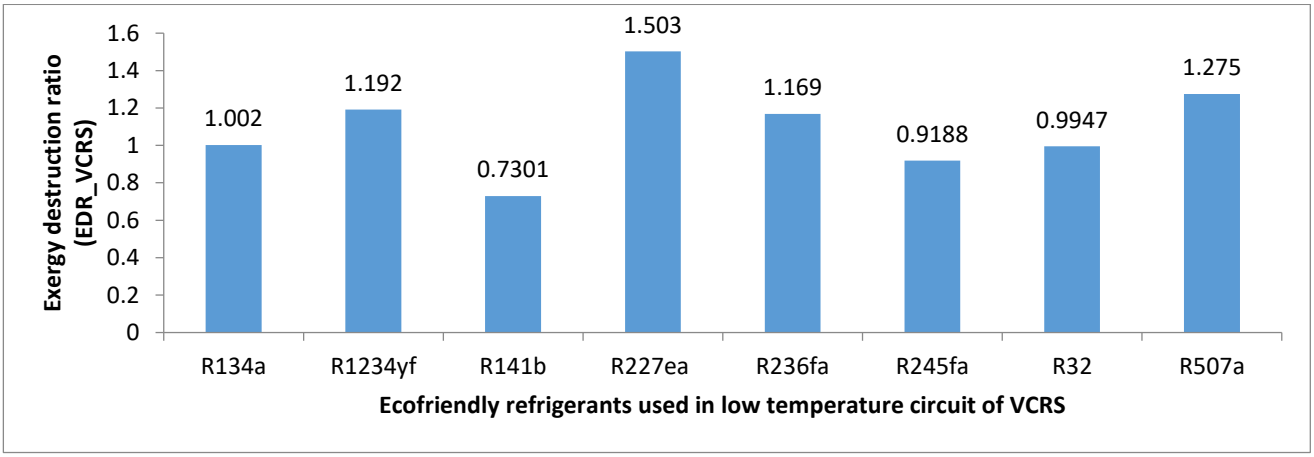


Figure 5: Thermal performances in terms of exergy destruction ratio (EDR_VCRS) of vapour compression system of vapour compression refrigeration system (COP_VCRS), of cascaded with single effect ammonia-water (NH_3-H_20) vapour absorption refrigeration system coupled with vapour compression refrigeration using ecofriendly refrigerants in the low temperature cycle of VCRS system

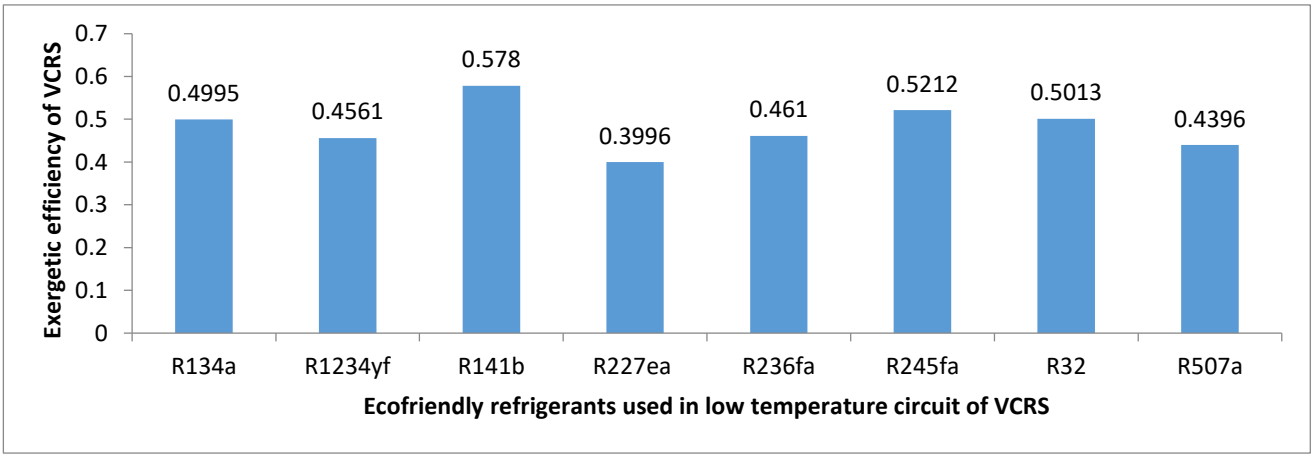


Figure 6: Thermal performances in terms of exergetic efficiency of vapour compression system of vapour compression refrigeration system (COP_VCRS), of cascaded with single effect ammonia-water(NH_3-H_20) vapour absorption refrigeration system coupled with vapour compression refrigeration using ecofriendly refrigerants in the low temperature cycle of VCRS system

The percentage improvement in thermal performance of combined novel vapour absorption refrigeration system coupled with vapour compression refrigeration system is shown in Table-2. It is found that this system combined single effect NH_3-H_2O vapour absorption system combined with vapour compression system using R141b ecofriendly refrigerant gives best first law performance(COP_Overall) improvement around 45.65% along with 45.73% improvement second law performance in terms of exergetic efficiency. However minimum exergy destruction ratio by using R227ea

Table-2: Percentage improvements in thermal performances of single effect NH_3_H_2O vapour absorption system cascaded with vapour compression refrigeration system using ecofriendly refrigerants

Performance Parameters	% First law Performance improvement (COP)	% II law Performance improvement (Exergetic)	% Reduction in Irreversibility (EDR)
R134a	41.428	34.34	34.29
R1234yf	38.60	28.20	29.0
R227ea	34.50	19.07	21.30
R236fa	38.912	28.96	29.88
R245fa	42.7	37.89	36.55
R32	41.55	35.03	34.51
R141b	45.65	45.73	41.71
R507a	37.45	25.61	27.12

4. Conclusions

The following conclusions were drawn.

(i) The thermodynamic performance in terms of first law efficiency and second law efficiency improved significantly by using vapour absorption system cascaded with vapour compression refrigeration system.

(ii) The 45.65% improvement in first law efficiency (i.e. over all COP) of combined single effect vapour absorption refrigeration cascade system using R141b refrigerant in the vapour compression cycle is found as compared to single effect NH_3H_2O vapour absorption refrigeration system

(iii) 45.73% increment of second law efficiency (i.e. exergetic efficiency) of the single effect NH_3H_2O vapour absorption refrigeration system cascaded with vapour compression refrigeration system is found as compared to single effect NH_3H_2O vapour absorption-refrigeration system

(iv) Minimum exergy destruction ratio in the single effect NH_3H_2O vapour absorption refrigeration system cascaded with vapour compression refrigeration system by using R227ea is found as compared to single effect NH_3H_2O vapour absorption- refrigeration system.

References

[1] Vaibhav Jain, S.S. Kachhwaha , Gulshan Sachdeva, Thermodynamic performance analysis of a vapour compression–absorption cascadedrefrigeration system, Energy conversion & Management, 2013, 685- 700.

[2] A Arora, Energy and exergy analyses of compression, absorption, and combined cycle cooling systems (Ph.D. Thesis), Centre for Energy Studies, IIT Delhi, India, 2009.

[3] Mishra R.S., Comparison of thermal performances of single effect, double effect and tripple effect LiBr-H2O absorption system cascaded with vapour compression refrigeration systems using ecofriendly refrigerants, International Journal of research in engineering and innovation , Vol-2, No-6 (2018), 610-621. .

[4] Riiffit S.B. , Shankland N, Integration of absorption and vapour-compression systems,Applied Energy, Volume-46, issue-4, 1993, 303-316.

[5] L. Kairouani, E. Nehdi, Cooling performance and energy saving of a compression–absorption refrigeration system assisted by geothermal energy, Applied Thermal Engineering, Vol- 26, 2006, 288–294.

Cite this article as: R.S. Mishra, Thermal performances (first law efficiency, exergy destruction ratio & exergetic efficiency) of cascade single effect ammonia-water (NH_3-H_20) vapour absorption refrigeration system coupled with vapour compression refrigeration using ecofriendly refrigerants in the low temperature cycle of VCRS system, *International journal of research in engineering and innovation (IJREI)*, vol 3, issue 1 (2019), 1-5.

International Journal of Research in Engineering and Innovation (IJREI)
journal home page: http://www.ijrei.com
ISSN (Online): 2456-6934

Thermodynamic analysis of vapour compression refrigeration system with mixing of TiO_2 nano material in HFO refrigerants for replacing HFC-134a

R.S. Mishra

Department of Mechanical & Production Engineering, Delhi Technological University Delhi, India

Abstract

In recent years, the climate change and environmental damage caused by the greenhouse gases have attracted increased attention to the environmental protection. Currently the refrigeration systems are widely using R11, R12, R22 & R502 as refrigerants. These refrigerants have chemical substances that damage the ozone layer and generates greenhouse effect. Montreal protocol requires for developed countries to completely phase out these refrigerants in 2010, and developing countries to phase out in 2020. Although R22 to be phaseout before 2030. R-134a, R404a, R407c & R410A is a substitute of R11, R12, R22 & R502 as refrigerants. The ODP of R22 is zero and the GWP value is 1924.The F-gas regulations are ended by the European Union in 2014, stipulate that refrigerators and freezers for home use, and those for business use, which contain HFCs and whose GWP value are above 150, are banned from market since January 1st 2015 and January 1st 2022 respectively. The new refrigerants (R1234yf & R1234ze), are environmental friendly refrigerants, with zero ODP value. The GWP value of R1234yf is 4, while GWP value of R1234ze is 6. The HFO refrigerants have a short atmospheric lifetime and its latent heat is small and its evaporation pressure and thermal conductivity is low, which will lead to a decline in system coefficient .of performance. The several methods were developed for enhancement in first law performance (COP) of vapour compression refrigeration systems. By using nano mixed refrigerants enhances first and second law performances. This paper mainly deals with optimal of utilization of TiO_2 in HFO-1234yf and R1234ze. The effect evaporator and condenser temperatures on compressor efficiencies have been discussed. 2018 ijrei.com. All rights reserved

Keywords: Thermodynamic performances, Energy-exergy Analysis, Eco friendly refrigerants, TiO_2 Nano- material

1. Introduction

The second law analysis (i.e. exergy Computation) is widely accepted as a useful tool for obtaining overall performances of any system for finding various exergy losses occurred in its components Exergy analysis also helps in taking account the important engineering decisions regarding design parameters of a system by finding maximum exergy destruction using entropy generation principle. A conventional exergetic analysis reveals irreversibilities within each component of a vapour compression refrigeration systems. Exergetic analysis provides the tool for a clear distinction between energy losses to the environment and internal irreversibilities in the process because exergy analysis is a methodology for the evaluation of the performance of devices and processes, and examining the exergy at different points in a series of energy-conversion steps. With this information, efficiencies can be evaluated, and the process steps having the largest losses (i.e., the greatest margin for improvement) can be identified. For these reasons, the modern approach uses the exergy analysis in the vapour compression refrigeration systems, which provides a more realistic view of the process and a useful tool for engineering evaluation Many researchers have carried out exergy studies of different thermal energy conversion systems describing various approach for exergy analysis and its usefulness for improving existing designs by reducing exergy destruction in a more simple and effective manner. Samuel yana mota [1] mainly focused on a thorough evaluation of the R22 replacement options for the medium temperature refrigeration applications and also included thermodynamic cycle performances. Comparison test of heat transfer and pressure drop characteristics, system performance comparisons, safety issues, determination of the environmental impact of refrigerant selection and three potentials alternatives to R22

Corresponding author: R. S. Mishra
Email Address: hod.mechanical.rsm@dtu.ac.in

were HFC (404A and R-410A) and HC (R-290) [1]. Syed Mohammad Said et.al, [2] had assessed theoretical performances of HCFC123, HFC134a, CFC11, and CFC12 as coolants. For a specific amount of desired exergy, more compression work is required for HCFC123 and HFC134a than for CFC11 and CFC12. The differences are not very significant at high evaporation temperatures and hence HCFC123 and HFC134a should not be excluded as alternative coolants and found optimum evaporation temperature for each condensation temperature which yields the highest exergetic efficiency. The exergetic assessment of the coolants HCFC123, HFC134a, CFC11, and CFC12 had done and found that the value of exergetic efficiency decreases with increasing the evaporator temperature. The highest exergetic efficiency occurs at the optimum evaporation temperature. Exergetic efficiency was decreased by 9.24, 12.03, 5.66, 13.78, 20.92, 9.53, 11.34 and 13.04% in R-134a, R-143a, R-152a, R-404A, R-407C, R-410A, R-502 and R-507A, respectively.

Yumrutas et. al [3] investigated of the effects of the evaporating and condensing temperatures on the pressure losses, exergy losses, second law of efficiency, and the COP of a vapour compression cycle. Dincer [4] asserts that conventional energy analysis, based on the first law of thermodynamics, evaluates energy mainly on its quantity but analysis that are based on second law considers not only the quality of energy, but also quantity of energy. Bejan[5] developed, thermodynamic model by using heat transfer irreversibility and showed that the exergetic efficiency decreases as evaporator temperature decreases. Mishra R.S.[6] carried out thermodynamic analysis of multi-evaporators single compressor and single expansion valve and liquid vapour heat exchanger(LVHE) in vapour compression refrigeration systems using thirteen ecofriendly refrigerants for reducing global warming and ozone depletion and concluded that the use of liquid vapour heat exchanger enhances the first law performance in terms of COP and second law performance in terms of exergetic efficiency is 20%. Jarall [7] proposed a theoretical and experimental analysis by using R1234yf in a small refrigeration system for performance comparison with R134a about the energetic characteristics of the refrigeration cycle with the refrigerants R134a and R1234yf and found that HFO-R1234yf could be alternative for replacing HFC-134a. The results showed a lower COP, smaller cooling capacity and lower compressor efficiency for R1234yf.

To explore its thermodynamic properties, applicability, compatibility, stability and safety in automotive air-conditioning systems, Ming Li [8] carried out experimental results are compared with R134a in the same conditions and found that HFO-1234yf could be an ideal alternative for R134a. Samaneh Daviram , et.al [9] is simulated automotive air conditioning system by considering HFO-1234yf (2,3,3,3-tetrafluoropropene) as the drop-in replacement of HFC-134a for finding thermal performance characteristics of system including COP and cooling capacity with changing different parameters. The simulated air conditioning system consists of a multi-louvered fin and flat-plate type evaporator, a wobble-plate type compressor, a mini-channel parallel-flow type condenser and a thermostatic expansion valve. The thermodynamic properties of the refrigerants are extracted from the REFPROP 8.0 software, and a computer program is developed for for finding thermal performances using thermodynamic analysis. In the theoretical analysis , the two different conditions have been considered for the cycle analysis. For the first state, the cooling capacity is taken as constant, and for the second state the fixed refrigerant mass flow rate is consideredAprea C, [10] Thermal analysis from a thermodynamic point of view, is carried out for evaluating the possible advantage of adopting a suction/liquid heat exchanger and developed a simplified criterion for also validating for many working fluids such as chlorofluorocarbon (CFC)s, hydrochlorofluorocarbon (HCFC)s and substitutes on the basis of their thermodynamic properties. The criterion is also presented in a graphical form using given two R502 and R32 examples Ming Li, et.al. [10] carried out Exergy analysis of automotive air-conditioning systems and found that useful exergy and energy outputs are 5.9% less than HFC-134a and found the input variables have significant effects on thermal efficiency and exergetic efficiency and found that the maximum exergy loss is due to condenser Lazarus Godson , B. Raja and D Mohan lal [11] observed that the colloidal mixture of nano-sized particles in a base fluid, called nanofluids, tremendously enhances the heat transfer characteristics of the original fluid, and is ideally suited for practical applications due to its marvelous characteristics. He has explained the unique features of nanofluids, such as enhancement of heat transfer, improvement in thermal conductivity, increase in surface volume ratio, Brownian motion, etc. and summarized the recent research in experimental and theoretical studies on forced and free convective heat transfer in nanofluids, their thermo-physical properties and their applications, and identifies the challenges and opportunities for future research. Dongsheng Wen , Guiping Lin Kai Zhang [12] reported the research carried out on nanofluids has progressed rapidly since its enhanced thermal conductivity and concluded that research on heat transfer applications of nanofluids with the aim of identifying the limiting factors so as to push forward their further development. Gabriela Huminic [13] studies theoretical & experimental results for the effective thermal conductivity, viscosity and the Nusselt number for the enhancement of the convection heat transfer in heat exchangers using nanofluids and explained the application of nanofluids in various types of heat exchangers: plate heat exchangers, shell and tube heat exchangers, compact heat exchangers and double pipe heat exchangers. .M.N. Pantzali, AA Mouza, S.V. Paras [14] investigated the efficiency of nanofluids as coolants. In the testing of nanofluids, he has found that the systematic measurements confirmed that the thermophysical properties of the base fluid are considerably affected by the nanoparticle addition. For a a typical nanofluid, namely a 4% CuO suspension in water, is selected and its thermal performance in a plate heat exchanger (PHE) is obtained experimentally. The new experimental data confirmed that besides the physical

properties, the type of flow inside the heat exchanging equipment also affects the efficiency of a nanofluid as coolant. The fluid viscosity seems also to be a crucial factor for the heat exchanger performance. It is concluded that in industrial heat exchangers, where large volumes of nanofluids are necessary and turbulent flow is usually developed, the substitution of conventional fluids by nanofluids seems inauspicious. Mishra et al. [15] experimentally evaluated the performance of a vapour compression refrigeration system by using Cu, Al_2O_3,CuO and TiO_2 based nano refrigerants in the primary circuit. The experimental results showed that the C.O.P of the system using Al_2O_3/R134a nano refrigerant was enhanced by 35% which was highest among all other nano refrigerant. Sabareesh et al. [16] experimentally investigated 17% increase in COP by using 0.01% by volume concentration TiO2 nano fluid in VCRS as a lubricant additive. Sajadi A.R. et.al. [17] experimentally investigated turbulent convective heat transfer coefficient and pressure drop of TiO2 dispersed in water nano fluid in the circular tube and also compared experimental results with correlation of Nusselt number and not concluded that how much (%) convective heat transfer coefficient increased. Huang Dan , et.al. [18] observed the effect of hybrid nano fluid mixture Al_2O_3 in the plate heat exchanger and found that convective heat transfer coefficient is increased as compared without nano fluid. Zeinali S Heris et.al [19] experimentally investigated the convective heat transfer increasement in the laminar flow forced convection heat transfer due to increase in the thermal conductivity of nano fluid due to nano particle fluctuations present in that fluid. Shengshan Bi et al. [20] found performance improvement reduction in power consumption upto 25% by mixed mineral oil TiO2 as the lubricant with refrigerant R600a. Subramani & Prakash [21] found improvement in performance by using Al_2O_3 at 0.06% weight in the mineral oil. Kumar et al. [18] found improvement in COP by 19.6% and reduction in power consumption by 11.5%. Due to enhancement in heat transfer coefficient using nanofluid Al_2O_3 & R600a/mineral oil as working fluid in a domestic refrigerator. Abbas et al. [22] performed the analysis of an air conditioning system by using a concentration of 0.01-0.1wt% of CNT Polyester oil with refrigerant R134a and found 4.2% enhancement in the COP was enhanced by using CNT particles concentration of 0.1% by weight. Hussen [23] showed the conventional refrigeration system performance improved with nano-refrigerant. Compressor work decreases by about 13% and system C.O.P. increases by about 12%.The above investigators have not studied in detail regarding performances of the vapour compression refrigeration systems in which nano refrigerants was circulated in the whole system. Therefore present investigation take care the overall system thermal performances in terms of first law efficiency (COP) and second law efficiency/ exergetic efficiency and various efficiencies of compressor used in the system.

2. Result and Discussion

2.1 Effect of condenser mass flow rate on thermal performances by mixing TiO_2 nano particles in the ecofriendly HFC-1234yf in the vapour compression refrigeration system

Table-1(a) shows the variation of condenser mass flow rate of water of vapour compression refrigeration system using ecofriendly HFO-1234yf refrigerant with thermal performances and it is found that condenser mass flow rate increases , the first law efficiency in terms of COP is increases and exergy destruction ratio of the system is decreases while second law efficiency is increases. Similarly evaporator convective overall heat transfer coefficient is decreases while condenser overall heat transfer coefficient is increases.

Table-1(a) Performance of vapour compression refrigeration system using R1234yf with Nano Particle (TiO_2) mixed with R-718, compressor speed (rpm) =2900, m_{brine} (kg/sec)=0.007, $L_{_eva}$=0.72m, $L_{_Cond}$=1.2m, P_brine=P_water=2.0 Bar

Condenser Mass flow rate of water (Kg/sec)	First law Efficiency (COP)	Exergy Destruction Ratio(EDR)	Exergetic Efficiency	Evaporator overall heat transfer coefficient (W/m^2K)	Condenser overall heat transfer coefficient (W/m^2K)
0.007	3.379	0.6218	0.3782	1327.54	692.96
0.008	3.477	0.6108	0.3892	1320.21	714.01
0.009	3.557	0.6018	0.3982	1315.88	731.28
0.010	3.625	0.5942	4058	1313.34	745.71

Table-1(b) Effect of evaporator Mass flow rate of brine on thermal performances and overall heat transfer coefficients of Vapour compression Refrigeration System using R1234yf with Nano Particle (TiO_2) mixed with R-718, compressor speed(rpm)=2900, m_{water} (kg/sec)=0.008, $L_{_eva}$=0.72m, $L_{_Cond}$=1.2m, P_brine = P_water P_brine =2.0 Bar

Evaporator Mass flow rate of brine (Kg/sec)	First law Efficiency (COP)	Exergy Destruction Ratio(EDR)	Exergetic Efficiency	Evaporator overall heat transfer coefficient (W/m^2K)	Condenser overall heat transfer coefficient (W/m^2K)
0.007	3.477	0.6108	0.3892	1320.21	714.01
0.008	3.549	0.6027	0.3973	1342.87	722.63
0.009	3.609	0.5961	0.4039	1361.93	729.54
0.010	3.658	0.5926	0.3974	1378.26	735.19

Table-1(b) shows the variation of evaporator mass flow rate of brine (Kg/sec) of vapour compression refrigeration system using ecofriendly HFO-1234yf refrigerant with the thermal performances and it is found that evaporator mass flow rate of brine (Kg/sec) increases , the first law efficiency in terms of COP is increases and exergy destruction ratio of the system is decreases while second law efficiency is increases. Similarly evaporator convective overall heat transfer coefficient is decreases while condenser overall heat transfer coefficient is increases.

Table-1(c) Effect of compressor speed on Performance of Vapour compression Refrigeration System using R1234yf with Nano Particle (TiO_2) mixed with R-718, m_{brine} (kg/sec)=0.007, m_{water} (kg/sec)=0.008, L_{eva}=0.72m, L_{Cond}=1.2m, P_brine=P_water=2.0 Bar

Speed of Compressor (R P M)	First law Effi. (COP)	System Exergy Destruction Ratio based on exergy of fuel	Second Law Efficiency/ Exergetic Efficiency	Exergy of product (W)	Exergy of fuel (W)
2500	3.631	0.5936	0.4064	23.68	100.6
2600	3.583	0.5989	0.4011	24.41	103.3
2700	3.542	0.6035	0.3965	25.11	105.9
2800	3.507	0.6074	0.3926	25.79	108.4
2900	3.477	0.6108	0.3892	26.45	110.7
3000	3.451	0.6137	0.3863	27.09	112.9

Table-1(c) shows the variation of compressor speed with thermal performances of vapour compression refrigeration system using ecofriendly HFO-1234yf refrigerant, it is found that compressor speed increases, the first law efficiency in terms of COP is decreases and exergy destruction ratio of the system is increases while second law efficiency is decreases. Similarly exergy of product is increases along with exergy of fuel (in terms of electrical power required to run compressor) is increases

2.2 Effect of condenser mass flow rate on thermal performances by mixing TiO_2 nano particles in the ecofriendly HFC-1234yf in the vapour compression refrigeration system

Table- 2(a): Variation of thermal performance (First law efficiency (COP) and Exergetic efficiency) of vapour compression refrigeration system using ecofriendly HFO-1234yf refrigerant with variation of Condenser temperature using TiO_2 mixed R1234yf for evaporator temp=268 K

Condenser Temperature (K)	COP	Rational EDR	Exergetic Efficiency
328	1.971	0.7848	0.2152
323	3.394	0.6962	0.3034
318	4.430	0.6157	0.3842
313	5.382	0.5272	0.4728
308	6.479	0.4165	0.5835

Table-2(a) shows the variation of condenser temperature with compressor performances, it is found that condenser temperature increases, first law performance in terms of COP is decreases the exergy destruction ratio is increases while exergetic efficiency is decreases. Table-2(b) shows the variation of condenser temperature with compressor performances, it is found that condenser temperature increases, the pressure ratio is increases and isentropic efficiency is decreases and volumetric efficiency of compressor is also decreases.

Table- 2(b): Variation of pressure ratio, isentropic Compressor efficiency and volumetric compressor efficiency of vapour compression refrigeration system using ecofriendly HFO-1234yf refrigerant with variation of Condenser temperature using TiO_2 mixed R1234yf for evaporator temp=268 K

Condenser Temperature (K)	Pressure Ratio (r_p)	Isentropic Compressor Efficiency	Volumetric Compressor Efficiency
328	6.461	0.8198	0.5523
323	5.744	0.8432	0.6722
318	5.088	0.8648	0.7272
313	4.490	0.8646	0.7554
308	3.947	0.9029	0.7736

2.3 Effect of condenser temperature on thermal performances by mixing TiO_2 nano particles in the ecofriendly HFC-1234ze in the vapour compression refrigeration system

Table- 2(c): Variation of thermal performance (First law efficiency (COP) and Exergetic efficiency) of vapour compression refrigeration system using ecofriendly HFO-1234ze refrigerant with variation of Condenser temperature using TiO_2 mixed R1234ze for evaporator temp=268 K

Condenser Temperature (K)	COP	Rational EDR	Exergetic Efficiency
328	1.971	0.8913	0.1087
323	3.394	0.7320	0.2680
318	4.430	0.6160	0.3804
313	5.382	0.5095	0.4905
308	6.479	0.3867	0.6133

Table-2(c) shows the variation of condenser temperature with variation of thermal performances (i.e. first and second law performances in terms of COP , Rational exergy destruction ratio and exergetic efficiency) of vapour compression refrigeration system using ecofriendly HFO-1234ze refrigerant and it is found it is found that condenser temperature increases , first law performance in terms of COP is decreases the exergy destruction ratio is increases while exergetic efficiency is decreases.

Table- 2(d): Variation of pressure ratio, isentropic compressor efficiency and volumetric compressor efficiency) of vapour compression refrigeration system using ecofriendly HFO-1234ze refrigerant with variation of Condenser temperature using TiO_2 mixed R1234ze for evaporator temp=268 K

Condenser Temperature (K)	Pressure Ratio (r_p)	Isentropic Compressor Efficiency	Volumetric Compressor Efficiency
328	7.312	0.7892	0.5426
323	6.451	0.8176	0.5738
318	5.669	0.8436	0.6040
313	4.961	0.8673	0.6334
308	4.269	0.8819	0.6619

Table-2(d) shows the variation of condenser temperature with compressor performances of vapour compression refrigeration system using ecofriendly HFO-1234ze refrigerant, it is found that condenser temperature increases, the pressure ratio is increases and isentropic efficiency is decreases and volumetric efficiency of compressor is also decreases.

2.4 Effect of evaporator temperature on thermal performances by mixing TiO_2 nano particles in the ecofriendly HFC-1234yf in the vapour compression refrigeration system

Table- 3(a): Variation of evaporator temperature with thermal performances (First law efficiency (COP) and Exergetic efficiency) of vapour compression refrigeration system using ecofriendly HFO-1234yf refrigerant with variation of evaporator temperature using TiO_2 mixed R1234yf for condenser temp=48^{0}C.

Evaporator Temperature (K)	COP	EDR	Rational EDR	Exergetic Efficiency
263	2.958	2.838	0.7398	0.2606
264	3.22	2.497	0.7141	0.2859
265	3.488	2.28	0.6952	0.3048
266	3.65	2.137	0.6812	0.3188
267	3.832	2.041	0.6712	0.3288
268	4.002	1.976	0.6640	0.3360
269	4.162	1.933	0.6591	0.3409
270	4.317	1.907	0.6560	0.3440
271	4.471	1.892	0.6542	0.3458
272	4.624	1.887*	0.6536*	0.3464*
273	4.78	1.889	0.6539	0.3461
274	4.939	1.898	0.6549	0.3451
275	5.105	1.913	0.6567	0.3433
276	5.276	1.934	0.6591	0.3409
277	5.456	1.960	0.6622	0.3378
278	5.642	1.994	0.6660	0.3340
283	6.762	2.274	0.6946	0.3054

Table-3(a) shows the variation of evaporator temperature with thermal performances (i.e. in terms of first law performance (COP) and second law performance (exergetic efficiency) and exergy destruction ratio) of vapour compression refrigeration system using ecofriendly HFO-1234yf refrigerant. It was found that the evaporator temperature is increases the first law performance (COP) of vapour compression refrigeration system is increases while exergy destruction ratio of vapour compression refrigeration system is decreases up to a optimum value and then started increases. Similarly exergetic efficiency of the system is increases as evaporator temperature is increases up to a optimum point and then decreases. The optimum value of evaporator temperature is found to be 272K (i.e. -1^{o}C) by using HFC-1234yf.

Table- 3(b): Variation of evaporator temperature with pressure ratio, isentropic Compressor Efficiency and volumetric compressor efficiency of vapour compression refrigeration system using ecofriendly HFO-1234yf refrigerant with variation of evaporator temperature using TiO_2 mixed R1234yf for evaporator temp=268 K

Evaporator Temperature (K)	Pressure Ratio (r_p)	Isentropic Compressor Efficiency	Volumetric Compressor Efficiency
263	6.558	0.8160	0.5653
264	6.322	0.8238	0.5737
265	6.096	0.8313	0.5819
266	5.879	0.8385	0.5895
267	5.673	0.8454	0.5977
268	5.475	0.8520	0.6052
269	5.285	0.8584	0.6127
270	5.104	0.8645	0.6199
271	4.930	0.8703	0.6270
272	4.763	0.8759	0.6339
273	4.604	0.8813	0.6407
274	4.451	0.8865	0.6473
275	4.304	0.8915	0.6538
276	4.163	0.8962	0.6602
277	4.028	0.9008	0.6664
278	3.898	0.9052	0.6725
283	3.322	0.9249	0.7015

Table-3(b) shows the variation of evaporator temperature with rational exergy destruction ratio (which is a ratio of total exergy destruction exergy (losses in the system was sum of exergy destruction in components to the exergy of fuel was evaluated based on exergy of fuel (i.e. total electrical power required for running compressor) of vapour compression refrigeration system using ecofriendly HFO-1234yf refrigerant and it was also observed that when evaporator temperature is increasing the rational EDR was decreasing. The isentropic compressor efficiency and volumetric efficiency is also increases with increasing evaporator temperature.

Table- 3(c): Variation of evaporator temperature with thermal performances (First law efficiency (COP) and Exergetic efficiency) of vapour compression refrigeration system using ecofriendly HFO-1234ze refrigerant with variation of evaporator temperature using TiO_2 mixed R1234ze for condenser temp=48 ^{0}C.

Evaporator Temperature (K)	COP	EDR	Rational EDR	Exergetic Efficiency
263	1.754	8.97	0.8997	0.1003
264	2.34	4.796	0.8285	0.1725
265	2.818	3.414	0.7734	0.2266
266	3.216	2.751	0.7334	0.2666
267	3.55	2.378	0.7039	0.2961
268	3.836	2.15	0.6826	0.3174
269	4.086	2006	0.6673	0.3327
270	4.310	1.913	0.6587	0.3433
271	4.56	1.854	0.6497	0.3503
272	4.711	1.819	0.6453	0.3547
273	4.899	1.80	0.6429	0.3571
274	5.085	1.795*	0.6422*	0.3578*
275	5.272	1.799	0.6427	0.3573
276	5.462	1.812	0.6444	0.3556
277	5.658	1.832	0.6469	0.3531
278	5.681	1.859	0.6503	0.3497
283	7.049	2.119	0.6794	0.3206

Table-3(c) shows the variation of evaporator temperature with thermal performances (i.e. in terms of first law performance (COP) and second law performance (exergetic efficiency) and exergy destruction ratio) of vapour compression refrigeration system using ecofriendly HFO-1234ze refrigerant. It was found that the evaporator temperature is increases the first law performance (COP) of vapour compression refrigeration system is increases while exergy destruction ratio of vapour compression refrigeration system is decreases up to a optimum value and then started increases. Similarly exergetic efficiency of the system is increases as evaporator temperature is increases up to a optimum point and then decreases. The optimum value of evaporator temperature to be 272K (i.e. 1^{o}C) by using HFC-1234ze respectively.

Table- 3(d): Variation of evaporator temperature with pressure ratio, isentropic Compressor Efficiency and volumetric compressor efficiency with variation of evaporator temperature of vapour compression refrigeration system using ecofriendly HFO-1234ze refrigerant using TiO_2 mixed R1234ze for evaporator temp=268 K

Evaporator Temperature (K)	Pressure Ratio (r_p)	Isentropic Compressor Efficiency	Volumetric Compressor Efficiency
263	7.452	0.7841	0.540
264	7.161	0.7938	0.5497
265	6.884	0.803	0.5592
266	6.62	0.8118	0.5684
267	6.369	0.8202	0.5773
268	6.129	0.8283	0.5860
269	5.90	0.8359	0.5944
270	5.682	0.8433	0.6026
271	5.473	0.8504	0.6106
272	5.274	0.8571	0.6184
273	5.083	0.8636	0.6260
274	4.901	0.8697	0.6335
275	4.727	0.8757	0.6407
276	4.561	0.8813	0.6478
277	4.401	0.8868	0.6547
278	4.249	0.892	0.6614
283	3.577	0.9151	0.6931

Table-3(d) shows the variation of evaporator temperature with rational exergy destruction ratio (which is a ratio of total exergy destruction exergy (losses in the system was sum of exergy destruction in components to the exergy of fuel was evaluated based on exergy of fuel (i.e. total electrical power required for running compressor) of vapour compression refrigeration system using ecofriendly HFO-1234ze refrigerant and it was also observed that when evaporator temperature is increasing the rational EDR was decreasing. The isentropic compressor efficiency and volumetric efficiency is also increases with increasing evaporator temperature.

3. Conclusions

Following conclusions were drawn while using ecofriendly HFO1234yf and HFO-1234ze and HFC-134a ecofriendly refrigerants by mixing TiO_2 refrigerants

- Thermal performances of vapour compression refrigeration using HFO-1234ze refrigerant by mixing TiO_2 nano particles is reduced as compared to TiO2 mixed HFO-1234yf refrigerant.
- The first law efficiency (COP) increases with increasing evaporator temperature
- The exergetic efficiency is increases with increasing evaporator temperature up to a certain temperature where exergetic efficiency, second law efficiency becomes optimum (i.e. maximum) and then started decreases with increasing evaporator temperature.
- The optimum value of evaporator temperature is found to be 274K (i.e. 1^{o}C) while in case of optimum second law efficiency, the evaporator temperature to be 271K (i.e. -2 ^{o}C) using HFC-134a
- The optimum value of evaporator temperature is found to be 272K (i.e. 1^{o}C) while in case of optimum second law efficiency, the evaporator temperature to be 269K (i.e. -4 ^{o}C) by using HFC-1234yf respectively
- The optimum value of evaporator temperature is found to be 274K (i.e. 1^{o}C) while in case of optimum second law efficiency, the evaporator temperature to be 272K (i.e. -41^{o}C) by using HFC-1234ze respectively.
- Exergy destruction ratio (EDR) is decreasing while increasing evaporator temperature.
- Exergy destruction ratio (EDR) is also increases with increasing condenser temperature.
- The volumetric efficiency for R1234yf and R1234ze is 4% and 5% lower compared with R134a.
- The first law efficiency (COP) values are about 8% lower

for R1234ye and 11% lower for R1234ze than those obtained using R134a while mixing TiO_2

- The best first law performances (COP) and exergetic efficiency were found using R290 hydrocarbon and R407c which is higher than R134a.
- Refrigerants R134a R404a and R507a give similar trends in their first law efficiency (COP), second law efficiency, exergetic efficiency and exergy destruction ratio, compressor efficiency, isentropic efficiency and volumetric efficiency with slightly variations.
- HFO-1234yf, R125 and R600a gives similar trends with slightly variation, however lower than R134a.
- Nano mixed R1234ze gives lower performance as compared with nano mixed HFO-1234yf
- The worst performances were found by using R410a, R236fa
- Super worst first and second law performances were observed by using Al2O3 mixed in R245fa, R123 refrigerants.
- The isentropic compressor efficiency and volumetric efficiency is also increasing with increasing evaporator temperature and it has optimum value at 274K (i.e. 1^{o}C).
- first law efficiency (COP) decreases with decreasing condenser temperature
- Similarly, isentropic efficiency and volumetric efficiency decreases by increasing condenser temperature.

References

[1] Mota-Babiloni A, et.al. .[2015] Analysis Based on EU Regulation No 517/2014 of new HFC/HFO Mixtures as Alternatives of High GWP Refrigerants in Refrigeration and HVAC Systems. International Journal of Refrigeration 52 , page-21-31

[2] Syed Mohammad Said et.al.[1994]Exergetic assessment of the coolants HCFC123, HFC134a, CFC11, and CFC12, Energy, Vol-19, No-11, page-1181–1186

[3] D. Yumrutas et. al [2002]Exergy analysis of vapour compression refrigeration systems, Exergy, an Int J, 2 (2002) 266-272

[4] Dincer I.[2003] Refrigeration systems and applications. London: Wiley; pp. 26–27.

[5] Bejan A,[1989], Theory of heat transfer irreversible refrigeration plants, Int J Heat mass transfer, 32(9), 1631-39

[6] Mishra R.S. [2013] Thermodynamic performance evaluation of multi evaporators single compressor and single expansion valve and liquid vapour heat exchanger in vapour compression refrigeration systems using thirteen ecofriendly refrigerants for reducing global warming and ozone depletion, International Journal of advance research and innovation, ISSN 2347 - 3258 , Volume 1, Issue 3 (2013) , page-220-228.

[7] Samaneh Daviran, Alibakhsh Kasaeian, Soudabeh Golzari, Omid Mahian, Shahin Nasirivatan, Somchai Wongwises [2017] , . comparative study on the performance of HFO-1234yf and HFC-134a as an alternative in automotive air conditioning systems, Applied Thermal Engineering , Vol-110 ,part- C , page-1091-1100

[8] Aprea C, Ascani M, De Rossi F. [1999], A Criterion for Predicting the Possible Advantage of Adopting a Suction/Liquid Heat Exchanger in Refrigerating System. Applied Thermal Engineering 19 ,page- 329-336

[9] Jarall S. [2012] Study of Refrigeration System with HFO-1234yf as a Working Fluid. International Journal of Refrigeration 35 , page-1668-1677.

[10] Ming Li, et.al [2014]Experimental Research on the Performance of HFO-1234yf in Automotive Air-Conditioning Systems. International journal of Energy conversion Vol 2, No 6.

[11] Lazarus Godson , B. Raja and D Mohan lal (2010)"Enhancement of heat transfer using nanofluids" - An overview, Renewable and Sustainable Energy Reviews, Volume 14, Issue 2, February 2010, Pages 629-641

[12] DongshengWen[a]. GuipingLin[b]. KaiZhang[c]. (2009) Review of nanofluids for heat transfer applications, Particuology Volume 7, Issue 2, April 2009, Pages 141-150

[13] Gabriela Huminic, AngelHuminic(2012) Application of nanofluids in heat exchangers: A review, Renewable and Sustainable Energy Reviews, Volume 16, Issue 8, October 2012, Pages 5625-5638

[14] M.N.Pantzali..A.A.Mouza..S.V.Paras (2009) Investigating the efficacy of nanofluids as coolants in plate heat exchangers Chemical Engineering ScienceVolume 64, Issue 14, 15 July 2009, Pages 3290-3300

[15] Mishra R S and Jaiswal Rahul Kumar [2015] Thermal Performance Improvements of Vapour Compression Refrigeration System Using Eco-Friendly Based Nanorefrigerants in Primary Circuit International Journal of Advance Research and Innovation 3, page-524-535.

[16] Sabareesh R K, Gobinath N, Sajith V, Das S and Sobhan C B [2012] Application of TiO 2 nanoparticles as a lubricant-additive _ for vapor compression refrigeration systems–An experimental investigation International journal of refrigeration 35, page-1989-1996

[17] Sajadi A.R. [2011].Investigation of turbulent convective heat transfer and pressure drop of TiO2/water nano fluid in circular tube. International communications in Heat and mass transfer, Elsevier,Vol-38, page-1474-1478

[18] Huang Dan , et.a. {2016] , Effect of hybrid nano fluid mixture in the plate heat exchangers, Experimental thermal and fluid science, Elsevier, Vol-72, page-190-196

[19] Zeinali S Heris et.al [2007] "Experimental investigation of convective heat transfer coefficient using Al_2O_3 /water nano fluid in circular tube" , J of Heat & fluid flow, Elsevier, Vol-28, page-203-210 .

[20] Bi Shengshan, [2011] Performance of a domestic refrigerator using TiO2-R600a nano-refrigerant as working fluid Energy Conversion and Management 52 733-737

[21] Subramani N and Prakash M J [2011] Experimental studies on a vapour compression system using nanorefrigerants International Journal of Engineering, Scie-nce and Technology ,3, page- 95-102

[22] Abbas M, [2013] Efficient Air—Condition Unit By Using Nano—Refrigerant 1st Engineering undergraduate research catalyst conference

[23] H.A. Hussen [2014], Experimental investigation for TiO_2 nanoparticles as a lubricant- Additive for a compressor of window type air-conditioner system J. Eng., 20 (2014), pp. 61-72

Cite this article as: R.S. Mishra, Thermodynamic analysis of vapour compression refrigeration system with mixing of TiO_2 nano material in HFO refrigerants for replacing HFC-134a, *International journal of research in engineering and innovation (IJREI)*, vol 2, issue 6 (2018), 589-595.

Variable Transconductance Voltage Differencing Current Conveyor and its Application in Filter Design

Suyash Kumar
Electrical Engineering Department
Delhi Technological University
Delhi-110042, India
suyash_bk201@hotmail.com

Gunit Dhingra
Electrical Engineering Department
Delhi Technological University
Delhi-110042, India
gu7nit@gmail.com

Pragati Kumar
Electrical Engineering Department
Delhi Technological University
Delhi-110042, India
pragati_1964@yahoo.co.in

***Abstract*—This paper proposes a novel design of variable transconductance voltage differencing current conveyor (VT-VDCC). The proposed design provides for increased tunability range of the transconductance of the VT-VDCC resulting in wide tuning range with low power dissipation. The performance of the proposed VT-VDCC has been verified by designing a current-mode universal filter. Workability of the designed circuit has been established with PSPICE simulations using TSMC 0.18μm CMOS process parameters.**

Keywords—Active Building Block; Transconductance Amplifier; Current Conveyor; Voltage Differencing Current Conveyor; Current-mode Biquad

I. INTRODUCTION

With technology scaling and increased need for portable and compact electronics, researchers are working towards the development of low-voltage high performance mixed mode signal processing circuits. Because of simultaneous integration of analog circuits with digital circuits on the same chip analog circuits must be designed to work at lower supply voltages. During the last few decades, many novel active building blocks (ABBs) have been proposed in the domain of analog signal processing. A detailed description of these ABBs is given in [1]. In most of these ABBs, a transconductor is used to generate current from a differential voltage input. Voltage Differencing Current Conveyor (VDCC) is one of the blocks that has been used in many applications like filter design [2-4], oscillator design [5-7] and inductance simulation [8-9]. In many of the above quoted structures, the characterizing parameters of the resulting applications depend on the transconductance value of the input transconductor present in the VDCC. Thus, to improve the range of tunability for any of the parameters of these structures, a wide tuning range for this transconductance stage must be obtained.

The main aim of this paper is to introduce a variable transconductance VDCC (VT-VDCC) with extended tunability range for the transconductance stage. This extension is obtained by the use of a diode-connected load in the input stage, which allows for further lowering of the transconductance with increased bandwidth. Several wideband variable gain amplifiers (VGAs) [10-11] have been proposed which use this diode-connected load for obtaining tunable voltage gains with high bandwidth.

As an application of the proposed VT-VDCC, a novel second order current-mode universal filter has been implemented using three VT-VDCCs and three passive components. The universal filter does not require any passive component matching for realization of allpass and notch responses. The pole frequency and quality factor can be tuned independently through transconductance control.

The paper has been organized as follows: section II describes the CMOS implementation of the proposed VT-VDCC. In section III, a VT-VDCC based novel second order universal filter has been presented. Section IV contains the simulation results which is followed by conclusion of the present paper in section V.

II. PROPOSED VARIABLE TRANSCONDUCTANCE VDCC

The symbol and behavioral model for VDCC is shown in Fig. 1 with its terminal characteristics given below in (1) [1].

$$\begin{bmatrix} I_N \\ I_P \\ I_Z \\ V_X \\ I_{WP} \\ I_{WN} \\ I_{zc} \\ I_{-ZC} \end{bmatrix} = \begin{bmatrix} 0 & 0 & 0 & 0 \\ 0 & 0 & 0 & 0 \\ g_m & -g_m & 0 & 0 \\ 0 & 0 & 1 & 0 \\ 0 & 0 & 0 & 1 \\ 0 & 0 & 0 & -1 \\ g_m & -g_m & 0 & 0 \\ -g_m & g_m & 0 & 0 \end{bmatrix} \begin{bmatrix} V_P \\ V_N \\ V_Z \\ I_x \end{bmatrix} \quad (1)$$

Only the x-terminal exhibits a low impedance while all other terminals P, N, Z, W_p and W_n are high impedance terminals. The proposed CMOS structure of the VT-VDCC consists of a modified transconductance stage and a translinear CCII [15]. Two z-copy terminals carrying complementary currents available at the z-terminal have been added to the OTA stage for filter design applications.

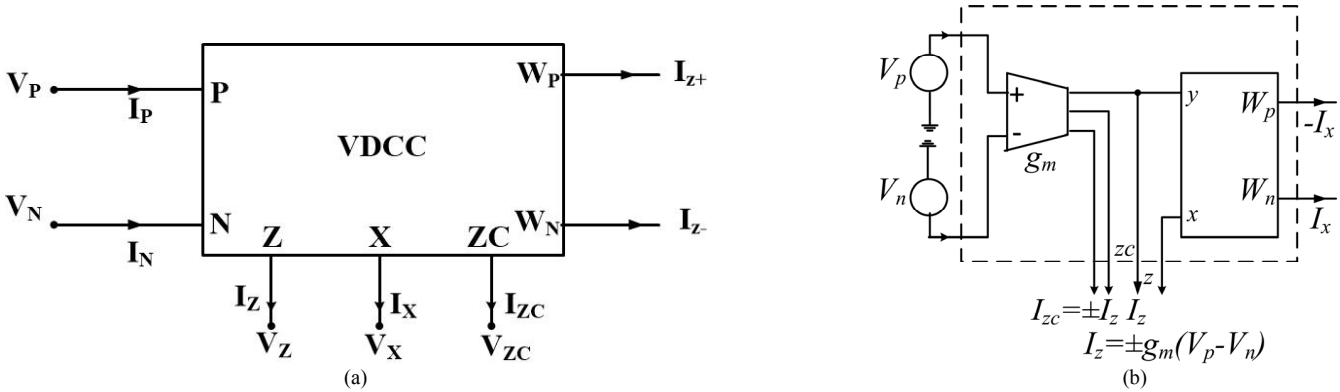


Fig 1: Voltage Differencing Current Conveyor (a) Symbol (b) Behavioral Model

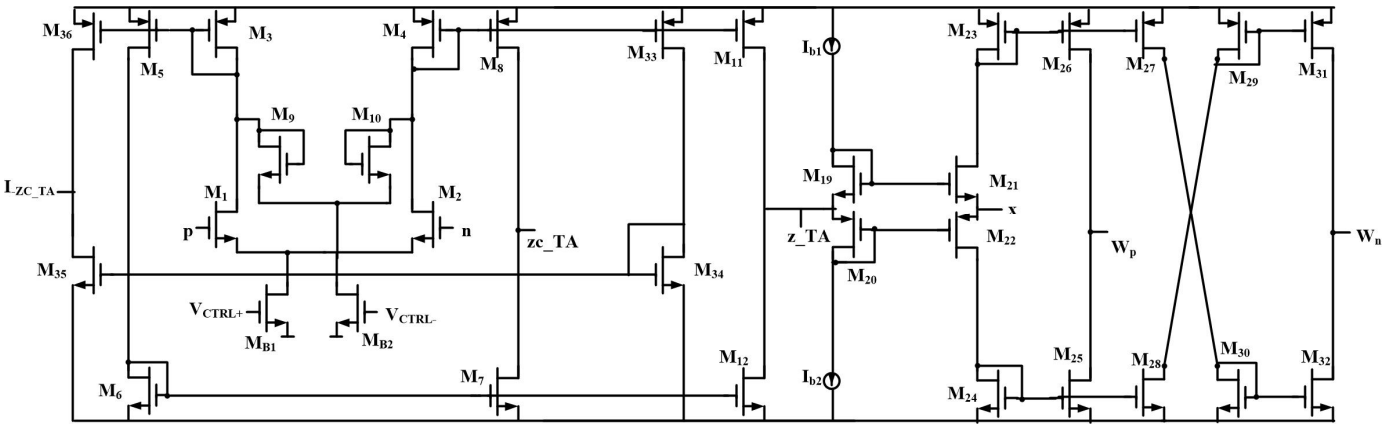


Fig 2: CMOS Implementation of the proposed VT-VDCC

In order to enhance the tunability range of the OTA stage of the VDCC, the structure of the conventional OTA is modified by adding the symmetric diode-connected load, formed by the transistors M9 and M10. This diode-connected load based control stage has been utilized in many low-voltage low-power variable gain amplifier designs [10, 11]. The transconductance of the input stage may be expressed as:

$$G_m = \frac{g_{m1,2}g_{m3,4}}{g_{m3,4} + g_{m9,10}} \tag{2}$$

$$= \frac{\mu_n C_{ox}\sqrt{\left(\frac{W}{L}\right)_{1,2}}\sqrt{\left(\frac{W}{L}\right)_{B}}\,(V_{CTRL+} - V_{SS} - V_{TH})}{1 + \frac{\left(\frac{W}{L}\right)_{9,10}}{\left(\frac{W}{L}\right)_{3,4}}\sqrt{\frac{1}{1 + \frac{(V_{CTRL+} - V_{SS} - V_{TH})^2}{(V_{CTRL-} - V_{SS} - V_{TH})^2}}}} \tag{3}$$

From the above equation it may be seen that as V_{CTRL+} is increased (while keeping V_{CTRL-} constant), the value of the transconductance increases. Also, when V_{CTRL-} is increased (while keeping V_{CTRL+} constant), the value of the transconductance decreases, thereby increasing the tuning range of the transconductance parameter.

III. Novel Current- Mode Universal Biquad

As an application of the VT-VDCC, a current-mode universal biquad is now presented. It consists of three VT-VDCCs, two grounded capacitors and one grounded resistor. The filter circuit is shown in Fig 3.

A routine analysis of the circuit gives the following current transfer functions:

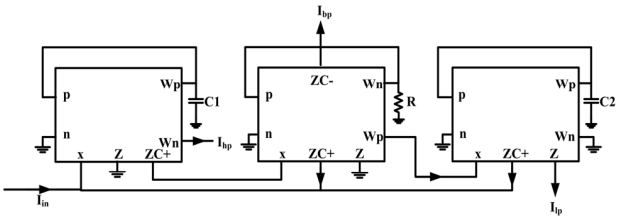


Fig 3: Circuit Diagram for proposed second order current-mode universal filter

$$\frac{I_{bp}}{I_{in}} = \frac{-sC_2 g_{m1} g_{m2} R}{D(s)} \tag{4}$$

$$\frac{I_{hp}}{I_{in}} = \frac{s^2 C_2 C_1}{D(s)} \tag{5}$$

$$\frac{I_{lp}}{I_{in}} = \frac{g_{m1}g_{m3}}{D(s)} \quad (6)$$

$$D(s) = s^2C_2C_1 + sC_2g_{m1}g_{m2}R + g_{m1}g_{m3} \quad (7)$$

$$\omega_o = \sqrt{\frac{g_{m1}g_{m3}}{C_1C_2}} \quad (8)$$

$$Q = \frac{1}{g_{m2}R}\sqrt{\frac{C_1g_{m3}}{g_{m1}C_2}} \quad (9)$$

The band-elimination and all-pass responses can be obtained by adding the high-pass and low-pass responses and high-pass, low-pass and inverted band-pass responses respectively. It is also evident from equations 8-9 that ω_o and Q are electronically tunable by varying the values of g_{m1}(or g_{m3}) and g_{m2} respectively. The active and passive sensitivities of the natural pole frequency ω and quality factor Q are computed as follows:

$S_{g_{m1}}^{\omega_o} = S_{g_{m3}}^{\omega_o} = \frac{1}{2}$; $S_{C_1}^{\omega_o} = S_{C_2}^{\omega_o} = -\frac{1}{2}$; $S_{g_{m2}}^{\omega_o} = S_R^{\omega_o} = 0$.

$S_{g_{m3}}^{Q} = S_{C_1}^{Q} = \frac{1}{2}$; $S_{g_{m1}}^{Q} = S_{C_2}^{Q} = -\frac{1}{2}$; $S_{g_{m2}}^{Q} = S_R^{Q} = -1$.

Thus it is observed that all the active and passive sensitivity coefficients are quite low.

IV. Simulation Results

To verify the workability of the proposed design, the VT-VDCC has been implemented using TSMC 0.18μm CMOS process parameters with DC supply voltage equal to $\pm$0.9V and $I_{B1} = I_{B2} = 10\mu A$. The aspect ratios for all the transistors have been shown in Table 1. The variation of the transconductance of the OTA stage with the variation of control voltage V_{CTRL+} has been shown in Fig. 4. As predicted, an increase in the control voltage V_{CTRL+} causes an increase in the transconductance values. Also, the variation in the transconductance values with change in control voltage V_{CTRL-} has also been shown in Fig. 5. The VT-VDCC transconductance was found to be tunable from 23μS to 919 μS.

TABLE I. Aspect Ratios of Transistors used in VT-VDCC

Transistor No.	*Width (µm)*	*Length (µm)*
M_1, M_2, M_9, M_{10}, M_{19}, M_{21}	50	0.5
M_{20}, M_{22}	25	0.5
M_{23}, M_{26}, M_{27}, M_{29}, M_{31}	10	0.5
M_{24}, M_{25}, M_{28}, M_{30}, M_{32}	10	0.5
M_3, M_4, M_5, M_8, M_{11}, M_{33}, M_{36}	4	0.5
M_6, M_7, M_{12}, M_{34}, M_{35}	10	0.5

A comparison of the proposed VT-VDCC with other VDCC circuits has been presented in Table 2.

The biquad filter shown in Fig. 3 was designed to have $Q = 0.707$ by appropriately setting $g_{m2} = 283\mu S$, $R = 5K\Omega$ and keeping $g_{m1} = g_{m3}$ and $C_1 = C_2 = 0.1nF$. Initially the value of $g_{m1} = g_{m3} = 628.28\mu S$ was selected to give f_o = 1 MHz. Appropriate values of the control voltages were selected to give $g_{m1} = g_{m3}$ = $628.28\mu S$, $315.09\mu S$, $157.73\mu S$ and $78.701\mu S$ so as to give f_o= 1MHz, 500kHz, 250kHz and 125kHz respectively. The tunability of the f_o is shown in Fig. 6. The frequency response for the universal biquad is shown in Fig 7.

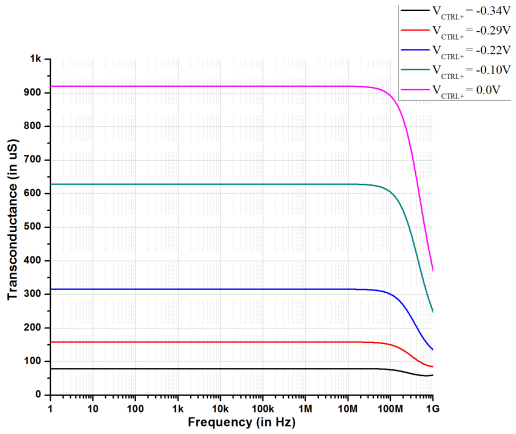


Fig. 4: Variation of Transconductance with V_{CTRL+} (V_{CTRL-} = -0.35V)

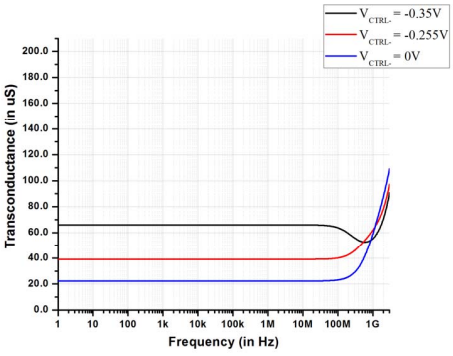


Fig. 5: Variation of Transconductance with V_{CTRL-} (V_{CTRL+} = -0.35V)

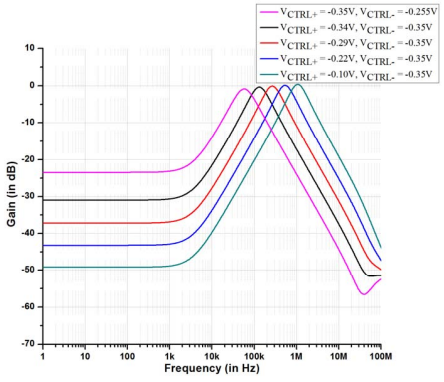


Fig. 6: Magnitude response of BP filter, showing pole frequency tunability

TABLE II. RANGE OF TRANSCONDUCTANCE FOR DIFFERENT ARCHITECTURES OF VDCC

Reference	Range of Transconductance	Controlling Parameter	Power Dissipation	Supply Voltage
[12]	0.27mS-2.81mS	V_{set_gm} = 0.16-1.4V	18mW	±2.5V
[13]	255μS-1919μS	I_{set_gm} = 10-150μA	-	±1.0V
[14]	14μS-2.8mS	V_{set_gm} = 0.07-1.4V	45mW	±2.5V
[9]	100.5μS-277mS	I_{B1} = 6.75-50μA	0.869mW	±0.9V
Proposed	23μS-783mS	V_{CTRL+}= -0.35V−0V, V_{CTRL-}= 0V− -0.35V	1.718mW	±0.9V

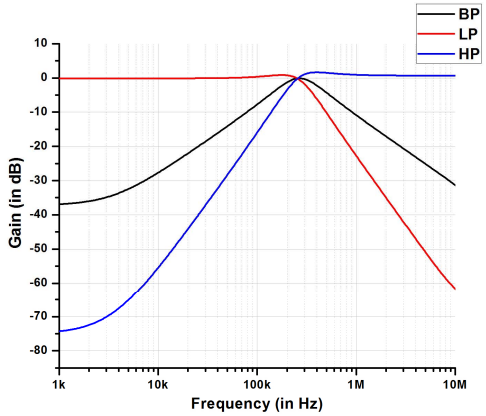


Fig. 7: Magnitude response of HP, BP, LP filters for a pole frequency of 250 kHz.

V. CONCLUSIONS

Our work presents a variable transconductance VDCC (VT-VDCC) with increased tunability range for the transconductance parameter for lower power dissipation than conventional VDCCs. The proposed design uses a symmetric diode-connected load based control stage for the enhancement of the tunability range. The proposed VT-VDCC has been used in the design of a novel second order current-mode universal biquad. The pole frequency of the biquad depends on the transconductance and therefore its enhanced tunability range has been demonstrated. The proposed filter is suitable for CMOS IC technology because of its electronic tunability and use of all grounded passive elements.

REFERENCES

[1] D. Biolek, R. Senani, V. Biolkova and Z. Kolka, "Active element for analog signal processing: classification, review, and new proposals," Radioengineering, vol. 17, no. 4, pp. I 5-32,2008.

[2] D. Prasad, A. Ahmad, A. Shukla, A. Mukhopadhyay, B. B. Sharma, "Novel VDCC Based Low-Pass and High-Pass Ladder Filters," In Proc. of Annual IEEE India Conference (INDICON 2015), 2015, p. 1-3.

[3] S. Rana, A. K. Kumawat and P. Kumar, "A universal current mode KHN biquad filter using voltage differencing current conveyor," 2016 IEEE 1st International Conference on Power Electronics, Intelligent Control and Energy Systems (ICPEICES), Delhi, 2016, pp. 1-5.

[4] R. Sotner, N. Herencsar, J. Jerabek, R. Prokop, A. Kartci, T. Dostal, K. Vrba, "Z-copy controlled-gain voltage differencing current conveyor: advanced possibilities in direct electronic control of first-order filter," Elektronika Ir Elektrotechnika, vol. 20, no. 6, pp. 77-83, 2014.

[5] D. Prasad, D. R. Bhaskar, M. Srivastava, "New Single VDCC-based Explicit Current-Mode SRCO Employing All Grounded Passive Components," Electronics, vol. 18, no. 2, pp. 81-88, 2014.

[6] R. Sotner, J. Jerabek, J. Petrzela and T. Dostal, "Voltage differencing current conveyor based linearly controllable quadrature oscillators," 2016 International Conference on Applied Electronics (AE), Pilsen, 2016, pp. 237-240.

[7] R. Sotner, J. Jerabek, J. Petrzela, N. Herencsar, R. Prokop, and K. Vrba,: 'Second-order simple multiphase oscillator using z-copy controlled gain voltage differencing current conveyor', Elektron. Elektrotech., 2014, 20, (9), pp. 13–18, doi: 10.5755/j01.eee.20.9.8709

[8] R. Sotner, J. Jerabek, N. Herencsar, J. Petrzela, A. Kartci and T. Dostal, "Discussion on two solutions of inductance simulators using single controlled gain voltage differencing current conveyor and the most important parasitic effects," 2016 26th International Conference Radioelektronika (RADIOELEKTRONIKA), Kosice, 2016, pp. 162-167.

[9] F. Kacar, A. Yesil, S. Minaei, H. Kuntman, "Positive/negative lossy/lossless grounded inductance simulators employing single VDCC, and only two passive elements," AEU – Int. Journal of Electronics and Communications, vol. 68, no. 1, pp. 73-78, 2014.

[10] Quoc-Hoang Duong, Le-Quan, and Sang-Gug Lee, "An All CMOS 84dB-Linear Low-Power Variable Gain Amplifier," Digest of Technical Papers Symposium on VLSI Circuits, pp. 114-117, 2005.

[11] Quoc-Hoang Duong, T. J. Park, E. J. Kim and Sang-Gug Lee, "An all CMOS 743 MHz variable gain amplifier for UWB systems," 2006 IEEE International Symposium on Circuits and Systems, Island of Kos, 2006, pp. 4 pp.-.

[12] R. Sotner, J. Jerabek, R. Prokop, V. Kledrowetz, J. Polak, L. Fujcik, and T. Dostal. "Practically implemented electronically controlled CMOS voltage differencing current conveyor." In Circuits and Systems (MWSCAS), 2016 IEEE 59th International Midwest Symposium on, pp. 1-4. IEEE, 2016.

[13] R. Sotner, J. Jerabek, N. Herencsar, T. Dostal, and K. Vrba. "Design of Z-copy controlled-gain voltage differencing current conveyor based adjustable functional generator." Microelectronics Journal 46, no. 2 (2015): 143-152.

[14] R.. Sotner, J. Jerabek, R. Prokop, and V. Kledrowetz. "Simple CMOS voltage differencing current conveyor-based electronically tunable quadrature oscillator." Electronics Letters 52, no. 12 (2016): 1016-1018.

[15] E. Brunn, "CMOS high speed, precision current conveyor and current feedback amplifier structures", Int. J. Electron, vol. 74, pp.93-100, 1993.

ACS APPLIED MATERIALS & INTERFACES

Subscriber access provided by DELHI TECH UNIV

Biological and Medical Applications of Materials and Interfaces

ZnO nanoparticles modified with an amphipathic peptide show improved photoprotection in skin

Anusha Aditya, Sabyasachi Chattopadhyay, Nidhi Gupta, Shamshad Alam, Archana Palillam Veedu, Mrinmoy Pal, Archana Singh, Deenan Santhiya, Kausar Mahmood Ansari, and Munia Ganguli

ACS Appl. Mater. Interfaces, **Just Accepted Manuscript** • DOI: 10.1021/acsami.8b08431 • Publication Date (Web): 03 Dec 2018

Downloaded from http://pubs.acs.org on December 9, 2018

Just Accepted

"Just Accepted" manuscripts have been peer-reviewed and accepted for publication. They are posted online prior to technical editing, formatting for publication and author proofing. The American Chemical Society provides "Just Accepted" as a service to the research community to expedite the dissemination of scientific material as soon as possible after acceptance. "Just Accepted" manuscripts appear in full in PDF format accompanied by an HTML abstract. "Just Accepted" manuscripts have been fully peer reviewed, but should not be considered the official version of record. They are citable by the Digital Object Identifier (DOI®). "Just Accepted" is an optional service offered to authors. Therefore, the "Just Accepted" Web site may not include all articles that will be published in the journal. After a manuscript is technically edited and formatted, it will be removed from the "Just Accepted" Web site and published as an ASAP article. Note that technical editing may introduce minor changes to the manuscript text and/or graphics which could affect content, and all legal disclaimers and ethical guidelines that apply to the journal pertain. ACS cannot be held responsible for errors or consequences arising from the use of information contained in these "Just Accepted" manuscripts.

ACS Publications

is published by the American Chemical Society. 1155 Sixteenth Street N.W., Washington, DC 20036

Published by American Chemical Society. Copyright © American Chemical Society. However, no copyright claim is made to original U.S. Government works, or works produced by employees of any Commonwealth realm Crown government in the course of their duties.

ZnO nanoparticles modified with an amphipathic peptide show improved photoprotection in skin

Anusha Aditya[a,b], *Sabyasachi Chattopadhyay*[a] , *Nidhi Gupta* [c], *Shamshad Alam*[d], *Archana Palillam Veedu*[a], *Mrinmoy Pal*[a], *Archana Singh*[a,b], *Deenan Santhiya*[c], *Kausar M. Ansari*[d], *Munia Ganguli*[a,b]*

[a] CSIR - Institute of Genomics and Integrative Biology, Mathura Road, New Delhi, India.

[b]Academy of Scientific and Innovative Research (AcSIR), Anusandhan Bhawan, 2 Rafi Marg, New Delhi-110001, India.

[c]Delhi Technological University, Department of Applied Chemistry and Polymer Technology, New Delhi-110042, India.

[d]CSIR-Indian Institute of Toxicology Research, Post Box no.-80, Mahatma Gandhi Marg, Lucknow, Uttar Pradesh-226001, India.

Contact address: Lab-219, Discovery Genomics Building, CSIR-Institute of Genomics and Integrative Biology, Mathura Road, New Delhi- 110025.

[*] Corresponding author email id: mganguli@igib.in, Tel: 011-29879225

KEYWORDS: ZnO nanoparticles, cell penetrating peptide, UV-B rays, photoprotection, cytotoxicity

ABSTRACT

ZnO nanoparticles of different sizes were functionalized with an amphipathic peptide and its effect on nanoparticle stabilization and UV photoprotective activity was studied in this article. The peptide modified nanoparticles exhibited lower aggregation, significant reduction in Zn^{2+} leaching *in-vitro* and even inside the cells for smaller particle sizes, reduced photocatalytic activity and reduced cellular toxicity under UV-B treated conditions. In addition, the peptide modified 60 nm sized ZnO nanoparticles showed lower genotoxicity, lower oxidative stress induction levels, less DNA damage responses and less immunogenic potential than the bare counterparts in presence of UV-B rays. They localized more in the stratum corneum and epidermis *ex-vivo* indicating better retention in epidermis and demonstrated improved UV-B protection and/or skin integrity in SKH-1 mice *in-vivo* as compared to unmodified nanoparticles and commercial UV protective agents tested. To our knowledge, this is the first report on application of peptide modified ZnO nanoparticles for improved photoprotection.

INTRODUCTION

Zinc oxide (ZnO) nanostructures exhibit diverse chemical, biological and clinical applications. Their unique properties like high refractive index and UV absorption over a wide wavelength range have been utilized for application in sunscreens[1], possibility of synthesis in a wide variety of shapes including nanosphere, nanorod, nanoflower, nanosheet or nanofiber[2-4] has been utilized for cargo delivery to cells[5], wide band gap (~3.4 eV) semiconductor property coupled with efficient near UV emission has been used in biosensors and bio-imaging applications[6] and photosensitive properties or formation of Reactive Oxygen Species (ROS) has led to applications as photodynamic therapeutic agent, antimicrobial agent or in combinatorial therapies[7-10].

Zinc oxide and Titanium oxide in both macro and nano sizes can offer UV protection in the UV-B range (290-320 nm) and UV-A range (320-400 nm)[11]. In case of nanoparticles, concerns have been raised about their permeation into deeper layers of skin and further into systemic circulation resulting in possible toxic and immune responses[12,13]. Although there are controversies regarding their penetration across the terminally differentiated and cornified layers of skin (stratum corneum)[14], it appears that there is minimal possibility of systemic exposure on topical application of ZnO nanoparticles[15,16]. Only under chemical (acetone) pretreatment/dermabrasion/ tape-stripped/flexed or massaged condition, the nanoparticles are found to be trapped in the hair follicular ostium or skin folds in pig-skin/human volunteers[17,18]. However, recent studies by Homes *et al* showed that hydrolysis of ZnO nanoparticles in the skin folds leads to formation of labile Zn^{2+} ions which permeate into viable epidermis and may elicit toxicity[19]. Moreover, repeated dosage of nanoparticle-based sunscreen in presence of UV-rays leads to the presence of Zn tracer element in blood and urine after 2 days which continued to increase up to 9 days[20,21]. It is also intuitive that Zn^{2+} penetration in skin and hence toxicity[22,23] can be accelerated due to the compromised barrier function of the skin due to age, presence of wounds or other skin disorders and also in presence of UV rays[24]. Several reports have also shown influence of size, shape and surface chemistry of ZnO nanoparticles on cytotoxicity, genotoxicity, mutagenicity as well as uptake routes in normal skin cell lines, skin tissue as well as compromised skin conditions in *in-vitro, ex-vivo* and *in-vivo* models[25-27]. Toxicity of ZnO nanoparticles has mainly been attributed to their propensity to dissolve into ionic state in the biological milieu depending upon their size, shape and surface charge[28].

In view of the above, a robust strategy to delimit Zn^{2+} ionic dissolution is necessary for improved application. The most common method of surface stabilization of ZnO nanoparticles is through covalent modification with triethoxysilyl moieties which subsequently undergo polymerization through formation of siloxane bridges[28]. However, such silane-modified

nanoparticles show limited stability in acidic pH when entrapped within lysosomal (pH 4.0) or late endosomal (pH 5.5) compartments and undergo dissolution to release Zn^{2+} ions at potentially cytotoxic levels[29]. Other strategies like iron doping[30] or poly(ethylene)Glycol (PEG) modification[31] of ZnO has also been used for this purpose. Though the photocatalytic potential decreases in this case, polymer modification generally delimits further applications of the nanoparticles as described in the literature[32].

Another major concern is the aggregation propensity of ZnO nanoparticles primarily in biological milieu[33] which leads to their spontaneous removal on sweating or wiping and also chances of mechanical disruption of the corneum layer[34]. Although covalent attachment of amphiphiles has been done in other metal oxide nanoparticles like silica and iron oxide to address such problems[35,36], these have not been attempted in case of ZnO nanoparticles.

In this study, we have developed an amphipathic peptide-coated ZnO nanoparticle assembly for improved stabilization of the nanoparticles and studied their UV protective activity. We observed that for all the nanoparticle sizes, the peptide modified nanoparticles showed lower aggregation, significant reduction in Zn^{2+} leaching *in vitro* and even inside the cells for smaller particle sizes, reduced photocatalytic activity and reduced cellular phototoxicity under UV-B treated conditions. Further, the 60 nm modified nanoparticles showed lower skin tissue penetration *ex vivo* (with maximum residence in the upper layer of the stratum corneum and epidermis) and demonstrated improved UV protection efficacy and skin integrity when applied to SKH-1 mice *in vivo* as compared to the commercial UV protective agents tested. In addition, the peptide modified 60 nm sized ZnO nanoparticles showed lower genotoxicity, lower oxidative stress induction levels, less DNA damage responses (CPD and 6,4-PP formation) and less immunogenic potential than the bare counterparts in presence of UV-B rays. To our

knowledge, this is the first report on improvement of stability of ZnO nanoparticles using amphipathic peptides for enhanced photoprotection.

RESULTS

Amphipathic peptide M9 can be attached to the surface of the ZnO nanoparticles

We modified ZnO nanoparticles with a secondary amphipathic peptide M9 (CRRLRHLRHHYRRRWHRFRC) to stabilize the nanoparticles, reduce aggregation and dissolution and analyze their UV photoprotective property. We first synthesized ZnO nanoparticles of 3 primary particle sizes (~30, 60 and 100 nm) using water as a variable to control nanoparticle growth (Ostwald ripening), as has been demonstrated earlier[37]. **Figure 1 a,b,c** are the representative Transmission Electron Microscopy (TEM) images of the nanoparticles of three different sizes (termed as ZnO-30, ZnO-60 and ZnO-100). The nanoparticles were then modified with surface amine groups using APTES (3-(Aminopropyl) triethoxysilane) and subsequently covalently linked to M9 peptide through NHS/EDC chemistry as described in the Materials and Methods section. TEM images depicting the morphology of the nanoparticles on APTES and M9 modification are shown in **Figure 1 d,e,f** and **Figure 1 g,h,i**. The Wide Angle X-ray diffraction (WAXRD) of the ZnO nanoparticles shows signatures corresponding to the ZnO [JCPDS-79-0205] phase suggesting that the nanoparticles are in crystalline state with majorly hexagonal wurtzite ZnO crystal structure (**Figure 1j**).

Figure 2a shows a schematic representation of the steps involved in creating the peptide modified ZnO nanoparticles**.** The success of each modification step was confirmed through Fourier Transform Infra-Red (FTIR) spectroscopy and Dynamic Light Scattering (DLS) as shown in **Figure 2b** and **Figure 2c** respectively for ZnO-30 nanoparticles. A strong Zn–O stretching band centered at 451 cm^{-1} and peaks at 1580 cm^{-1} and 1407 cm^{-1} (due to the

symmetrical and asymmetrical stretching modes of carboxylate groups arising from the zinc acetate precursor) could be identified from the spectra. APTES modification showed a slight shift and a decrease in the intensity in these peaks in relation to the diagnostic band of Zn-O stretching[38]. Moreover, an additional strong band at 1005 cm^{-1} , which corresponds to Zn-O-Si stretching vibrations, was observed. The peaks at about 1574 cm^{-1} and 1517 cm^{-1} could be attributed to the bending vibration of N–H and the band at about 690 cm^{-1} to the Si-O-Si bond stretching vibration. An additional shoulder at 2937 cm^{-1} corresponded to the C–H stretch of alkane groups present in APTES[39]. After attachment with M9, the peaks at 1407 and 1574 cm^{-1} shifted, indicating the replacement of acetate groups, and a new band at 1650cm^{-1} indicated characteristic amide (-CO-NH-) stretching vibration arising from the peptide[40]. The appearance of two main characteristic peaks of arginine at 1453 cm^{-1} (amide II) and 1651 cm^{-1} also indicated successful conjugation[41]. The N–H stretching of primary and secondary amine groups of guanidine were observed near 3100–3500 cm^{-1}. The intense peak at 1020-1250 cm^{-1} indicated C-N stretching vibrations arising from primary aliphatic amines present in M9-peptide. Similar patterns were observed in case of peptide modification of ZnO-60 and ZnO-100 nanoparticles(data not shown).

The hydrodynamic diameter (size by number) and TEM sizes of both the modified and unmodified nanoparticles as well as the alterations in surface charges with different modification steps (as indicated by zeta potential measurements) were measured and are summarized in Table 1. Increase in size and surface charge has been noted in all the cases on modification, as expected. A range of concentrations of peptide was used for attachment on nanoparticle surface from which an appropriate concentration was chosen (see **Figure S1** for further explanation).

Modification with M9 peptide decreases aggregation and dissolution of ZnO nanoparticles

Subsequently we monitored the propensity of the nanoparticles towards aggregation and dissolution after being surface-modified with the peptide M9. Aggregation was first monitored in water through size by intensity measurements using Dynamic Light Scattering. Size by intensity considers particles of all sizes present in the sample and thereby gives an appropriate reflection of presence of aggregates. **Figure 3a** represents the average size by intensity values of the bare and modified nanoparticles of all the sizes with time. Bare ZnO-30 nanoparticles showed an average size of 115.9±0.9 nm at 0 hr which increased to 461.6±10.45 nm after 4 hours. On the other hand, ZnO-30+M9 nanoparticles showed an almost constant size by intensity over a period of 4 hours indicating a homogeneous population. Both ZnO-60 and ZnO-100 nanoparticles showed very high average particle size, 181.9±2.90 nm and 227.7±9.70 nm respectively at 0 hr. The aggregate size of ZnO-60 became 607.9±16.01 nm after 4 hours and ZnO-100 grew to 414.6±62.00 nm after 2 hours, beyond which it was impossible for analysis due to precipitation of large aggregates. The aggregate size was considerably lower in case of ZnO-60+M9 which showed initial size of 278.30±0.88 nm and remained stable up to 4 hours at 251.90±52.85 nm. Although no precipitation was observed in case of ZnO-100+M9 as well even after 4 hours, the aggregate size was as high as 670.5±62.60 nm. Similar aggregation trend was also noticed in DMEM complete media although there seemed to be better stabilization of both the unmodified and the modified nanoparticles as compared to that observed in water **(Figure S2).**

Stability against ionic dissolution was also measured for both the unmodified and peptide modified ZnO nanoparticles *in vitro* and also inside the keratinocyte cells in culture using the zinquin assay[31,42]. As shown in **Figure 3b**, the ionic concentration of zinc (free Zn^{2+}) increases over a period of 4 hours. All the three sizes of bare nanoparticles showed almost similar dissolution with time as indicated by the fluorescence intensity of the Zn^{2+} bound to zinquin ester. However, the peptide-modified nanoparticles attained a maximum fluorescence intensity

which was ten times lower than that of the unmodified ones at the longest measured time point indicating considerably less Zn^{2+} dissolution.

In order to check the dissolution inside the cells, we first checked cellular toxicity profile of the nanoparticles of all three sizes and their M9 modified counterparts in HaCaT cells at 24 hours in order to choose an appropriate concentration for administration of nanoparticles. While the cells tolerated 25µg/ml of most of the unmodified and all the modified nanoparticles, most of the unmodified nanoparticles were quite toxic to the cells beyond a concentration of 50µg/ml (**Figure S3).** Therefore, cellular uptake was measured at a concentration of 40 µg/ml which is in between these two concentrations. We confirmed that both the unmodified and modified nanoparticles were taken up by the HaCaT cells at this concentration by quantitaing through flow cytometry (see **Figure S4 a**) and fluorescence microscopy (**Figure S4 b**). In order to ensure that the signals are not due to the detached peptides carrying the fluorophore, TEM images of cells containing unlabeled nanoparticles of 60 nm size were also analyzed (**Figure S4 c**). The nanoparticles were observed in the cytoplasmic region of the cells and ZnO-60 nanoparticles were also observed to be entrapped in endocytotic vessicles. All subsequent experiments were carried out at this concentration of nanoparticles.

Figure 3c demonstrates the dissolution of the nanoparticles to release free Zn^{2+}inside the cells. The 30nm bare ZnO nanoparticles showed strong cellular leaching as indicated by the high fluorescence positive cells and high intensity of fluorescence as well. However, there was less leaching from the higher sized nanoparticles inside the cells as compared to that observed *in vitro*. In all the cases, the M9 modified nanoparticles showed low ionic dissolution.

Photocatalytic degradation is observed in bare but not in peptide modified ZnO nanoparticles

We also checked the photostability of the modified and unmodified nanoparticles using a protocol described in the Materials and Methods section. In a photocatalytic degradation experiment, absorption spectra measurement when bare ZnO nanoparticles were used showed 60-90% decrease of the maximum absorption peak of Rhodamine at 554 nm (**Figure 4 a,c,e**) after 3 hours of exposure to sunlight indicating poor photostability of the nanoparticles. This was not the case for M9 modified ZnO nanoparticles of smaller sizes. As seen in **Figure 4b** and **Figure 4d**, ZnO-30+M9 and ZnO-60+M9 were stable even after 3 hours, showing ~10-20% degradation whereas ZnO-100+M9 showed higher decrease in the maximum absorption (**Figure 4f**). Thus, modification with M9 peptide enhanced the photostability in case of ZnO-30+M9 and ZnO-60+M9 nanoparticles while the effect, although present, is milder in case of the ZnO-100+M9 nanoparticles.

Peptide modification reduces cellular toxicity on UV-B irradiation

We next wanted to see the effect of these nanoparticles on cellular toxicity in presence of UV-B rays at a concentration of 40 µg/ml. As shown in **Figure 4g**, toxicity measurement using MTT assay 24 hours after the incubation indicates the following- a) for all the nanoparticle sizes, the M9 modified nanoparticles exhibited significantly higher cell viability in comparison to bare ZnO nanoparticles even in the presence of UV-B rays b) while treatment with UV-B rays without any nanoparticle treatment left only 74.47% cells viable after 24 hours, pre-treatment with unmodified nanoparticles showed more toxicity in all the cases, leaving only 65.37%, 52.8% and 65.74% cells viable 24 hours after UV-B irradiation in case of ZnO-30, ZnO-60 and ZnO-100 nanoparticles respectively. This might happen due to the photodynamic effect of ZnO nanoparticles which has been reported earlier[43]. On the other hand, pre-treatment with M9 modified ZnO nanoparticles showed much less toxicity in presence of UV-B rays and high cell viability was noted in all the cases.

All these results indicate that although modification with M9 peptide causes less aggregation, dissolution, confers photocatalytic stability and reduces phototoxicity for all the nanoparticle sizes, the largest sized nanoparticles of 100 nm size still showed strong aggregation and more tendency of photocatalytic degradation as compared to the others. The effect of stabilization on M9 modification was similar for 30 nm and 60 nm sized nanoparticles. However, smaller sized nanoparticles are generally not preferred for sunscreen applications[44]. Hence, we carried out all subsequent experiments using ZnO-60 nanoparticles.

Modified ZnO nanoparticles are primarily present in the epidermis when administered *ex vivo* to human skin tissue

We next analyzed transdermal penetration and localization of the nanoparticles in the skin *ex-vivo* and *in-vivo*. Independent administration of 200 μg/cm^{2}of ZnO-60 and ZnO-60+M9 to Strat-M membrane (which mimics skin tissue) in stirring condition in a Franz Diffusion Apparatus showed minimal transdermal permeation with only 1.73% and 0.02% of ZnO-60 and ZnO-60+M9 respectively being detected in the receptor chamber after 4 hours and 2.83% and 0.01% respectively after 24 hours (**Figure 5a**). Transmission Electron Microscopy experiments indicate that when human skin tissue was exposed to 200 μg/ml or 0.156 mg/cm^2 of ZnO-60 or ZnO-60+M9 in independent experiments consecutively for 3 days, ZnO-60 nanoparticles were present in the stratum corneum, viable epidermis as well as in the dermis in small quantities as seen through visual observation while ZnO-60+M9 nanoparticles were found mostly in the outer stratum corneum and the viable epidermis (**Figure 5b**). The observation was further confirmed through Scanning Electron Microscopy coupled with Energy Dispersive X-ray spectroscopy (**Figure 5c** and **Figure 5d**). With the same exposure of nanoparticles, dermis from the human foreskin tissue was recovered (details in Materials and

Methods section) and analyzed for Zn content. As shown in **Figure 5d**, there was a higher presence of Zn in the dermis when ZnO-60 nanoparticles were administered whereas Zn from ZnO-60+M9 was undetectable in the dermis similar to the control (see also **Table S1**). These results indicate higher retention in the epidermis in case of the peptide modified nanoparticles and minimal dermal or transdermal presence.

ZnO+M9 nanoparticles offer protection against UV-B radiation in SKH-1 mice

The *in-vivo* effect of UV-B radiation after administration of the unmodified and modified 60 nm sized ZnO nanoparticles was studied in SKH-1 mice model according to the study plan shown in **Figure 6a**. UV-B radiation can cause cutaneous toxicity or inflammation as well as enhancement in epidermal thickness and integrity loss of the skin. In our study, SKH-1 mice exposed to repeated UV-B dosages for 3 consecutive days started showing visible erythema or redness. The change in epidermal thickness is evident on visual observation (**Figure 6b)** and depicted quantitatively in **Figure 6c**. It is observed that the epidermal thickness increased in case of UV-B treatment by 1.96 folds with respect to control, thereby indicating high inflammation. Bare ZnO-60 nanoparticle treatment also increased the epidermal thickness 1.90 times higher with respect to the control. With pre-treatment of bare ZnO-60 nanoparticles (doses mentioned in the Materials and Methods section) followed by UV-B exposure, the epidermal thickness increased to 3.06 folds with respect to control, showing phototoxicity over and above the effect of only UV-B treatment. On the other hand, ZnO-60+M9 nanoparticles showed mild or no inflammation by themselves, and even when coupled with UV-B treatment, there was minimum inflammation and epidermal thickness was similar to that of control mice skin, indicating photoprotection. Interestingly, known commercial UV-protective formulation -either without ZnO nanoparticles (Formulation A) or with ZnO nanoparticles (Formulation B) caused either huge inflammation with increase of epidermal thickness of around 4.05 folds at this UV-B dosage (Formulation A) or visible tissue damage of the dermis as indicated by large

vesicle formation (Formulation B). Thus, there seems to be less protection from UV-B radiation in case of these formulations as compared to ZnO-60+M9. **Figure 6d** shows the quantification of Zn in full thickness skin as measured through Atomic Absorption Spectroscopy in absence and presence of UV-B radiation after exposure to nanoparticles. ZnO-60 nanoparticles showed 11.79 folds higher presence of Zn with respect to the control in absence of UV-B radiation as compared to a lower value of around 2.75 fold in case of ZnO-60+M9 nanoparticles under the same condition. Interestingly, we found marked increase in presence of ZnO-60 nanoparticle (15.75 folds w.r.t control) and marginal increase in ZnO-60+M9 nanoparticles (5.89 folds w.r.t control) under UV-B exposure. We also compared the Zn concentration levels with known formulations- Formulation A without ZnO nanoparticles and Formulation B with ZnO nanoparticles. As expected, there was nearly undetectable presence of Zn in Formulation A. However, even in Formulation B, we observed small but insignificant presence of Zn.

Administration of M9-modified ZnO nanoparticles to skin cells can reduce deleterious effects of UV-B radiation on them

Effect on Genotoxicity

We also studied the possible DNA damage to keratinocytes on pre-treatment of the cells with modified and unmodified ZnO-60 nanoparticles followed by UV-B treatment. As shown in **Figure 7a** and **Figure 7b**, there was a significant increase in the DNA damage measured by tail extent moment which increased from a mean of 1.41 in untreated cells to 7.24 on 200mJ/cm^2 of UV-B treatment. Bare ZnO-60 nanoparticles by themselves caused significant DNA damage with a mean tail extent moment of 6.85 with respect to untreated samples while ZnO-60+M9 caused significantly less damage of DNA with a mean tail extent moment of 1.02. Interestingly, in presence of UV-B rays, ZnO-60 showed higher DNA damage (tail extent moment=10.41) with respect to only UV-B induced damage (tail extent moment=7.24). In

contrast, ZnO-60+M9 nanoparticles decreased the DNA damage in presence of UV-B rays quite significantly as seen from the Tail extent moment of 2.1.

Effect on production of Reactive Oxygen Species (ROS) and level of anti-oxidant enzyme

As seen in **Figure 7c** bare ZnO-60 nanoparticles alone could induce 3.93 times ROS production than control un-irradiated cells while ZnO-60+M9 under un-irradiated conditions retained the basal ROS levels necessary for proper functioning of different organelles. While UV-B rays increased the basal ROS levels 1.73 times with respect to control un-irradiated cells, there was 4.29 times increase when a pre-treatment of ZnO-60 nanoparticles was given. On the other hand, in case of ZnO-60+M9, the ROS levels increased marginally by 3.01 times with respect to control un-irradiated cells and 1.73 times with respect to UV-B irradiated cells. On measurement of the activity of the ROS scavenging enzyme Superoxide dismutase (SOD), we observed that the inhibition rate of SOD was significantly higher with pretreatment of ZnO-60 in absence of UV-B rays then the UV-B control **(Figure 7d).** On the other hand, SOD inhibition rate in the presence of UV-B and ZnO-60 pretreatment, showed impaired enzyme activity accounting for higher toxicity. In case of ZnO-60+M9, both in presence and absence of UV-B radiation, similar SOD activity was observed as in the control UV-B treated and untreated cells.

In such a situation, though ROS production is high, higher SOD activity might be able to quench excess free radicals present thus showing less toxicity. In case of ZnO-60+M9, both in presence and absence of UV-B radiation, similar SOD activity of 174.26% and 190.06% respectively was observed which was similar to the control UV-B treated and untreated cells. In such a situation, though ROS production is high, higher SOD activity might be able to quench excess free radicals present thus showing less toxicity. The M9 modified ZnO-60 nanoparticles also showed better membrane integrity of keratinocytes both in presence and

absence of UV-B rays, as confirmed by Lactate Dehydrogenase assay **(Figure S5 a).** The high ROS production and impaired SOD activity might eventually lead to reduced activity of final apoptotic signaling markers (Caspase3/Caspase9) which showed minimal expression in cells with ZnO-60 nanoparticle and UV-B treatment **(Figure S5 b).**

Effect on cell cycle

We also checked if there is any aberration to normal cell cycle distribution 24 hours after irradiation with UV-B rays. As shown in **Figure 7e** and **Figure 7f**, control samples showed 52.7±1.83% cells in G0/G1 phase, 21.23±1.55% in S phase and 26.06±1.4% cells in the G2/M phase. However, we observed a G2/M phase arrest as the number of cells in the G0/G1 phase decreased to 30.95±3.46% and the percentage cells in G2/M phase increased to 42.25±0.21% on treatment with ZnO-60. Interestingly pre-incubation with ZnO-60 nanoparticles followed by UV-B treatment showed both S phase and G2/M phase arrest as the percentage cells in G0/G1 phase decreased to 33.23±1.24% and that in S phase increased to 33.5±5.3% while that in G2/M phase increased to 33.27±4.30%. In contrast, both in the presence of only ZnO-60+M9 nanoparticles (G0/G1: 54.03±3.69%, S: 25.13±1.82%, G2/M: 20.83±1.90%) and in the presence of both ZnO-60+M9 nanoparticles and UV-B rays (G0/G1:48.3±2.8%, S: 26.03±1.79%, G2/M: 25.67±1.67%), the cell cycle progressed in a similar fashion to that of normal control cells.

Effect on UV induced dimer formation:

As shown in **Figure S6 a** and **Figure S6 b**, we observed that bare ZnO-60 nanoparticles induced CPD formation which is 2.5 times more than that induced by only UV-B radiation but ZnO-60+M9 nanoparticles seemed to perform a protective function by decreasing CPD formation in comparison to that obtained on UV-B treatment. In case of 6,4-PP production,

both ZnO-60 and ZnO-60+M9 nanoparticles seemed to show some protection with respect to the cells exposed to only UV-B treatment.

Effect on production of pro-inflammatory cytokines:

As shown in **Figure S6 c** and **Figure S6 d,** significant drop in production level of proinflammatory cytokines IL-6 and TNF-α level was observed when ZnO-60+M9 pretreated keratinocyte cells were exposed to UV-B radiation in comparison to those treated with ZnO-60 nanoparticles under similar conditions. As shown in **Figure S6 e** and **Figure S6 f**, the expression of other cytokines like IL-2 and IL-12 were maintained at a low level of 1.5-2 pg/ml in case of pretreatment of both ZnO-60 and ZnO-60+M9 both in presence and absence of UV-B radiation.

All these observations indicate that treatment of keratinocytes with ZnO-60+M9 nanoparticles show better viability, lower DNA damage, less oxidative stress, less UV- induced dimer production, better cell cycle distribution and less immune response both in presence and absence of UV-B radiation as compared to the bare ZnO-60 nanoparticles.

DISCUSSION

Zinc oxide nano-formulations are increasingly preferred over micron-sized particles in sunscreens since they are transparent in nature and protect the skin against both UV-A and UV-B rays. However, despite their widespread use, a lot of controversies have arisen regarding their possible toxic effects. The discussion centers around two main points- a) strategies towards maintaining good dispersion stability and low aggregation propensity of the nanoparticles while achieving photoprotection and b) understanding the extent of penetration

of the ZnO nanoparticles, including Zn^{2+} leaching, and its possible associated toxicity. Our study addresses these two major aspects using peptide modified ZnO nanoparticles.

In order to prevent sunlight induced erythema, UV filters should ideally spread over a large surface area of the skin instead of forming patches because of aggregation[45]. Since ZnO nanoparticles have inherent tendency to form agglomerates and aggregates in formulations[11] as well as in biological milieu, various coatings of ZnO nanoparticles with aluminum oxide, silicon oxide or silicone oils has been used to increase dispersion stability[46]. In our study, we have tried to achieve this by using an amphipathic peptide M9 as a coating on the ZnO surface. It has been shown in the literature that combination of hydrophobic and hydrophilic residues in the peptide can expel water from the core and help in self-assembly and dispersion in aqueous media[47,48]. In an attempt at self-assembly of hydrophobic peptides on silica nanoparticles, it has been demonstrated that the 7-mer peptides in a solution with pH 7.4 can exhibit adsorption on the nanoparticle surface when peptide-surface interactions are favored, and this can reduce aggregation of the nanoparticles[49]. We therefore expected the amphipathic M9 peptide modification to be an appropriate choice. Moreover, we rationalized that the presence of nine arginines and four histidines in the sequence would impart positive charge on the ZnO surface when coated, and also help in reducing their aggregation. This peptide has high skin compatibility and long residence (up to 24 hours) in the upper layers of the skin (stratum corneum and epidermis) with no toxicity and negligible transdermal penetration[50-52]. Literature reports indicate that the interaction of nanoparticles with the upper epidermal lipids and the capability to adhere to the skin might help in better efficacy as UV protectant[45,53]. Since this peptide was previously demonstrated to interact with skin lipids and allow mild fluidization[50] along with interaction with the corneo-desmosomal proteins, we presumed that coating ZnO with this peptide could lead to better retention of the nanoparticles in skin, limited transdermal penetration and thereby possibility of improved photoprotective

efficiency. M9 is additionally known to enter skin cells, and thus was likely to further enhance the uptake of the modified nanoparticles in keratinocytes in the epidermis. We also speculated that the coating is likely to delimit dissolution of the nanoparticles into free Zn^{2+} due to the shielding effect of the peptide . We also independently coated ZnO nanoparticles with a known cell penetrating peptide (TAT) and a polymer (PEI). ZnO+M9 showed superior cell viability in presence of UV-B radiation *in-vitro* as compared to the others indicating that the choice of coating plays a role in determining the extent of toxicity (**Figure S7a**). Additionally, a comparison of the cytotoxicity of ZnO and ZnO+M9 nanoparticles was carried out with 4 commercial products: ZnO-APTES, ZnO coated with silicone oil, ZnO-SiO_2 core-shell structure and ZnO microparticles. It was observed that both ZnO-60 and ZnO-60+M9 have higher cellular viability both in presence/absence of UVB rays (**Figure S7b**) at multiple concentrations. This indicates that the peptide modification can be an improved strategy over known and commonly used commercial strategies for nanoparticle stabilization.

Through a series of systematic studies using ZnO nanoparticles of three different sizes (30nm, 60 nm and 100 nm), we have established the role of M9 peptide to counter the problems related to aggregation and dissolution. The 30 and 60 nm bare nanoparticles show similar aggregation kinetics (**Figure 3a and Figure S8a**) and the peptide modification led to lowering of the aggregation propensity in water as well as in DMEM (**Figure 3a** and **Figure S2**). Overall aggregation on peptide modification is significantly lower in DMEM in all the cases presumably because of the high negative charge imparted by multiple serum proteins[54]. However, such a coating on the peptide-modified ZnO might not be useful for further applications because of limited penetrability and possible immunogenic reactions. 30 nm sized bare ZnO nanoparticles had higher aggregation than its modified counterpart mainly because it had near-neutral surface potential[55] (**Table 1**). In the case of bare 60 nm and 100 nm sized nanoparticles, nucleation played a major role because of wet-chemical method of synthesis

employed in this case[37]. Due to this, dispersion of 60 nm and 100 nm sized nanoparticles in water leads to 'seeded growth' or 'nucleation' where energy of a favorable bonding between a monomer and a cluster leads to a lowering of the Gibbs bulk free energy[56]. Nanoparticles of 100 nm size showed maximum aggregation in the bare form, and also when modified with the peptide. In the other cases, the modified nanoparticles had sufficient positive charge on its surface imparted by the M9 peptide in order to repel each other by electrostatic forces and maintain homogeneity and stability. Of these, ZnO-100+M9 had the least positive charge and the highest aggregation (**Figure 3a** and **Table 1**).

The dissolution studies indicate that under intracellular conditions, only bare ZnO-30 nanoparticles showed significant Zn^{2+} formation **(Figure 3c)**. This phenomenon can be supported by previous literature where smaller sized nanoparticles were shown to have higher dissolution rates under the same pH conditions. The size dependent dissolution phenomenon has been mainly attributed to the Noyes-Whitney equation which describes that smaller sized nanoparticles due to higher exposed surface area and higher surface energy usually leads to high dissolution propensity[57,58]. However, *in-vitro*, nanoparticles of all the three sizes show similar dissolution kinetics (**Figure 3b** and **Figure S8b**). It is possible that the intracellular aggregation of the larger sized nanoparticles (ZnO-60/ ZnO-100) led to lower dissolution rates in cells in comparison to that observed *in-vitro* and in some cases might completely stagnate the process[59]. All the M9 modified nanoparticles showed less dissolution as compared to the unmodified ones **(Figure 3b and Figure S8b),** a result of shielding effect by the M9 peptides attached to the surface of ZnO nanoparticles. Dissolution was still higher in the smaller nanoparticles than for the 100 nm nanoparticles.

Our study also established how cellular toxicity is affected by the administration of these nanoparticles to skin cells. The M9 modified nanoparticles were tolerated by the cells even up to a concentration range of 40-50 µg/ml showing limited toxicity unlike the bare nanoparticles

(**Figure S3** and **Figure 4g**). Even in presence of UV-B radiation, at a concentration of 40 µg/ml, the modified nanoparticles were very well tolerated while the bare nanoparticles were more toxic to the cells for all the particle sizes. The maximum difference with and without modification was observed in case of the 60 nm nanoparticles which also showed the highest uptake in keratinocytes (**Figure S4**). This might be attributed to the membrane wrapping process and phagocytic properties of keratinocyte cells. The binding of nanoparticle to cell membrane receptors produces a localized decrease in Gibbs free energy thus wrapping the membrane and budding off as endosomal vesicles. The process is size-dependent because small nanoparticles (5-40 nm) have less nanoparticle-receptor interaction and larger nanoparticles (>100 nm) have a large nanoparticle-receptor interaction per particle leading to limited uptake in both cases[60]. The low uptake of ZnO-100 nanoparticles might be responsible for their lower toxicity to cells while for ZnO-30, although the uptake is low, high intracellular dissolution could be contributing to toxicity. Bare ZnO-60 nanoparticles in comparison had high uptake and showed dissolution as well as aggregation leading to high toxicity. M9 modified nanoparticles, in spite of enhanced uptake, exhibited less toxicity presumably by arresting dissolution into Zn^{2+} ions in case of bare nanoparticles.

Literature suggests that ZnO nanoparticles impart maximum photoprotective efficacy at 60-100 nm range[61]. This is because very small size (10-50 nm) generally shows attenuation of UV rays only at the lower wavelengths[44]. However, in our study, the 100 nm nanoparticles showed high aggregation and high photocatalytic property (**Figure 4**) neither of which is suitable for *in vivo* applications. Therefore, we restricted further study to the 60 nm nanoparticles. Peptide modification not only enhanced the cellular viability of the ZnO-60 nanoparticles, other parameters like genotoxicity, ROS production, cytokine release, cell cycle regulation etc. were also favorably affected in presence of UV-B radiation (see **Figure 7, Figure S5, Figure S6).**Bare ZnO nanoparticles exhibited a broad UV absorption peak at 360-370 nm in agreement

with existing literature[11,44]. The modified nanoparticles did not show any significant shift from that range thereby ensuring proper attenuation of UV rays (**Figure S9a**).

The UV absorption peak was not very clearly observed in case of commercial products ZnO-APTES, ZnO coated with silicone oil and ZnO-SiO_2 core-shell structure (**Figure S9 b**). This seems to indicate that these nanoparticles may differ in their UV characteristics from the unmodified ZnO and may not function efficiently for UV protection. A slight shoulder was observed clearly in case of ZnO microparticles around 360 nm. However, microparticles have problems related to patchy and opaque appearances on skin and may not be preferred for UV protection.

In the context of residence of the nanoparticles in skin, most of the early studies indicate that ZnO nanoparticles of the size range of 15-40 nm do not cross the stratum corneum even up to 24 hours of exposure[61]. Other studies on pig skin reported ZnO nanoparticles of 15-200 nm size range which were entrapped only in the stratum corneum reducing toxicity concerns. But recent evidence by Gulson *et al*[21] and Holmes *et al*[19], contradict this point of view and indicate that the labile Zn^{2+} generating spontaneously from the nanoparticles may have a deeper penetration capability. The Zn^{2+} dissolution increases with higher surface-to-volume ratio of the nanoparticles, acidic pH of the skin and perma-selectivity of skin to cationic Zn is even aggravated in compromised skin under abraded, epilated, UV damaged, psoriatic or any other skin condition. Previously, researchers have tried to modify nanomaterials in a manner that its cutaneous penetration can be restricted to the upper layers of the skin with minimal chances of systemic exposure[62]. In our study, we have shown that the coating of ZnO nanoparticles with M9 not only reduces Zn^{2+} dissolution but also entraps the particles only in the upper epidermal layers as measured by ICP-MS technique (**Figure S10a**) and observed visually (**Figure 5b**). There was also minimum trace in the dermis (**Figure 5 c,d**) and negligible transdermal

penetrance (**Figure 5a**) of the modified nanoparticles. This temporary increase in local concentration of ZnO nanoparticles in the epidermis, coupled with their entry in skin cells after application might help in a longer residence time in skin. The keratinocytes of the epidermal layers have a turnover rate of 7 days. Therefore, there is no major concern of biodegradation as the nanoparticles will be eventually removed from the body along with the dead and differentiated corneocytes. To confirm the clearance of the particles, when the nanoparticles were applied on SKH-1 mice and checked after 7 days of administration, the skin tissue analysis showed only trace amount of Zn present in case of ZnO-60+M9. In contrast, in case of ZnO-60 nanoparticles, considerable amount (~50 μg/g concentration of Zn) was still present in the mice skin (**Figure S10b**). The skin integrity was also retained on application of the nanoparticles (**Figure S10 c, d, e**). Moreover, the serum concentration of Zn analysed after 7 days of similar topical administration to the mouse skin *in vivo* showed negligible presence of applied Zn in blood for both ZnO-60 and ZnO-60+M9 (**Table S2**).

The photoprotective property of the nanoparticles was also validated *in-vivo* in SKH-1 mice (**Figure 6d**) where after washing the surface which removes the nanoparticles on the stratum corneum, there was lower presence of Zn in case of the modified ZnO nanoparticles in the full thickness mice skin. Improved photo-protectivity with lower skin thickening and/or unaltered skin integrity was observed in case of application of the modified nanoparticles as compared to both bare ZnO and known sunscreen formulations (**Figure 6b and Figure 6c**). The ZnO-60+M9 were applied in a formulation base of Pentalan-408 in the *in vivo* experiments; however, the nanoparticles were also found to be photostable in known formulation base CCT (also present in the Formulation B of this study) (see **Fig S10)** thereby indicating the possibility of its further application as a commercial formulation in future.

CONCLUSION

In summary, this study demonstrates that ZnO-60 nanoparticles surface-modified with the amphipathic peptide M9 can reside in the upper skin layers, enter keratinocytes with minimal toxicity and show efficient photoprotection and minimum phototoxicity. This modification confers stability and reduces aggregation and dissolution of the nanoparticles. Moreover, the nanoparticles do not go into systemic circulation, and are cleared from the skin in seven days. All these features make these nanoparticles a suitable choice for further development as a photoprotective agent as compared to other core-shell and coated ZnO nanoparticles or ZnO nanoformualations that are commercially available.

MATERIALS AND METHODS

MATERIALS

Zinc acetate dehydrate, methanol, sodium hydroxide(NaOH), (3-Aminopropyl)triethoxysilane (APTES), Fluorescein isothiocyanate (FITC), N-Hydroxysuccinimide (NHS), 1-ethyl-3-(3-dimethylaminopropyl) carbodiimide hydrochloride(EDC), Zinquin ethyl ester dye were obtained from Sigma Aldrich. ZnO coated with APTES (commercial) was obtained from Nanostructured & Amorphous Materials, Inc, Zinc Oxide ZnO, 98+%, 30 nm, silicone oil coated, ZnO-SiO2 core shell nanoparticle and ZnO microparticles were obtained from Intelligent Materials, Inc. MTT (3-(4,5-Dimethylthiazol-2-yl)-2,5-Diphenyltetrazolium Bromide) was obtained from USB, Affymetrix. M9, M9 peptides modified with FITC were purchased from SBS Genentech, China. Copper grids for generating TEM micrographs were obtained from TEDPELLA, USA. Solvents like methanol, ethanol were obtained from SRL Enterprises. 4′,6-diamidino-2-phenylindole (DAPI) and Cellmask™ Orange were obtained from Thermo Fisher Scientific. All other chemicals were obtained from Sigma Aldrich, unless mentioned otherwise. Formulation A (sunscreen emulsion without ZnO nanoparticles) and Formulation B (Capric-caprylic triglyceride (CCT) based known sunscreen emulsion with ZnO

nanoparticles) were obtained from commercial companies-Natural, India and Lakme, India respectively.

METHODS

Synthesis of bare and M9 modified ZnO nanoparticles

Zinc oxide nanoparticles were synthesized using solvo-thermal method as reported earlier[37]. Briefly, 1.98 g of zinc acetate dihydrate was dissolved in 40 mL of methanol. With the addition of 7 ml, 12.5 ml and 25 ml of water, variable nanoparticle size of ~30 nm, ~60 nm and ~100 nm (ZnO-30/ZnO-60/ZnO-100) respectively was achieved. After addition of water, 30 mL of a methanol solution containing 0.72 g of NaOH was added dropwise to the resulting solution and the final solution was refluxed for 30 minutes at room temperature. The precipitate thus obtained was centrifuged at 3000 rpm and washed several times with a mixture of ethanol: acetone in the ratio of 1:1. Finally it was dried in a vacuum dryer for 3 hrs and stored in powdered form. Distilled water accelerated the nucleation of the nanoparticles and acted as a controlling factor for the size of the nanoparticles. Bare ZnO nanoparticles were subsequently modified with APTES[39], which introduces free-NH_2 groups for further functionalization. Briefly, 100 mg of ZnO nanoparticle was dispersed in 20 ml ethanol through probe sonication for 10 minutes. 45µL of APTES and 15 µl TEOS were added into the solution, and the mixture was stirred for 5 h. The final conjugate was precipitated at 5000 rpm, washed several times with ethanol and then kept overnight in vacuum for drying. For analyzing cellular uptake using fluorescence microscopy and flow cytometry, FITC modified ZnO nanoparticles were prepared. Briefly, 30 mg Fluorescinisothiocyanate (FITC) was added to 100 µl APTES in 5 ml ethanol and kept under stirring conditions for 24 hrs. The FITC-APTES conjugate was then loaded onto 20ml of 1mg/ml methanolic dispersion of unmodified ZnO nanoparticles. The

nanoparticles were subjected to 3 cycles of washing and re-dispersion in ethanol to remove excess FITC and dried overnight under vacuum.

To prepare the peptide modified nanoparticles (with and without FITC modification), the -COOH group of M9 or M9-FITC peptide was covalently conjugated to $-NH_2$ group of $ZnO+NH_2$ with the help of NHS/EDC heterobifunctional linker[63]. Briefly, M9: EDC: NHS was added in 2:2:5 molar ratios in PBS solution (pH 7.4) and mixture were stirred for 15 mins before addition of 1mg/ml PBS solution of ZnO nanoparticles (previously dispersed under sonication). Excess EDC, NHS and M9 were removed by repeated centrifugation and washing with MilliQ water.

Characterization of nanoparticles

Size and surface charge determination: The size of all the nanoparticles was measured using both TEM and DLS. All samples (1mg/ml in MilliQ) were sonicated for 10 mins before measurements. For TEM, 5 µl of each sample was loaded on copper grids and left for 1 min for drying. Excess liquid was removed using blotting paper. TEM images were obtained on a TECNAI-G electron microscope operating at an accelerating voltage of 200 kV and analyzed through ImageJ (NIH, USA) software and average size across 10 fields were analyzed using MedCalc version 15.0 (MedCalc Software, Ostend, Belgium). Hydrodynamic size measurements were carried out in Malvern Nano-ZS90 particle size analyzer and expressed in terms of size by number in order to make direct comparison with TEM images. The size by number values were calculated from the size by intensity plots using the instrument software by taking into account the size of the largest peak in the intensity distribution. This does not take into account particles of larger size that could be present in the sample in small amounts. In order to use this information, the size by intensity data was generated at different time points and has been used to study aggregation with time (Fig 3a). This is because the scattering

intensity of spherical particles is proportional to sixth power of the size, therefore even if there is a small number of particles of a higher size in an otherwise homogeneous distribution, the contribution from these higher size particles (including aggregates) can be noted. This, when measured over time, can therefore give a measure of the changes in aggregation pattern.

For surface charge determination, the samples were suspended in MilliQ at a concentration of 1 mg/ml, sonicated for 10 mins and zeta potential measurements were recorded. Refractive index of ZnO was set to 2.0. To evaluate the crystalline nature of the sample powder X-ray diffraction experiments were performed on a Bruker D4 X-ray diffractometer operating at 30 kV and 15 mA using CuK alpha radiation. The XRD patterns were collected in the 2 theta range of 10 to 60 with a step size of 0.02 and a counting time of 6 s per step.

For FTIR spectroscopy, dried nanoparticles were ground and mixed thoroughly with potassium bromide at the ratio of 1: 100 and made into pellets. The FTIR spectra of the pellets were then recorded using a NICOLET 380 FTIR spectrometer operating in the range of 400–4000 cm^{-1} with a resolution of 4 cm^{-1}.

UV absorbance spectra of all the nanoparticles- synthesized bare ZnO nanoparticles, ZnO+M9 nanoparticles, M9 peptide and precursor Zinc acetate as well as commercial ZnO coated with APTES, ZnO coated with silicone oil, ZnO-SiO2 core shell nanoparticles and ZnO microparticles were recorded from 200 to 600 nm at a step count of 1 nm in a Cary Series UV-Vis spectrophotometer (Agilent Technologies).

Aggregation propensity measurement

Dried powder of unmodified ZnO-30/ZnO-60/ZnO-100 and modified ZnO-30+M9/ZnO-60+M9/ZnO-100+M9 was independently dissolved in MilliQ at a concentration of 0.5 mg/ml.

The solution was sonicated for 15 minutes (pulse on: 50 seconds and pulse off: 10 seconds cycle) and immediately taken for particle size measurement. Size by intensity measurements were carried out in a Malvern Nano-ZS90 particle size analyzer. Data were recorded up to 4 hours at intervals of 1 hour. Intensity weighted distribution (size by intensity) reflects the diversity of population by size present in the sample. Similar experiment was also carried out with Dulbecco's Modified Eagle's media (DMEM).

Ionic Zn detection *in vitro*

Dried powder of unmodified ZnO-30/ZnO-60/ZnO-100 and modified ZnO-30+M9/ZnO-60+M9/ZnO-100+M9 was independently dissolved in MilliQ at a concentration of 0.5 mg/ml. The solution was sonicated for 15 minutes (pulse on: 50 seconds and pulse off: 10 seconds cycle). Consequently, the suspension was centrifuged at 8000 r.p.m at different time points. 100 µl of supernatant was mixed with 25µM of zinquin ethyl ester dye (Ex 364 nm/Em 385 nm) in order to quantitate Zn^{2+} in the solution. Fluorescence reading was captured from 0^{th} hour to 4 hours at an interval of 1 hour.

Intracellular Zn detection

HaCaT cells were seeded in 24 well plates at a concentration of 30,000 cells/well and on confluency, it was pretreated with nanoparticles. 4 hours after nanoparticle treatment, intracellular zinc ions were measured by zinquin ethyl ester, a UV excitable fluorescent zinc indicator (Ex 364 nm/Em 385 nm) as mentioned previously[31]. After incubation with zinc indicator for 30 mins at dark, cells were washed with PBS and harvested. Subsequently, cells were analyzed by flow cytometry (FACSARIA III, Becton Dickinson, USA) using 375 nm laser.

Photocatalytic assay

The photocatalytic assay of ZnO nanoparticles was carried out as mentioned previously[44] with some modifications. Briefly, 6 volumetric flasks of 10 ml water/CCT compound were each were filled with 30 ppm Rhodamine B dye and mixed well. 10 mg of powdered nanoparticles-ZnO-30/60/100 and ZnO-30+M9/60+M9/100+M9 were added to the flask and stirred well for 1 hour. Subsequently, these flasks were exposed to sunlight (28.7041° N, 77.1025° E co-ordinates) at a power of 840 to 880 W/m^2 recorded through a Tenmars TM-207 Solar power meter. At time points of 1 hour/2 hours/3 hours, the reaction mixture was sampled and centrifuged for 5 mins at 3000 r.p.m. Following that, the supernatant was collected and absorption spectra were measured to detect any photocatalytic effects as indicated by the intensity of the absorption spectrum of Rhodamine. Blank experiments were carried out on a Rhodamine solution containing no ZnO nanoparticles and there was negligible degradation of the dye upon exposure to sunlight for up to 3 hours.

Franz diffusion assay

For Franz diffusion assay, commercially available skin equivalent (Strat-M®, 47mm discs, Merck Millipore**)** was procured for transdermal diffusion study. The membranes were placed in between the donor and receptor chamber of Franz diffusion apparatus and held together by means of a spring clip. The receptor chamber was filled with 20 ml PBS solution (pH 7.4). To check transdermal diffusion of ZnO nanoparticles, 200 µl of 1 mg/ml ZnO-60/ZnO-60+M9 was added to the donor chamber and the fluid was collected from the receptor chamber through the sampling port at 4 hours and 24 hours. The sampling fluid was subjected to zinc content analysis by Atomic Absorption Spectroscopy (PinAAcle 900F, Perkin Elmer) to analyze whether there is any infiltration of elemental zinc.

Tissue SEM/TEM/ICP-MS

Human full thickness foreskin was obtained under the approval by institutional human ethics committee [Approval Number: IGIB/HEC/09/13] in transportation media (Hank's Balanced Salt Solution or HBSS from Invitrogen). The experiments were carried on immediately after skin was excised, washed three times alternately with PBS and 70% alcohol solution to clear the contamination if any. The subcutaneous fat was carefully removed with a blade and the skin was sectioned into 0.5 cm X 0.5 cm pieces. The sectioned skin was placed in small inserts in 24 well plates to avoid sideways infiltration of nanoparticles. The skin was equilibrated in 300 µl K-SFM (Keratinocyte-Serum free media) for 24 hours, following which 100 µl of 200 µg/ml ZnO-60/ ZnO-60+M9 suspended in PBS was added to the tissue thrice at an interval of 24 hrs. After this, the tissue was fixed using a 4% paraformaldehyde/2.5% glutaraldehyde for 4 hours at room temperature and then left overnight at 4^0C for proper fixation. Next, the sections were washed in 1% Osmium tetroxide in sodium cacodylate buffer in ice and stained with uranyl acetate and lead citrate. Following this, the tissue section was washed with a gradient of different percentage of ethanol (50%, 75%, 95%,100%) and suspended in propylene oxide for 15 mins twice. The sections were paraffinized in Epon 812 hard resin and small blocks were cut using RMC ultramicrotome. Samples were then visualized on TECNAI G2 20 twin (FEI) Transmission Electron Microscope at a magnification of 500X, 1000X and 5500X (for viewing the nanoparticles).

To analyze the penetration of ZnO nanoparticles beyond the epidermis, the epidermis was separated from the full thickness skin by overnight incubation with 0.25% dispase at 37^0C. After careful removal of the epidermis, the skin tissue was fixed with 2.5% glutaraldehyde in 0.1 M cacodylate buffer for 4 hours at 4°C followed by post-fixation in 1% OsO4. Following this, the samples were loaded on a double-sided conducting carbon tape over aluminum stubs and coated with gold under argon atmosphere by means of a sputter coater (SC7620, Mini sputter coater, Quorum Technology Ltd, U.K.). These samples were analyzed for their surface

features using SEM (FEI Quanta 200F). EDX analysis of the tissue sections was performed to evaluate the Zn content of the samples.

To analyze the localization of the nanoparticles, dermis and epidermis was separated using above mentioned protocol and then each of these layers were subjected to analysis of Zn content using Inductively Coupled Plasma Mass Spectrometry (ICP-MS) technique in a Agilent ICP-MS 7900 analyzer.

***In-vivo* studies**

Female SKH-1 hairless mice (5-6 week old) of 20±3 g were purchased from Charles River Laboratories (Wilmington, MA, USA) and all the experiments were approved by the institutional animal ethics committee of CSIR-Indian Institute of Toxicology Research, Lucknow (CSIR-IITR/IAEC/30/12). 10% (wt/v) ZnO nanoparticles formulation (ZnO-60/ZnO-60+M9) were prepared in Pentalan-408 (Pentaerythritoltetraethylhexanoate) according to a previous report[23] to the dorsal surface of mouse (4cm^2 area) for 3 consecutive days (n=5). Each day, 30 mins after the application of the formulation, the mice were exposed to 200 mJ/cm^2 UV-B radiation in an irradiation chamber with a distance of 22 cm between the light source and the target skin from a band of four 100W TL01 fluorescent lamps (Phillips, India). 24 hours after the treatment, the mice were sacrificed and the skin sections were removed and fixed with 4% neutral buffered paraformaldehyde. The skin tissue was then embedded in paraffin and sectioned into 6µm sections and stained with H&E for histological studies. ZnO-60 and ZnO-60+M9 systems were compared to Formulation A (sunscreen emulsion without ZnO nanoparticles) and Formulation B (Capric-caprylic triglyceride(CCT) based known sunscreen emulsion with ZnO nanoparticles). Images were analyzed for epidermal thickness, measured from the top of stratum granulosum to the basal membrane at 5 equidistant sites using ImageJ software (NIH). Remaining tissue from the mice was were

predigested in 3 ml of ultrapure nitric acid overnight and subsequently heated to 160°C, digested with perchloric acid subjected to Atomic Absorption Spectroscopy (PinAAcle 900F, Perkin Elmer) for zinc content analysis. To check the clearance of ZnO-60 and ZnO-60+M9, the compounds were applied on SKH-1 mice skin as mentioned above, and kept for 7 days. After that, the mice were sacrificed and skin section as well as serum sample was subjected to Atomic Absorption Spectroscopy (as mentioned above).

Cell culture experiments with keratinocytes

Human keratinocyte HaCaT cells were maintained in DMEM F12 media supplemented with 10% (v/v) Fetal bovine serum (Life Technologies, USA) at 37 °C and 5% CO_2 in humidified incubator. For all the experiments the cells were allowed to reach 70-80% confluency when nanoparticle treatment was done at mentioned concentrations.

Cellular uptake of ZnO and ZnO+M9 nanoparticles

Flow cytometry

HaCaT cells were seeded in 24 well plates at a density of 30,000 cells per well and treated with 40 µg/ml ZnO+FITC and ZnO+M9-FITC of all the sizes independently for 4 hours at 37 °C. After incubation, the media containing the nanoparticles was removed and cells were washed twice with PBS supplemented with heparin (1mg/ml). The cells were then treated with trypsin (0.25%) for 10 min and harvested in media, pelleted down, washed and resuspended in PBS, then analyzed on FACS-Accuri™ (Becton Dickinson, USA) using BD Accuri™ software. The FITC labeled nanoparticles were excited using 488 nm laser and detected with 530/30 nm (FL1) band pass filter.

Confocal microscopy

HaCaT cells were seeded at density of $1x10^5$ cells per well on 18X10 mm square coverslips in 6 well plates and incubated for 24 hours. At 70-80% confluency, the cells were treated with 40 µg/ml final concentration of ZnO-30/ZnO-60/ZnO-100/ZnO-30+M9/ZnO-60+M9/ZnO-100+M9 coated with FITC nanoparticles and incubated for 4 hours in Opti-MEM. Subsequently, cells were fixed using 4% paraformaldehyde for 10 minutes at 37 °C and washed thrice for 5 min with PBS. The cells were then treated with 100 µl PBS solution of 300 nM DAPI nuclear stain and incubated for 10 minutes, washed thrice with PBS and mounted with anti-fade mounting media onto glass slides (75X25 mm). Imaging was done on an inverted laser scanning microscope (Leica TCS SP8) using 63X magnification and 405 and 488 nm laser lines. For bright field microscopy, same technique was used but the cells were treated with unlabeled ZnO-60 and ZnO-60+M9 nanoparticles.

Transmission Electron Microscopy

HaCaT cells were seeded at density of $1x10^5$ cells per well in 6 well plates and incubated for 24 hours. At 70-80% confluency, the cells were treated with 40 µg/ml final concentration of ZnO-60 or ZnO-60+M9. 24 hours after treatment, the cells were centrifuged at 1000 r.p.m for 5 minutes and the pellets were fixed using a 4% paraformaldehyde/2.5% glutaraldehyde for 4 hours at room temperature and then left overnight at 4^0C. Next, the cells were washed in 1% Osmium tetroxide in sodium cacodylate buffer in ice and stained with uranyl acetate and lead citrate. Following this, the tissue section was washed with a gradient of different percentage of ethanol (50%, 75%, 95%,100%) and suspended in propylene oxide for 15 mins twice. The sections were paraffinized in Epon 812 hard resin and small blocks were cut using RMC ultramicrotome. Samples were then visualized on TECNAI G2 20 twin (FEI) Transmission Electron Microscope at a magnification of 1000X, 5500X (for viewing the nanoparticles).

UV-B exposure

4 hours after nanoparticle treatment, the cells were washed with PBS twice to remove the nanoparticles and Dulbecco's Phosphate Buffer saline was added before UV-B irradiation. The cells were then irradiated with UV-B (280-320 nm) source consisting of 20 watt F20T12BL lamps (UV cabinet, Daavlin, Bryan, OH 43506) at dosage of 200mJ/cm^2. 24 hours after the irradiation, cells were harvested and subjected to following assays.

Cytotoxicity of ZnO and ZnO+M9 nanoparticles

Cell viability was assessed by MTT assay in human keratinocyte cells with and without ZnO treatment. Briefly, HaCaT cells (10,000 per well) in 100 µL DMEM with 10% FBS culture medium were plated in 96-well plate and incubated in 5% CO_2 at 37 °C. After 24 h, the medium was replaced with 100 µL of Opti-MEM medium containing 0-200 µg/ml sonicated ZnO-30/ZnO-60/ZnO-100 and ZnO-30+M9/ZnO-60+M9 and ZnO-100+M9 and incubated for 4 h. Next, the nanoparticles were removed and cells were washed with PBS and replaced with complete media. 100 µL of MTT reagent (1mg/ml) was added to the media and incubated for 3 hours. The purple formazan crystals thus formed were dissolved in 100 µl DMSO. The absorbance was measured using an ELISA reader at a test wavelength of 540 nm and a reference wavelength of 620 nm. Percentage viable cells were expressed considering untreated cells as 100% viable. In another experimental setup, 40 µg/ml of final concentration of ZnO-30/ZnO-60/ZnO-100/ ZnO-30+M9/ZnO-60+M9/ZnO-100+M9 were added and cells were irradiated with UV-B as mentioned earlier. Following this, similar cytotoxicity assay was carried out. Similar assay was carried out with ZnO coated with poly(ethylenimine) and ZnO coated with poly(ethyleneglycol) (synthesized) as well as commercially obtained ZnO coated with APTES, ZnO coated with silicone oil, ZnO-SiO_2 core shell nanoparticles and ZnO microparticles, in independent experiments.

Genotoxicity assessment of ZnO and ZnO+M9 nanoparticles

Genotoxicity of the nanoparticles was determined using Comet assay, with some modifications. HaCaT cells were plated in 24 well plates at concentration of 30,000 cells per well in complete medium. After 24 hours of incubation, 40 µg/ml of final concentration of ZnO-30/ZnO-60/ZnO-100/ ZnO-30+M9/ZnO-60+M9/ZnO-100+M9 were added to the wells in duplicates in independent experiments. After 4 hours of incubation, cells were irradiated with UV-B radiation as mentioned earlier. Then, following 24 hours of incubation, cells were washed with PBS and approximately 50µl suspension of 30,000 cells was added to 550 µl of 0.75% of Low melting Agarose. Single cell suspensions of these cells were loaded on 75X25 mm glass slides pre-coated with 0.1% Low melting Agarose and allowed to cool for 2-3 minutes at room temperature. The slides were then dipped into Alkaline lysis buffer (NaCl-2.5 mM, EDTA 100 µM, Tris base 10mM, Sodium sarcosinate 1%, DMSO 5%) for 20 minutes at 4^0C, washed in MilliQ and again incubated in Alkaline electrophoresis buffer (NaOH 0.3 M, EDTA 3 mM) at 4^0C for 40 minutes. The slides were then run in freshly prepared alkaline electrophoresis buffer at 2 V/cm and 300 mA for 20 mins. Finally the excess alkali was neutralized for 5 mins in a neutralization buffer (Tris base 0.4 M). The slides were then dried at 50^0C and kept overnight at 4^0C for drying, and loaded with 50µM of propidium iodide stain to track the DNA elements. Images were obtained in a Leica DMI6000B microscope system at 40X magnification. Olive tail moment and tail DNA (%) was measured for 50 random cells (25 from each replicate) and analyzed using Komet 5.0 software (ANDOR technology, Belfast, UK).

Intracellular ROS production in ZnO and ZnO+M9 nanoparticles

Intracellular ROS generation in HaCaT cells was determined using a ROS fluorescent probe CM-H_2DCFDA. Briefly, HaCaT cells were seeded in 6-well plates at a concentration of $1x10^5$

cells per well. A final concentration of 40µg/ml of ZnO-60/ ZnO-60+M9 nanoparticles were added to the wells in duplicates. After 4 hours of incubation, cells were treated with 200 mJ/cm^2 of UV-B rays and after 24 hours of incubation, cells were treated with 10 µM CM-H_2DCFDA in cultured medium and incubated at 37 °C for 20 min. The cells were then treated with trypsin (0.25%) for 10 min and harvested in media, pelleted down washed with PBS, resuspended in PBS having 1% BSA and then analyzed on FACS- Accuri™(Becton Dickinson, USA) using 488 nm laser and detected with 530/30 nm (FL1) band pass filter and analyzed using BD Accuri™ software. Cellular integrity was determined through CytoTox-ONE™ Homogeneous Membrane Integrity Assay kit (Promega).

Superoxide dismutase assay

HaCaT cells were seeded in 96 well plates at a concentration of 5000 cells/well. At 70% confluency, cells were pretreated with nanoparticles and post-treated with UV-B as mentioned above. 24 hours after treatment, SOD activity (%inhibition rate) was determined using SOD Assay Kit-WST (Sigma Aldrich, Cat no: 19160), according to manufacturer's protocols.

Cell cycle analysis

HaCaT cells were synchronized using serum free medium for 48 hours. Cells were pretreated with nanoparticles and post-treated with UV-B as mentioned above. Following this, cells were harvested, washed with PBS, fixed with cold 70% ethanol for 30 mins at 4^0C and permeabilized with 0.5% NP-40. After 2 washes with PBS cells were treated with 100µg/ml RNAase and incubated with 50µg/ml Propidium iodide for 30 mins at dark. Percentage cells at different phases (G0/G1, S and G2/M) were determined by analyzed on FACS-Accuri™ (Becton Dickinson, USA) using BD Accuri™ software. Untreated cells were taken as controls for interpreting the results. Cell cycle distribution and percentages were quantitated for 10,000 cells using the Multicycle AV cell cycle program (Phoenix Flow Systems, San Diego, CA).

ELISA for DNA damage measurement, cytokine profiling

HaCaT cells were seeded in 24 well plates at a density of 30,000 cells/well and pre-incubated with respective treatments and then UV-B irradiated as mentioned above. After 24 hours, the cells were washed in PBS twice and subsequently DNA was isolated using Blood genomic DNA extraction kit (Helix Biosciences, FABGK 100). DNA concentration and purity was measured on NanoDrop^{TM}ND-1000 platform and following this, Cyclobutane pyrimidine dimmers (CPD) and 6-4 Photoproduct (6,4-PP) were quantified with an Oxiselect Cellular UV-induced DNA damage ELISA kit from Cell Biolabs (San Diego, CA, USA) according to the manufacturer's instructions.

After 24 hours of incubation, spent media was collected and stored at -20^{0}C and divided into small 200 µl aliquots to avoid repeated freeze-thaw cycles. The media containing extracellular cytokines was thawed just before analysis. Cytokine profiling was done for UV-B mediated proinflammatory TNF-α and IL-6 cytokines (eBiosciences, BMS 223HS and BMS213HS respectively) and general inflammatory markers related to immunosuppression, IL-2 and IL-12 (eBiosciences, BMS221HS and BMS238HS).

Caspase 3 and Caspase 9 levels were checked through Human Caspase-3 Instant ELISA (eBiosciences, BMS2012INST) and Human Caspase-9 Platinum ELISA (eBiosciences, BMS2025) respectively.

Statistical analysis

All data are expressed as mean ± SD and n = number of experiments conducted. Differences between the treatments were evaluated by Student's t-test using GraphPad Prism 6 software. P-value < 0.05 has been considered to be statistically significant. In all the graphical

representations, * implies p-value <0.05, ** implies p-value <0.01, *** implies p-value <0.001, ns=not significant.

Data availability: The authors declare that all data supporting the findings of this study are available within the article and its Supplementary Information Files or from the corresponding author on reasonable request.

REFERENCES:

1. Osmond, M. J.; McCall, M. J. Zinc Oxide Nanoparticles in Modern Sunscreens: An Analysis of Potential Exposure and Hazard. *Nanotoxicology* 2010, 4, 15–41.

2. Fan, Z.; Lu, J. G. Zinc Oxide Nanostructures: Synthesis and Properties. *J. Nanosci. Nanotechnol* 2005,5, 1561–1573.

3. Mclaren, A.; Valdes-Solis, T.; Li, G.; Tsang, S. C. Shape and Size Effects of ZnO Nanocrystals on Photocatalytic Activity. *J. Am. Chem. Soc* 2009,131, 12540–12541.

4. Pacholski, C.; Kornowski, A.; Weller, H. Self-assembly of ZnO: From Nanodots to Nanorods. *Angew. Chemie - Int. Ed* 2002, 41, 1188–1191.

5. Nie, L.; Gao, L.; Feng, P.; Zhang, J.; Fu, X.; Liu, Y.; Yan, X.; Wang,T. Three-Dimensional Functionalized Tetrapodlike ZnO Nanostructures for Plasmid DNA Delivery. Small. 2006, 2, 621–625.

6. Hong, H.; Shi, J.; Yang, Y.; Zhang, Y.; Engle, J.W.; Nickles, R.J.; Wang, X.; Chaibo W. Cancer Targeted Optical Imaging with Fluorescent Zinc oxide Nanowires. *Nano Lett.* 2011, 11, 3744–3750.

7. Zhang, Y.; Nayak, T. R.; Hong, H.; Cai, W. Biomedical Applications of Zinc Oxide Nanomaterials. *Curr Mol Med.*2013,13, 1633–1645.

8. Pati, R.; Mehta, R.K.; Mohanty, S.; Padhy, S.; Sengupta, M.; Vaseeharan, B.; Goswami, C.; Sonawane, A. Topical Application of Zinc Oxide Nanoparticles Reduces Bacterial Skin Infection in Mice and Exhibits Antibacterial Activity by Inducing Oxidative Stress Response and Cell Membrane Disintegration in Macrophages. *Nanomedicine Nanotechnology, Biol. Med.*2014*,* 10, 1195–1208 .

9. Li, J.; Guo, D.; Wang, X.; Wang,H.; Jiang, H.; Jiang, H.; Chen, B. The Photodynamic Effect of Different Size ZnO Nanoparticles on Cancer Cell Proliferation In vitro. *Nanoscale Res. Lett.*2010*,*5, 1063–1071.

10. Zhang, H.; Chen, B.; Jiang, H.; Wang, C.; Wang, H.; Wang, X. A Strategy for ZnO Nanorod Mediated Multi-mode Cancer Treatment. *Biomaterials* 2011*,* 32, 1906–1914.

11. Wang, S. Q.; Tooley, I. R. Photoprotection in the Era of nanotechnology. *Semin. Cutan. Med. Surg.*2011*,*30, 210–213.

12. Burnett, M. E.; Wang, S. Q. Current Sunscreen Controversies: a Critical Review. *Photodermatol. Photoimmunol. Photomed.*2011*,*27, 58–67.

13. Baroli, B. Penetration of Nanoparticles and Nanomaterials in the Skin: Fiction or Reality? *J. Pharm. Sci.*2010*,*99, 21–50.

14. Nohynek, G. J.; Lademann, J.;Ribaud, C.; Roberts, M. S. Grey Goo On The Skin? Nanotechnology, cosmetic and sunscreen safety. *Crit. Rev. Toxicol.*2007*,*37, 251–277.

15. Filipe, P.; Silva, J.; Silva, R. A. R.; Cirne de castro, J. L.; Gomes M. M.; Alves, C. L.; Santus, R.; Pinheiro, T. Stratum Corneum is an Effective Barrier to TiO2 and ZnO Nanoparticle Percutaneous Absorption. *Skin Pharmacol. Physiol.* 2009*,* 22, 266–275 .

16. Schulz, J.; Hohenberg, H.; Pflucker, F.; Gartner, E.; Will, T.; Pfeiffer, S.; Wepf, R.; Wendel, V.; Barlag, G, H.; Wittern, K, P. Distribution of Sunscreens on Skin. in *Advanced Drug Delivery Reviews,*2002*,* 54, S157-S163.

17. Gamer, A. O.; Leibold, E.; Van Ravenzwaay, B. The In vitro Absorption of Microfine Zinc oxide and Titanium Dioxide through Porcine Skin. *Toxicol. Vitr.2006,*20, 301–307.

18. Becker, W.; Jeffrey, E.; Benson, H. A. E.; Roberts, M. S. Effect of Flexing and Massage on In vivo Human Skin Penetration and Toxicity of Zinc Oxide Nanoparticles. *Nanomedicine (Lond).*2016, 11, 1193–1205.

19. Holmes, A. M.; Song, Z.; Moghimi, H. R.; Roberts, M. S. Relative Penetration of Zinc Oxide and Zinc Ions into Human Skin after Application of Different Zinc Oxide Formulations. *ACS Nano.*2016*,* 10,1810-1819 .

20. Gulson, B.; Mccall, M.; Korsch, M.; Gomez, L.; Casey, P.; Oytam, Y.; Taylor, A.; Mcculloch, M.; Trotter, J.; Kinsley, L.; Greenoak, G. Small Amounts of Zinc from Zinc Oxide Particles in Sunscreens Applied Outdoors are Absorbed through Human Skin. *Toxicol. Sci.* 2010*,* 118, 140–149.

21. Gulson, B.; McCall, M. J.; Bowman, D. M.; Pinheiro, T. A Review of Critical Factors for Assessing the Dermal Absorption of Metal Oxide Nanoparticles From Sunscreens Applied to Humans, and a Research Strategy to Address Current Deficiencies. *Arch. Toxicol.*2015*,*89, 1909–1930 .

22. Monteiro-Riviere, N. A.; Wiench, K.; Landsiedel, R.; Schulte, S.; Inman, A.O.; Riviere, J.E. Safety Evaluation of Sunscreen Formulations Containing Titanium Dioxide and Zinc Oxide Nanoparticles in UVB Sunburned Skin: An In vitro and in vivo study. *Toxicol. Sci.*2011*,* 123, 264–280 .

23. Pal, A.; Alam, S.; Chauhan, L.K.S.; Saxena, P.N.; Kumar, M.; Ansari, G.N.; Singh, D.; Ansari, K.M. UVB Exposure Enhanced the Dermal Penetration of Zinc Oxide Nanoparticles and Induced Inflammatory Responses through Oxidative Stress Mediated by MAPKs and NF-κB Signaling in SKH-1 Hairless Mouse Skin. *Toxicol. Res.*2016*,* 5, 1066–1077 .

24. Biniek, K.; Levi, K.; Dauskardt, R. H. Solar UV Radiation Reduces the Barrier Function of Human Skin. *Proc. Natl. Acad. Sci. U. S. A.*2012*,*109, 17111–17116.

25. Vandebriel, R. J.; Jong, D.W. H. A Review of Mammalian Toxicity of ZnO Nanoparticles. *Nanotechnol. Sci. Appl.*2012*,* 5, 61–71 .

26. Kocbek, P.;Teskač, K.; Kreft, M. E.; Kristl, J. Toxicological Aspects of Long-term Treatment of Keratinocytes with ZnO and TiO2 Nanoparticles. *Small.* 2010*,* 6, 1908–1917 .

27. Sharma, V.; Singh, S. K.; Anderson, D.; Tobin, D. J.; Dhawan, A. Zinc Oxide Nanoparticle Induced Genotoxicity in Primary Human Epidermal Keratinocytes. *J. Nanosci. Nanotechnol.*2011*,*11, 3782–3788.

28. Shen, C.; James, S.A.; de jonge, M.D.; Turney, T.W.; Wright, P.F.; Feltis, B.N. Relating Cytotoxicity, Zinc Ions, and Reactive Oxygen in ZnO Nanoparticle-Exposed Human Immune Cells. *Toxicol. Sci.*2013*,* 136, 120–130 .

29. Krumpfer, J. W.; Schuster, T.; Klapper, M.; Müllen, K. Make it Nano-Keep it Nano. *Nano Today.*2013*,*8, 417–438.

30. George, S.; Pokhrel, S.; Xia, T.; Gilbert, B.; Ji, Z.; Schowalter, M.; Rosenauer, A.; Damoiseaux, R.; Bradley, K, A.; Madler, L.; Nel, A.E. Use of a Rapid Cytotoxicity Screening Approach To Engineer a Safer Zinc Oxide Nanoparticle through Iron Doping. *ACS Nano.* 2010, 4, 15–29.

31. Luo, M.; Shen, C.; Feltis, B. N.; Martin, L.L.; Hughes, A.E.; Wright, P.; Turney, W. T. Reducing ZnO Nanoparticle Cytotoxicity by Surface Modification. *Nanoscale* 2014,6, 5791–5798.

32. Pombo García, K. *et al.* Zwitterionic-Coated 'Stealth' Nanoparticles for Biomedical Applications: Recent Advances in Countering Biomolecular Corona Formation and Uptake by the Mononuclear Phagocyte System. *Small.* 2014,10, 2516–2529.

33. Han, Y.; Kim, D.; Hwang, G.; Lee, B.; Eom, I.; Kim, P. J.; Tong, M.; Kim, H. Aggregation and Dissolution of ZnO Nanoparticles Synthesized by Different Methods: Influence of Ionic Strength and Humic acid. *Colloids Surfaces A-Physicochemical Eng. Asp* 2014,451, 7–15.

34. Labouta, H. I.; Schneider, M. Interaction of Inorganic Nanoparticles With the Skin Barrier: Current Status and Critical review. *Nanomedicine Nanotechnology, Biol. Med.* 2013, 9, 39–54 .

35. Nam, J.; Won, N.; Bang, J.; Jin, H.; Park, J.; Jung, S.; Jung, S.; Park, Y.; Kim, S.Surface Engineering of Inorganic Nanoparticles for Imaging and Therapy. *Adv. Drug Deliv. Rev.*2013*,* 65, 622–648.

36. Veiseh, O.; Gunn, J. W; Zhang, M. Design and Fabrication of Magnetic Nanoparticles for Targeted Drug Delivery and Imaging. *Adv. Drug Deliv. Rev.*2010*,* 62, 284–304.

37. Aditya, A.; Chattopadhyay, S.; Jha, D., Gautam, H.K.; Maiti, S.; Ganguli, M. Zinc Oxide Nanoparticles Dispersed in Ionic Liquids Show High Antimicrobial Efficacy to Skin-Specific Bacteria. *ACS Applied Materials & Interfaces* 2018,10(18), 15401-15411.

38. Zhang, Y.; Wu, H.; Huang, X.; Zhang, J.; Guo, S. Effect of Substrate (ZnO) Morphology on Enzyme Immobilization and its Catalytic Activity. *Nanoscale Res. Lett.*2011*,* 6, 450-456.

39. Zhao, L.; Zhang, R.; Zhang, J; Sun, S. Synthesis and Characterization of Biocompatible ZnO Nanoparticles. *CrystEngComm* 2012*,*14, 945-950.

40. Jung, H. S.; Kong, W. H.; Sung, D. K.; Lee, M.; Beack, S. E. Nano Graphene Oxide – Hyaluronic Acid Conjugate for Photothermal Ablation Therapy of Skin Cancer. *ACS Nano*. 2014, 8, 260-268 .

41. Imani, R.; Emami, S. H.; Faghihi, S. Synthesis and Characterization of an Octaarginine Functionalized Graphene oxide Nano-carrier for Gene Delivery Applications. *Phys. Chem. Chem. Phys.*2015*,* 17, 6328–6339 .

42. Coyle, P.; Zalewski, P, D.; Philcox, J, C.; Forbes, I, J.; Ward, A.D.; Lincoln, S.F.; Mhadevan, I.; Rofe, A. M. Measurement of Zinc in Hepatocytes by Using a Fluorescent Probe, Zinquin: Relationship to Metallothionein and Intracellular Zinc. *Biochem. J.*1994*,*303 , 781–786 .

43. Chen, W.; Zhang, J. Using Nanoparticles to Enable Simultaneous Radiation and Photodynamic Therapies for Cancer Treatment. *J. Nanosci. Nanotechnol.*2006*,*6, 1159–1166.

44. Antonio J. R.; Antônio C. R.; Cardeal I. L. S.; Ballavenuto J. M. A.; Oliveira J. R. Nanotechnology in Dermatology. *Anais Brasileiros de Dermatologia*. 2014, 89, 126-136.

45. Barre, G. Biodegradable Polymer Nanocapsules Containing a Sunscreen Agent : Preparation and Photoprotection. *Eur J Pharm Biopharm.* 2001, 52, 191–195.

46. Karadzovska, D.; Brooks, J. D.; Monteiro-Riviere, N. A.; Riviere, J. E. Predicting Skin Permeability From Complex Vehicles. *Adv. Drug Deliv. Rev.*2013*,* 65, 265–277.

47. Lévy, R.; Thanh, T.K.N.; Doty, R.C.; Hussain, I.; Nichols, R.J.; Schiffrin, D. J.; Brust,M.; Fernig, D. G. Rational and Combinatorial Design of Peptide Capping Ligands for Gold Nanoparticles. *J. Am. Chem. Soc 2004.*126, 10076–10084 .

48. Guerrero, S.; Araya, E.; Fiedler, J.L.; Arias, J.I.; Adura, C.; Albericio, F.; Giralt, E.; Arias J.L.; Fernandez M.S.; Kogan M.J. Improving the Brain Delivery of Gold Nanoparticles by Conjugation With an Amphipathic Peptide. *Nanomedicine (Lond).*2010*,*5, 897–913 .

49. Puddu, V.; Perry, C. C. Peptide Adsorption on Silica Nanoparticles: Evidence of Hydrophobic Interactions. *ACS Nano.* 2012*,*6, 6356–6363.

50. Vij, M.; Natarajan,P.; Pattnaik, B.R.; Alam, S.; Gupta, N.; Santhiya, D.; Sharma, R.; Singh, A.; Ansari K. M.; Gokhale R.S.; Natarajan V.T.; Ganguli, M. Non-invasive Topical Delivery of Plasmid DNA to the Skin Using a Peptide Carrier. *J. Control. Release* 2016*,* 222, 159–168.

51. Vij, M.; Alam, S.; Gupta, N.; Gotherwal, V.; Non-invasive Oil-Based Method to Increase Topical Delivery of Nucleic Acids to Skin. *Mol Ther.*2017*,* 25, 1–11.

52. Sharma, R.; Nisakar, D.; Shivpuri, S.; Ganguli, M. Contrasting Effects of Cysteine Modification On the Transfection Efficiency of Amphipathic Peptides. *Biomaterials.*2014*,*35, 6563–6575 .

53. Yener, G.; Incegül, T.; Yener, N. Importance of Using Solid Lipid Microspheres as Carriers for UV Filters on the Example Octyl Methoxy Cinnamate.*Int J Pharm* 2003*,*258, 203–207 .

54. Wells, M. A.; Abid, A.; Kennedy, I. M.; Barakat, A. I. Serum Proteins Prevent Aggregation of Fe2O3 and ZnO Nanoparticles. *Nanotoxicology* 2012*,* 6, 837–846 .

55. Hotze, E. M.; Phenrat, T.; Lowry, G. V. Nanoparticle Aggregation: Challenges to Understanding Transport and Reactivity in the Environment. *J. Environ. Qual.*2010*,*39, 1909-1924 .

56. Polte, J. Fundamental Growth Principles of Colloidal Metal Nanoparticles – a New Perspective. *CrystEngComm.*2015*,* 17, 6809–6830.

57. Bian, S. W.; Mudunkotuwa, I. A.; Rupasinghe, T.; Grassian, V. H. Aggregation and Dissolution of 4 nm ZnO Nanoparticles in Aqueous Environments: Influence of pH, Ionic Strength, Size, and Adsorption of Humic Acid. *Langmuir.*2011*,*27, 6059–6068 .

58. Yang, Z.; Xie, C. Zn2+ Release from Zinc and Zinc Oxide Particles in Simulated Uterine Solution. *Colloids Surfaces B Biointerfaces.*2006*,* 47, 140–145.

59. Zhang, W. Nanoparticle Aggregation: Principles and Modeling. *Adv. Exp. Med. Biol.*2014*,* 811, 20–43.

60. Albanese, A.; Tang, P. S.; Chan, W. C. W. The Effect of Nanoparticle Size, Shape, and Surface Chemistry on Biological Systems. *Annu. Rev. Biomed. Eng.*2012*,* 14, 1–16.

61. Cross, S. E.; Innes, B.; Roberts, M. S.; Tsuzuki, T.; Robertson T. A.; McCormick, P. Human Skin Penetration of Sunscreen Nanoparticles: In-vitro Assessment of a Novel Micronized Zinc Oxide Formulation. *Skin Pharmacol. Physiol.*2007,20, 148–154.

62. Deng, Y.; Ediriwickrema, A.; Yang, F.; Lewis, J.; Girardi, M.; Saltzman, W. M. A Sunblock Based on Bioadhesive Nanoparticles. *Nat. Mater.,* 2015,14, 1278–1285.

63. Pan, L.; He, Q.; Liu, J.; Chen, Y.; Ma, M.; Zhang, L.; Shi, J. Nuclear-targeted Drug Delivery of TAT Peptide-conjugated Monodisperse Mesoporous Silica Nanoparticles. *J Am Chem Soc.*2012, 134, 5722-5725.

ACKNOWLEDGMENT

This work was supported by CSIR, Government of India and Network project TOUCH (Project Code BSC0302), AA acknowledges CSIR, Govt. of India for fellowship. The authors are thankful to Dr. Sevi Murugavel, Department of Physics and Dr. Indrajit Roy, Department of Chemistry, University of Delhi for help in BET surface area measurements, FTIR, and valuable suggestions on synthesis and modification of nanoparticles. The authors are thankful to Mr. Manish Kumar (CSIR-IGIB) and Project code BSC0403 for help in acquiring confocal microscopy images.

SUPPORTING INFORMATION:

TEM images and Zeta potential values of APTES and M9 modified ZnO nanoparticles; Aggregation and dissolution propensities of modified and unmodified ZnO nanoparticles in DMEM and different pHs; Cell viability and uptake behavior of modified and unmodified ZnO nanoparticles; Cellular-TEM images for understanding localization of modified and unmodified ZnO nanoparticles; Membrane integrity assay; Apoptotic marker ELISA assay; Cytotoxicity in comparison of commercial compounds; Aggregation and dissolution kinetics; Absorbance spectra; ICP-MS study; Tissue integrity through TEM analysis; AAS spectra in mice skin; Photocatalytic assay in CCT oil; Elemental analysis using EDX.

AUTHOR INFORMATION

Corresponding Author: Dr. Munia Ganguli

Address - RoomNo-225/Lab No-219,

CSIR-Institute of Genomics and Integrative Biology,

Mathura Road, New Delhi-110020.

Email id-mganguli@igib.res.in, mganguli@igib.in

Ph. No. - 91-11-29879 225/ +91 9871607437

AUTHOR CONTRIBUTIONS

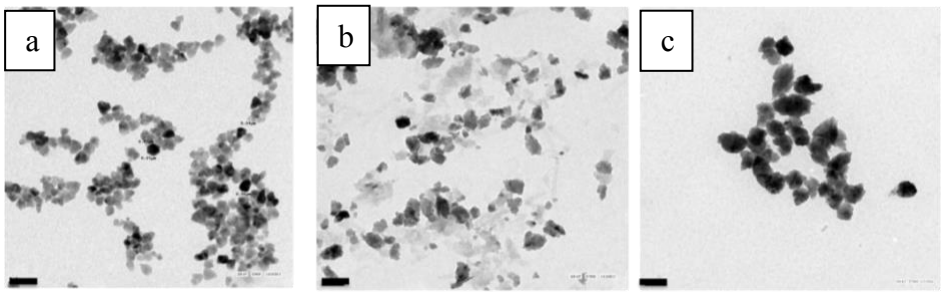
AA, SC, AP and MP have carried out the experimental part. NG and DS have contributed in the XRD and FTIR recording and analysis. SA and KMA have helped in carrying out the animal experiments. MG and AA have conceptualized and executed the necessary details of the project and written the manuscript. All authors have given approval to the final version of the manuscript.

NOTES The authors declare no competing financial interest.

ZnO-30

ZnO-60

ZnO-100



30.04±3.5 nm

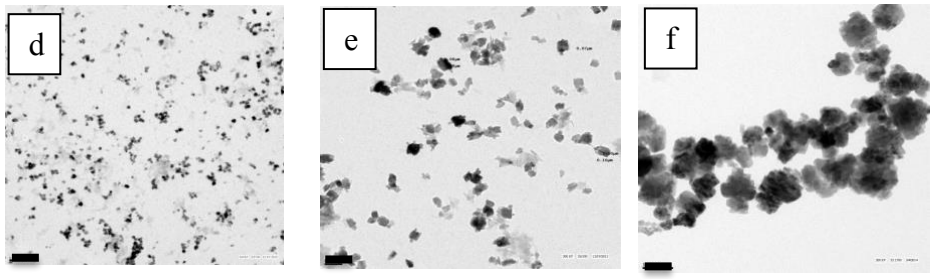
65.8±1.7 nm

102.42±83 nm

ZnO-30+APTES

ZnO-60+APTES

ZnO-100+APTES



32.1±3.20 nm

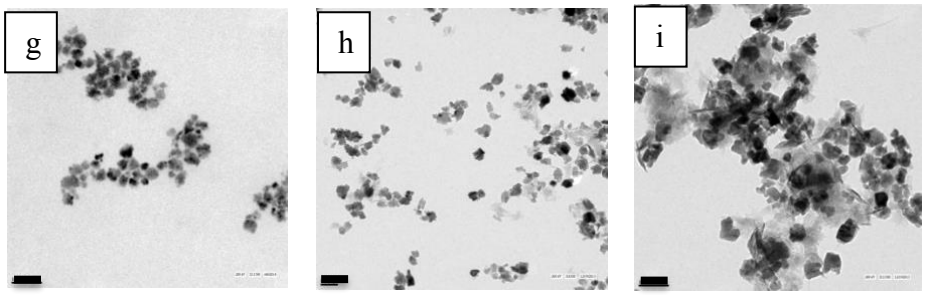
65.8±1.70 nm

103.8±80 nm

ZnO-30+M9

ZnO-60+M9

ZnO-100+M9



40.6±7.90 nm

69.3±3.61 nm

110.15±17.9 nm

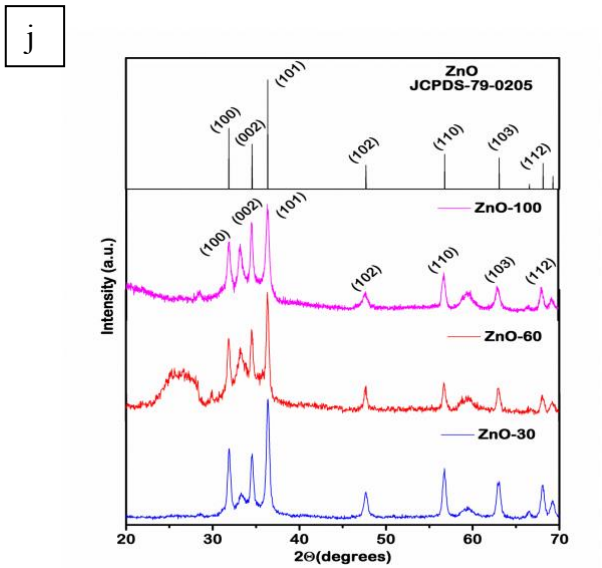


Figure 1: Characterization of bare ZnO nanoparticles: Transmission Electron Microscopy images of Zinc oxide nanoparticles a) bare 30 nm (ZnO-30) b) bare 60 nm (ZnO-60) and c) bare 100 nm (ZnO-100) nanoparticles. Characterization of amine modified d) 30 nm (ZnO-30+APTES), e) 60 nm (ZnO-60+APTES) and f) 100 nm (ZnO-100+APTES) nanoparticles. Characterization of M9 peptide modified g) 30 nm (ZnO-30+M9), h) 60 nm (ZnO-60+M9) and i) 100 nm (ZnO-100+M9) nanoparticles. Scale bar 100 nm. Size of nanoparticles is expressed as mean±S.D across 10 fields and ~100 nanoparticles have been analyzed through Image J software, j) X-ray diffraction of ZnO-30, ZnO-60 and ZnO-100 nanoparticles.

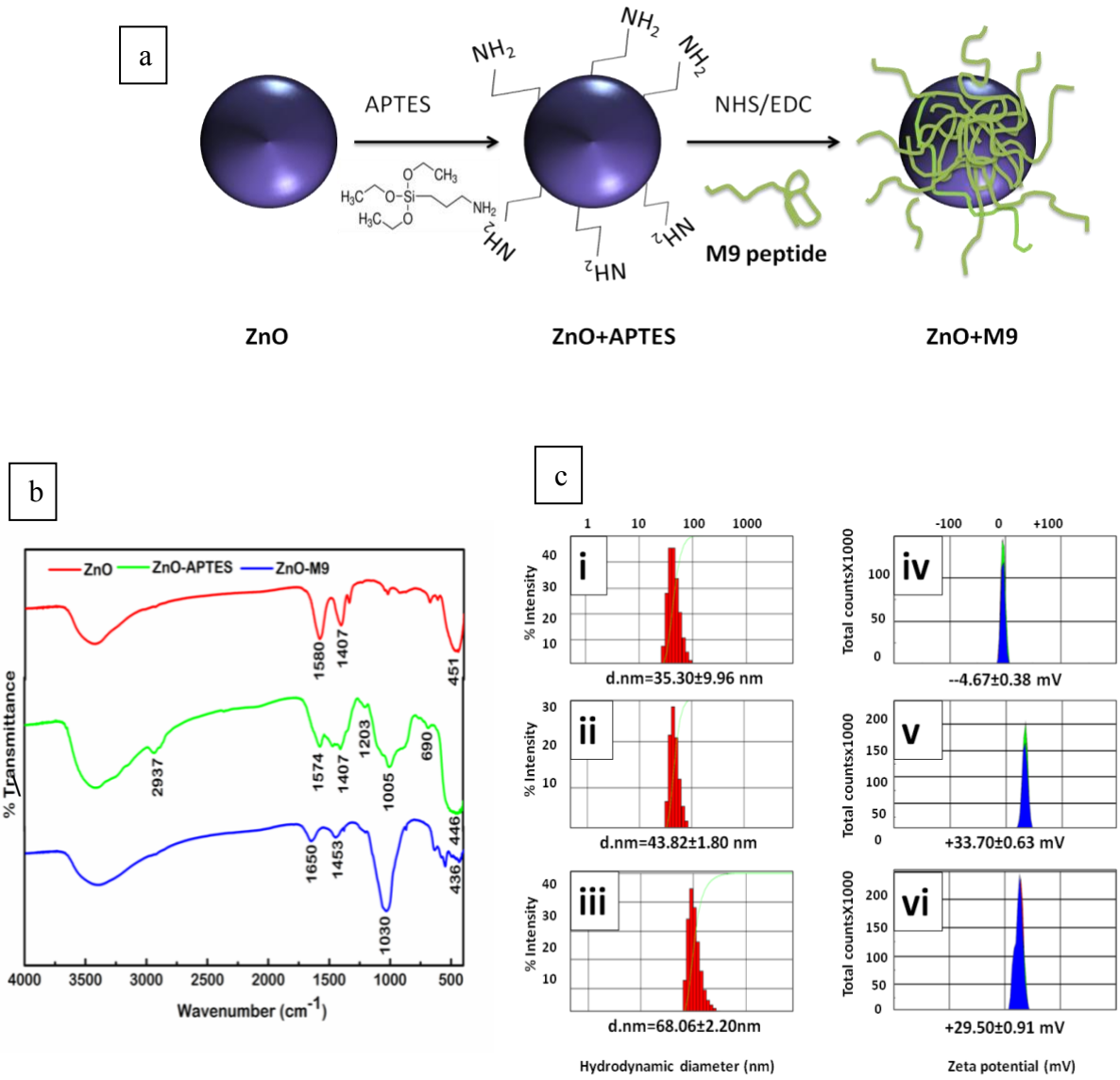


Figure 2: Characterization of M9 modified ZnO nanoparticles: a) Schematic representation of preparation of ZnO+M9 assembly, b) FTIR spectra for bare ZnO-30, ZnO-30 modified with APTES, ZnO-30 modified with M9. c) i-iii represents the hydrodynamic diameter of ZnO-30, ZnO-30+APTES and ZnO-30+M9 respectively and iv-vi represent zeta potential values of ZnO-30, ZnO-30+APTES and ZnO-30+M9 respectively, data obtained from 3 independent readings.

	Size measured by TEM (nm)	Hydrodynamic diameter (nm)	Zeta potential (mV)
ZnO-30	30.04±3.5	35.3±9.96	-4.67±0.38
ZnO-30+APTES	32.1±3.2	43.82±1.80	+33.7±0.63
ZnO-30+M9	40.59±7.9	68.06±2.20	+29.5±0.91
ZnO-60	64.4±4.1	87.1±7.19	-33.6±4.48
ZnO-60+APTES	65.8±1.7	93.61±6.86	+40.1±0.32
ZnO-60+M9	69.3±3.61	98.33±4.12	+27.5±0.28
ZnO-100	102.4±2.83	119.04±1.17	-22.9±0.86
ZnO-100+APTES	103.0±8.00	176.56± 10.44	+35.3±0.18
ZnO-100+M9	110.15±17.9	225.76±12.13	+6.15±0.33

Table-1: Size measured by TEM, hydrodynamic diameter (size by number) obtained from DLS and zeta potential values of bare 30 nm (ZnO-30), ZnO-30+APTES, ZnO-30+M9/bare 60 nm (ZnO-60), ZnO-60+APTES, ZnO-60+M9 nanoparticles, and bare 100 nm (ZnO-100), ZnO-100+APTES, ZnO-100+M9 nanoparticles. Measurements are expressed as mean±S.D across 3 measurements.

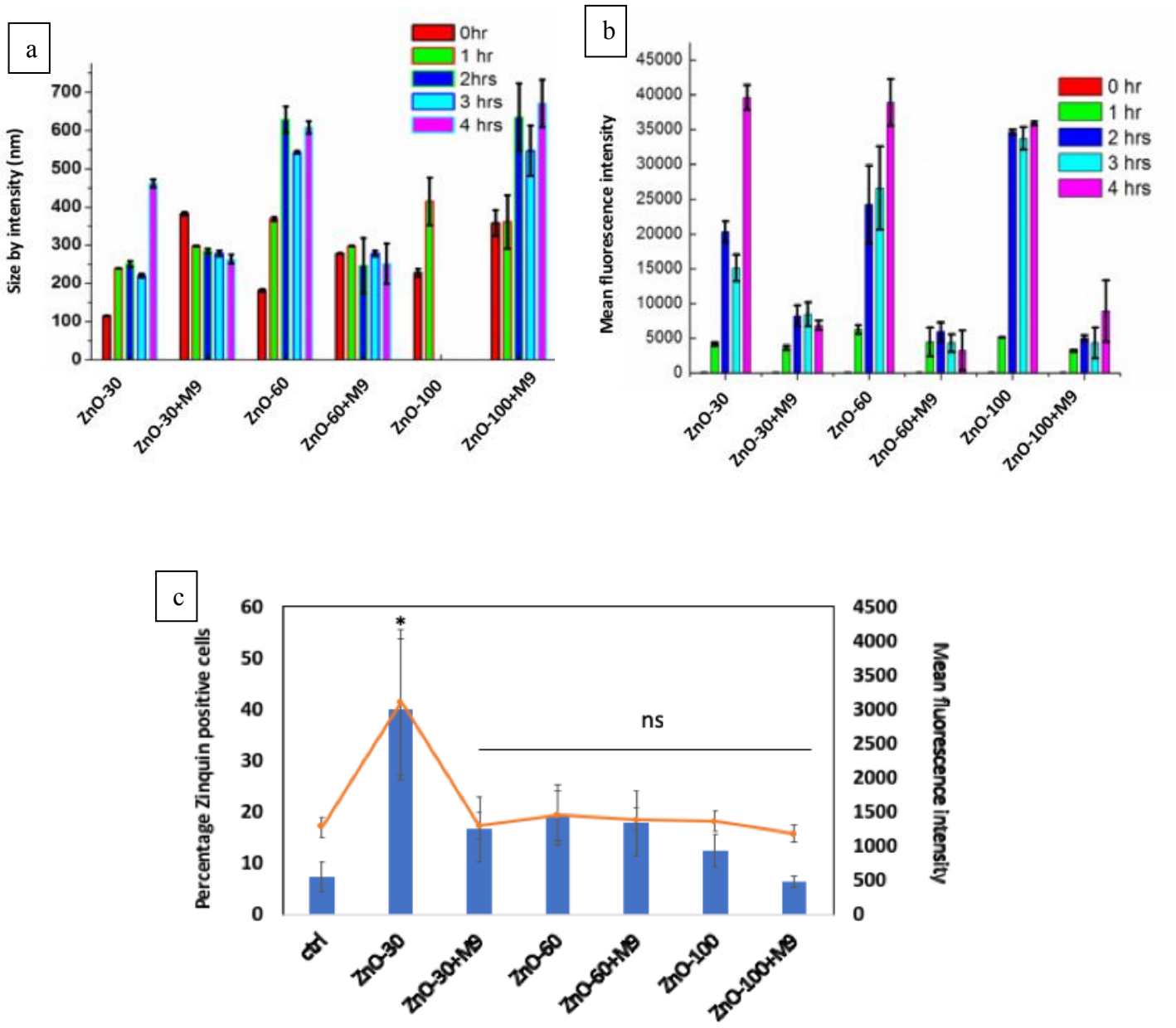


Figure 3: Analysis of aggregation and dissolution propensity of ZnO nanoparticles-a) Aggregation propensity of bare ZnO-30/ZnO-60/ZnO-100 and modified ZnO-30+M9/ZnO-60+M9/ZnO-100+M9 was recorded through size intensity measurements (DLS), b) Zn^{2+} dissolution levels in water quantitated through UV excitable zinquin ethyl ester (25µM) and analysed in fluorescence plate reader (for experimental details, see Materials and Methods section) c) Intracellular Zn^{2+} dissolution levels as quantitated through UV excitable zinquin ethyl ester (25µM) and analysed through flow cytometry. Bars represent percentage positive cells and line represents mean intensity of zinquin expression per cell. Data expressed as mean±SD, n=3. (p-value *p<0.05, ns=not significant)

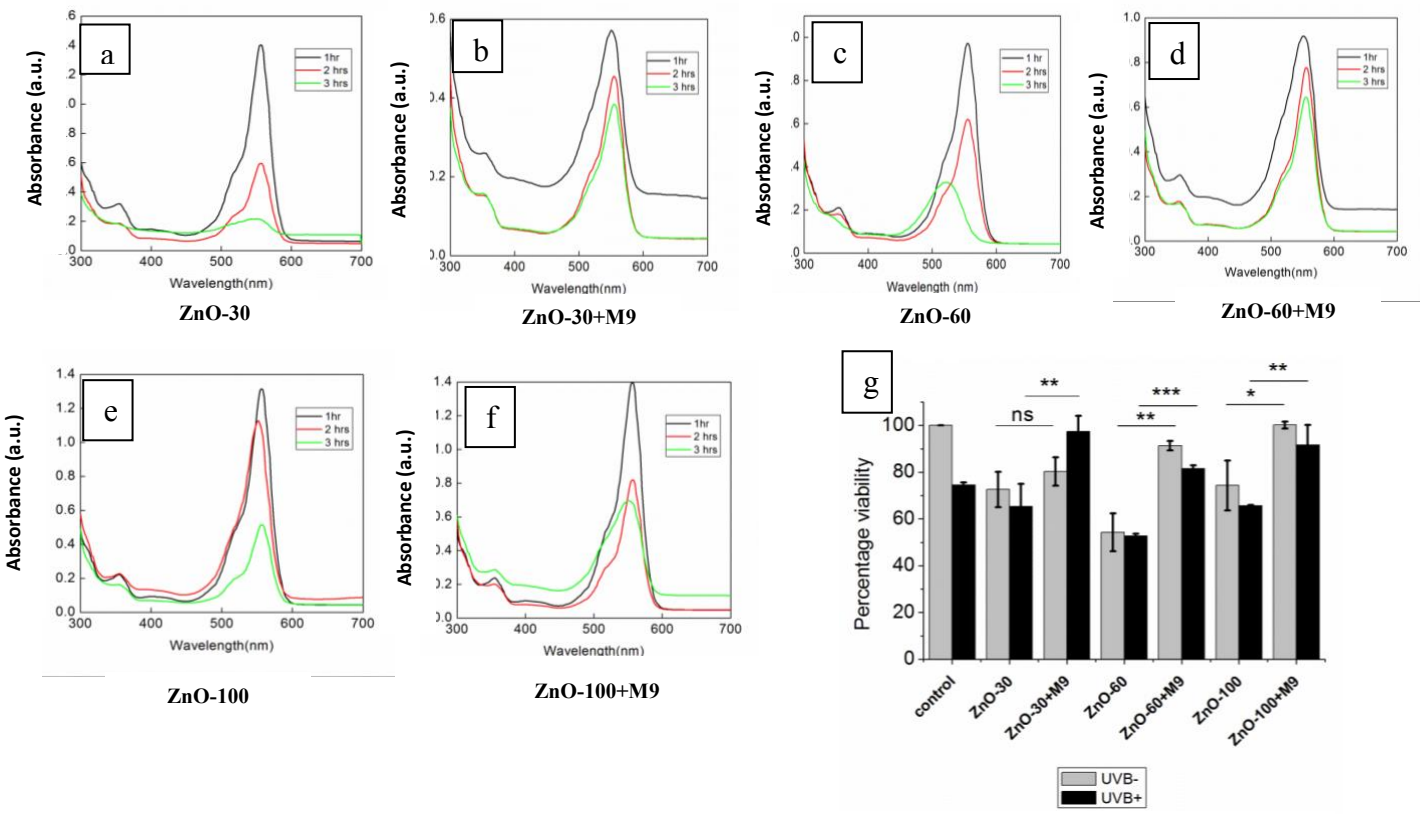


Figure 4: Photocatalytic degradation and cytotoxicity in presence of UV-B radiation - Absorption spectra of Rhodamine dye in aqueous solutions containing **a)** ZnO-30, **b)** ZnO-30+M9, **c)** ZnO-60, **d)** ZnO-60+M9, **e)** ZnO-100, **f)** ZnO-100+M9 nanoparticles after exposure to sunlight for a time period of maximum three hours; **g)**. Percentage viable cells as measured after 24 hrs, after administration of 40 µg/ml ZnO nanoparticles of all the three sizes with and without M9 modification in presence and absence of 200 mJ/cm^2 UV-B rays. Data expressed as mean±SD, n=3. (p-value *** p <0.001, ** p<0.01, *p<0.05, ns=not significant)

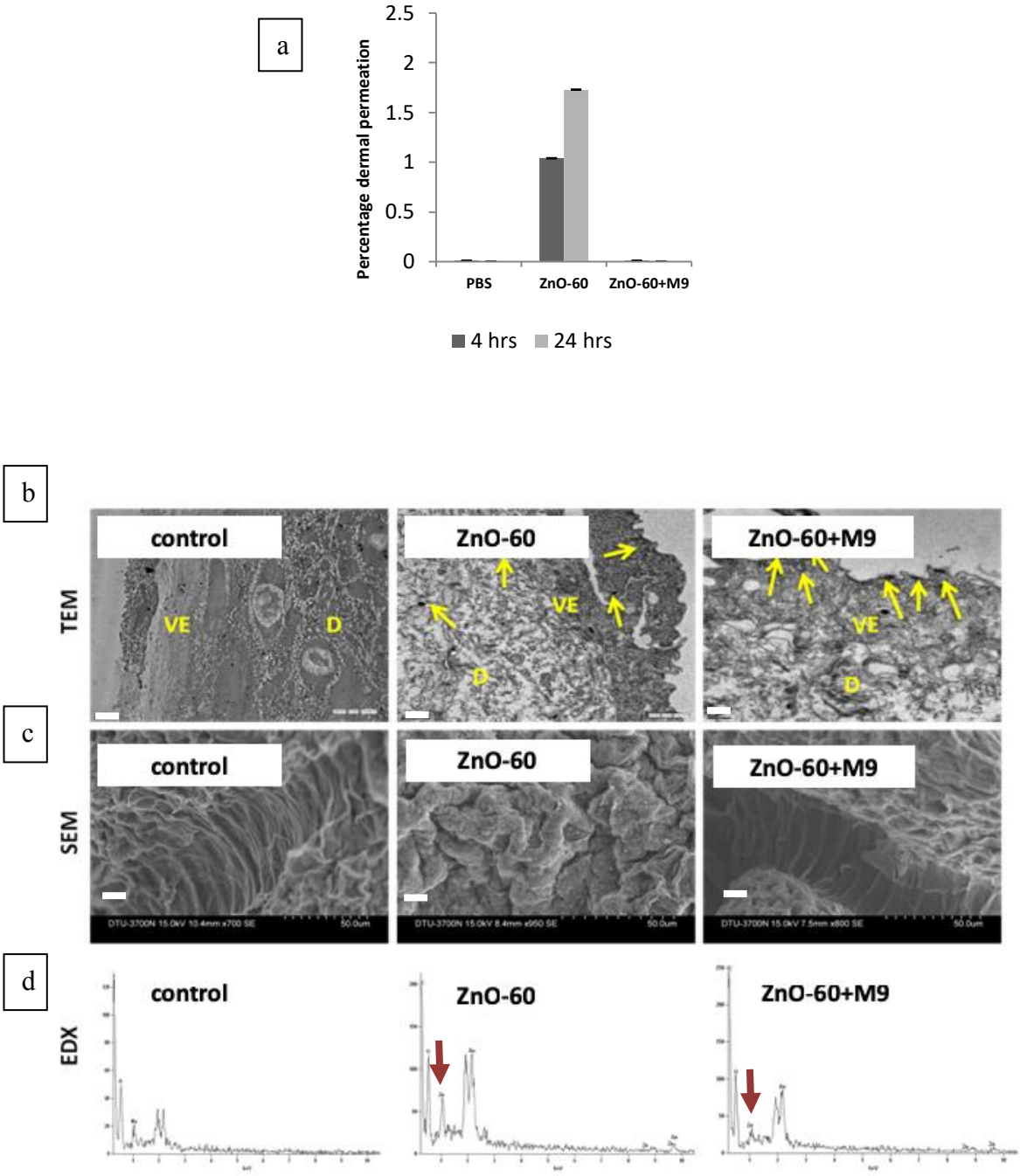
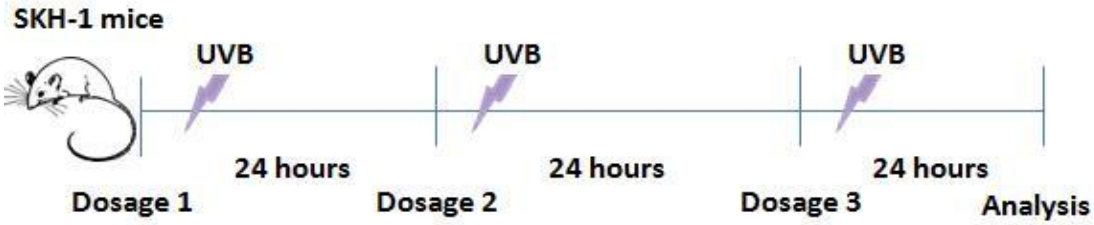
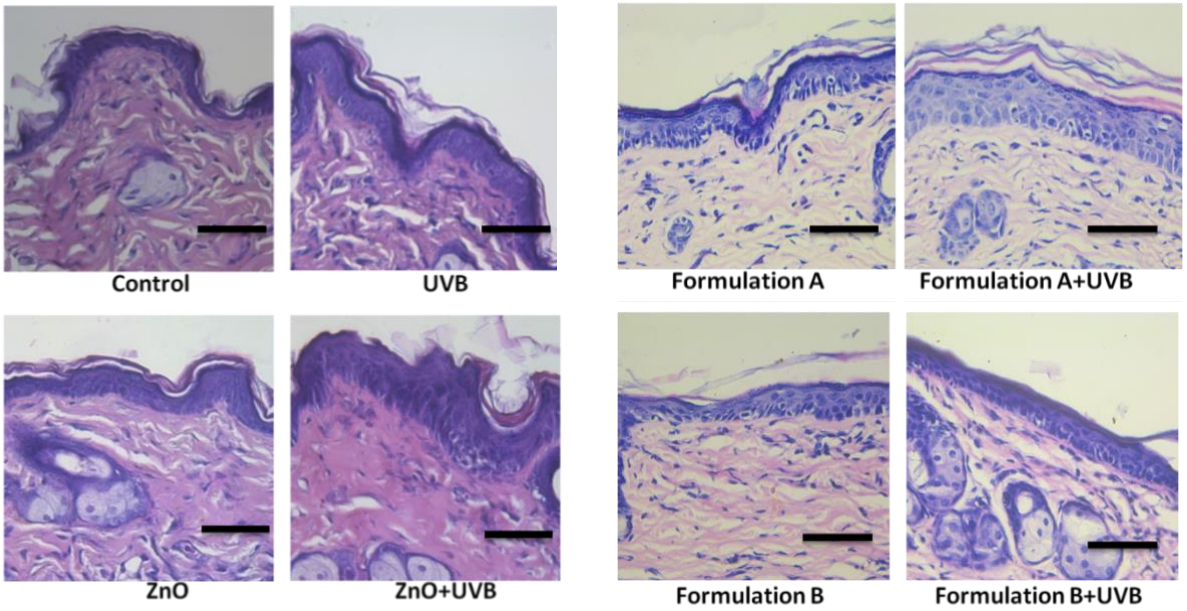


Figure 5: Ex-vivo penetration of M9 modified and unmodified ZnO nanoparticles a) Atomic Absorption Spectroscopy (AAS) showing the Zn penetrance on ZnO-60/ZnO-60+M9 administration across Strat-M membrane (expressed as percentage permeation). Bars are represented as an average of 3 readings and expressed as mean ± S.D, b) Transmission Electron Microscopy to check the localization of ZnO nanoparticles in human foreskin tissue, Scale bar=100 nm, Yellow arrows indicate presence of nanoparticles, c) and d) Scanning Electron Microscopy and elemental analysis of zinc to check the dermal localization of nanoparticles. Arrows represent Zn peak in the EDX patterns. Scale bar = 100 nm. Red arrows indicate elemental Zn abundance in the scanning electron microscopy window.

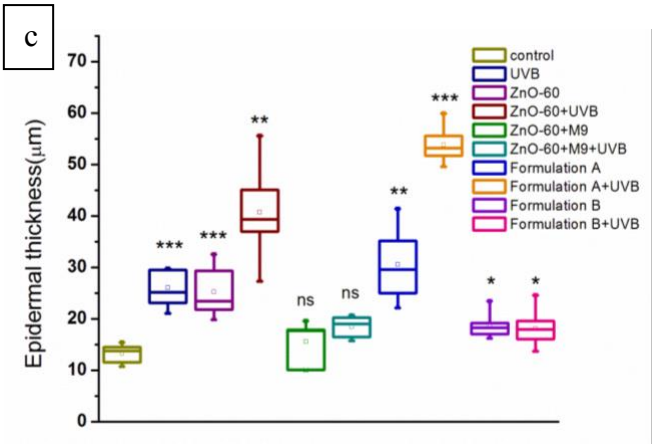
a


SKH-1 mice
UVB
UVB
UVB
24 hours
24 hours
24 hours
Dosage 1
Dosage 2
Dosage 3
Analysis

b


Control
UVB
Formulation A
Formulation A+UVB
ZnO
ZnO+UVB
Formulation B
Formulation B+UVB
ZnO+M9
ZnO+M9+UVB

c


Epidermal thickness(μm)
control
UVB
ZnO-60
ZnO-60+UVB
ZnO-60+M9
ZnO-60+M9+UVB
Formulation A
Formulation A+UVB
Formulation B
Formulation B+UVB
ns
ns

d

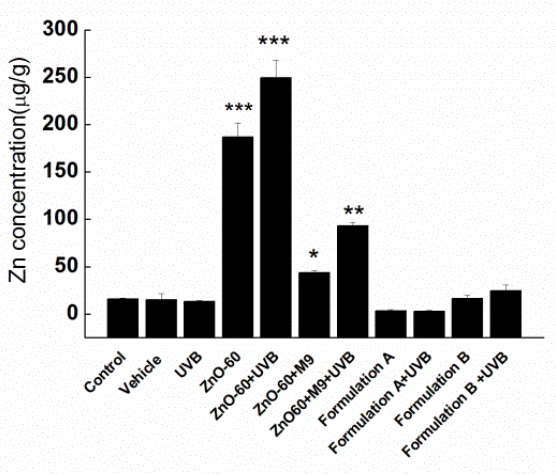

Zn concentration(μg/g)
Control
Vehicle
UVB
ZnO-60
ZnO-60+UVB
ZnO-60+M9
ZnO60+M9+UVB
Formulation A
Formulation A+UVB
Formulation B
Formulation B +UVB

Figure 6: *In-vivo* photoprotection and quantitation of Zn in the mice skin after administration of ZnO nanoparticles- a) Schematic representation of the study design for *in-vivo* ZnO-60 /ZnO-60+M9/Formulation treatment and UV-B exposure, b) Representative images of histopathological sections of SKH-1 mice skin after ZnO-60/ ZnO-60+M9/Formulation A/Formulation B pre-treatment and UV-B exposure. Scale bar = 5μm. c) Epidermal thickness of control and treatment group quantitated by ImageJ software and represented as an average of 5 readings, expressed as mean ± S.D. d) Atomic absorption spectroscopy (AAS) showing the Zn penetrance across full thickness SKH-1 mice skin on ZnO-60,ZnO-60+M9,Formulation A, Formulation B administration. Bars represent an average of 3 readings and are expressed as mean ± S.D. (p-value *** $p < 0.001$, ** $p < 0.01$, *$p < 0.05$, ns=not significant)

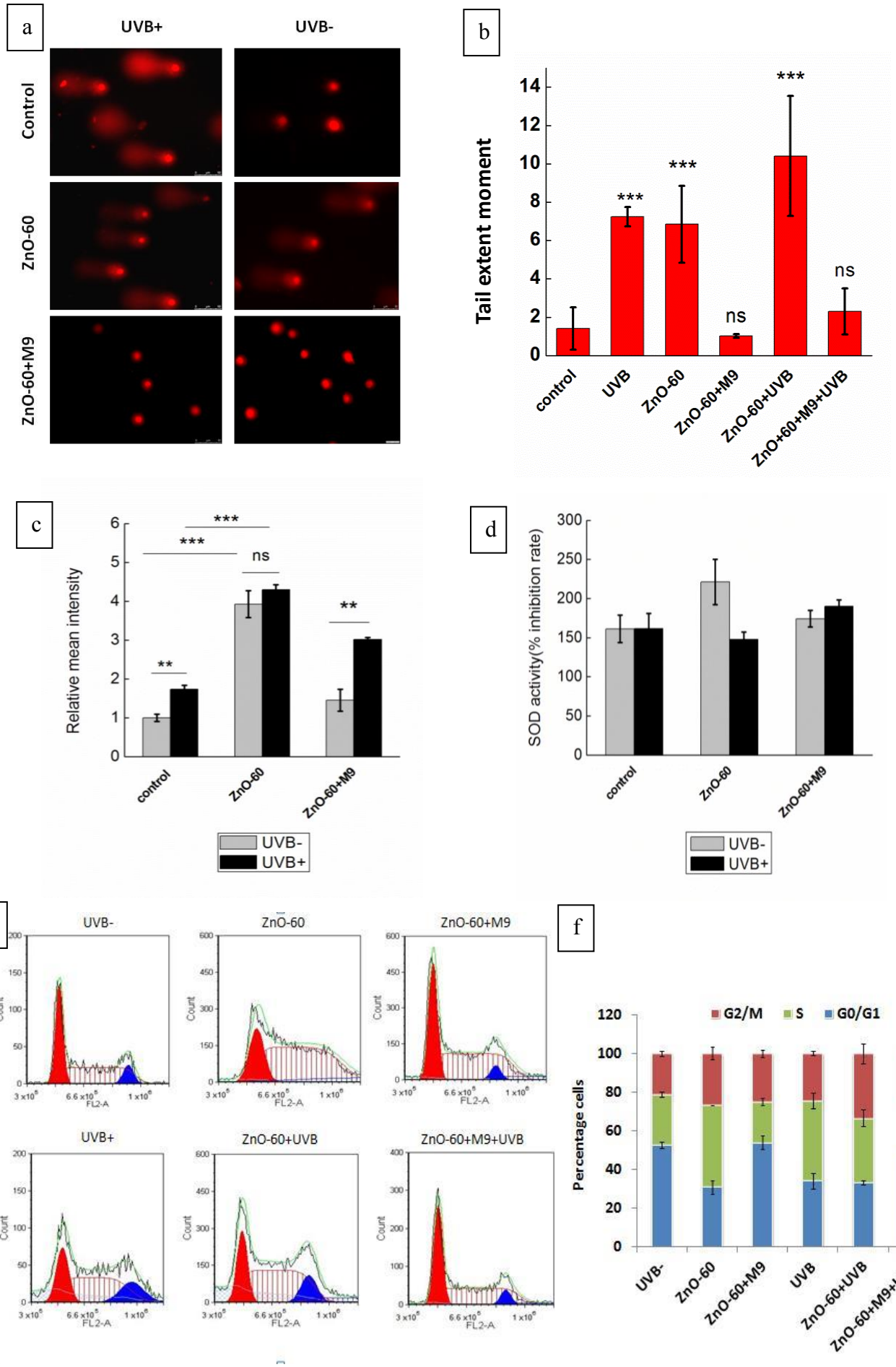

a
UVB+
UVB-
Control
ZnO-60
ZnO-60+M9
b
Tail extent moment
***
***
***
ns
ns
control
UVB
ZnO-60
ZnO-60+M9
ZnO-60+UVB
ZnO+60+M9+UVB
c
Relative mean intensity
***
***
ns
**
**
control
ZnO-60
ZnO-60+M9
UVB-
UVB+
d
SOD activity(% inhibition rate)
control
ZnO-60
ZnO-60+M9
UVB-
UVB+
e
UVB-
ZnO-60
ZnO-60+M9
UVB+
ZnO-60+UVB
ZnO-60+M9+UVB
Count
FL2-A
f
G2/M
S
G0/G1
Percentage cells
UVB-
ZnO-60
ZnO-60+M9
UVB
ZnO-60+UVB
ZnO-60+M9+UVB

Figure 7: *In-cellulo* photoprotection analysis- HaCaT cells ($30X10^3$ /well) were seeded in 24 well plates after 80% confluency was achieved, cells were incubated with 40 µg/ml concentration of ZnO-60/ ZnO-60+M9 and incubated for 4 hours. Cells were subsequently irradiated with 200 mJ/cm^2 UV-B rays. 24 hours after irradiation the following were measured. a) Representative images of Comet assay performed to understand DNA damage effects b) Tail extent moment was quantitated for 50 comets across (n=2) and represented as mean ± SD. c) ROS production was quantitated using CM-H_2DCFDA dye. Bars represent mean± SD, n=3 d) Superoxide dismutase levels (% inhibition rate) was quantitated using WST assay, bars represent mean± SD, n=3, e) Cell cycle distribution across G0/G1, G2/M and S phases for 10,000 cells was plotted using the Multicycle AV cell cycle program. f) Percentage cells in each phase was quantitated and bars represent mean± SD, n=3, (p-value *** $p < 0.001$, ** $p < 0.01$, *$p < 0.05$, ns=not significant)

TABLE OF CONTENTS (TOC):

